Energy, Environment, and Sustainability
Series Editor: Avinash Kumar Agarwal

Himanshu Tyagi
Prodyut R. Chakraborty
Satvasheel Powar
Avinash Kumar Agarwal *Editors*

Solar Energy

Systems, Challenges, and Opportunities

Springer

Energy, Environment, and Sustainability

Series Editor

Avinash Kumar Agarwal, Department of Mechanical Engineering, Indian Institute of Technology Kanpur, Kanpur, Uttar Pradesh, India

This books series publishes cutting edge monographs and professional books focused on all aspects of energy and environmental sustainability, especially as it relates to energy concerns. The Series is published in partnership with the International Society for Energy, Environment, and Sustainability. The books in these series are edited or authored by top researchers and professional across the globe. The series aims at publishing state-of-the-art research and development in areas including, but not limited to:

- Renewable Energy
- Alternative Fuels
- Engines and Locomotives
- Combustion and Propulsion
- Fossil Fuels
- Carbon Capture
- Control and Automation for Energy
- Environmental Pollution
- Waste Management
- Transportation Sustainability

More information about this series at http://www.springer.com/series/15901

Himanshu Tyagi · Prodyut R. Chakraborty ·
Satvasheel Powar · Avinash Kumar Agarwal
Editors

Solar Energy

Systems, Challenges, and Opportunities

Springer

Editors
Himanshu Tyagi
Department of Mechanical Engineering
Indian Institute of Technology Ropar
Rupnagar, India

Prodyut R. Chakraborty
Department of Mechanical Engineering
Indian Institute of Technology Jodhpur
Jodhpur, India

Satvasheel Powar
School of Engineering
Indian Institute of Technology Mandi
Mandi, India

Avinash Kumar Agarwal
Department of Mechanical Engineering
Indian Institute of Technology Kanpur
Kanpur, India

ISSN 2522-8366 ISSN 2522-8374 (electronic)
Energy, Environment, and Sustainability
ISBN 978-981-15-0674-1 ISBN 978-981-15-0675-8 (eBook)
https://doi.org/10.1007/978-981-15-0675-8

This Springer imprint is published by the registered company Springer Nature Singapore Pte Ltd.
The registered company address is: 152 Beach Road, #21-01/04 Gateway East, Singapore 189721, Singapore

Preface

Energy demand has been rising remarkably due to increasing population and urbanization. Global economy and society are significantly dependent on the energy availability because it touches every facet of human life and activities. Transportation and power generation are two major examples. Without the transportation by millions of personalized and mass transport vehicles and availability of 24×7 power, human civilization would not have reached contemporary living standards.

The International Society for Energy, Environment and Sustainability (ISEES) was founded at Indian Institute of Technology Kanpur (IIT Kanpur), India, in January 2014, with an aim to spread knowledge/awareness and catalyze research activities in the fields of energy, environment, sustainability, and combustion. The Society's goal is to contribute to the development of clean, affordable, and secure energy resources and a sustainable environment for the society and to spread knowledge in the above-mentioned areas and create awareness about the environmental challenges, which the world is facing today. The unique way adopted by the society was to break the conventional silos of specializations (engineering, science, environment, agriculture, biotechnology, materials, fuels, etc.) to tackle the problems related to energy, environment, and sustainability in a holistic manner. This is quite evident by the participation of experts from all fields to resolve these issues. The ISEES is involved in various activities such as conducting workshops, seminars, and conferences in the domains of its interests. The society also recognizes the outstanding works done by the young scientists and engineers for their contributions in these fields by conferring them awards under various categories.

Third International Conference on "Sustainable Energy and Environmental Challenges" (III-SEEC) was organized under the auspices of ISEES from December 18 to 21, 2018, at Indian Institute of Technology Roorkee. This conference provided a platform for discussions between eminent scientists and engineers from various countries including India, USA, Norway, Finland, Sweden, Malaysia, Austria, Hong Kong, Bangladesh, and Australia. In this conference, eminent speakers from all over the world presented their views related to different aspects of energy, combustion, emissions, and alternative energy resource for sustainable development and cleaner

environment. The conference presented five high-voltage plenary talks from globally renowned experts on topical themes, namely "The Evolution of Laser Ignition Over more than Four Decades" by Prof. Ernst Wintner, Technical University of Vienna, Austria; "Transition to Low Carbon Energy Mix for India" by Dr. Bharat Bhargava, ONGC Energy Center; "Energy Future of India" by Dr. Vijay Kumar Saraswat, Hon. Member (S&T) NITI Aayog, Government of India; "Air Quality Monitoring and Assessment in India" by Dr. Gurfan Beig, Safar; and "Managing Large Technical Institutions and Assessment Criterion for Talent Recruitment and Retention" by Prof. Ajit Chaturvedi, Director, IIT Roorkee.

The conference included 24 technical sessions on topics related to energy and environmental sustainability including 5 plenary talks, 27 keynote talks, and 15 invited talks from prominent scientists, in addition to 84 contributed talks and 50 poster presentations by students and researchers. The technical sessions in the conference included Advances in IC Engines, Solar Energy, Environmental Biotechnology, Combustion, Environmental Sustainability, Coal and Biomass Combustion/Gasification, Air and Water Pollution, Biomass to Fuels/Chemicals, Combustion/Gas Turbines/Fluid Flow/Sprays, Energy and Environmental Sustainability, Atomization and Sprays, Sustainable Transportation and Environmental Issues, New Concepts in Energy Conservation, and Waste to Wealth. One of the highlights of the conference was the Rapid-Fire Poster Sessions in (i) Engine/Fuels/Emissions, (ii) Renewable and Sustainable Energy, and (iii) Biotechnology, where 50 students participated with great enthusiasm and won many prizes in a fiercely competitive environment. 200+ participants and speakers attended this four-day conference, which also hosted Dr. Vijay Kumar Saraswat, Hon. Member (S&T) NITI Aayog, Government of India, as the chief guest for the book release ceremony, where 14 ISEES books published by Springer, Singapore, under a special dedicated series "Energy, environment and sustainability" were released. This was second time in a row that such significant and high-quality outcome has been achieved by any society in India. The conference concluded with a panel discussion on "Challenges, Opportunities and Directions for National Energy Security," where the panelists were Prof. Ernst Wintner, Technical University of Vienna; Prof. Vinod Garg, Central University of Punjab, Bhatinda; Prof. Avinash Kumar Agarwal, IIT Kanpur; and Dr. Michael Sauer, Boku University of Natural resources, Austria. The panel discussion was moderated by Prof. Ashok Pandey, Chairman, ISEES. This conference laid out the road map for technology development, opportunities and challenges in energy, environment, and sustainability domain. All these topics are very relevant to the country and the world in present context. We acknowledge the support received from various funding agencies and organizations for the successful conduct of the Third ISEES Conference (III-SEEC), where these books germinated. We would, therefore, like to acknowledge NIT Srinagar, Uttarakhand (TEQIP) (special thanks to Prof. S. Soni, Director, NIT, UK), SERB, Government of India (special thanks to Dr. Rajeev Sharma, Secretary); UP Bioenergy Development Board, Lucknow (special thanks to Sh. P. S. Ojha), CSIR, and our publishing partner Springer (special thanks to Swati Meherishi).

The editors would like to express their sincere gratitude to large number of authors from all over the world for submitting their high-quality work in a timely manner and revising it appropriately at a short notice. We would like express our special thanks to all the reviewers who reviewed various chapters of this monograph and provided their valuable suggestions to improve the manuscripts.

Rupnagar, India — Himanshu Tyagi
Jodhpur, India — Prodyut R. Chakraborty
Mandi, India — Satvasheel Powar
Kanpur, India — Avinash Kumar Agarwal

Contents

Editors and Contributors

About the Editors

Dr. Himanshu Tyagi is currently working as an Associate Professor in the School of Mechanical, Materials and Energy Engineering at IIT Ropar. He has previously worked at the Steam Turbine Design Division of Siemens (Germany and India) and at the Thermal and Fluids Core Competency Group of Intel Corp (USA). He received his Ph.D. from Arizona State University, in the field of heat transfer and specifically looked for the radiative and ignition properties of nanofluids. He and his co-workers proposed the concept of direct absorption solar collectors using nanofluids which won the Best Paper Award at the ASME Energy Sustainability Conference at Long Beach, CA. He obtained his master's degree from University of Windsor, Canada, and his bachelor's from IIT Delhi, in Mechanical Engineering. At present, he is working to develop nanotechnology-based clean and sustainable energy sources with a team of several Ph.D., postgraduate, and undergraduate students. Among other awards, he has received Summer Undergraduate Research Award (SURA) from IIT Delhi, International Graduate Student Scholarship from University of Windsor Canada, Indo-US Science and Technology Forum (IUSSTF) grant awarded for organizing an Indo-US Workshop on 'Recent Advances in Micro/Nanoscale Heat Transfer and Applications in Clean Energy Technologies' at IIT Ropar.

Dr. Prodyut R. Chakraborty is an Assistant Professor in the Mechanical Engineering, IIT Jodhpur since February 2013. He received his Bachelor degree of Mechanical Engineering from the North Bengal University in 2000, and his M.Sc Engineering in 2004, and PhD in 2011 both from the Department of Mechanical Engineering, Indian Institute of Science Bangalore. Prior to his joining at IIT Jodhpur, he worked for two years at the Department of Material Physics in Space in German Aerospace Center (DLR) Cologne as a postdoctoral research fellow. He also worked as a Research Analyst at the Applied CFD Lab, G.E. Global Research Centre Bangalore from 2004 to 2005. His primary area of research is numerical modeling of alloy solidification, latent heat based energy storage systems for high temperature applications, Thermal management and thermal comfort, and sorption cooling.

Dr. Satvasheel Powar is an Assistant Professor in the School of Engineering, IIT Mandi since June 2015. He received his Bachelors (Production Engineering) from Shivaji University in 2003, and Masters (Mechanical Engineering) from the Dalarna University, Sweden in 2005. He then worked with Greatcell Solar S.A., Switzerland, and G24i, the UK. He received his Ph.D. in Chemistry/Materials Engineering from the Monash University, Australia in 2013. Before joining at IIT Mandi, he worked for two and half years at the Nanyang Technological University, Singapore as a postdoctoral research fellow. His primary area of research is new generation solar photovoltaic and solar thermal utilization. He was recently awarded the Bhaskara Advanced Solar Energy fellowship by Indo-US Science and Technology Forum (IUSSTF) to visit Lawrence Berkeley National Laboratory, University of California, Berkeley, USA for three months.

Prof. Avinash Kumar Agarwal joined IIT Kanpur in 2001. He worked at the Engine Research Center, University of Wisconsin at Madison, USA as a Post-Doctoral Fellow (1999–2001). His interests are IC engines, combustion, alternate and conventional fuels, lubricating oil tribology, optical diagnostics, laser ignition, HCCI, emissions and particulate control, and large bore engines. Prof. Agarwal has published 270+ peer reviewed international journal and conference papers, 35 edited books, and 63 books chapters. He is an associate editor of ASME Journal of Energy Resources Technology, and has edited the Handbook of Combustion, Wiley VCH, Germany. Prof. Agarwal is a Fellow of SAE, ASME, NASI, Royal Society of Chemistry, ISEES, and INAE. He has been the recipient of several prestigious awards such as Clarivate Analytics India Citation Award-2017 in Engineering and Technology, NASI-Reliance Industries Platinum Jubilee Award-2012; INAE Silver Jubilee Young Engineer Award-2012; Dr. C. V. Raman Young Teachers Award: 2011; SAE Ralph R. Teetor Educational Award -2008; INSA Young Scientist Award-2007; UICT Young Scientist Award-2007; INAE Young Engineer Award-2005. Prof. Agarwal received Prestigious Shanti Swarup Bhatnagar Award-2016 in Engineering Sciences.

Contributors

Avinash Kumar Agarwal Department of Mechanical Engineering, Indian Institute of Technology Kanpur, Kanpur, Uttar Pradesh, India

Sana Fatima Ali Centre for Energy Studies, Indian Institute of Technology Delhi, New Delhi, India

Bhabajit Baruah Department of Mechanical Engineering, Girijananda Chowdhury Institute of Management and Technology, Guwahati, India

Anirban Bhattacharya School of Mechanical Sciences, IIT Bhubaneswar, Bhubaneswar, Odisha, India

Santosh B. Bopche Department of Mechanical Engineering, NIT Hamirpur, Hamirpur, India

Prodyut R. Chakraborty Department of Mechanical Engineering, Indian Institute of Technology Jodhpur, Jodhpur, Rajasthan, India

Laltu Chandra Department of Mechanical Engineering, IIT BHU, Varanasi, India

Rajesh Choudhary Lovely Professional University, Phagwara, Punjab, India

Ambesh Dixit Department of Physics, Indian Institute of Technology Jodhpur, Jodhpur, India

Kapil Garg School of Mechanical, Materials and Energy Engineering, Indian Institute of Technology Ropar, Rupnagar, Punjab, India

Shanal Shalindra Bandara Gunasekera Department of Chemistry, Faculty of Science, University of Peradeniya, Peradeniya, Sri Lanka

Samodha Subhashini Gunathilaka Department of Chemistry, Faculty of Science, University of Peradeniya, Peradeniya, Sri Lanka

Md. Amirul Islam Kyushu University Program for Leading Graduate School, Green Asia Education Center, IGSES, Kyushu University, Fukuoka, Japan;
International Institute for Carbon-Neutral Energy Research (WPI-I²CNER), Kyushu University, Fukuoka, Japan;
Department of Electronics and Telecommunication Engineering, Bangabandhu Sheikh Mujibur Rahman Science and Technology University, Gopalganj, Bangladesh

Kazuhide Ito Interdisciplinary Graduate School of Engineering Sciences, Kyushu University, Kasuga-shi, Fukuoka, Japan

S. C. Kaushik Centre for Energy Studies, Indian Institute of Technology Delhi, New Delhi, India

Vikrant Khullar Mechanical Engineering Department, Thapar Institute of Engineering and Technology Patiala, Patiala, Punjab, India

Ravindra Kumar Defence Laboratory, Jodhpur, India

Rohitash Kumar Defence Laboratory, Jodhpur, India;
Department of Physics, Indian Institute of Technology Jodhpur, Jodhpur, India

Janethri B. Liyanage Department of Chemistry, University of Peradeniya, Peradeniya, Sri Lanka

Amaresh Mishra School of Chemistry and Nano Research Centre, Sambalpur University, Sambalpur, India

Bobin Mondal Defence Laboratory, Jodhpur, India

Deepak Moudgil Mechanical Engineering Department, Thapar Institute of Engineering and Technology Patiala, Patiala, Punjab, India

Bandi Sai Mukesh Department of Mechanical Engineering, Indian Institute of Technology Jodhpur, Jodhpur, Rajasthan, India

Sudipto Mukhopadhyay Department of Mechanical Engineering, Indian Institute of Technology Jodhpur, Jodhpur, Rajasthan, India

Mahbubul Muttakin International Institute for Carbon-Neutral Energy Research (WPI-I²CNER), Kyushu University, Nishi-ku, Fukuoka, Japan;
Interdisciplinary Graduate School of Engineering Sciences, Kyushu University, Kasuga-shi, Fukuoka, Japan

Rakesh Nath Department of Mechanical Engineering, Girijananda Chowdhury Institute of Management and Technology, Guwahati, India

Ravi Teja Parella Department of Mechanical Engineering, Indian Institute of Technology Jodhpur, Jodhpur, Rajasthan, India

Sasanka Peiris Sri Lanka Institute of Nanotechnology, Homagama, Sri Lanka

Ishanie Rangeeka Perera Department of Chemistry, Faculty of Science, Postgraduate Institute of Science, University of Peradeniya, Peradeniya, Sri Lanka

Satvasheel Powar School of Engineering, Indian Institute of Technology Mandi, Mandi, Himachal Pradesh, India

Dibakar Rakshit Centre for Energy Studies, Indian Institute of Technology Delhi, New Delhi, India

R. J. K. U. Ranatunga Department of Chemistry, Faculty of Science, Postgraduate Institute of Chemistry, University of Peradeniya, Peradeniya, Sri Lanka

Bidyut Baran Saha Kyushu University Program for Leading Graduate School, Green Asia Education Center, IGSES, Kyushu University, Fukuoka, Japan;
International Institute for Carbon-Neutral Energy Research (WPI-I²CNER), Kyushu University, Fukuoka, Japan;
Mechanical Engineering Department, Kyushu University, Nishi-ku, Fukuoka, Japan

Satish Sangwan Department of Mechanical Engineering, Indian Institute of Technology Jodhpur, Jodhpur, Rajasthan, India

Rajat Saxena Centre for Energy Studies, Indian Institute of Technology Delhi, New Delhi, India

Naveen Sharma DVR & Dr. HS MIC College of Technology, Kanchikacherla, Andhra Pradesh, India

K. V. S. Teja School of Mechanical, Materials and Energy Engineering, Indian Institute of Technology Ropar, Rupnagar, Punjab, India

Himanshu Tyagi Department of Mechanical Engineering, School of Mechanical, Materials and Energy Engineering, Indian Institute of Technology Ropar, Rupnagar, Punjab, India

Sumita Vyas Defence Laboratory, Jodhpur, India

Part I
General

Chapter 1
Introduction to Solar Energy: Systems, Challenges, and Opportunities

Himanshu Tyagi, Prodyut R. Chakraborty, Satvasheel Powar and Avinash Kumar Agarwal

Abstract Solar energy-based technologies have seen remarkable development in the last decades. This is observed all across the world. The concerns related to cost and availability of fossil fuels, effects of climate change due to use of fossil fuels are the primary drivers behind the usages of these technologies. With such motivation, several research groups around the world are working in the field of solar energy. Since this field is quite diverse, it includes academicians of diverse background such as physics, chemistry, materials science, mechanical engineering, electrical engineering etc. This monograph is an effort to present the collection of such effort with an aim to present the developments at the system-level as well as the challenges and opportunities that are present at the technical level. It includes chapters covering the following themes—overview of energy usage in developing countries, solar thermal systems (heating and cooling), energy storage, and solar cells.

Keywords Solar energy · Energy storage · Heating · Cooling · Phase change materials · Solar cells · Sustainability

H. Tyagi (✉)
Department of Mechanical Engineering, Indian Institute of Technology Ropar, Rupnagar, Punjab 140001, India
e-mail: himanshu.tyagi@iitrpr.ac.in

P. R. Chakraborty
Department of Mechanical Engineering, Indian Institute of Technology Jodhpur, Jodhpur, Rajasthan 342037, India
e-mail: pchakraborty@iitj.ac.in

S. Powar
School of Engineering, Indian Institute of Technology Mandi, Mandi, Himachal Pradesh 175005, India

A. K. Agarwal
Department of Mechanical Engineering, Indian Institute of Technology Kanpur, Kanpur, Uttar Pradesh 208016, India

H. Tyagi et al. (eds.), *Solar Energy*, Energy, Environment, and Sustainability, https://doi.org/10.1007/978-981-15-0675-8_1

This chapter presents an outline of the whole monograph, along with collection of the abstract of each chapter. The whole monograph has been divided into five parts. Each part deals with a unifying theme. The monograph begins with Part I where the overall usage of energy is put into context, especially with a focus on the progress of developing countries (such as India, China, Brazil). It also includes chapters which highlight the usage of solar energy-based technologies in remote areas of India, and also the optimum usage of energy in buildings for thermal comfort. This part consists of four chapters (including this Introduction chapter). The abstracts of each of these chapters are as follows.

Chapter 2: Sustainable Development Goals calls for a substantial increase in the share of solar energy in the global energy mix, as well as for a more efficient use of energy. With the considerable cost of degradation in the environment at USD80 billion annually, which is equivalent to 5.7% of GDP in 2009, a major constraint in sustaining future economic growth could be the environment. In this present work, an attempt has been made to outline and focus on the goals set by BRICS countries with the aid of the major financial institutions and the socio economic groups for these five countries and the action plans taken as an initiative for the sustainable development of the energy sector at large and solar energy in specific. India is planning to increase the production of renewable energy by 40% within 2030 and in turn reduce emissions intensity by 33–35% over 2005 levels. China on the other hand intends to reduce emission intensity by 60–65% over 2005 levels by increasing its solar energy capacity from 43 GW at the end of 2015 to 127 GW by 2020. Russia's current emissions are around 40% lower than 1990 levels which are greater than the target set of 25–30% over 1990 levels. More emphasis is given in developing sustainable renewable green energy. Brazil is arguably in the best position to achieve its goals in renewable energy sphere, as in 2015, 74% of its energy came from renewable sources. South Africa has a very far way to go in the field of renewable energy as at present more than 90% of the energy are still generated from fossil fuels though the country has targets to commission another 17.8 GW of renewable energy capacity by 2020.

Chapter 3: The solar energy is available at free of cost and cleanest source of renewable type energy that can be utilized as a better substitute to the fossil fuel energy. These days lot of research is going on in extracting maximum possible heat energy from the solar irradiation. From solar systems practicability and remotely located societal upliftment point of view, it's a big challenge to erect and run continuously or effectively the solar energy systems in remotely located or hilly areas of Himachal Pradesh, India. This chapter discusses various applications of the solar concentrating collector technology that may help remotely located people get rid of their day to day problems e.g. water freezing, water pumping, cooking, drying of agricultural products, air conditioning etc. The challenges to be faced by the community people to meet household and agricultural demands and ways to get better the performance of solar-energy based systems along with opportunities for solar energy systems to meet the requirements of remotely located people are also discussed in this chapter.

Chapter 4: Energy efficiency and conservation measures in buildings are the focus in today's design and construction practices. One of the major reasons for energy

consumption in buildings is maintaining thermal comfort. Providing a thermally comfortable environment with an energy efficient design will not only lead to energy and cost savings, but will also have other intangible benefits, such as enhanced productivity, and health and well-being of the occupants. Studies have reported that buildings have 50–60% energy saving potential by means of an efficient design. This study aims at utilizing passive design strategies, such as provision of insulation and window glazing, to analyse their effects on thermal comfort of the occupants inside an office room. Measurements of indoor environmental quality parameters was done for the room, and Predicted Mean Vote and Percentage People Dissatisfied models, given in ASHRAE Standard 55, have been used in this study to assess the existing comfort levels of the occupants. A parametric study to examine their influence on the thermal environment using these models has been done using IDA ICE Beta 4.7 software. It was observed that application of the passive techniques although enhanced the thermal environment of the room, the comfort levels were still not within the ideal range specified by ASHRAE. The study concluded that more passive strategies can be employed to enhance the comfort levels. This would help in reducing the need for alternate methods of space conditioning, hence, leading to energy conservation.

The next part in this monograph, (Part II) consists of three chapters which deal with the heating aspects of solar thermal systems. It contains chapters which study the solar water heating system as well as solar air heaters. Moreover it contains a chapter highlighting the mathematical model of a solar updraft tower where a buoyancy driven-flow (heated by solar energy) drives turbine for power generation. The abstracts of each of these three chapters are as follows.

Chapter 5: Solar energy is a promising renewable source to support the growing energy demand. This energy is widely harnessed for solar water heating systems to provide hot water for both domestic and industrial sectors thus reducing use of conventional energy sources. In this work, a concentrated solar water heater (CSWH) system is designed and fabricated at IIT Jodhpur. The main objectives are development of a point focus based direct solar water heating system and preliminary experiment based evaluation of the designed system. The system envisages a flux concentration of 100 Suns, which will enable receiver area reduction and the use of other heat transfer fluids like oil in future. The CSWH system consists of (a) receiver and (b) parabolic dish with two-axis sun tracking provision. In the conventional solar water heater system the irradiance from sun is directly collected by the collector whereas in concentrated solar water heater the reflected irradiance is received by the receiver. The reflector consists of a reflecting surface mounted on a parabolic structure and the cavity receiver consists of consists of a serpentine copper tube exposed to concentrated irradiance. The receiver will be insulated from top in order to prevent heat loss from one of its surface. An optical model of parabolic dish and receiver has been developed using TracePro software. This model is used as reference to generate the flux density distribution. The experimental setup consists of a parabolic dish, a receiver with thermocouples, a Coriolis flow meter, pump, water tank and NI DAQ. Coriolis flow meter is used to measure the mass flow rate in the system. K-type thermocouples are attached on to the receiver and the temperature

is recorded using NI DAQ system. The theoretical geometric concentration ratio predicted is 115 but from the experiment a flux concentration ratio 94 is measured.

Chapter 6: To achieve maximum thermohydraulic performance, by maximizing the heat transfer and minimizing the pumping power, for a ribbed solar air heater, a Taguchi method has been used to predict the optimal set of design and flow parameters. An L_{16} (4^3) orthogonal array is selected as an investigational plan to perform the computational fluid dynamics (CFD) simulations for investigating the effect of design parameters, i.e. Reynolds number (4000–16,000), rib pitch to height ratio (3–12), and rib geometry due to change in inclination angle of front face of the rib ($\alpha = 45°$–$90°$) on the effectiveness of a solar air heater. Nusselt number, friction factor and thermohydraulic performance are considered as performance indexes, and the minimization of pumping power (minimum pressure drop) and the maximization of heat transfer and overall performance are taken as the optimization criteria. Results show that Reynolds number has the greatest influence on the heat transfer as well as thermohydraulic performance, while rib spacing on the friction factor ratio. The best combinations of design factors for heat transfer, pressure drop, and thermohydraulic performance are $A_4B_4C_1$, $A_4B_1C_1$, and $A_1B_4C_1$, respectively. Numerical results validate the aptness of the proposed methodology, so, this investigation suitably offers an improved rib design for internal fluid flow investigations related to effective heat transfer applications.

Chapter 7: Solar updraft tower power plant is a way to harness energy from the sun. It is a simple concept which requires low maintenance and utilises land that is already being used for growing plants, and generates power from it. A prototype plant was setup in Manzanares, Spain. Numerical analysis on power generation is performed for a similar plant assuming it is setup in Ropar. By considering losses via convection and radiation through the top surface of the collector, collector efficiency is calculated. Two cases arise here, 1. With 100% collector efficiency and 2. Collector efficiency is obtained after subtracting convection and radiation losses. The influx of solar radiation is highest in June. Hence, the variation of parameters like temperature, velocity, power output, efficiency with time of the day is done by taking averages for the month of June. Next the impact of physical parameters like chimney height, chimney radius and collector radius are studied on 21st June 11:00 to 12:00. How each parameter impacts the output of the plant is studied by creating a mathematical model of the power plant. Methods to improve the power output are discussed.

Part III of the monograph contain three chapters which discuss the possibilities of space cooling using non-conventional sources of energy, such as solar thermal powered adsorption cooling. The abstracts of each of these three chapters are as follows.

Chapter 8: Adsorption based cooling systems are gaining considerable attention since it can utilize low grade thermal energy, which otherwise could go as a waste. Heat sources possessing a temperature of as low as 60 °C can drive an adsorption chiller and that temperature requirement is even lower in the case of multi-stage adsorption cooling systems. A typical flat plate solar collector can provide hot water having a temperature of 65 °C in most of the countries in the Asian region. The temperature of evacuated tube collectors' water outlet can reach above 95 °C. In order

to make use of such collectors, in conjunction with other auxiliary heat sources, for providing heat to power an adsorption chiller, it is imperative to have a proper mathematical model. This can aid in designing the network and predicting the performance of the whole system, prior to installation. This chapter focuses on the modelling of a system that incorporates flat plate collectors, evacuated tube collectors and a thermally powered adsorption chiller. Here, mathematical equations to calculate the efficiency of flat plate and evacuated tube collectors are presented; processes that are involved in a typical two bed adsorption cooling system are explained in brief, and a mathematical model of an adsorption chiller, that employs mass and heat recovery schemes is developed. Finally, the simulation results of the model are presented, and the performance of the chiller is investigated to demonstrate a clear understanding of its operation.

Chapter 9: Conventional cooling and refrigeration systems already evolved to efficient design, have higher COP and compact size. However, the compressor part of such system consumes a tremendous amount of electricity and contribute indirectly to global warming. The working fluids of these systems are typically HFC or HFC blends which possess very high global warming potential. A significant percentage of working fluid is leaked from the high-pressure side of the system and directly contribute to global warming. The summation of indirect and direct warming impact, namely, total equivalent warming impact (TEWI) of the vapour compression cooling systems are significantly high. Adsorption cooling system (ACS) can resolve this critical issue. In ACS, the mechanical compressor of the traditional cooling system is replaced by a thermal compressor, namely, a pair of adsorption beds. Highly porous adsorbent material (silica gel, activated carbon, zeolite and so forth) is the key component of an adsorption bed. These materials have the capability to capture and hold certain types of fluid. This phenomenon is known as adsorption. Upon heating, the adsorbed fluid is liberated from the pores (desorption process) and gets thermally compressed. Solar thermal energy is the most prospective option for the desorption process to occur. Since there is no mechanical compressor, electricity consumption is deficient, which significantly minimizes the indirect warming impact. Moreover, natural or alternative refrigerants are used as the working fluid, which has zero/negligible GWP. Hence, the direct warming impact is also shallow. In this chapter, the working principle and governing equations of a solar energy driven adsorption cooling system will be elaborated. Besides, TEWI assessment procedure will be explained and compared for both vapour compression and adsorption cooling systems.

Chapter 10: The present study focuses on the thermodynamic analysis of zeolite-water and activated carbon-ethanol based adsorption cooling systems. The performance of the system depends critically on four operating temperatures namely maximum desorption temperature, minimum adsorption temperature, condensing temperature, and evaporating temperature and also on the ratio of specific heat of structural material and the specific heat of adsorbent. Dubinin-Astakhov equation is used to estimate the equilibrium uptake of working pairs. A comparative study is made between these working pairs for the air-conditioning applications.

The next part in this monograph, (Part IV) consists of four chapters which deal with the critical issue of energy storage. Phase change materials (PCM) can be used for the purpose of storing thermal energy. This allows the end-user to store energy for those periods where direct solar energy may not be available. Moreover PCMs can also be used to offset cooling loads for buildings in warmer climatic zones. The abstracts of each of these four chapters are as follows.

Chapter 11: Efficient storage of solar thermal energy has been a key research area in recent years. Among the various methods for energy storage, phase change material (PCM) based latent heat systems have shown a lot of promise due to their high energy storage densities and smaller system sizes. However, the low thermal conductivities of PCM pose a significant challenge in designing such systems, therefore, augmentation with suitable thermal conductivity enhancers becomes necessary to improve their energy charging and discharging performances. The use of metal foam structures embedded in PCM to form composite PCM-metal foam energy storage system can improve the effective thermal conductivity remarkably due to the high surface area for heat transfer between the metal foam and the PCM. This chapter presents a study of PCM-metal foam composite systems for solar energy storage. At first, a brief overview of the relevant thermal enhancement methods with particular emphasis on metal foam systems is presented. This is followed by the description of a typical PCM-metal foam composite system and the important parameters governing its energy storage performance. Different modelling approaches for such systems and their advantages and disadvantages are presented. The effect of important factors for metal foam-PCM composite systems are analyzed by performing pore-scale simulations. It is shown that factors such as metal foam porosity, pore size distribution, foam material, phase change material and overall system size contribute significantly towards the melting pattern and energy storage characteristics of these systems.

Chapter 12: In the present work, we propose thermal energy storage by direct photo-thermal energy conversion (referred to as optical charging) using nanoparticles laden phase change materials (PCMs). In the conventional thermal storage systems, the absorbed solar energy is indirectly transferred to the PCM (primarily through conduction and convection heat transfer mechanisms) and is subsequently stored in the form of latent heat of the PCM (referred to as thermal charging). Opposed to the conventional thermal storage strategies; optical charging involves direct interaction of the sunlight with the phase change material (radiation being the predominant heat transfer mechanism). Broad absorption-based nanoparticles (amorphous carbon) have been seeded into the pristine phase change material (paraffin wax) to enhance photo-thermal conversion efficiency. Particularly, we investigate the effect of adding nanoparticles to conventional PCMs during optical charging process. To understand the role of nanoparticles; samples of pristine paraffin wax and nano-PCMs [different concentrations of nanoparticles (0.05, 0.1, 0.2, 0.4, wt%) dispersed in the pristine paraffin wax] have been optically heated. Furthermore, optical charging has been compared with the conventional thermal charging process. As per the experimental observations, the optical charging scheme significantly improves the thermal charging rate (by more than 157%) at optimum nanoparticle concentration (0.2%, in the present study) as compared to conventional thermal charging.

Chapter 13: Buildings use more than 40% of the total power consumed in India. Therefore, implementing energy conservation within buildings is of prime concern. Utilization of passive design parameters, such as Phase Change Material (PCM) incorporation, for energy conservation in buildings is thus a lucrative option. Incorporating PCMs within elements result in lowering of heat gain and temperature within the building. A number of simulation and experimental studies on PCM incorporated buildings, have been carried out. The advancements made in last forty years in the field of PCMs and their utilization as Thermal Energy Storage (TES) medium for buildings have been reviewed and presented in this study. This study focuses on PCM incorporation which is sensitive to its properties and climatic parameters of the location. Thus, there is a need of benchmarking the PCM for their application in buildings. Focus is on buildings in tropical hot climatic conditions, where reduction in cooling load is a challenge. This study lays emphasis on using an appropriate PCM selection. Thus, phase change temperature forms and important criteria for PCM selection. Thermal conductivity, specific heat and latent heat are other properties which must be evaluated before PCM selection and implementation within buildings. The study also encompasses different methods of PCM incorporation being implemented across the world and have marked advantages and disadvantages of each followed by their impact in terms of energy savings.

Chapter 14: Metastable supercooled liquid phase change material (MSLPCM) is prepared by homogeneous mixing of sodium acetate trihydrate (SAT), water and ethylene glycol (EG) in 92:5:3 weight fractions, respectively. A stainless steel (SS-306) triggering disk of size 20 mm (L) × 18 mm (W) × 0.2 mm (T) is fabricated by engraving of grooves on SS disk for initiating nucleation in heat pack and release of heat at the time of requirement. The PCM heat pack containing 300 g PCM and a triggering disk is fabricated using high frequency PVC sealing machine. Thermal performance of identical PCM heat pack and water pack (300 g water) is carried out inside temperature history measuring setup at 0 °C ambient temperature. The temperature of PCM heat pack and water heat pack reduces from 70 to 30 °C in 210 and 48 min, respectively at 0 °C ambient temperature. The heating time of PCM heat pack is ~4.4 times compared to water heat packs.

The last part of this monograph, (Part V) consists of four chapters deal with the technological advancements in the field of solar cells. New types of solar cells (DSSC and OSC, which stand for 'Dye Sensitized Solar Cells' and 'Organic Solar Cells', respectively) have the potential to generated electricity at very low cost, however they require further improvements. The abstracts of each of these four chapters are as follows.

Chapter 15: Utilization of renewable sources can reduce the impact of increasing global energy demand on the rate of depletion of fossil fuels. One of the most studied and implemented routes to meet this energy demand is to harvest solar energy. Among solar-energy harvesting devices, dye-sensitized solar cells have been recognized as some of the cheapest and most environment friendly technologies, since they do not require high purity of starting materials or advanced fabrication techniques. A dye-sensitized solar cell is composed of a working electrode, in which the light

absorbing sensitizer is chemisorbed onto the surface of a wide bandgap semiconductor; a redox electrolyte, that is placed in between two electrodes and functions to regenerate the sensitizer; and a counter electrode, which is a catalyst which accelerates a redox reaction with the electrolyte. Titanium dioxide (anatase phase) is the most widely used semiconductor material in dye-sensitized solar cells due to its low cost, chemical stability and optical properties. In this chapter, the literature on optimizing TiO_2 as a semiconductor material for n-type DSCs is reviewed. The evolution of TiO_2 nanostructures and techniques such as doping, composite preparation and surface modification are elaborated on. These methods have enhanced both the chemical and physical properties of TiO_2 nanostructures. Moreover, despite good overall performance, rapid recombination kinetics are a major disadvantage inherent in TiO_2. Thus, research has been carried out to substitute TiO_2 with alternative semiconductor. In view of this, other potential competitors for photo-anode material are reviewed and assessed. Finally, the prospects of an ideal semiconductor material for dye-sensitized solar cells is discussed.

Chapter 16: The energy crisis is a global problem that drives investment on renewable energy sources worldwide. Utilization of solar energy has become an effective strategy for sustainable energy generation, as it has the potential to fill the energy gap created due to the depletion of fossil fuel. On the ever-extending ladder of solar harvesting technologies, third generation dye-sensitized solar cells (DSCs) have the advantages of better cost effectiveness and environmental footprint when compared to the first-generation silicon solar cells and second-generation thin film photovoltaics. The ultimate goal of constructing high-efficiency multi-junction devices has set the target of improving single junction components of DSCs (n- and p-type), separately. The pace of development of single junction p-DSCs has been much slower than that of n-DSCs. Discovery of suitable materials and techniques have lifted the performance of n-DSCs to more than 14% since it was first reported in 1991. On the other hand, p-DSCs have a maximum efficiency of 2.51%. It is important to bridge the gap between the efficiencies of these single junction configurations, in order to adopt the concept of multi-junction/tandem-DSCs that have the potential to reach higher efficiencies by harvesting a larger fraction of the solar spectrum. This chapter focuses on reviewing literature on development of p-DSCs. First, as an introduction, the structure, function and kinetics of p-DSCs are described. Next, the two main factors that affect the overall performance of a p-DSC; light harvesting capacity, and energy loss within the device, are comprehensively discussed.

Chapter 17: Dye-sensitized solar cells (DSCs) are third generation photovoltaic devices capable of harvesting solar energy to generate electricity. DSCs have gained significant research interest during past decades due to its high theoretical power conversion efficiencies and most importantly the cost effectiveness and environment friendly fabrication process. Firstly, in this chapter, the function of the counter electrode (CE) in a DSC has been discussed in brief. The CE participates in the electron transfer from the external circuit back to the redox mediator thereby catalyzing its regeneration reaction. In the state of art DSCs, Pt has been the preferred CE material. Properties such as promising conductivity and high electrocatalytic activity towards the process of reduction of I_3^- to I^- which is the typical redox

mediator, contributes to its applicability as the preferred CE material. However, the use of Pt CE adhere major drawbacks such as the high cost and its susceptibility to undergo corrosion. These limitations have emphasized the importance of exploring alternative cost effective functional materials with better conductivity and electrocatalytic properties. Subsequently, the limitations of using Pt as the CE materials, and the advantages and challenges associated with alternative materials have been elaborated. Conducting polymers with extended conjugate electron systems are a promising substitute material for Pt in DSCs. A wide range of conducting polymers and polymer hybrid composites have been investigated for their applicability as CEs in DSCs. These polymers have gained popularity not just due to cost effectiveness compared to Pt but also due to their promising conductivity, superior electrocatalytic properties, easy preparation and fabrication. Different types of conjugated polymers and polymer hybrid composites, their synthetic methods, fabrication processes and their respective photovoltaic performances are then reviewed. Finally, the future prospects of conducting polymers as CE material has been discussed.

Chapter 18: Organic solar cell (OSC) is one of the promising photovoltaic technology for next generation low-cost renewable energy sources. The power conversion efficiencies (PCE) of OSCs have reached above 14% in single-junction and ~17% in tandem OSCs. This rapid increase in the performance is mostly profited from the synergetic advances in rational molecular design, device processing and interfacial layer modifications. In addition to the development of efficient photoactive materials, interfacial design plays a crucial role in the improvement of device performance and stability. Most importantly, the interfacial layer is responsible for establishing good ohmic contact in the device, thus minimize the resistance, interfacial recombination and improve charge selectivity. In this chapter, we present the recent development in the electron and hole transporting interfacial materials design for both single-junction and tandem OSCs. Special attention will be paid to the design principles of interfacial materials which includes inorganic metal oxides, composite materials, oligomeric and polymeric molecules and their use as cathode and anode interlayer for high efficiency devices. The structure-property relationships of various interfacial materials will be analyzed as an approach towards high performance OSCs. Finally, we will discuss the current challenges with possible solutions and perspectives for performance enhancement in OSCs.

The lists of specific topics included in this monograph are as follows:

- Sustainable Development Goals in context to BRICS Countries
- Installations of Solar Systems in Remote Areas of Himachal Pradesh, India: Challenges and Opportunities
- Utilising Passive Design Strategies for Analysing Thermal Comfort Levels inside an Office Room using PMV-PPD Models
- Design and Development of a Concentrated Solar Water Heating System
- Multi-objective Performance Optimization of a Ribbed Solar Air Heater
- Mathematical Modelling of Solar Updraft Tower
- Solar Thermal-Powered Adsorption Chiller
- TEWI Assessment of Conventional and Solar Powered Cooling Systems

- Thermodynamic Analysis of Activated Carbon-Ethanol and Zeolite-water Based Adsorption Cooling Systems
- PCM-Metal Foam Composite Systems for Solar Energy Storage
- Direct Photo-Thermal Energy Storage Using Nanoparticles Laden Phase Change Materials
- Review on PCM application for cooling load reduction in Indian buildings
- Fabrication and thermal performance evaluation of Metastable supercooled liquid PCM based Heat pack
- Yet to be Challenged: TiO_2 as the Photo-anode Material in Dye-sensitized Solar Cells
- p-type Dye Sensitized Solar Cells: An Overview of Factors Limiting Efficiency
- Conducting Polymers as Cost Effective Counter Electrode Material in Dye-sensitized Solar Cells
- Interfacial Materials for Organic Solar Cells.

In this monograph the various chapters are arranged into five different parts: (i) General, (ii) Solar Thermal Systems: Heating, (iii) Solar Thermal Systems: Cooling, (iv) Energy Storage, and (v) Solar Cells.

Chapter 2
Sustainable Development Goals in Context to BRICS Countries

Bhabajit Baruah and Rakesh Nath

Abstract Sustainable Development Goals calls for a substantial increase in the share of solar energy in the global energy mix, as well as for a more efficient use of energy. With the considerable cost of degradation in the environment at USD80 billion annually, which is equivalent to 5.7% of GDP in 2009, a major constraint in sustaining future economic growth could be the environment (Griffith-Jones in A BRICS development bank: a dream coming true? (No. 215), 2014). In this present work, an attempt has been made to outline and focus on the goals set by BRICS countries with the aid of the major financial institutions and the socio economic groups for these five countries and the action plans taken as an initiative for the sustainable development of the energy sector at large and solar energy in specific. India is planning to increase the production of renewable energy by 40% within 2030 and in turn reduce emissions intensity by 33–35% over 2005 levels (Schmidt and Sewerin in Nat Energy 2(6):17084, 2017). China on the other hand intends to reduce emission intensity by 60–65% over 2005 levels by increasing its solar energy capacity from 43GW at the end of 2015 to 127GW by 2020. Russia's current emissions are around 40% lower than 1990 levels which are greater than the target set of 25–30% over 1990 levels. More emphasis is given in developing sustainable renewable green energy. Brazil is arguably in the best position to achieve its goals in renewable energy sphere, as in 2015, 74% of its energy came from renewable sources (Schmidt and Sewerin in Nat Energy 2(6):17084, 2017). South Africa has a very far way to go in the field of renewable energy as at present more than 90% of the energy are still generated from fossil fuels though the country has targets to commission another 17.8 GW of renewable energy capacity by 2020.

Keywords Smart grid · Renewable energy · Solar photovoltaic · Sustainable energy

B. Baruah (✉) · R. Nath
Department of Mechanical Engineering, Girijananda Chowdhury Institute of Management and Technology, Guwahati 781017, India
e-mail: bhabajit_me@gimt-guwahati.ac.in

H. Tyagi et al. (eds.), *Solar Energy*, Energy, Environment, and Sustainability, https://doi.org/10.1007/978-981-15-0675-8_2

List of Symbols

GDP	Gross domestic product
USD	United States dollar
BRICS	Acronym for Brazil, Russia, India, China and South Africa
GW	Giga watt
MW	Mega watt
NDB	New Development Bank
SE for All	Sustainable energy for All
SDG	Sustainable development goals
HIO	High impact opportunities
PV	Photovoltaic
kWh	Kilowatt hour
IEEFA	Institute for energy economics and financial analysis
NOx	Nitrogen oxide
SO_2	Sulphur dioxide
PFF	Project financing facility
EDB	Eurasian Development Bank
CO_2	Carbon dioxide
T&D	Transmission and distribution
IRP	Integrated resource plan
RE	Renewable energy

2.1 Introduction

2.1.1 Economic Analysis

Sustainable Development Goals calls for a substantial increase in the field of renewable sources i.e. solar, wind, geothermal and hydropower in the global energy mix, as well as for more efficient use of energy. With the considerable cost of degradation in the environment at USD 80 billion annually, which is equivalent to 5.7% of GDP in 2009, a major constraint in sustaining future economic growth could be the environment (Griffith-Jones 2014). It is worthy to note that, it might be practically impossible or too expensive to clean up later. Certain model simulations indicate that policy interventions such as taxes in the environment could be used to render positive environmental and health benefits with minimum economic costs (Griffith-Jones 2014). In this context, BRICS energy ministers are committed to:

- Emphasizing for the use of natural resources;
- Reducing the use of fossil fuels by promoting energy efficient technologies;
- Strengthening energy security cooperation with the aid of joint research on strategic reserves, energy efficiency and renewable energy;

- Seeking investment opportunities for the New Development Bank (NDB) in the fields of energy efficiency and renewable energy.

Several initiatives were set up to pursue these goals. In 2017, countries launched an Energy Research Cooperation Platform to support their work on energy efficiency and energy more widely. Its purpose is to conduct research and analysis, contribute to implementing BRICS investment projects in the energy sector, develop cooperation on energy technology, and improve training for personnel in BRICS countries. The platform is supported by two additional initiatives: the BRICS Network University and the BRICS Think Tank Council. To mobilize investments, Energy and Green Economy Working Group was established to encourage public-private partnerships for energy-efficient technologies. The Working Group is part of the BRICS Business Council, which was created in 2013 with a vision to strengthen and promote business, trade, and investment amongst the BRICS business communities.

In 2014, the BRICS forum set up the New Development Bank to assist fund infrastructure in the BRICS countries. One of the key objectives of the NDB's job is to lay energy targets for the BRICS countries to provide reliable and sustainable investment for the BRICS countries to build their independent renewable energy capacity (Council 2015). The targets laid down by the NDB triggered the BRICS countries to develop plans and execute new and existing renewable capacity. In this regard to achieve these goals, the bank offer loans quickly and flexibly to the BRICS countries. It's a great step towards sustainability in the energy field. And these concerns of BRICS counties can lead to better cooperation between them in the future.

Though the NDB has brought remarkable advances in the field of renewable capacity for the BRICS countries, some of them have been seen to miss their targets. Thereby demand has been placed for the NDB and other multilateral development banks and financial institutions to increase investment such that the BRICS could have a massive impact on the environmental damage currently being created by their energy systems (Council 2015). One of the most perspective and rapidly developing fields in renewable energy is the Smart grid communications market. It has been predicted that the Smart grid communications market would reach USD 9.5 billion by 2020 among the BRICS countries (News on Renewable 2019). The market is expected to grow rapidly over the next eight years which would be followed by three distinct phases. In the first phase, a two-way communication system would be established between utilities and subscribers by the deployment of smart meters. That would be followed by the incorporation of the new sensors and other devices at prime junctures of the network. This would help the utilities to develop value-added services to aid their smart grid infrastructure (News on Renewable 2019; Trindade et al. 2017). The final phase would comprise of the development of new services and software for the optimization of smart meter establishment and overall grid.

2.2 BRICS: Role of India

The Sustainable Energy for All (SEforALL) report on India reflects that the Government has launched numerous schemes for its cities and villages to transform to meet the Sustainable Development Goals (SDGs) for energy. As per the report, over 300 million Indians in rural areas are having no power connections. The government of India had set a target for universal household electrification within December 2018. The report also identifies short, medium and long term High Impact Opportunities (HIO's) which would support sustainable energy for all sectors. Some of the HIO's include renewable energy sources, storage facilities of these energies and implementation of smart grids, solar energy efficient pumps for agriculture, etc.

India, being one of the fastest growing countries in the field of renewable energy, is planning to increase the production of renewable energy by 40% within 2030 (Chu and Majumdar 2012). This would increase the capacity of renewable energy to 175 GW. The incorporation of such huge capacity in the field of renewable energy would, in turn, reduce emissions intensity by 33–35% over 2005 levels (Solar Power in India 2019). To reach this rather ambitious aim India undertakes the following steps:

In June 2018, Siemens Gamesa, Renewable solution provider, addressed that it has bagged an order in the field of Wind Energy from India's largest renewable energy Independent Power Producer, Re New Power, for the construction of a 150 MW wind farm located in the Kutch district of Gujarat. Since 2009, Siemens Gamesa has installed over 5 GW of renewable energy in various parts of the country. One of the fastest developing energy sectors in India is Solar Energy. The Government of India had a target to increase the capacity by 20 GW by the year 2022. According to the report by the Indian Government, this target was fulfilled way before four years than the stipulated time and as of 31 March 2019; the country's solar installed capacity already reached 28.18 GW. With the increasing capture of the market by the solar sector, this target was raised to 100 GW of solar capacity by 2022 of which 40 GW was the target set for rooftop solar (News on Renewable 2019). The budget set for the total investment was USD100 billion. Following the target set, 3 GW of solar capacity was commissioned in 2015–2016, 5 GW in 2016–2017 and over 10 GW in 2017–2018 which bought down the price of solar electricity by 18% below the price of the electricity produced by coal (Solar Power in India 2019).

In addition to its solar photovoltaic (PV) large scale grid connection, India is expanding its off-grid solar energy local urban and rural energy needs. The rapid growth of solar energy has reduced drastically the use of kerosene in rural areas. Developer Azure Power has commissioned its largest solar-power project in the Indian state of Punjab, with a capacity of 150 MW (Goswami and Zhao 2009). The project occupies 713 acres of land and will cater to the power requirements of the local community while generating an estimated 1000 jobs within the community. The new plant constitutes a portfolio of three projects each with a capacity of 50 MW. The company noted that the weighted average tariff on these projects is INR 5.63 (USD0.083) per kWh and Azure Power will supply Punjab State Power Corporation

for 25 years. Achieving these impressive targets, additional funding was required. In this regard, Canara Bank came forward to finance renewable energy projects through Canara Renewable Energy Financing Scheme. The objective of the scheme was similar to that of the New Development Bank's (NDB) to provide green financing and increase the rate of renewable energy development. The loans provided for the infrastructural development of the renewable energy sector by NDB would be on-lent through Canara Bank to the renewable energy sub-projects that primarily include solar, wind, biomass, geothermal, small hydropower, waste-to-energy, and other projects. This will, in turn, mobilize long term financing to renewable energy projects. Canara Renewable Energy Financing Scheme is estimated to have an overall capacity of USD 500 million (New Development Bank 2019).

2.3 BRICS: Role of China

China's target to reduce emission intensity by 60–65% over 2005 levels (News on Renewable 2019) makes it even greater than any other country, according to the IEEFA report. China has targeted increasing its solar capacity from 43 GW at the end of 2015 to 127 GW by 2020, and wind capacity to 250 GW by 2020 from 145 GW in 2015. Since the forecasting of China's development of renewable energy is rather high, the issue of financing the majority of the deal is also significantly important which makes it unavoidable to turn to the NDB that is currently engaged in three big energy ventures in China. China follows its age-old tradition of driving the agenda forward, as the country edges closer to a more sustainable pattern of growth (Liu et al. 2010). China's desire for a significant rise in renewable energy in the energy mix market makes China's aim to increase the use of renewables to 15% of its energy consumption by 2020. By 2020, China should be declared as a nation of 50 GW solar powers as addressed by the National Energy Administration. In this context, roof-top solar power technology was designed and supported by the Lingang Distributed Solar Power Project. The project with the aid of the NDB has accelerated green financing and promotes clean energy (New Development Bank 2019).

The prime objective of this project is to promote roof-top solar energy by incorporating solar photovoltaic power technology for the generation of electricity in Shang-hai Lingang Industrial Area and reduce carbon emission. The project aims to generate electricity through 100 MW roof-top solar photovoltaic powers by reducing 73,000 tons of carbon emission every year. The project also aids in saving the cost of losses in potential transmission by importing energy from places outside Shanghai. Subsequently, the project has been divided into many sub-projects to be implemented within 3 years until the end of 2019. To prove the concept, an onsite 3 MW pilot project has already been implemented successfully. The agreement has been made and the state grid would procure the electricity generated from the roof-top by solar photovoltaic power technology. The project aligns with the NDB's focus to support projects that aim at developing renewable energy sources. The project also estimates to reduce carbon dioxide emissions by approximately 73,000 tons per year and NOx

emissions by 1300 tons per year. The project will meet the desire need of saving gas consumption by 23,000 tons per year and coal consumption by about 32,000 tons per year (New Development Bank 2019).

Putian Pinghai Bay Offshore Wind Power Project is the second major initiative of the Government of China to increase offshore wind power capacity and provides sufficient electricity supply to Fujian and to stimulate the development of offshore wind energy with technological advances. Its focus aligns with NDB to offer financial support to projects aiming at developing renewable energy sources. The NDB will also provide financial support to the cost incurred for the procurement of equipment and other civil works. The project has been estimated to provide an effective electricity generation of 3490 h per year. Apart from providing electricity of 873 million kWh per year to meet the increasing demand for power consumption in Fujian, the capacity would also have a total targeted capacity of 700 MW offshore wind power (New Development Bank 2019). The increasing demand for offshore wind power would help China to sustain a greener and healthier environment and thus reducing carbon emissions with a target of avoiding 869,900 tons of carbon emissions per year. Meanwhile, the project also estimates the elimination of harmful components of emissions such as 26,175 tons of SO_2, 13,090 tons of NOx, and 237,300 tons of flue gas. It would also avoid the consumption of coal by 314,100 tons. With a vision to create employment opportunities and help the local economy to grow, a new industrial cluster has been initiated keeping in mind the socio-economic aspects of the society.

The third project, the Jiangxi Industrial Low Carbon Restructuring and Green Development Pilot Project aims at upgrading the traditional industries to achieve energy conservation and reduce emissions. Financial assistance would be provided to the Project by NDB through a Project Financing Facility (PFF) loan of up to USD 200 million. The Project comprises lengthy sub-projects, which as a whole will promote conservation of energy, regeneration of waste and emission of pollutants will be reduced. It will also promote the reutilization of industrial water in the Jiangxi Province.

The approved subprojects will acknowledge the contribution to an energy saving level of 95,118 tons of coal equivalents per annum and a carbon emission reduction of 263,476 tons per annum on an aggregate level, through increased recycling ratios, upgraded factory machinery, increased utilization of heat waste and improved energy conservation.

2.4 BRICS: Role of Russia

Russia's advancement amongst other BRICS nations is slightly above par as it has already met the expectations defined in its annual forum. The goal was to reduce emissions over 1990 levels by 25–30%, and Russia's emissions are around 40% lower than 1990 levels currently. However, by the end of 2020, the country is planning a production hike of 4.5% in the amount of renewable energy. The progress is

predominantly sluggish as compared to what has already been predicted due to the lack of investment from the country itself. It has allocated a share of USD 1billion for renewable technologies in all 17 Russian states in 2014 (Cherepovitsyn and Tcvetkov 2017).

Russia accounts for untapped renewable resources of energy. The non-fossil fuel based energy of Russia contributes to only 3% of the total primary energy consumption of the country (Kutsenko 2015). Karelia, a federal subject of Russia, has a low capacity of energy generation. It is still not sufficient as it imports power from other regions of Russia. Hence, the Nord-Hydro model project is designed for the enhancement in the capacity of power generation in the region and to facilitate the development of renewable energy. The project in alignment with the New Development Bank has accelerated green financing and promotes clean energy development. Two loans will be provided by the NDB in order to support the Eurasian Development Bank (EDB) and International Investment Bank for renewable energy projects. The loans will accelerate the business scenario of the Nord-Hydro project to increase the supply of energy through the renewable energy source in the Karelia region. The Russian government supports the project with a preferential tariff. This project initiates the construction of a small dam and two hydroelectric, providing an installed capacity of 49.8 MW in total. As much as 48,000 tons of carbon dioxide emissions per year will be avoided with the proposed power generation.

Meanwhile, a rather challenging project is being developed in the Russian Federation Territory. The project is designed in January 2015 to run smart grids in Ufa which slated to continue till 2019 as was planned. Concerning the expectation, after the smart grids are deployed, the Bashkiria project implementation will raise the region's power supply to a whole new qualitative level without a surge in the investment planned. It is further expected to reduce power losses in Ufa by a factor of two which in money terms would translate to 400 million rubles annually (Cherepovitsyn and Tcvetkov 2017). The experience is extensive and can be replicated in any region where the power grid infrastructure properties are the same as Russia's. The prospects of exporting this technology are significant.

2.5 BRICS: Role of Brazil

Brazil, the energy surplus country, is undoubtedly in a comfortable position to achieve its goals in the renewable energy horizon. In 2015, about 74% of the total energy generated came from renewable sources. Brazil has been one of the largest nations since 2007, contracting renewable energy through auction bidding. A pool of sophisticated and new technologies has been adopted at regular intervals by the auction bidding mechanism (La Rovere et al. 2011).

According to the IEEFA's report, "Brazil's 2024 Energy Plan envisages an increase in total installed renewable capacity, including large hydropower, from 106.4 GW in 2014 to 173.6 GW in 2024." But the current political situation prevents the development of this field. With the declined GDP growth, the country had to witness a

major drop in electric power load projections. It has been predicted that the demand in energy load would reduce to an extent of 3480 MW in 2019 which can be reflected by the fall in electricity consumption by 0.9% in 2016. The dip in electricity consumption sends negative feedback to the industries. In December 2016, the solar and wind energy auction was canceled which seemed to shake the confidence of the investors as 1260 projects were registered for the auction out of which 841 numbers were under wind energy and 419 numbers were under solar photovoltaic (PV), totaling to 35,147 MW of installed capacity (New Development Bank 2019). The cancellation decision by the government brought doubt on the minds of investor's on the intention of the government to support energy projects which were going well forward. Since that was the only tender in the year for renewable energy, its cancellation brought a halt in the process of commissioning wind and solar capacity for that year. The investors felt that this decision rather would bring a long-term impact on renewable energy investment in the country and hence slowing down the investment process in that sector.

The New Development Bank hasn't financed any renewable energy project in Brazil since 2017 which also illustrates the complicities in the renewable energy field. With the growing pace, Brazil is expected to have a jump of 44% in solar installed capacity in 2019, which would enhance the solar capacity by another 3.3 GW. With an expected demand in electricity consumption between 2018 and 2022 at an average of 3.8% annually, the need for further investment in infrastructure in the renewable energy sector becomes more prominent (New Development Bank 2019).

Brazil has been a great supporter and promoter of renewable energy for years. But due to the inadequate infrastructure in transmission lines, several projects have been delayed. This made the Brazilian Government set prior conditions for the investors to have secure transmission lines before participation in the auctions. This would not only reduce the problem of delays due to insufficient transmission infrastructure but would also accelerate to drive the market for T&D equipment.

2.6 BRICS: Role of South Africa

The most developed economy in Sub-Saharan Africa is the Republic of South Africa, yet the slow growth is the strong headwinds the country is facing at present. Frequent disruption in the electricity seems to complicate and bring challenges for the economic growth of the country (Conway et al. 2015). Moreover, the grid facilities also need up gradation as they are outdated. As per the National Treasury of South Africa, if the issue of electricity shortage is well addressed, then GDP growth is expected to increase by 2% roughly. Therefore it has become a major matter of concern for the government to secure energy supply and develop renewable energy (Martin 2017).

As per the national commitment for the transition from high carbon to low carbon economy, IRP was formulated to set an ambitious target of 17 800 MW of renewable energy in 2010 to be achieved by 2030 (Wentworth 2014). About 5000 MW of renewable energy was planned to be operational by 2019 within this frame time of 20 years.

This would be followed by another 2000 MW of RE by 2020. Ministerial Determinations are entrusted for the proper implementation of the IRP 2010 that is being regulated by Act No. 4 of Electricity Regulations, 2006 (Kok 2014). It is through the bidding windows that the country has procured 6 422 MW of electricity from 112 Renewable Energy Independent Power Producers in 2017. By the end of June 2017, a total of 3 162 MW of electricity generation capacity was already connected to the national electricity grid. In this regard, the NDB's PFF supported the infrastructural development of the grid connection. With such an objective, NDB would provide a PFF loan to Eskom Holdings State Owned Company Limited of USD180 million. This would, in turn, reduce the dependency of the country on fossil fuels and thus would aid towards the sustainable development of energy and increasing electricity supply. Considering the volume of projects to be funded, the PFF has been divided into sub-projects. Currently, the sub-projects under commissioning include infrastructural development of expedited independent power producer project for Upington, the establishment of substation and transmission lines for Soweto area and Ankerlig-Sterrekus (Martin 2017). With the approval and selection criteria from NDB, future sub-projects would be proposed to ensure the overall development objective of the project.

Through the implementation of the project, Eskom is expected to generate a total of 670 MW of RE to the grid. This would meet 10% of the national target for RE capacity from 2020 to 202 (Solar Power in India 2019). Once the transmission lines are developed to meet the demand for electricity, prospects in the development of RE could be established.

It is to be noteworthy that out of all the BRICS countries, South Africa has a very far way to go in the field of renewable energy as at present more than 90% of the energy are still generated from fossil fuels through the country has targets to commission another 17.8 GW of renewable energy capacity by 2020 (Solar Power in India 2019).

2.7 Conclusion

In the context of the BRICS countries based on their geographic advantages shown by the perceptible economic growth in the early 21st century, the current piece of work tries to analyze the possibility of the BRICS countries for sustainable development and discussed the necessary conditions to be fulfilled. Every effort should be made to focus on the proper utilization of their abundant potential natural resources, land and population by effective technological advancement to encourage sustainable development. India, China, and South Africa being the energy deficit countries, has a great role to play in the field of solar renewable energy to overcome the shortage of energy in the context of the global energy mix. On the other hand, Brazil and Russia being the energy surplus countries could utilize the excess form of renewable energy in exporting to the other nations to meet the demand for energy in the global energy mix.

References

Cherepovitsyn A, Tcvetkov P (2017) Overview of the prospects for developing a renewable energy in Russia. In: 2017 International conference on green energy and applications (ICGEA). IEEE, pp 113–117

Chu S, Majumdar A (2012) Opportunities and challenges for a sustainable energy future. Nature 488(7411):294

Conway D, Van Garderen EA, Deryng D, Dorling S, Krueger T, Landman W, Lankford B, Lebek K, Osborn T, Ringler C, Thurlow J (2015) Climate and southern Africa's water–energy–food nexus. Nat Clim Chang 5(9):837

Council BTT (2015) Towards a long-term strategy for BRICS: a proposal by the BRICS think tanks council

Goswami DY, Zhao Y (Eds) (2009) Proceedings of ISES world congress 2007, vol. 1–5. Solar Energy and Human Settlement. Springer Science & Business Media

Griffith-Jones S (2014) A BRICS development bank: a dream coming true? (No. 215). In: United Nations conference on trade and development

Kok N (2014) South Africa's peacebuilding and PCRD activities: the role of IBSA and BRICS

Kutsenko E (2015) Pilot innovative territorial clusters in Russia: a sustainable development model. Forsat 9(1 (eng))

La Rovere EL, Pereira AS, Simões AF (2011) Biofuels and sustainable energy development in Brazil. World Dev 39(6):1026–1036

Liu LQ, Wang ZX, Zhang HQ, Xue YC (2010) Solar energy development in China—A review. Renew Sustain. Energy Rev 14(1):301–311

Martin B (2017) The politics of electricity planning in South Africa: a review of dominant advocacy coalitions seeking to influence the Integrated Resource Plan of 2010 (IRP2010), and its update in 2013 (Doctoral dissertation, University of Cape Town)

New Development Bank (NDB) (2019) https://www.ndb.int/. Accessed on 15th June 2019

News on Renewable (2019) Nuclear, fossil, technology, market data—power technology, https://www.power-technology.com/. Accessed on 15th June 2019

Schmidt TS, Sewerin S (2017) Technology as a driver of climate and energy politics. Nat Energy 2(6):17084

Solar Power in India (2019) https://en.wikipedia.org/wiki/Solar_power_in_India. Accessed on 15th June 2019

Trindade EP, Hinnig MPF, Moreira da Costa E, Marques J, Bastos R, Yigitcanlar T (2017) Sustainable development of smart cities: A systematic review of the literature. J. Open Innov.: Technol., Mark., Complex. 3(3):11

Wentworth L (2014) Creating incentives for green economic growth: green energy in South Africa

Chapter 3
Installations of Solar Systems in Remote Areas of Himachal Pradesh, INDIA: Challenges and Opportunities

Santosh B. Bopche

Abstract The renewable energy is an energy obtained from natural replenishable resources. It consists of wind, water power, tidal power, solar, biomass and energy recovered from wastes. The solar energy is available at free of cost and cleanest source of renewable type energy that can be utilized as a better substitute to the fossil fuel energy. These days lot of research is going on in extracting maximum possible heat energy from the solar irradiation. From solar systems practicability and remotely located societal upliftment point of view, it's a big challenge to erect and run continuously or effectively the solar energy systems in remotely located or hilly areas of Himachal Pradesh, INDIA. The present chapter discusses various applications of the solar concentrating collector technology that may help remotely located people get rid of their day to day problems e.g. water freezing, water pumping, cooking, drying of agricultural products, air conditioning etc. The challenges to be faced by the community people to meet household and agricultural demands and ways to get better the performance of solar-energy based systems along with opportunities for solar energy systems to meet the requirements of remotely located people are also discussed in this chapter.

Keywords Solar energy · Systems · Challenges · Opportunities · Rural · Remote

3.1 Introduction

The distantly located and interior/disconnected community of Himachal Pradesh faces so many problems in their day to day routine endeavors. It comprises; for cooking they have to still rely on conventional fuels e.g. woods, kerosene etc. For cooking purposes bio gas can be generated more effectively with the assistance of solar energy. Solar cookers energized by concentrating collectors can be made easily available to such communities. During winter, at hill top locations, the pipe lines meant for water supply gets chocked due to formation of ice. This type of problem can completely be overcame by employing solar collector cum thermal energy storage

S. B. Bopche (✉)
Department of Mechanical Engineering, NIT Hamirpur, Hamirpur 177001, India
e-mail: santoshbopche@nith.ac.in

H. Tyagi et al. (eds.), *Solar Energy*, Energy, Environment, and Sustainability, https://doi.org/10.1007/978-981-15-0675-8_3

systems, so that water shall remain in circulation all times. Solar driven pumps can be erected in such areas to fulfill the household as well as irrigation water supply necessities. Solar dryers can be employed for drying of agricultural products. The people can be made aware about the construction of their houses so that cool air shall remain in circulation and serve the purpose of air conditioning.

Conventional means for production of electricity to meet the energy demands is Diesel Generator which is considered as an economic burden to remotely located poor and backward communities. These systems are non-environment friendly and less reliable. Solar dependent energy systems could be better option to meet routine energy demands (Khatib et al. 2018).

An anticipated solar energy potential of INDIA is about 748 GW, according to MNRE, INDIA (Padmanathan et al. 2018). In India, about 61% of the overall installed electricity generation is generated using coal/lignite however contribution of renewable energy resources is only about 13%. Despite growth in power generation capacity of about 272.5 GW, around 75.02 million inhabitants of rural and remote areas are deprived of electricity. According to Census 2011, among 75.02 million inhabitants, 72.04 million people uses kerosene as a primary illumination source and 0.92 million households use renewable (solar) energy as a primary light source. The success with erection of solar photovoltaic (PV) technology is quite limited although it is a better alternative in terms of quality of lighting, permanence and resourcefulness. The challenges faced in deploying solar PV panels in remotely located areas contains unavailability of solar PV products market in order to build connectivity between service providers and the end user(s), unavailability of active financing agencies in order to make the products quite affordable to the consumers, and unawareness among the society members about the solar based technologies e.g., PV or other renewable energy technology based appliances like solar cookers, solar water heaters, solar air heaters etc. (Anand and Rao 2016).

3.2 Challenges/Limitations of Concentrating Solar Power Technology in Remote Regions

For individual house power generation, concentrating solar power technology is realistic and convincing in remote areas. Lots of challenges are to be faced for efficient and uninterrupted operation of such systems. The limitations comprise: water consumption, water availability, transmission of electricity, power supply security, materials design, selection of heat transfer fluids, viability of thermal energy storage & design of receiver subsystems in addition to commercial feasibility and ecological effects. Some of the technical challenges are discussed as follows (Xu et al. 2016).

1. **Water consumption**

The availability and easy reach to water is a basic concern in remotely located areas. Large quantity of water is necessary for extracting energy from solar energized absorbers/receivers and for cleaning of reflecting surfaces e.g. mirrors, polished aluminium or stainless steel. The availability of water is a prime concern in some remotely located regions. The predicted water requirement ranges from 3 to 3.50 m^3/kW. The 95% of total water requirement is generally utilized at cooling towers and 5% is consumed in general for reflective surfaces cleaning. The implementation of dry mirror cleaning techniques/technologies are really helpful in mitigating the usage of water consumption in solar-based power generation units.

2. **Drycooling**

Lots of concentrating solar based power units are working on Rankine cycle with steam as a working fluid. In steam condenser, steam cooling is achieved using ordinary cooling water. Better cycle efficiency can be attained at lower steam-condensation temperature. Studies of NREL (National Renewable Energy Laboratory) have revealed that dry-cooling would preserve water usage by more than 90%. However, the difference of temperature between the cooing water and the dry cooling medium may differ the yield of cycle thermal efficiency.

3. **Dust-cleaning**

The collection/optical efficiency of concentrating collectors depend on the reflectivity of surfaces e.g. parabolic dish/cylindrical concentrator, heliostats and transmissivity of the solar absorber cover tubes. Optical efficiency drops due to accumulation of dust particles and therefore the overall performance of the systems. The studies have disclosed that about 40% of the solar-thermal to electric power conversion decreases due to formation of a dust layer of size 4.84 g/m^2. It also influences the optical-performance of a concentrating solar power reflective surfaces. Is also observed that 1% drop in the reflectivity raises the levelized cost of electricity by 1%. Regularly washing mirrors with the help of water and maintaining reflective surface's parabolic profile/orientation of heliostats are the most effective ways maintaining collector's performance. At remotely located/rural areas it's a big challenge to arrange water for the cleaning task (Xu et al. 2016).

4. **Concentrating Solar Power (CSP) desalination cogeneration**

This is nowadays an attractive option in remotely situated rural/agricultural areas. The steam generated using CSP cycle is utilized to support the desalination processes. It may also fulfill the water demands of the remotely situated population facing dearths.

5. **Heat transfer/working fluid**

The heat exchange fluid is an important component of CSP technologies, which is doing a job of collecting energy effectively from the concentrated solar radiation to the steam driven prime mover. These are water/steam, air, thermal-oils, organic as

well as molten-salts. It also serves the purposes of energy storage. It may need to remain stable or sustain temperatures up to 700 °C and must be corrosion resistant. Higher viscosity increases the pumping power whereas higher specific heat is good to make the systems more compact. The air is reported as a best option for heat transfer fluid meeting all above discussed criterias.

6. **Environmental impacts**

It is well known that CSP systems are climate friendly. The researches in this area and widespread of this CSP technology may fulfill household power needs in a more effective way by capturing free and clean source of solar irradiation.

Living creatures e.g. flying birds gets burnt badly due to accidental exposure to concentrated solar radiation beams focussing at absorber locations.

After usage, the heat transfer fluids like synthetic-oils, organic fluids, hydraulic fluids, molten salts, lubricant as well as coolants in CSP collecting systems, exposing it to the clean outer ambience may not be climate friendly. Better reuse/effluent practices need to be pursued in order to minimize the environmental impacts caused using such hazardous fluids/compounds. The organo-compounds e.g., Biphenyl/Diphenyl oxide used in CSP systems are very poisonous and inflammable also.

7. **Higher capital costs**

The initial cost of CSP technology based power unit is higher. The pursual of mass production techniques, availability of sales and services in remote locations and research innovations in heat transfer fluids, higher temperature range storage systems and thermodynamic cycles may decrease the capital, running and maintenance cost by around 60% in coming future.

So, it can be concluded that setting up of solar thermal power units in remotely situated areas for a bigger capacity, say above 100 kW is problematic to maintain and operate. In such areas, solar thermal power plant of less than or equal to 5 kW capacity for an individual home may prove beneficial to meet the routine/daily household needs.

Interruptions in the power supply may occur due to natural constraints like cloudy weather, rains, heavy rainfall, heavy wind, snowfall, fall of bigger sized ice pellets that may cause damage to the renewable energy systems, failure of solar tracking systems, instrumentation devices. In addition to this, interruptions in electricity supply to the accessories associated with the solar collectors may occur due to longer hours load shedding.

The use of locally available renewable energy options e.g., solar, wind and biomass would be extra efficient than long distance transmission of electric power for supply to remotely located agricultural areas, in order to evolve self-sustained methods to cope up with the crisis of fossil based fuel depletion and weather change in long run. It leaves smaller carbon footprints behind.

The solar thermal based systems have poor solar thermal efficiency. The disadvantage associated with power transmission through longer distances is transmission loss and towers as well as cable installation cost. For such circumstances, erection

of a local standalone microgrid sourced by hybrid renewable energy system (HRES) could be the best alternative of electricity production (Li et al. 2018).

3.3 Opportunities for Renewable Energy Installations

In order to electrify remotely located regions, economically and efficiently there are lots of prospects for renewable energy based installations.

Bioenergy is a renewable energy which is generally obtained from biomass processed by various biochemical as well as thermochemical actions in order to convert it as a syngas, biooil and biochar. The thermochemical processes involves combustion, pyrolysis and gasification to transform agricultural waste biomass to electricity. Biochar is a Carbon rich solid residue obtained from pyrolysis and gasification. An availability of biomass is an important parameter to judge production of Biochar as well of energy generation (Li et al. 2018).

The ***solar home system*** (SHS) is also an important option for meeting cooking and illumination needs of remote locations. It involves; solar cooker, solar powered LED lamps, and solar charged battery to run home appliances. The disadvantages associated with parabolic concentrating energized cooker comprise potentially risky and faster operation due to concentrated radiation and uncontrolled heating rate.

An ***Off-grid PV (Photovoltaic) system*** may supply electricity/power to meet daily basic domestic needs. However, solar home systems cover illuminating, refrigerating, charging, pumping, electric mosquito shocking, fanning, air conditioning needs most of which are not extensively examined and evolved. Using SHSs would save time spend for doing domestic basic tasks and would preserve a healthy environment. It would promote educational creative activities and finally would take advantage of scoring innovations in energy efficiency and developing cost effective systems.

Khatib et al. (2018) have developed a product called S***olar Box (Solenx)*** serves three basic applications e.g., lightening LED lamps, a mini Insulin-refrigerator, two USB ports, electric mosquito shocker or a battery charger. A mini Insulin refrigerator is used to keep Insulin (used for Diabetic patients) under suitable thermal conditions (Within 2–8 °C for 25 °C ambient temperature). It can also be used to store Veterinary medicines and various animal health products. An electric mosquito shocker consisting of electric grid and a light source used to attract flying objects which may be harmful causing Leishmaniasis, Malaria as well as Dengue Fever. These insects, gets burned after coming in contact with its wire mesh due to higher grid voltage (Khatib et al. 2018).

For energizing an individual home, a ***solar home system*** for fulfilling daily power demand of about 0.75 kW-h is also suggested by Zubi et al. (2019), for illuminating LED lamps and cooking with the help of energy proficient multicooker.

Energy scarcity alleviation can be done by adopting solar house technology to renovate a rural home. In solar house, solar-air source heating system and floor radiative heating systems are installed (Liu et al. 2018).

About 20% of the world's residents live in remotely and electrically disconnected areas. Electrifying these areas by conventional ways imply huge capital investments and intense infrastructures. However, ***Microgrids*** (DC microgrids) based on renewable energy sourced generation and storage systems may be appropriate and cost effective solution. The systems working on direct current supply have its own benefits like lesser complexity and affordable operating systems. The difficulties involved in case of AC based electrical generators are as: synchronizing complexity, optional requirement of last stage inverter, huge investment and losses associated with it. All these shortcomings are totally removed in case of DC generators. The DC based home appliances comprise LED lighting, TVs, Laptops, charging units etc. The AC based appliances include fans, refrigerators/air conditioning systems. Such efficient appliances drastically reduce the domestic electricity consumption leading to cheaper and compact systems. Electrification of rural and remotely based locations is a big and inevitable challenge in order to empower the life of millions of inhabitants of such places, in a maintainable ways (Gandini and Almeida 2017).

Wazed et al. (2017) have evolved and examined the ***Solar Powered Irrigation Systems*** energized by Photo-Voltaic and solar based thermal technologies, which may be utilized by individual agriculturalists in small-scale remote rural agricultural lands. The remote hilly areas of Himachal Pradesh have been facing inconsistent water availability and supplies issues since longer time. The only dependable source is ground water supply. The remotely located farmers and localities have to cope up with larger installation investments required for the erection of bore wells and purchase of generator and pumps. The operational costs are also higher due to day by day hiking of conventional fuel prices and routine maintenance requirements. The technology desires to be evolved and importance/stress/emphasis should be put on the renewables based energy options.

An irrigation system based on renewable energy option uses PV panels for generating electrical power by extracting energy from solar power. It may be used for energizing electric motor in order to run/drive a pump. The system may be improved with the employ of batteries and storage water tanks. Solar PV panels produce DC power, which needs to be supplied to AC motor pump unit via an inverter. In modern times the PV based irrigation systems become more reachable to the remotely located agriculturists, by mitigating the installation as well as operational costs of PV based power generation technology. It is reported that in order to irrigate one hectare farm land a power of about 1 kW is required, which can be meet through the use of PV panels. The permanent magnet type DC motors are preferred for irrigation purposes owing to its high efficiency, torque and easy starting capabilities as compared to AC motors. The positive displacement pump and diaphragm type pump are generally used for higher and lower water head requirements, respectively.

A PV power based solution scheme proposed for retrieving ground water for the purpose of irrigation of farm land is as shown in Fig. 3.1.

The drawbacks of PV technology comprise: (1) degradation of PV cells due to long term exposure (0.8% per year), (2) harmful manufacturing technology of PV cells, (3) use of batteries and transportation may promote carbon footprints of the technology and (4) performance loss due to accumulation of dust (Wazed et al. 2017).

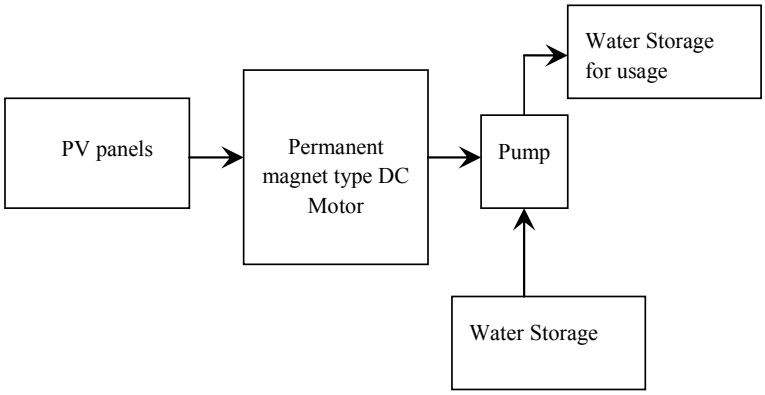

Fig. 3.1 PV power based water pumping system

Solar Driven Heat Engines: Another technology proposed is solar thermal based irrigation system, as depicted in Fig. 3.2. This technology utilizes concentrated solar energy to produce mechanical power via an engine operated on Stirling, Rankine or Brayton engine. The power/work generated may be directly used to drive pumps or to produce electrical power for driving pump motors (Wazed et al. 2017).

The solar irrigation can be a best alternative to increase the production of agricultural products by not levying extra burden on the power grid or diesel consumption. It also helps keeping clean an environment. The diesel based pumps planted on agricultural lands may need to be replaced by solar driven irrigations pumps all over the country. Providing subsidy and related incentives from the government will encourage and give confidence to farmers to cultivate more and more land using solar based irrigation technique (Islam et al. 2017).

Fig. 3.2 Solar thermal power based irrigation system

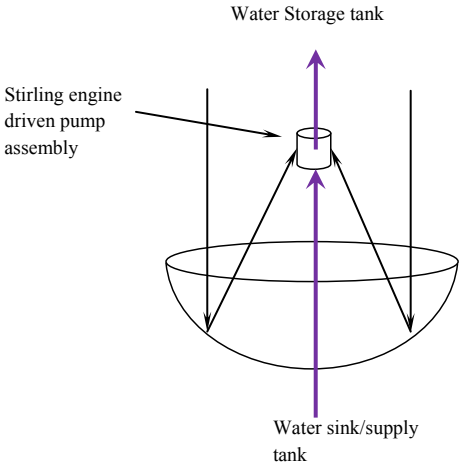

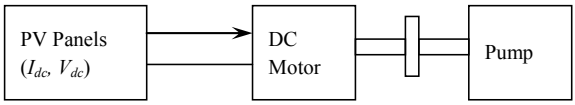

Fig. 3.3 Directly coupled DC motor based Solar-irrigation-system. Adapted from Islam et al. (2017)

A Photovoltaic array system is used to energize motors of the irrigation pumps. In order to transform variable magnitude DC voltage into a constant magnitude AC or DC power electronic inverter circuit is generally used, before energizing AC or DC motors. For solar irrigation system dynamic as well as displacement type pumps are preferred. The displacement type pumps are reported to be more efficient than the dynamic type. The performance of dynamic pump is solar insolation dependent. The additional unutilized energy obtained from solar irrigation systems can be used for providing energy/work for rice-parboiling-systems (Islam et al. 2017).

The schematic diagram of directly coupled solar-irrigation-system is as depicted in Fig. 3.3.

Irrigation using Solar based Thermal Systems: Thermal energy can be obtained from the Sun with the help of a solar-concentrating surface. It can be transferred to the working fluid, which directly or indirectly executes Rankine, Brayton or Stirling cycle engines. Mechanical work is obtained from these heat engines used to drive the generator in order to drive the motors for energizing various household and agricultural appliances. This solar thermal technology can also be used to drive the pumps for irrigation purposes, which has not been researched extensively in last 10–15 years. A schematic showing, solar driven irrigation pump run by Stirling engine is as depicted in Fig. 3.4 (Wazed et al. 2018).

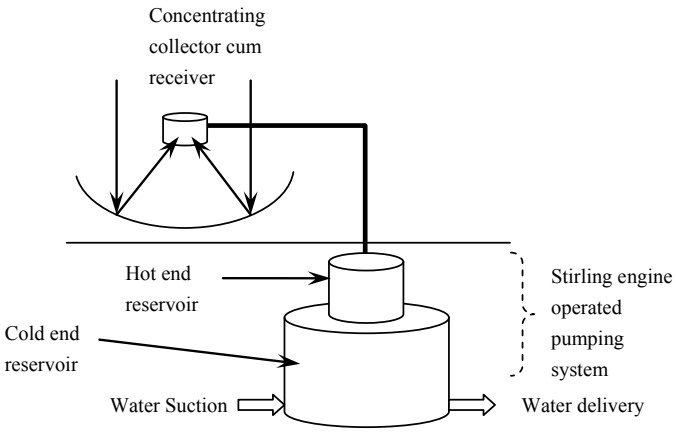

Fig. 3.4 Schematic of solar driven stirling engine. Adapted from Wazed et al. (2018)

A metal hydride based pumping system, wherein, a metal hydride is heated using solar energy which produces a Hydrogen gas. It then pressurizes a piston which ultimately produces a water-head up to 15 m on Sunny days (Wazed et al. 2018).

The solar thermal based pumping systems exhibited an efficiency of about 3% in comparison to 6% of that of Photovoltaic systems. But efficiency shall not be the prime concern in case the systems working on renewable sources. For remotely located society irrigation purposes, a locally evolved solar thermal based irrigation system is reported to be more cost effective and ecofriendly as compared to PV technology (Wazed et al. 2018).

Electricity generation through solar based Micro-grid: The lowest ever rural electricity tariff in the world is at Myanmar. Xu et al. (2019) have provided an economic comparison of various microgrid systems e.g., Solar PV based microgrid, diesel based microgrid, biogas based microgrid, solar PV cum diesel based microgrid, and solar PV cum biogas based microgrid. In their study, rice husk is used as a source for biogas energized micro-grid. Among these five types of microgrids, solar PV based microgird generated an excess electricity of about 30% more than the local requirements. It is attributed to the hourly variation of the incoming solar radiation (Xu et al. 2019).

Energy Generation from Biogas: Energy can also be obtained from biogas, which can be produced using household waste products. The disadvantage of having lesser energy production efficiency can be improved by uniting it with a solar power. This technology is termed as solar assisted biogas power generation unit. Biogas is generally produced from biodegradation of organic wastes/resources, by bacteria under anaerobic condition. Such biogas generation units can be installed anywhere either in urban area or in remotely located hilly rural area. It comprises Methane with some amount of Carbon Dioxide, and little proportion of Hydrogen Sulphide. Based on a large scale production of biogas, electricity generation unit can also be evolved. The overall performance of the biogas generation unit can be controlled by maintaining suitable range of parameters e.g., pH, system temperature, loading rate and agitation etc. The correct temperature range is 30–60 °C for anaerobic bio-degradation process and pH range need to be maintained at optimum loading rate is 6.8–7.2. Among all parameters, temperature is the main concern contributing in overall production of biogas. The length of fermentation also depends on temperature of the biogas generation system. This temperature can also be maintained using external sources e.g. heat of exhaust gases leaving from power generating engine driven by biogas, electrical heat and heat yielded from any adjacent combustion unit or from biofuel or from any of the renewable sources i.e., solar energy. The heat obtained from solar energy, can be utilized to heat biogas digester above the ambient, may be by means of hot water production. It is circulated through the jacket of the biogas digester. It may reduce the time required for attaining the optimum temperature required for biogas production. At lower temperatures, production of biogas is reduced and may even discontinue.

An advantage associated with solar assisted biogas generating unit is that it improves the production rate of biogas due to solar assistance. The installation cost of such modified systems is more. It needs special attention for the operation and

maintenance of the solar panels due to dust accumulation and atmospheric calamities like thunderstorm, heavy winds and heavy snow-ball falls. Solar energy is not a continuous source. During nights, it is very difficult to maintain performance of the biogas generation unit (Mahamudul et al. 2019).

There are other problems that reduce the performance of the Solar Collector based systems. These can be overcame by routine and timely look-after and maintenance.

3.4 Improvement of the Performance of Solar-Based Power Units/Set Ups

The methods that may increase the efficiency of the solar based power units are as dictated follows.

(1) In order to pick the power plant performance up, dust accumulation on the reflecting surfaces need to be prevented, by regular dry/wet cleaning. Since, it is observed that the glass plates transmittance reduces by 39.4%, on an average on account of exposure to the solar radiation for say about 38 days. Super-hydrophobic materials are specifically recommended to inherit the self-cleaning and anti-contamination properties in the concentrating solar power mirror (Xu et al. 2016).

(2) The heat transfer fluids which are thermally more stable even at higher temperatures also mend the solar energy system's performance. The requirement of pumping power reduces for lesser viscous heat transfer fluids. The sizes of thermal energy storage tanks can be mitigated by using working fluids having higher values of specific heats. These two factors help increasing the efficiency of a solar collector system (Xu et al. 2016).

(3) The performances of solar systems can also be improved by replacing the aluminium concentrator by galvanized steel structure. In addition, Aluminium polymeric reflector be replaced by thin-silvered glass reflector and by providing selective surface coatings on the absorber surface of a receiver in a way to improve the outcome of the system. A practice of using of steel and thin glass reflector also raise the performance of the system by about 12% that may diminish the cost of energy to be supplied by about 25% (Njoh et al. 2019).

(4) The use mirrors having high reflective qualities allow more than 98.5% reflectivity to the solar rays incident on the reflector surface, also assist enhancing the system performance (Price et al. 2002).

3.5 Concluding Remarks

In order to cope up domestic energy poverty, the developing countries should keep on high priority an access to electricity to each and every remotely located region. It may

be by adopting grid expansion, distributed smaller power capacity units, micro-grid projects and solar home systems. Therefore, serious attention may needs to be focused to give more and more renewable energy solutions, specifically to tackle power supply, power security and local (in-house) as well as global climatic concerns. Every household should have access to lower cost/affordable electricity. Such conditions may definitely progress living standards, economic increase, development of human as a whole, mitigate gender-inequality, pick up an initial age education standards, protect the atmosphere and circumvent the negative health consequences of indoor flames/fires (Zubi et al. 2019).

A Solar Photovoltaic-biomass-biogas hybrid system as presented by Ganthia et al. (2018) has been proved to be an easy solution for meeting daily electricity needs of remotely located societies. Its advantages are: (i) lesser maintenance cost, (ii) emission-less, (iii) no requirement of conventional fuels, (iv) easy installation and (v) easy operation. The disadvantage of Solar PV water pumping system reported is having higher Initial cost. In addition to all above-discussed systems, windmill based water pumping system can also be employed for irrigation purposes. Its advantages comprise; no emission, no requirement of conventional fuels and longer working life. Its disadvantages are; higher initial/maintenance cost and limited availability of market for sales and service. This energy is wind speed dependent (Rathore et al. 2018).

The unavailability of market and skilled manpower for sales, supplies and maintenance of these solar energy systems at such remotely located areas is a big challenge in a path of making local communities aware of using renewable energy technologies for fulfilling their daily energy needs.

The challenges/problems faced in remote locations comprise: variation of solar radiation topography, wind speed (lesser wind speeds means no possibility of wind propelled turbines in order to assist solar based power generation), rainfall (cloudy weather hinders solar irradiation), community spirit, unorganized administrative structure, lack of respect for nature, self-help ethos, sparsely distributed houses (increases the cost of cabling etc.), lack of renewable energy infrastructure (It incurs extra high initial cost), Human capital (lack of skilled workers for initial installation and post installation routine maintenances), small market size, no funding sources, scarce income opportunities (Njoh et al. 2019).

The adaption to the solar energy by remotely located homes depends on social-economic, demographic and approach of the government towards rural, remotely located electrification. Solar home systems have assisted socio-economic activities and have improved the living standards of rural localities especially house women. It also has reduced the house pollution which used to occur due to use of Kerosene and other conventional fuels. This technology adaptation is constrained by unavailability of skilled personnel (Mishra et al. 2016).

Acknowledgements This chapter work is motivated by the research project, entitled 'Solar Thermal Collection Efficiency Improvement using Multistaging of Parabolic Dish Collector', by State Council for Science, Technology & Environment, Shimla, H.P. INDIA (Grant No. SCST&E (R&D)/2017–18).

References

Anand S, Rao AB (2016) Models for deployment of solar PV lighting applications in rural India. Energy Proc 90:455–462

Gandini D, Almeida ATD (2017) Direct current microgrids based on solar power systems and storage optimization, as a tool for cost-effective rural electrification. Renew Energy 111:275–283

Ganthia BP, Sasmita S, Rout K, Pradhan A, Nayak J (2018) An economic rural electrification study using combined hybrid solar and biomass-biogas system. Mater Today Proc 5:220–225

Islam MR, Sarker PC, Ghosh SK (2017) Prospect and advancement of solar irrigation in Bangladesh: a review. Renew Sustain Energy Rev 77:406–422

Khatib T, Shaar A, Alhamad F, Dwikat H, Shunnar R, Othman M (2018) Development of solenx: a reliable and cost effective solar aid box for underserved and rural areas in Palestine. Energy Convers Manag 174:863–873

Li L, You S, Wang X (2018) Optimal design of standalone hybrid renewable energy systems with biochar production in remote rural areas: a case study. In: 10th International conference on applied energy. ICAE 2018. Hong Kong, China, 22–25 Aug 2018

Liu Z, Wu D, He BJ, Liu Y, Zhang X, Yu H, Jin G (2018) Using solar house to alleviate energy poverty of rural Qinghai-Tibet region, China: a case study of a novel hybrid heating system. Energy Build 178:294–303

Mahamudul HM, Rasul MG, Akbar D, Mofijur M (2019) Opportunities for solar assisted biogas plant in sub-tropical climate in Australia, a review. Energy Proc 160:683–690

Mishra P, Behera B (2016) Socio-economic and environmental implications of solar electrification: experience of rural Odisha. Renew Sustain Energy Rev 56:953–964

Njoh AJ, Etta S, Ngyah-Etchutambe Ijang B, Enomah Lucy ED, Tabrey HT, Essia U (2019) Opportunities and challenges to rural renewable energy projects in Africa: lessons from the Esaghem village, cameroon solar electrification project. Renew Energy 131:1013–1021

Padmanathan K, Govindarajan U, Ramachandaramurthy VK, Rajagopalan A, Pachaivannan N, Sowmmiya U, Padmanaban S, Nielsen JBH, Xavier S, Periasamy SK (2018) A sociocultural study on solar photovoltaic energy system in India: stratification and policy implication. J Cleaner Prod. Accepted manuscript. https://doi.org/10.1016/j.jclepro.2018.12.225

Price H, Lupfert E, Kearney D, Zarza E, Gee GCR, Mahone R (2002) Advances in parabolic trough solar power technology. J Sol Energy Eng ASME 124:109–125

Rathore PKS, Das SS, Chauhan DS (2018) Perspectives of solar photovoltaic water pumping for irrigation in India. Energy Strategy Rev 22:385–395

Wazed SM, Hughes BR, O'Connor D, Calautit JK (2017) Solar driven irrigation systems for remote rural farms. In: 9th international conference on applied energy, ICAE 2017, 21–24 Aug 2017, Cardiff UK. Energy Proc 142:184–191

Wazed SM, Hughes BR, O'Connor D, Calautit JK (2018) A review of sustainable solar irrigation systems for Sub-Saharan Africa. Renew Sustain Energy Rev 81:1206–1225

Xu X, Vignarooban K, Xu B, Hsu K, Kannan AM (2016) Prospects and problems of concentrating solar power technologies for power generation in the desert regions. Renew Sustain Energy Rev 53:1106–1131

Xu D, Mumata M, Mogi G (2019) Economic comparison of microgrid systems for rural electrification in Myanmar. Energy Proc 159:309–314

Zubi G, Fracastoro GV, Lujano-Rojas JM, Bakari KE, Andrews D (2019) The unlocked potential of solar home systems; an effective way to overcome domestic energy poverty in developing regions. Renew Energy 132:1425–1435

Chapter 4
Utilising Passive Design Strategies for Analysing Thermal Comfort Levels Inside an Office Room Using PMV-PPD Models

Sana Fatima Ali and Dibakar Rakshit

Abstract Energy efficiency and conservation measures in buildings are the focus in today's design and construction practices. One of the major reasons for energy consumption in buildings is maintaining thermal comfort. Providing a thermally comfortable environment with an energy efficient design will not only lead to energy and cost savings, but will also have other intangible benefits, such as enhanced productivity, and health and well-being of the occupants. Studies have reported that buildings have 50–60% energy saving potential by means of an efficient design. This study aims at utilizing passive design strategies, such as provision of insulation and window glazing, to analyse their effects on thermal comfort of the occupants inside an office room. Measurements of indoor environmental quality parameters was done for the room, and Predicted Mean Vote and Percentage People Dissatisfied models, given in ASHRAE Standard 55, have been used in this study to assess the existing comfort levels of the occupants. A parametric study to examine their influence on the thermal environment using these models has been done using IDA ICE Beta 4.7 software. It was observed that application of the passive techniques although enhanced the thermal environment of the room, the comfort levels were still not within the ideal range specified by ASHRAE. The study concluded that more passive strategies can be employed to enhance the comfort levels. This would help in reducing the need for alternate methods of space conditioning, hence, leading to energy conservation.

Keywords Thermal comfort · Passive design · IDA ICE

S. F. Ali · D. Rakshit (✉)
Centre for Energy Studies, Indian Institute of Technology Delhi, Hauz Khas, New Delhi 110016, India
e-mail: dibakar@ces.iitd.ac.in

S. F. Ali
e-mail: esz178538@ces.iitd.ac.in

H. Tyagi et al. (eds.), *Solar Energy*, Energy, Environment, and Sustainability, https://doi.org/10.1007/978-981-15-0675-8_4

Notations

A_{Du}	Dubois area (m^2)
C_{res}	Heat exchange by convection in breathing (W/m^2)
E_c	Heat exchange by evaporation on skin (W/m^2)
E_{res}	Evaporative heat exchange in breathing (W/m^2)
f_{cl}	Clothing surface area factor
H	Sensitive Heat Losses (W/m^2)
$Ht.$	Height of a person (cm)
h_c	Convective Heat Transfer Coefficient (W/m^2 K)
I_{cl}	Clothing insulation (m^2 K/W)
L	Thermal load on the body of an occupant (W/m^2)
M	Metabolic Rate (W/m^2)
PMV	Predicted Mean Vote
PPD	Percentage People Dissatisfied
p_a	Water Vapor Partial Pressure (kPa)
p_s	Partial Vapor Pressure of Saturated Air (kPa)
RH	Relative Humidity
t_a	Air Temperature (°C)
t_{cl}	Surface temperature of clothing (°C)
t_g	Globe temperature (°C)
t_r	Mean Radiant Temperature (°C)
t_{sk}	External skin temperature (°C)
t_W	Wet Bulb temperature (°C)
v_a	Velocity of air (m/s)
v_{ar}	Relative velocity of air (m/s)
W	Effective Mechanical Power (W/m^2)
$Wt.$	Weight of a person (kg)

4.1 Introduction

4.1.1 Energy Conservation in Buildings

Buildings are necessary to provide shelter to the occupants, to provide a safe environment and for carrying out various activities inside a space. Thus, growth in building sector is at an all-time rise as a result of the increase in population. National Statistical Organization reported that currently, buildings stand at consuming approximately 40% of the total electricity and one of the major factors in consumption of electricity is maintaining comfort of the occupants, be it thermal or visual (02 Energy and Buildings 2014). Generation of electricity still relies on non-renewable energy sources and hence, to cater to the increasing demand, resource depletion would take place along

with leading to an unnecessary wastage of money. Bureau of Energy Efficiency reports that buildings can potentially save up to almost 50% of the electricity (02 Energy and Buildings 2014).

The energy expenditure in buildings can be truncated to a large extent by putting into practice measures such as climate responsive design, modifying the construction of building, making use of local resources, etc. Such measures form a part of the passive techniques in buildings, which do not rely on any supporting electrical or mechanical systems. Apart from this, efficient space conditioning, or lighting systems can be employed in buildings, as part of the active measures in buildings, which involve the utilisation of building services systems.

Several studies have been carried out which focus on employing passive techniques to alleviate the energy expenditure. Sharma et al. evaluated the impact of the orientation of the building on its energy expenditure (Sharma et al. 2015). One such study by Kumar et al. focused on changing the construction material, the platform area and the orientation of the building to examine their effect on the energy need (Sushil Kumar et al. 2016). Another such study by Lee et al. concentrated on optimising a window system on the basis of its type and properties to examine their effects on the total load of the building, including thermal and lighting, and thus minimizing it (Lee et al. 2013). Such studies prove that implementing passive measures in buildings as a first step has a lot of potential to curb the energy requirements in buildings, and hence, such measures should be encouraged. However, employing such techniques, should also have a positive effect on the comfort level of the occupants, apart from its objective of saving energy in buildings. Therefore, the effect of the techniques employed should be examined not only for the energy requirements of the building but also for the comfort requirement of the occupants.

4.1.2 Meeting the Indoor Environmental Quality (IEQ)

In addition to meeting the energy requirements in a building, the indoor environment should also meet the comfort criteria since it affects the health, comfort, safety and productivity of the occupants, making it an intangible asset. It incorporates distinct parameters such as air quality, odor, lighting, noise, and thermal comfort (ISHRAE 2015). Fulfilling the requirements of the indoor environmental quality leads to augmenting occupant's life span, benefits the resale worth of the building, and brings down the accountability and liability of the owners. Whilst the elements of the IEQ should be restricted to their allowable limits, such as noise and odor, there are still some facets which cannot be eluded, and thus, can only be regulated according to the requirements. One of the parameters fitting to this description is the thermal comfort, which also utilises a major portion of the electricity in buildings. The aim of regulating the parameter implies optimising the conditions of the most favorable environment for occupants within available funds and resources.

4.1.3 Thermal Comfort: A Necessity

ASHRAE Standard 55 (ASHRAE 2010) defines thermal comfort as the condition of the occupants in agreement with their thermal environment, estimated subjectively. It represents a balanced state between the occupants and their environment determined when heat by occupant's metabolism process is dispersed into the environment.

Nowadays, designing an efficient building solely on the basis of energy requirements is not sufficient. The thermal comfort of the occupants, along with other comfort criteria should be met for a building to be called efficient. The occupants incline towards easier methods of retaining a thermally comfortable environment, hence opt for auxiliary systems of space conditioning. This results in an increase in the consumption of energy in buildings. Hence, passive methods should be adopted in buildings to the greatest extent possible not only for lowering down the demand for energy, but also for sustaining the recommended thermal comfort. Studies have proven that passive techniques are useful in achieving comfort conditions. There have been many such studies, such as that done by Haase and Amato (2009) wherein they checked the influence of natural ventilation and orientation in improving the thermal comfort of the occupants, by Ravikumar and Prakash (2009) wherein the size of the openings were adjusted in order to achieve thermal comfort conditions, by Liu et al. (2018) where an optimum window-to-wall ratio and optimum thicknesses of the insulation for the building envelope for meeting the required comfort was found, by Berkovic et al. (2012) where a particular configuration as well as orientation of a building was proposed for thermal comfort, or study of different arrangements for window-door by Daghigh et al. (2009), or provision of a partition wall for comfort improvement, as shown by Aryal and Leephakpreeda (2016), etc. The various passive techniques that can be employed in buildings for maintaining comfort conditions for the occupants are (Haase and Amato 2009; Ravikumar and Prakash 2009; Liu et al. 2018; Daghigh et al. 2009; Aryal and Leephakpreeda 2016; Gadi 2010; Zahiri and Altan 2016; Kamal 2012; Berkovic et al. 2012):

- Orientation
- Building Form
- Window-to-Wall Ratio
- Arrangement and Size of Openings
- Envelope Construction
- Envelope Materials
- Thermal Insulation
- Glazing
- Provision of Shading Devices
- Provision of Partition Walls
- Induced Ventilation Techniques (such as solar chimneys, wind towers, etc.)
- Earth Coupling Techniques (such as provision of earth air tunnels, etc.)
- Provision of Thermal Storage Components (such as Trombe walls, water walls, etc.).

In case if the passive techniques employed are not able to meet the required comfort, then efficient active techniques should be implemented in order to fill the

gap. Standards recommend that a minimum of 80% of the occupants need to be thermally satisfied with their environment (ASHRAE 2010; ISO 2005).

4.1.4 Thermal Comfort Evaluation

A variety of factors dictate the occupant comfort conditions, which may differ from one person to another. These factors include rate of metabolism of human beings (M), clothing insulation (f_{cl}), air speed (v_{ar}), air temperature (t_a), mean radiant temperature (t_r) and relative humidity (RH), which establish the heat exchange between the occupants and surroundings.

Numerous models are available to determine the comfort level of the occupants, formulated on the basis of the factors affecting it, such as Effective Temperature (ET), Corrected Effective Temperature (CET), Operative Temperature (OT), Tropical Summer Index (TSI), etc. (Auliciems and Szokolay 1997). However, two of the most recognised models for determining thermally comfortable environment are the Predicted Mean Vote (PMV) and the Percentage People Dissatisfied models, which are also accepted as the standard indices for evaluating thermal comfort by ASHRAE Standard 55 (ASHRAE 2010), and ISO 7730 (ISO 2005). Studies by researchers such as Pourshaghaghy and Omidvari (2012), Azad et al. (2018), Nematchoua et al. (2017), Rupp and Ghisi (2017), Katafygiotou and Serghides (2014), Calis and Kuru (2017), Pazhoohesh and Zhang (2018), Stamou et al. (2007) etc., have successfully utilised these PMV-PPD models for predicting the comfort conditions within the indoor spaces.

Predicted Mean Vote (PMV). The standards (ASHRAE 2010; ISO 2005) describe the predicted mean vote index for evaluating thermal comfort of the occupants in a space, according to which, the condition of the comfort can be envisaged by the PMV values. This index, developed by P. O. Fanger, represents a scale of thermal perception, having 7 points representing sensations of the occupants. It spans from a value of −3.0, representing a cold environment to +3.0, representing a hot environment, as shown in Table 4.1 (ASHRAE 2010; ISO 2005). The ideal thermal comfort conditions are represented by the PMV range of −0.5 to +0.5, as recommended by the standards (ASHRAE 2010; ISO 2005).

The different environmental factors (air temperature—t_a, mean radiant temperature—t_r, air velocity—v_{ar} and relative humidity—RH), which can be measured, as well as the physiological factors (rate of metabolism—M and clothing insulation—f_{cl}), which are the expected parameters, form the main basis of assessing the PMV values.

Table 4.1 ASHRAE scale of thermal sensation of occupants

Thermal sensation	Cold	Cool	Slightly cool	Neutral	Slightly warm	Warm	Hot
PMV scale	−3.0	−2.0	−1.0	0.0	1.0	2.0	3.0

The PMV values of a space for occupants can be assessed from the heat transfer balance equations, as given by Eq. (4.1) (ASHRAE 2010; ISO 2005):

$$PMV = (0.303e^{-0.036M} + 0.028) \times L \tag{4.1}$$

Here, L illustrates the different thermal loads on the human body, which can be evaluated using Eq. (4.2)

$$L = M - W - H - E_c - C_{res} - E_{res} \tag{4.2}$$

In Eq. (4.2), M can be taken from the table given in Annexure A of ASHRAE standard 55 (ASHRAE 2010), found to be 1.2 met for the present case. Additionally, the remaining terms on the right hand side of the equation can be calculated using the following equations:

$$H = 3.96 \times 10^{-8} \times f_{cl} \times [(t_{cl} + 273)^4 - (t_r + 273)^4] - f_{cl} h_c (t_{cl} - t_a) \tag{4.3}$$

$$E_c = 3.05 \times [5.73 - 0.007 \times (M - W) - p_a] - 0.42[(M - W) - 58.15] \tag{4.4}$$

$$C_{res} = 0.0014 \times M \times (34 - t_a) \tag{4.5}$$

$$E_{res} = 0.0173 \times M \times (5.87 - p_a) \tag{4.6}$$

These equations also constitute a term f_{cl}, which can be evaluated using Eq. (4.7) or Eq. (4.8):

$$f_{cl} = 1 + 1.29 I_{cl}\,;\ \text{If } I_{cl} \leq 0.078\,\text{m}^2\,\text{K/W} \tag{4.7}$$

$$f_{cl} = 1.05 + 0.645\, I_{cl}\,;\ \text{If } I_{cl} > 0.078\,\text{m}^2\,\text{K/W} \tag{4.8}$$

Here, the value of I_{cl} can be obtained from another table given in annexure B of ASHRAE Standard 55 (ASHRAE 2010), which was found to be 1.2 clo for the present study. Apart from this, the values of h_c and p_a can be obtained from Eq. (4.9) or Eqs. (4.10) and (4.11) respectively.

$$h_c = 2.38 \times |t_{cl} - t_a|^{0.25}\,;\ \ \text{If}\left(2.38 \times |t_{cl} - t_a|^{0.25}\right) > \left(12.1 \times \sqrt{v_{ar}}\right) \tag{4.9}$$

$$h_c = 12.1 \times \sqrt{v_{ar}}\,;\ \text{If}\left(2.38 \times |t_{cl} - t_a|^{0.25}\right) \leq \left(12.1 \times \sqrt{v_{ar}}\right) \tag{4.10}$$

$$p_a = 1000 \times \frac{RH}{100} \times p_s \tag{4.11}$$

where,

$$p_s = e^{\left(16.6536 - \frac{4030.183}{t_a + 235}\right)} \tag{4.12}$$

Another term, v_{ar} mentioned in the above equations can be found from Eq. (4.13):

$$v_{ar} = v_a + 0.005\left(\frac{M}{A_{Du} \times 58} - 58.15\right) \tag{4.13}$$

Here, the term A_{Du} can be attained using Eq. (4.14):

$$A_{Du} = (Ht.)^{0.725} \times (Wt.)^{0.425} \times 0.007184 \tag{4.14}$$

Additionally, another term used in the above mentioned equations is t_{cl}, the value of which, can be obtained using the iterative Eq. (4.15):

$$\begin{aligned} t_{cl} = t_{sk} - I_{cl} \times 3.96 \times 10^{-8} \times f_{cl} \times [(t_{cl} + 273)^4 - (t_r + 273)^4] \\ -I_{cl} \times f_{cl} \times h_c \times (t_{cl} - t_r) \end{aligned} \tag{4.15}$$

where,

$$t_{sk} = 35.7 - 0.028(M - W) \tag{4.16}$$

Percentage People Dissatisfied (PPD). Whilst determining the PMV value is crucial to acquire an idea about the thermal perception of the occupants of their environment, it is also critical to analyse whether the occupants are feeling content with their environment or not. This led P. O. Fanger to devise another model: The Percentage People Dissatisfied (PPD) Model. This index establishes a relationship between the occupant's satisfaction with their thermal environment and the PMV values attained. Standards recommend a PPD value of ≤20% (ASHRAE 2010; ISO 2005). Moreover, the minimum PPD value is 5%, lying at 0 PMV value, which suggests that at least 5% of the occupants feel discomfort even in a thermally neutral environment (ASHRAE 2010; ISO 2005).

The PPD values rely solely on the PMV values, and hence, can be found using Eq. (4.17) (ASHRAE 2010; ISO 2005):

$$PPD = 100 - 95 \times e^{[-(0.3353PMV^4 + 0.2179PMV^2)]} \tag{4.17}$$

4.2 Methodology

A small office room, established on the first floor of a G + 1 building in Delhi, has been selected for the study of thermal comfort. The room has dimensions 7.62 × 6.1 × 3 m^3, with the floor area being 37.2 m^2. The room has three windows with

dimensions 1.52 × 1.52 × 0.02 m^3 each, with two windows in west direction and one window in east direction, along with two doors of dimensions 2.32 × 0.91 × 0.04 m^3 each, where one faces the north-west direction, while the entrance lies in the north-eastern direction, as shown in Fig. 4.1. The thickness of the walls is 0.23 m, while 12 mm thick clear glass single pane windows have been used. The building element details and associated properties have been mentioned in Tables 4.2 and 4.3 (SP 1987).

The study has been carried out for a period of two months (December to February). An IEQ sensor, called Active Space Indoor Environmental Quality Sensor, consisting of different industrial sensors together, was stationed at the occupant's working table surface to continuously measure and record the readings of the environmental parameters, such as relative humidity, air velocity, air temperature and mean radiant temperature, at time steps of 1–2 min. The readings were registered for all the occupancy days (weekdays) and occupancy hours (10:00–18:30 h) for the period of study.

The equations for assessing the PMV and PPD indices were then used to evaluate the existing comfort level of the occupants analytically on the basis of the observations taken.

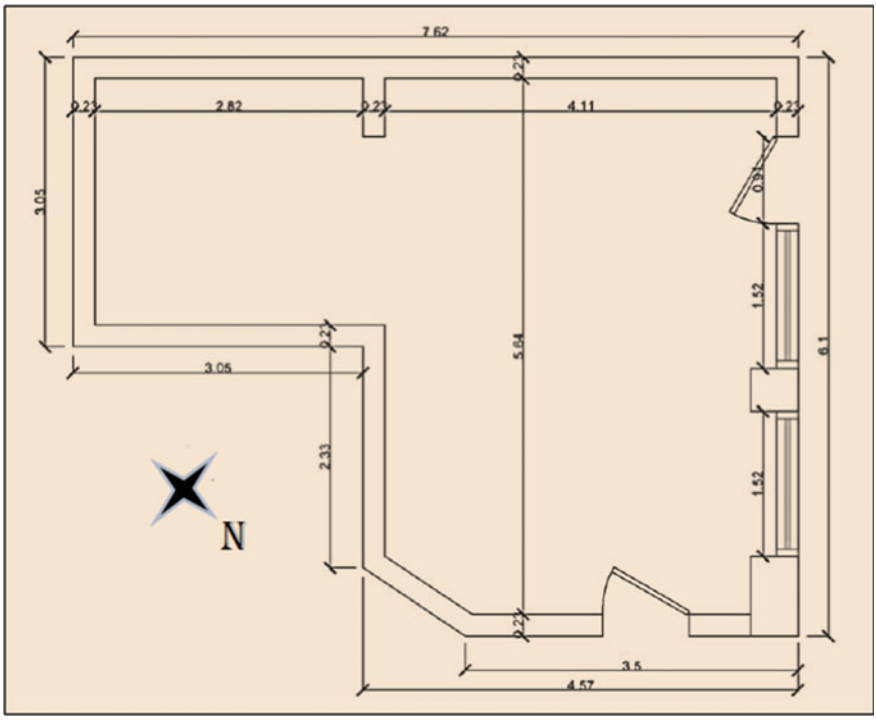

Fig. 4.1 Plan of the office room (dimensions in m)

Table 4.2 Building element details

Building element	Layer	Thickness (m)	Thermal conductivity (W/m K)	Specific heat capacity (kJ/kg K)	Density (kg/m^3)
External walls	Gypsum plaster	0.012	0.22	1.09	970
	Bricks	0.230	0.58	0.84	1500
	Gypsum plaster	0.012	0.22	1.09	970
Roof	Gypsum plaster	0.012	0.22	1.09	970
	Concrete slab	0.127	1.70	0.88	2300
	Cement mortar slurry	0.100	0.72	0.92	1648
	Mud phuska	0.102	0.52	0.88	1622
	Brick tiles	0.038	0.79	0.88	1892
Floor	Concrete slab	0.13	1.7	0.88	2300
	Gypsum plaster	0.012	0.22	1.09	970
	Marble tiles	0.039	3.00	0.88	2300
Doors	Wood	0.039	0.14	0.50	2300

Table 4.3 Window properties of the building

Properties	Thickness (m)	Solar heat gain coefficient (SHGC)	Transmittance		U-value (W/m^2 K)	Emissivity	
			Solar	Visible		Internal	External
Values	0.012	0.68	0.60	0.74	1.90	0.84	0.84

In addition to the experimental work, a simulation study analysis has been performed to investigate the impact of different passive parameters on the occupant's thermal comfort, for which, IDA ICE 4.7 Beta software has been used. The design input parameters of the study include the time zone of the location—+5.5 h and the latitude and longitude of the place, being N 28° 36′ E 77° 12′ respectively. The office room has been modeled as a single zone in the software and the construction and material details, as given in Tables 4.2 and 4.3, have also been specified (SP 1987). The model of the office room is shown in Fig. 4.2.

Other software inputs required were the no. and schedule of the occupants as well as the lighting and equipment, which were the occupancy hours of the office room, as mentioned above. The lighting and equipment load included taking into

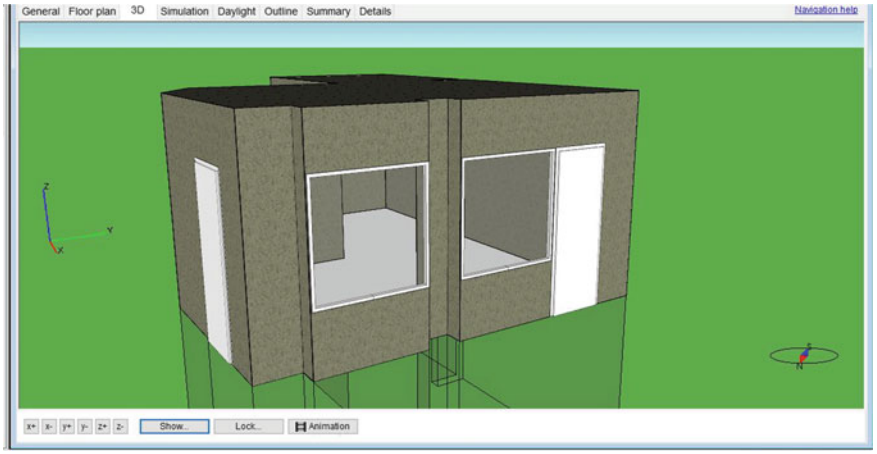

Fig. 4.2 Model of the office room

consideration 11 PCs, 3 tube-lights and 4 bulbs. Furthermore, the infiltration rate, holiday list, the simulation period, etc., also needs to be provided as an input.

The thermal comfort of the occupants in terms of the PMV and PPD values have been determined with the help of the software as well and validated against the experimental results. The changes in building construction along with their corresponding properties was later carried out in order to analyse the impact of these modifications on the comfort levels of the occupants.

4.3 Results and Discussion

4.3.1 Experimental Results

The experimental observations led to determining the PMV and PPD values analytically at each instant. Results suggested that the PMV values obtained has a minimum value of -1.21 and a maximum value of 1.11, and the rest of the values at other instances vary between these two extents. This implies that the mostly cooler conditions were persisting in the office room, since the minimum PMV value is farther from the -0.5 to $+0.5$ ideal range recommended by standards (ASHRAE 2010; ISO 2005). This is in agreement with the aspect that the experiments were conducted in the winter season in an unconditioned building. However, there were only a few instants of time when the PMV values ranged in the ideal zone, while at other instants the values were far from the values corresponding to the comfort conditions. Hence, suggesting that measures should be taken to improve the comfort conditions of the occupants.

Similarly, PPD values were also estimated corresponding to each of the PMV value obtained for each instant of time. With the minimum PPD value being 5%, the maximum PPD value reached 36.01%, which is again much beyond the 20% restriction, as recommended by the standards (ASHRAE 2010; ISO 2005). The PPD results also suggest that though there have been instances where the PPD values lie within the 20% range, but there are other cases as well wherein the PPD values have crossed the 20% cap, suggesting that for the study duration, a maximum of 36.01% of the occupants are dissatisfied with their thermal environment. Therefore, this value should also be tried to be brought down in order to reach the ideal conditions.

A graph between the two values has also been plotted, as shown in Fig. 4.3, which agrees well with the ideal PMV versus PPD curve, that can be obtained from any literature (ASHRAE 2010; ISO 2005). The graph between the two values obtained indicates that the minimum PPD value of 5% corresponds to the 0 PMV value, implying that even at thermally neutral conditions, at least 5% of the occupants remain dissatisfied, as stated in Sect. 4.1.4. The graph also depicts that moving away from the 0 PMV value, towards either negative or positive sides of the graph, the percentage of dissatisfied occupants is increasing, while only a very small percentage of people are feeling comfortable with their thermal environment, and hence, lie within the zone of −0.5 to +0.5. It also implies that some percentage of occupants still feel thermally satisfied with their environment on moving only a little away from the ideal zone. However, as the threshold crosses 20%, measures need to be taken to maintain the thermal environment within the ideal range and reduce the percentage of people dissatisfied with their thermal environment.

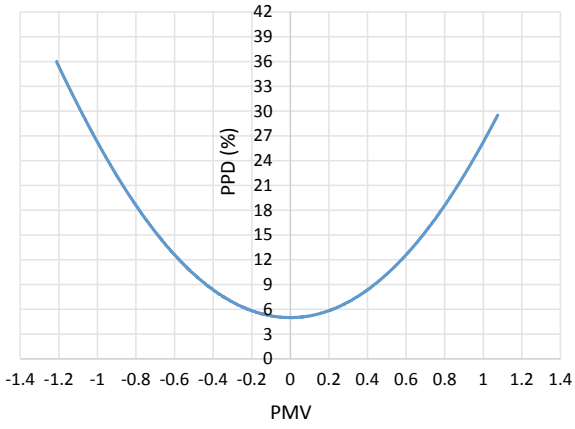

Fig. 4.3 Experimental results

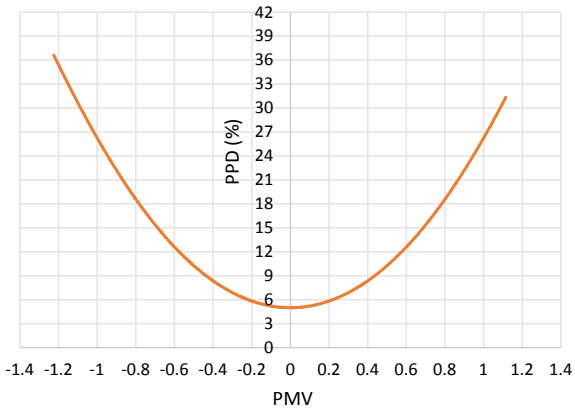

Fig. 4.4 Simulation software results

4.3.2 Analysis Led Design Results and Validation

The PMV and PPD values estimated with the help of the software were then tabulated and plotted in the form of a graph, as shown in Fig. 4.4. Simulation results yielded the minimum PMV value as −1.22 and the maximum PMV value as 1.11. These results too indicate thermally cooler conditions prevailing in the office room for most of the cases. The corresponding maximum PPD value reached is 36.61% in this case, which also indicates the percentage of people not feeling comfortable with their thermal environment.

On comparing the experimental results with that obtained from simulation, it was found that the two curves were approximately identical with each other and with the ideal PMV versus PPD curve. However, a little deviation in the outcomes was found, with the maximum deviation between the experimental and simulation results being 2.78%, which falls within the range of permissible errors, i.e., 15%. It implies the validation of the simulation results with the experimental ones. Hence, it was suggested that the simulation software could be used to proceed further with the study.

4.3.3 Passive Design Strategies for Thermal Comfort Analysis

The results of the study indicated that the thermal environment of the office room for the period of study was not favorable to the occupants, and lied in the zone of a cooler environment, with the PMV values being within −1.22 and 1.11. This is in conformity with the case that experiments were performed on an unconditioned building in the winter season. The results also concluded that the percentage of occupants not comfortable with their thermal environment was high (36.61%), suggesting that measures should be taken to bring down this value and make the indoor zone within

Table 4.4 Insulation material's properties

Material	Specific heat (kJ/kg K)	Thermal conductivity (W/m K)	Density (kg/m^3)
Cellulose foam	2.02	0.035	57
Mineral wool	0.84	0.038	40
Fiber glass	0.85	0.040	48
Polyurethane foam	1.80	0.026	30
Expanded polystyrene	1.30	0.038	15

a comfortable range. Thus, passive design strategies should be employed to the building to tend to this issue. Though numerous strategies can be applied to the building, however, this study has been conducted for incorporating provision of wall insulation, provision of roof insulation and provision of window glazing.

Provision of Wall Insulation. Insulation acts as a barrier between the ambient conditions and the indoor conditions of a space and maintains an appropriate required temperature inside in both summers as well as in winters (https://www.greenmatch.co.uk/blog/2014/08/insulation-why-is-it-important). It basically restricts the heat flow inside or outside of the space, thus, making a building energy efficient (https://www.usiinc.com/blog/insulation/why-you-should-insulate-your-walls/).

There are various insulation materials available in the market, however, the most commonly employed insulation materials are the cellulose foam, mineral wool, fiber glass, polyurethane foam and expanded polystyrene (EPS), which have been selected for the purpose of this study for analysing their effects on the comfort level of the occupants. The properties of these materials have been depicted in Table 4.4 (http://www.greenspec.co.uk/building-design/insulation-materials-thermal-properties/):

In the simulation software, the construction of the wall was changed by employing each of these insulations one by one with a constant thickness 0.04 m for the sake of drawing comparisons between these materials and their impact on the thermal comfort (Kapoor et al. 2016). Simulation was run for each of the case by providing the values of the rest of the input parameters same as that of the base case.

Figure 4.5 depicts the results of the case when cellulose foam has been used as the insulation material. It can be observed from the plot of PMV versus PPD for this material that in contrast to the base case, the minimum PMV value has reduced from −1.22 to −0.43 and the maximum PMV value has reduced from 1.11 to 0.98. This implies that provision of this insulation has led to causing the PMV range of the office room closer to the ideal range, though it still does not make for the ideal comfort conditions. However, another point to be noted in this is that in comparison to the base case, the curve has shifted towards the warmer side of the PMV scale, denoting that cellulose foam insulation of 40 mm thickness is creating a barrier for the heat inside the office room to cross and flow towards the ambient, hence,

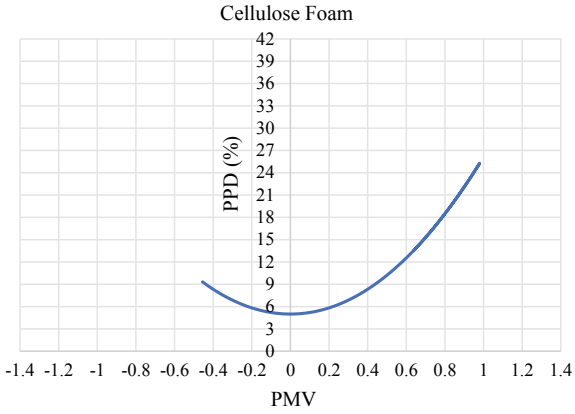

Fig. 4.5 PMV versus PPD curve for cellulose foam wall insulation

creating a zone of warmer environment. It can also be spotted that the PPD value has decreased as well, from a value of 36.61 to 25.24%, indicating that even though the environment is warmer, more percentage of occupants are feeling satisfied with their thermal environment, as during the winter season, people tend to opt for warmer indoor spaces.

Likewise, each of the material was applied to the wall construction and similar results were obtained, as that in Fig. 4.4, for each of the case, with slight deviations in the extents of the PMV and PPD ranges, which can be observed from Table 4.5. It can be established from the results that there is a reduction in the minimum and maximum PMV values in all the cases. These materials brought the range of PMV of the room closer to the ideal range, and in each of the case, curves of PMV versus PPD have shifted from a cooler side of the scale to the warmer side of the PMV scale owing to the reason that the colder conditions inside the unconditioned building due to the ambient are transforming into warmer conditions because of the restriction to the heat flow from the inside to the outside due to provision of insulation. Consequently, the PPD value too has decreased in each case. Additionally, these results also suggest that after provision of these insulating materials, people might feel discomfort because of the resulting warmer environment rather than the colder one. On comparing the results of the comfort indices for each of the insulating materials, it can be perceived

Table 4.5 Results of provision of wall insulation

Insulation material	Cellulose foam	Mineral wool	Fiber glass	Polyurethane foam	Expanded polystyrene
Minimum PMV	−0.43	−0.46	−0.45	−0.41	−0.44
Maximum PMV	0.98	0.97	0.97	1.01	0.98
Maximum PPD	25.24	25.13	24.82	26.54	25.19

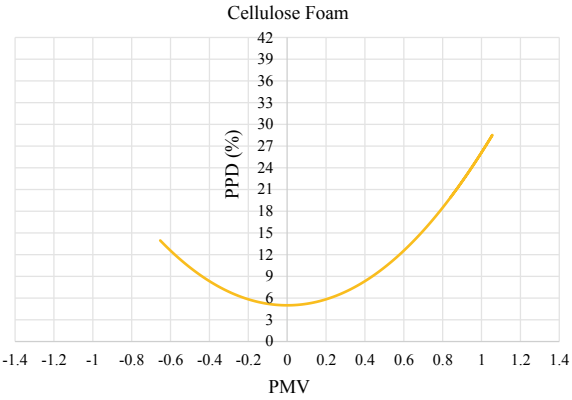

Fig. 4.6 PMV versus PPD curve for cellulose foam roof insulation

that though they are all following the same trend, still there are slight differences in the magnitude of these materials, which might be possible because of the different thermal properties they possess, as mentioned in Table 4.4. On assessing the results in these cases against each other, it is observed that the fiber glass insulation for the same thickness is performing better in improving the comfort conditions of the occupants inside the office space, as compared to the base case, while the least enhancement was seen in the case of polyurethane foam insulation.

Provision of Roof Insulation. The materials selected for studying the effect of provision of wall insulation have also been applied for analysing the effect of provision of roof insulation on the comfort of the occupants. Similar to the previous case, each of the insulation with a constant thickness of 0.04 m was applied to the existing roof construction and the rest of the input parameters same as the base case, so that their effects on the comfort levels can be analysed and compared with each other (Kapoor et al. 2016).

The results of the case when cellulose foam has been applied as the roof insulation can be seen in Fig. 4.6. The results clearly indicate an improvement in the comfort levels as against the base case. In this case, the minimum PMV value has reduced from −1.22 to −0.64, while there is only a slight reduction in the maximum PMV value from 1.11 to 1.06, implying that there is a shift in the curve towards the warmer side of the PMV scale, in comparison to the base case. This indicates that a 40 mm thick cellulose foam roof insulation is acting as a barrier between the ambient and the indoor conditions of the space, and hence, restricts the inside heat to cross and flow towards the ambient, thus, leading to a zone of warmer environment. This warmer zone, however, is still an improvement over the base case, as the maximum PMV corresponding to this zone is still less than the maximum PMV value corresponding to the warmer zone of the base case. This case also signifies that the PMV range has come closer to the ideal range, in comparison to the base case, still it is far from the ideal comfort range. In addition to this, it can be seen from Fig. 4.6 that the PPD value too has decreased from 36.61 to 28.52%, suggesting that bringing the maximum PMV value closer to ideal range has also led to a decrease in the percentage of people

feeling dissatisfied with their thermal environment, since during the winter season, people tend to opt for warmer indoor spaces.

In a similar manner, each of the material was applied to the roof construction, which yielded similar results for each of the case, as that in Fig. 4.6, but with slight variations in the maximum and minimum PMV as well as PPD values, as shown in Table 4.6. The results clearly indicate that there is a reduction in the minimum and maximum PMV values in all the cases. Each of these materials brought the range of PMV of the room closer to the ideal range, and in each of the case, curves of PMV versus PPD have shifted from a cooler side of the scale to the warmer side of the PMV scale because of the fact that the colder conditions inside the unconditioned building due to the ambient are converting into warmer conditions because of the barrier to the heat flow from the inside to the outside due to provision of insulation. Subsequently, the PPD value as well has decreased in each case. In addition to these, the results also indicate that in comparison to the base case, where occupants were uncomfortable due to the colder environment persisting inside the office room, the occupants would now feel discomfort due to resulting warmer environment persisting in the room due to the application of these insulation materials on roof. However, the percentage of people dissatisfied with their thermal environment would still be less in each of these cases, as against the base case, hence, signifying improvements in the comfort conditions. The comparison of the results of the comfort indices for each of the insulating materials demonstrate that though they are all following the same trend, there are still some minor differences in the magnitudes of these materials, which might be because of the different thermal properties they possess, as mentioned in Table 4.4. On evaluating these case results against each other, it is observed that in this case as well, the fiber glass insulation for the same thickness, is performing better in improving the comfort conditions of the occupants inside the office space, as compared to the base case, while the least enhancement was seen in the case of mineral wool roof insulation.

Provision of Window Glazing. Glazing has an impact on the flow of heat across windows in buildings as the heat is directly transferred through the window glazing, along with absorbing some portion of it which is consequently transmitted to the inside space through radiation and convection (http://www.greenspec.co.uk/building-design/windows/). Hence, the type of window and the glazing is another

Table 4.6 Results of provision of roof insulation

Insulation material	Cellulose foam	Mineral wool	Fiber glass	Polyurethane foam	Expanded polystyrene
Minimum PMV	−0.64	−0.66	−0.46	−0.64	−0.66
Maximum PMV	1.06	1.07	0.80	1.04	1.06
Maximum PPD	28.52	29.30	18.61	27.92	28.65

Table 4.7 Window glazing properties

Parameters	Solar heat gain coefficient (SHGC)	U value (W/m^2 K)	Emissivity		Solar transmittance (T)
			Internal	External	
Double pane clear glass	0.76	2.9	0.84	0.84	0.70
Triple pane clear glass	0.68	1.9	0.84	0.84	0.60
Tinted glass	0.60	5.7	0.5	0.1	0.47
Low-e glass	0.62	3.8	0.1	0.5	0.58

important parameter for analysing heat exchange through fenestrations. This study has been done considering four different types of glazing systems—double pane clear glass, triple pane clear glass, tinted glass and low-emissivity (low-e) glass, with their properties mentioned in Table 4.7 (http://glassed.vitroglazings.com/topics/how-low-e-glass-works; EQUA 2013; https://www.commercialwindows.org/tints.php).

The input parameters for each of the three windows were modified according to each of the case mentioned above and simulations were run for the cases to obtain the thermal comfort indices for each of them throughout the simulation period. Figure 4.7 represents the PMV versus PPD curve for the case of double pane windows with clear glass. The graph depicts that similar to the case of provision of wall insulation, the PMV as well as PPD values have decreased in this case too. It can be observed that the minimum PMV value has reduced from −1.22 to −0.61 and the maximum PMV value has decreased from 1.11 to 0.85. The possible reason behind this could be that its SHGC as well as transmittance value is comparatively high while its U value is comparatively lower, hence admitting the solar heat to the inside while restricting the heat from the inside to the outside. Correspondingly, the PPD value obtained in this case has also reduced from 36.61 to 20.55%. It can be seen in this case as well that the PMV as well as PPD ranges have been brought closer to the ideal ranges

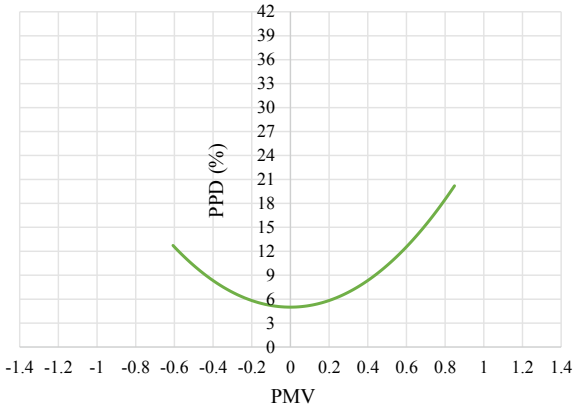

Fig. 4.7 PMV versus PPD curve for double pane clear glass window

Table 4.8 Results of provision of window glazing

Type	Double pane clear glass	Triple pane clear glass	Tinted glass	Low-e glass
Minimum PMV	−0.61	−0.59	−0.81	−0.63
Maximum PMV	0.85	0.82	1.06	0.77
Maximum PPD	20.55	19.25	28.86	17.47

recommended by standards (ASHRAE 2010; ISO 2005) and the curve dominates towards the zone of positive PMV values, making the environment comparatively warmer, and resulting in attaining a maximum PPD value because of that. However, that maximum PPD value is still approximately equal to the upper limit of the required PPD, even though the PMV value is a little beyond the maximum tolerable PMV value.

Analogously, the window properties were modified according to the cases undertaken for the study and the simulation was run for each of them. The thermal comfort indices obtained using the simulation analysis for each of the case were plotted against each other and it was noticed that the PMV versus PPD curves of the cases followed the same trend as depicted in Fig. 4.7, though with different PMV as well as PPD ranges. The results of these cases are tabulated in Table 4.8. Both the PMV and PPD values in each of the cases were observed to have comparatively shrunk down and tended towards the ideal range, with a considerable shift from a cooler environment to a warmer one. This suggests that changing the glazing type to the cases chosen can result in admitting the heat inside and restricting its flow to the ambient. Moreover, comparison of the results of these cases revealed that the difference in their magnitudes are due to the different thermal properties they possess, enlisted in Table 4.7. Comparison of results against each of the cases suggests that the low-e glass has a better performance since the maximum reduction in values were observed in this case, while minimum improvement was observed in the case of tinted glass.

4.3.4 Optimal Solution for Maximum Thermal Comfort

Implementing passive design technologies in buildings have a huge impact on the energy consumption as well as maintaining comfort of occupants. Section 4.3.3 dealt with examining the impact of different passive strategies applied to the building, for which, other parameters were kept constant as the base case, on the basis of which, a certain strategy giving the finest outcome is chosen. However, if more than one strategy is applied to a building, the result of these techniques do not just add up to each other. They have different interactions with the environment. They might behave differently when alone or when in conjunction with other parameters. Hence, the effects of these strategies should be studied when applied together in order to analyse their inter relationships and to come to a conclusion on the basis of their

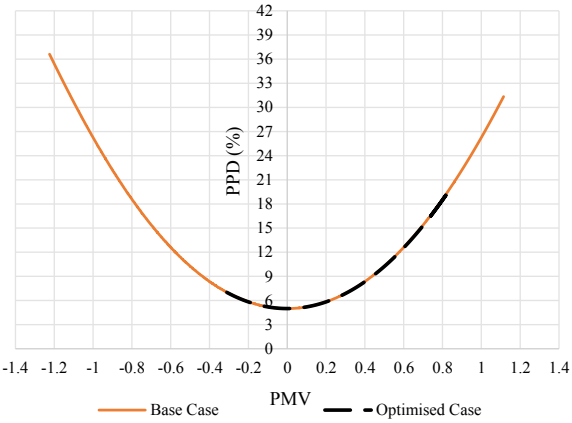

Fig. 4.8 PMV versus PPD curve for optimised case compared to base case

objectives. The study involved analysing the effect of provision of wall insulation and provision of roof insulation, both of which yielded fiber glass insulation in each of their cases as the best among other options on the basis of maximum improvement in thermal comfort of the occupants. Similarly, low-e glass windows provided better results as compared to the other cases. However, for analysing the inter relationships of these parameters, a combination of each of the type of window glazing was checked and simulated with each of the case of provision of insulations in order to maximize the thermal comfort goal. The simulation was run for the each combination and the results in the form of thermal comfort indices was obtained. On comparing the simulation results with each other, it was learnt that although individual strategies applied showed different results, but if those strategies are used in conjunction, the maximum improvement in comfort conditions was for the case of cellulose foam wall insulation with fiber glass roof insulation of 40 mm thicknesses each, along with triple pane clear glass window. The results of this case has been plotted in Fig. 4.8, which depicts that there is a reduction in the minimum as well as maximum PMV values, as compared to the base case. The minimum PMV value has reduced from −1.22 to −0.31, while the maximum PMV value has decreased from 1.11 to 0.84. It can be observed that when only individual strategies were taken into consideration, the results with respect to the type of the insulation or glazing provisions were different. However, when these strategies are combined, better results were obtained with different type of insulation and glazing combination, rendering it as an optimal solution for the cases studied. The combined effect of these strategies was that it reduced the coolness in the inside zone and brought its minimum value down to −0.31, which is within the ideal environmental condition (ASHRAE 2010; ISO 2005), whereas, while doing that, the combined strategy led to shifting of the zone more towards a warmer side for most of the instances, hence, most of the values of the curve lie on the positive side of the PMV scale. Consequently, the PPD value too dropped substantially, reaching to a value of 19.81% from 36.61%, indicating that a larger percentage of occupants would be satisfied with their thermal environment.

Moreover, this has resulted in bringing the PPD value within the range specified by standards, however, the value is nearer to the upper limit of the PPD range (ASHRAE 2010; ISO 2005). It is worth mentioning here that this forms the optimal solution for the cases explored in this study, which has tried to improve the thermal comfort conditions of the office room, still has not been successful in completely bringing it within the ideal range for a comfort zone, hence, more passive strategies should be explored and employed in order to maintain a thermally comfortable environment for the occupants.

4.4 Conclusions

Building designers should focus on the comfort requirements of the occupants as well, in addition to other goals. Employing passive design strategies can not only lead to lowering the energy requirements of the building, but can also aid in improving the thermal comfort in addition to other comfort parameters. The existing comfort level for an office room has been determined, using the PMV and PPD models, and the impact of different passive strategies on the comfort levels of the occupants have been assessed. It was observed that application of different passive technologies resulted in an improvement in the comfort conditions of the occupants. As compared to the base case, the curve of PMV versus PPD approached closer to the ideal comfort range, however, it was noticed that in each case, the curve shifted towards the positive side of the PMV scale, indicating a zone of warmer environment. This resulted from the fact that the cooler conditions inside the unconditioned building due to the ambient were transforming into warmer conditions because of the heat being admitted inside from the windows and the restriction to the heat flow from the inside to the outside due to provision of different passive techniques. This, however, is still an improvement over the base case as the maximum values of PMV as well as PPD was found to decrease, since the study was done in the winter season, during which, a warmer environment is preferred by the occupants.

An optimal solution with respect to the strategies explored in the study has been proposed for the office room under analysis, which resulted in enhancement of the comfort conditions. It has been observed that it is not necessary that the solution obtained from employing individual strategies shall correspond to the optimal solution when a combination of the different passive techniques are used. When the passive strategies were employed individually, the optimal solution for provision of wall insulation was the fiber glass insulation of thickness 40 mm, which resulted in percentage improvements of 63.11% and 12.61% on the negative and positive sides of the PMV scale respectively, and 32.20% improvement in PPD value. Optimal roof insulation, obtained with 40 mm thick fiber glass resulted in percentage improvements of 62.29% and 27.93% in minimum and maximum PMV values respectively, and 49.17% in PPD. Similarly, low emissivity glazing was yielded as the optimal solution out of the different window glazing studied, which resulted in percentage improvements of 48.36%, 30.63% and 52.28% in the values of minimum PMV,

maximum PMV and PPD respectively. However, it was observed that the comfort indices and the optimal solutions obtained in the cases when individual techniques were employed in the building were different from the optimal solution obtained when these techniques were applied in conjunction with each other. The optimised case resulted when cellulose foam wall insulation was applied with fiber glass roof insulation of 40 mm thicknesses each, along with triple pane clear glass windows, which caused the percentage improvements of 74.59% and 24.32% on the negative and positive sides of the PMV scale respectively, while 45.89% improvement in the PPD value. This shows the different behavior and interaction of these parameters with the environment and their interdependency which led to a change in the final result of the comfort indices. It has also been seen that the optimal solution on the basis of the strategies undertaken in this study though improved the conditions as compared to the base case, but were still not enough to completely transform the indoor space into a comfortable environment. Thus, additional passive strategies can be employed to bring the comfort indices within the ideal range, and hence maintain a thermally comforting environment.

Acknowledgements Authors are thankful to Global Evolutionary Energy Design (GEED), New Delhi, India, where the experimental work for this study was conducted.

References

02 Energy and Buildings (2014) New Delhi

Aryal P, Leephakpreeda T (2016) Effects of partition on thermal comfort, indoor air quality, energy consumption, and perception in air-conditioned buildings. J Sol Energy Eng 138:051005. https://doi.org/10.1115/1.4034072

ASHRAE (2010) ANSI/ASHRAE standard 55-2010, thermal environmental conditions for human occupancy, 1st edn. American Society of Heating, Refrigerating and Air-conditioning Engineers, Inc., Atlanta, Georgia, USA

Auliciems A, Szokolay SV (1997) Thermal comfort. PLEA in association with Department of Architecture, University of Queensland

Azad AS, Rakshit D, Wan MP, Babu S, Sarvaiya JN, Kumar DEVSK, Zhang Z, Lamano AS, Krishnasayee K, Gao CP, Valliappan S, Goh A, Seoh A (2018) Evaluation of thermal comfort criteria of an active chilled beam system in tropical climate: a comparative study. Build Environ 145:196–212. https://doi.org/10.1016/J.BUILDENV.2018.09.025

Berkovic S, Yezioro A, Bitan A (2012) Study of thermal comfort in courtyards in a hot arid climate. Sol Energy 86:1173–1186. https://doi.org/10.1016/J.SOLENER.2012.01.010

Calis G, Kuru M (2017) Assessing user thermal sensation in the Aegean region against standards. Sustain Cities Soc 29:77–85. https://doi.org/10.1016/J.SCS.2016.11.013

Daghigh R, Adam N, Sopian K, Sahari B (2009) Thermal comfort of an air-conditioned office through different windows-door opening arrangements. Build Serv Eng Res Technol 30:49–63. https://doi.org/10.1177/0143624408099448

EQUA (2013) User manual, IDA indoor climate and energy, version 4.6. EQUA Simulation AB, Sweden

Gadi MB (2010) Application of design and passive technologies for thermal comfort in buildings in hot and tropical climates. Mater Energy Effic Therm Comf Build 681–708. https://doi.org/10.1533/9781845699277.3.681

Greenspec: Windows: heat loss & heat gain. http://www.greenspec.co.uk/building-design/windows/. Accessed 1 Jun 2019

Haase M, Amato A (2009) An investigation of the potential for natural ventilation and building orientation to achieve thermal comfort in warm and humid climates. Sol Energy 83:389–399. https://doi.org/10.1016/J.SOLENER.2008.08.015

How low-e glass works. http://glassed.vitroglazings.com/topics/how-low-e-glass-works. Accessed 15 Feb 2017

Insulation materials and their thermal properties. http://www.greenspec.co.uk/building-design/insulation-materials-thermal-properties/. Accessed 9 Feb 2017

Insulation—why is it important? | GreenMatch. https://www.greenmatch.co.uk/blog/2014/08/insulation-why-is-it-important. Accessed 2 Jun 2019

ISHRAE (2015) ISHRAE position paper on indoor environmental quality. New Delhi

ISO (2005) Ergonomics of the thermal environment—analytical determination and interpretation of thermal comfort using calculation of the PMV and PPD indices and local thermal comfort criteria. ISO, Switzerland

Kamal MA (2012) An overview of passive cooling techniques in buildings: design concepts and architectural interventions. Acta Tech Napocensis Civ Eng Archit 55

Kapoor R, Roulet C-A, Maithel S, Bhanware P (2016) Thermal insulation of buildings for energy efficiency

Katafygiotou MC, Serghides DK (2014) Thermal comfort of a typical secondary school building in Cyprus. Sustain Cities Soc 13:303–312. https://doi.org/10.1016/J.SCS.2014.03.004

Lee JW, Jung HJ, Park JY, Lee JB, Yoon Y (2013) Optimization of building window system in Asian regions by analyzing solar heat gain and daylighting elements. Renew Energy 50:522–531. https://doi.org/10.1016/J.RENENE.2012.07.029

Liu S, Huang C, Liu Y, Shen J, Li Z (2018) Retrofitting traditional Western Hunan dwellings with passive strategies based on indoor thermal environment. J Archit Eng 24:04018017. https://doi.org/10.1061/(ASCE)AE.1943-5568.0000316

Nematchoua MK, Ricciardi P, Reiter S, Asadi S, Demers CM (2017) Thermal comfort and comparison of some parameters coming from hospitals and shopping centers under natural ventilation: the case of Madagascar Island. J Build Eng 13:196–206. https://doi.org/10.1016/J.JOBE.2017.07.014

Pazhoohesh M, Zhang C (2018) Investigating occupancy-driven air-conditioning control based on thermal comfort level. J Archit Eng 24:04018003. https://doi.org/10.1061/(ASCE)AE.1943-5568.0000295

Pourshaghaghy A, Omidvari M (2012) Examination of thermal comfort in a hospital using PMV–PPD model. Appl Ergon 43:1089–1095. https://doi.org/10.1016/J.APERGO.2012.03.010

Ravikumar P, Prakash D (2009) Analysis of thermal comfort in an office room by varying the dimensions of the windows on adjacent walls using CFD: a case study based on numerical simulation. Build Simul 2:187–196. https://doi.org/10.1007/s12273-009-9317-7

Rupp RF, Ghisi E (2017) Predicting thermal comfort in office buildings in a Brazilian temperate and humid climate. Energy Build 144:152–166. https://doi.org/10.1016/J.ENBUILD.2017.03.039

Sharma P, Azad AS, Rakshit D (2015) Quantitative evaluation of directional influence on building performance in India. In: International conference on advances in power generation from renewable energy sources (APGRES 2015), Kota, Rajasthan

SP 41 (1987) Handbook on functional requirements of a building (other than industrial buildings) (parts 1–4). Bureau of Indian Standards, New Delhi

Stamou AI, Katsiris I, Schaelin A (2007) Evaluation of thermal comfort in indoor stadiums of the Athens 2004 Olympic Games with CFD models: case of Nikea Indoor Stadium. J Archit Eng 13:130–135. https://doi.org/10.1061/(ASCE)1076-0431(2007)13:3(130)

Sushil Kumar TVK, Chandrasekar J, Moorthy SK, Sakthikala A, Arvind Bharath SR (2016) Optimization of building envelope to reduce air conditioning. Indian J Sci Technol 9. https://doi.org/10.17485/ijst/2016/v9i4/79072

Why you should insulate your walls | USI Building Solutions. https://www.usiinc.com/blog/insulation/why-you-should-insulate-your-walls/. Accessed 3 May 2019

Windows for high-performance commercial buildings. https://www.commercialwindows.org/tints.php. Accessed 29 Jan 2017

Zahiri S, Altan H (2016) The effect of passive design strategies on thermal performance of female secondary school buildings during warm season in a hot and dry climate. Front Built Environ 2:3. https://doi.org/10.3389/fbuil.2016.00003

Part II
Solar Thermal Systems: Heating

Chapter 5
Design and Development of a Concentrated Solar Water Heating System

Bandi Sai Mukesh, Ravi Teja Parella, Sudipto Mukhopadhyay and Laltu Chandra

Abstract Solar energy is a promising renewable source to support the growing energy demand. This energy is widely harnessed for solar water heating systems to provide hot water for both domestic and industrial sectors thus reducing use of conventional energy sources. In this work, a concentrated solar water heater (CSWH) system is designed and fabricated at IIT Jodhpur. The main objectives are development of a point focus based direct solar water heating system and preliminary experiment based evaluation of the designed system. The system envisages a flux concentration of 100 Suns, which will enable receiver area reduction and the use of other heat transfer fluids like oil in future. The CSWH system consists of (a) receiver and (b) parabolic dish with two-axis sun tracking provision. In the conventional solar water heater system the irradiance from sun is directly collected by the collector whereas in concentrated solar water heater the reflected irradiance is received by the receiver. The reflector consists of a reflecting surface mounted on a parabolic structure and the cavity receiver consists of consists of a serpentine copper tube exposed to concentrated irradiance. The receiver will be insulated from top in order to prevent heat loss from one of its surface. An optical model of parabolic dish and receiver has been developed using TracePro software. This model is used as reference to generate the flux density distribution. The experimental setup consists of a parabolic dish, a receiver with thermocouples, a Coriolis flow meter, pump, water tank and NI DAQ. Coriolis flow meter is used to measure the mass flow rate in the system. K-type

B. S. Mukesh · R. T. Parella · S. Mukhopadhyay
Department of Mechanical Engineering, Indian Institute of Technology Jodhpur, Jodhpur, Rajasthan 342037, India
e-mail: bandisaimukesh@gmail.com

R. T. Parella
e-mail: teja.1@iitj.ac.in

S. Mukhopadhyay
e-mail: smukhopadhyay@iitj.ac.in

L. Chandra (✉)
Department of Mechanical Engineering, IIT BHU, Varanasi 221 005, India
e-mail: chandra.mec@iitbhu.ac.in

H. Tyagi et al. (eds.), *Solar Energy*, Energy, Environment, and Sustainability, https://doi.org/10.1007/978-981-15-0675-8_5

thermocouples are attached on to the receiver and the temperature is recorded using NI DAQ system. The theoretical geometric concentration ratio predicted is 115 but from the experiment a flux concentration ratio 94 is measured.

5.1 Introduction

Solar energy is a promising renewable source to meet the growing energy demand. From the direct normal irradiance (DNI) map of India the abundance of solar radiation in Rajasthan, Gujarat, and Ladakh is obvious with an availability of more than 5.5 kWh/m^2/day NREL (2019). This energy can be harnessed for solar water heating systems to provide hot water for both domestic and industrial sectors which will reduce the electrical energy consumption. The solar water heater has many advantages, such as negligible global warming potential, lower payback period, ease of manufacturing, and less maintenance Singh et al. (2016).

A large variety of solar water heater designs exist each with its own set of advantages and disadvantages. Flat plate solar water heaters consist of pipes welded onto a metal plate collector, which is placed inside a rectangular case covered by a glass with efficiency as high as 44% Ayompe and Duffy (2013a). Sae-Jung et al. (2015) conducted experiments on a thermos-syphon based solar water heater, which resulted in enhanced efficiency of 56%. Evacuated tube collectors consist of glass vacuum-sealed metal absorber tube. Ayompe and Duffy (2013b) studied the thermal performance of solar water heating system with evacuated heat-pipe tubular collector and achieved efficiency of 62%. In general, evacuated tube collectors have higher efficiency in comparison to flat-plate collectors. Diego-Ayala and Carrillo (2016) compared performance of flat-plate water heating systems with thermos-syphon and forced flow. They reported higher efficiency with forced flow in comparison to thermos-syphon based system. Kakaza and Folly (2015) compared the alternative energy sources to be provided for a particular demand. Results revealed that heat pump based solar water heaters have short payback period even though the initial investment is high. Papadimitratos et al. (2016) developed a new design by integrating evacuated tube solar collectors with phase change material (PCM) based thermal energy storage. Here, heat pipe is immersed inside the phase change material, where heat is effectively accumulated and stored for an extended period of time. Evacuated tube collectors also have better thermal insulation in comparison to a flat-plate collector, which enhances the overall efficiency. The efficiency of the Dual-PCM solar water heater system has increased 26% compared with standard system. Xue (2016) reported experimental investigation of a domestic solar water heater coupled with phase change material based energy storage. Robles et al. (2014) conducted experiments on a non-evacuated aluminium based mini channel solar water heater, which resulted in an average increase in thermal efficiency of 13% compare to flat plate collector. Deng et al. (2015) presented a novel flat plate solar water heater using micro heat pipe array sprayed with solar selective coating and arranged closely as the absorber of collector.The experiment was conducted on a 2 m^2 flat plate collector

and showed an efficiency of 64.25%. Some of the involved process parameters are summarized in Table 5.1. Currently flat-plate solar water heater systems are widely utilized. However, flat plate collectors suffer from disadvantages like occupying more roof area and are corrosion prone. This has led to design and development of concentrated solar heating systems.

In concentrated solar water heating systems, compound parabolic concentrators (CPCs) are one of the majorly used collectors for domestic water heating purposes after conventional flat plate collectors. Hadjiat et al. (2018) proposed design and analysis of a novel integrated collector storage (ICS) solar water heater. The system consists of CPC reflectors where solar collector and water storage are integrated as single unit with the geometric concentration ratio of collector being around 1.22 and the highest temperature of water in tank is around 50 °C. Benrejeb et al. (2015) proposed an ICS solar water heater system with improved optical and thermal efficiencies. The geometric concentration ratio was improved from 1.05 in old design to 1.34 in new design and the highest temperature attained was 65 °C. Harmim et al. (2019) proposed a design of ICS solar water heater for integration into building facade. A linear parabolic reflector was used as concentrator, with the maximum water temperature obtained varying from 40 to 49 °Cand the geometric concentration ratio reported is 3.3. Chong et al. (2012) investigated solar water heater using stationary V-trough collector. The geometry is simpler as compared to that of a CPC. The set up was designed for solar concentration ratio of 1.8 suns whereas from the experiments it achieved a concentration ratio of 1.41 suns and the highest water temperature attained in the tank is 85.9 °C. Rajamohan et al. (2017) carried out analysis on a solar water heater with parabolic dish concentrator and a conical absorber. Water is the working fluid, and as solar radiation is concentrated onto the absorber the water in the absorber evaporates and converts into vapor phase. The vapor is passed into a heat exchanger where heat transfer between vapor and fresh cold water occurs with the vapor condensing to liquid phase. The working fluid returns to the bottom of the conical absorber under gravity and continues as a cyclic process inside the system. The highest water temperature achieved is 65 °C and the average system efficiency achieved is 55.40%. The available literature in concentrated solar water system is not abundant. Further, design of simple systems which can be easily fabricated and can produce a high concentration ratio is desirable. In this work, a concept of concentrating solar water heating (CSWH) system is proposed and evaluated. This system is expected to be versatile with multifaceted applications such as:

- Reduce the rate of heat loss by means of reducing the surface area while keeping the water temperature comparable to conventional systems. This is expected to increase the overall system efficiency.
- The proposed CSWH system envisages a flux concentration of about 100 Suns. This may allow in future evaluation of other heat transfer fluids like oil by elevating the operating temperature.
- The reduction of receiver area may allow implementation of such a system in cold deserts or high-altitude by mitigating the freezing related issues.

Table 5.1 Parameters of various solar water heater systems

Reference/ parameters	AP16 Papadimitratos et al. (2016)	AR14 Robles et al. (2014)	SX16 Xue (2016)	UDA16 Diego-Ayala and Carrillo (2016)	LMA13 Ayompe and Duffy (2013a)	AD13 Ayompe and Duffy (2013b)	SJ15 Sae-Jung et al. (2015)
Power output, P_{out} (kW)	0.4	1.8	0.5	0.5	1	1.2	0.8
Power input, P_{in} (kW)	1.5	2.6	0.8	1.1	2.4	2.1	1.4
Solar irradiance, q'' (W/m^2)	947	822	700	1200	633	701	700
Inlet temperature, T_i (°C)	25–42	28–53	16–35	40	23–60	23–51	44
Outlet temperature, T_o (°C)	33–50	33–58	21–40	48.6	28–66	29–57	69
Ambient temperature, T_a (°C)	25	25	16	26	19	16	34
Thermal efficiency, η (%)	27.8	68	56.8	47	44	56	56.4
Mass flow rate, $\dot{m}$ (kg/s)	0.0126	0.109	0.02	0.014	0.047	0.047	0.008
Tube diameter, D (mm)	–	1.42	8	16	12	–	–
Length of tube (mm)	–	2912	1800	–	–	–	1800
Collector area (m^2)	1.6	3.2	1.27	0.9	4	3	2.16

Most of the CSWH systems reported in literature are mostly based on a parabolic trough concentrator with oil as working fluid to best of our knowledge. Water is used as the secondary fluid, which is indirectly heated via a thermal energy storage, see e.g. Prasartkaew (2018). In the proposed system, water serves as heat transfer fluid as well as the storage. Thus, the present system is different and more compact.

With the above mentioned objectives, the design of the proposed CSWH system is discussed followed by the experimental set up description. Finally results of the experiments are presented.

5.2 Design of Concentrated Solar Water Heating System

The CSWH system consists of a receiver and a parabolic dish with two-axis sun tracking mechanism. The schematic of the proposed receiver assembly is shown in Fig. 5.1. In conventional solar water heater system, the irradiance from sun is directly collected by the collector whereas in concentrated solar water heater the irradiance reflected from the reflector is received by the receiver. Thus, the amount of heat flux incident on the receiver in CSWH is greater than that collected by the collector in conventional solar water heater. A parabolic dish reflector consists of a reflecting surface mounted on a parabolic profile reflector. The surface of parabolic dish is covered with aluminum foil which is a good reflector available at low cost. A two-axis sun tracking system mechanism tracks the sun such that the sunrays are always incident normally on the parabolic reflector. The reflected DNI from the parabolic dish reflector is concentrated onto the focal point of parabolic dish where the receiver is placed to heat the water. The area of receiver is 400 cm^2, which is substantially lower compare to flat-plate solar collector, which is typically around 2–3 m^2 for similar thermal power. The receiver has square-shaped aperture of 20 cm × 20 cm. Thus, the thermal losses will be reduced substantially as compared to a flat-plate type system under the same operating conditions.

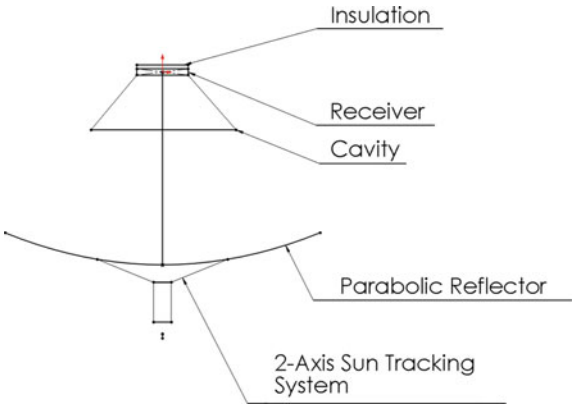

Fig. 5.1 Schematic of concentrated solar water heating (CSWH) system

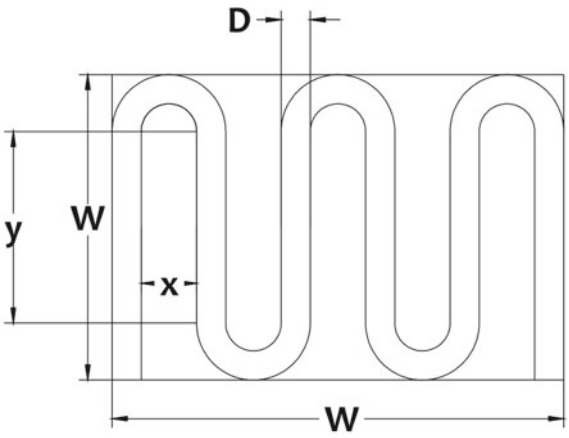

Fig. 5.2 Top view of serpentine tube receiver

Figure 5.2 depicts the proposed receiver assembly comprising of serpentine tubes inside a cuboid shaped receiver. The selection of receiver dimension is based on a preliminary analysis of the spot size of concentrated solar irradiance from parabolic dish. The receiver will be insulated from top in order to prevent heat loss from one of its surface. The serpentine tube and receiver is made of copper with high thermal conductivity of 401 W/mK at 300 K Incropera (2006). For higher absorption of solar flux, the serpentine pipe is painted with black colour whose absorptivity is 0.98 Incropera (2006). The entire receiver is enclosed inside a cavity made up of glass as depicted in Fig. 5.1. Due to the presence of cavity the ambient air will not be in direct contact with the base of the receiver where the reflected irradiation is concentrated. This will reduce losses by convective heat transfer. The glass may be coated with a solar selective anti-reflective coating to reduce transmission of reflected thermal radiation. Such a design is envisaged to be useful for high-altitude areas with low ambient temperature, to avoid reaching freezing point temperature of water.

According to the NASA Surface meteorology, the monthly averaged DNI is 5–6 kWh/m^2/day NREL (2019) in desert and high-altitude regions of India. Taking 9 hours of effective sun per day, the average solar irradiation on the dish is more than 600 W/m^2. In CSWH, the geometric concentration ratio (C) is defined as the ratio of reflector (A_{pd}) to the receiver area (A_R) as given in Eq. (5.1). In the present case, $C \sim 115$ and the corresponding heat flux onto receiver is given by Eq. (5.2).

$$C = \frac{A_{pd}}{A_R} \tag{5.1}$$

$$q''_R = C \times q''_{pd} \tag{5.2}$$

5.2.1 Parabolic Dish Design

The parabolic dish reflector is designed for an input power of 2 kW thermal power i.e. the reflector area collects 2 kJ/s from DNI. Aluminum foil used as the reflector material on the dish has a reflectivity 0.85. For an average DNI 641.1 W/m^2, the required minimum area of reflector is 4.3 m^2. For a parabolic dish with aperture of W = 2.4 m and focal length f = 1.5 m where long focal length is chosen such that the shadow effects are minimized, the depth of the parabolic dish Z_R is calculated as 0.24 m using Eq. (5.3).

$$f = \frac{W^2}{16 Z_R} \tag{5.3}$$

The central role of the parabolic dish in solar concentrator systems is its ability to focus parallel rays to a point, at distance f from its vertex as shown in Fig. 5.3. The rim angle ϕ_R is the angle between the axis and a line from the focus to physical edge of the concentrator. Together the focal length and rim angle of a parabolic concentrator completely define its cross-sectional geometry. The rim angle (ϕ_R) is given by

$$\tan \phi_R = \frac{0.5W}{f - Z_R} \tag{5.4}$$

where W is the width of parabola and Z_R is the depth of the parabola.

The parabolic effect of focusing to a single point only occurs with perfectly parallel incoming rays. Each point on the parabolic mirror will reflect a cone of rays that matches the angular distribution of the solar source (half angle size θ_s). The size of the spot formed by the cone of rays reflected from the points on the mirror, when incident on a flat target placed in the focal plane is shown in Fig. 5.3. The rays from the rim will form the widest spot on the flat receiver. The reflected cone from the

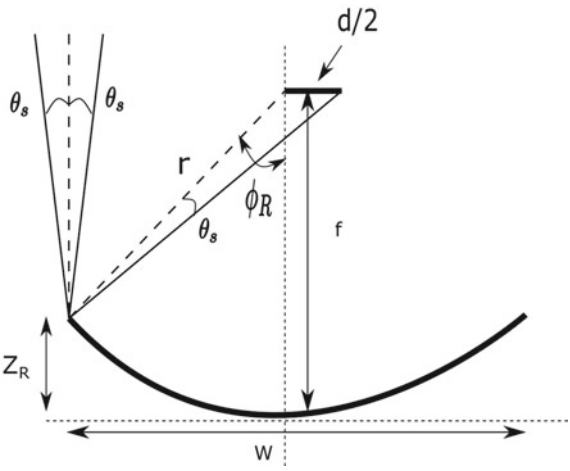

Fig. 5.3 Parabolic dish with ray tracing for calculation of spot diameter on the receiver

single spot on the mirror will actually form an elliptical spot on the target with a major axis length of d Lovegrove and Pye (2012). The width of the focal spot on the focal plane is given by Eqs. (5.5) and (5.6)

$$d = \frac{2P \sin\theta_s}{\cos\phi_R} \tag{5.5}$$

where

$$P = \frac{0.5W}{\sin\phi_R} \tag{5.6}$$

A parabolic dish of focal length (f) = 1.5 m, aperture (W) = 2.4 m and depth of parabola (Z_R) = 0.24 m has been designed with a collector aperture area of ~4.6 m^2. This gives an input power of ~2.5 kW. For the calculation of input power an average irradiance of 641.1 W/m^2 is taken. The sun rays reflected from the parabolic dish is concentrated onto the receiver. These rays form an elliptical spot. Taking the value of angular distribution of the solar source (half angle θ_s) as 0.0046 rad, and using Eq. (5.4), ϕ_R comes out to be 0.76 rad. Now using Eq. (5.5), the width of the focal spot obtained is 2.25 cm. To increase the width of spot on the receiver, flexibility is provided in the design for a movement of 5–10 cm along the vertical direction. The optical model as shown Fig. 5.4 is designed using TracePro software to calculate the receiver travel so that the width of the spot is 20 cm.

The solar radiation incident on the parabolic dish is reflected on to the receiver at the focus. This model is used as reference to generate flux density distribution. Figure 5.5 shows the flux distribution and width size at focal point i.e., receiver is placed at 1.5 m vertical from the vertex of parabolic dish. To get a spot of width 20 cm, the receiver is moved down by ~10 cm. The spot of width 20 cm covering the receiver

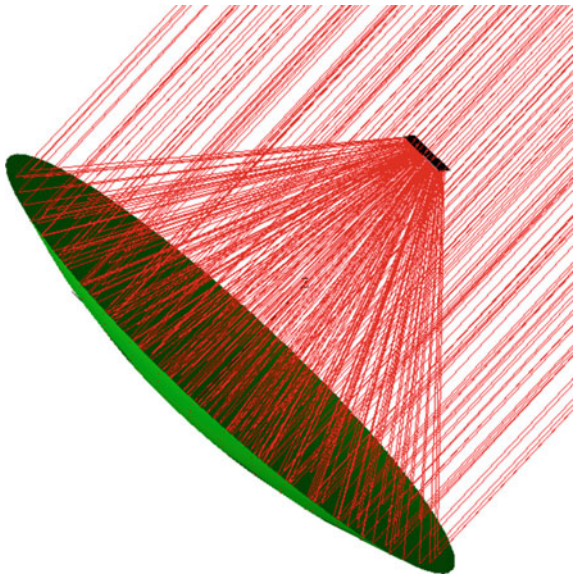

Fig. 5.4 Optical model for ray-tracing

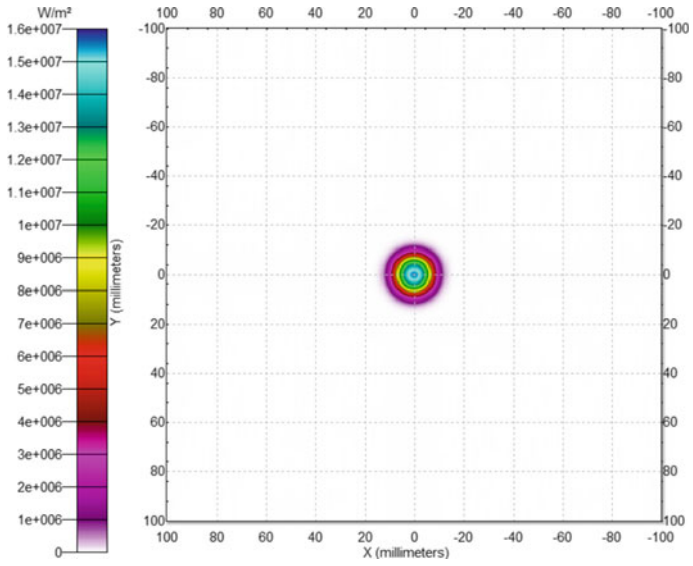

Fig. 5.5 Flux distribution on receiver at focus

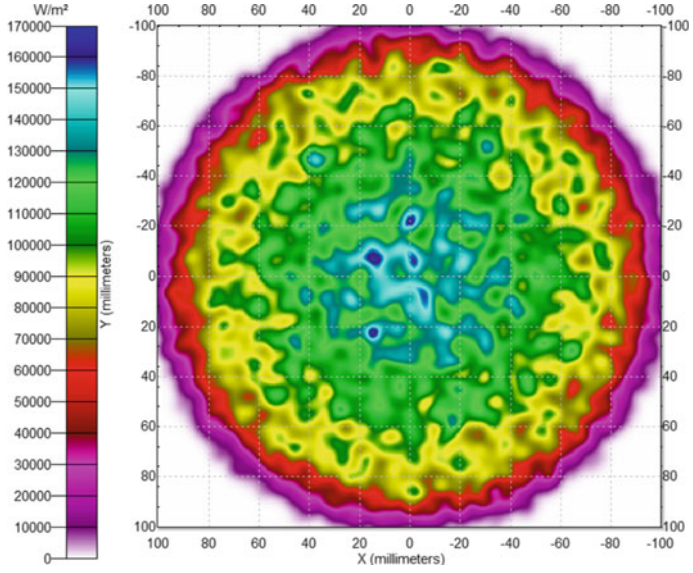

Fig. 5.6 Gaussian flux distribution on the receiver

is shown in Fig. 5.6. In parabolic collector based systems, the flux concentrating on to the receiver is not constant, the flux is distributed on the surface with a Gaussian profile. The Gaussian flux distribution on the surface of the receiver is shown in Fig. 5.6 having a spot diameter of 20 cm which is modeled in the ray tracing software, TracePro. It is observed from Fig. 5.6 that the flux at the center of the receiver surface is high and decreases with the increasing radius of spot. Here all the TracePro simulations are done for average DNI of 641.1 W/m^2 for Jodhpur.

5.2.2 Receiver Design

As shown in Fig. 5.2, the receiver consists of a serpentine tube. The surface of the receiver, which is exposed to concentrated solar irradiance, is 20 cm × 20 cm in dimensions. Let, the outer diameter of pipe be D_o = 10 mm. Thus, maximum of 20 parallel pipes can be fitted on receiver with surface area of 20 cm × 20 cm. However, the direct contact of pipe must be avoided to allow flow development and heating up with distance. Consequently, there must be a gap between these pipes. For n number of parallel pipes there will be $n - 1$ number of gaps in the serpentine tube receiver as in Fig. 5.2, let x is the size of gap between the pipes, y is the length of the parallel pipes with uniform spacing. Therefore, the total length of receiver is given by:

$$D_o n + x(n-1) = 20 \tag{5.7}$$

$$y + x + 2D_o = 20 \tag{5.8}$$

The total length of pipe is given by:

$$L = ny + (n-1)\frac{\pi}{2}(x + D_o) + x + 2D_o \tag{5.9}$$

For the current purpose Re_D >5000 is considered in view of turbulent flow and the associated higher heat transfer compared to laminar flow. This will mitigate to some extent the heat loss by reduced surface temperature of copper pipe. The temperature difference between the inlet and outlet of the receiver for a total tube length of L is given by Eq. (5.6) Incropera (2006) and the efficiency of CSWH is given by Eq. (5.11).

$$\Delta T = \frac{q''_R \pi D_o L}{\dot{m} c_p} \tag{5.10}$$

$$\eta = \frac{\dot{m} c_p \Delta T}{q'' A_{pd}} \tag{5.11}$$

Table 5.2 Variation of ΔT with length of pipe

n	gap, x(mm)	Length, L(m)	ΔT(°C) for $\dot{m}$ = 0.03 kg/s	ΔT(°C) for $\dot{m}$ = 0.035 kg/s
11	9.5	2.2	9	7.6
12	7.8	2.4	9.7	8.3
13	6.3	2.6	10.5	9
14	5.1	2.8	11.3	9.7
15	4.1	3.0	12.2	10.4

Table 5.3 Receiver geometry design parameters

Parameter	Value
width of absorber, w	20 cm
Length of pipe, L	2.6 m
Outer diameter of pipe, D_o	9.525 mm
Inner diameter, D_i	7.747 mm
No of loops, n	13

Table 5.2 shows the variation of temperature rise with length of pipe. The length of 2.6 m is chosen for the design as it gives a temperature rise of 10 °C and also for ease of manufacturing of the serpentine receiver. The parameters of serpentine receiver are shown in Table 5.3.

5.3 Manufacturing of CSWH

The development of the CSWH system involved the fabrication of parabolic dish, copper tube receiver, selection of required accessories and assembling the system. At first, mild steel strips with the required co-ordinates are forged and assembled into a parabolic skeleton. Channels are fitted on to the skeleton and aluminium sheets (reflectivity 0.85) are fixed on the channels with screws, forming the parabolic dish of required depth and aperture. The receiver is made by using copper tube. A copper tube of length 2.6 m and outer diameter 9.525 mm is cut and brazed with elbows to form the required shape according to the design specifications. The receiver is insulated with a pack of glass wool on the backside. A cavity is made with aluminium sheets on the receiver to reduce the losses and increase efficiency. Cavity receiver is mounted on to the parabolic dish with steel angles. Manual tracking mechanism is incorporated on the parabolic dish for tracking the sun. Hose pipes of diameter 12.7 mm are used to connect the inlet and outlet of the receiver to the reservoir tank of capacity 200 L. An electric pump is installed for circulating the water in the system along with a seat valve to control the mass flow rate at the inlet (Figs. 5.7 and 5.8).

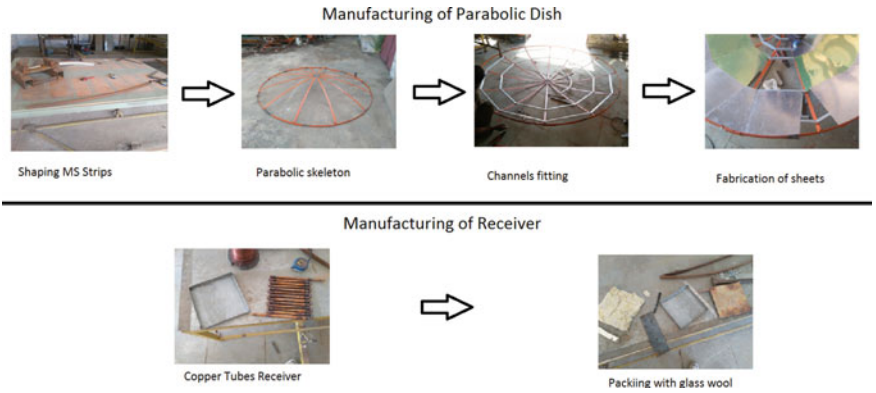

Fig. 5.7 Manufacturing of parabolic dish and receiver

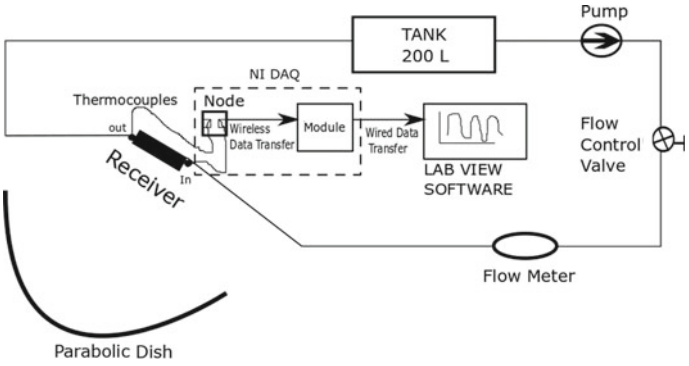

Fig. 5.8 Experimental layout of concentrated solar water heating (CSWH) system

5.4 Experimental Setup

The experimental setup consists of a parabolic dish, a receiver with thermocouples, a Coriolis flow meter, a 0.5 hp pump, 200 L tank and data acquisition system (make NI). Coriolis flow meter is used to measure the mass flow rate in the system. The K-type thermocouples are attached on to the receiver and the temperature is recorded using NI DAQ system. The water is pumped using a 0.5 hp pump from the reservoir filled with 200 L of water and mass flow rate is controlled using a seat valve. The mass flow rate in the experiment is 0.03 kg/s and the parabolic dish is tracked manually with respect to sun. Solar radiation is reflected by the parabolic dish on to the receiver and this radiation is absorbed by the serpentine copper tubes. The water is kept circulating inside the copper tubes with the help of pump. The heat transfer takes place between the copper tube and the water flowing through it and the temperature rises. It is to be noted here that the system is single pass and hence the temperature rise is limited by that. The serpentine pipe is coated with black paint for higher

absorptivity. The storage tank is also an insulated tank to minimize the heat loss to the ambient. The experiment is carried out from 4:05 p.m. to 5:15 p.m. in the month of April at IIT Jodhpur and the DNI data at the time of experiment is obtained from the DNI measuring station at IIT Jodhpur. The experiments are performed manually by aligning the dish at an interval of 15 min following the shadow of receiver at the center of dish. The day time was selected in view of clear sky, low wind speed and low dust condition. Further, experiments at different times of day will be conducted in future. The actual experimental setup and the zoomed in view of the focused receiver is shown in Fig. 5.9.

5.5 Results and Discussions

From the DNI data on 16-04-2017, the measured average flux is 322.08 W/m^2 (from 4:25 p.m. to 4:30 p.m.). The ambient temperature at the time of the experiment is 314 K and and mass flow rate of water is 0.03 Kg/s. It is observed in the experiments that the spot size on the receiver is 30 cm, which is larger than the theoretical spot size. So reflectors are folded about the receiver as shown in Fig. 5.9 which resembles a cavity to reflect the solar radiation on the serpentine copper tube. The outlet temperature and inlet temperature of fluid obtained from the experiment is shown in Fig. 5.10. It must be mentioned here that since the system is single pass, the outlet temperature attained is relatively low. The highest temperature difference between inlet and outlet attained is 6.6 and the average temperature difference is 6 °C. A multipass system can easily produce hot water for domestic use within reasonable time duration. The flux estimated from the water inlet and outlet experimental temperatures is 30.58 kW/m^2. In the experiments, the power input to CSWH is around 1.4kW and the efficiency of CSWH excluding the pump power is 59%.

Fig. 5.9 Parbolic dish and receiver with zoomed in view of receiver

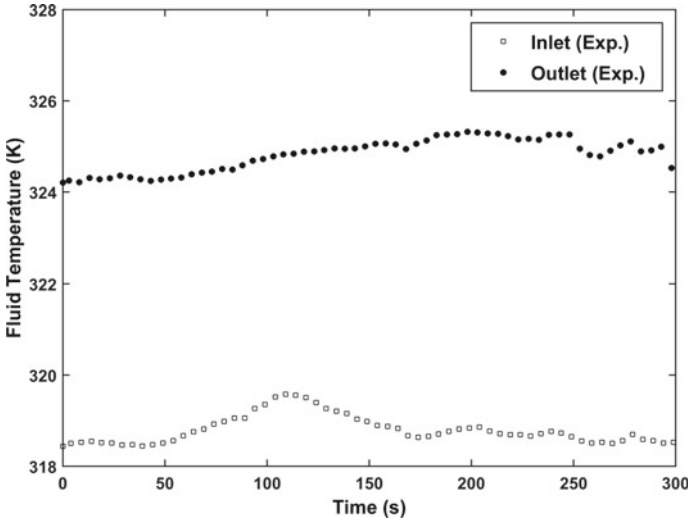

Fig. 5.10 Inlet and outlet temperature from the single pass CSWH system

The theoretically predicted geometric concentration ratio is 115 but from the experiment the flux concentration ratio obtained is 94. The obtained outlet experimental temperature can be used for validation of the numerical model of this system.

5.6 Conclusions

A concept of concentrated solar water heater (CSWH) system is proposed, designed and developed from easily available and low cost materials. This is based on the point focusing concept using parabolic dish onto a small receiver. This aims to reduce the exposed surface area of receiver to ambient and thus, reduce heat loss. The presented CSWH system shows a thermal efficiency of about 59% at a lesser power input and smaller HTF mass flow rate as compared to system LMA13 as in Table 5.1 Ayompe and Duffy (2013a), which is a non-concentrating solar water heating system with thermal efficiency of 44%. The theoretical geometric concentration ratio is 115 and from the experiments conducted a flux concentration ratio of 94 is obtained. The first level design with the measured efficiency of about 59% compares well with that of the existing systems. Further improvements are foreseen with a cavity to mitigate the direct heat loss. Due to the ease of the fabrication, easy availability of the materials used and low cost the presented CWSH system can be widely used.

References

Ayompe L, Duffy A (2013) Analysis of the thermal performance of a solar water heating system with flat plate collectors in a temperate climate. Appl Therm Eng 58(1–2):447–454

Ayompe L, Duffy A (2013) Thermal performance analysis of a solar water heating system with heat pipe evacuated tube collector using data from a field trial. Solar Energy 90:17–28

Benrejeb R, Helal O, Chaouachi B (2015) Optical and thermal performances improvement of an ics solar water heater system. Solar Energy 112:108–119

Chong K, Chay K, Chin K (2012) Study of a solar water heater using stationary v-trough collector. Renew Energy 39(1):207–215

Deng Y, Zhao Y, Quan Z, Zhu T (2015) Experimental study of the thermal performance for the novel flat plate solar water heater with micro heat pipe array absorber. Energy Procedia 70:41–48. International Conference on Solar Heating and Cooling for Buildings and Industry, SHC 2014

Diego-Ayala U, Carrillo J (2016) Evaluation of temperature and efficiency in relation to mass flow on a solar flat plate collector in mexico. Renew Energy 96:756–764

Hadjiat M, Hazmoune M, Ouali S, Gama A, Yaiche M (2018) Design and analysis of a novel ics solar water heater with cpc reflectors. J Energy Storage 16:203–210

Harmim A, Boukar M, Amar M, Haida A (2019) Simulation and experimentation of an integrated collector storage solar water heater designed for integration into building facade. Energy 166:59–71

Incropera FP (2006) Fundamentals of heat and mass transfer. Wiley

Kakaza M, Folly K (2015) Effect of solar water heating system in reducing household energy consumption. IFAC-PapersOnLine 48(30):468–472. 9th IFAC Symposium on Control of Power and Energy Systems CPES 2015

Lovegrove K, Pye J (2012) 2 - fundamental principles of concentrating solar power (csp) systems. In: Lovegrove K, Stein W (eds) Concentrating solar power technology. Woodhead Publishing Series in, Energy, Woodhead Publishing, pp 16–67

NREL. *DNI Map of India*

Papadimitratos A, Sobhansarbandi S, Pozdin V, Zakhidov A, Hassanipour F (2016) Evacuated tube solar collectors integrated with phase change materials. Solar Energy 129:10–19

Prasartkaew B (2018) Efficiency improvement of a concentrated solar receiver for water heating system using porous medium. In: IOP conference series: materials science and engineering, vol 297, Jan, p 012059

Rajamohan G, Kumar P, Anwar M, Mohanraj T (2017) Analysis of solar water heater with parabolic dish concentrator and conical absorber. In: IOP conference series: materials science and engineering, vol 206, Jun, p 012030

Robles A, Duong V, Martin AJ, Guadarrama JL, Diaz G (2014) Aluminum minichannel solar water heater performance under year-round weather conditions. Solar Energy 110:356–364

Sae-Jung P, Krittayanawach T, Deedom P, Limmeechokchai B (2015) An experimental study of thermo-syphon solar water heater in thailand. Energy Procedia 79:442–447. 2015 International Conference on Alternative Energy in Developing Countries and Emerging Economies

Singh R, Lazarus IJ, Souliotis M (2016) Recent developments in integrated collector storage (ics) solar water heaters: a review. Renew Sustain Energy Rev 54:270–298

Xue HS (2016) Experimental investigation of a domestic solar water heater with solar collector coupled phase-change energy storage. Renew Energy 86:257–261

Chapter 6
Multi-objective Performance Optimization of a Ribbed Solar Air Heater

Naveen Sharma and Rajesh Choudhary

Abstract To achieve maximum thermohydraulic performance, by maximizing the heat transfer and minimizing the pumping power, for a ribbed solar air heater, a Taguchi method has been used to predict the optimal set of design and flow parameters. An L_{16} (4^3) orthogonal array is selected as an investigational plan to perform the computational fluid dynamics (CFD) simulations for investigating the effect of design parameters, i.e. Reynolds number (4000–16000), rib pitch to height ratio (3–12), and rib geometry due to change in inclination angle of front face of the rib ($\alpha = 45°–90°$) on the effectiveness of a solar air heater. Nusselt number, friction factor and thermohydraulic performance are considered as performance indexes, and the minimization of pumping power (minimum pressure drop) and the maximization of heat transfer and overall performance are taken as the optimization criteria. Results show that Reynolds number has the greatest influence on the heat transfer as well as thermohydraulic performance, while rib spacing on the friction factor ratio. The best combinations of design factors for heat transfer, pressure drop, and thermohydraulic performance are $A_4B_4C_1$, $A_4B_1C_1$, and $A_1B_4C_1$, respectively. Numerical results validate the aptness of the proposed methodology, so, this investigation suitably offers an improved rib design for internal fluid flow investigations related to effective heat transfer applications.

Keywords Computational fluid dynamics · Heat transfer · Pumping power · Optimization · Solar air heater · Thermohydraulic performance

6.1 Introduction

In today's scenario, the demand of energy is increasing continuously owing to the industrial development and increasing population. With limited and rapidly decreasing conventional energy sources, the supply of consistent and continual energy has

N. Sharma (✉)
DVR & Dr. HS MIC College of Technology, Kanchikacherla, A.P 521180, India
e-mail: sharma.naveen28@yahoo.com

R. Choudhary
Lovely Professional University, Phagwara, Punjab 144411, India

H. Tyagi et al. (eds.), *Solar Energy*, Energy, Environment, and Sustainability, https://doi.org/10.1007/978-981-15-0675-8_6

turned into a global concern. Therefore, use of renewable energy sources and designing compact and efficient thermal systems are urgent requirements to have a sustainable future. Solar air heater (SAH), act as heat exchangers, uses solar energy to produce low to moderate temperatures which have a number of applications such as solar water heaters, in preserving industrial and agricultural products and heating/cooling of buildings (Siddhartha et al. 2012). Admittedly, the solar air heaters have simple design and easy operation, but also have fewer problems, for instance, such as less heat storage capacity and low performance. Therefore, substantial efforts are required to make these thermal systems more appropriate and cost-effective.

For improving the performance of heat exchanging devices, the researchers and scientists working in the pertinent field have suggested numerous heat transfer enhancement (active/passive) techniques (Webb 1994). Generally, heat transfer enhancement techniques such as rib turbulators, winglets and extended surfaces control the flow passively and cause turbulence in the near wall region which leads to reduction in the thermal resistance compared to a conventional heat exchanger and provide enhanced heat transfer. Along with enhanced heat transfer rates, the pressure penalty also increases with the introduction of rib turbulators (Tariq et al. 2018). These conflicting perspectives motivate the researchers and designers to find the solution how much should be the modification required in the rib geometry for achieving the best performance. Significant amount of research activity has been devoted to the understanding of detailed heat transfer and fluid flow in rib turbulated ducts for different applications (Kumar et al. 2019; Sharma et al. 2018; Jin et al. 2019). Nowadays, researchers have more focused towards employing soft computing approaches such as ANN, RSM, Jaya algorithm, GA, and Taguchi method for selecting optimal blends of design parameters in different heat transfer applications (Rao et al. 2018; Aidinlou and Nikbakht 2017; Sharma et al. 2017; Nagaiah and Geiger 2019).

It is evident that for predicting the optimal sets of design factors corresponding to maximum heat transfer, minimum friction factor and highest thermohydraulic performance, there is no need to perform all the simulations/experiments ($a^n = a \times a \times \ldots n$ times). Conducting all the experiments/CFD simulations consumes too much time and also costly affair; but, the Taguchi method effectively predicted the optimum values with a few experiments/simulations and short span of time. Therefore, in the present work also Taguchi method has been successfully applied with a very limited number CFD simulations for prediction of the best sets of design parameters.

Numerous investigations have been performed to design and optimize the design parameters of heat exchangers mounted with ribs, wire inserts, fins for various heating/cooling applications using Taguchi Method (Yun and Lee 2000; Bilen et al. 2001; Wang et al. 2009; Aghaie et al. 2015; Chamoli 2015; Caliskan et al. 2016; Kotcioglu et al. 2018; Sahin et al. 2019). Yun and Lee (2000) systematically analyzed the influence of slit fins on the aerothermal characteristics using the Taguchi method. Four design parameters among considered eight parameters have significant contributions, i.e. 39%, 28%, 20% and 9% contributions of fin pitch, slit pattern angle, length and height of the slit, respectively, on the performance of the slit finned heat exchanger. The contribution of Reynolds number and rectangular block positions, i.e. angular displacement, span wise and stream wise disposition, placed on a heat

transferring surface on heat transfer enhancement have been studied using Taguchi Method (Bilen et al. 2001). The most significant parameter influencing heat transfer is the Reynolds number, which is followed by the turning angle of the block. It was also reported that the heat transfer rate increases with increasing Reynolds number and turning angle of the block. The cooling effectiveness of a reactor with/without noise sinking shield was studied by Wang et al. (2009) for avoiding the overheating problem using a systematic CFD-Taguchi approach. The radius of the bottom and the top opening of noise reducing cover are found to be the most significant with contribution ratios of 49.5% and 23%, respectively, to the natural convection cooling performance. The performance of a ribbed SAH was studied by Aghaie et al. (Aghaie et al. 2015) using CFD-Taguchi approach at a Reynolds number of 10000. The authors optimized a general rib geometry, which can produce triangular, trapezoidal and rectangular geometries by varying its parameters, while considering maximization of thermal performance as the criteria of optimization. It was found that relative rib pitch and height have the greatest influence on performance improvement. Triangular rib geometry was found to be the optimum configuration. Chamoli (Chamoli 2015) optimized different design parameters, i.e. Reynolds number (Re), open perforation ratio (β), relative baffle height (e/H) and relative baffle pitch (p/e), of a rectangular duct roughened with perforated V-down baffle. Maximum heat transfer and minimum friction factor conditions were found at p/e = 2, e/H = 0.4, β = 12%, Re = 18600 and p/e = 4, e/H = 0.285, β = 44%, Re = 14800 respectively. Caliskan et al. (2016) studied the impact of design parameters on heat transfer distribution for a surface attached with V-shaped and convergent-divergent shaped ribs. Results revealed that Reynolds number was the most dominant factor influencing heat transfer, and the highest thermal performance was obtained for V-shaped ribs at Reynolds number of 10000. The aerothermal features of a cross flow heat exchanger with pin-fins have been studied by Kotcioglu et al. (2018) using Taguchi method with L_{25} orthogonal array. The best thermal performance was observed for hexagonal pin-fins, followed by square-angle pin-fins. Recently, the design parameters, i.e. corner angle, inclination angle, baffle height, baffle length, baffle width and Reynolds number, of a heat sink fixed with hollow trapezoidal baffles have been optimized to enhance the performance (Sahin et al. 2019). The length of the baffle is the greatest influencing factor, with contribution ratio of 32.5%, on the pumping power and Reynolds number, with influence ratio of 80%, for heat transfer.

The above discussed studies reveal that the rib design parameters i.e. shape, size, spacing, inline or staggered arrangement, number of ribbed walls, perforation, rib inclination, and Reynolds number, have significant impact on the overall performance of the heat exchanger mounted with ribs. It has also been reported that the CFD-Taguchi scheme can be employed easily and also economically for a reliable and robust optimization (Wang et al. 2009; Aghaie et al. 2015). Therefore, the present research work is primarily concentrated on the prediction of best rib design parameters for a ribbed SAH using Taguchi method. The ribs have been provided on the bottom surface, which was exposed to constant heat flux. Firstly, the profound impacts of design parameters, i.e. rib geometry (see Fig. 6.1), rib spacing and

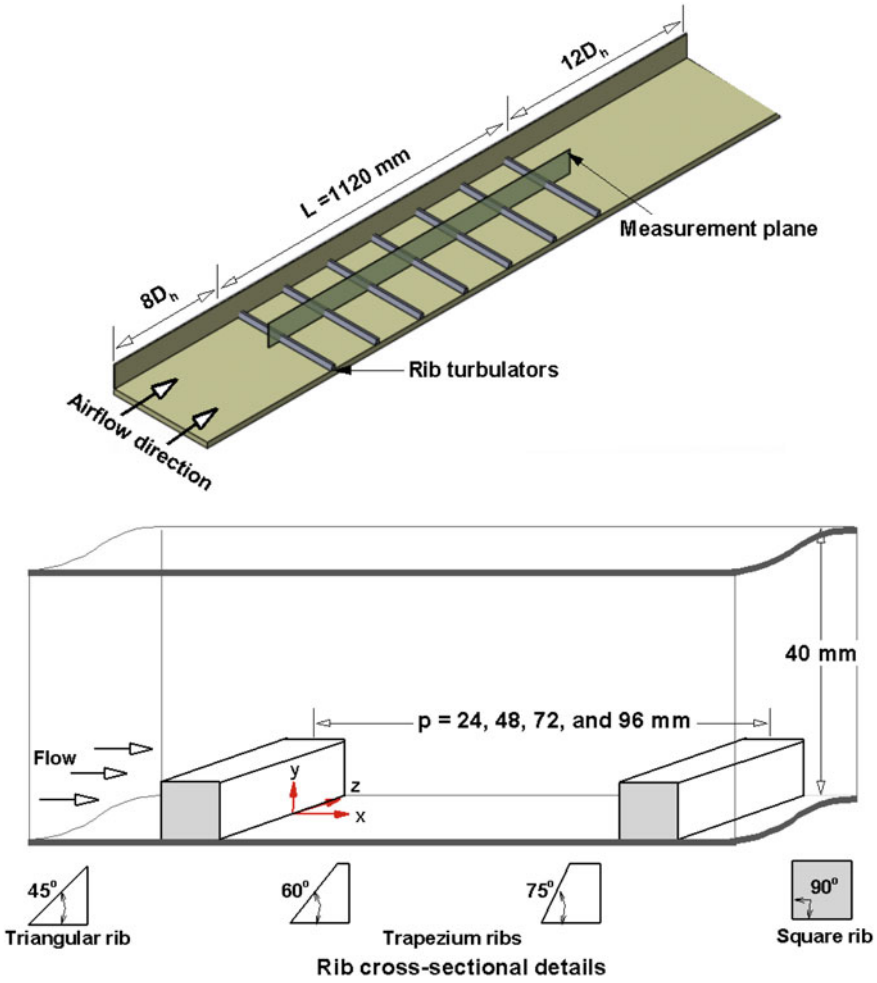

Fig. 6.1 Details of SAH and considered rib geometries

Reynolds number, on flow structures variation has been studied from CFD simulations. Subsequently, the performance indexes, i.e. heat transfer in terms of Nusselt number, pumping power in terms of friction factor, and effectiveness in terms of thermohydraulic performance, have been determined. The proposed innovative geometry (Fig. 6.1), that can produce right angle triangular, square and trapezium ribs, has been optimized using Taguchi method, and then the order of most influential parameters on performance indexes has been assessed.

6.2 Geometric Modeling

A 2-dimensional model of a SAH inserted with periodic ribs, whose front side is inclined at different angles (45°, 60°, 75°, and 90°), has been developed to understand the flow and heat transfer features (see Fig. 6.1).

The desired airflow, at atmospheric temperature and pressure, is provided by selecting suitable Reynolds number (Re = 4000, 8000, 12000 and 16000) in order to deduce forced convective heat transfer in the duct. The lower ribbed surface is provided with continuous heat flux of 4000 W/m^2, while the other sides are adiabatic in nature. The cross-section of the rib is square, i.e. e = w = 8 mm, while the duct height (H) and hydraulic diameter (D_h) are 40 and 80 mm (2H). The spacing between two consecutive ribs is varied as 3e, 6e, 9e, and 12e. Depending upon front face inclination, the type of rib geometry changes from triangular at inclination angle of 45° to trapezoidal for inclination angles of 60° and 75°, and square at inclination angle of 90° (Fig. 6.1).

The computational domain, as shown in Fig. 6.1, is judiciously decided so as to settle a uniform flow at inlet and fully developed flow at outlet (Aghaie et al. 2015). Numerical simulations have been carried out with certain assumptions, i.e. the flow is steady and fully developed turbulent flow, pressure variation and shear forces in wall normal direction are considered as zero, body forces due to gravity are neglected, working fluid is considered as an incompressible, and the axial heat conduction in the fluid is negligible.

6.2.1 Mathematical Modeling

The flow and heat transfer behaviour inside a ribbed SAH are mathematically described by some governing equations, i.e. continuity, momentum and energy equations, as given below in Cartesian coordinate system (Fluent 2006):

Mass conservation (Continuity equation):

$$\frac{\partial}{\partial x_i}(\rho u_i) = 0 \tag{6.1}$$

Momentum equation:

$$\frac{\partial}{\partial x_j}\left(\rho\, u_i\, u_j\right) = \frac{\partial}{\partial x_j}\left[\mu\left(\frac{\partial u_i}{\partial x_j} + \frac{\partial u_j}{\partial x_i}\right) - \frac{2}{3}\delta_{ij}\frac{\partial u_k}{\partial x_k}\right] + \frac{\partial}{\partial x_j}\left(-\rho\overline{u_i'\, u_j'}\right) - \frac{\partial P}{\partial x_i} \tag{6.2}$$

Energy Equation:

$$\frac{\partial}{\partial x_j}\left(\rho\,\mu_j\,T\right) = \frac{\partial}{\partial x_j}\left[\left(\Gamma + \Gamma_t\right)\frac{\partial T}{\partial x_j}\right] \tag{6.3}$$

RNG k-ε model with "enhanced wall treatment" has been reported as the finest turbulence model to foresee the aerothermal characteristics inside a duct with attached mechanical devices (Wang et al. 2009; Aghaie et al. 2015; Akcayoglu and Nazli 2018). Therefore, the RNG k-ε model, which holds turbulent kinetic energy (k) and turbulence dissipation rate (ε) is employed here (Fluent 2006):

$$\frac{\partial}{\partial x_i}(\rho\,k\,u_i) + \rho\,\varepsilon = \frac{\partial}{\partial x_j}\left(\mu_{eff}\,\alpha_k\frac{\partial k}{\partial x_j}\right) + G_k \tag{6.4}$$

$$\frac{\partial}{\partial x_i}\left(\rho\,\varepsilon\,u_j\right) - \frac{\partial}{\partial x_j}\left(\mu_{eff}\,\alpha_{\mathcal{E}}\frac{\partial \varepsilon}{\partial x_j}\right) + R_{\mathcal{E}} = C_{1\varepsilon}\frac{\mathcal{E}}{k}(G_k) - C_{2\varepsilon}\rho\frac{\varepsilon^2}{k}(G_k) \tag{6.5}$$

where, α_k and α_ε are the effective turbulent Prandtl number for k and ε. μ_t $(=\rho C_\mu\,(k^2/\varepsilon))$ is turbulent viscosity and μ_{eff} is effective turbulent viscosity.

6.2.2 Numerical Solution Procedure

The commercial software ANSYS 15.0 has been used for solving the governing equations by using Finite Volume Method (FVM) with segregated solution approach. The second order upwind scheme has been used to the governing equations. QUICK differencing scheme has been employed for solving momentum equation. The pressure–velocity-coupled solution is obtained by SIMPLE algorithm (Fluent 2006). Air is considered as working fluid. The convergence conditions of 10^{-3} and 10^{-6} have been applied for momentum and energy equations, respectively. After grid independency, a mesh grid consisting of 1.81×10^5 cells has been found to be suitable for CFD simulations, and further increase in number of cells has negligible effect on heat transfer results with a maximum deviation of about 1.5%.

The averaged heat transfer distribution, Nu, is assessed from the local convective heat transfer coefficient, $h(\mathrm{x})$, and expressed as (Aghaie et al. 2015):

$$Nu = \frac{1}{L}\int \frac{h(\mathrm{x})D_h}{k} \tag{6.6}$$

The friction factor, f, is the parameter refers to pressure penalty (ΔP) and measured over the length of test section, L, with a flow velocity of u as (Webb 1994; Tariq et al. 2018):

$$f = \frac{2 \times \Delta P \times D_h}{\rho u^2 L} \tag{6.7}$$

To study the combined effect of turbulence on heat transfer augmentation and increase in pressure drop, the thermohydraulic performance is introduced as (Webb 1994; Tariq et al. 2018),

$$\eta = \frac{Nu/Nu_s}{(f/f_s)^{1/3}} \tag{6.8}$$

here, subscript s refers to the smooth duct results.

Further, Dittus-Boelter and modified Blasius correlations are used to find the Nusselt number and friction factor inside a smooth SAH, respectively, as (Aghaie et al. 2015):

$$Nu_s = 0.024 \times \mathrm{Re}^{0.8} \times \mathrm{Pr}^{0.4} \tag{6.9}$$

$$f_s = 0.085 \times \mathrm{Re}^{-1/4} \tag{6.10}$$

6.3 Taguchi Approach

Taguchi approach is initially proposed as a method for enhancing the quality of products. It is usually embraced for optimizing the design parameters, in any case, by using two basics ideas. First idea is that the quality loss should be characterized as deviances from the major goals, not conformity to random details, and the other idea is accomplishing high system quality ranks, from financial aspects, allocated to the quality products. To accomplish attractive product quality, Taguchi recommends a three-stage process, i.e. design of system, parameter and tolerances.

Since the experimental techniques are costly and tedious, the requirement to fulfill the design goals with the minimum number of assessments (experimental/simulation) is evidently a vital prerequisite. Therefore, Taguchi robust design strategy, which utilizes the potential of numerical tools called Orthogonal Array (OA) and signal to noise (S/N) ratio, can be suitably used for a wide range of process parameters with few experiments. The careful selection of controlled parameters and response parameters is essential for accurate results. In the present work, the controllable parameters are Reynolds number, relative rib pitch and inclination angle (α) as described in Table 6.1. The response factors are heat transfer (Nu), friction factor (f) and thermohydraulic performance (η). Taguchi investigation is executed with Minitab 17.0 software. A L_{16} (4^3) OA is utilized, which inferred completing 16 tests with 3 factors of 4 levels that are documented in Table 6.2. Based on the proposed OA, the CFD simulations have been performed to obtain the values of response parameters, as presented in Table 6.2.

Table 6.1 Taguchi parameters and their levels

Code	Parameters	Levels			
		1	2	3	4
A	Reynolds Number (Re)	4000	8000	12000	16000
B	Rib pitch to height ratio (p/e)	3	6	9	12
C	Inclination angle (α)	45°	60°	75°	90°

Table 6.2 Chosen L_{16} (4^3) orthogonal array and corresponding simulation results

Number of test	Factors and their levels			Simulation results		
	A (Re)	B (p/e)	C (α)	*Nu*	*f*	η
1	1	1	1	40.98	0.010555451	2.58
2	1	2	2	38.459	0.013026767	2.26
3	1	3	3	39.701	0.015456197	2.20
4	1	4	4	41.014	0.017508645	2.18
5	2	1	2	54.02	0.009832906	1.89
6	2	2	1	64.803	0.010942903	2.19
7	2	3	4	65.44	0.011844515	2.15
8	2	4	3	66.955	0.013529408	2.11
9	3	1	3	68.318	0.009229039	1.71
10	3	2	4	75.682	0.010104006	1.83
11	3	3	1	90.06	0.011697562	2.08
12	3	4	2	89.525	0.012511095	2.02
13	4	1	4	83.63	0.008236498	1.68
14	4	2	3	93.063	0.008874747	1.83
15	4	3	2	99.059	0.010604145	1.83
16	4	4	1	111.21	0.012571249	1.94

Taguchi method strongly recommends the use of signal-to-noise (S/N) ratios. Maximizing the S/N ratio results in minimization of the losses related with the process. There are numerous S/N ratios accessible relying upon the sort of characteristics. The S/N ratio attributes can be partitioned into three classifications, stated by Eqs. (6.11)–(6.13) when the characteristic is continuous (Ross 1995):

Smaller is better:

$$\frac{S}{N} = -10\log\left(\frac{\sum y^2}{n}\right) \tag{6.11}$$

Nominal is best:

$$\frac{S}{N} = -10\log\left(\frac{\sum \overline{Y}/S_{\overline{Y}}^2}{n}\right) \tag{6.12}$$

Larger is better:

$$\frac{S}{N} = -10\log\left(\frac{\sum 1/y^2}{n}\right) \tag{6.13}$$

where, y and $\overline{Y}$ is the local and averaged observed data of n number of observations, respectively, while $S_{\overline{Y}}^2$ is variance of y. Suitably "larger is better" characteristic is used for maximization of heat transfer (*Nu*) and performance (η), while "smaller is better" characteristic is employed for minimization of pumping power (*f*).

6.4 Results and Discussion

Before performing simulations for all the cases as mentioned in Table 6.2, the numerical results obtained using RNG *k*-*ε* turbulence model for smooth duct are compared with Dittus-Boelter (Eq. 6.9) and modified Blasius (Eq. 6.10) correlations and presented in Fig. 6.2. The CFD simulation results are showing good agreement with standard correlations with the maximum deviation of ±5.23% for Nu and ±7.84% for *f*.

The profound impact of rib installation, which plays a decisive role in varying the flow patterns, has been shown in Fig. 6.3. From computational results, a trapped vortex is found at the lowest rib spacing (p/e ≤ 6), whereas the flow reattaches on the

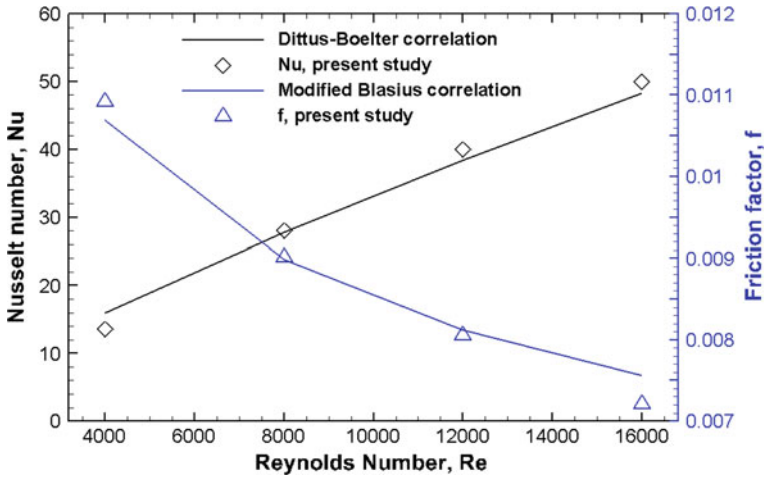

Fig. 6.2 Validation of computational results with standard correlations

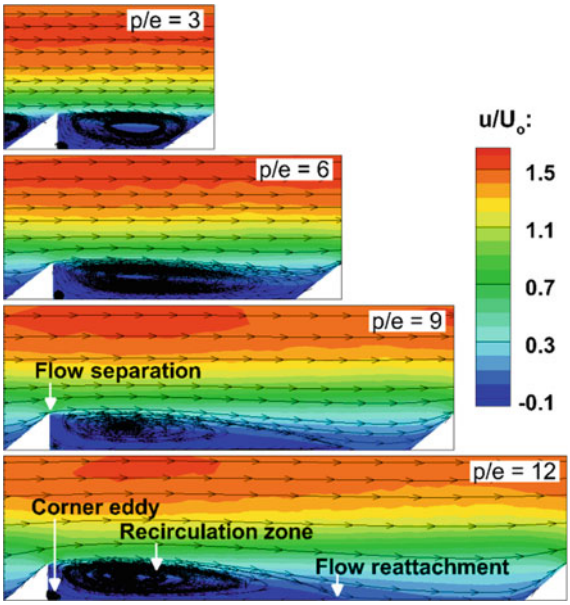

Fig. 6.3 Effect of rib spacing on flow structures

surface, but without boundary layer redevelopment, at the intermediate rib spacing ($6 < p/e < 9$). Markedly, flow reattachment along with a fresh boundary layer restoration is observed at higher rib spacing ($p/e \geq 9$).

Figure 6.4 shows the definable mean flow patterns in the enclosure between ribs. Evidently, the global flow structures, i.e. corner eddies (secondary recirculation bubble at the downstream rib corner and a separation bubble at upstream rib corner) and recirculation bubbles, and sizes (i.e. reattachment length, L_r) are strongly dependent on rib configurations (see Fig. 6.4). The reattachment length increases with decrease in inclination angle. Interestingly, the separation bubble has been appeared for the ribs with higher inclination angle i.e. $\alpha \geq 75°$.

The outcomes of CFD simulations, as reported in Table 6.2, are converted into S/N ratios by Taguchi analysis. Assigned enactments with their conforming outcomes are displayed in Table 6.3 for all performance indexes. The general means of S/N ratios for performance indexes have been calculated and found to be 36.44 dB for Nusselt number, 38.84 dB for friction factor and 6.097 dB for performance factor.

The response tables of S/N ratios for heat transfer, pressure drop and performance factor are presented in Tables 6.4, 6.5 and 6.6, and plotted in Figs. 6.5, 6.6 and 6.7, respectively. The importance of design factors for the studied performance indexes is rated in the last penultimate row of the tables (see Tables 6.4, 6.5 and 6.6). The parameter having the maximum difference between the highest and the lowest values of S/N ratio has the greatest influence on the performance indexes.

The heat transfer augments with the increase of average fluid velocity, i.e. parameter Re (A), as expected (Fig. 6.5). Therefore, heat transfer can suitably be controlled by the flow Reynolds number. The heat transfer increases with increasing p/e

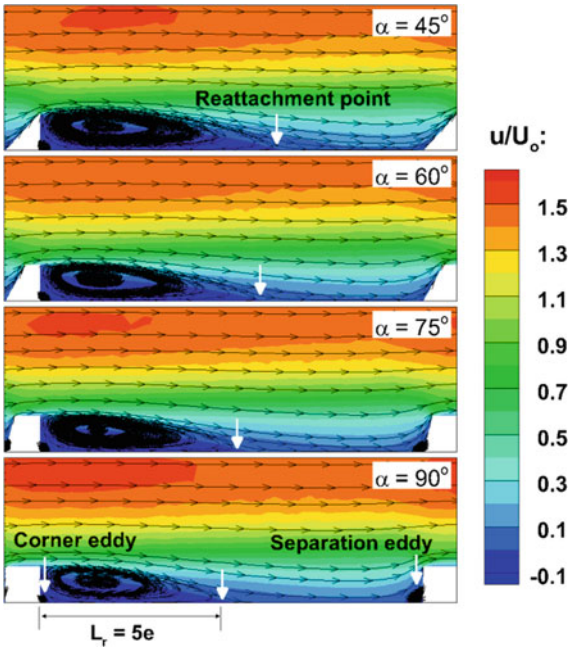

Fig. 6.4 Effect of inclination angle on flow structures

Table 6.3 Taguchi S/N ratios for performance indexes

Number of test	Factors and their levels			Signal to noise (S/N) ratios		
	A	B	C	$S/N_{(Nu)}$	$S/N_{(f)}$	$S/N_{(\eta)}$
1	4000	3	45°	32.25	39.53	8.24
2	4000	6	60°	31.70	37.70	7.08
3	4000	9	75°	31.98	36.22	6.86
4	4000	12	90°	32.26	35.13	6.78
5	8000	3	60°	34.65	40.15	5.53
6	8000	6	45°	36.23	39.22	6.80
7	8000	9	90°	36.32	38.53	6.65
8	8000	12	75°	36.52	37.37	6.47
9	12000	3	75°	36.69	40.70	4.64
10	12000	6	90°	37.58	39.91	5.27
11	12000	9	45°	39.09	38.64	6.35
12	12000	12	60°	39.04	38.05	6.11
13	16000	3	90°	38.45	41.69	4.52
14	16000	6	75°	39.38	41.04	5.23
15	16000	9	60°	39.92	39.49	5.26
16	16000	12	45°	40.92	38.01	5.77

Table 6.4 Response table for Nusselt number

Levels	A	B	C
1	32.05	35.51	37.12
2	35.93	36.22	36.33
3	38.1	36.83	36.14
4	39.67	37.18	36.15
Delta	7.62	1.67	0.98
Rank	1	2	3
Contribution ratio (%)	74.20	16.26	9.54

Table 6.5 Response table for friction factor

Levels	A	B	C
1	37.15	40.51	38.85
2	38.82	39.47	38.85
3	39.32	38.22	38.83
4	40.06	37.14	38.81
Delta	2.91	3.37	0.03
Rank	2	1	3
Contribution ratio (%)	46.12	53.41	0.47

Table 6.6 Response table for thermohydraulic performance

Levels	A	B	C
1	7.241	5.731	6.79
2	6.362	6.094	5.993
3	5.591	6.281	5.8
4	5.194	6.282	5.805
Delta	2.047	0.55	0.991
Rank	1	3	2
Contribution ratio (%)	57.05	15.33	27.62

(B), because with increasing p/e the flow reattaches on the heat transferring surface (Fig. 6.3), thereby providing more heat transfer rate. The heat transfer decreases with increase in inclination angle (C) of the front face of the rib. Further inspection reveals the blends of design parameters, which result in better heat transfer rate, are as follows: Re = 16000 (A_4), p/e = 12 (B_4), and $\alpha = 45°$ (C_1). Consequently, $A_4B_4C_1$ is found to be the ideal sets of design parameters, which provide the highest heat transfer (Table 6.7).

Figure 6.6 illustrates the pronounced influence of control parameters on friction factor. It increases with increase in Re (A). The pressure drop decreases significantly with increasing rib spacing (B), while reduces slightly with rise in inclination angle (C). The optimal sets of the design factors corresponding to minimum pumping power

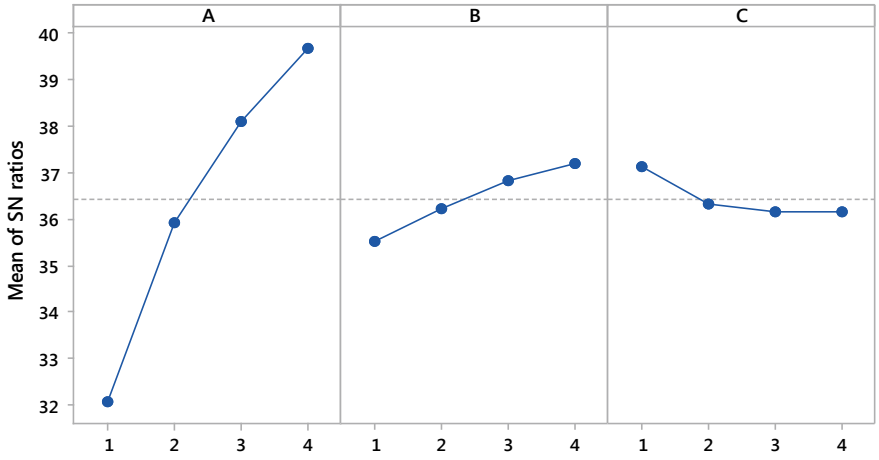

Fig. 6.5 Taguchi—S/N ratios for Nusselt number

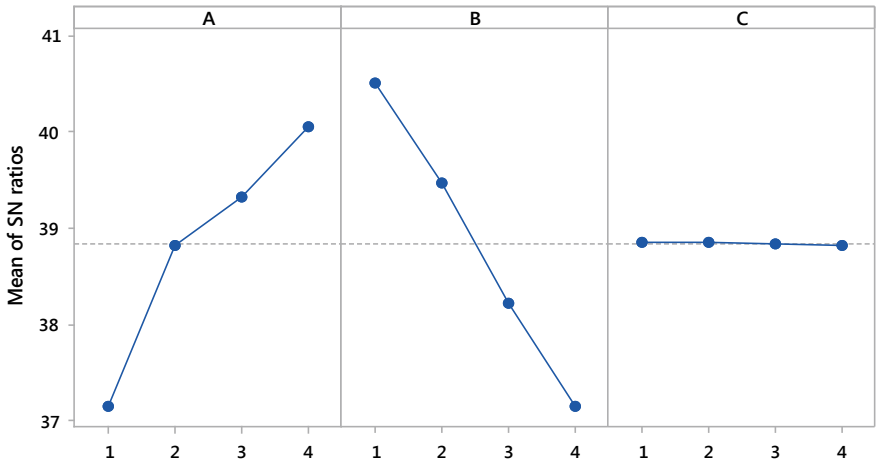

Fig. 6.6 Taguchi—S/N ratios for friction factor

are as follows: Re = 16000 (A_4), p/e = 3 (B_1), and $\alpha = 45°$ (C_1). Consequently, $A_4B_1C_1$ is found as the best grouping of design factors associated with the lowest pressure drop (see Table 6.7).

Figure 6.7 elucidates the prominent impact of design parameters on thermohydraulic performance factor. Thermohydraulic performance decreases with increase in Re (A), because of significant increase in pressure penalty. While η tends to increase with the increase of p/e (B). The reason can be attributed to enhancement in heat transfer and also decrease in friction factor with the increase in rib spacing. However, the η shows same trend as that of *Nu* with inclination angle, it decreases with

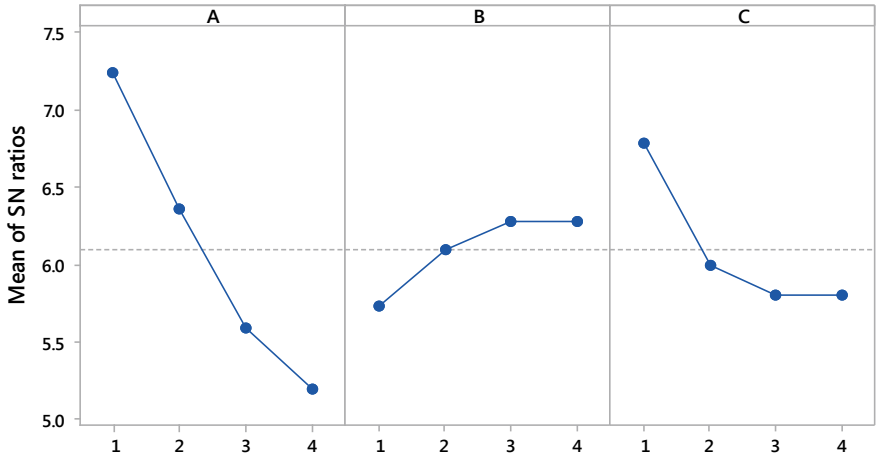

Fig. 6.7 Taguchi—S/N ratios for thermohydraulic performance

Table 6.7 Optimum conditions and performance values

Levels		Factors			Value
		A (Re)	B (p/e)	C (α)	
Nu	Best level	4^a	4^b	1^c	111.2
	Best value	16000	12	45°	
f	Best level	4^b	1^a	1^c	0.00812
	Best value	16000	3	45°	
η	Best level	1^a	4^c	1^b	2.71
	Best value	4000	12	45°	

[a, b, c]represents the order of most dominant factor

increase in the inclination angle (C). The optimal values of the design parameters for the maximum performance are as follows: Re = 4000 (A_1), p/e = 12 (B_4), and $\alpha = 45°$ (C_1). Consequently, $A_1B_4C_1$ is found as the optimal combination of design parameters associated with the highest performance as per the "larger is the better" condition for thermohydraulic performance factor (see Table 6.7).

The delta is the difference of the greatest and the least value of S/N ratios for each design factor. The contribution ratio is equivalent to the ratio of delta estimations of individual factor to the cumulative delta estimation, and here introduced in the last line of Tables 6.4, 6.5 and 6.6.

The contribution ratio of each controllable design factor to performance indexes is depicted in Fig. 6.8. Figure 6.8 shows that the factor A (Re) contributes to 74.2% of the aggregate impact, thereby signifying that Re has the greatest influence on heat transfer. It can be seen that factors B (p/*e*) and C (α) are the second and third most dominant factors, respectively. In view of Fig. 6.8, the factor B (p/e), having

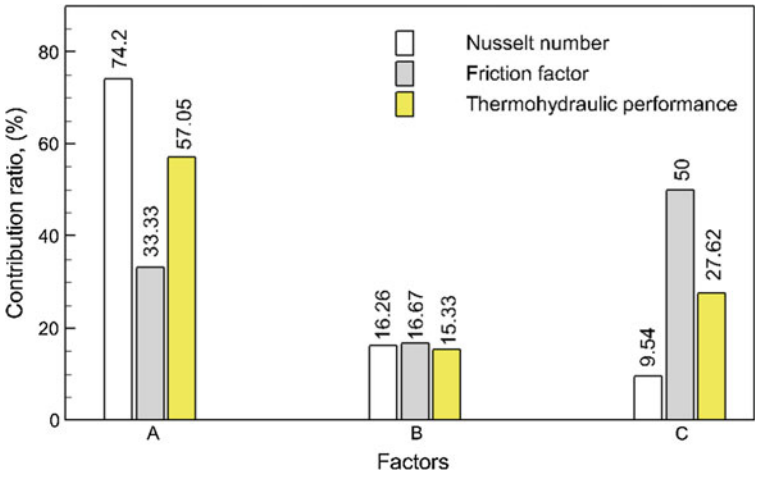

Fig. 6.8 Impact of each factor on performance indexes

a contribution ratio of 53.41%, is considered as the most dominant factor affecting pressure penalty. The factors A and C add to 46.12% and 0.47% of the aggregate impact on friction factor, respectively.

Further analysis reveals that Re has the greatest impact, around 57.05%, on the thermohydraulic performance factor. This implies that the Reynolds number (parameter A) is the most influential one on η, followed by inclination angle (C) and p/e (B) with contribution ratio of 27.62% and 15.33%, respectively. The ideal level of design parameters for heat transfer, pressure penalty and thermohydraulic performance are $A_4B_4C_1$, $A_4B_1C_1$ and $A_1B_4C_1$, respectively depicted in Table 6.7. The coefficients a, b, and c signify the first, second, and third most dominant factor, respectively.

6.5 Confirmation Tests

The confirmation test, last step in DOE process, has been performed at the optimum settings of the design factors, as described in Table 6.7, to confirm the interpretation made from analysis of the results. Table 6.8 depicts the results of confirmation tests for all the performance indexes, where the predicted S/N ratios have been estimated using Eqs. (6.14), (6.15), and (6.16), respectively (Ross 1995).

$$\chi_{Nu} = \overline{T} + \left(\overline{A_4} - \overline{T}\right) + \left(\overline{B_4} - \overline{T}\right) + \left(\overline{C_1} - \overline{T}\right) \tag{6.14}$$

$$\chi_{f} = \overline{T} + \left(\overline{A_4} - \overline{T}\right) + \left(\overline{B_1} - \overline{T}\right) + \left(\overline{C_1} - \overline{T}\right) \tag{6.15}$$

$$\chi_{\eta} = \overline{T} + \left(\overline{A_1} - \overline{T}\right) + \left(\overline{B_4} - \overline{T}\right) + \left(\overline{C_1} - \overline{T}\right) \tag{6.16}$$

Table 6.8 Confirmation results for performance indexes

		Initial parameter	Optimum factors	
			Prediction	Simulation
Nu	Level	$A_1B_1C_1$	$A_4B_4C_1$	$A_4B_4C_1$
	S/N ratio (dB)	31.81	41.10	40.92
f	Level	$A_1B_1C_1$	$A_4B_1C_1$	$A_4B_1C_1$
	S/N ratio (dB)	38.84	41.75	41.81
η	Level	$A_1B_1C_1$	$A_1B_4C_1$	$A_1B_4C_1$
	S/N ratio (dB)	7.57	8.12	8.66

where χ and $\overline{T}$ refer to the predicted and overall averaged values of S/N ratios of 16 simulations, respectively, while $\overline{A}$, $\overline{B}$ and $\overline{C}$ indicate towards the average S/N ratios of considered parameters at selected levels. From Table 6.8, it is clear that the predicted and confirmation tests results show a good agreement with maximum deviation of ± 1, $\pm 1\%$ and $\pm 6.5\%$ in the heat transfer, friction factor, and thermo-hydraulic performance factor, respectively. Therefore, it can be concluded that the Taguchi method can be considered as a reliable soft computing tool for optimization in heat transfer researches.

6.6 Conclusions

In this research work, the effects of the rib geometry and rib pitch to height ratio are investigated by using CFD-Taguchi approach at Reynolds number varying from 4000 to 16000 on the aerothermal characteristics. The significant results can be summarized as follows:

1. The flow patterns between two neighboring ribs are dependent on rib configuration, rib spacing as well as Reynolds number.
2. With increase in inclination angle, from 45° to 90°, the size of primary recirculation bubble decreases. In addition, a separation eddy has been appeared in front of the ribs with higher inclination angle i.e. $\alpha \geq 75°$.
3. Reynolds number is the most dominant parameter in respect of heat transfer and thermohydraulic performance. The optimal conditions of design parameters for maximization of heat transfer and thermal performance are $A_4B_4C_1$ (Re = 16000, p/e = 12, and $\alpha = 45°$) and $A_1B_4C_1$ (Re = 4000, p/e = 12, and $\alpha = 45°$).
4. For friction factor, the rib spacing is the key parameter having contribution ratio of 53.41%, which is followed by the Reynolds number (46.12%) and have negligible effect of rib configuration (0.47%). Ideal set of design parameters providing minimum friction factor is $A_4B_1C_1$ (Re = 16000, p/e = 3, and $\alpha = 45°$).
5. Rib with inclination angle of 45° provides the highest average heat transfer and the lowest friction along with the best thermohydraulic performance among the

tested configurations. So, this investigation offers an improved rib design suitable in various heat exchanging devices for improved overall performance.

References

Aghaie AZ, Rahimi AB, Akbarzadeh A (2015) A general optimized geometry of angled ribs for enhancing the thermo-hydraulic behavior of a solar air heater channel—a Taguchi approach. Renew Energy 83:47–54

Aidinlou HR, Nikbakht AM (2017) Intelligent modeling of thermohydraulic behavior in solar air heaters with artificial neural networks. Neural Comput Appl 1–15

Akcayoglu A, Nazli C (2018) A comprehensive numerical study on thermohydraulic performance of fluid flow in triangular ducts with delta-winglet vortex generators. Heat Transf Eng 39(2):107–119

Bilen K, Yapici S, Celik C (2001) A Taguchi approach for investigation of heat transfer from a surface equipped with rectangular blocks. Energy Convers Manag 42:951–961

Caliskan S, Nasiri Khalaji M, Baskaya S, Kotcioglu I (2016) Design analysis of impinging jet array heat transfer from a surface with V-shaped and convergent–divergent ribs by the Taguchi method. Heat Transf Eng 37(15):1252–1266

Chamoli S (2015) A Taguchi approach for optimization of flow and geometrical parameters in a rectangular channel roughened with V-down perforated baffles. Case Studies Therm Eng 5:59–69

Fluent (2006) Fluent 6.3-User's guide. Fluent Inc.

Jin D, Quan S, Zuo J, Xu S (2019) Numerical investigation of heat transfer enhancement in a solar air heater roughened by multiple V-shaped ribs. Renew Energy 134:78–88

Kotcioglu I, Khalaji MN, Cansiz A (2018) Heat transfer analysis of a rectangular channel having tubular router in different winglet configurations with Taguchi method. Appl Therm Eng 132:637–650

Kumar R, Kumar A, Goel V (2019) Simulation of flow and heat transfer in triangular cross-sectional solar-assisted air heater. J Solar Energy Eng 141(1):011007-1-12

Nagaiah NR, Geiger CD (2019) Application of evolutionary algorithms to optimize cooling channels. Int J Simul Multi Design Optim 10:A4

Rao RV, Saroj A, Ocloń P, Taler J, Taler D (2018) Single-and multi-objective design optimization of plate-fin heat exchangers using Jaya algorithm. Heat Transf Eng 39(13–14):1201–1216

Ross PJ (1995) Taguchi techniques for quality engineering, 2nd edn. McGraw-Hill, New York

Sahin B, Ates I, Manay E, Bayrakceken A, Celik C (2019) Optimization of design parameters for heat transfer and friction factor in a heat sink with hollow trapezoidal baffles. Appl Therm Eng 154:76–86

Sharma N, Sharma V, Tariq A (2017) Performance optimization of trapezium rib parameters using response surface methodology. In: ASME 2017 gas turbine India conference, American Society of Mechanical Engineers, Bangalore, India, , pp. V001T03A016-1-8

Sharma N, Tariq A, Mishra M (2018) Detailed heat transfer and fluid flow investigation in a rectangular duct with truncated prismatic ribs. Exp Thermal Fluid Sci 96:383–396

Siddhartha V, Sharma N, Varun G (2012) A particle swarm optimization algorithm for optimization of thermal performance of a smooth flat plate solar air heater. Energy 38:406–413

Tariq A, Sharma N, Mishra M (2018) Aerothermal characteristics of solid and slitted Pentagonal rib turbulators. J Heat Transf 140(6):061901-1-14

Wang Q, Chen Q, Zeng M (2009) A CFD-Taguchi combined method for numerical investigation of natural convection cooling performance of air-core reactor with noise reducing cover. Numer Heat Transf Part A Appl 55(12):1116–1130

Webb RL (1994) Principles of enhanced heat transfer. Wiley, New York

Yun JY, Lee KS (2000) Influence of design parameters on the heat transfer and flow friction characteristics of the heat exchanger with slit fins. Int J Heat Mass Transf 43(14):2529–2539

Chapter 7
Mathematical Modelling of Solar Updraft Tower

K. V. S. Teja, Kapil Garg and Himanshu Tyagi

Abstract Solar updraft tower power plant is a way to harness energy from the sun. It is a simple concept which requires low maintenance and utilises land that is already being used for growing plants, and generates power from it. A prototype plant was setup in Manzanares, Spain. Numerical analysis on power generation is performed for a similar plant assuming it is setup in Ropar. By considering losses via convection and radiation through the top surface of the collector, collector efficiency is calculated. Two cases arise here, 1. With 100% collector efficiency and 2. Collector efficiency is obtained after subtracting convection and radiation losses. The influx of solar radiation is highest in June. Hence, the variation of parameters like temperature, velocity, power output, efficiency with time of the day is done by taking averages for the month of June. Next the impact of physical parameters like chimney height, chimney radius and collector radius are studied on 21st June 11:00 to 12:00. How each parameter impacts the output of the plant is studied by creating a mathematical model of the power plant. Methods to improve the power output are discussed.

Keywords Solar energy · Solar updraft tower · Collector · Chimney · Wind turbine

Nomenclature

A	Area (m^2)
C	Power coefficient for wind turbine, $C = 0.45$
C_p	Specific heat at constant pressure for air (J/kg K), $C_p = 1007$ J/kg K
g	Acceleration due to gravity (m/s^2), $g = 9.81$ m/s^2
G_{sc}	Solar constant (W/m^2), $G_{sc} = 1367$ W/m^2
h	Convective heat transfer coefficient (W/m^2 K)
H	Height (m)
I_o	Hourly incident solar energy on an extra-terrestrial horizontal surface (J/m^2)

K. V. S. Teja (✉) · K. Garg · H. Tyagi
School of Mechanical, Materials and Energy Engineering, Indian Institute of Technology Ropar, Rupnagar, Punjab 140001, India
e-mail: 2018mem1016@iitrpr.ac.in

H. Tyagi et al. (eds.), *Solar Energy*, Energy, Environment, and Sustainability, https://doi.org/10.1007/978-981-15-0675-8_7

m	Refractive index
$\dot{m}$	Mass flow rate of air (kg/s)
n	Day of the year
p	Pressure (Pa)
P	Power (kW)
Q	Heat (W)
Q''	Hourly average incident heat flux (W/m^2)
r	Radius (m)
R	Characteristic gas constant (J/kg K), $R = 287$ J/kg K
T	Temperature (°C)
v	Velocity (m/s)

Greek symbols

ε	Emissivity
η	Efficiency (%)
ρ	Density (kg/m^3)
σ	Stefan-Boltzmann's constant (W/m^2 K^4), $\sigma = 5.67 \times 10^{-8}$ W/m^2 K^4
τ	Transmissivity

Subscripts

chim	Chimney
coll	Collector
conv	Convection
i	Inlet of turbine/chimney
o	Ambient
ovr	Overall
rad	Radiation
turbine	Turbine

7.1 Introduction

Over the past few decades, the population has been rising at a very steep rate. This leads a proportional growth in the energy requirement. Current major sources of energy production have been through fossil fuels like coal, oil, natural gas. These fossil fuels account for about 80% of total energy supply. But these resources are not infinite and are going to deplete sometime in the near future. So, in order to

tackle such a huge demand in energy, we need to start using renewable sources like: hydro-electric, wind, solar etc. Among the renewable energy sources, solar energy and wind energy are the most abundant, easily available and environment friendly.

Without a doubt, fossil fuels are much more efficient and effective ways to produce power. But keep in mind that these sources are going to deplete one day and they also have huge adverse impact on the environment. Hence, the need to find more and better ways to use these forms of energy arises (Shahzad 2012). Solar updraft tower is one such way to harness energy from the sun. It is a very simple construction. The power plant consists of three major components: 1. Greenhouse (collector), 2. Chimney, 3. Wind turbine.

The greenhouse is made of glass or plastic. These materials act as transparent medium for shorter-wavelengths and opaque for longer-wavelengths. Hence, the heat from the sun gets trapped inside the greenhouse. A chimney is placed at the centre. During the day, the solar irradiation falling onto the collector heats up the air inside the greenhouse. Since, temperature and density are inversely related for constant pressure (from ideal gas equation); density of air is lower inside when compared to the ambient air. This density difference creates pressure gradient between the base and ambient air inside the chimney. This pressure gradient when created over a large area, gets converted in kinetic energy, and used to run a turbine and extract energy. For the purpose of this plant, a vertical axis wind turbine is used to generate power.

During the night, the ground is hot because it absorbs the sun's radiation during the day. The hot ground heats up the air inside the greenhouse at night. Hence, this type of plant can operate for 24 h a day. The land can be utilised by planting crops. Even though a very large area is required for such a plant to generate significant power output, the land is not wasted and can be utilised in a number of ways such as, planting crops, solar panels can also be set up on the ground.

A solar updraft tower power plant prototype has been set up in Manzanares, Spain. This working prototype used the above-mentioned principles. The plant in Manzanares operated between 1981 and 1989. Various parameters of this plant have been listed in Table 7.1 (Schlaich et al. 2005; Agarwal et al. 2018). Average power output of 50 kW has been reported for this plant. Despite being a very simple concept, it involves a lot of fluid mechanics and heat transfer phenomenon. There are numerous parameters like height of the chimney, chimney radius, collector radius,

Table 7.1 Various physical parameters of the Manzanares plant

Chimney height	194.6 m
Chimney radius	5.08 m
Mean collector radius	122 m
Mean roof height	1.85 m
Number of turbine blades	4
Typical collector air temperature increase	$\Delta T = 20$ °C
Average power output	50 kW
Turbine blade profile	FX W-151-A

Table 7.2 Correlation between plant dimensions and power output

Capacity	MW	5	30	100	200
Chimney height	m	550	750	1000	1000
Chimney radius	m	45	70	110	120
Collector radius	m	1250	2900	4300	7000

greenhouse height, chimney profile, inclination of the greenhouse etc., which affect the output power that can be extracted from the system. Various studies, simulations and experiments were carried out to analyse these parameters. By increasing the height of chimney and collector diameter, the power output can be increased by a large factor. In Table 7.2 (Schlaich et al. 2005; Agarwal et al. 2018), the relation between the physical parameters of the plant and its power output are listed. The date was not specified for this data hence, it can be assumed as the averaged values taken over the year.

Haaf et al. (1983) studied the working principle and construction of the prototype located in Manzanares, Spain. They were the first to realise that increase in collector area increases the power output but reduces the efficiency of the plant (Haaf et al. 1983; Haaf 1984). Increasing chimney height leads to an increase in the velocity of air, which causes an increase in the mass flow rate (Pasumarthi and Sherif 1998a, b). A detailed journal on the power generation, efficiency and costs involved in setting up the plant were studied by Lodhi (1999). A similar study on the working and economics was done on the Manzanares plant by Schlaich et al. (1996). Koonsrisuk and Chitsomboon (2013) determined that the efficiency and power output vary linearly with chimney height. It has also been observed by Chitsomboon (2001) that the efficiency has almost no correlation with solar insolation, height of the greenhouse roof and the chimney diameter.

Optimal dimensions of the plant can be obtained only by considering economic constraints because increase in solar insolation, collector diameter and chimney height will also increase the power output. Fasel et al. (2013) studied the plant using ANSYS Fluent, which is a commercial CFD tool. They have performed a CFD analysis to determine temperatures and air velocities in the system. Agarwal et al. (2018) also did a CFD analysis on ANSYS Fluent for the plant at Manzanares, Spain. They have considered a full scale 3-D model, performed simulation for steady state with/without radiation and transient state with/without thermal storage on 8th June. Results show that the simulation with radiation model showed very close values of various parameters when compared to the actual prototype's observed data. Also using water as thermal storage lowers the velocity of air but compensates for the intermittent availability of solar insolation. The Manzanares plant operates for about 8–9 h a day and requires a minimum velocity of 2.5 m/s for the turbine to be operational.

Overall efficiency of the system is the product of turbine efficiency, chimney efficiency and the collector efficiency. For a wind turbine, the Betz limit is 59.25%. Which means that the maximum amount of power extracted is 59.25% of the kinetic

energy of air at the inlet. Actual efficiency is always less than this limit. Generally, it lies between 35 and 45%. For this study, the turbine efficiency is taken as 45%.

Two different cases were analysed using the dimensions of the Manzanares plant. In case 1, the collector efficiency is assumed to be 100%. And in case 2, both convection and radiation losses through the top surface of the greenhouse roof were accounted and calculated the collector efficiency. The ground is assumed to be a black body to calculate the tower efficiency.

7.2 Mathematical Modelling of the Power Plant

For this analysis, consider a hypothetical solar updraft tower power plant located in Ropar, India (Latitude = 30.97° N). Assume the dimensions to be similar to the plant in Manzanares, Spain (Agarwal et al. 2018). The aim is to calculate the power that can be extracted using this setup.

Initially it is assumed that the collector is circular, with a radius of 122 m. The height and radius of the chimney are taken as 194.6 m and 5.08 m respectively. A vertical axis wind turbine is set up inside the chimney. The blade radius of the turbine is assumed to be equal to the chimney radius. The turbine efficiency is taken as 45%. All calculations are done from sunrise to sunset.

The schematic diagram of the setup is shown in Fig. 7.1. For simplifying the calculations, the greenhouse roof is taken as horizontal with respect to the ground. Chimney radius is constant throughout its height. For better efficiency and power generation, a sloped roof and a chimney with a tapered or hyperbolic profile is taken. Another novel concept of combining a thermal power plant's cooling tower with

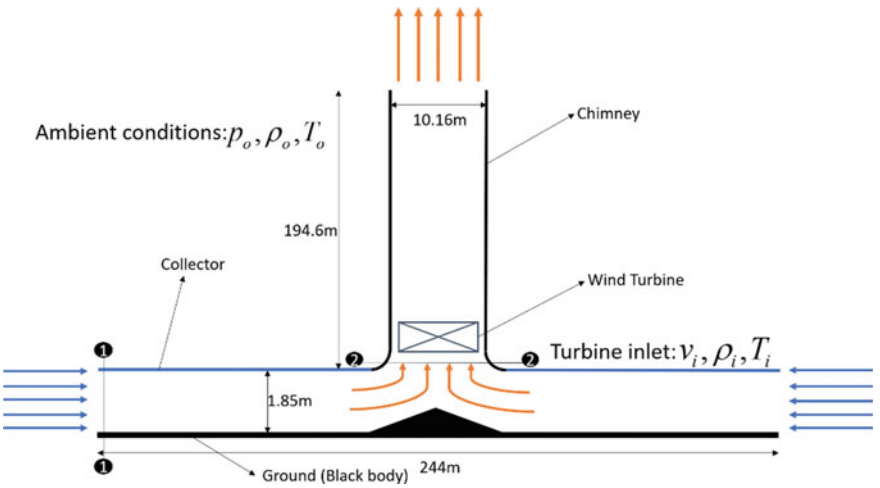

Fig. 7.1 Schematic diagram of the Manzanares plant showing physical dimensions of the plant

a solar chimney was proposed by Zandian and Ashjaee (2013). By doing so, the efficiency of solar updraft towers was improved. Also, the power generated by these units was around 10 times more than the one located in Manzanares.

By using water or some other fluid as thermal storage medium, plant can be operational even during the night. But here, the plant is assumed to be operational during the day only (i.e. from sunrise to sunset). Also, neglect the losses due to atmospheric interactions like fog, rain, clouds. Power output was calculated for sunny day. Ambient temperature is taken as the monthly average temperature of Ropar from sunrise to sunset. The ground is assumed to be a black body.

In order to calculate the power output of the system, heat flux incident on the ground must be calculated. The incident solar energy per unit area from ω_2 to ω_1 hour angles is obtained using the following relation (Duffie and Beckman 2003).

$$I_o = \frac{24 * 3600 * G_{sc}}{\pi} * \left(1 + 0.033 * \cos\left(\frac{360 * n}{365}\right)\right) * \left[\cos\phi * \cos\delta * (\sin\omega_2 - \sin\omega_1) + \frac{\pi * (\omega_2 - \omega_1)}{180} * \sin\phi * \sin\delta\right] \quad (7.1)$$

Solar constant is taken as 1367 W/m^2. Latitude angle for Ropar is +30.97°. n ranges from 1 to 365. By taking ω_2 and ω_1 in 15° intervals, the hourly incident solar energy per unit area from sunrise to sunset can be calculated.Declination is given by (Duffie and Beckman 2003)

$$\delta = 23.45 * \sin\left(360 * \frac{284 + n}{365}\right) \quad (7.2)$$

Once I_o is calculated, incident heat flux can be calculated using the following equation

$$Q'' = I_o * \frac{(\omega_2 - \omega_1)}{15 * 3600} \quad (7.3)$$

Ambient temperature is taken as the monthly average temperature from sunrise to sunset for Ropar. Collector is assumed to be a circle with radius 122 m. Chimney radius is taken as 5.08 m. Areas of collector and chimney are 46,759.465 m^2 and 81.073 m^2 respectively.

7.2.1 Case 1 (Without Losses)

In case 1, the collector efficiency is taken as 100%. This means all the incident flux is used to raise the temperature of the air inside the greenhouse i.e.

$$Q'' * A_{coll} = \dot{m} C_p (T_i - T_o) \quad (7.4)$$

Here, mass flow rate of air unknown. It can be calculated using

$$\dot{m} = \rho_i * A_{chim} * v_i. \tag{7.5}$$

In order to simplify the calculations, approximate $\rho_i = \rho_o$. Mass flow rate of air after approximation is given by

$$\dot{m} \approx \rho_o * A_{chim} * v_i \tag{7.6}$$

By taking the above approximation, the equation to obtain temperature at turbine inlet becomes a linear equation rather than a cubic equation. This simplifies the calculations significantly. Velocity at the bottom of the chimney is given by (Schlaich et al. 2005).

$$v_i = \sqrt{2 * g * H_{chim} * \frac{T_i - T_o}{T_o}} \tag{7.7}$$

Put the values of velocity in Eq. (7.6) to get the mass flow rate. Substitute $\dot{m}$ in Eq. (7.4). Here, T_i is the only unknown. Making T_i the subject gives us a relation to obtain the average temperature of air at chimney entrance.

$$T_i = T_o \left[1 + \left(\frac{(Q'' * A_{coll} * R)^2}{(P_o * A_{chim} * C_p)^2 * 2 * g * H_{chim}} \right)^{1/3} \right] \tag{7.8}$$

Once T_i is obtained, velocity of air at chimney entrance (v_i) can be calculated using Eq. (7.7). Using air velocity, the power generated by the wind turbine is given by

$$P_{out} = C * \frac{1}{2} * \rho_i * A_{chim} * v_i^3 \tag{7.9}$$

where C is assumed to be 0.45 for this wind turbine. Efficiency of the chimney is defined as the ratio of kinetic energy of air at chimney entrance to the heat absorbed by the air.

$$\eta_{chim} = \frac{\frac{1}{2} * \rho_i * A_{chim} * v_i^3}{\dot{m} * C_p (T_i - T_o)} \tag{7.10}$$

Putting the values of $\dot{m}$ and v_i as defined earlier in Eqs. (7.5) and (7.7), this can be simplified to

$$\eta_{chim} = \frac{g * H_{chim}}{C_p * T_o} \tag{7.11}$$

Clearly, it can be observed that the efficiency of the plant is a function of the chimney height. Depending on mechanical and economic constraints, the chimney height must be kept as high as possible.

7.2.2 Case 2 (with Losses)

For case 2, the collector losses from the top surface are taken into account. Additionally, the reflectivity and absorptivity of glass is taken into account. Assuming refractive index of glass (m) as $1.5+10^{-7}i$, the average wavelength of solar spectrum is assumed to be 0.5 μm. The corresponding reflectivity, absorptivity and transmissivity are calculated. Transmissivity is found to be around 0.912, which shows the fraction of solar radiation that actually is incident on the ground.

Accordingly, the temperature of the glass roof is calculated. From the top surface of the greenhouse roof, convective and radiative losses are calculated and subtracted from the incident heat flux and the power output is calculated again. The results obtained in case 1 and case 2 are compared.

In order to calculate the roof temperature, certain assumptions have to be taken, as analytical solution for this is not easily obtained. First of all, the roof temperature is assumed to be constant throughout. This temperature is assumed to be equal to the average of ambient temperature and mean air temperature inside the plant. It is known that the temperature at the periphery is equal to the ambient atmospheric temperature and temperature at the centre is equal to the temperature at the chimney entrance. So, assuming the temperature distribution along the radial direction to be linear, assume the mean temperature of the air is the temperature of air at the $A_{coll}/2$ mark along the radial direction. At radius $r_{coll} = 86.267$ m, the area $= A_{coll}/2$. Using linear interpolation, temperature at $r_{coll} = 86.267$ m can be calculated. Now, roof temperature can be determined.

Convection losses

Assuming wind velocity as 0, the convection losses take place via natural convection only. But in reality, the wind velocity cannot be determined theoretically and is constantly fluctuating. So, if only natural convection is considered, the Nusselt number is calculated and then heat transfer coefficient is obtained to be around 1.8 W/m^2 K (Incropera et al. 1993). Actual heat transfer coefficient is obviously higher than that, hence it is assumed to be around 5 W/m^2 K.

$$Q_{conv} = h * A_{coll} * (T_{coll} - T_o) \tag{7.12}$$

Radiation losses

Emissivity of glass roof is taken as 0.95 to determine radiation losses. Assume sky temperature and ambient temperatures are equal.

$$Q_{rad} = \varepsilon_{coll} * A_{coll} * \sigma * (T_{coll}^4 - T_o^4) \tag{7.13}$$

After calculating the losses from the top surface of the roof, new value of heat input to the system is given by

$$Q = \tau * Q'' * A_{coll} - Q_{conv} - Q_{rad} \tag{7.14}$$

This is the actual input to the system. Using this, new value of temperature at turbine inlet is calculated, which is obviously less than the old value. There is a significant difference in both these values, hence new value of roof temperature is calculated and 6 such iterations are performed until almost no change in old and new values of chimney inlet temperature is observed.

Using the final temperature at chimney inlet, determine other parameters like velocity, power output and efficiency. New parameter collector efficiency is also obtained in this case.

$$\eta_{coll} = \frac{Q}{Q'' * A_{coll}} = \left(\tau - \frac{Q_{conv} + Q_{rad}}{Q'' * A_{coll}}\right) \tag{7.15}$$

Overall efficiency is given by

$$\eta_{ovr} = \eta_{turbine} * \eta_{chim} * \eta_{coll} \tag{7.16}$$

7.3 Results and Discussions

7.3.1 Impact of Solar Radiations on Performance of the Plant

This setup relies almost exclusively on solar radiations to generate power. Other forms such as wind have a small impact in air velocity at the inlet and losses through the collector roof. Since solar radiation is the major factor here, its variation must be thoroughly studied. If we consider the hour of the day for any particular day, then the hourly heat flux from the sun starts at minimum in the morning and reaches maximum at solar noon and then symmetrically reaches minimum again at sunset. But the same cannot be said about the temperature distribution. It is significantly hotter in the afternoon session when compared to forenoon. Due to this the plant generates more power in the afternoon session. The ambient temperature here is taken as the monthly average temperature of Ropar taken on an hourly interval.

However, if the day off the year is varied keeping the hour of the day constant, it is observed that since Ropar lies in the Northern hemisphere, solar radiation is highest in the month of May and June. Hence the power output is maximum on these months. And expectedly, the solar radiation is minimum in December and January. Hence the

output of the plant reaches minimum in these months. However, the variation is not exactly smooth. The increment is very steep and then it remains almost constant for a few months before it decreases in a similar manner and again remains constant for a few more months.

In order to study the variation in output parameters, June month is selected here and studied. There are 4 major parameters that affect the performance of the plant.

1. Hour of the day
2. Collector radius
3. Chimney radius
4. Collector height.

Other parameters like slope of the collector roof, profile of the chimney, wind velocity, cloud coverage, day of the year etc. also affect the performance. But the main focus here was the physical parameters like collector radius, chimney radius, chimney height and hour of the day. Since the calculations were performed for June, day of the year is not a major factor because the temperature range over one month is not much.

4 different cases are now created. The aim here is to keep 3 of the above listed parameters as constants and vary one parameter. For both case 1 and case 2 all parameters are varied and compared.

7.3.2 Hour of the Day

Using Eq. (7.1), the hourly incident heat flux was calculated for everyday of the year. Since the maximum heat flux is incident in the month of May and June, the power output is also highest for these months. All calculations were performed focussing majorly on the month of June. Using the heat flux, the rise in temperature within the system was calculated. The variation of temperature at the chimney inlet versus time of the day can be observed in Fig. 7.2. It shows the variation between case 1 and case 2. Variation not symmetric between forenoon and afternoon for temperature because the ambient temperature is higher afternoon compared to forenoon even though the heat flux distribution is symmetric about 12:00 noon.

From Eq. (7.7), velocity at chimney inlet for every hour was calculated for June. Corresponding power output was calculated. Monthly averaged values of velocity and power output were calculated. Variation of velocity at chimney inlet and power output against time of the day can be observed in Fig. 7.3. Power output is proportional to the cube of velocity. Hence, their trends are similar when varied with time. Start low at sunrise and reach maximum around midday and then decrease till sunset. Distribution is almost symmetric between forenoon and afternoon.

The above curves are similar of case 1 and case 2 but efficiency is very different. This is because the collector efficiency is also accounted in case 2. This can be seen in Fig. 7.4. Maximum chimney efficiency is observed when ambient temperature is minimum i.e. at sunrise. But collector efficiency is maximum at 12:00 noon. This

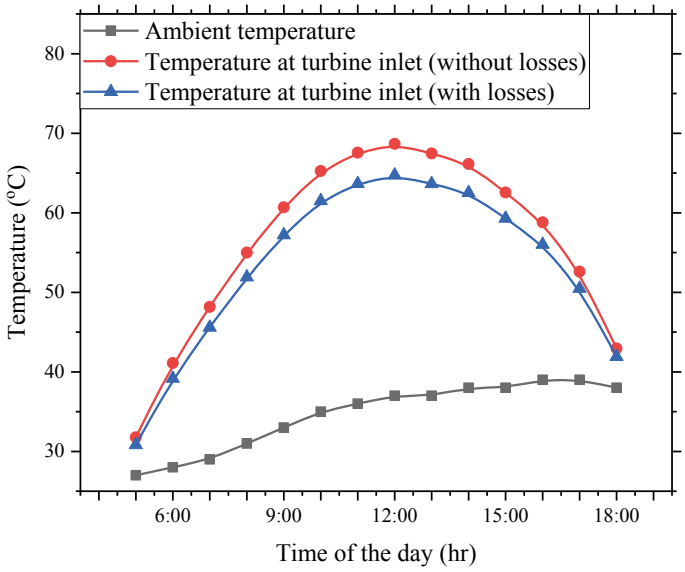

Fig. 7.2 Variation of ambient temperature and temperature at turbine inlet for both cases from sunrise to sunset for June

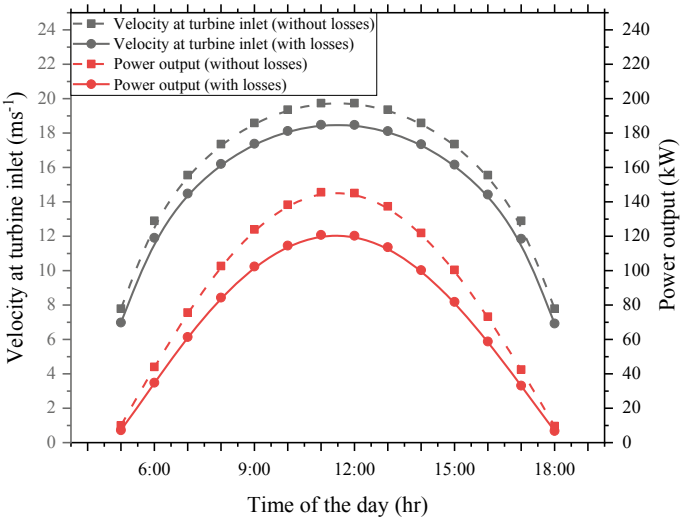

Fig. 7.3 Variation of velocity at turbine inlet and power output from sunrise to sunset for June

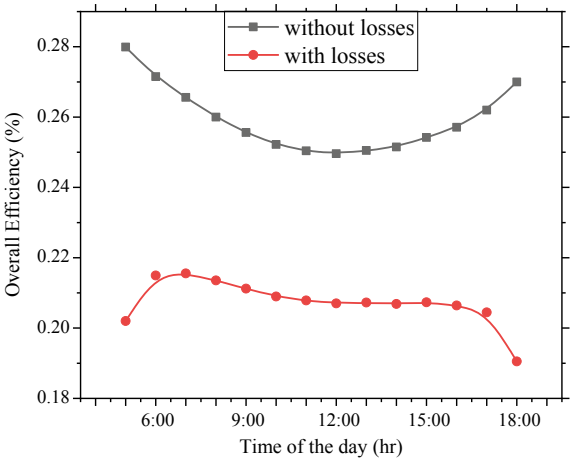

Fig. 7.4 Comparison of overall efficiency for case 1 and case 2 from sunrise to sunset for June

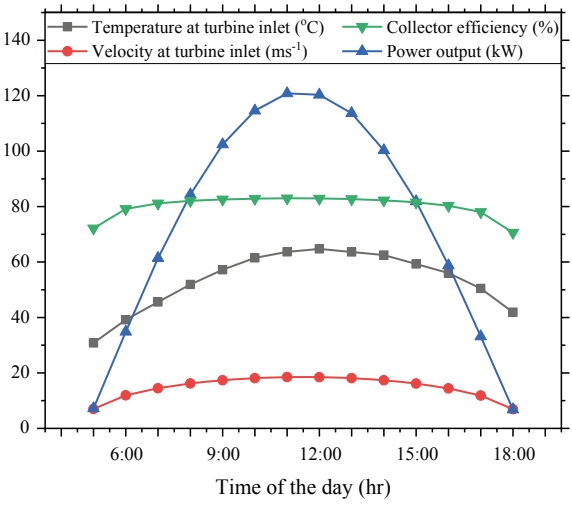

Fig. 7.5 Comparison of various parameters versus time of the day for June when convection and radiation losses through collector roof are accounted

makes it difficult to predict when the overall efficiency will be maximum. Variation of all the parameters with time for case 2 can be observed in Fig. 7.5.

7.3.3 Collector Radius

Keeping chimney height as 200 m, chimney radius as 5 m, varying the collector radius from 100 to 300 m, all the parameters were calculated for 21st June 11:00 to 12:00. From Figs. 7.6, 7.7 and 7.8 it is observed that as collector radius increases, the temperature and velocity at the chimney inlet increase almost linearly. Also, power

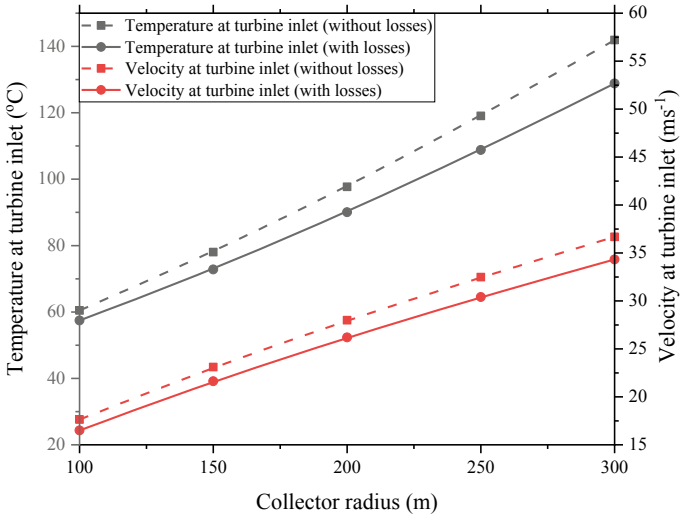

Fig. 7.6 Variation of velocity and temperature at turbine inlet calculated on June 21st between 11:00 and 12:00 for both cases when collector radius is varied

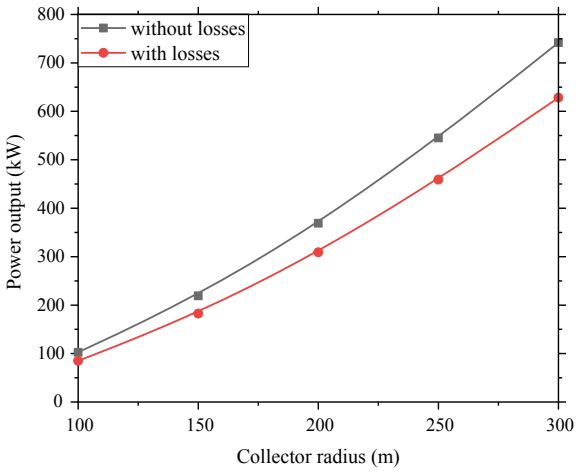

Fig. 7.7 Variation of power output calculated on June 21st between 11:00 and 12:00 for both cases when collector radius is varied

output increases as well but efficiency of the plant decreases. This shows that the collector radius must be as large as possible. The only constraint is the availability of land and the costs involved.

The incident solar radiation flux remains constant regardless of the plant dimensions but, when the collector radius increases, the heat input increases because the area increases. But for a given increase in heat flux, the corresponding velocity increment is much lower. Hence, the power output increases at a slower rate compared

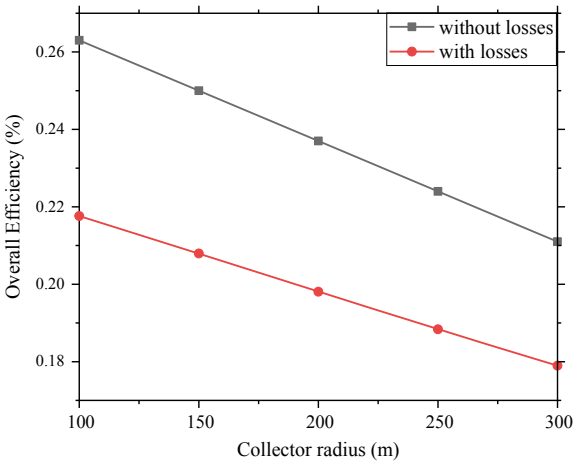

Fig. 7.8 Variation of overall efficiency calculated on June 21st between 11:00 and 12:00 for both cases when collector radius is varied

to the input heat. Due to this reason the ratio between these two i.e., the efficiency decreases with increase in collector radius.

7.3.4 Chimney Radius

Here, chimney height is kept at 200 m, collector radius is kept at 150 m and the power output, temperature and velocity variations are observed as chimney radius varies from 2 to 10 m on 21st June 11:00 to 12:00. Figures 7.9 and 7.10 show these variations for both case 1 and case 2. While the velocity and temperature at chimney inlet decrease as the radius is increased, the power output as well as efficiency increases. The variation is very steep when the radius is small, but as radius increases, the slope of all these curves approaches zero. This implies that the radius of tower should be significantly large, but increasing it beyond a certain point will yield poor cost to power ratio.

7.3.5 Chimney Height

Finally, chimney height is varied from 100 to 300 m keeping collector radius at 300 m, and chimney radius at 5 m on 21st June 11:00 to 12:00. The temperature of the air at chimney entrance decreases as height increases. Velocity of air, power output and efficiency increase with increase in height. Which means the chimney height must be as high as possible keeping structural and cost constraints into account. Figures 7.11 and 7.12 show the variation of various parameters with height.

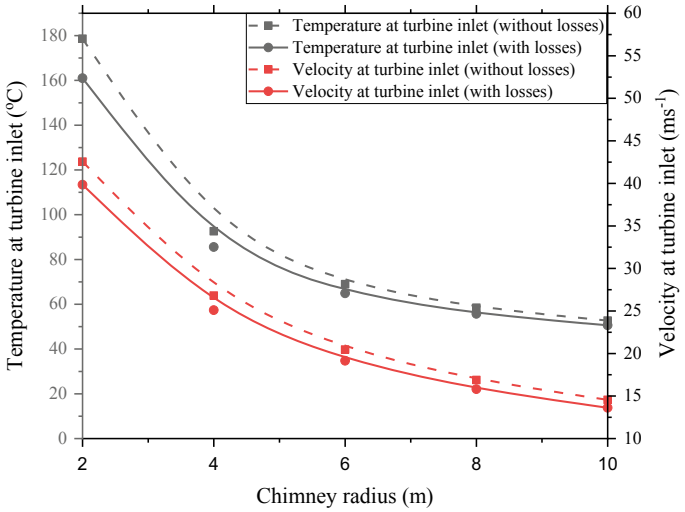

Fig. 7.9 Variation of temperature and velocity at turbine inlet calculated on 21st June between 11:00 and 12:00 for both cases when chimney radius is varied

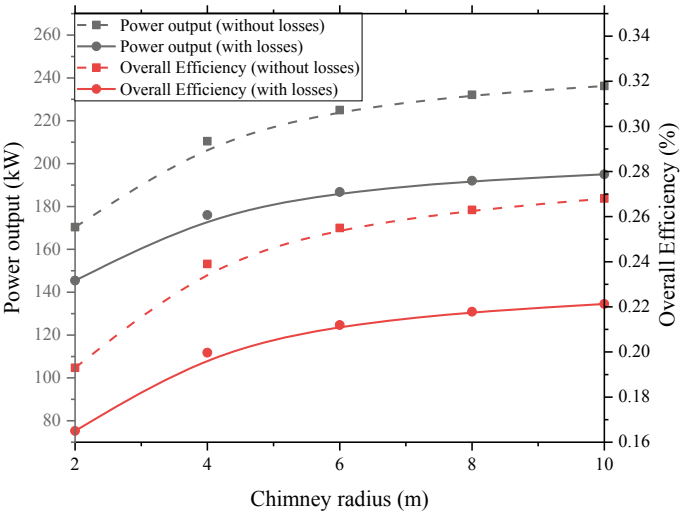

Fig. 7.10 Variation of power output and overall efficiency calculated on 21st June between 11:00 and 12:00 for both cases when chimney radius is varied

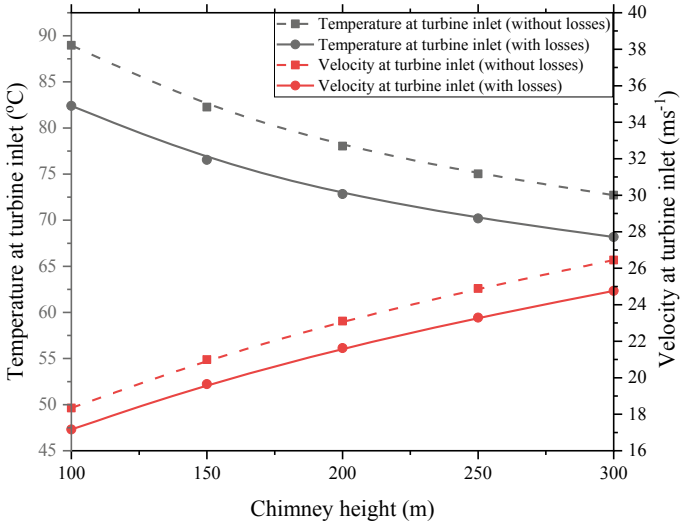

Fig. 7.11 Variation of temperature and velocity at turbine inlet calculated on 21st June between 11:00 and 12:00 for both cases when chimney height is varied

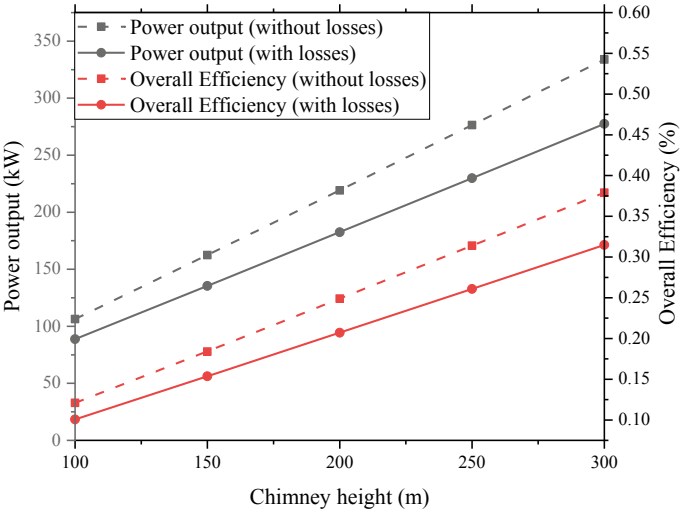

Fig. 7.12 Variation of output power and overall efficiency calculated on 21st June between 11:00 and 12:00 for both cases when chimney height is varied

Additionally, it is observed that the velocity of air reaches a maximum at the top of the chimney. But it is infeasible to install a turbine at such a large height.

7.3.6 Comparison of Power Output Between 21st June and 21st December

In order to get an idea about the average performance of the plant, a comparison between 21st June and 21st December is necessary because, these are the days with the maximum and minimum incident solar radiation respectively. By doing an analysis on 21st December similar to the earlier one, the range of power outputs that can be obtained using the plant is calculated. It is found that the power output between 11:00 and 12:00 ranges from 118.81 to 145.43 kW in case 1 and from 91.41 to 120.67 kW. Also, by varying the physical parameters like collector radius, chimney radius and chimney height, the variation between the power outputs on 21st June and 21st December for case 2 can be observed in Figs. 7.13, 7.14 and 7.15. Obviously, the trend remains the same, but the rate of change varies slightly. The minimum power output is generally observed to be 75–80% of the maximum power output. From these figures, average power output over the year can be estimated theoretically.

Since, the power output increases with increase in each of the 3 mentioned physical parameter, there is no optimum dimension that can be theoretically obtained. As the plant dimensions increase, the power output also continuously increases. However, by considering the limiting temperature at which plants can grow healthily inside the greenhouse and by performing an economic analysis and considering the cost and material constraints, it is possible to arrive at an optimum value of the plant dimensions. These dimensions can vary vastly depending on the requirement, climatic conditions etc.

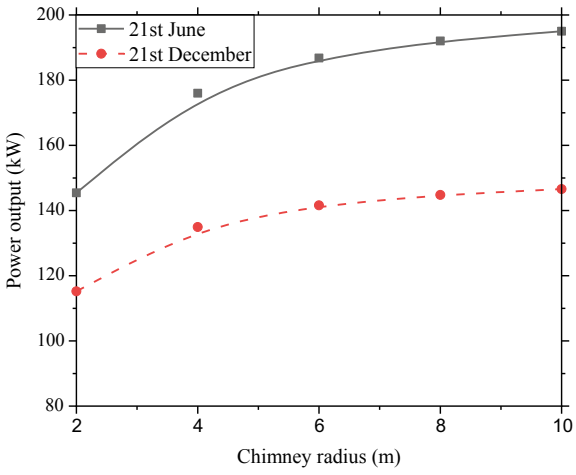

Fig. 7.13 Comparison between power output generated on 21st June and 21st December 11:00 to 12:00 for case 2 when chimney radius is varied

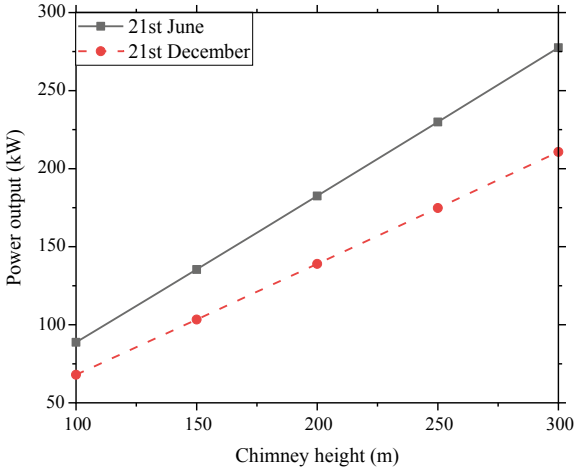

Fig. 7.14 Comparison between power output generated on 21st June and 21st December 11:00 to 12:00 for case 2 when chimney height is varied

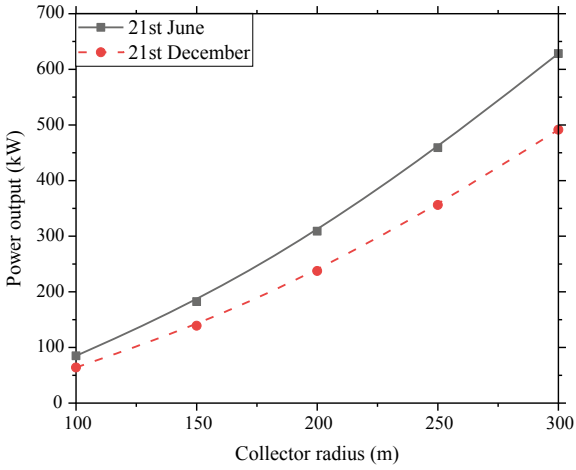

Fig. 7.15 Comparison between power output generated on 21st June and 21st December 11:00 to 12:00 for case 2 when collector radius is varied

7.4 Conclusions

Mathematical modelling of a hypothetical solar updraft tower with dimensions identical to the prototype located in Manzanares, Spain was done. Numerical analysis on various parameters like temperature, velocity, power output, efficiency was performed. From the above analysis, it can be inferred that

1. For case 1, no losses through the top surface of the collector were accounted. The power output for this case was found to be around 75 kW when averaged from sunrise to sunset for all days of the year. For the month of June, the average power output was around 90 kW.

2. In case 2, convective as well as radiative losses through the collector roof were calculated. Also, the absorptivity and reflectivity of the roof was determined. Thus, the actual heat flux involved in power generation was calculated for June and corresponding power output was estimated to be around 74 kW and the collector efficiency turned out to be nearly 80%. Theoretically, when averaged over the year, the power output could be around 60 kW, which is around 20% more than the plant in Manzanares.
3. The peak power output for case 1 was found to be nearly 145 kW and for case 2, it was around 120 kW.
4. The prototype in Manzanares was producing around 50 kW on average. The difference in power output is due to many factors like the cloud coverage, latitude, actual collector area, the ground not being a black body, effect of shadowing, difference in the ambient temperature etc.
5. Physical parameters like collector radius, chimney radius and chimney height were varied and their impact on the power output was observed.
6. Power output increases with increase in each of the above-mentioned parameters, but the nature of the increment is different. The increment is linear when chimney height is increased. When plotted against collector radius, the graph is concave upwards and against chimney radius, it is convex upwards.
7. This type of plant can be established wherever plants are being grown and thus the land is fully utilised. Also, it can be run at night by storing the heat from the sun using water or some other means. By doing so, the power generation during the day would be less when compared to a plant that does not utilise thermal storage. But the plant can run day and night and produce more power when averaged over the entire day.

Acknowledgements The authors (K. V. S. T., K. G. and H. T.) wish to express their gratitude to the School of Mechanical Material and Energy Engineering at Indian Institute of Technology Ropar for their support.

References

Agarwal A, Kumar P, Mehta B (2018) Solar updraft tower—a potential for future renewable power generation: a computational analysis. In: Tyagi H, Agarwal AK, Chakraborty PR, Powar S (eds) Applications of solar energy. Springer, Singapore, pp 319–339

Chitsomboon T (2001) A validated analytical model for flow in solar chimney

Duffie JA, Beckman WA (2003) Solar radiation

Fasel HF, Meng F, Shams E, Gross A (2013) CFD analysis for solar chimney power plants. Sol Energy 98:12–22

Haaf W (1984) Solar chimneys. Part II: preliminary test results from the Manzanares pilot plant. Int J Sol Energy 2(2):141–161

Haaf W, Friedrich K, Mayr G, Schlaich J (1983) Part I: principle and construction of the pilot plant in Manzanares. Int J Sol Energy 2(1):3–20

Incropera FP, Dewitt DP, Bergman TL, Lavine AS (1993) Fundamentals of heat and mass transfer

Koonsrisuk A, Chitsomboon T (2013) Mathematical modeling of solar chimney power plants. Energy 51:314–322

Lodhi MAK (1999) Application of helio-aero-gravity concept in producing energy and suppressing pollution. Energy Convers Manag 40(4):407–421

Pasumarthi N, Sherif SA (1998a) Experimental and theoretical performance of a demonstration solar chimney model—Part II: experimental and theoretical results and economic analysis. Int J Energy Res 22(5):443–461

Pasumarthi N, Sherif SA (1998b) Experimental and theoretical performance of a demonstration solar chimney model—Part I: mathematical model development. Int J Energy Res 22(3):277–288. Fuel Energy Abstr 39(3):201

Schlaich J (1996) The solar chimney: electricity from the sun, p 55

Schlaich J, Bergermann R, Schiel W, Weinrebe G (2005) Design of commercial solar updraft tower systems—utilization of solar induced convective flows for power generation. J Sol Energy Eng 127(1):117

Shahzad U (2012) The need for renewable energy sources. ITEE J 1(1):30–38

Zandian A, Ashjaee M (2013) The thermal efficiency improvement of a steam rankine cycle by innovative design of a hybrid cooling tower and a solar chimney concept. Renew Energy 51:465–473

Part III
Solar Thermal Systems: Cooling

Chapter 8
Solar Thermal-Powered Adsorption Chiller

Mahbubul Muttakin, Kazuhide Ito and Bidyut Baran Saha

Abstract Adsorption based cooling systems are gaining considerable attention since it can utilize low grade thermal energy, which otherwise could go as a waste. Heat sources possessing a temperature of as low as 60 °C can drive an adsorption chiller and that temperature requirement is even lower in the case of multi-stage adsorption cooling systems. A typical flat plate solar collector can provide hot water having a temperature of 65 °C in most of the countries in the Asian region. The temperature of evacuated tube collectors' water outlet can reach above 95 °C. In order to make use of such collectors, in conjunction with other auxiliary heat sources, for providing heat to power an adsorption chiller, it is imperative to have a proper mathematical model. This can aid in designing the network and predicting the performance of the whole system, prior to installation. This chapter focuses on the modelling of a system that incorporates flat plate collectors, evacuated tube collectors and a thermally powered adsorption chiller. Here, mathematical equations to calculate the efficiency of flat plate and evacuated tube collectors are presented; processes that are involved in a typical two bed adsorption cooling system are explained in brief, and a mathematical model of an adsorption chiller, that employs mass and heat recovery schemes is developed. Finally, the simulation results of the model are presented, and the performance of the chiller is investigated to demonstrate a clear understanding of its operation.

M. Muttakin · B. B. Saha (✉)
International Institute for Carbon-Neutral Energy Research (WPI-I^{2}CNER), Kyushu University, 744 Motooka, Nishi-ku, Fukuoka 819-0395, Japan
e-mail: saha.baran.bidyut.213@m.kyushu-u.ac.jp

M. Muttakin
e-mail: muttakin@kyudai.jp

M. Muttakin · K. Ito
Interdisciplinary Graduate School of Engineering Sciences, Kyushu University, Kasuga-Koen 6-1, Kasuga-shi, Fukuoka 816-8580, Japan
e-mail: ito@kyudai.jp

B. B. Saha
Mechanical Engineering Department, Kyushu University, 744 Motooka, Nishi-ku, Fukuoka 819-0395, Japan

H. Tyagi et al. (eds.), *Solar Energy*, Energy, Environment, and Sustainability, https://doi.org/10.1007/978-981-15-0675-8_8

Keywords Adsorption chiller · Evacuated tube collector · Mathematical modelling · Solar collector

8.1 Introduction

Global environmental concern and the increasing cost of fossil fuels press scientists to make renewable energy sources more sustainable and cost effective. Solar energy has been found to be the most widely used renewable energy sources over the last few decades. The early researches on solar energy had been conducted in the early' 40s by Hottel (1942). He (Hottel 1954; Zarem and Erway 1963; Hottel and Whillier 1955) continued his extensive research on solar energy, and all the early works are summarized by Duffie and Beckman (1974) in his book. Later Kalogirou (2004) presented a summary on various types of solar thermal collectors and their applications. Solar thermal collectors convert solar radiation into heat energy, which can be utilized in various applications. One of the promising application of thermal energy is cooling and dehumidification through the utilization of adsorption refrigeration technology.

With the rapid growth of the economy and development of infrastructure, energy consumption is increasing at a fast pace, and it is estimated to rise 28% within the next 20 years (Conti et al. 2016). Furthermore, according to the estimation of the International Institute of Refrigeration in Paris (Coulomb 2006), 15% of the world's total produced electricity is spent on air-conditioning and refrigeration processes of various kinds. In the present scenario, vapor compression refrigeration technology is predominant in the market, which is highly energy intensive. Furthermore, it uses CFC, HCFC based refrigerants, which are being considered as the major culprits for global warming and ozone depletion. Adsorption based refrigeration technology is environmentally benign, as it can use natural refrigerants (e.g. water, CO_2). Instead of electricity, it is primarily driven by low grade heat having a temperature of as low as 60 °C (Muttakin et al. 2018; Mitra et al. 2017; Saha et al. 2006). A typical low cost flat plate solar collector is able to provide heat at such low temperature. Hence solar thermal powered adsorption chiller is gaining considerable attention, particularly by the environmental scientists.

Scientists (Muttakin 2013) worked on the modeling and optimization of solar thermal systems utilizing various computer based simulation programs. Modelling of adsorption chiller (Wang 2001) is also necessary to make the system efficient and economically viable. The computer modelling of any system has numerous advantages (Kalogirou and Papamarcou 2000),

- Prediction of system performance.
- Optimization of the system to make it more economical and energy efficient.
- Reduction or elimination of the cost of building prototypes.
- Estimation of system performance under variable operating conditions.
- Sensitivity analysis of different design parameters.

In this book chapter model equations of a solar thermal powered adsorption chiller are presented. First, the system is briefly explained in Sect. 8.2. In the next section, the construction of a flat plate collector is described, which is followed by the derivation of different heat transfer components to calculate its efficiency. Section 8.4 models an evacuated tube collector to estimate its dynamic performance. Next model equations of a typical commercial adsorption chiller are explained, and simulation results of a 10-RTon chiller are presented under specific operating conditions. Finally, the chapter ends with a conclusion.

8.2 System Description

An adsorption chiller requires low grade heat for its operation. Hence the heat from flat plate collectors or evacuated tube collectors can drive the system. The main components of a two-bed adsorption chiller are two ad/de-sorption beds with adsorbents, one evaporator and one condenser. A schematic of a solar thermal powered adsorption chiller is shown in Fig. 8.1.

A typical ad/de-sorption bed has finned tube heat exchanger, and the adsorbents are placed between the fins. The chiller works in cycles. The four major steps of an adsorption chiller are adsorption, mass recovery, heat recovery and desorption. During the adsorption phase, cold water flows through the tubes of the adsorbent bed and during the desorption phase, hot water from the hot water tanks flows through those tubes. The difference between the temperatures of hot and cold water is known

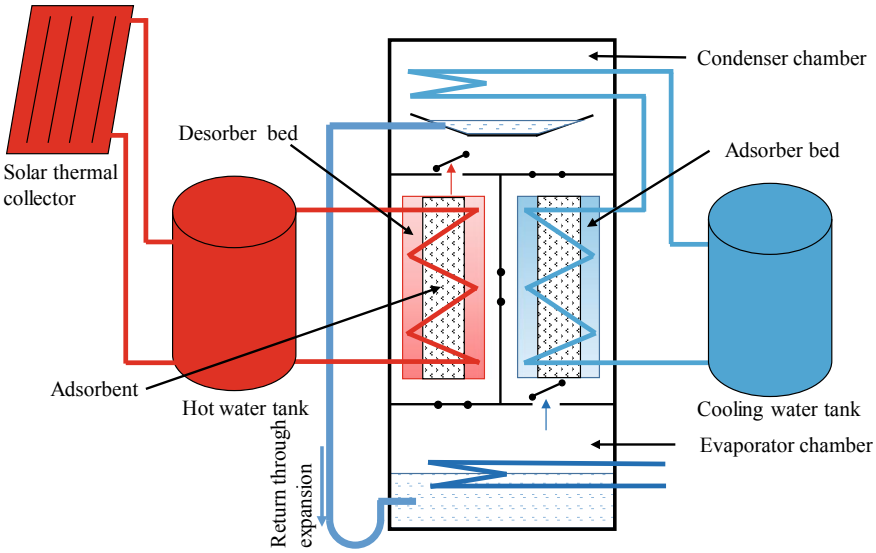

Fig. 8.1 Schematic diagram of a solar thermal powered adsorption chiller

as temperature swing. For a typical single stage silica gel—water adsorption chiller, the temperature of the hot water requires to be 60–80 °C. However, a multistage adsorption chiller can be operated at a temperature swing of 10 °C (Saha and Kashiwagi 1997). Theoretically, a temperature swing of 2.2 °C can be utilized to drive a 10-stage adsorption chiller (Saha et al. 2007).

In a solar thermal-powered adsorption chiller, heat is obtained primarily from the solar thermal collectors. However, an auxiliary electrical heater is often used to maintain the temperature in the hot water tank. This is required as the performance of the solar thermal collector strongly depends on the environmental condition. It is obvious that during rainy days, the output from the collector will be significantly lower when compared to the same during bright sunny days. The poor solar irradiance in rainy days results in lower absorbed energy by the solar thermal collector, which in turn reduces its output.

8.3 Model Equations of a Flat Plate Collector

A typical solar thermal system includes solar thermal collectors, water storage tanks and necessary piping. An adsorption chiller requires a low temperature heat source to be driven efficiently, and flat plate collectors (FPC) are the most popular solar thermal collectors considering low temperature application.

8.3.1 Components of an FPC

As can be seen in Fig. 8.2, the major components of a flat plate collector are;

- Glazing: A glazing material is placed on the top of the FPC. Glass is the most widely used glazing material because of its ability to transmit 90% of the incoming shortwave solar irradiation while being opaque to longwave radiation emitted outward by the absorber plate (Duffie and Beckman 1974).
- Absorber plate: The role of an absorber plate is to support the tubes and fins. In some collectors, it may be integrated with the tubes. The three most important materials that are used as absorber plates are copper, aluminium and stainless steel.
- Tubes: Tubes provide the path for the flow of heat-transfer fluid from inlet to outlet.
- Header: The header provides the passage for cold water inlet and hot water outlet.
- Insulation: Insulation prevents the loss of heat from the collector through its bottom and its side.
- Housing: The housing holds all the components as well as protects the system from moisture, dust etc.

An FPC is a non-concentrating type of solar thermal collector, i.e., its concentration ratio is one. The concentration ratio signifies the amount of transmitted solar

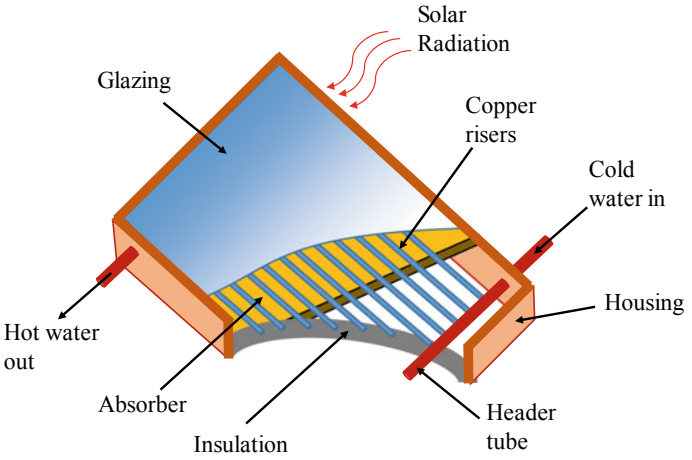

Fig. 8.2 Components of a flat plate collector

energy that causes the rise of temperature of the heat-transfer fluid and can be defined as the ratio of aperture area of the collector to its absorber area.

Prior to modelling a flat plate collector, it is important to define two parameters that play vital roles in the performance of the collector; these are, absorptance α and emittance ε. The monochromatic, directional absorptance is a surface property, defined as the fraction of the incident radiation of wavelength ψ from the direction μ, φ, that is absorbed by the surface. Mathematically it can be shown as,

$$\alpha_{\psi}(\mu, \varphi) = \frac{I_{\psi,abs}(\mu, \varphi)}{I_{\psi,inc}(\mu, \varphi)} \tag{8.1}$$

Here μ is the cosine of the polar angle and φ is the azimuth angle; I represents the radiant exposure and subscripts *abs* and *inc* stand for absorbed and incident, respectively.

On the other hand, the monochromatic directional emittance, of a surface is the ratio of the monochromatic intensity emitted by the surface in a specific direction to the same that would be emitted by a blackbody maintained at the same temperature (Duffie and Beckman 1980). Mathematically it can be written as,

$$\varepsilon_{\psi}(\mu, \varphi) = \frac{I_{\psi}(\mu, \varphi)}{I_{\psi,b}} \tag{8.2}$$

where subscript b represents blackbody.

8.3.2 Efficiency of an FPC

An efficient solar collector should possess high absorptance for radiation in the solar energy spectrum. At the same time, in order to minimize the losses, it must have low emittance for long wave radiation. The efficiency (η) of an FPC is defined as the ratio of useful gain (Q_u) to the incident solar radiation power (Q_T),

$$\eta = \frac{Q_u}{Q_T} = \frac{Q_u}{GA_c} \tag{8.3}$$

where G represents the solar irradiance in W/m^2, and A_c represents an aperture area of the collector. With G_s being the absorbed energy, the useful energy gain can be defined by,

$$Q_u = A_c[G_S - U_L(T_c - T_a)] \tag{8.4}$$

where U_L is the overall heat transfer coefficient, T_c and T_a are the mean absorber plate temperature and ambient air temperature, respectively. Hence, $U_L(T_c - T_a)$ is the thermal energy lost from the collector to the ambient through conduction, convection and infrared radiation.

In order to determine the efficiency of the collector, all the parameters of Eq. (8.4) must be known. The parameters G, A_c, T_c and T_a can be measured through experiments. The absorbed energy G_s can be calculated from,

$$G_S = G(\tau\alpha)_{eff} \tag{8.5}$$

where $(\tau\alpha)_{eff}$ is called the effective transmittance-absorptance coefficient. It can be approximated from the known value of incidence angle modifier of a collector, as defined by,

$$K_{\tau\alpha} = \frac{(\tau\alpha)_{eff}}{(\tau\alpha)_n}$$

where $(\tau\alpha)_n$ is transmittance-absorptance normal to the collector surface. For FPC with flat covers, the incidence angle modifier depends on the angle of incidence θ following the below equation (Souka and Safwat 1966),

$$K_{\tau\alpha} = 1 + b_0\left(\frac{1}{\cos\theta} - 1\right)$$

where b_0 is the incidence angle modifier constant, and it has a positive value.

The thermal network of an FPC with two covers is shown in Fig. 8.3. The absorbed energy G_s is converted to useful energy gain Q_u after losing a portion to the ambient environment through the top and bottom of the collector. At some typical location, let T_p be the absorber plate temperature. From the top of the collector, heat loss is due to

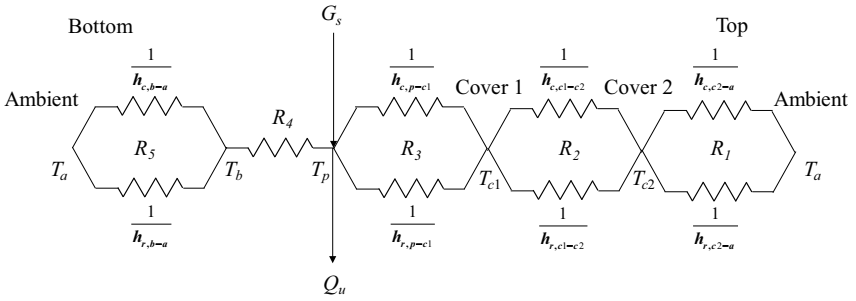

Fig. 8.3 Thermal model of an FPC having two covers

convection and radiation heat transfer to the ambient. This heat loss is essentially the same as the steady state energy transfer between the plate at T_p and the first cover at T_{c1} and is equal to the energy transfer between any other two adjacent covers. Hence, the heat loss through the top of the FPC can be expressed by,

$$Q_{top,coll} = h_{c,p-c1}(T_p - T_{c1}) + \frac{\sigma(T_p^4 - T_{c1}^4)}{\frac{1}{\varepsilon_p} + \frac{1}{\varepsilon_{c1}} - 1} \tag{8.6}$$

where $h_{c,p-c1}$ is the convection heat transfer coefficient between two inclined parallel plates, σ is the Stefan-Boltzmann constant which is equal to 5.6697×10^{-8} W/(m^2 °C^4), and ε_p and ε_{c1} are the directional emittances of absorber plate and cover 1, respectively. Equation (8.6) can be written in terms of radiation heat transfer coefficient $h_{r,p-c1}$ as,

$$Q_{top,coll} = (h_{c,p-c1} + h_{r,p-c1})(T_p - T_{c1}) \tag{8.7}$$

$h_{r,p-c1}$ can be calculated from,

$$h_{r,p-c1} = \frac{\sigma(T_p + T_{c1})(T_p^2 + T_{c1}^2)}{\frac{1}{\varepsilon_p} + \frac{1}{\varepsilon_{c1}} - 1} \tag{8.8}$$

Thus the resistance R_3 can be written as,

$$R_3 = \frac{1}{h_{c,p-c1} + h_{r,p-c1}} \tag{8.9}$$

The resistance, R_2, between the two covers can have a similar expression, and the expression is essentially of the same form for further adjacent covers. However, considering practical applications, the maximum limit of the number of covers of an FPC is two. The resistance to heat loss, R_1, from the top cover to the ambient, can be represented following the similar expression,

$$R_1 = \frac{1}{h_w + h_{r,c2-a}} \tag{8.10}$$

where resistance to radiation heat transfer accounts for radiation exchange with the sky having a temperature T_{sky};

$$h_{r,c2-a} = \frac{\sigma \varepsilon_c (T_{c2} + T_{sky})(T_{c2}^2 + T_{sky}^2)(T_{c2} - T_{sky})}{T_{c2} - T_a} \tag{8.11}$$

For free-convection conditions, the minimum values of convection heat transfer coefficient are 5 and 4 W/(m^2 °C) for temperature differences of 25 and 10 °C, respectively. But for forced-convection conditions, it can be calculated following the expression obtained from Mitchell's (1976) experimental results,

$$h_w = \frac{c_0 \left(\frac{v}{v_0}\right)^{0.6}}{\left(\frac{L}{L_0}\right)^{0.4}} \tag{8.12}$$

where $v_0 = 1$ m/s, $c_0 = 8.6$ W/(m^2 °C) and $L_0 = 1$ m. L is the cubic root of the collector house volume in m and v represents the wind speed in m/s. For the simultaneous occurrence of free and forced convections, it is recommended (McAdams 1954) to use the larger value of the convection heat transfer coefficients; hence it can be expressed as,

$$h_w = \max\left[5, \frac{8.6\left(\frac{v}{v_0}\right)^{0.6}}{\left(\frac{L}{L_0}\right)^{0.4}}\right] \text{W/(m}^2\,^\circ\text{C)} \tag{8.13}$$

Thus, for an FPC having two covers, the mathematical expression of the top loss coefficient from the collector to the surroundings becomes,

$$U_{top,coll} = \frac{1}{R_1 + R_2 + R_3} \tag{8.14}$$

On the other hand, losses through the back of the collector can be obtained from,

$$U_{bot,coll} = \frac{1}{R_4} = \frac{\kappa_{ins,coll}}{\delta_{ins,coll}} \tag{8.15}$$

where $\kappa_{ins,coll}$ and $\delta_{ins,coll}$ are the thermal conductivity and thickness of the insulation, respectively.

It needs mentioning that, for a well-designed system, the edge loss from the collector can be neglected as its value is very small compared to other heat losses from the collector. With edge loss coefficient-area product of $(UA)_{edge}$, the losses

through the edges of the collector can be calculated from,

$$U_{edge,coll} = \frac{(UA)_{edge,coll}}{A_C} \tag{8.16}$$

The overall heat transfer coefficient, U_L, is essentially the summation of all the loss coefficients. Adding Eqs. (8.14)–(8.16),

$$U_L = U_{top,coll} + U_{bot,coll} + U_{edge,coll} \tag{8.17}$$

Putting the value of U_L into Eq. (8.4), one can determine the useful energy gain Q_u, which can be utilized to determine the FPC efficiency η using Eq. (8.3).

8.4 Model Equations of an Evacuated Tube Collector

An evacuated tube collector (ETC) comprises an absorber plate attached to a heat pipe, placed inside a vacuum-sealed tube, as can be seen in Fig. 8.4. Since the plate and the heat pipe are surrounded by the vacuum, the heat loss to the environment by convection and conduction is very minimal. This results in higher efficiency of ETC when compared to FPC.

The solar energy absorbed by the plate, through both direct and diffuse radiation, is transferred to the heat-transfer fluid kept inside the heat pipe. Receiving heat, the fluid, e.g. methanol, evaporates and rises upward to the heat sink where it condenses again releasing heat to the flow-fluid, e.g. water. After condensing, the heat transfer

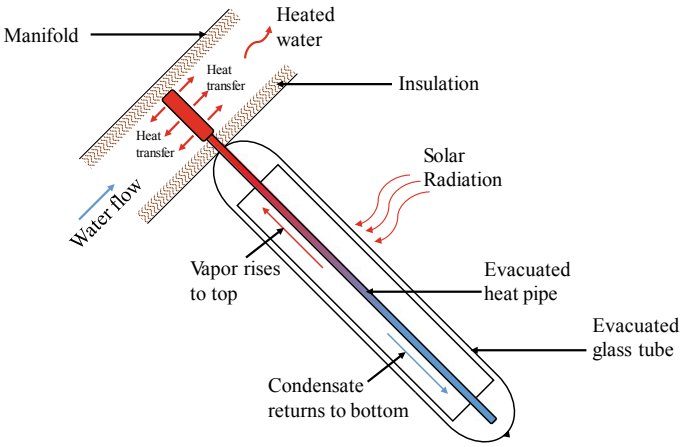

Fig. 8.4 Schematic of a heat pipe evacuated tube collector

fluid returns to the collector for receiving heat from the absorbed solar energy again. Thus it undergoes an evaporating—condensing cycle.

8.4.1 Efficiency of an ETC

The efficiency and useful energy gain of such a collector can be obtained using the same equations as used for FPC, i.e. Eqs. (8.3) and (8.4).

$$\eta = \frac{Q_u}{Q_T} = \frac{Q_u}{G A_c}$$
$$Q_u = A_c[G_S - U_L(T_c - T_a)]$$

Also from Eq. (8.5), we know, $G_S = G(\tau\alpha)_{eff}$. For evacuated tube collectors, the overall incidence angle modifier $K_{\tau\alpha}$ is equal to the product of incidence angle modifier in transverse plane K_t and that in longitudinal plane K_l,

$$K_{\tau\alpha} = K_t.K_l = \frac{(\tau\alpha)_{eff}}{(\tau\alpha)_n}$$

In order to determine the efficiency and useful energy gain, it is important to know the thermal model of an ETC, which is shown in Fig. 8.5. The energy absorbed by the plate is first transmitted to the heat-transfer fluid (e.g., methanol) placed inside the heat pipe, which transfers it to the manifold fluid (e.g., water). This causes the rise of the temperature of the manifold fluid.

Now, the steady state heat transfer rate from plate to heat transfer fluid can be represented by,

$$Q_{c-h} = h_e A_C (T_c - T_h) \tag{8.18}$$

where T_h represents the mean temperature of the heat-transfer fluid, and h_e is the heat transfer coefficient. This heat transfer rate Q_{c-h} is essentially the same as the

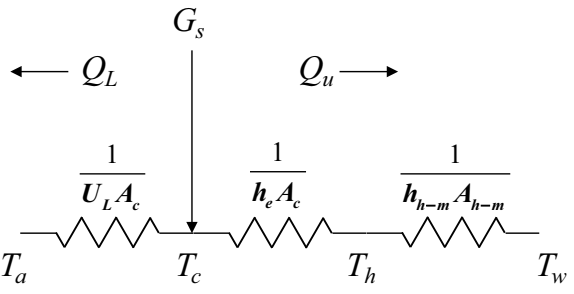

Fig. 8.5 Thermal model of a typical ETC

useful energy gain Q_u, i.e. $Q_{c-h} = Q_u$. Eliminating T_c and from Eqs. (8.4), (8.5) and (8.18), we can write,

$$Q_{c-h} = \frac{h_e/U_L}{h_e/U_L + 1} A_C[G(\tau\alpha)_{eff} - U_L(T_h - T_a)] \tag{8.19}$$

The steady state energy transfer from the heat-transfer fluid to the manifold fluid can be expressed by,

$$Q_{h-m} = h_{h-m} A_{h-m} \left(T_h - T_f\right) \tag{8.20}$$

where, h_{h-m} represents the heat transfer coefficient for this heat flow, A_{h-m} is the area of the heat pipe in contact with the manifold fluid and T_f is the mean temperature of the working fluid.

Again, since $Q_{c-h} = Q_{h-m}$, eliminating T_h from Eqs. (8.19) and (8.20) we can write,

$$\begin{aligned} Q_{h-m} &= \frac{A_C}{(U_L A_C / h_{h-m} A_{h-m}) + (U_L/h_e + 1)} [G(\tau\alpha)_{eff} - U_L(T_f - T_a)] \\ &\Rightarrow Q_{h-m} = F_r A_C [G(\tau\alpha)_{eff} - U_L(T_f - T_a)] \end{aligned} \tag{8.21}$$

where

$$F_r = \frac{1}{(U_L A_C / h_{h-m} A_{h-m}) + (U_L/h_e + 1)} \tag{8.22}$$

F_r is known as the heat removal factor and can be defined as the ratio of the actual amount of heat transferred to the manifold fluid to the heat that would be transferred if the entire collector were at the fluid inlet temperature. From Eq. (8.22), it can be said that the value of F_r is dependent on three ratios, U_L/h_e, U_L/h_{h-m} and A_{h-m}/A_c.

Since $Q_{h-m} = Q_u$, from Eqs. (8.3) and (8.21), collector efficiency can be written as,

$$\eta = F_r(\tau\alpha)_{eff} - F_r U_L \frac{(T_f - T_a)}{G} \tag{8.23}$$

Thus the steady state efficiency of an ETC has a linear form; however, in real applications, it may not be linear and may be difficult to obtain solving all the parameters. To overcome this shortcoming, Cooper and Dunkle (1981) proposed a second order efficiency equation with the assumption,

$$F_r U_L = a + b(T_f - T_a) \tag{8.24}$$

Substituting Eq. (8.24) into the Eq. (8.23), we obtain,

$$\eta = \underbrace{F_r(\tau\alpha)_{eff}}_{\eta_0} - a\frac{\left(T_f - T_a\right)}{G} - b\frac{\left(T_f - T_a\right)^2}{G} \tag{8.25}$$

where η_0, a and b are constants and are usually furnished by the collector manufacturer. The mean manifold fluid temperature T_f can be considered as an average of the fluid temperatures at the inlet (T_i) and at the outlet (T_0), i.e.,

$$T_f = \frac{T_i + T_0}{2}$$

and thus the efficiency can be calculated from,

$$\eta = \eta_0 - a\frac{\left(T_f - T_a\right)}{G} - b\frac{\left(T_f - T_a\right)^2}{G} \tag{8.26}$$

It needs mentioning that the efficiency of an FPC can be expressed by the same equation as Eq. (8.26) shown above.

8.4.2 Dynamic Modelling of an ETC

In an evacuated tube collector, there are two fluids, heat transfer fluid or refrigerant and manifold fluid (water is considered in the current modelling). The current model is based on the assumption that there is no refrigerant present in the ETC, rather, water is assumed to flow directly through the heat pipes. The major assumptions are summarized below,

- There is no presence of refrigerant. Water flows directly through the heat pipes.
- The flow of water is only in the positive x direction.
- The heat conduction in the fluid moving direction is neglected.
- The temperature dependence of thermo-physical properties of water is considered.
- Properties of glass and absorber do not depend on temperature and are assumed to be constant.
- The infrared emissivity of the sky is unity ($\varepsilon_{sky} = 1$).

Based on the stated assumptions, the heat influx to various components of an ETC is depicted in Fig. 8.6. As shown in the figure, the model (Praene et al. 2005) consists of 3 thermal nodes. These are, the transparent glass cover, the absorber plate and the fluid (water) having temperatures T_g, T_c and T_f, respectively. The heat transfer between the sky and the glass cover is by radiation only. Again, since the absorber plate is surrounded by the vacuum, heat transfer between the glass cover and absorber plate, is entirely by radiation. Convective heat transfer is existent between the glass cover and the ambient environment, and between the absorber plate and water.

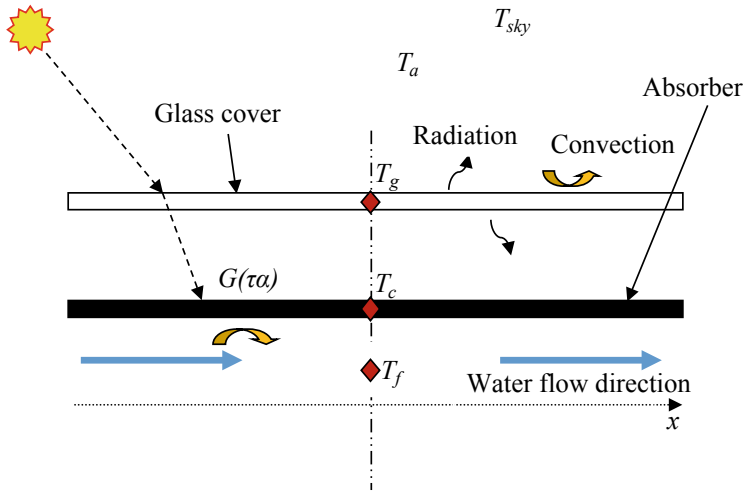

Fig. 8.6 Assumed model of ETC

Now, the governing equation that explains the time dependence of the temperature of the glass cover is,

$$Cp_g\delta_g\rho_g\frac{dT_g}{dt} = \varepsilon_g\sigma(T_{sky}^4 - T_g^4) + h_{g,a}(T_a - T_g) + \frac{\varepsilon_c\varepsilon_g}{\varepsilon_c + \varepsilon_g - \varepsilon_c\varepsilon_g}\sigma(T_c^4 - T_g^4) \tag{8.27}$$

where subscripts g, a, c and *sky* stand for glass cover, ambient, absorber plate and the sky, respectively. Cp represents the specific heat capacity, T is the temperature in K; δ stands for the thickness, and ρ represents the density. Using Swinbank's formula (Swinbank 1963) $T_{sky} = pT_a^{1.5}$ where $p = 0.0552\ \mathrm{K}^{-1/2}$, the sky temperature can be obtained from the ambient temperature.

Now, for the absorber plate, the governing equation can be expressed as,

$$Cp_c\delta_c\rho_c\frac{dT_c}{dt} = G(\tau\alpha) + \frac{\varepsilon_c\varepsilon_g}{\varepsilon_c + \varepsilon_g - \varepsilon_c\varepsilon_g}\sigma(T_g^4 - T_c^4) + h_{f,c}(T_f - T_c) \tag{8.28}$$

where subscript f stands for fluid (water). The plate receives radiative heat from the glass cover and transfers it to the working fluid predominantly in convective mode.

Finally, the temperature of the fluid, having a velocity of u along the positive x axis, depends on time and its position in the flow channel. The governing equation to describe the change in fluid temperature with time and position is,

$$Cp_f\rho_f\frac{\pi d_{in}^2}{4}\left(\frac{dT_f}{dt} + u\frac{dT_f}{dx}\right) = \pi d_{in}h_{f,c}(T_c - T_f) \tag{8.29}$$

where d_{in} represents the diameter of the absorber tube that contains the fluid.

Thus Eqs. (8.27)–(8.29) are the governing dynamic equations to determine the temperatures of the glass cover, absorber plate and working fluid (with both time and position) respectively.

8.5 Modelling of an Adsorption Chiller

The major components of a two-bed adsorption chiller are evaporator, condenser and two adsorber beds. An adsorber bed is necessarily a heat exchanger, filled with the adsorbent material, e.g., silica gel, packed between the fins of that finned tube heat exchanger. Adsorption and desorption are exothermic and endothermic processes, respectively. To extract the heat of adsorption, it is necessary to circulate cooling water through the tubes of the adsorber bed during the adsorption process. Furthermore, during this process, the bed is connected to the evaporator in order to receive the adsorbate vapor, e.g., water vapor, to be adsorbed by the adsorbent. Consequently, the other bed goes through the desorption process and is connected to the condenser. The hot water, flowing through its tubes, provide the necessary heat required for desorption.

Thus an adsorption chiller works in a cyclic manner. Each cycle consists of three operating modes (a) adsorption/desorption, (b) mass recovery and (c) heat recovery. This section will state the lumped analytical simulation model equations of an adsorption chiller that uses silica gel as the adsorbent and water as the adsorbate. The model is based on the following assumptions,

- The porous properties of the adsorbent are constant.
- The kinetics parameters, i.e. the diffusivity and activation energy, are independent of temperature and pressure.
- At the first time step of any phase, the model does not consider the water flow condition within the bed in the previous time step.
- The isotherm and kinetics equations for adsorption and desorption are same.

8.5.1 Description of Operating Modes

8.5.1.1 Mode (a): Adsorption/Desorption

In the operating mode (a) (see Fig. 8.7), Bed 1 goes through the desorption phase, and adsorption is taking place in Bed 2. Bed 1 is heated up by the hot water streams, which also raises the pressure of Bed 1.

The connecting valve between Bed 1 and condenser is open at this stage, and the desorbed vapor is then condensed in the condenser and returned back to the evaporator through an expansion valve. The other bed (Bed 2) is connected to the

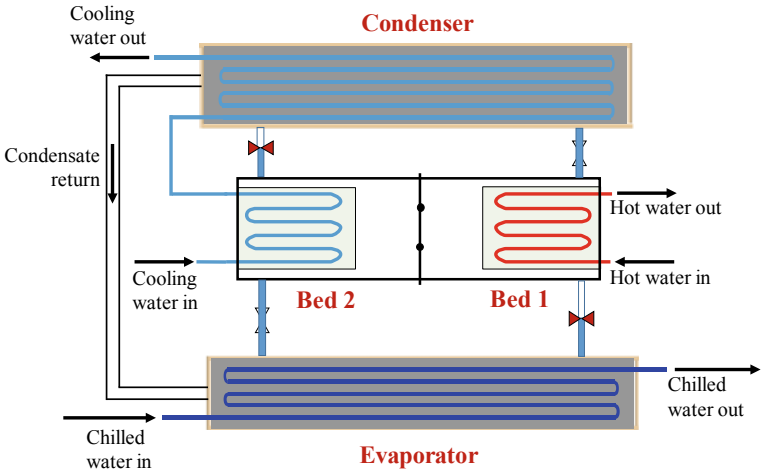

Fig. 8.7 Schematic of an adsorption chiller. Mode (a): Bed 1 goes through desorption and Bed 2 goes through adsorption

evaporator to adsorb the evaporated vapor, and this evaporation produces the desired cooling effect. The cooling water exiting from Bed 2 flows through the condenser to condense the desorbed vapor. The heated cooling water is usually cooled by a cooling tower.

8.5.1.2 Mode (b): Mass Recovery

At the end of ad/de-sorption, pressure in Bed 1 becomes higher than that in Bed 2. In the mass recovery mode (see Fig. 8.8), the bypass valve between the two beds is opened which causes flow of water vapor from hot Bed 1 to comparatively cooler Bed 2 by means of pressure swing. The mass recovery time is adjusted to attain the mechanical equilibrium between the two beds, while the excess time is not recommended.

8.5.1.3 Mode (c): Heat Recovery

Due to the flow of hot and cooling water through Bed 1 and Bed 2, respectively, the temperature of Bed 1 becomes higher than that of Bed 2.

In the heat recovery mode (see Fig. 8.9) the cooling water first flows through Bed 1, extracting heat from the bed the water releases it to Bed 2. This causes an increase and reduction of temperatures of Bed 2 and Bed 1, respectively. Thus heat recovery reduces the total amount of heat required, which ultimately increases the system's coefficient of performance (COP).

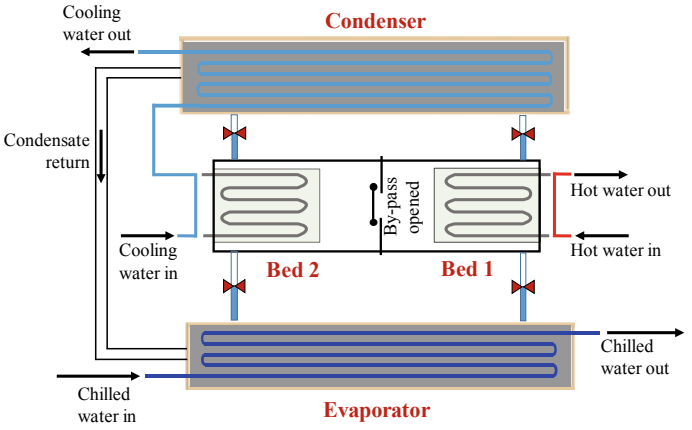

Fig. 8.8 Schematic of an adsorption chiller. Mode (b): Mass recovery. Water vapor flows from Bed 1 to Bed 2 due to the difference in pressure

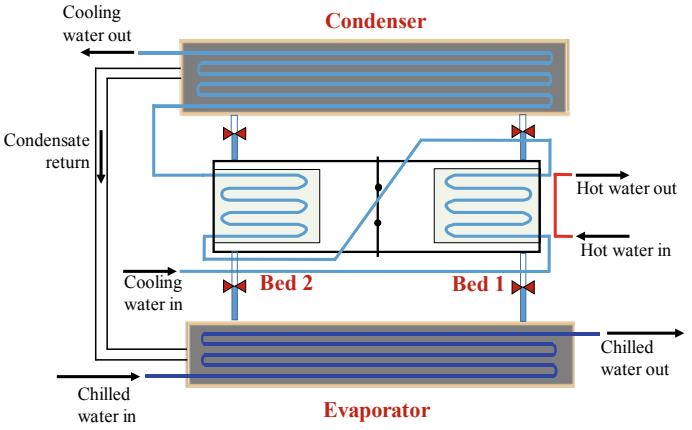

Fig. 8.9 Schematic of an adsorption chiller. Mode (c): Heat recovery. Cooling water extracts heat from Bed 1 and releases it to Bed 2 before flowing through the condenser

Thus one cycle is complete and in the next stage, the cycle is repeated, and the beds perform an alternating role. Bed 1 starts adsorbing and is connected to the evaporator and Bed 2 starts desorbing and gets connected to the condenser. The pressure of Bed 1 becomes essentially the same as that of evaporator and Bed 2 attains the same pressure as of condenser. Hence in the mass recovery mode, the desorbed vapor of Bed 2 is further passed to Bed 1 in order to achieve the mechanical equilibrium between the two beds. The heat is extracted from the hot Bed 2 by the cooling water and released to comparatively cooler Bed 1, during the heat recovery mode.

8.5.2 Model Equations for the Adsorbent—Adsorbate Pair

Prior to modelling different components (beds, evaporator, condenser) of an adsorption chiller, it is required to define the models of two most important parameters of an adsorbent—adsorbate pair; these are isotherm and kinetics.

8.5.2.1 Isotherm Model

Adsorption isotherm defines the maximum amount of adsorbate that can be adsorbed by the adsorbent at a particular pressure. The values of isotherm parameters are determined by correlating the experimental data of equilibrium uptake with the model. For silica gel—water pair, S-B-K model (Saha et al. 1995) can be used to determine the equilibrium adsorption uptake,

$$w* = A(T_{ads})\left[\frac{P_{sat}\left(T_{ref}\right)}{P_{sat}(T_{ads})}\right]^{B(T_{ads})} \tag{8.30}$$

where,

$$A(T_{ads}) = A_0 + A_1 T_{ads} + A_2 T_{ads}^2 + A_3 T_{ads}^3$$
$$B(T_{ads}) = B_0 + B_1 T_{ads} + B_2 T_{ads}^2 + B_3 T_{ads}^3.$$

T_{ads} and T_{ref} are the adsorption temperature and saturation temperature, respectively, and P_{sat} is the saturation pressure. The values of the parameters A_0, A_1, A_2, A_3, B_0, B_1, B_2, B_3 are determined by fitting the model with experimental uptake data.

8.5.2.2 Kinetics Model

Adsorption kinetics can be defined as the rate of adsorption, which essentially determines the cycle time of the adsorption chiller. The faster the kinetics, the smaller the cycle time required, hence the greater the specific cooling produced. The most widely used kinetics models are linear driving force (LDF) model, Fickian diffusion (FD) model, Langmuir model, semi-infinite model etc. Some models are also proposed by implementing suitable modifications of the above mentioned models. In the current modelling of the adsorption chiller LDF model is utilized to simulate the adsorption kinetics, which assumes that the adsorption rate is proportional to the difference between the equilibrium uptake (w*) and the instantaneous uptake (w),

$$\frac{dw}{dt} = k_s a_v [w * -w(t)] \tag{8.31}$$

where $k_s a_v$ is the overall mass transfer coefficient. Due to the spherical shape of silica gel adsorbent, the overall mass transfer coefficient can be written as,

$$k_s a_v = \frac{15 D_s}{R_p^2},$$

where D_s is the diffusion time constant, and R_p is the adsorbent particle radius. D_s depends on the temperature T, following equation,

$$D_s = D_{so} \exp\left(\frac{-E_a}{RT}\right)$$

where D_{so} is the pre-exponential constant, E_a is the activation energy, and R is the universal gas constant. The values of D_{so} and E_a can be obtained from the experimental data by plotting $\ln D_s$ against $1/T$ as described by the equation stated below,

$$\ln D_s - \ln D_{so} = \left(\frac{-E_a}{RT}\right)$$

This plot is known as the Arrhenius plot. The slop yields $-E_a/R$ and the intercept provides the constant, D_{so}. Hence, for an adsorption chiller comprising silica gel—water pair, Eq. (8.31) can be rewritten as,

$$\frac{dw}{dt} = \frac{15 D_{so}}{R_p^2} \left\{ \exp\left(\frac{-E_a}{RT}\right) \right\} (w * -w) \tag{8.32}$$

8.5.3 Model Equations of the Chiller

The energy balance equations of different components (beds, evaporator, condenser) can be generalized as follows,

$$\left[MC_p\right]_{H.Ex} \frac{dT_k}{dt} = M_{bed} h_{ads} \frac{dw}{dt} + \left[\dot{m} C_p (T_{in} - T_{out})\right]_{H.Ex.fluid} \tag{8.33}$$

where M is the mass, C_p is specific heat capacity, M_{bed} is the mass of adsorbent used, and h_{ads} is the isosteric heat of adsorption/desorption. k indicates various components of adsorption chiller, i.e., adsorbing/desorbing bed, evaporator and condenser. Subscripts *H.Ex* and *H.Ex.fluid* stand for heat exchanger and heat transfer fluid respectively; *in* and *out* represent inlet and outlet respectively. The left-hand side of Eq. (8.33) represents the rate of change of enthalpy of the particular heat exchanger component (adsorbing/desorbing bed, evaporator, condenser). The first term on the right-hand side indicates the amount of heat released or absorbed by the adsorbent

during the process of adsorption or desorption. And the last term indicates the sensible heat transfer between the heat transfer fluid and the respective component.

The solution of Eq. (8.33) provides the temperature T_k of the heat exchanger components. But that requires the outlet temperature T_{out} to be known. In order to determine T_{out}, the log mean temperature difference (LMTD) of the energy balance equation for heat transfer fluid is employed. According to that method, the amount of heat transfer,

$$\dot{Q} = UA\Delta T_{\ln} \tag{8.34}$$

where U and A are the overall heat transfer coefficient and heat transfer surface area of the heat exchanging component respectively, and ΔT_{ln} represents LMTD. Again $\dot{Q} = \dot{m}C_p(T_{out} - T_{in})$ gives,

$$\Delta T_{\ln} = \frac{\dot{m}C_p(T_{out} - T_{in})}{UA} \tag{8.35}$$

But ΔT_{ln} is defined by the equation,

$$\Delta T_{\ln} = \frac{(T - T_{in}) - (T - T_{out})}{\ln\left(\frac{T-T_{in}}{T-T_{out}}\right)} \tag{8.36}$$

Hence, from Eqs. (8.35) and (8.36), we can determine T_{out}, as given in the equation below,

$$T_{out} = T - \left[(T - T_{in})\exp\left(-\frac{UA}{\dot{m}C_p}\right)\right] \tag{8.37}$$

Substituting T_{out} into Eq. (8.33), it can be written as,

$$\left[MC_p\right]_{H.Ex}\frac{dT_k}{dt} = M_{bed}h_{ads}\frac{dw}{dt} + \left[\dot{m}C_p(T_{in} - T_k)\left\{1 - \exp\left(-\frac{UA}{\dot{m}C_p}\right)\right\}\right]_{H.Ex.fluid} \tag{8.38}$$

Thus, Eq. (8.38) is the energy balance equation, which is valid for all the heat exchanger components of the chiller.

8.5.3.1 Modelling of Adsorber/Desorber Bed

An adsorber/desorber bed comprises several modules where each module is necessarily a finned tube heat exchanger, and the adsorbents are packed between the fins. The mass of adsorbent loaded in each bed depends on the cooling capacity of the chiller. Figure 8.10 represents a typical module of a finned-tube heat exchanger.

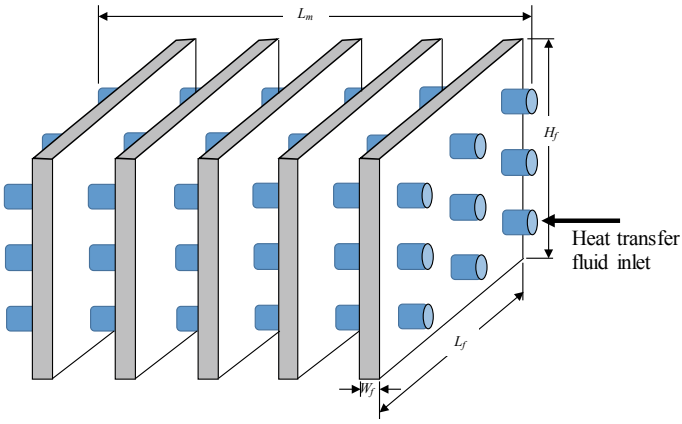

Fig. 8.10 A module of a finned-tube heat exchanger

Let us consider a bed containing N_m number of modules. Length of each module is $L_{m,}$ and each module contains N_t a number of tubes having outside and inside diameters $D_{m,o}$ and $D_{m,i}$ respectively. If the tube material density is denoted by ρ_t, the total mass of the tubes can be determined by,

$$M_t = \frac{\pi}{4}\left(D_{m,o}^2 - D_{m,i}^2\right) L_m N_t \rho_t \tag{8.39}$$

If L_f, H_f and W_f are the fin's length, height and width respectively, the fin surface area that is in contact with the adsorbent can be calculated from,

$$A_f = L_f H_f - \frac{\pi}{4} D_{m,o}^2 N_t \tag{8.40}$$

If there are N_f number of fins in each module and the density of the fin material is ρ_f, the total mass of the fins can be expressed by,

$$M_f = A_f W_f \rho_f N_f \tag{8.41}$$

Now, let us assume $C_{p,t}$, $C_{p,f}$ and $C_{p,s}$ are the specific heat capacities of tube material, fin material and silica gel. If M_{bed} is the amount of adsorbent used in each bed, we can write,

$$\left[MC_p\right]_{bed} = \left(M_t C_{p,t} + M_f C_{p,f}\right) N_m + M_{bed} C_s \tag{8.42}$$

The adsorbent bed goes through adsorption, desorption, mass recovery and heat recovery phases. Hence the model equations for each phase is narrated in the following sub-sections.

Bed Equations During Adsorption-Desorption

Let us assume, at a certain point of time, Bed 1 is at the desorption phase, and Bed 2 is at adsorption phase. The desorber bed, i.e., Bed 1, is then connected to the condenser. Hot water flows through the tubes of the heat exchanger, providing the necessary heat for the process of desorption. The hot water outlet temperature depends on the rate of heat transfer between the tubes and the adsorbent bed. For the desorber bed, Eq. (8.38) can be written as,

$$\left[MC_p\right]_{bed,des}\frac{dT_{bed,des}}{dt} = M_{bed}h_{ads}\left(\frac{dw}{dt}\right)_{des} + \dot{m}_{hot}C_{p,hot}(T_{in,hot} - T_{bed,des})\left\{1 - \exp\left(-\frac{(UA)_{bed}}{\dot{m}_{hot}C_{p,hot}}\right)\right\} \tag{8.43}$$

where, $T_{bed,des}$ is the temperature of the desorbing bed, $\dot{m}_{hot}$ and $C_{p,hot}$ are the flow rate and specific heat capacity of hot water. $\left(\frac{dw}{dt}\right)_{des}$ is the rate of desorption and can be calculated using Eq. (8.32). The equilibrium uptake w^* at any time step can be determined using Eq. (8.30). It needs mentioning that in the case of a desorber bed, $P_{sat}(T_{ref})$ is essentially the condenser pressure and $P_{sat}(T_{ads})$ corresponds to the saturation pressure of water at the bed temperature. $\left[MC_p\right]_{bed,des}$ can be obtained from,

$$\left[MC_p\right]_{bed,des} = \left[MC_p\right]_{bed} + wM_{bed}C_{p,des}$$

where, $C_{p,des}$ is the specific heat capacity of water vapor at the desorber bed temperature. $T_{in,hot}$ is the inlet temperature of hot water, and the hot water outlet temperature can be determined from,

$$T_{out,hot} = T_{bed,des} - \left[\left(T_{bed,des} - T_{in,hot}\right)\exp\left(-\frac{(UA)_{bed}}{\dot{m}_{hot}C_{p,hot}}\right)\right] \tag{8.44}$$

Similar to desorber bed, the model equation for adsorber bed, i.e., for Bed 2, can be written as,

$$\left[MC_p\right]_{bed,ads}\frac{dT_{bed,ads}}{dt} = M_{bed}h_{ads}\left(\frac{dw}{dt}\right)_{ads} + \dot{m}_{cool}C_{p,cool}(T_{in,cool} - T_{bed,ads})\left\{1 - \exp\left(-\frac{(UA)_{bed}}{\dot{m}_{cool}C_{p,cool}}\right)\right\} \tag{8.45}$$

where subscripts *ads* and *cool* represent adsorption and cooling water, respectively. The outlet temperature of cooling water can be calculated from,

$$T_{out,cool} = T_{bed,ads} - \left[\left(T_{bed,ads} - T_{in,cool}\right)\exp\left(-\frac{(UA)_{bed}}{\dot{m}_{cool}C_{p,cool}}\right)\right] \tag{8.46}$$

Since the adsorber bed is connected to the evaporator, the equilibrium uptake w^* is a function of evaporator pressure and saturation pressure of water at the bed temperature.

Bed Equations During Mass Recovery

In the mass recovery stage, there is no water flow through any of the bed, as can be seen in Fig. 8.8. Hence the outlet temperatures of hot and cooling water will remain the same as their inlet temperatures. The beds are also isolated from the evaporator and condenser. At the end of the ad/de-sorption phase, the pressure at Bed 1 becomes higher than that at Bed 2. The opening of the by-pass valve in the mass recovery stage initiates the flow of excess vapor from Bed 1 to Bed 2 due to pressure swing, and the process is usually continued (accomplished by appropriate determination of cycle time) until the mechanical equilibrium between the two beds is attained. The flow rate of vapor, from Bed 1 to Bed 2, during this stage can be determined from Thu et al. (2017),

$$\frac{dw}{dt} = 1.41576 Y A_{bp}\sqrt{\frac{\Delta P \rho}{K}} \tag{8.47}$$

where Y is the expansion factor (Shashi Menon 2015), A_{bp} is the cross-section area of the bypass valve, ΔP is the pressure difference between the two beds and K is the total resistance coefficient. It needs mentioning that the reversed vapor flow due to pressure changes is also accounted for in the above model. K can be calculated from,

$$K = f\frac{L}{D} + \sum_i \xi_i$$

where ξ is the minor loss coefficient for different components, L and D are the length and width of the bypass valve, respectively. f is the friction factor given as,

$$f = \begin{cases} \frac{64}{\mathrm{Re}}\ for\ \mathrm{Re} < 2300 \\ \frac{1.325}{\left[\ln\left(\frac{e}{3.7D} + \frac{5.74}{\mathrm{Re}^{0.9}}\right)\right]^2}\ for\ 5000 \le \mathrm{Re} \le 10^8 \& 10^{-6} \le \frac{e}{D} \le 10^{-2} \end{cases}$$

The energy balance equations for mass recovery can be written as follows;
for Bed 1,

$$\left[MC_p\right]_{bed,des}\frac{dT_{bed,des}}{dt} = -M_{bed}h_{ads}\frac{dw}{dt} \tag{8.48}$$

and for Bed 2,

$$\left[MC_p\right]_{bed,ads}\frac{dT_{bed,ads}}{dt} = M_{bed}h_{ads}\frac{dw}{dt} \tag{8.49}$$

Bed Equations During Heat Recovery

In the heat recovery stage, the beds are isolated from evaporator, condenser and also from each other. As a result, there is no flow of water vapor through the beds. The temperature of hot water at the outlet remains the same as it is at the inlet since there is no flow of hot water through the bed (see Fig. 8.9**).** The cooling water extracts heat from the desorbed bed (Bed 1) and heats up the adsorbed bed (Bed 2) on its way to the condenser. The cooling water outlet temperature from Bed 1 can be written as,

$$T_{out,des} = T_{bed,des} - \left[\left(T_{bed,des} - T_{in,cool}\right)\exp\left(-\frac{(UA)_{bed}}{\dot{m}_{cool}C_{p,cool}}\right)\right] \tag{8.50}$$

And the cooling water outlet temperature from Bed 2 can be calculated from,

$$T_{out,ads} = T_{bed,ads} - \left[\left(T_{bed,ads} - T_{out,des}\right)\exp\left(-\frac{(UA)_{bed}}{\dot{m}_{cool}C_{p,cool}}\right)\right] \tag{8.51}$$

The energy balance equations for the two beds can be expressed by;
for Bed 1,

$$\left[MC_p\right]_{bed,des}\frac{dT_{bed,des}}{dt} = \dot{m}_{cool}C_{p,cool}\left(T_{in,cool} - T_{bed,des}\right)\left\{1 - \exp\left(-\frac{(UA)_{bed}}{\dot{m}_{cool}C_{p,cool}}\right)\right\} \tag{8.52}$$

for Bed 2,

$$\left[MC_p\right]_{bed,ads}\frac{dT_{bed,ads}}{dt} = \dot{m}_{cool}C_{p,cool}\left(T_{bed,des} - T_{bed,ads}\right)\left\{1 - \exp\left(-\frac{(UA)_{bed}}{\dot{m}_{cool}C_{p,cool}}\right)\right\} \tag{8.53}$$

8.5.3.2 Modelling of the Evaporator

An evaporator is usually a shell and tube type heat exchanger comprising a series of tubes. Chilled water flows through the tubes while the refrigerant vapor evaporates from the shell side. During the ad/de-sorption phase, the evaporator is connected to the adsorber bed, and the evaporated vapor gets adsorbed by the adsorbent. Let us assume, the evaporator has $N_{t,evap}$ number of tubes and mass, length and inside diameter of each tube are $M_{t,evap}$, $L_{t,evap}$, and $D_{e,i}$ respectively. Hence, at any instant,

the amount of chilled water present within the tubes of the evaporator is,

$$M_{ch,evap} = \frac{\pi}{4} D_{e,i}^2 L_{t,evap} N_{t,evap} \rho_{ch} \tag{8.54}$$

where ρ_{ch} is the density of chilled water. $\left[MC_p\right]_{bed,des}$ can be calculated from,

$$\left[MC_p\right]_{evap} = M_{ch,evap} C_{p,ch} + M_{t,evap} N_{t,evap} C_{p,t,evap} \tag{8.55}$$

where, $C_{p,ch}$ and $C_{p,t,evap}$ are the specific heat capacities of chilled water and evaporator tube material respectively.

Let $h_{fg,evap}$ be the latent heat of evaporation of water at the evaporation temperature. The energy balance equation for the evaporator during ad/de-sorption phase can be written as,

$$\begin{aligned}\left[MC_p\right]_{evap} \frac{dT_{evap}}{dt} = &-M_{bed}\left(\frac{dw}{dt}\right)_{ads} \left\{h_{fg,evap} + C_{p,ads}\left(T_{bed,ads} - T_{evap}\right)\right\} \\ &+ \dot{m}_{ch} C_{p,ch}\left(T_{in,ch} - T_{evap}\right)\left\{1 - \exp\left(-\frac{(UA)_{evap}}{\dot{m}_{ch} C_{p,ch}}\right)\right\}\end{aligned} \tag{8.56}$$

where subscript *ch* stands for chilled water. *UA* value of the evaporator, i.e., $(UA)_{evap}$, is determined to utilize the LMTD method, as mentioned in Sect. 5.3.

The chilled water outlet temperature is determined from,

$$T_{out,ch} = T_{evap} - \left[\left(T_{evap} - T_{in,ch}\right) \exp\left(-\frac{(UA)_{evap}}{\dot{m}_{ch} C_{p,ch}}\right)\right] \tag{8.57}$$

During mass and heat recovery stages, the evaporator is isolated from the beds. Hence, the temperature of the evaporator and chilled water remain unchanged at these stages.

8.5.3.3 Modelling of the Condenser

Cooling water flows through the tubes of the condenser condensing the desorbed vapor that comes from the desorber bed. Similar to evaporator modelling, let us assume, the condenser has $N_{t,cond}$ number of tubes and mass, length and inside diameter of each tube are $M_{t,cond}$, $L_{t,cond}$, and $D_{c,i}$ respectively. Then for condenser, Eqs. (8.54) and (8.55) can be written as,

$$M_{cool,cond} = \frac{\pi}{4} D_{c,i}^2 L_{t,cond} N_{t,cond} \rho_{cool} \tag{8.58}$$

and,

$$\left[MC_p\right]_{cond} = M_{cool,cond}C_{p,cool} + M_{t,cond}N_{t,cond}C_{p,t,cond} \tag{8.59}$$

where subscripts *cool* and *cond* represent cooling water and condenser, respectively. During the ad/de-sorption stage, the cooling water from the outlet of Bed 1 enters the condenser. Hence, the energy balance equation can be written as,

$$\left[MC_p\right]_{cond}\frac{dT_{cond}}{dt} = -M_{bed}\left(\frac{dw}{dt}\right)_{des}\left\{h_{fg,cond} + C_{p,des}\left(T_{bed,des} - T_{cond}\right)\right\} + \dot{m}_{cool}C_{p,cool}\left(T_{out,cool} - T_{cond}\right)\left\{1 - \exp\left(-\frac{(UA)_{cond}}{\dot{m}_{cool}C_{p,cool}}\right)\right\} \tag{8.60}$$

The water temperature at the outlet of the condenser can be expressed as,

$$T_{out,cond} = T_{cond} - \left[\left(T_{cond} - T_{out,cool}\right)\exp\left(-\frac{(UA)_{cond}}{\dot{m}_{cool}C_{p,cool}}\right)\right] \tag{8.61}$$

In the mass recovery stage, the condenser is not connected to any bed. Thus, the temperatures of the condenser and cooling water don't change at this stage.

During the heat recovery stage, the condenser is isolated from the beds and water from Bed 1 first flows through Bed 2, before entering the condenser. Thus the energy balance for this stage can be modeled as,

$$\left[MC_p\right]_{cond}\frac{dT_{cond}}{dt} = \dot{m}_{cool}C_{p,cool}\left(T_{out,ads} - T_{cond}\right)\left\{1 - \exp\left(-\frac{(UA)_{cond}}{\dot{m}_{cool}C_{p,cool}}\right)\right\} \tag{8.62}$$

The water temperature at the outlet of condenser is,

$$T_{out,cond} = T_{cond} - \left[\left(T_{cond} - T_{out,ads}\right)\exp\left(-\frac{(UA)_{cond}}{\dot{m}_{cool}C_{p,cool}}\right)\right] \tag{8.63}$$

8.5.3.4 Performance Parameters

An adsorption chiller is usually specified by its cooling capacity and coefficient of performance (*COP*). The cooling capacity can be defined as the amount of cooling effect that an adsorption chiller is able to produce. For a chiller having a cycle time of t_{cycle}, the cooling capacity can be defined by,

$$Q_c = \frac{\int_0^{t_{cycle}} \dot{m}_{ch}C_{p,ch}\left(T_{in,ch} - T_{out,ch}\right)dt}{t_{cycle}} \tag{8.64}$$

The rate of heat input to drive an adsorption chiller can be expressed by,

$$Q_h = \frac{\int_0^{t_{cycle}} \dot{m}_{hot} C_{p,hot} \left(T_{in,hot} - T_{out,hot}\right) dt}{t_{cycle}} \tag{8.65}$$

The *COP* of the chiller is defined by the ratio of useful cooling capacity produced to the heat input to the chiller. Mathematically it can be shown as,

$$COP = \frac{Q_c}{Q_h - Q_{rec}} \tag{8.66}$$

where Q_{rec} is the rate of heat recovered during the heat recovery stage.

8.5.4 Typical Simulation Results

In this subsection, simulation results of a typical 10-ton capacity adsorption chiller are shown. Let us consider the inlet temperatures of the cold water, hot water and chilled water are 27, 80 and 13 °C respectively and their flow rates are 10, 15 and 6 m^3/h respectively. These values are assumed to be constant throughout the operation of the chiller. However, they may not be such a uniform in real-life application. The chiller uses silica gel as the adsorbent and water as the refrigerant. The isotherm parameters of the S-B-K model are furnished in Table 8.1 (Rezk and Al-Dadah 2012). The isosteric heat of ad/de-sorption for the pair is found to be, $h_{ads} = 2.8 \times 10^4$ J/kg.

The particle radius of the silica gel adsorbent is considered as $R_p = 0.17$ mm. The adsorption rate is determined using the LDF model and the values of its kinetics parameters (Saha et al. 1995) are $D_{so} = 2.54 \times 10^{-4}$ m^2/s and $E_a = 4.2 \times 10^4$ J/mol. The assumed specifications of different components of the chiller are shown in Table 8.2.

In the current simulation, the time required for the ad/de-sorption, mass recovery and heat recovery are considered as 300 s, 20 s and 10 s, respectively. The typical simulation results are shown in Figs. 8.11, 8.12 and 8.13. The average cooling capacity of the chiller is found to be 10.03 RTon with a *COP* of 0.51.

Figure 8.11 shows the variation of temperature of different components of the chiller obtained from the simulation results. The experimental data can be obtained

Table 8.1 Isotherm properties of the silica gel—water pair

Parameter	Value	Parameter	Value
A_0	-6.5314	B_0	-15.587
A_1	0.7245×10^{-1}	B_1	0.15915
A_2	-0.23951×10^{-3}	B_2	-0.50612×10^{-3}
A_3	0.25493×10^{-6}	B_3	0.53290×10^{-6}

Table 8.2 Specifications of different components of the adsorption chiller

Ad/de-sorber bed	
Mass of adsorbent used, M_{bed}	80 kg
Number of modules, N_m	10
Length of each module, L_m	3.65 m
Tube material	Copper
Number of tubes in each module, N_t	3
Outside diameter of the tube, $D_{m,o}$	16.6 mm
Inside diameter of the tube, $D_{m,i}$	15 mm
Fin material	Aluminium
Number of fins in each module, N_f	3310
Length of the fin, L_f	342 mm
Height of the fin, H_f	30 mm
Width of the fin, W_f	0.105 mm
Evaporator	
Tube material	Copper
Number of tubes, $N_{t,evap}$	115
Length of the tube, $L_{t,evap}$	3.9 m
Mass per tube, $M_{t,evap}$	1.4 kg
Inner diameter of the tube, $D_{e,i}$	17.65 mm
Condenser	
Tube material	Copper
Number of tubes, $N_{t,cond}$	220
Length of the tube, $L_{t,cond}$	2.65 m
Mass per tube, $M_{t,cond}$	0.96 kg
Inner diameter of the tube, $D_{e,i}$	17.65 mm

from the test results of commercial adsorption chiller and can be utilized to validate the model. The variation of temperature and uptake of the beds is depicted in Fig. 8.12. As expected, the bed temperature increases during desorption and decreases during adsorption. The instantaneous cooling capacity at different stages of cycle time can be seen in Fig. 8.13. It needs mentioning that in determining the average cooling capacity and *COP*, the simulation result of the first cycle is ignored. It is done as the initial results are strongly influenced by the values used for initialization, and the model requires a few time steps to stabilize.

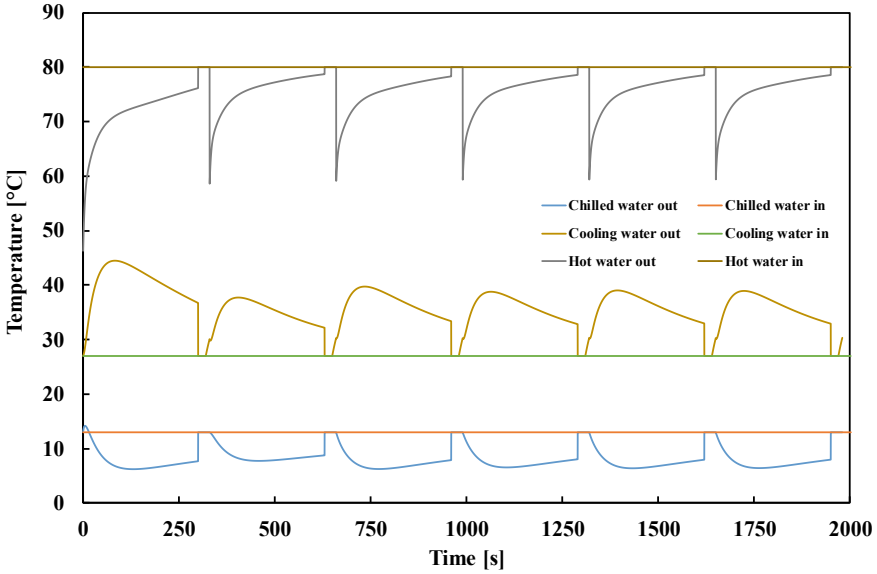

Fig. 8.11 Typical simulation results showing the variation of temperature with time of different components of an adsorption chiller

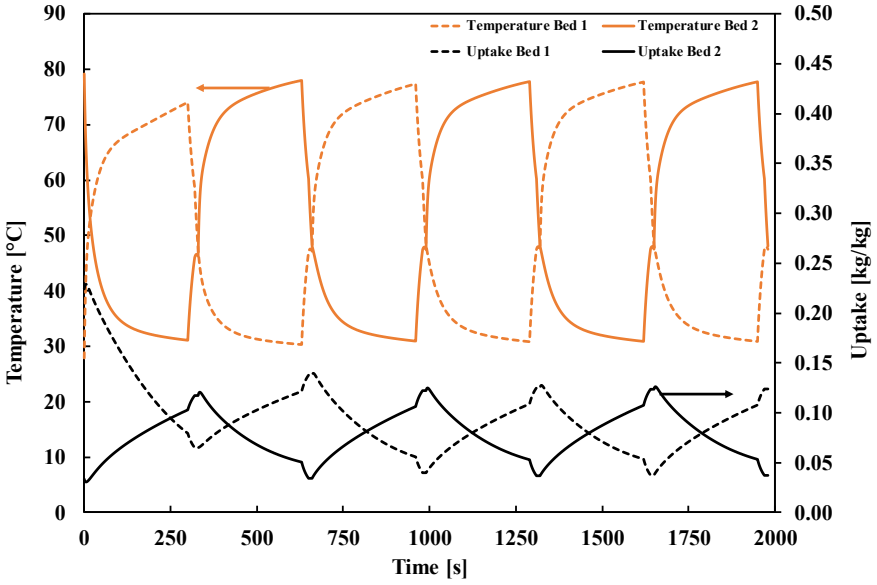

Fig. 8.12 Simulation results showing the temperature of beds and uptakes at different stages of operation of an adsorption chiller

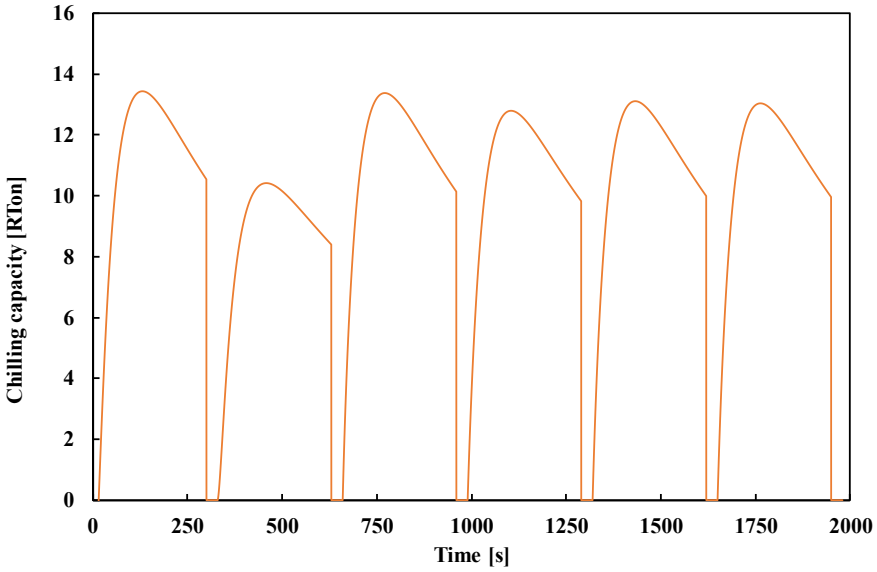

Fig. 8.13 The instantaneous cooling capacity of the chiller

8.6 Conclusion

Flat plate collectors have widely been used for domestic water heating. On the other hand, the evacuated tube collector is the cheapest and most preferred option for boiler water preheating. In this chapter, the model equations of these two types of collectors are presented. Furthermore, a commercial adsorption chiller is modelled, and the simulation results of the model are presented. The design parameters of the chiller may be varied to observe their effects on its performance. The model can be utilized to predict the performance of the chiller under variable operating conditions. It can also play a vital role in designing different components of the chiller to make the system more efficient and cost effective.

References

Conti J, Holtberg P, Diefenderfer J, LaRose A, Turnure JT, Westfall L (2016) International energy outlook 2016 with projections to 2040. USDOE Energy Information Administration (EIA), Washington, DC, USA

Cooper PI, Dunkle RV (1981) A non-linear flat-plate collector model. Sol Energy 26:133–140

Coulomb D (2006) Statement by the Director of the International Institute of Refrigeration. In: United Nations climate change conference, Nairobi. http://www.un.org/webcast/unfccc/2006/statements/061117iir_e.pdf

Duffie JA, Beckman WA (1974) Solar energy thermal processes. University of Wisconsin-Madison, Solar Energy Laboratory, Madison, WI

Duffie JA, Beckman WA (1980) Solar engineering of thermal processes. Willey, New York
Hottel HC (1942) Performance of flat-plate solar heat collectors., Trans ASME 64:91
Hottel C (1954) Performance of flat plate energy collectors: space heating with solar energy. In: Course symposium. Cambridge
Hottel H, Whillier A (1955) Evaluation of flat-plate solar collector performance. In: Transdisciplinary conference on the use of solar energy
Kalogirou SA (2004) Solar thermal collectors and applications. Prog Energy Combust Sci 30: 231–295. https://doi.org/10.1016/j.pecs.2004.02.001
Kalogirou SA, Papamarcou C (2000) Modelling of a thermosyphon solar water heating system and simple model validation. Renew Energy 21:471–493
McAdams WH (1954) Heat transmission. McGraw-Hill, New York, pp 252–262
Mitchell JW (1976) Heat transfer from spheres and other animal forms. Biophys J 16:561–569
Mitra S, Thu K, Saha BB, Dutta P (2017) Performance evaluation and determination of minimum desorption temperature of a two-stage air cooled silica gel/water adsorption system. Appl Energy 206:507–518. https://doi.org/10.1016/j.apenergy.2017.08.198
Muttakin M (2013) Optimization of solar thermal collector systems for the tropics. National University of Singapore. https://scholarbank.nus.edu.sg/handle/10635/47365
Muttakin M, Mitra S, Thu K, Ito K, Saha BB (2018) Theoretical framework to evaluate minimum desorption temperature for IUPAC classified adsorption isotherms. Int J Heat Mass Transfer 122:795–805. https://doi.org/10.1016/j.ijheatmasstransfer.2018.01.107
Praene J-P, Garde F, Lucas F (2005) Dynamic modelling and elements of validation of solar evacuated tube collectors. In: Ninth international IBPSA conference
Rezk ARM, Al-Dadah RK (2012) Physical and operating conditions effects on silica gel/water adsorption chiller performance. Appl Energy 89:142–149. https://doi.org/10.1016/j.apenergy.2010.11.021
Saha BB, Kashiwagi T (1997) Experimental investigation of an advanced adsorption refrigeration cycle. ASHRAE Trans 103:50–58
Saha BB, Boelman EC, Kashiwagi T (1995) Computational analysis of an advanced adsorption-refrigeration cycle. Energy 20:983–994
Saha BB, El-Sharkawy II, Chakraborty A, Koyama S, Banker ND, Dutta P, Prasad M, Srinivasan K (2006) Evaluation of minimum desorption temperatures of thermal compressors in adsorption refrigeration cycles. Int J Refrig 29:1175–1181. https://doi.org/10.1016/j.ijrefrig.2006.01.005
Saha BB, Chakraborty A, Koyama S, Srinivasan K, Ng KC, Kashiwagi T, Dutta P (2007) Thermodynamic formalism of minimum heat source temperature for driving advanced adsorption cooling device. Appl Phys Lett 91. https://doi.org/10.1063/1.2780117
Shashi Menon E (2015) Meters and valves. Trans Pipeline Calc Simul Manual 431–471. https://doi.org/10.1016/b978-1-85617-830-3.00012-2
Souka AF, Safwat HH (1966) Determination of the optimum orientations for the double-exposure, flat-plate collector and its reflectors. Sol Energy 10:170–174
Swinbank WC (1963) Long-wave radiation from clear skies. Q J R Meteorol Soc 89:339–348
Thu K, Saha BB, Mitra S, Chua KJ (2017) Modeling and simulation of mass recovery process in adsorption system for cooling and desalination. Energy Procedia 105:2004–2009. https://doi.org/10.1016/j.egypro.2017.03.574
Wang RZ (2001) Performance improvement of adsorption cooling by heat and mass recovery operation Â lioration de la performance d' un syste Á me de Ame Á adsorption a Á l' aide de re Â cupe Â ration de masse refroidissement a et de chaleur. Int J Refrig 24:602–611. https://doi.org/10.1016/j.ijrefrig.2014.04.018
Zarem A, Erway D (1963) Introduction to the utilization of solar energy. McGraw-Hill, New York

Chapter 9
TEWI Assessment of Conventional and Solar Powered Cooling Systems

Md. Amirul Islam and Bidyut Baran Saha

Abstract Conventional cooling and refrigeration systems already evolved to efficient design, have higher COP and compact size. However, the compressor section of such system consumes a tremendous amount of electricity and contribute indirectly to global warming. The working fluids of these systems are typically HFC or HFC blends which possess very high global warming potential. A significant percentage of working fluid is leaked from the high-pressure side of the system and directly contribute to global warming. The summation of indirect and direct warming impact, namely, total equivalent warming impact (TEWI) of the vapour compression cooling systems are significantly high. Adsorption cooling system (ACS) can resolve this critical issue. In ACS, the mechanical compressor of the traditional cooling system is replaced by a thermal compressor, namely, a pair of adsorption beds. Highly porous adsorbent material (silica gel, activated carbon, zeolite and so forth) is the key component of an adsorption bed. These materials have the capability to capture and hold certain types of fluid. This phenomenon is known as adsorption. Upon heating, the adsorbed fluid is liberated from the pores (desorption process) and gets thermally compressed. Solar thermal energy is the most prospective option for the desorption process to occur. Since there is no mechanical compressor, electricity consumption is deficient, which significantly minimizes the indirect warming impact. Moreover, natural or alternative refrigerants are used as the working fluid, which has zero/negligible GWP. Hence, the direct warming impact is also shallow. In this chapter, the working

Md. A. Islam · B. B. Saha (✉)
Kyushu University Program for Leading Graduate School, Green Asia Education Center, IGSES, Kyushu University, Kasuga-Koen 6-1, Kasuga-shi, Fukuoka 816-8580, Japan
e-mail: saha.baran.bidyut.213@m.kyushu-u.ac.jp

Md. A. Islam
e-mail: toha_apece@yahoo.com

International Institute for Carbon-Neutral Energy Research (WPI-I^{2}CNER), Kyushu University, 744 Motooka, Nishi-ku, Fukuoka 819-0395, Japan

Md. A. Islam
Department of Electronics and Telecommunication Engineering, Bangabandhu Sheikh Mujibur Rahman Science and Technology University, Gopalganj 8100, Bangladesh

H. Tyagi et al. (eds.), *Solar Energy*, Energy, Environment, and Sustainability, https://doi.org/10.1007/978-981-15-0675-8_9

principle and governing equations of a solar energy driven adsorption cooling system will be elaborated. Besides, TEWI assessment procedure will be explained and compared for both vapour compression and adsorption cooling systems.

Keywords Adsorption cooling · GWP · HFC · Solar thermal energy · TEWI · Vapor compression refrigeration

9.1 Introduction

The main objectives behind the invention of cooling systems are to attain thermal comfort during summer and to preserve various goods (fish, meat, vegetable, and so forth) that usually rots very fast at ambient conditions (Arora 2010; Islam et al. 2017). The conventional cooling systems have four major building blocks: evaporator, compressor, condenser and expansion device. A working fluid (namely refrigerant) flows through these components, change the phase due to pressure variation and removes heat from a low-temperature source to a relatively higher temperature sink (Wang 2000). Electricity is required to run this cooling system, and the mechanical compressor consumes about 90% of that electricity. Electricity generation sources are mainly fossil fuel based and release greenhouse gases during electricity production (Rahman and de Castro 1995; Bose 2010; Cherp et al. 2017). Briefly, a cooling system indirectly contributes to global warming by using electricity. Moreover, refrigerant leakage is inevitable from joints and seals, mechanical failure or during servicing (Tassou and Grace 2005; Francis et al. 2016). Previous generation refrigerants such as ethers, NH_3, SO_2 have toxicity problem; H_2O has narrow operating temperature range; CFCs and HCFCs have ozone depletion potential and high global warming impact; HCs are unsafe due to their high flammability issue although they have very low GWP and wider operation range (Calm 2008; Sarbu 2014). The properties of some refrigerants are shown in Table 9.1. Currently employed refrigerants in the cooling systems are mostly HFCs and have a very high global warming impact. Hence, the leaked refrigerant contributes directly to global warming. The summation of indirect and direct warming impact, namely, total equivalent warming impact (TEWI) of the conventional cooling systems are significantly high (Calm 2002; Makhnatch and Khodabandeh 2014; Davies and Caretta 2004; Kruse 2000). Hence, the adsorption cooling system is becoming popular, which can be driven by solar thermal energy or any low-temperature heat source (Saha et al. 2006; Kayal et al. 2016; Thu et al. 2013; El-Sharkawy et al. 2008). Electricity consumption of this system is very low. Moreover, natural refrigerants can be used as working fluids which have zero or negligible global warming impact (Habib et al. 2014; Kasaeian et al. 2018; Saha et al. 2001). According to history, Faraday discovered the adsorption cooling phenomenon in 1948. He observed that NH_3 adsorption onto AgCl could produce cooling. G. E. Hulse proposed an adsorption refrigeration system with silica gel as adsorbent and SO_2 as the refrigerant in the 1920s (Wang et al. 2014). Nowadays, many renowned

Table 9.1 Properties of the selected refrigerants

	R22	R32	R134a	R404A	R410A	R717	R718	Methanol
Chemical formula (Kohler et al. 2016)	$CHClF_2$	CH_2F_2	CH_2FCF_3	R125 (44%) R134a (4%) R143a (52%)	R32 (50%) R125 (50%)	NH_3	H_2O	CH_3OH
GWP (kg–CO_2 eq.)	1760 (Mota-Babiloni et al. 2017)	677 (Stocker et al. 2019)	1300 (Stocker et al. 2019)	3922 (Vaitkus and Dagilis 2017)	2088 (Mota-Babiloni et al. 2017)	0	0	0
ODP	0.055 (Deveciog and Oruç 2017)	0	0	0	0	0	0	0
Critical pressure (MPa) (Lemmon et al. 2018)	4.99	5.78	4.06	3.73	4.9	1.14	2.21	8.10
Critical temperature (°C) (Lemmon et al. 2018)	96.15	78.11	101.06	72.12	71.34	132.41	373.95	239.45
Normal boiling point (°C) (Lemmon et al. 2018)	− 40.81	− 51.65	− 26.07	− 46.22	− 51.44	− 33.32	99.97	64.48

(continued)

Table 9.1 (continued)

	R22	R32	R134a	R404A	R410A	R717	R718	Methanol
Latent heat of evaporation at 25 °C (kJ/kg) (Lemmon et al. 2018)	182.74	270.91	177.79	138.99	190.6	1165.8	2441.7	1169.0
ASHRAE safety group (Kohler et al. 2016)	A1	A2L	A1	A1	A1	B2L	A1	N/A
Flammability (Kohler et al. 2016)	No	Yes (mild)	No	No	No	Yes (mild)	No	Yes (Machiele 1987)
Toxicity (Kohler et al. 2016)	No	No	No	No	No	Yes	No	Yes (Machiele 1987)

industries such as Mitsubishi (2012), Tokyo Boeki Machineries (2019), Bry-Air (2019), Mayekawa (2019), and SorTech (2009) are commercially manufacturing high capacity adsorption chillers.

9.2 Cooling Systems

The refrigerant fluid changes its phase between vapour and liquid in various sections of the cooling system due to pressure variation, which is the fundamental working principle of any cooling system (Ahamed et al. 2010; Gill and Singh 2018; Yumrutaş et al. 2002; Yang and Yeh 2015). Most common types of cooling system utilize electrical energy to achieve the desired pressure. Moreover, researchers have developed new systems that are capable of doing the same job using thermal energy such as (solar energy, waste heat, geothermal energy, and so forth) (Carotenuto et al. 2017; Ghaebi et al. 2018; Ng et al. 2001, 2006; Habib et al. 2013; Choudhury et al. 2013; Alahmer et al. 2016; Khan et al. 2007).

9.2.1 Vapor Compression Refrigeration (VCR)

A conventional VCR system comprises of four major parts: evaporator, compressor, condenser and expansion device. A refrigerant (pure/blends) is the primary working fluid which changes phase in evaporator and condenser to perform the cooling (Cengel 2004). The schematic and working principle of a VCR is shown in Fig. 9.1.

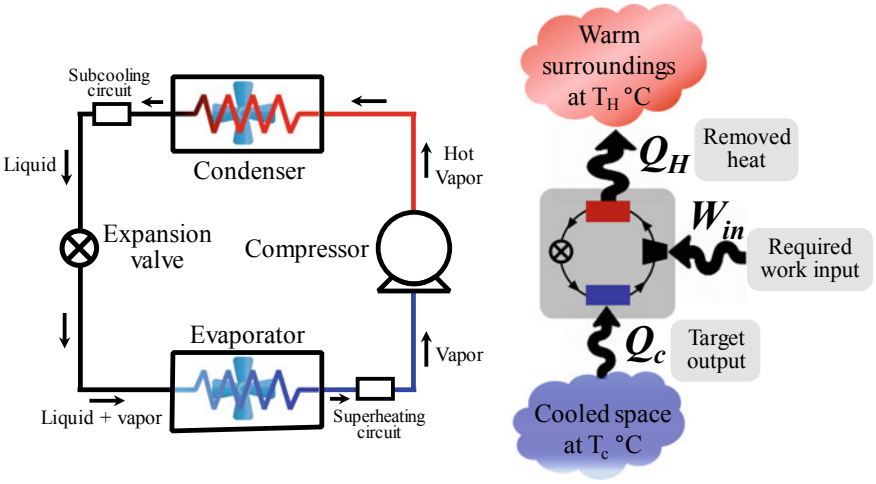

Fig. 9.1 Schematic and norm of a conventional vapor compression system

9.2.1.1 Evaporator

The liquid refrigerant evaporates at low pressure in the evaporator. During evaporation, liquid refrigerant accumulates latent heat from the surroundings. Evaporation is an isothermal process. A heat exchanger fluid (air/water) is flown to the evaporator coil for efficient cooling. Most of the evaporator is followed by an auxiliary circuit for superheating the vapour which ensures that the liquid refrigerant is completely evaporated before leaving the evaporator. Superheating prevents the damage of the compressor and increases the efficiency of the system.

9.2.1.2 Compressor

Vapour refrigerant is fed into the suction line of the compressor and compressed until the condenser pressure. The compression process of an ideal compressor is isentropic. However, in practice, there is no idea compressor. Hence, the compression is non-isentropic. According to Gay-Lussac's gas law, the temperature increases during the compression. Modern compressors are variable in speed and electricity consumption is very low.

9.2.1.3 Condenser

Hot vapour refrigerant discharges from compressor outlet and flows through the condenser coil. The coil has fins, and the air is flown for faster heat transfer. Heat is released from the refrigerant to the surroundings and gets liquefied. Released refrigerant from the condenser is passed through an additional circuit which subcools the liquid refrigerant to ensure that all the refrigerant is in the liquid state before entering expansion device.

9.2.1.4 Expansion Device

The high-pressure liquid refrigerant is forced through a small orifice of the expansion valve, which causes a sudden pressure and temperature drop. Refrigerant is in two-phase condition after the expansion device. This refrigerant reenters into the evaporator and the cycle continues to repeat.

9.2.2 Solar Cooling

Unlike the VCR system, work input of a solar cooling system is thermal energy instead of electricity. The mechanical compressor of a VCR is replaced with a thermal compressor, namely adsorption bed (Sayigh and McVeigh 1992; Chang

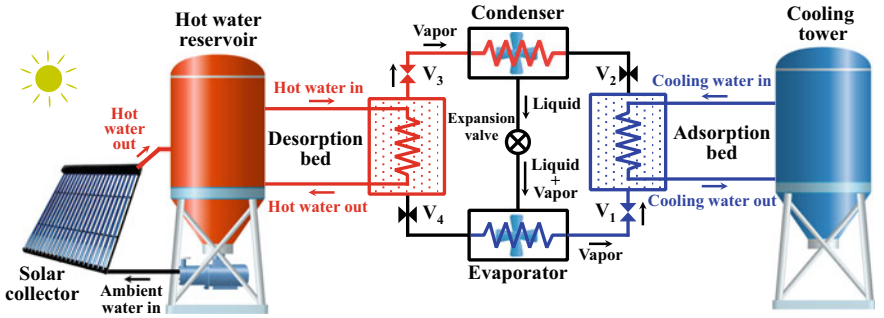

Fig. 9.2 Adsorption cooling system by using solar thermal energy

et al. 2007; Cho and Kim 1992; Bassols-Rheinfelder 1985; Buonomano et al. 2018; Tangkengsirisin et al. 1998; Al Mers et al. 2006; Chang et al. 2009). Other three components of the system are the same as VCR. Some additional components are also required in the solar cooling system for the cooling to happen. The complete system is entitled as adsorption cooling system (ACS), which is shown in Fig. 9.2.

The main component of an adsorption bed is the adsorbent. An adsorbent material contains millions of pores and capable of adsorbing (capture and hold) the refrigerant (also called adsorbate) molecules. Choosing the appropriate adsorbent/adsorbate is crucial to design an efficient adsorption cooling system.

9.2.2.1 Adsorption/Desorption

Adsorption is the phenomenon to trap and retain refrigerant molecules into the adsorbent pores. Adsorption capacity depends on the porous properties (surface area, pore width, pore volume) of the adsorbent and also surrounding conditions (temperature and pressure). Hence, choosing the adsorbent is crucial for a solar cooling system. Properties of some common adsorbents are shown in Table 9.2.

The refrigerant molecules need to be regenerated and recirculated to complete the refrigeration cycle. The regeneration process is called desorption. Hot water is passed through the heat exchanger coil, which is placed inside the adsorption/desorption bed for the regeneration. Required hot water for the desorption is obtained from solar thermal energy.

9.2.2.2 Solar Collector

A solar collector is an apparatus that accumulates or concentrates solar insolation. There are various types of solar collectors such as flat plate collector, parabolic collector, direct absorption collector, photovoltaic thermal (PVT) collector, hybrid photovoltaic and thermal collector (Khullar et al. 2012; Phelan et al. 2013; He et al.

Table 9.2 Porous properties of some well-known adsorbents

Adsorbent name	BET surface area, A ($m^2\ g^{-1}$)	Pore width, w (Å)	Pore volume, υ ($cm^3\ g^{-1}$)
Activated carbon (Maxsorb III) (El-Sharkawy et al. 2014)	3045	11.20	1.70
Activated carbon from waste palm trunk (Pal et al. 2017)	2927	16.80	2.41
Activated carbon from Mangrove (Pal et al. 2017)	2924	14.70	2.13
Activated carbon fiber (A20) (El-Sharkawy et al. 2006)	1900	21.60	0.765
Activated carbon fiber (A15) (El-Sharkawy et al. 2006)	1400	21.75	1.028
Silica gel (RD) (Ng et al. 2001)	650	21.00	0.35
Silica gel (type A) (Ng et al. 2001)	650	22.00	0.36
Zeolite (AQSOA Z01) (Kayal et al. 2016)	132	7.40	0.087
Zeolite (AQSOA Z02) (Kayal et al. 2016)	590	3.70	0.2769

2006; Fudholi et al. 2014; Tyagi et al. 2012; Khelifa et al. 2015). Necessary heat for desorption can be arranged by employing one of those collectors.

9.3 Total Equivalent Warming Impact (TEWI)

Every refrigeration system contributes to global warming, either directly or indirectly. TEWI is the overall quantity of direct and indirect GWP released from a system.

The compressor (desorption bed for a solar cooling system) and condenser sections operate at a high temperature and pressure than the atmospheric. Although all the sections are properly sealed, a significant amount of leakage (about 20%) can occur from joints and seals, due to mechanical failure or during servicing (Tassou and Grace 2005; Reddy et al. 2012). This leakage will lead to performance degradation and will increase energy consumption (Du et al. 2016; McIntosh et al. 2000). Moreover, the leaked refrigerants have high GWP, which will eventually contribute directly to global warming (Davies and Caretta 2004).

Indirect emission occurs due to the electricity consumption of the refrigeration system since a major share of the electricity is generated from fossil fuel.

A cooling system is mostly made with metals such as stainless steel, aluminium, and copper. These materials production requires a lot of energy which indirectly contribute to global warming.

Hence, TEWI can be assessed from the following equation:

$$\begin{aligned} TEWI &= direct\ emission + indirect\ emission \\ &= (GWP_r \times L) \times n + [(E \times \varepsilon) \times n + m \times GWP_m] \end{aligned} \tag{9.1}$$

Here,

GWP_r	Global warming potential of the selected refrigerant (kg-CO_2 eq.)
L	Annual leakage rate of charged refrigerant (%)
n	Duration to calculate TEWI (year)
E	Electricity consumption (kWh)
ε	CO_2 emission factor for per unit electricity generation (kg-CO_2 eq./kWh)
m	Mass of the raw materials that are used to build the cooling system (kg)
GWP_m	CO_2 emission factor for per unit raw material production (kg-CO_2 eq./kg).

9.3.1 TEWI of Conventional Cooling System

Operating conditions and assumptions are required to set before the TEWI assessment of a conventional VCR system. The complete set of parameters are listed in Table 9.3.

9.3.1.1 Assessment Parameters

Evaporation Temperature

Different cooling applications require a different degree of cooling. For example, in summer, the temperature of the room air-conditioning system is set to 20–25 °C for thermal comfort. However, beverages, vegetables, fruits and many other products are preserved at 2–5 °C to prevent from rotting. These products are called medium temperature (MT) cooling loads. Moreover, Fish, meat, ice-cream requires much lower (about −20 °C) temperature for preservation. These are called low temperature (LT) cooling loads. Another important application of low-temperature requirement is data storage centers.

Evaporation temperature of the VCR is set about 5°–10° lower than the target temperature. Hence, three different evaporation temperature is considered (Table 9.3) for three types of cooling applications.

Table 9.3 Operating conditions and assumptions for a conventional cooling system

Parameter	Quantity
Evaporation temperature for specific applications, T_{eva}	12 °C (room air-conditioning) – 7 °C (medium temperature applications) – 25 °C (low temperature applications)
Condensation temperature, T_{con}	40 °C
Selected refrigerants	R32 (Difluoromethane: CH_2F_2) R134a (1,1,1,2-Tetrafluoroethane: $C_2H_2F_4$) R404A (44% R125, 4% R134a, 52% R143a) (Lemmon et al. 2018)
GWP and ODP of the considered refrigerants, GWP_r and ODP_r	Refer to Table 9.1
Cooling load, Q_c	10 kW
Suction gas superheat, T_{sup}	8 °C
Degree of subcooling, T_{sub}	5 °C
Isentropic efficiency of the compressor, η_{isen}	70% (room air-conditioning) 65% (medium temperature applications) 60% (low temperature applications)
Initial refrigerant charging amount	1 kg for per kW room air-conditioning cooling load 2 kg for per kW medium temperature load 3 kg for per kW room air-conditioning load (Poggi et al. 2008)
Annual leakage rate of refrigerant, L_a	15% (Tassou and Grace 2005; Francis et al. 2016)
GWP for electricity generation, ε	0.518 (kg-CO_2/kWh) (Electricity Review Japan 2018)
Product weight (indoor + outdoor unit), m	60 kg (10 kW room air-conditioning) (Hitachi Room Aircon Product Brochure 2019; General 2018) 80 kg (10 kW medium temperature system) 100 kg (10 kW low temperature system)
Weight percentage of raw materials to build a cooling system	Stainless steel: 50% Copper: 20% Aluminium: 20% Others (refrigerant, plastic, paint etc.): 10%
GWP of per kg material production, GWP_m	Stainless steel: 2.13 kg-CO_2 eq. (Chisalita et al. 2019) Copper: 4.97 kg-CO_2 eq. (Kosai and Yamasue 2019) Aluminum: 9.17 kg-CO_2 eq. (Kosai and Yamasue 2019)
System lifespan	15 years
System runtime	12 h/day

Condensation Temperature

The assessment has been performed for the summer season when the ambient temperature is around 30 °C. The condensation temperature is always higher than the ambient temperature so that heat exchange can occur naturally. In this assessment, the condensation temperature is considered constant (40 °C).

Selected Refrigerants and Their Environmental Impact

Global warming potential (GWP) is the quantity of heat that a greenhouse gas can grasp in the atmosphere for a specific duration, relative to CO_2. Each refrigerant has a certain amount of GWP when released to the environment. Previously used CFCs and HCFCs have very high GWP. Those refrigerants are also responsible for ozone layer depletion (ODP), which is located at the lower portion of the stratosphere. ODP value of a fluid is the measure of destructive effects compared to the reference substance R11 (or CFC-11 or CCl_3F or Trichlorofluoromethane). HFC based refrigerants are used in modern domestic air-conditioning and refrigeration systems. Most frequently used refrigerants for room air-conditioning systems are R134a and R32. However, R22 is still used in room air-conditioning system in some developing and underdeveloped countries. Besides, HFC blend R404A and R410A are predominantly used in commercial refrigeration systems and low-temperature applications. Hence, these three refrigerants (R32, R134a and R404A) are selected for the assessment. Analysis with R22 (for room air-conditioning application) and R410A (for medium and low temperature applications) are also presented in the appendix section for the readers' convenience.

Cooling Load

The cooling load is the quantity of heat energy that needs to be removed from the cooling space (evaporation surroundings) to maintain the target temperature. Usually, a standard 20 m^2 room (typical height −2.44 m) can be cooled with a 5 kW air-conditioner (Quick calculations for walk-in coolers and freezers 2019). A typical two-room house with 10 kW air-conditioning cooling load is considered for this assessment. Medium temperature (MT) and low temperature (LT) cooling loads are also considered 10 kW. Since, MT and LT loads are mostly used for food preservation; the cooled space is smaller compared to room air-conditioning system.

Superheat and Subcool

A certain degree of superheating is applied after the evaporator to ensure that the liquid refrigerant is completely vaporized before it reaches the suction line of the compressor. Likewise, subcooling is performed after condenser to confirm that the

refrigerant is completely liquefied before entering the expansion device. Superheating and subcooling of the refrigerant prevent damage of the components and increase the efficiency of the system. The typical value of superheating and subcooling is in the range of 5–10 K. In this assessment, superheating has been considered 8 K and subcooling is 5 K.

Isentropic Efficiency

When a thermodynamic process is adiabatic and completely reversible, the process is called isentropic. Isentropic efficiency of an ideal compressor is hundred-percent. An ideal compressor has to be frictionless, and there should be no heat transfer during the operation. In reality, there is no ideal compressor, and we consider a certain value for the isentropic efficiency. In principle, the compression ratio increases when the difference between the evaporation temperature and condensation temperature increases. Therefore, the isentropic efficiency of the compressor is lower for low-temperature applications. Hence, isentropic efficiency values are different in Table 9.3, depending on the application.

Refrigerant Charging

Initially, each cooling system requires a certain amount of refrigerant charging. The actual initial charging amount depends on the evaporator cooling capacity, condenser capacity, evaporator and condenser heat exchanger size, heat transfer coefficients, operating conditions, refrigerant type, and so forth. Approximately, the required refrigerant amount can be expressed in terms of cooling capacity. For domestic cooling systems, the amount is 0.24–1 (in kg) times of the cooling load (kW). For medium and low-temperature applications, the amount is higher (2–3.4 times) (Poggi et al. 2008). In order to simplify the calculation, a certain amount of refrigerant charge has been considered and shown in Table 9.3.

Leakage Rate

Although the compressor is hermetically sealed, 15–20% of the charged refrigerant might be leaked from joints and seals, mechanical failure or during servicing (Tassou and Grace 2005; Francis et al. 2016). This leakage will lead to performance degradation and will increase energy consumption. Modern refrigeration system manufacturers claim that their system has a very low leakage rate, which could be as low as 5% per year. Hence, the sensitivity of direct emission with the leakage rate is presented in the appendix section.

GWP for Electricity Generation

Electricity is required to drive the VCR, and most of the electricity generation sources are fossil fuel based. For example, in Japan, the most share of the electricity is generated from gas (39.2%), coal (33.7%) and oil (8.2%). Other sources are hydro (8.2%), solar PV (4.9%), waste (1.8%), nuclear (1.7%), biofuels (1.4%), wind (0.6%), and geothermal (0.2%) (IEA 2018). Combined CO_2 emission factor for per unit electricity generation is 0.518 kg for Japan (Electricity Review Japan 2018). Developing and underdeveloped countries have much higher GWP for per unit of electricity generation.

Weight of the Cooling System

Choosing raw materials is crucial to building various parts of an air-conditioner. The objective is to reduce the mass, increase the efficiency and decrease the cost. Different parts of the air conditioners are made of different metals, plastic and steel (Rude 2019). Frames and base structures are usually made of corrosion resistant stainless steel. Heat exchangers and fins are typically made of Aluminum. Additionally, copper is chosen for tubing of condenser and evaporator. Copper has relatively higher thermal conductivity, higher tensile strength, lower thermal expansion coefficient than Aluminum. However, Aluminum is lighter and cheaper than Copper. In this assessment, we have considered that 50% is stainless steel, 20% is copper, 20% is Aluminum and 10% other materials of total weight.

GWP of Raw Materials Production

Building materials of a cooling system are mostly metals. These metals are usually extracted from ores. The extraction process includes heating in high temperature furnace, electrolysis of molten compounds, refining, shaping, cutting, and so forth. A large amount of energy is required to obtain the metals in usable form to build a cooling system. Hence, the raw materials that are used in the cooling system also contribute to global warming.

System Lifespan

An average life expectancy of the cooling system is considered 15 years. Since TEWI is usually calculated on per year basis, lifespan is necessary to calculate the annual indirect warming impact to build the system.

System Runtime

A cooling system is not always running. Either the system is turned off by the user or the system turns itself off when it reaches the desired temperature. Hence, a certain runtime is considered for this assessment.

9.3.1.2 Assessment Results

In order to determine the indirect emission, electricity consumption is required. Electricity consumption depends on the COP of the system, which is ultimately obtained from the thermodynamic properties of the refrigerant by using REFPROP (Lemmon et al. 2018) and the equations from (9.2) to (9.10).

$$P_{d'} = P_d = P_a = P_{a'} \tag{9.2}$$

$$P_{b''} = P_{b'} = P_b = P_c = P_{c'} \tag{9.3}$$

$$T_a = T_{eva} \tag{9.4}$$

$$T_{a'} = T_{eva} + T_{\text{sup}} \tag{9.5}$$

$$h_{c'} = h_{d'} \tag{9.6}$$

$$s_{a'} = s_{b'} \tag{9.7}$$

$$T_b = T_c = T_{con} \tag{9.8}$$

$$T_{c'} = T_{con} - T_{sub} \tag{9.9}$$

$$\eta_{isen} = \frac{h_{b'} - h_{a'}}{h_{b''} - h_{a'}} \tag{9.10}$$

Here, T, P, s, h, and η represents temperature, pressure, entropy, enthalpy and isentropic efficiency, respectively.

Table 9.4 shows thermodynamic quantities of room air-conditioning system. A similar data set can be evaluated for the medium and low-temperature system. Refrigeration cycles for these three systems are drawn in Fig. 9.3 from those three sets of thermodynamic data.

The cooling cycle consists of isobaric, isentropic, isenthalpic and isothermal processes. State lines of the cooling cycle is explained in Table 9.5.

Table 9.4 Thermodynamic quantities at state points of room air-conditioning system

State point	Explanation	Temperature T (°C)	Pressure P (kPa)	Enthalpy h (kJ kg^{-1})	Entropy s (kJ kg^{-1} K^{-1})
a	Saturated vapor	12.00	1174.18	516.80	2.111
a′	Superheated vapor	20.00	1174.18	527.36	2.148
b″	Hot vapor with non-isentropic compression	78.97	2478.31	571.15	2.186
b′	Hot vapor with isentropic compression	68.91	2478.31	558.02	2.148
b	Saturated vapor	40.00	2478.31	512.71	2.009
c	Saturated liquid	40.00	2478.31	275.61	1.252
c′	Subcooled liquid	35.00	2478.31	265.08	1.218
d′	Expanded two-phase refrigerant when subcooled	12.00	1174.18	265.08	1.229
d	Expanded two-phase refrigerant without subcooling	12.00	1174.18	275.61	1.266

Theoretical maximum COP of the system is denoted as Carnot COP and can be expressed by the following equation,

$$COP_{carnot} = \frac{273.15 + T_{eva}}{T_{con} - T_{eva}} \tag{9.11}$$

A practical system has frictional and other losses in various sections. Hence, the actual COP is lower than COP_{carnot}. The ratio of cooling load and work of compression is the practical COP of the system, which can be calculated by the following equation.

$$COP = \frac{h_{a'} - h_{d'}}{h_{b''} - h_{a'}} \tag{9.12}$$

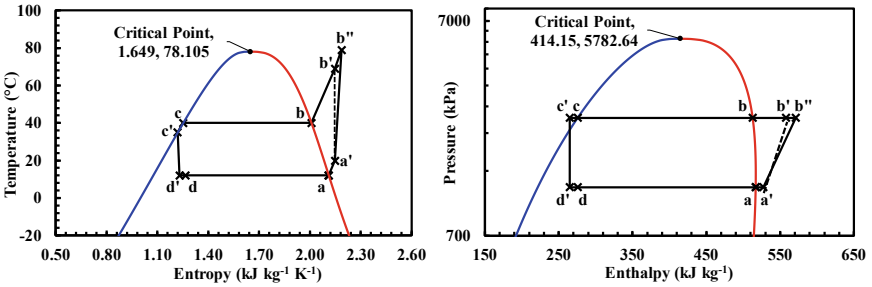

(a) Room air-conditioning cycle with R32.

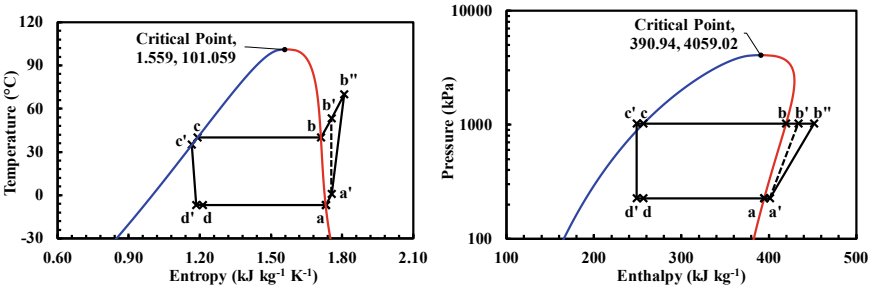

(b) Medium temperature (–7 °C) refrigeration cycle with R134a.

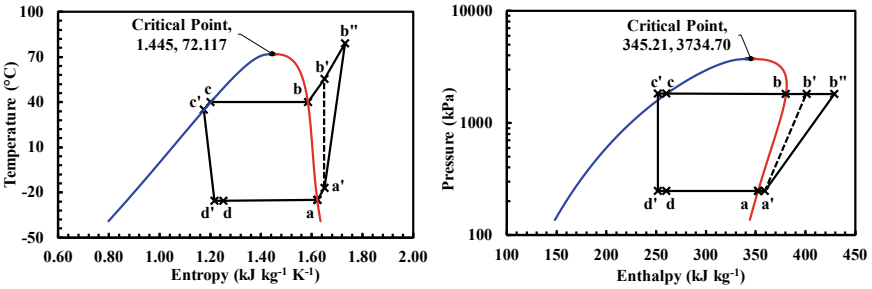

(c) Low temperature (–25 °C) refrigeration cycle with R404A.

Fig. 9.3 T-s and P-h diagram for various cooling applications

Electric power consumption is dependent on the COP of and can be determined by the following equation,

$$E_p = \frac{Q_c}{COP} \tag{9.13}$$

The mass flow rate of the refrigerant can be calculated by the following equation,

$$\dot{m} = \frac{h_{a'} - h_{d'}}{Q_c} \tag{9.14}$$

Table 9.5 Illustration of the cooling cycle

State line	Description
a–a″	This is the superheating line, which is an isobaric process. 8 °C temperature increases for the current application
a′–b″	Non-isentropic compression happens along this line. Discharged vapour refrigerant has a very high temperature and pressure at b″ (if we consider an ideal case, the compression process is isentropic, and the state line will be a′–b′)
b″–b	Isobaric cooling of compressed hot vapour refrigerant until it reaches condensation temperature in the outdoor unit (for ideal case, the line will be b′–b)
b–c	The phase change of saturated vapour to saturated liquid through the two-phase region. The process is isothermal and isobaric
c–c′	Isobaric liquid subcooling process. In this case, 5 °C temperature decrement from condensation temperature
c′–d′	Isenthalpic expansion of liquid refrigerant
d′–a	Isobaric evaporation of liquid refrigerant. The process requires latent heat for phase change, and hence, there is no temperature change along this line

The performance of a system can be estimated by the equations from (9.11) to (9.14). All these parameters can be obtained from assumptions and state diagrams.

The results clearly indicate that the performance of the system deteriorates when the temperature requirement is lower. It happens due to the higher compression ratio requirement to reach a lower evaporation temperature. Hence, the electricity requirement and indirect warming impact both increases. Indirect warming impact is lower than direct warming for room air-conditioning system and medium temperature system. However, the value exceeds the indirect warming impact on the low-temperature system (Table 9.6). Higher GWP value of the refrigerant R404A is responsible for that. Direct warming impact will substantially increase if R404A is used in the medium temperature system or room air-conditioning system. However, the application of R404A is limited in the commercial and low-temperature refrigeration system due to their thermodynamic properties.

A small 10 kW conventional cooling system can produce 4.816–31.346 tonne equivalent CO_2 emission every year depending on the application. The emission amount could be higher if the system is situated in an underdeveloped or developing country where electricity is primarily generated from coal, gas and other fossil fuel based sources. Additionally, TEWI would increase for tropical countries where the exterior temperature is higher than the considered temperature. Environmental impact would further increase, (i) for lower temperature applications because COP and isentropic efficiency is lower, (ii) with aging of the system because the system would be more prone leakage and will consume more electricity, (iii) if selected refrigerant have higher GWP or poor thermodynamic property in the operation condition.

Table 9.6 Results of assessment: conventional cooling system

Parameter	System type		
	Room air-conditioning (R32)	Medium temperature refrigeration (R134a)	Low-temperature refrigeration (R404A)
COP_{carnot}	10.184	5.663	3.818
COP	5.989	3.029	1.660
Refrigerant flow rate, $\dot{m}$ (kg h^{-1})	137.257	236.251	143.344
Discharge temperature of refrigerant (°C)	78.971	69.950	160.416
Discharge pressure of refrigerant (kPa)	2478.310	1016.592	2478.31
Compression ratio	2.111	4.509	7.408
Annual electricity consumption (kWh)	7312.923	14,462.196	26,392.087
Annual indirect warming impact on electricity consumption (t-CO_2 eq.)	3.788	7.491	13.671
Total indirect warming impact for building the cooling system (t-CO_2 eq.)	0.234	0.311	0.389
Annual indirect warming impact for building the cooling system (t-CO_2 eq.)	0.016	0.021	0.026
Annual direct warming impact (t-CO_2 eq.)	1.013	3.900	17.649
Annual TEWI (t-CO_2 eq.)	4.816	11.412	31.346

9.3.2 TEWI of Solar Cooling System

Operating conditions and assumptions for the solar cooling system is summarized in Table 9.7. Same operating temperatures (T_{eva} and T_{con}), operation hours and cooling capacity have been set for the adsorption cooling system to compare the results with the conventional cooling system. Natural refrigerants (GWP = 0) have been chosen to decrease environmental impact. Three different functional pairs have been selected for three different applications. Silica gel/water pair is suitable for the temperature range of room air-conditioning systems. Moreover, medium temperature

Table 9.7 Operating conditions and assumption for the solar cooling system

Parameter	Quantity
Evaporation temperature for specific applications, T_{eva}	12 °C (room air-conditioning) −7 °C (medium temperature applications) −25 °C (low temperature applications)
Condensation temperature, T_{con}	40 °C
Selected refrigerants	R717 (Ammonia: NH_3), R718 (Water: H_2O), MetOH (Methanol: CH_3OH)
Functional adsorbent/adsorbate pairs	Silica gel/water (room air-conditioning) (Tokyo Boeki Machineries 2019; Bry-Air 2019) Activated carbon/methanol (medium temperature applications) (Attalla et al. 2018) Activated carbon/ammonia (low temperature applications) (Wang et al. 2009; Askalany et al. 2013)
GWP of the considered refrigerants, GWP_r	GWP_{water}: 0 kg-CO_2 eq. (Bolaji and Huan 2013), $GWP_{methanol}$: 0 kg-CO_2 eq. (Rosset et al. 2018), $GWP_{ammonia}$: 0 kg-CO_2 eq. (Abas et al. 2018)
Cooling load, Q_c	10 kW
Thermal co-efficient of performance, $COP_{thermal}$	0.6 (room air-conditioning) (Bry-Air 2019; Stryi-Hipp 2016) 0.4 (medium temperature applications) 0.2 (low temperature applications)
Electricity consumption (for pumps and valves)	0.8 kW (room air-conditioning) (Bry-Air 2019) 1.4 kW (medium temperature applications) 2.0 kW (low temperature applications)
Required adsorbent amount (two beds)	50 kg (room air-conditioning) (Bry-Air 2019) 70 kg (medium temperature applications) 90 kg (low-temperature applications)
Initial refrigerant charging amount	30 kg (room air-conditioning) (Bry-Air 2019) 50 kg (medium temperature applications) 70 kg (low-temperature applications)
The annual leakage rate of refrigerant, L_a	15%
GWP for electricity generation, ε	0.518 (kg-CO_2/kWh) (Electricity Review Japan 2018)
Product weight, m	900 kg (10 kW room air-conditioning) (Bry-Air 2019) 1200 kg (10 kW medium temperature system) 1500 kg (10 kW low-temperature system)

(continued)

Table 9.7 (continued)

Parameter	Quantity
The weight percentage of raw materials to build a cooling system	Stainless steel: 60% Copper: 10% Aluminum: 10% Others (refrigerant, adsorbent, cooling/chilled water etc.): 20%
GWP of per kg material production, GWP_m	Stainless steel: 2.13 kg-CO_2 eq. (Chisalita et al. 2019) Copper: 4.97 kg-CO_2 eq. (Kosai and Yamasue 2019) Aluminum: 9.17 kg-CO_2 eq. (Kosai and Yamasue 2019)
System lifespan	25 years (Bry-Air 2019)
System runtime	12 h/day

and low-temperature applications require different working fluids, such as methanol and ammonia (Ebrahimi and Keshavarz 2014). Activated carbon is suitable for the adsorption of these refrigerants.

COP of the adsorption cooling system can be expressed in two ways which are shown in Eqs. (9.15) and (9.16). Thermal input is very high compared to cooling output for adsorption cooling system. Hence, thermal COP is usually very low. Moreover, electricity input is much lower for a solar cooling system, and therefore electrical COP is very high. Thermal COP of the chiller for room air-conditioning system is the range of 0.5–0.6 (Bry-Air 2019; Stryi-Hipp 2016). COP decreases for lower evaporation temperature. In this assessment, we have considered COP values 0.6, 0.4 and 0.2 for room air-conditioning, medium temperature and low-temperature cooling systems, respectively.

$$COP_{thermal} = \frac{Q_{eva}}{Q_{des}} \tag{9.15}$$

$$COP_{elctrical} = \frac{Q_{eva}}{E_{in}} \tag{9.16}$$

Here,

Q_{eva} Evaporator cooling capacity (kJ)
Q_{des} Required thermal input for desorption (kJ)
E_{in} Required electrical power input (kWh) or (kJ).

The adsorption chillers require a small amount of electricity to run the pumps (chilled water, cooling water) and control the valves. A 10 kW chiller requires about 0.8 kW electricity according to the manufacturer's specification (Bry-Air 2019). Medium and low-temperature applications require a considerably higher amount

of electricity, which is shown in Table 9.7. The required amount of adsorbent and refrigerant also increases for lower temperature applications.

An adsorption system has two or more beds. The frames of the beds are usually made of stainless steel. The beds contain adsorbent and heat exchangers. Hence, the weight of an adsorption system is ten times or higher than the conventional system of the same cooling capacity. The weight of a 10 kW solar room air-conditioning cooling system is about 900 kg according to manufacturer's specification. Weight of medium and low-temperature systems have been considered higher due to the higher adsorbent and heat exchanger requirement. The weight percentage of steel, aluminum, copper and other materials have been modified due to the constructional difference with the conventional cooling system. The system has a higher lifetime and requires lower maintenance than the conventional systems because there are very few moving parts in this system.

The results of the assessment for the solar cooling system is summarized in Table 9.8. Thermal COP, electricity consumption, indirect emission due to electricity consumption, direct emission and TEWI of the considered solar cooling systems

Table 9.8 Results of assessment: solar cooling system

Parameter	System type		
	Room air-conditioning (Silica gel/water)	Medium temperature refrigeration (Activated carbon/methanol)	Low temperature refrigeration (activated carbon/ammonia)
$COP_{thermal}$	0.6	0.4	0.2
$COP_{electrical}$	12.5	7.143	5
Annual electricity consumption (kWh)	3504	6132	8760
Annual indirect warming impact on electricity consumption (t-CO_2 eq.)	1.815	3.176	4.538
Total indirect warming impact for building the cooling system (t-CO_2 eq.)	2.423	3.230	4.038
Annual indirect warming impact for building the cooling system (t-CO_2 eq.)	0.097	0.129	0.162
Annual direct warming impact (t-CO_2 eq.)	0	0	0
Annual TEWI (t-CO_2 eq.)	1.912	3.306	4.699

are lower than the conventional system. Since the weight of the adsorption cooling system is much higher, the indirect warming impact for building the cooling system is higher. However, TEWI of the solar cooling systems is much lower than the conventional systems.

9.4 Results Comparison and Discussions

The conventional vapour compression system is very compact in size and COP is also high. COP of adsorption cooling system is very low because of the huge loss of thermal energy conversion during operation. Hence, the COP of adsorption cooling system is often referred to as thermal COP. Electrical COP (ratio of cooling capacity to electricity input) is much higher for the solar cooling system, which is shown in Fig. 9.4. COP decreases for both conventional and solar cooling system when the evaporation temperature requirement is lower.

In Fig. 9.5, electricity consumption is compared between the conventional and solar cooling system. Inevitably the consumption is lower for the solar cooling system since the desorption (often referred to as thermal compression) is carried out by solar thermal input.

Indirect and direct emissions are individually drawn in Fig. 9.6 for conventional and solar cooling system for three different applications. Last two bars of each application are the TEWI for that particular application which is obtained by aggregating the direct and indirect emissions.

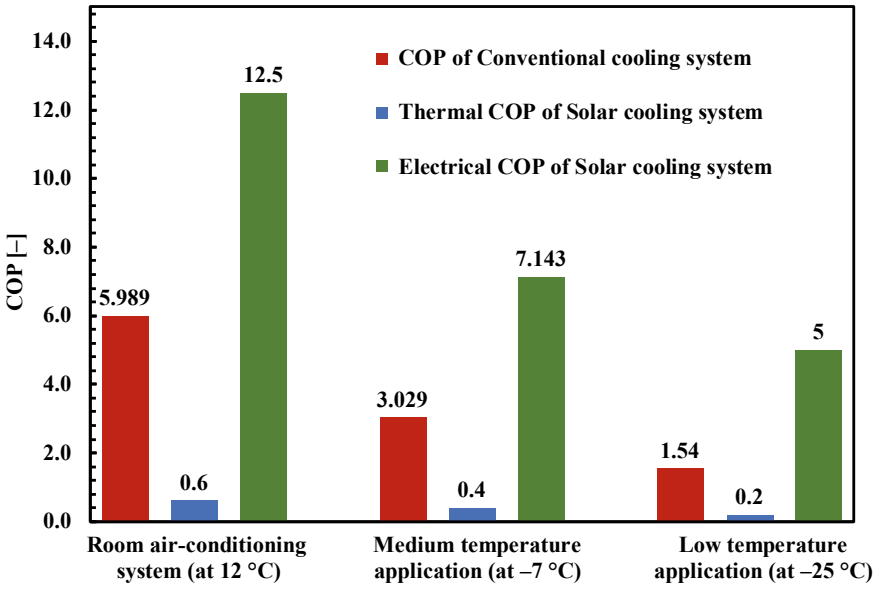

Fig. 9.4 COP variation for different applications: conventional vs solar cooling system

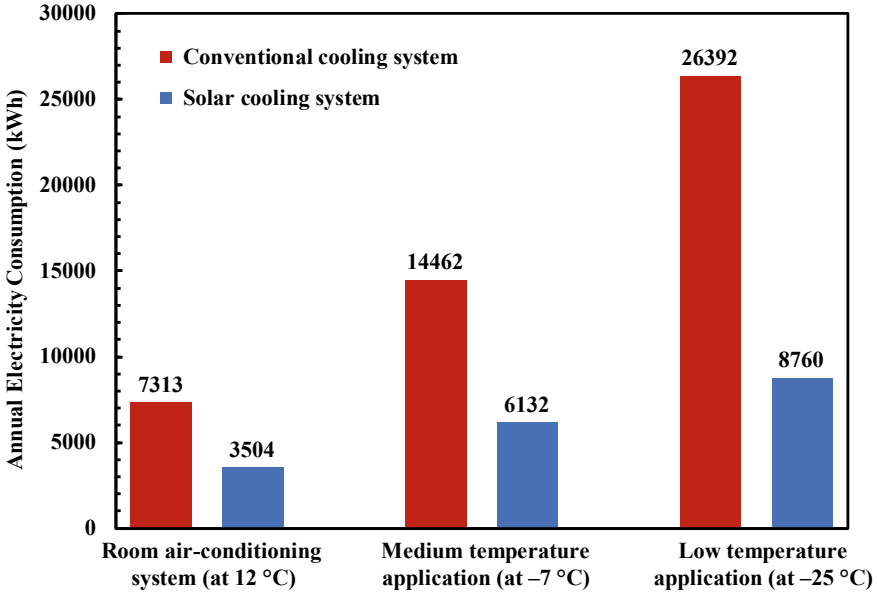

Fig. 9.5 Electricity consumption for various applications: conventional vs solar cooling

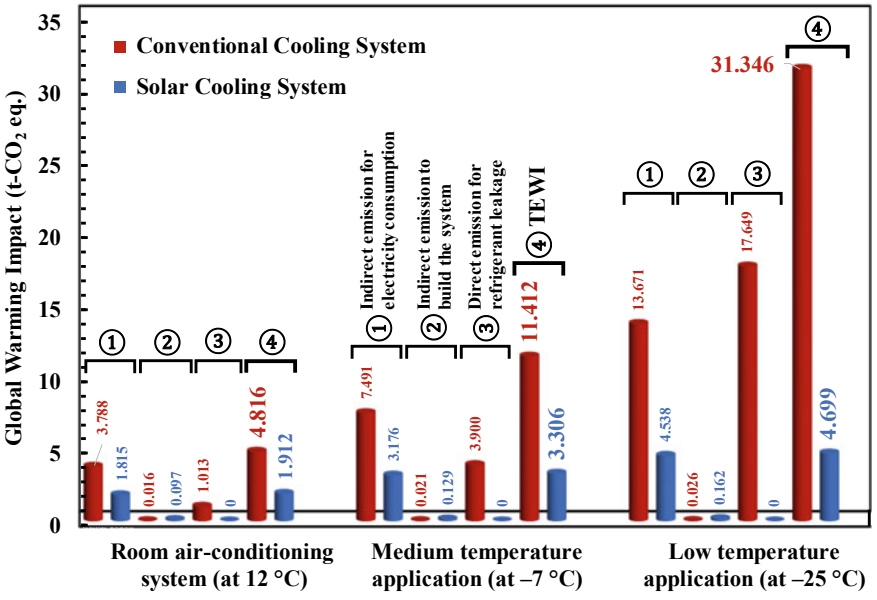

Fig. 9.6 Indirect, direct and total equivalent warming impact comparison

Since the solar cooling system has low electricity consumption, indirect emission is also lower for all three applications. However, the dimension and weight of the solar cooling system are much higher than the conventional system. Hence, indirect emission for raw materials is higher for the adsorption cooling system. Additionally, direct emission for the solar cooling system is zero because of deploying natural refrigerants as working fluid.

Total equivalent warming impact is much higher for conventional cooling systems, as shown in Fig. 9.6. Lower evaporation temperature causes higher TEWI.

9.5 Conclusions

In this assessment, performance and environmental impact of conventional and solar cooling system have been evaluated and compared. Three different applications: room air-conditioning (T_{eva} at 12 °C), medium temperature application (T_{eva} at − 7 °C) and low-temperature applications (T_{eva} at −25 °C) have been considered for both the systems. R32, R134a and R404A have been selected as working fluid for the conventional system. Whereas, silica gel/water, activated carbon/methanol and activated carbon/ammonia pairs have been considered for the solar cooling system. A constant cooling load of 10 kW is considered for all the applications. The results indicate that COP of the conventional cooling system is higher than thermal COP of the solar cooling system. However, electrical COP of the solar cooling system is considerably high due to the thermal input for desorption (thermal compression).

Indirect emission for electricity consumption is definitely higher for the conventional cooling system. It happens due to the huge electricity consumption by the mechanical vapour compressor. However, the weight of the used raw materials is very high that build the solar cooling system. Hence, annual indirect warming impact to build the system is relatively higher for the solar cooling system. In the case of direct emission, the solar cooling system is better because it uses natural refrigerants, and the GWP of those refrigerants are zero. Currently deployed refrigerants (R32, R134a, R404A, etc.) in conventional systems have high GWP, and hence, the direct warming impact is higher. However, the situation might change if low GWP refrigerants are introduced in conventional systems.

Currently, TEWI (summation of indirect and direct emissions) is very high for conventional cooling systems. Therefore, now is the appropriate time to switch from conventional systems to solar cooling technology.

Appendix 1

The Sensitivity of TEWI with a Refrigerant Leakage Rate

The refrigerant leakage rate of a conventional cooling system could vary for several reasons such as evaporation and condensation temperature, selected refrigerant and

Table 9.9 Emission sensitivity with leakage rate

System type	Emission	Annual leakage rate from the initial amount			
		$L_a = 5\%$	$L_a = 10\%$	$L_a = 15\%$	$L_a = 20\%$
Room air-conditioning system (R32)	Direct emission (t-CO_2 eq.)	0.338	0.675	1.013	1.350
	TEWI (t-CO_2 eq.)	4.141	4.479	4.816	5.154
	Change of TEWI	−14.02%	−7.00%	0	+7.02%
Medium temperature refrigeration (R134a)	Direct emission (t-CO_2 eq.)	1.3	2.6	3.9	5.2
	TEWI (t-CO_2 eq.)	8.812	10.112	11.412	12.712
	Change of TEWI	−22.78%	−11.39%	0	+11.39%
Low temperature refrigeration (R404A)	Direct emission (t-CO_2 eq.)	5.883	11.766	17.649	23.532
	TEWI (t-CO_2 eq.)	20.646	26.529	31.346	38.295
	Change of TEWI	−36.30%	−18.15%	0	+18.15%

system-manufacturing process. When the difference between evaporation and condensation temperature is large, the compression ratio is high, which leads to a higher leakage rate. Besides, each refrigerant possesses different pressure at the operating conditions. Hence, the leakage rate also depends on the selected refrigerant type. Moreover, the leakage rate depends on the sealing method of refrigerant compression chamber and airtightness of the refrigerant flowing channels. This part is solely dependent on the design of the system manufacturer. The annual leakage rate is varied from 5 to 20%, and the assessment result is compared in Table 9.9. One percent leakage rate reduction can decrease the total equivalent warming impact 1.4% for room air-conditioning system with R32 working fluid. The reduction is about 2.28% and 3.63% for medium and low temperature applications with R134a and R404A, respectively.

The solar cooling system would not be affected by the leakage amount since all the selected refrigerants have zero GWP.

Appendix 2

Effect of Refrigerant Type on TEWI

The current assessment is carried out considering R32, R134a and R404A as a refrigerant for room air-conditioning, medium temperature and low temperature systems, respectively. Once the refrigerant is changed, the refrigeration cycle will be affected, which would ultimately have an impact on the indirect emission. Moreover, GWP of the refrigerants are different, and hence, the direct emission will be changed. In this section, the assessment is performed with R22 for room air-conditioning system, and

Table 9.10 Results of assessment with different refrigerant: conventional cooling system

Parameter	System type		
	Room air-conditioning (R22)	Medium temperature refrigeration (R410A)	Low-temperature refrigeration (R410A)
COP_{carnot}	10.184	5.663	3.818
COP	6.261	2.828	1.621
Refrigerant flow rate, $\dot{m}$ (kg h^{-1})	208.749	211.302	221.665
Discharge temperature of refrigerant (°C)	69.396	86.749	115.333
Discharge pressure of refrigerant (kPa)	1533.570	2418.695	2418.695
Compression ratio	2.122	3.813	7.343
Annual electricity consumption (kWh)	6995.385	15,488.595	27,018.872
Annual indirect warming impact on electricity consumption (t-CO_2 eq.)	3.624	8.023	13.996
Total indirect warming impact for building the cooling system (t-CO_2 eq.)	0.234	0.311	0.389
Annual indirect warming impact for building the cooling system (t-CO_2 eq.)	0.016	0.021	0.026
Annual direct warming impact (t-CO_2 eq.)	2.64	8.352	9.396
Annual TEWI (t-CO_2 eq.)	6.279	16.396	23.418

R410A is considered for both medium and low temperature system. All the other parameters are the same, as shown in Table 9.3. Result of the assessment is shown in Table 9.10.

COP of the room air-conditioning system is higher when R22 is deployed instead of R32. Hence, electricity consumption and direct emission due to electricity consumption are lower. However, GWP of R22 is much higher than R32, which results in about 23% higher TEWI for room air-conditioning system.

Contrarily, replacing R134a with R410A for medium temperature applications gives a huge hike in TEWI, which is about 30%. However, TEWI could be decreased by about 25% by deploying R410A in exchange for R404A for low temperature applications.

Most of the adsorption cooling systems are using natural refrigerants. However, conventional refrigerants such as R32 and R134a have higher adsorption capacity, which could lead to develop an efficient adsorption cooling system (Saha et al. 2012; Askalany and Saha 2015). In that case, there would be direct warming impact from the adsorption cooling system. Since currently available systems only use natural refrigerants, the direct emission is considered to be zero.

References

Abas N, Kalair AR, Khan N, Haider A, Saleem Z, Saleem MS (2018) Natural and synthetic refrigerants, global warming: a review. Renew Sustain Energy Rev 90:557–569. https://doi.org/10.1016/j.rser.2018.03.099

Adsorption Chiller: Adref-Noa; Friendly to mankind and to the earth (2019). Mayewaka-Mycom; Mayekawa Mfg. Ltd. http://www.mayekawa.co.id/pic/AdRef-Noa—English-828.pdf. Accessed 24 Apr 2019

Ahamed JU, Saidur R, Masjuki HH (2010) A review on exergy analysis of vapor compression refrigeration system. Renew Sustain Energy Rev 15:1593–1600. https://doi.org/10.1016/j.rser.2010.11.039

Al Mers A, Azzabakh A, Mimet A, El Kalkha H (2006) Optimal design study of cylindrical finned reactor for solar adsorption cooling machine working with activated carbon–ammonia pair. Appl Therm Eng 26:1866–1875. https://doi.org/10.1016/j.applthermaleng.2006.01.021

Alahmer A, Wang X, Al-Rbaihat R, Amanul Alam KC, Saha BB (2016) Performance evaluation of a solar adsorption chiller under different climatic conditions. Appl Energy 175:293–304. https://doi.org/10.1016/j.apenergy.2016.05.041

Arora RC (2010) Refrigeration and air conditioning, 1st edn. PHI Learning Pvt., Ltd., New Delhi

Askalany AA, Saha BB (2015) Experimental and theoretical study of adsorption kinetics of Difluoromethane onto activated carbons. Int J Refrig 49:160–168. https://doi.org/10.1016/j.ijrefrig.2014.10.009

Askalany AA, Salem M, Ismael IM, Ali AHH, Morsy MG, Saha BB (2013) An overview on adsorption pairs for cooling. Renew Sustain Energy Rev 19:565–572. https://doi.org/10.1016/j.rser.2012.11.037

Attalla M, Sadek S, Salem Ahmed M, Shafie IM, Hassan M (2018) Experimental study of solar powered ice maker using adsorption pair of activated carbon and methanol. Appl Therm Eng 141:877–886. https://doi.org/10.1016/j.applthermaleng.2018.06.038

Bassols-Rheinfelder J (1985) Solar cooling using an open-cycle adsorption system with adiabatical mass transfer and external heat exchange. Sol Energy 35:93–104. https://doi.org/10.1016/0038-092X(85)90040-4

Bolaji BO, Huan Z (2013) Ozone depletion and global warming: case for the use of natural refrigerant—a review. Renew Sustain Energy Rev 18:49–54. https://doi.org/10.1016/j.rser.2012.10.008

Bose B (2010) Global warming: energy, environmental pollution, and the impact of power electronics. IEEE Ind Electron Mag 4:6–17. https://doi.org/10.1109/MIE.2010.935860

Buonomano A, Calise F, Palombo A (2018) Solar heating and cooling systems by absorption and adsorption chillers driven by stationary and concentrating photovoltaic/thermal solar collectors: Modelling and simulation. Renew Sustain Energy Rev 81:1112–1146. https://doi.org/10.1016/j.rser.2017.07.056

Calm JM (2002) Emissions and environmental impacts from air-conditioning and refrigeration systems. Int J Refrig 25:293–305. https://doi.org/10.1016/S0140-7007(01)00067-6
Calm JM (2008) The next generation of refrigerants—historical review, considerations, and outlook. Int J Refrig 31:1123–1133. https://doi.org/10.1016/j.ijrefrig.2008.01.013
Carotenuto A, Figaj RD, Vanoli L (2017) A novel solar-geothermal district heating, cooling and domestic hot water system: dynamic simulation and energy-economic analysis. Energy 141:2652–2669. https://doi.org/10.1016/j.energy.2017.08.084
Cengel YA (2004) Thermodynamics, an engineering approach, 5th edn. McGraw-Hill, New York
Chang W-S, Wang C-C, Shieh C-C (2007) Experimental study of a solid adsorption cooling system using flat-tube heat exchangers as adsorption bed. Appl Therm Eng 27:2195–2199. https://doi.org/10.1016/j.applthermaleng.2005.07.022
Chang W-S, Wang C-C, Shieh C-C (2009) Design and performance of a solar-powered heating and cooling system using silica gel/water adsorption chiller. Appl Therm Eng 29:2100–2105. https://doi.org/10.1016/j.applthermaleng.2008.10.021
Cherp A, Vinichenko V, Jewell J, Suzuki M, Antal M (2017) Comparing electricity transitions: a historical analysis of nuclear, wind and solar power in Germany and Japan. Energy Policy 101:612–628. https://doi.org/10.1016/j.enpol.2016.10.044
Chisalita D-A, Petrescu L, Cobden P, van Dijk HA, Cormos A-M, Cormos C-C (2019) Assessing the environmental impact of an integrated steel mill with post-combustion CO_2 capture and storage using the LCA methodology. J Clean Prod 211:1015–1025. https://doi.org/10.1016/j.jclepro.2018.11.256
Cho S-H, Kim J-N (1992) Modeling of a silica gel/water adsorption-cooling system. Energy 17:829–839. https://doi.org/10.1016/0360-5442(92)90101-5
Choudhury B, Saha BB, Chatterjee PK, Sarkar JP (2013) An overview of developments in adsorption refrigeration systems towards a sustainable way of cooling. Appl Energy 104:554–567. https://doi.org/10.1016/j.apenergy.2012.11.042
Davies TW, Caretta O (2004) A low carbon, low TEWI refrigeration system design. Appl Therm Eng 24:1119–1128. https://doi.org/10.1016/j.applthermaleng.2003.12.026
Deveciog AG, Oruç V (2017) The influence of plate-type heat exchanger on energy efficiency and environmental effects of the air-conditioners using R453A as a substitute for R22 2017. https://doi.org/10.1016/j.applthermaleng.2016.10.180
Du Z, Domanski PA, Payne WV (2016) Effect of common faults on the performance of different types of vapor compression systems. Appl Therm Eng 98:61–72. https://doi.org/10.1016/j.applthermaleng.2015.11.108
Ebrahimi M, Keshavarz A (2014) Combined cooling, heating and power. Elsevier. https://doi.org/10.1016/C2013-0-18763-6
Electricity Review Japan (2018) The federation of electric power companies 2018. http://www.fepc.or.jp/english/library/electricity_eview_japan/index.html. Accessed 14 Feb 2019
El-Sharkawy II, Kuwahara K, Saha BB, Koyama S, Ng KC (2006) Experimental investigation of activated carbon fibers/ethanol pairs for adsorption cooling system application. Appl Therm Eng 26:859–865. https://doi.org/10.1016/j.applthermaleng.2005.10.010
El-Sharkawy II, Saha BB, Koyama S, He J, Ng KC, Yap C (2008) Experimental investigation on activated carbon–ethanol pair for solar powered adsorption cooling applications. Int J Refrig 31:1407–1413. https://doi.org/10.1016/j.ijrefrig.2008.03.012
El-Sharkawy II, Uddin K, Miyazaki T, Saha BB, Koyama S, Miyawaki J et al (2014) Adsorption of ethanol onto parent and surface treated activated carbon powders. Int J Heat Mass Transf 73:445–455. https://doi.org/10.1016/j.ijheatmasstransfer.2014.02.046
Francis C, Maidment G, Davies G (2016) An investigation of refrigerant leakage in commercial refrigeration. Int J Refrig 74:12–21. https://doi.org/10.1016/j.ijrefrig.2016.10.009
Fudholi A, Sopian K, Yazdi MH, Ruslan MH, Ibrahim A, Kazem HA (2014) Performance analysis of photovoltaic thermal (PVT) water collectors. Energy Convers Manag 78:641–651. https://doi.org/10.1016/j.enconman.2013.11.017

General (2018) Product catalogue 2018—air conditioners lineup. https://www.fujitsu-general.com/shared/g-eu/pdf-geur-support-ctlg-3eg019-1801e-01.pdf. Accessed 8 Apr 2019

Ghaebi H, Shekari Namin A, Rostamzadeh H (2018) Performance assessment and optimization of a novel multi-generation system from thermodynamic and thermoeconomic viewpoints. Energy Convers Manag 165:419–439. https://doi.org/10.1016/j.enconman.2018.03.055

Gill J, Singh J (2018) Component-wise exergy and energy analysis of vapor compression refrigeration system using mixture of R134a and LPG as refrigerant. Heat Mass Transf Und Stoffuebertragung 54:1367–1380. https://doi.org/10.1007/s00231-017-2242-x

Habib K, Choudhury B, Chatterjee PK, Saha BB (2013) Study on a solar heat driven dual-mode adsorption chiller. Energy 63:133–141. https://doi.org/10.1016/j.energy.2013.10.001

Habib K, Saha BB, Koyama S (2014) Study of various adsorbent-refrigerant pairs for the application of solar driven adsorption cooling in tropical climates. Appl Therm Eng 72:266–274. https://doi.org/10.1016/j.applthermaleng.2014.05.102

He W, Chow TT, Ji J, Lu J, Pei G, Chan LS (2006) Hybrid photovoltaic and thermal solar-collector designed for natural circulation of water. Appl Energy 83:199–210. https://doi.org/10.1016/j.apenergy.2005.02.007

Hitachi Room Aircon Product Brochure (2019) http://www2.tochi.hitachi.co.jp/ra.drowing/zumen/JT90J2E7.PDF. Accessed Apr 8 2019

IEA (2018) International Energy Agency. Key world energy statistics. https://www.iea.org/countries/Japan/. Accessed 13 Feb 2019

Islam MA, Srinivasan K, Thu K, Saha BB (2017) Assessment of total equivalent warming impact (TEWI) of supermarket refrigeration systems. Int J Hydrogen Energy 42:26973–26983. https://doi.org/10.1016/j.ijhydene.2017.07.035

Kasaeian A, Hosseini SM, Sheikhpour M, Mahian O, Yan WM, Wongwises S (2018) Applications of eco-friendly refrigerants and nanorefrigerants: a review. Renew Sustain Energy Rev 96:91–99. https://doi.org/10.1016/j.rser.2018.07.033

Kayal S, Baichuan S, Saha BB (2016) Adsorption characteristics of AQSOA zeolites and water for adsorption chillers. Int J Heat Mass Transf 92:1120–1127. https://doi.org/10.1016/j.ijheatmasstransfer.2015.09.060

Khan MZI, Saha BB, Alam KCA, Akisawa A, Kashiwagi T (2007) Study on solar/waste heat driven multi-bed adsorption chiller with mass recovery. Renew Energy 32:365–381. https://doi.org/10.1016/j.renene.2006.02.003

Khelifa A, Touafek K, Ben Moussa H, Tabet I, Hocine HB, Cheikh El, Haloui H (2015) Analysis of a hybrid solar collector photovoltaic thermal (PVT). Energy Proc 74:835–843. https://doi.org/10.1016/j.egypro.2015.07.819 (Elsevier)

Khullar V, Tyagi H, Phelan PE, Otanicar TP, Singh H, Taylor RA (2012) Solar energy harvesting using nanofluids-based concentrating solar collector. In: ASME 2012 third international conference on micro/nanoscale heat mass transfer, vol 3. ASME, p 259. https://doi.org/10.1115/mnhmt2012-75329

Kohler JA, Briley GC, Clark EM, Dorman DR, Duda SW, Halel DM, et al (2016) ANSI/ASHRAE standard 15-2016. Safety standard for refrigeration systems

Kosai S, Yamasue E (2019) Global warming potential and total material requirement in metal production: identification of changes in environmental impact through metal substitution. Sci Total Environ 651:1764–1775. https://doi.org/10.1016/j.scitotenv.2018.10.085

Kruse H (2000) Refrigerant use in Europe. ASHRAE J 42:16–24. https://www.usgbc.org/drupal/legacy/usgbc/docs/LEED_tsac/Energy/ASHRAEJournal09-00RefrigerantUseinEurope.pdf

Lemmon EW, Bell IH, Huber ML, McLinden MO (2018) NIST standard reference database 23: reference fluid thermodynamic and transport properties-REFPROP, version 10.0. National Institute of Standards and Technology. https://dx.doi.org/10.18434/T4JS3C

Machiele PA (1987) Flammability and toxicity tradeoffs with methanol fuels, vol 2018. https://doi.org/10.4271/872064

Makhnatch P, Khodabandeh R (2014) The role of environmental metrics (GWP, TEWI, LCCP) in the selection of low GWP refrigerant. Energy Proc 61:2460–2463. https://doi.org/10.1016/j.egypro.2014.12.023

McIntosh IBD, Mitchell JW, Beckman WA (2000) Fault detection and diagnosis in chillers—part I: model development and application. ASHRAE Trans 106:268

Mitsubishi Plastics launches a compact adsorption chiller with the highest cooling capacity per volume in the world (2012) https://www.m-chemical.co.jp/en/news/mpi/201203140474.html. Accessed 24 Mar 2019

Mota-Babiloni A, Navarro-Esbrí J, Makhnatch P, Molés F (2017) Refrigerant R32 as lower GWP working fluid in residential air conditioning systems in Europe and the USA. Renew Sustain Energy Rev 80:1031–1042. https://doi.org/10.1016/j.rser.2017.05.216

Ng KC, Chua HT, Chung CY, Loke CH, Kashiwagi T, Akisawa A et al (2001) Experimental investigation of the silica gel-water adsorption isotherm characteristics. Appl Therm Eng 21:1631–1642. https://doi.org/10.1016/S1359-4311(01)00039-4

Ng KC, Wang X, Lim YS, Saha BB, Chakarborty A, Koyama S et al (2006) Experimental study on performance improvement of a four-bed adsorption chiller by using heat and mass recovery. Int J Heat Mass Transf 49:3343–3348. https://doi.org/10.1016/j.ijheatmasstransfer.2006.01.053

Pal A, Thu K, Mitra S, El-Sharkawy II, Saha BB, Kil HS et al (2017) Study on biomass derived activated carbons for adsorptive heat pump application. Int J Heat Mass Transf 110:7–19. https://doi.org/10.1016/j.ijheatmasstransfer.2017.02.081

Phelan P, Otanicar T, Taylor R, Tyagi H (2013) Trends and opportunities in direct-absorption solar thermal collectors. J Therm Sci Eng Appl 5:021003. https://doi.org/10.1115/1.4023930

Poggi F, Macchi-Tejeda H, Leducq D, Bontemps A (2008) Refrigerant charge in refrigerating systems and strategies of charge reduction. Int J Refrig 31:353–370. https://doi.org/10.1016/j.ijrefrig.2007.05.014

Quick calculations for walk-in coolers and freezers (2019). Heatcraft Refrigeration Products LLC. http://www.uscooler.com/blog/load-calc.pdf. Accessed 9 Apr 2019

Rahman S, de Castro A (1995) Environmental impacts of electricity generation: a global perspective. IEEE Trans Energy Convers 10:307–314. https://doi.org/10.1109/60.391897

Reddy VS, Panwar NL, Kaushik SC (2012) Exergetic analysis of a vapour compression refrigeration system with R134a, R143a, R152a, R404A, R407C, R410A, R502 and R507A. Clean Technol Environ Policy 14:47–53. https://doi.org/10.1007/s10098-011-0374-0

Rosset K, Mounier V, Guenat E, Schiffmann J (2018) Multi-objective optimization of turbo-ORC systems for waste heat recovery on passenger car engines. Energy 159:751–765. https://doi.org/10.1016/j.energy.2018.06.193

Rude J (2019) How products are made. http://www.madehow.com/Volume-3/Air-Conditioner.html. Accessed 10 Apr 2019

Rupp J (2009) SolarCombi+, SorTech package solution description. http://www.solarcombiplus.eu/docs/d44_sortech_v02_english.pdf. Accessed 23 Apr 2019

Saha BB, Akisawa A, Kashiwagi T (2001) Solar/waste heat driven two-stage adsorption chiller: the prototype. Renew Energy 23:93–101. https://doi.org/10.1016/S0960-1481(00)00107-5

Saha BB, El-Sharkawy II, Chakraborty A, Koyama S, Banker ND, Dutta P et al (2006) Evaluation of minimum desorption temperatures of thermal compressors in adsorption refrigeration cycles. Int J Refrig 29:1175–1181. https://doi.org/10.1016/j.ijrefrig.2006.01.005

Saha BB, El-Sharkawy II, Thorpe R, Critoph RE (2012) Accurate adsorption isotherms of R134a onto activated carbons for cooling and freezing applications. Int J Refrig 35:499–505. https://doi.org/10.1016/j.ijrefrig.2011.05.002

Sarbu I (2014) A review on substitution strategy of non-ecological refrigerants from vapour compression-based refrigeration, air-conditioning and heat pump systems. Int J Refrig 46:123–141. https://doi.org/10.1016/j.ijrefrig.2014.04.023

Sayigh AAM, McVeigh JC (1992) Solar air conditioning and refrigeration, 1st edn. Pergamon Press, New York

Standard specification of adsorption chiller (2019). Tokyo Boeki Machinery, Japan. http://www.tokyo-boeki-machinery.jp/adsorption_chiller/siyou.html. Accessed 23 Apr 2019

Stocker TF, Qin D, Plattner GK, Tignor M, Allen SK, Boschung J, Nauels A, Xia Y, Bex V, Midgley PM (eds) (2019) Contribution of working group i to the fifth assessment report of the intergovernmental panel on climate change. Cambridge University Press, Cambridge. http://www.climatechange2013.org/images/report/WG1AR5_ALL_FINAL.pdf. Accessed 23 Apr 2019

Stryi-Hipp G (2016) Renewable heating and cooling: technologies and applications, 1st edn. Woodhead Publishing, Amsterdam

Tangkengsirisin V, Kanzawa A, Watanabe T (1998) A solar-powered adsorption cooling system using a silica gel-water mixture. Energy 23:347–353. https://doi.org/10.1016/S0360-5442(98)00002-4

Tassou SA, Grace IN (2005) Fault diagnosis and refrigerant leak detection in vapour compression refrigeration systems. Int J Refrig 28:680–688. https://doi.org/10.1016/j.ijrefrig.2004.12.007

Technical specification of 10 kW Bry-Chill adsorption chiller (2019) Bry-Air (Asia) Pvt. Ltd. https://www.bryair.com/products-solutions/adsorption-chillers/brychilltm-adsorption-chiller/. Accessed 23 Apr 2019

Thu K, Chakraborty A, Saha BB, Ng KC (2013) Thermo-physical properties of silica gel for adsorption desalination cycle. Appl Therm Eng 50:1596–1602. https://doi.org/10.1016/j.applthermaleng.2011.09.038

Tyagi VV, Kaushik SC, Tyagi SK (2012) Advancement in solar photovoltaic/thermal (PV/T) hybrid collector technology. Renew Sustain Energy Rev 16:1383–1398. https://doi.org/10.1016/j.rser.2011.12.013

Vaitkus L, Dagilis V (2017) Analysis of alternatives to high GWP refrigerants for eutectic refrigerating systems. Int J Refrig 76:160–169. https://doi.org/10.1016/j.ijrefrig.2017.01.024

Wang SK (2000) Handbook of air conditioning and refrigeration, 2nd edn. McGraw-Hill, New York

Wang LW, Wang RZ, Oliveira RG (2009) A review on adsorption working pairs for refrigeration. Renew Sustain Energy Rev 13:518–534. https://doi.org/10.1016/j.rser.2007.12.002

Wang R, Wang L, Wu J (2014) Adsorption refrigeration technology—theory and application. Wiley, Singapore

Yang MH, Yeh RH (2015) Performance and exergy destruction analyses of optimal subcooling for vapor-compression refrigeration systems. Int J Heat Mass Transf 87:1–10. https://doi.org/10.1016/j.ijheatmasstransfer.2015.03.085

Yumrutaş R, Kunduz M, Kanoğlu M (2002) Exergy analysis of vapor compression refrigeration systems. Exergy An Int J 2:266–272. https://doi.org/10.1016/S1164-0235(02)00079-1

Chapter 10
Thermodynamic Analysis of Activated Carbon–Ethanol and Zeolite–Water Based Adsorption Cooling Systems

Satish Sangwan and Prodyut R. Chakraborty

Abstract The present study focuses on the thermodynamic analysis of zeolite–water and activated carbon–ethanol based adsorption cooling systems. The performance of the system depends critically on four operating temperatures namely maximum desorption temperature, minimum adsorption temperature, condensing temperature, and evaporating temperature and also on the ratio of specific heat of structural material and the specific heat of adsorbent. Dubinin–Astakhov equation is used to estimate the equilibrium uptake of working pairs. A comparative study is made between these working pairs for the air-conditioning applications.

Keywords Adsorption · Zeolite · Activated carbon · Ethanol

10.1 Introduction

The world is getting warmer, the average global temperature of earth has increased by 0.8 °C since 1880 and most of this increase occurred since 1975 (Hansen et al. 2010). Due to this increase in average temperature, demand of refrigeration and air-conditioning is increasing continuously. It is approximated by the international Institute of Refrigeration in Paris that 15% of the total electricity production across the world is used for cooling applications and it is also estimated that the 45% of the total households and commercial buildings energy consumption is consumed for air-conditioning applications (Choudhury et al. 2013). Traditional methods of cooling uses CFC, HCFC and HFC as a refrigerant which are the major cause of ozone layer depletion and global warming. So the demand of environment friendly refrigeration and air-conditioning technologies is under continuous research focus. One more problem with the traditional refrigeration systems is energy consumption. Conventional vapor compression cooling systems uses electricity as source of energy. The energy efficiency of electricity production is about 40–50%, so most of the energy is released in atmosphere as waste heat at a temperature of 70–200 °C (Wang

S. Sangwan · P. R. Chakraborty (✉)
Department of Mechanical Engineering, Indian Institute of Technology Jodhpur, Jodhpur 342037, Rajasthan, India
e-mail: pchakraborty@iitj.ac.in

H. Tyagi et al. (eds.), *Solar Energy*, Energy, Environment, and Sustainability, https://doi.org/10.1007/978-981-15-0675-8_10

et al. 2014). Energy consumption problems can be solved by developing cooling technologies which utilizes low grade heat as source of power.

Adsorption cooling has gained attention as a novel technology. The main advantage with this technology is having zero ODP (ozone depleting potential) and GWP (global warming potential) values as it uses natural ingredients as refrigerants alternative to refrigerants containing CFC, HCFC, or HFC (Saha et al. 2007). Since 1970s, adsorption technology have been focused more among other sorption technologies. In comparison to other sorption systems which uses low grade energy as source of heat, adsorption systems has variety of adsorbents such as physical, chemical and composite adsorbents and these can be used over a range of temperatures (50–400 °C). Secondly, this technology doesn't require solution pump and rectification equipment. Adsorption cooling systems are devoid of problems faced by absorption systems like solution crystallization and use of pollution prone refrigerants. But adsorption refrigeration systems are less efficient as compared to absorption refrigeration, and another disadvantage this technology have, is that the systems are of large volume. Due to these merits and demerits, this technology is given recognition by academicians as a complementary technology for absorption refrigeration.

Adsorption systems uses zeolite–water, silica gel–water, and activated carbon–methanol/ethanol/ammonia, as working pairs (Lu et al. 2006). Many researchers have studied adsorption systems based on these working pairs.

10.2 History of Adsorption Cooling Technology

In 1848, Faraday discovered that the cooling effect can be produced when AgCl adsorbed NH_3 (Wang et al. 2014). In the 1920s, Hulse suggested a silica gel–SO_2 based cooling system for storing the food and heat source for this system was combustion of propane and air was used for cooling. Lowest temperature achieved was 12 °C (Hulse 1929). Activated carbon–methanol based cooling system was introduced by Plank and Kuprianoff (Wang et al. 2014). Adsorption refrigeration was not given importance by scientists and researchers for a long period due to improvement in the efficiency of vapor compression refrigeration systems and adsorption technology was not able to compete with efficient CFCs systems.

Due to energy crisis which occurred in the 1970s, adsorption refrigeration technology got a chance for the development because adsorption systems can be driven by waste heat sources and solar energy. The problem of environmental pollution became very serious from 1990 onward with the major drawbacks of CFC being the significant contributor to ozone layer depletion and global warming. Because of this adsorption cooling technology was given recognition by researchers and academicians. Till now air conditioning systems for automobiles, marine refrigeration and heat pump systems are focused more under adsorption technology (Suzuki 1993) because these systems have no moving parts and perform well in vibrating conditions (Jones and Golben 1985).

In early years, focus of research was on the performance of the working pairs. The main objective was to use this technology to practical applications. Adsorbents which were studied are silica gel, activated carbon, zeolite, $CaCl_2$, hydride and the refrigerants under focus were methanol, ammonia, water, hydrogen (Critoph and Vogel 1986). Initial research work suggested improvements in adsorption refrigeration cycles are required especially to address the intermittent behaviour of the cycle, and low COP and SCP issues. Other major issue was low heat and mass transfer performance inside the adsorption bed. For solving the above stated problems, researchers mainly focused on aspects like adsorption properties, heat and mass transfer, and advanced adsorption refrigeration cycles were proposed e.g. heat recovery cycle, mass recovery cycle, thermal wave cycle (Wang 2001b), convective thermal wave cycle (Critoph 1994) and cascading cycle (Douss and Meunier 1989). In some references (Wang et al. 2004; Aristov et al. 2002; Mauran et al. 1993) working pairs with good adsorption characteristics e.g. composite adsorption working pairs were proposed and adsorption cycles were analysed for the proposed working pairs.

Till 1992, most of the work was based on theoretical analysis of different adsorption cycles and mainly on the effect of cycle parameters on the performance of adsorption cycle (Luo and Feidt 1992; Hajji et al. 1991; Cacciola and Restuccia 1995). Based on the theoretical and experimental analysis researchers focused on the design of an adsorbent bed which enhances the heat and mass transfer performance (Restuccia et al. 1988).

In the 1990s, European Union listed a project on the adsorption (JOULE0046F) into their research and the members of the research group for this project were Meunier from France (zeolite–water), Cacciola from Italy (zeolite–water), Critoph from England (activated carbon–ammonia), Groll from German (metal hydrides-Hydrogen), Spinner from France, Zigler from German (nickel chloride-ammonia). In 1999, International Journal of Refrigeration published the results of the JOULE research plan (Wang et al. 2014).

10.3 Current Research on Adsorption Refrigeration

Countries like Italy, France, USA, UK, and India are working on adsorption heat pump and cooling systems, and, the main focus is on the heat and mass transfer performance of adsorbent beds, working pairs, and adsorption cycles. The development in this field can be summarized as working pairs; structure of cooling system; enhancement in the heat and mass transfer performance of adsorbent bed.

A. **Adsorption working pairs**: Working pair used in adsorption refrigeration is a key element for the system. Coefficient of performance of the system is influenced by the thermal properties of the working pair. For the better performance of the system selection of a suitable working pair is required and this selection must be based on the available heat source temperature and application requirements. Commonly used working pairs are activated carbon–ammonia, activated

carbon–ethanol, silica gel–water, zeolite–water, metal hydrides–hydrogen, calcium chloride–ammonia and strontium chloride–ammonia etc. (Srivastava and Eames 1998). Activated carbon–methanol has high adsorption and desorption capacity with low heat of adsorption of the order of 1800–2000 kJ/kg. Desorption temperature cannot exceed 120 °C, because above this temperature methanol will start decomposing. Activated carbon–ammonia with similar heat of adsorption as activated carbon–methanol pair, has the advantage of low evaporation temperature of refrigerant and is used for high temperature heat source. Silica gel–water is generally used for low temperature heat source because silica gel will be destroyed at temperature higher than 120 °C. Zeolite–water has wide range of desorption temperature from 70 to 250 °C and, the heat of adsorption is around 3200–4200 kJ/kg, which is a disadvantage of this working pair. Activated carbon–ethanol has the advantage of high adsorption/desorption capacity but has low value of latent heat of vaporization approximately 30% lower than methanol. It has saturation pressure similar to methanol. Activated carbon–ethanol works best around desorption temperature of 100 °C.

B. **Low grade heat utilization**: Adsorption Refrigeration Technology is suitable for recovery of thermal energy from low grade heat sources by using working pairs such as Activated carbon–methanol. On the other hand, activated carbon–ammonia can be used for high temperature heat source. As compared to absorption systems, adsorption refrigeration technology is more suitable in vibratory systems because of solid adsorbent. Therefore in the recent past, researchers focused on the use of low grade heat in adsorption cooling.

   Suzuki (1993) worked on zeolite–water based automobile air conditioner and observed that heat and mass transfer properties of bed plays an important role in minimizing the cycle time and mass of the system. Lavan (Mei et al. 1979) worked out on the probability of a system that utilizes the exhaust gas of trucks. Zhu et al. (1992) worked on the adsorption system used for fish storage on boats. SJTU also developed some adsorption cooling systems (Wang et al. 2004; Wang 2001a) mainly activated carbon–ammonia based 5 kW air conditioner, zeolite–water based 5 kW system for locomotive cab and an ice maker based on activated carbon–methanol.

   Saha et al. (2007) studied an adsorption system based on activated carbon fiber–ethanol which works on low temperature waste heat source (60–95 °C). *COP* of the system is 0.6 with cycle time of 600–700 s.

C. **Solar energy utilization**: Solar energy based sorption cooling systems got attention due to the seasonal matching of cooling requirements and heat supply. Use of low temperature heat as source of energy by adsorption cooling systems makes them more suitable for solar energy applications as compared to absorption systems.

   Tchernev (Wang et al. 2014) developed a zeolite–water based adsorption cooling system, and from then onwards, researchers focused on the adsorption systems driven by solar energy. In France, Guilleminot and Pons (Grenier et al. 1988) investigated adsorption cooling systems which utilizes solar energy as heat source, working pairs used were activated carbon–methanol and zeolite–water,

and it is observed that the COP of zeolite–water system is 0.10 having collector area of 20 m^2 and mass of adsorbent is 360 kg. The COP of activated carbon–methanol system (Pons and Guilleminot 1986) was found out to be 0.12–0.14 having collector area of 6 m^2 and mass of adsorbent is 20–24 kg/m^2. Sumathy et al., studied an activated carbon–methanol system driven by solar energy, and observed that output of the system is 4–5 kg of ice per day and the COP is about 0.1–0.2 with collector area of 0.92 m^2 (Sumathy and Zhongfu 1999). Li et al., at Guangzhou Institute of Energy Conversion and Tan at South China University of Technology developed a refrigeration system powered by solar energy having similar performance to the system developed by Sumathy (Wang et al. 2014).

To enhance the energy efficiency a compound refrigerator and water heater system based on solar energy was developed by SJTU (Wang et al. 2000) and in 2004, SJTU also developed a solar energy based adsorption chiller which uses silica gel–water as working pair for building and grain storage hall.

El-Sharkawy et al. (2008) worked on activated carbon–ethanol based solar powered adsorption system. Ideal *COP* of the system is 0.8 at an evaporator temperature of 15 °C and desorption temperature of 80 °C.

10.4 Adsorption Process and Selection Criteria for Working Pairs

Adsorption is a surface phenomenon in which molecules of one substance adheres to the surface of another. This results in an increase in concentration at the interface. The solid which adsorbs the molecules called adsorbent and the liquid or gas which is getting adsorbed is called adsorbate. Adsorption is of mainly two types, physical adsorption (Ponec et al. 1974) and chemisorption (Wang 2005). Driving force in case of physisorption is weak wander wall force of attraction whereas in case of chemisorption adsorbent and adsorbate undergo a chemical reaction (Gasser and Ehrlich 1987). Chemisorption is an endothermic process and is not reversible. Physisorption is an exothermic process and the heat released during this process is known as adsorption heat. This process is reversible in nature, means desorption occurs when heat is supplied to the adsorbent and this heat can be acquired using solar energy and waste heat from automobiles or any other sources.

Basic requirements for the selection of adsorbent are as follows:

1. Should desorb large amount of adsorbate over a given range of temperature.
2. Should have low specific heat.
3. Should have high conductivity.
4. Should be stable with adsorbate/refrigerant used.
5. Should be easily available and have low cost.

Basic requirements for the selection of adsorbate are as follows:

1. Should have high latent heat of vaporization to minimize the amount of adsorbent needed.
2. The saturation pressure corresponding to the evaporating temperature should be above atmospheric pressure so that the system always runs on positive pressure.
3. The saturation pressure corresponding to the condensing temperature should be as low as possible.
4. Should be thermally and chemically stable.
5. Non-toxic, non-flammable and should have low cost.

10.5 Adsorption Refrigeration Cycle

An adsorption refrigeration cycle consist of adsorber/desorber, a condenser, an evaporator and an expansion valve (Meunier 2001). The mechanical compressor which is an integral part of traditional VCR systems is replaced by low grade energy driven adsorbent bed. Single bed adsorption refrigeration cycle is intermittent in nature and consists of four processes.

I. Sensible Heating
II. Desorption and Condensation
III. Sensible Cooling
IV. Adsorption and Evaporation

The desorption and adsorption occurs at constant pressure (isobaric process), whereas the sensible heating and cooling occurs at constant concentration (isosteric process). To deal with the problem of intermittent nature of single bed cycle, we are considering two bed system in which both the beds will work simultaneously, one will undergo adsorption process, at the same time other will undergo desorption process. Schematic of two bed adsorption refrigeration system (Basic cycle) with uniform bed temperature assumption and representative ideal thermodynamic cycle for the beds is shown in Fig. 10.1, the system operates in the following way.

Sensible Heating
This is the period from a to b as shown in Fig. 10.1. During this process concentration of refrigerant or adsorbate remains constant or at maximum ($x_a = x_b$) and the bed is sensibly heated from T_a to T_b, resulting an increase in pressure from P_e (evaporating pressure) to P_c (condensing pressure).

Heating, Desorption and Condensation
This is the period from b to c as shown in Fig. 10.1. At T_b pressure in the adsorber is equal to the condensing pressure P_c and desorption starts. During desorption temperature of the bed increases along isobar until the refrigerant concentration reaches X_{min}. This desorbed refrigerant get condensed in the condenser releasing the latent heat of condensation to atmosphere.

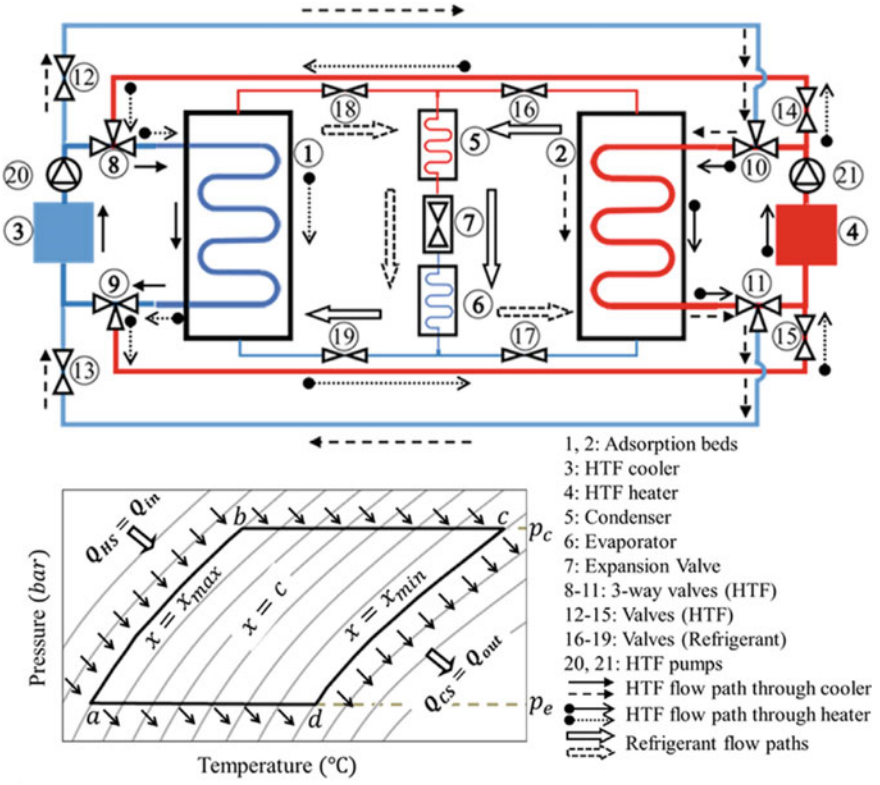

Fig. 10.1 Schematic of two bed adsorption cooling system (basic cycle) and representative ideal thermodynamic cycle for the beds

Cooling and Depressurization

This is the period from c to d as shown in Fig. 10.1. After the completion of desorption process, the bed is at highest temperature and needs to be cooled for re-adsorption of refrigerant. So the bed is sensibly cooled resulting in decrease in temperature from T_c to T_d and pressure for P_c to P_e while the concentration of refrigerant remains constant ($x_c = x_d$).

Cooling, Adsorption and Evaporation

This is the period from d to a as shown in Fig. 10.1. During this process refrigerant get evaporated inside the evaporator absorbing the heat from the surroundings. Then refrigerant comes out of evaporator and enters into the adsorbent bed, where re-adsorption of refrigerant occurs and as adsorption is an exothermic process the bed needs to be cooled simultaneously. This process continues until the cycle is completed and the system is returned to its original temperature of T_a.

10.6 Heat Recovery Cycle

The schematic of two bed adsorption cooling system with heat recovery and associated thermodynamic cycle for the beds is shown in Fig. 10.2. At the completion of each half of the cycle, desorption bed will be at highest temperature (T_c) and adsorption bed will be at lowest temperature (T_a). The bed at lowest temperature requires heat to undergo desorption process while the bed at highest temperature needs to be cooled, so that it can undergo adsorption process. Part of the heat rejected during cooling (process c-d-a) can be utilized to preheat the desorbing bed (process a-b-c), reducing the total amount of external heating and cooling requirements. It will also result in the improvement of *COP* and second law efficiency of the system.

The heat recovery can be achieved by circulating a heat transfer fluid between both the beds as shown in Fig. 10.3. But heat can only be recovered till both the beds attains thermal equilibrium (point e and f in thermodynamic cycle).

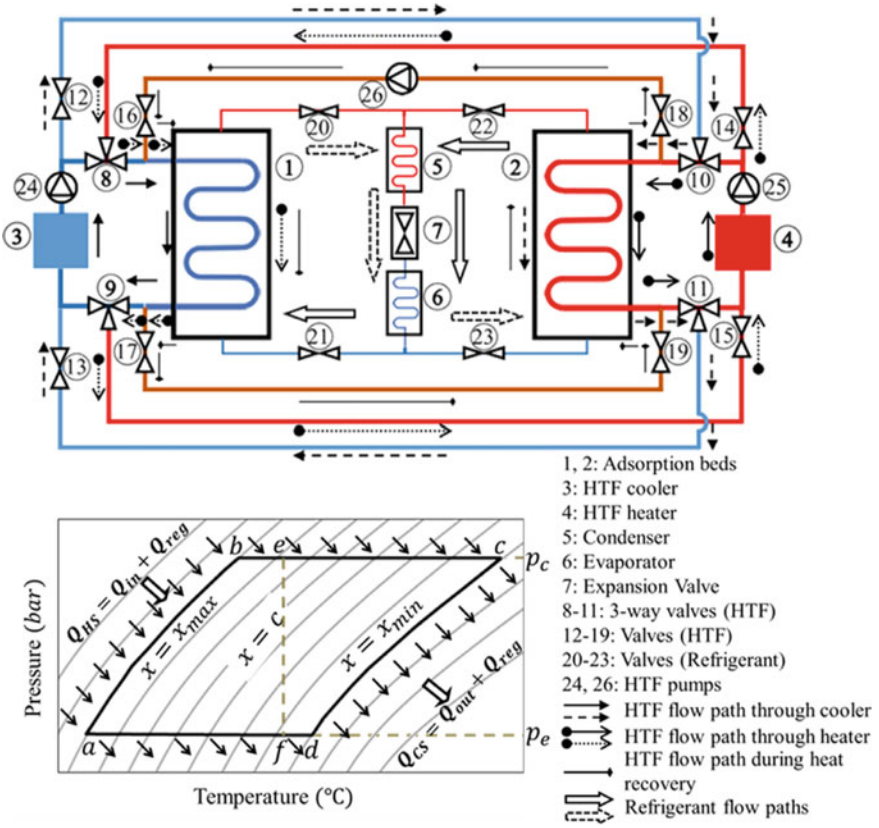

Fig. 10.2 Schematic of two bed adsorption cooling system with heat recovery and associated thermodynamic cycle for the beds

10.7 Mathematical Modelling

The mathematical model is derived on the basis of simple thermodynamic cycles described in Fig. 10.1. This model is based on the adsorption equilibrium equations of the working pair and heat flows. The assumptions made to simplify the calculations are as follows. (i) Equilibrium condition is reached in adsorbent bed during both adsorption and desorption process, it implies that the amount of adsorbate adsorbed or desorbed is calculated using equilibrium adsorption equation. (ii) The pressure, temperature and concentration of adsorbate are uniform throughout the adsorbent bed. (iii) No change in the concentration of adsorbate during sensible heating and cooling of adsorbent bed. (iv) Specific heat of refrigerant is considered to be constant over the working temperature range. (v) Temperature difference between the heat transfer fluid and the adsorbent bed is considered to be negligible. (vi) Temperature difference between the heat transfer fluid and the refrigerant is considered to be negligible in the evaporator/condenser. And, (vii) system is well insulated i.e., no heat loss from the system to the environment.

The Dubinin–Astakhov (D-A) equation is used to calculate sorption uptake of adsorbate in the adsorbent bed as a function of temperature (T) and pressure (P) (Tamainot-Telto and Critoph 1997; Critoph and Turner 1988; Saha et al. 2009, 2011).

$$x(T, T_{psat}) = x_0 \exp\left[-k\left(\frac{T}{T_{psat}} - 1\right)^n\right] \tag{10.1}$$

where, x_o is the maximum concentration of adsorbate obtained under saturated concentration, k and n are empirical coefficients. Values x_o, k, and n depends on the nature of adsorbent-adsorbate pair and are constants for a given adsorbent-adsorbate pair. T is the temperature of the bed in Kelvin and T_{psat} is the saturation temperature (K) of adsorbate at the bed pressure (p).

Heat analysis of basic cycle

Sensible heat (Q_{sh}) is the energy required to increase the bed temperature from minimum adsorption temperature T_a to minimum desorption temperature T_b and pressure from p_e to p_c prior to the onset of desorption process (process a-b on thermodynamic cycle in Fig. 10.1). Q_{sh} heat supply per unit kg of adsorbent is given by:

$$Q_{sh} = \int_{T_a}^{T_b} c_{ad}(T)\, dT + \int_{T_a}^{T_b} R_m c_{ad}^{ref}\, dT + \int_{T_a}^{T_b} c_{vr} x_a\, dT \tag{10.2}$$

where, c_{ad} is the specific heat of activated carbon, c_{ad}^{ref} is the specific heat of activated carbon at reference temperature (300 K) and c_{vr} is average constant volume specific heat of liquid and gaseous refrigerant. $R_m = (c_m m_m)/(c_{ad}^{ref} m_{ad})$ is defined as the ratio of heat capacity of the combined container material of the adsorber bed and HTF

with that of adsorbent. c_m is the combined specific heat capacity of the structural material of bed and HTF, and m_m is the combined mass of the same ($c_m m_m = c_{st} m_{st} + c_{HTF} m_{HTF}$ and $m_m = m_{st} + m_{HTF}$). $x_a = x_b$ is the maximum concentration of adsorbate adsorbed in the bed.

The heat input per unit kg of adsorbent during the desorption process Q_{de} (process *b*–*c* in Fig. 10.1) can be estimated as:

$$Q_{de} = \int_{T_b}^{T_c} c_{ad}(T)\, dT + \int_{T_b}^{T_c} R_m c_{ad}^{ref}\, dT + \int_{T_b}^{T_c} c_{pr} x(T, T_{csat})\, dT - \int_{x_b}^{x_c} h_d\, dx \quad (10.3)$$

where, c_{pr} is average constant pressure specific heat of liquid and gaseous refrigerant. Once again, coexistence of gaseous and liquid refrigerant at equilibrium in the bed leads to estimation of c_{pr} on the basis of the average between gas-phase and liquid phase constant pressure specific heats of refrigerant. Last term in Eq. 10.3, represents the amount of heat required for desorption as desorption is an endothermic process and the negative sign is due to the fact that the term dx is negative during desorption.

The sensible cooling per unit kg of adsorbent (Q_{sc}) of the bed prior to onset of adsorption process (process *c*–*d* in Fig. 10.1) brings down the pressure of the bed from condensing pressure p_c to evaporating pressure p_e accompanied by a decrease in bed temperature from maximum desorption temperature (T_c) to maximum adsorption temperature (T_d). Q_{sc} can be estimated as:

$$Q_{sc} = \int_{T_c}^{T_d} c_{ad}(T)\, dT + \int_{T_c}^{T_d} R_m c_{ad}^{ref}\, dT + \int_{T_c}^{T_d} c_{vr} x_c\, dT \quad (10.4)$$

Process *c*–*d* being isosteric $x_c = x_d$, $x_c = x_d$ is the minimum concentration of refrigerant adsorbed in the bed.

Re-adsorption of adsorbate occurs at evaporation pressure p_e (isobaric process d-an in Fig. 10.1). Adsorption being exothermic process, heat removal from the bed is essential during this process. The bed temperature reduces from maximum adsorption temperature T_d to minimum adsorption temperature T_a during this process. The heat removal (Q_{ad}) required per kg of adsorbent can be found out to be:

$$Q_{ad} = \int_{T_d}^{T_a} c_{ad}(T)\, dT + \int_{T_d}^{T_a} R_m c_{ad}^{ref}\, dT + \int_{T_d}^{T_a} c_{pr} x(T, T_{esat})\, dT - \int_{x_d}^{x_a} h_a\, dx + \int_{x_d}^{x_a} c_{pr}(T - T_{esat})\, dx \quad (10.5)$$

Last term in Eq. 10.5, is included to take care of the cooling effect provided by the refrigerant coming from evaporator as it will be at a lower temperature compared to bed temperature. Second last term is adsorption heat.

During the cooling process of adsorption bed, heat can be directly rejected to the ambient till the adsorption bed reaches the ambient temperature. If the minimum adsorption temperature (T_a) is lower than that of ambient temperature, cooling of the adsorber bed below the ambient will require a special cooling arrangement. In order to be on the safer side, cooling of the adsorption bed from condensation temperature T_{csat} to minimum adsorption temperature T_a is considered as the external cooling requirement. If we denote cooling requirement (per kg of adsorbent) of the adsorption bed below T_{csat} as $Q_{<T_{csat}}$, it can be expressed as:

$$Q_{<T_{csat}} = \int_{T_{csat}}^{T_a} c_{ad}(T)\,dT + \int_{T_{csat}}^{T_a} R_m c_{ad}^{ref}\,dT + \int_{T_{csat}}^{T_a} c_{pr} x(T, T_{esat})\,dT - \int_{x_{csat}}^{x_a} h_a\,dx + \int_{x_{csat}}^{x_a} c_{pr}(T - T_e)\,dx \tag{10.6}$$

If T_a is greater than T_{csat} then $Q_{<T_{csat}} = 0$.

After desorption gaseous refrigerant at high temperature and superheated state enters the condenser, and condenses to a state of saturated liquid at condensing pressure p_c by releasing heat to the ambient. The heat released to the atmosphere (per kg of adsorbent) can be estimated as:

$$Q_{cond} = -\left[(x_b - x_c)h_{fg} + \int_{x_b}^{x_c} c_{pr}(T - T_{csat})\,dx\right] \tag{10.7}$$

An additional cooling (per unit kg of adsorbent) of refrigerant is required during the free expansion of saturated liquid from p_c to p_e as the refrigerant flows through the expansion valve between the condenser and evaporator, which is given by:

$$Q_{co} = \int_{T_{csat}}^{T_{esat}} c_{rl}(T)(x_b - x_c)\,dT \tag{10.8}$$

where, c_{rl} is the temperature dependent specific heat of liquid refrigerant.

Refrigeration effect per kg of adsorbent Q_{evap} can be estimated as

$$Q_{evap} = (x_b - x_c)h_{fg} \tag{10.9}$$

It is pertinent to mention here that the signs of estimated values of Q_{sh}, Q_{de}, and Q_{evap} is positive and the signs of estimated values of Q_{sc}, Q_{ad}, $Q_{<T_{csat}}$, Q_{cond}, Q_{co} are negative. The *SCE* and *COP* of the system can be estimated as:

$$SCE = Q_{evap} - Q_{co} - Q_{<T_{csat}} \tag{10.10}$$

$$COP = \frac{SCE}{Q_{de} + Q_{sh}} \tag{10.11}$$

Heat recovery cycle (analysis)
The thermodynamic cycle of the heat recovery process is shown in Fig. 10.2. The heat recovery can be attained till thermal equilibrium is established between the beds so that both the beds reach a common temperature (described by sates e and f on the thermodynamic cycle in Fig. 10.2). The estimation of equilibrium temperature of the two beds T_e and T_f ($T_e = T_f = T_{eq}$) is be based on two alternative formulations based on relative values of T_b and T_d. If the condition $T_b \geq T_d$ is satisfied, then T_{eq} can be estimated from the following formulation.

$$Q_{sh}|_{T_a}^{T_{eq}} = \left| Q_{sc}|_{T_c}^{T_{eq}} \right| \tag{10.12}$$

On the other hand if the condition $T_b < T_d$ is satisfied, then T_{eq} needs to be estimated from the following formulation.

$$Q_{sh} + Q_{de}|_{T_b}^{T_{eq}} = \left| Q_{sc} + Q_{ad}|_{T_d}^{T_{eq}} \right| \tag{10.13}$$

$Q_{sh}|_{T_a}^{T_{eq}}$, $Q_{de}|_{T_b}^{T_{eq}}$, $Q_{sc}|_{T_c}^{T_{eq}}$, and $Q_{ad}|_{T_d}^{T_{eq}}$ can be obtained from Eqs. 10.2–10.5 by changing the upper limits of integrations to e and f respectively. Although the temperatures T_e and T_f are equal at state points e and f, the concentrations of refrigerant at desorbing and adsorbing beds are not equal, i.e. $x_e(T_e, T_{csat}) \neq x_f(T_f, T_{esat})$; and one should be careful while calculating $Q_{de}|_{T_b}^{T_{eq}}$ and $Q_{ad}|_{T_d}^{T_{eq}}$ from Eqs. 10.3 and 10.5. By substituting appropriate expressions of $Q_{sh}|_{T_a}^{T_{eq}}$, $Q_{sc}|_{T_c}^{T_{eq}}$, Q_{sh}, Q_{sc}, $Q_{de}|_{T_b}^{T_{eq}}$, and $Q_{ad}|_{T_d}^{T_{eq}}$ in Eq. 10.12 or 10.13, we obtain an equation with a single unknown T_{eq} and Eq. 10.12 or 10.13 can be rewritten as:

$$F(T_{eq}) = 0 \tag{10.14}$$

where, $F(T_{eq})$ is a nonlinear function of T_{eq}. Equation 10.14 can be solved by using iterative secant method to determine the value of T_{eq} in the following manner.

$$T_{eq}^{(i)} = T_{eq}^{(i-1)} - F^{(i-1)} \frac{T_{eq}^{(i-1)} - T_{eq}^{(i-2)}}{F^{(i-1)} - F^{(i-2)}} \tag{10.15}$$

where, i represents the iteration step. The two initial guesses to initiate the iteration has been considered to be T_b, and T_d.

If $T_b \geq T_d$, regenerated or recovered heat per kg of adsorbent Q_{reg} can be simply estimated as:

$$Q_{reg} = Q_{sh}|_{T_a}^{T_{eq}} = \left| Q_{sc}|_{T_c}^{T_{eq}} \right| \tag{10.16}$$

On the other hand, for $T_b < T_d$, Q_{reg} can be simply estimated as:

$$Q_{reg} = Q_{sh} + Q_{de}|_{T_b}^{T_{eq}} = \left| Q_{sc} + Q_{ad}|_{T_d}^{T_{eq}} \right| \tag{10.17}$$

The net heat input from the external heat source per kg of adsorbent Q_{in} is estimated as:

$$Q_{in} = Q_{sh} + Q_{de} - Q_{reg} \tag{10.18}$$

Since $T_{eq} > T_{csat}$, the net external cooling requirement per kg of adsorbent Q_{out} is:

$$Q_{out} = Q_{<T_{csat}} \tag{10.19}$$

The *SCE* is same as given by Eq. 10.10, however, the *COP* of the system can be estimated as:

$$COP = \frac{SCE}{Q_{in}} \tag{10.20}$$

Second Law Efficiency

The analysis will remain incomplete if we do not discuss the second law efficiencies of each of these adsorption refrigeration cycles. From the first law of thermodynamics for the half cycle we obtain the following heat balance equation.

$$(Q_{de} + Q_{sh}) + (Q_{evap} - Q_{co} - Q_{<T_{csat}}) = Q_{cond} + (Q_{ad} + Q_{sc} - Q_{<T_{csat}}) \tag{10.21}$$

From the second law: $\Delta S_{uni} = \Delta S_{sys} + \Delta S_{sur} \geq 0$. Noting that $\Delta S_{sys} = 0$ for a closed cycle, net entropy increase of the surrounding must be greater than or equal to zero ($\Delta S_{sur} \geq 0$). The change in entropy of the surrounding can be expressed as.

$$-\frac{(Q_{de} + Q_{sh})}{T_c} - \frac{(Q_{evap} - Q_{co} - Q_{<T_{csat}})}{T_{esat}} + \frac{Q_{cond}}{T_{csat}} + \frac{(Q_{ad} + Q_{sc} - Q_{<T_{csat}})}{T_{amb}} \geq 0 \tag{10.22}$$

where, T_{amb} is the ambient temperature, and all the temperatures values are in absolute temperature scale (K). It is desired that the ambient temperature should be less than saturation temperature at condenser pressure ($T_{amb} < T_{csat}$). However, in worst case scenario, T_{amb} should at least be equal to T_{csat}. Putting this condition in Eq. 10.22, we obtain the following expression for entropy generation of the surrounding.

$$-\frac{(Q_{de} + Q_{sh})}{T_c} - \frac{(Q_{evap} - Q_{co} - Q_{<T_{csat}})}{T_{esat}} + \frac{Q_{cond}}{T_{csat}} + \frac{(Q_{ad} + Q_{sc} - Q_{<T_{csat}})}{T_{csat}} \geq 0 \tag{10.23}$$

Finally, combining Eqs. 10.23 and 10.21, and rearranging the terms we obtain the expression for maximum coefficient of performance (COP_{max}) given by:

$$COP_{max} = \frac{Q_{evap} - Q_{co} - Q_{<T_{csat}}}{(Q_{de} + Q_{sh})} \leq \left(\frac{T_c - T_{csat}}{T_c}\right)\left(\frac{T_{esat}}{T_{csat} - T_{esat}}\right) \quad (10.24)$$

The second law efficiencies of the cycles described earlier are defined as:

$$\eta_{II} = \frac{COP_{cycle}}{COP_{max}} \quad (10.25)$$

10.8 Results

COP, SCE, η_{II} values of the two cycles for both the working pairs are plotted against five input parameters (maximum desorption temperature (T_c), minimum adsorption temperature (T_a), condensing temperature (T_{csat}), evaporating temperature (T_{esat}) and the heat capacity ratio (R_m) between structural material and adsorbent). Activated Carbon–Ethanol and Zeolite–Water are used as working pairs for the present analysis. Adsorption parameters such as x_o, k, and n and thermos-physical properties used for the analysis are given in Tables 10.1 and 10.2 respectively.

Table 10.1 Adsorption parameters of working pairs

Working pair	x_0 (kg of refrigerant/kg of adsorbent)	k	n
Activated carbon–ethanol (Uddin et al. 2014)	1.2	25.587	1.8
Zeolite–water (Wang et al. 2014)	0.302	4.40	2

Table 10.2 Thermo-physical properties

Property	Unit	Activated carbon–ethanol	Zeolite–water
c_{ad} (Turner 1992; Sharafian and Bahrami 2015)	kJ/kg K	$0.175 + 2.245 \times 10^{-3} \times T$	0.836
c_{rl} (Sharafian and Bahrami 2015)	kJ/kg K	2.87	4.185
c_{pr} (Sharafian and Bahrami 2015)	kJ/kg K	1.687	1.880
c_{vr} (Sharafian and Bahrami 2015)	kJ/kg K	1.5063	1.419
h_{fg} (Wang et al. 2014)	kJ/kg	842	2258
R	kJ/kg K	0.1807	0.462
C	K	4659	4897

Figure 10.3 shows the effect of varying maximum desorption temperature (T_c) and heat capacity ratio (R_m) on *COP* of the basic cycle keeping all other input parameters constant i.e. $T_a = T_{csat} = 300$ K and $T_{esat} = 273$ K for both the working pairs. From Fig. 10.3a and b, it is clear that with the increase in maximum desorption temperature, *COP* also increases and attains maxima for a particular value of T_c (370 K for Activated carbon ethanol and around 450 K for Zeolite–water pair) but with further increase in temperature it starts decreasing because a fixed amount of refrigerant is adsorbed inside the adsorbent and no more desorption occurs after a particular temperature. With the increase heat capacity ratio more amount of input heat will be absorbed by the structural material and it will affect the COP adversely which can also be seen from Fig. 10.3.

Figure 10.4 shows the effect of varying maximum desorption temperature (T_c) and heat capacity ratio (R_m) on *COP* of the heat recovery cycle keeping all other input parameters constant i.e. $T_a = T_{csat} = 300$ K and $T_{esat} = 273$ K for both the working pairs. Heat recovery cycle also follows the same trend with respect to maximum desorption temperature as followed by the basic cycle. Heat recovery cycle resulted in higher *COP* as compared to basic cycle. From Fig. 10.4a and b, it can be noticed that there is a sudden change in the *COP* gradient with respect to T_c at $T_c = 365$ K (activated carbon–ethanol) and $T_c = 360$ K (zeolite–water). This change is due to the fact that condition $T_b \geq T_d$ prevails till $T_c = 365$ K (activated carbon–ethanol) and $T_c = 360$ K (zeolite–water), and the estimation of equilibrium bed temperature T_{eq} is obtained from Eq. 10.16 pertaining to sensible heating and cooling. On the other hand, for $T_c > 365$ K (activated carbon–ethanol) and $T_c > 360$ K (zeolite–water) the condition $T_b < T_d$ gets satisfied and estimation of T_{eq} is obtained from Eq. 10.17 involving adsorption and desorption cooling along with sensible heating or cooling process.

Figure 10.5 shows the effect of varying minimum adsorption temperature on *COP* while all other parameters are kept constant i.e. $T_c = 370$ K (activated carbon–ethanol), $T_c = 450$ K (Zeolite–water), $T_{csat} = 300$ K, and $T_{esat} = 273$ K. It is evident from Fig. 10.5a and b that with the increase in minimum adsorption temperature *COP*, increases and is maximum at $T_a = T_{csat} = 300$ K. With further increase in temperature *COP* starts decreasing, this can be explained using Eqs. 10.6 and 10.8–10.10, when T_a approaches T_{csat}, $Q_{<T_{csat}}$ approaches zero and at the same time the value of $(x_b - x_c)$ also reduces which causes decrease in Q_{evap} (Eq. 10.9) and Q_{co} (Eq. 10.8) but the net effect is increase in SCE and COP values. For the case when T_a is greater than T_{csat}, $Q_{<T_{csat}} = 0$ and the net effect of increase in T_a will be decrease in *SCE* and *COP* values. It can be concluded that for maximum *COP* both T_a and T_{csat} should be kept same.

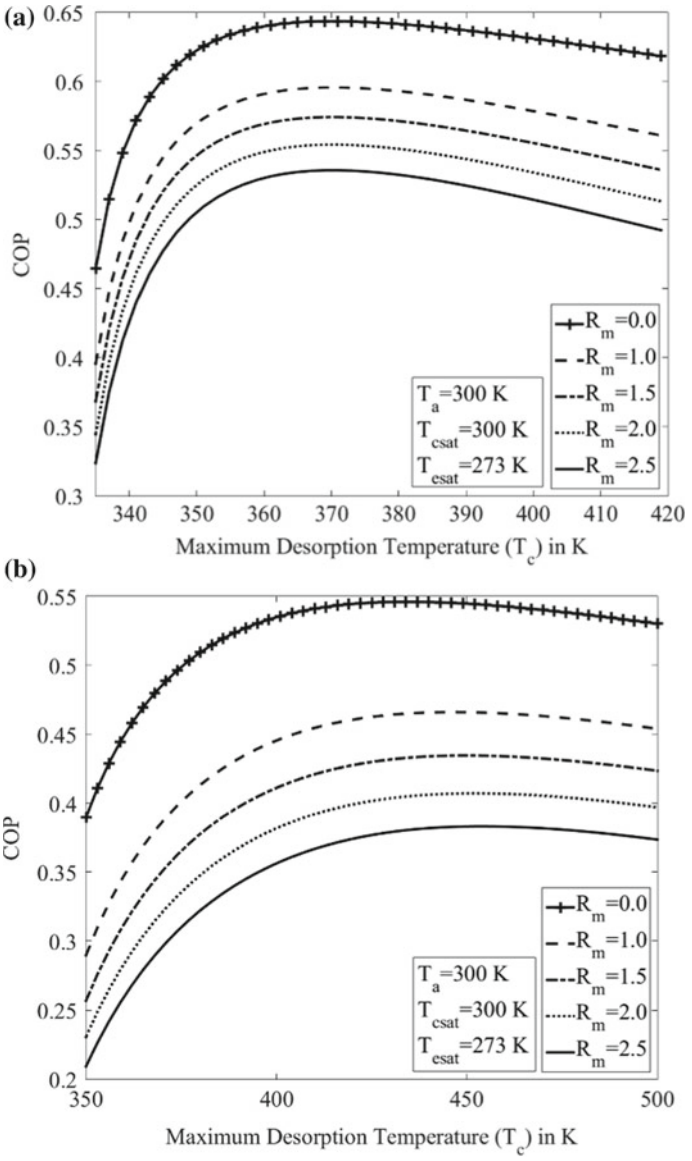

Fig. 10.3 Variation of COP of basic cycle with maximum desorption temperature (T_c) and R_m, **a** activated carbon–ethanol and **b** zeolite–water

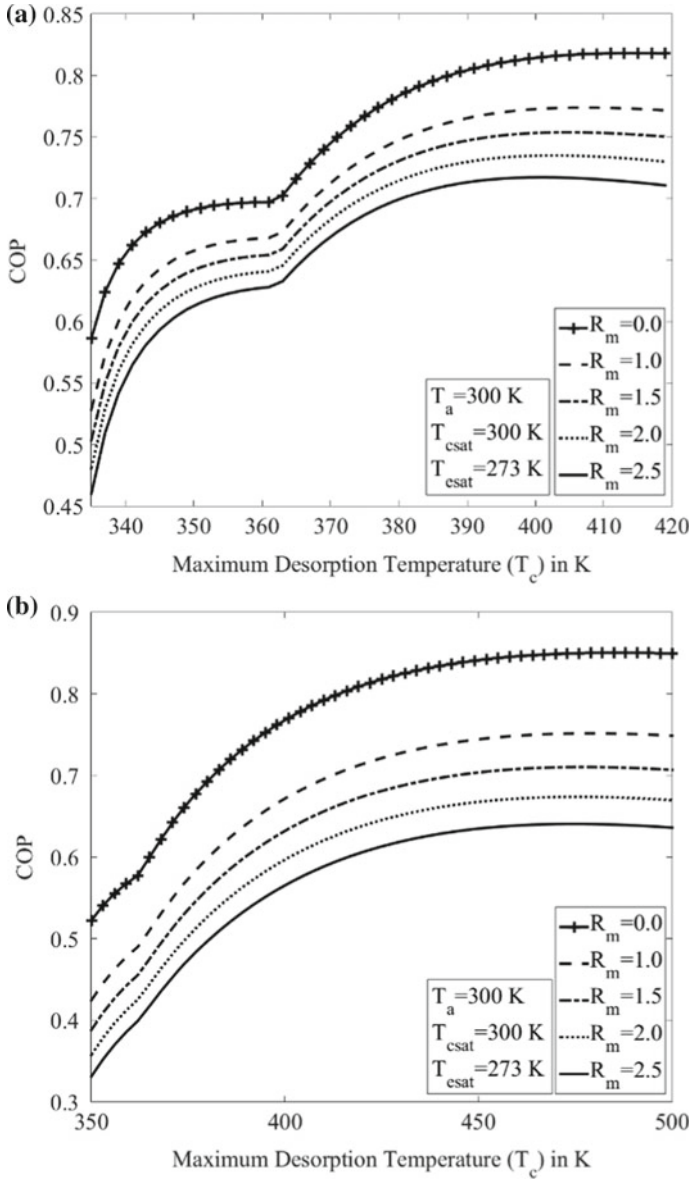

Fig. 10.4 Variation of COP of heat recovery cycle with maximum desorption temperature (T_c) and R_m, **a** activated carbon–ethanol and **b** zeolite–water

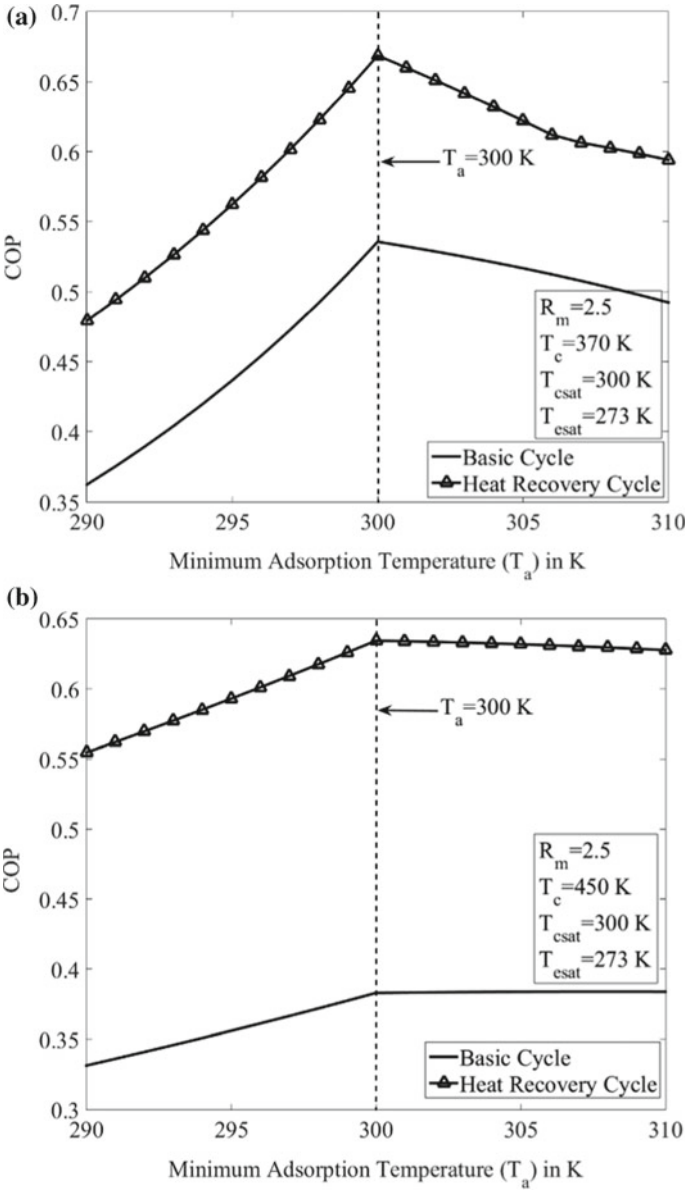

Fig. 10.5 Variation of COP with minimum adsorption temperature (T_a) **a** activated carbon–ethanol and **b** zeolite–water

Figure 10.6 shows the effect of varying condensing temperature (T_{csat}) on *COP*, keeping all other parameters constant i.e. $R_m = 2.5$, $T_c = 400\,\text{K}$ (activated carbon–ethanol), $T_c = 450\,\text{K}$ (Zeolite–water), $T_a = 300\,\text{K}$, and $T_{esat} = 273\,\text{K}$. Condensing temperature has an adverse effect on *COP*, with increase in T_{csat} value of *COP* decreases monotonically. It can be explained physically as well as using Eqs. 10.1 and 10.8–10.10. From Eq. 10.1 it is clear that higher the T_{csat} higher will be the x_c and hence lower the difference $x_b - x_c$, this will decreases the value of *SCE* and *COP*.

Figure 10.7 shows the effect of varying evaporating temperature (T_{esat}) on *COP*, keeping all other input parameters constant, i.e. $R_m = 2.5$, $T_c = 400\,\text{K}$ (activated carbon–ethanol), $T_c = 450\,\text{K}$ (Zeolite–water), $T_a = T_{csat} = 300\,\text{K}$. Evaporating temperature has positive impact on *COP*, means increase in T_{esat} increases the value of *COP*. It can be explained the same way as the effect of condensing temperature.

Figure 10.8 shows the variation of *SCE* with respect to maximum desorption temperature (T_c) at $R_m = 2.5$, $T_a = T_{csat} = 300\,\text{K}$, and $T_{esat} = 273\,\text{K}$. *SCE* increases with increase in maximum desorption temperature (T_c).

Figure 10.9 shows the effect of variation of maximum desorption temperature on second law efficiency for two cycles under consideration. From Figs. 10.3, 10.4, and 10.9, it is clear that maxima of *COP* and maxima of second law efficiency (η_{II}) are not in the same range. That is why there needs to be a trade off in choosing T_c in the best possible way such that neither *COP* nor η_{II} is sacrificed too much in the interest of improving the individual entities. In order to obtain a common scale for *COP* and η_{II} both the parameters are normalized within a range of zero to one by dividing *COP* and η_{II} with corresponding maximum values COP_{max} and η_{IImax} respectively. COP/COP_{max} and η_{II}/η_{IImax} are then plotted simultaneously for varying T_c values (Fig. 10.10). The intersection point of COP/COP_{max} versus T_c plot with η_{II}/η_{IImax} versus T_c plot provides the required optimized values of *COP*, η_{II}, and T_c.

From Figs. 10.3, 10.4, 10.5, 10.6, 10.7, 10.8 and 10.9, it is evident that activated carbon–ethanol working pair has higher values of *COP*, *SCE*, and η_{II} as compared to zeolite–water. From Fig. 10.2, we can observe that maxima for activated carbon ethanol occurs in the range 360–375 K, whereas for zeolite–water maxima occurs around 445–460 K. So zeolite–water working pair can be used at higher desorption temperatures while activated carbon–ethanol is suitable for lower desorption temperature. Typical *COP* values heat recovery cycle for both the working pairs for air conditioning applications ($T_{esat} = 283\,\text{K}$) at desorption temperature of 100 °C (373 K) and at condensing temperature of 27, 37, and 47 °C are given in Table 10.3.

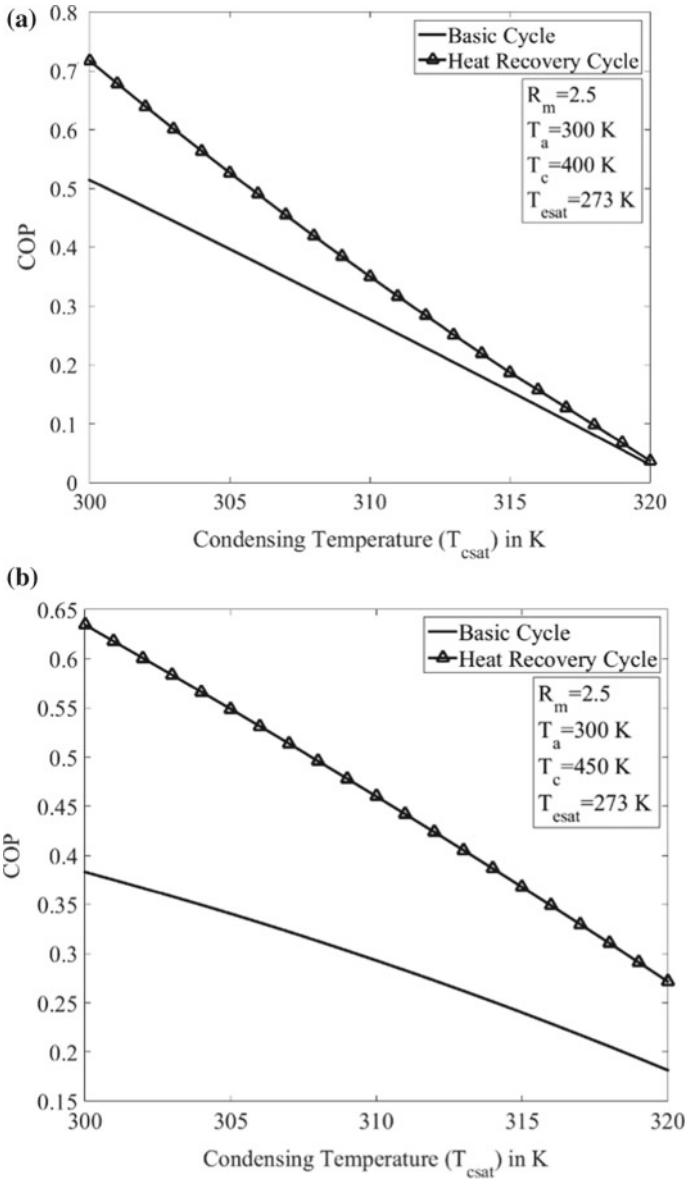

Fig. 10.6 Variation of COP with condensing temperature (T_{csat}) **a** activated carbon–ethanol and **b** zeolite–water

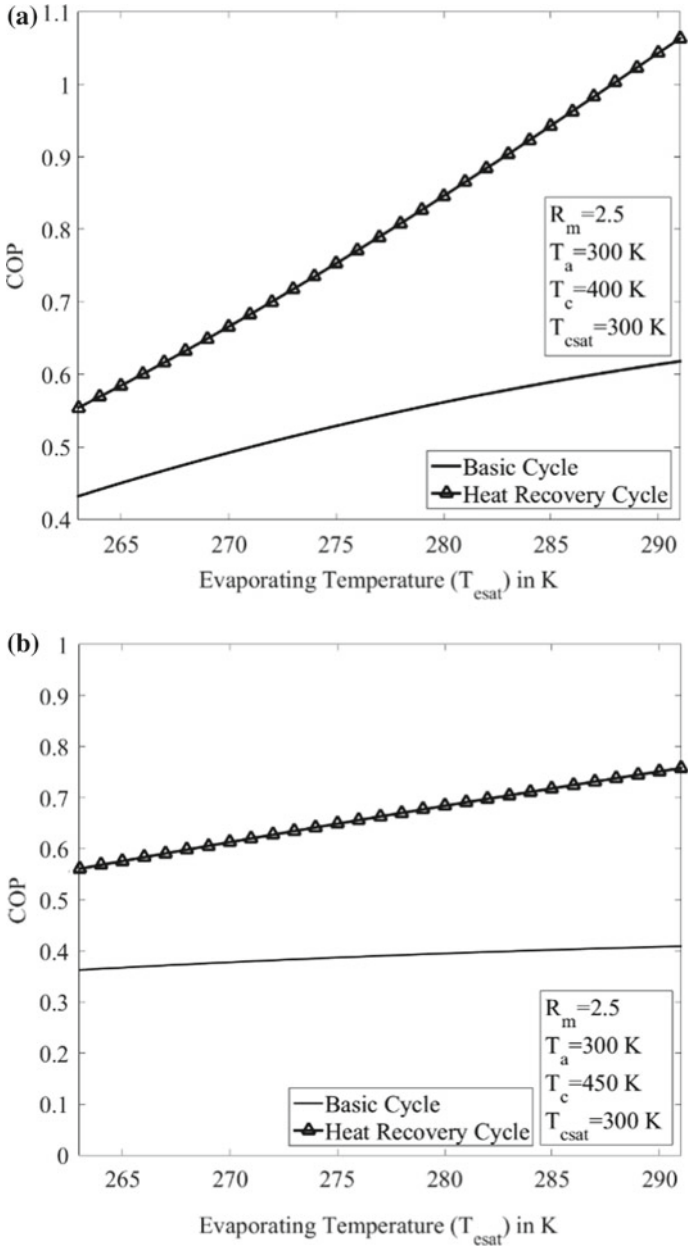

Fig. 10.7 Variation of COP with evaporating temperature (T_{esat}) **a** activated carbon–ethanol and **b** zeolite–water

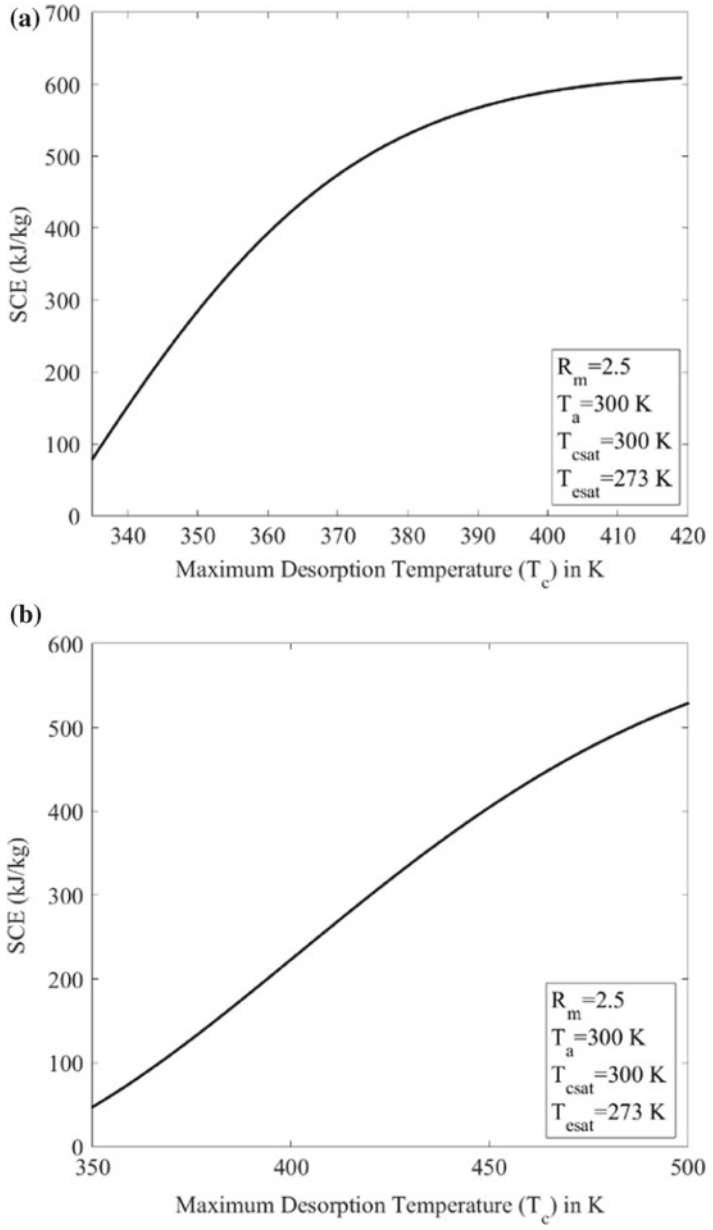

Fig. 10.8 Variation of SCE with maximum desorption temperature (Tc), **a** activated carbon–ethanol and **b** zeolite–water

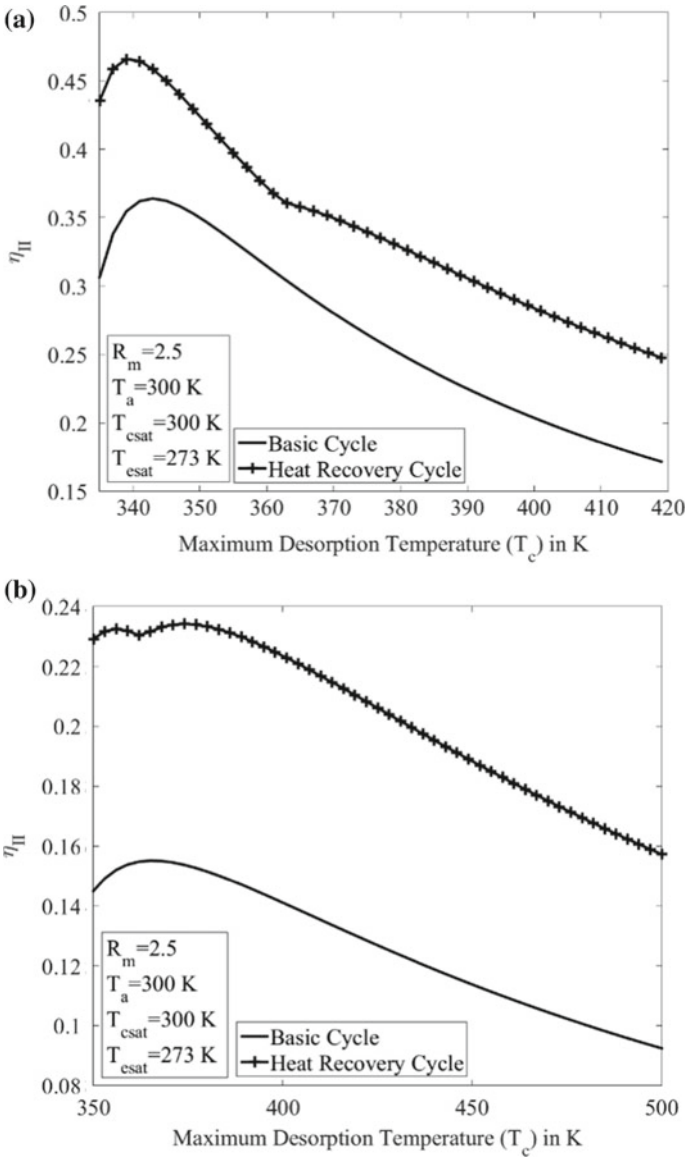

Fig. 10.9 Variation of second law efficiency η_{II} with T_c for two cycles **a** activated carbon–ethanol; **b** zeolite–water

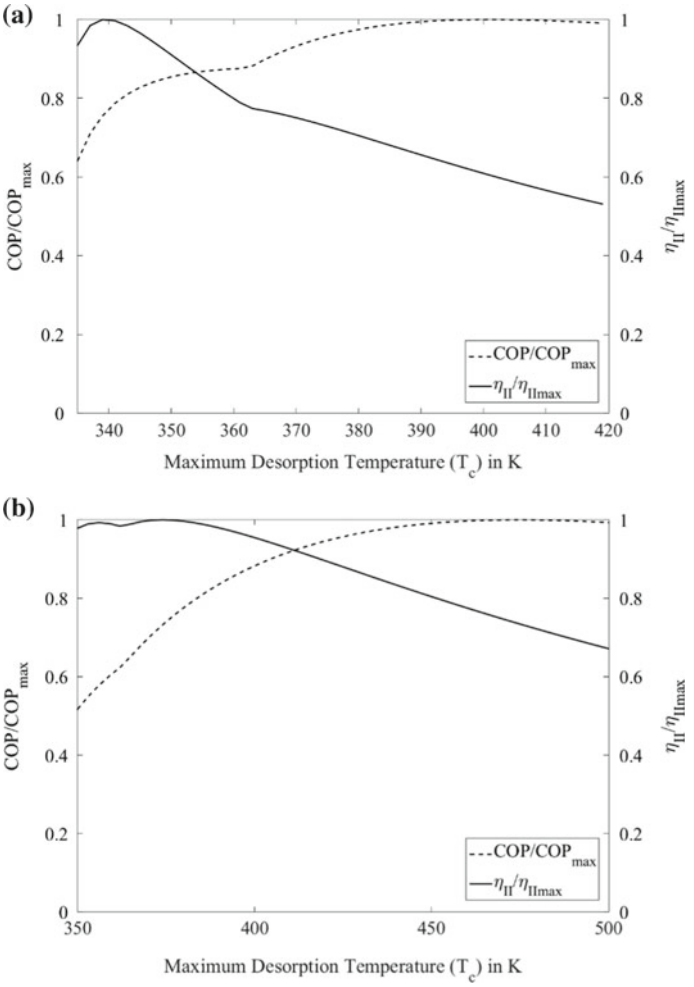

Fig. 10.10 Optimized COP, η_{II}, and T_c obtained from intersection point of COP/COP_{max} versus T_c and η_{II}/η_{IImax} versus T_c plots **a** activated carbon–ethanol; **b** zeolite–water

Table 10.3 COP values for air conditioning applications at different condensing temperatures

$T_{csat} = T_a$ (K)	$T_{esat} = 283$ K	
	Activated carbon–ethanol	Zeolite–water
300	0.9040	0.5712
310	0.6341	0.3938
320	0.4704	0.2147

10.9 Conclusion

Thermodynamics analysis of two cycles namely basic cycle and heat recovery cycle is presented for activated carbon–ethanol and zeolite–water. Coefficient of performance (*COP*), Specific cooling effect (*SCE*), and Second law efficiency (η_{II}) are studied with respect to five input i.e. maximum desorption temperature, minimum adsorption temperature, condensing temperature, evaporating temperature, and heat capacity ratio. Maximum desorption temperature plays significant role in finding the maxima of *COP* and Second law efficiency (η_{II}). But the maxima of both the parameters found to be at different range of temperature. A graphical method to find common temperature so that neither COP nor second law efficiency is sacrificed in maximizing the individual entities is discussed. Activated carbon–ethanol performs better at low desorption temperature while zeolite–water is suitable for high desorption temperature applications.

References

Aristov YI, Restuccia G, Cacciola G, Parmon VN (2002) A family of new working materials for solid sorption air conditioning systems. Appl Therm Eng 22(2):191–204

Cacciola G, Restuccia G (1995) Reversible adsorption heat pump: a thermodynamic model. Int J Refrig 18(2):100–106

Choudhury B, Saha BB, Chatterjee PK, Sarkar JP (2013) An overview of developments in adsorption refrigeration systems towards a sustainable way of cooling. Appl Energy 104:554–567

Critoph RE (1994) Forced convection enhancement of adsorption cycles. Heat Recovery Syst CHP 14(4):343–350

Critoph RE, Turner HL (1988) Performance of ammonia–activated carbon and ammonia–zeolite heat pump adsorption cycles. In: Proceedings of the international conference on Pompes a Chaleur Chimiques de Hautes Performances, Perpignan, France, pp 202–11

Critoph RE, Vogel R (1986) Possible adsorption pairs for use in solar cooling. Int J Ambient Energy 7(4):183–190

Douss N, Meunier F (1989) Experimental study of cascading adsorption cycles. Chem Eng Sci 44(2):225–235

El-Sharkawy II, Saha BB, Koyama S, He J, Ng KC, Yap C (2008) Experimental investigation on activated carbon–ethanol pair for solar powered adsorption cooling applications. Int J Refrig 31(8):1407–1413

Gasser RPH, Ehrlich G (1987) An introduction to chemisorption and catalysis by metals. Phys Today 40:128

Grenier P, Guilleminot JJ, Meunier F, Pons M (1988) Solar powered solid adsorption cold store. J Sol Energy Eng 110(3):192–197

Hajji A, Worek WM, Lavan Z (1991) Dynamic analysis of a closed-cycle solar adsorption refrigerator using two adsorbent-adsorbate pairs. J Sol Energy Eng 113(2):73–79

Hansen J, Ruedy R, Sato M, Lo K (2010) Global surface temperature change. Rev Geophys 48(4)

Hulse GE (1929) Freight car refrigeration by an adsorption system employing silica gel. Refrig Eng 17(2):41–53

Jones JA, Golben PM (1985) Design, life testing, and future designs of cryogenic hydride refrigeration systems. Cryogenics 25(4):212–219

Lu ZS, Wang RZ, Wang LW, Chen CJ (2006) Performance analysis of an adsorption refrigerator using activated carbon in a compound adsorbent. Carbon 44(4):747–752
Luo L, Feidt M (1992) Thermodynamics of adsorption cycles: a theoretical study. Heat Transfer Eng 13(4):19–31
Mauran S, Prades P, L'haridon F (1993) Heat and mass transfer in consolidated reacting beds for thermochemical systems. Heat Recovery Syst CHP 13(4):315–319
Mei V, Chaturvedi SK, Lavan BZ (1979) A truck exhaust gas operated absorption refrigeration system. ASHRAE Trans 85:66–76
Meunier F (2001) Adsorptive cooling: a clean technology. Clean Prod Process 3(1):8–20
Ponec V, Knor Z, Černý S, Smith D, Adams NG (1974) Adsorption on solids. Butterworths, London
Pons M, Guilleminot JJ (1986) Design of an experimental solar-powered, solid-adsorption ice maker. J Sol Energy Eng 108(4):332–337
Restuccia G, Recupero V, Cacciola G, Rothmeyer M (1988) Zeolite heat pump for domestic heating. Energy 13(4):333–342
Saha BB, El-Sharkawy II, Chakraborty A, Koyama S (2007) Study on an activated carbon fiber–ethanol adsorption chiller: Part I—system description and modelling. Int J Refrig 30(1):86–95
Saha BB, Habib K, El-Sharkawy II, Koyama S (2009) Adsorption characteristics and heat of adsorption measurements of R-134a on activated carbon. Int J Refrig 32(7):1563–1569
Saha BB, Jribi S, Koyama S, El-Sharkawy II (2011) Carbon dioxide adsorption isotherms on activated carbons. J Chem Eng Data 56(5):1974–1981
Sharafian A, Bahrami M (2015) Critical analysis of thermodynamic cycle modeling of adsorption cooling systems for light-duty vehicle air conditioning applications. Renew Sustain Energy Rev 48:857–869
Srivastava NC, Eames IW (1998) A review of adsorbents and adsorbates in solid–vapour adsorption heat pump systems. Appl Therm Eng 18(9):707–714
Sumathy K, Zhongfu L (1999) Experiments with solar-powered adsorption ice-maker. Renew Energy 16(1):704–707
Suzuki M (1993) Application of adsorption cooling systems to automobiles. Heat Recovery Syst CHP 13(4):335–340
Tamainot-Telto Z, Critoph RE (1997) Adsorption refrigerator using monolithic carbon–ammonia pair. Int J Refrig 20(2):146–155
Turner L (1992) Improvement of activated charcoal-ammonia adsorption heat pumping/refrigeration cycles: investigation of porosity and heat/mass transfer chacteristics
Uddin K, El-Sharkawy II, Miyazaki T, Saha BB, Koyama S (2014) Thermodynamic analysis of adsorption refrigeration cycles using parent and surface treated Maxsorb III/ethanol pairs
Wang RZ (2001a) Adsorption refrigeration research in Shanghai Jiao Tong University. Renew Sustain Energy Rev 5(1):1–37
Wang RZ (2001b) Performance improvement of adsorption cooling by heat and mass recovery operation. Int J Refrig 24(7):602–611
Wang LW (2005) Performances, mechanisms and application of a new type compound adsorbent for efficient heat pipe type refrigeration driven by waste heat. Doctor Dissertation, Shanghai Jiao Tong University, Shanghai, China
Wang RZ, Li M, Xu YX, Wu JY (2000) An energy efficient hybrid system of solar powered water heater and adsorption ice maker. Sol Energy 68(2):189–195
Wang LW, Wang RZ, Wu JY, Wang K (2004) Compound adsorbent for adsorption ice maker on fishing boats. Int J Refrig 27(4):401–408
Wang R, Wang L, Wu J (2014) Adsorption refrigeration technology: theory and application. Wiley
Zhu R, Han B, Lin M, Yu Y (1992) Experimental investigation on an adsorption system for producing chilled water. Int J Refrig 15(1):31–34

Part IV
Energy Storage

Chapter 11
PCM-Metal Foam Composite Systems for Solar Energy Storage

Anirban Bhattacharya

Abstract Efficient storage of solar thermal energy has been a key research area in recent years. Among the various methods for energy storage, phase change material (PCM) based latent heat systems have shown a lot of promise due to their high energy storage densities and smaller system sizes. However, the low thermal conductivities of PCM pose a significant challenge in designing such systems, therefore, augmentation with suitable thermal conductivity enhancers becomes necessary to improve their energy charging and discharging performances. The use of metal foam structures embedded in PCM to form composite PCM-metal foam energy storage system can improve the effective thermal conductivity remarkably due to the high surface area for heat transfer between the metal foam and the PCM. This chapter presents a study of PCM-metal foam composite systems for solar energy storage. At first, a brief overview of the relevant thermal enhancement methods with particular emphasis on metal foam systems is presented. This is followed by the description of a typical PCM-metal foam composite system and the important parameters governing its energy storage performance. Different modelling approaches for such systems and their advantages and disadvantages are presented. The effect of important factors for metal foam-PCM composite systems are analyzed by performing pore-scale simulations. It is shown that factors such as metal foam porosity, pore size distribution, foam material, phase change material and overall system size contribute significantly towards the melting pattern and energy storage characteristics of these systems.

Keywords Solar energy storage · Phase change material · Metal foam · Thermal enhancement

11.1 Introduction

Solar energy is one of the most promising sources of renewable energy. It is universally available, can be harnessed safely and relatively easily, and is unlimited in nature. Solar energy can be harnessed at various scales starting from small roof-top

A. Bhattacharya (✉)
School of Mechanical Sciences, IIT Bhubaneswar, Bhubaneswar, Odisha 752050, India
e-mail: anirban@iitbbs.ac.in

H. Tyagi et al. (eds.), *Solar Energy*, Energy, Environment, and Sustainability, https://doi.org/10.1007/978-981-15-0675-8_11

units to large scale solar power plants. One of the major drawbacks of solar energy is its intermittent nature. Not only the solar energy is unavailable at night, during daytime also the availability of solar insolation varies significantly depending on local weather pattern and cloud formation. This necessitates the use of suitable energy storage devices which can distribute the available energy evenly over the required time period.

11.1.1 Types of Energy Storage

In the recent past, several forms of energy storage devices have been proposed. Energy storage devices can use different mechanisms for energy storage and can store the energy in different forms such as chemical energy, mechanical energy, thermal energy and electrical energy. The suitability of the type of energy storage device depends on the mechanism of solar energy collection. For example, thermal energy storage devices may be better suited for solar thermal power plants while chemical energy based batteries or electrical storage units may be more suitable for direct electricity generation through the use of photovoltaic (PV) cells. Other important factors such as safety, ease of installation and operation and maintenance costs also need to be accounted for. Out of all the different modes of energy storage proposed, thermal energy storage systems show a lot of potential and have been studied widely.

11.1.2 Thermal Energy Storage Systems

Thermal energy storage systems are systems which store energy in the form of heat. Depending on the form of energy storage, thermal energy storage systems can be classified into sensible heat based systems and latent heat based systems. Sensible heat based systems, such as molten salt thermocline systems, store the entire energy by temperature increase of the storage medium. Various designs have been studied such as single medium storage where the heat transfer fluid itself acts as the storage medium. On the other hand dual media systems have a filler material in addition to the charging and discharging fluid which is cost effective for large systems. Latent heat based systems store energy in terms of latent heat transfer during phase change process. It consists of a suitable material which melts and solidifies at the required temperature and stores energy during melting and releases it during solidification.

Compared to other forms of energy storage, latent heat energy storage (LHES) systems have high storage densities which leads to smaller overall system sizes. Also, as the phase change process occurs at a constant temperature or over a narrow band of temperature, LHES systems can be designed to operate at specific required temperatures. Various materials have been used for LHES systems ranging from organic compounds such as fatty acids and esters to inorganic salts, collectively called as phase change materials (PCM). A classification of different types of PCM

is present in Pielichowska and Pielichowski (2014), Zalba et al. (2003) and Nazir et al. (2019). The main factor for the selection of storage medium is the operating temperature of the system. PCM based energy storage systems have been discussed in details in Sharma et al. (2009), Kenisarin and Mahkamov (2007), Farid et al. (2004), Agyenim et al. (2010) and Xu et al. (2015).

11.1.3 Thermal Enhancement of Latent Heat Energy Storage Systems

Among all the energy storage media, PCMs, in particular organic PCMs, have been studied and used most widely. PCMs have high latent heat of fusion and thus can store large quantities of energy in a limited size. However, PCMs typically have low thermal conductivities. As a result, the full storage potential of a system cannot be used if the operating time cycle is of short duration as the entire PCM cannot be melted in that time. Various mechanisms for increasing the heat transfer in the PCM has been proposed such as the use of high thermal conductivity fins, use of flow channels, use of filler materials, nanoparticles, encapsulated PCM distributed in the heat transfer fluid and porous metal matrix structures such as metal foam. Extensive discussion about various thermal enhancement mechanisms have been presented in Fan and Khodadadi (2011), Liu et al. (2016), Ibrahim et al. (2017), Qureshi et al. (2018) and Lin et al. (2018).

11.2 PCM-Metal Foam Hybrid System

11.2.1 Concept

The main concept of thermal enhancement of PCM based LHES systems involves the use of a high thermal conductivity secondary material whose main function is to distribute the heat quickly to different parts of the energy storage unit. Increasing the amount of this material increases the overall heat transfer rate of the system but at the cost of reduced energy storage due to the reduced amount of PCM present in the system. Another important parameter for designing these systems is the area of contact between the PCM and the high thermal conductivity material. Based on these criteria, metal foam structures are among the best mechanisms for thermal conductivity enhancement of PCM based energy storage systems.

Metal foams are metallic structures with high porosity. As a result, they have low weight but very high surface area. Metal foam structures with different geometries can be produced such as structures with regular geometries consisting of arranged array of cells or irregular geometries with randomly distributed pores. At lower porosity, the foam structure may consist of large number of pores embedded within a metallic

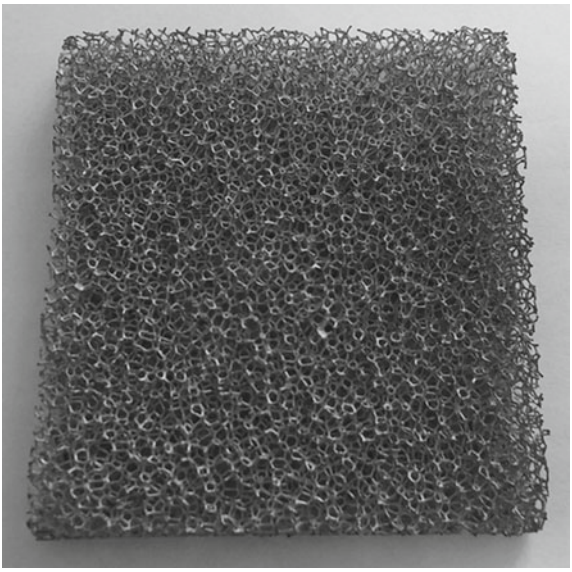

Fig. 11.1 Typical metal foam structure with irregular geometry

base while at very high porosity the foam structure resembles an intricate network of metallic wires. Metal foam structures also depend on the manufacturing method. Metal foams are typically produced by foaming agents generating gas bubbles during solidification of metal from a melt pool or by passing a foaming gas during solidification. This results in an irregular geometry with pores of various sizes interlinked with each other. Foam with regular geometry can be created through direct molding or additive manufacturing techniques. Figure 11.1 shows the structure of a typical metal foam with irregular geometry.

These metallic foam structures may be filled with PCM to develop metal foam-PCM composite structures for thermal energy storage. Due to the large contact area, significant amount of heat transfer can occur between the metal foam and PCM. Also due to the low volume fraction of metals in metal foams, the quantity of PCM can be relatively high resulting in higher energy storage capacity as compared to other thermal enhancement mechanisms such as use of fins. The intricate network of metallic structure can transfer heat to all parts of the PCM such that there are no large areas of continuous PCM, unlike metal fin systems.

11.2.2 Design and Construction

Composite metal foam-PCM systems typically have a cylindrical or rectangular cuboid geometry. The external container contains the metal foam whose pores are filled with PCM. Air gaps need to be removed to preserve high effective thermal conductivity of the system. The entire structure is insulated to prevent heat loss.

Energy is transferred to the system by heating it from one side. This may be directly heated by incoming solar radiation or more typically heated by the heat transfer fluid circulated from the collector. Multiple metal foam-PCM composite systems are needed to limit the size of each storage unit.

11.2.3 Materials

Various materials have been proposed and tested for the metal foam structure as well as for the PCM. Aluminum and copper are the most widely tested material for metal foam as they offer excellent thermal conductivity (Hong and Herling 2006; Siahpush et al. 2008; Wang et al. 2016; Mancin et al. 2015; Xiao et al. 2013). Graphite foams, although not technically metal, have also been tested (Ji et al. 2014; Lafdi et al. 2008; Zhang et al. 2012; Zhao et al. 2014). For the PCM, the choice of material depends on the temperature range of application as well as its suitability for use with a metallic foam. The PCM must not react with the metal foam structure or corrode the surface of the foam. Typical materials which can be used are different types of organic compounds such as paraffin.

11.3 Important Design Parameters for a PCM-Metal Foam System

The performance of a composite metal-foam PCM system depends on various factors. The important factors are: thermo-physical properties of the foam material and PCM, the foam structure, foam porosity and overall storage unit size and aspect ratio. Each of these is discussed in the following sub-sections.

11.3.1 Thermo-physical Properties of Foam Material

The properties of the foam material play a vital role in the performance of the storage system. The foam material should have very high thermal conductivity and high specific heat for better heat transfer and sensible energy storage characteristics. Low density of the material is desirable for reducing the overall weight of the system. However, low density also leads to lower sensible heat storage and thus reduces the energy storage capacity of the system. Low thermal coefficient of expansion is necessary so that the foam structure does not change much during the charging or discharging process. Relatively good mechanical properties such as strength are

also desirable to maintain the integrity of the system. The foam material and PCM combination should also have high wettability to prevent formation of air pockets due to shrinkage of PCM during solidification.

11.3.2 Thermo-physical Properties of PCM

The most important property of PCM is high latent heat of fusion as this is the critical factor which governs the total energy storage capacity of the system. PCM should also have relatively high thermal conductivity for better heat transfer to the interior regions and high specific heat for better sensible heat storage. As mentioned before, PCM should also have high wettability with the metal foam structure. Another important property is the change in density during solidification and melting. Typically, PCMs undergo shrinkage due to volume contraction during solidification. Ideally, shrinkage should be as minimum as possible. Shrinkage can be very detrimental to the performance of energy storage system as it can lead to the formation of air pockets between the metal foam and PCM thus drastically reducing the effective thermal conductivity of the system. Other important properties of PCM are chemical inertness and stability. Initial filling up of the metal foam with PCM also requires the PCM to have lower viscosity.

11.3.3 Foam Porosity

The overall porosity of the metal foam has to be carefully chosen based on detailed analysis. Lower porosity results in higher heat transfer rates leading to faster charging and discharging of energy. On the other hand, higher porosity, leads to larger volume fraction of PCM leading to higher overall energy storage capacity. The sensible heat capacity of the metal foam and PCM needs to be considered to calculate the required porosity of the system.

11.3.4 Foam Structure

The structure of the metal foam plays an important role in the performance of a metal foam-PCM energy storage system. It has been shown that foams with lower pore size and higher pore density have higher heat transfer rates due to the more intricate network of metal structure (Lafdi et al. 2007; Ren et al. 2017; Dinesh and Bhattacharya 2019). Also, open cell foams with high porosity enables significant convective heat transfer which contributes towards the overall heat transfer rate. On the other hand, closed foams or nearly closed foam structures have conduction as the dominant heat transfer mechanism. Foams with regular structure and irregular structure may also have different heat transfer characteristics.

11.3.5 Overall Size and Aspect Ratio

The overall dimensions of the storage unit has to be designed such that the energy charging and discharging can be completed during the required time period. However, if the storage unit is too small, a large number of units will be necessary thus increasing the overall cost. Aspect ratio also is an important parameter as it defines the farthest distance of PCM from the heat transfer surface. A broad and shallow design where the wall opposite to the heat transfer surface is relatively near is better as energy can be transported to the entire PCM in less time.

11.4 Previous Studies on PCM-Metal Foam Hybrid Systems

11.4.1 Experimental Studies

A number of experimental investigations have been performed to study the effect of aluminum, copper and nickel foam on the heat transfer characteristics of PCM based storage systems (Siahpush et al. 2008; Xiao et al. 2013, 2014; Zhao et al. 2010; Chen et al. 2014; Zhu et al. 2018; Zheng et al. 2018). The main findings from the experimental studies can be summarized as follows.

- Comparison of pure PCM systems and metal foam-PCM systems show that use of metal foam drastically improves the heat transfer characteristics of the system and the effective thermal conductivity of the composite structure is many times higher than that of the PCM.
- Metal foam structure plays an important role in determining the system characteristics. Lower porosity leads due to higher heat conduction whereas higher porosity leads to higher convection and energy storage capacity.
- Foam material has a strong influence on the heat transfer.

11.4.2 Numerical Modelling

Numerical modelling of metal foam-PCM composite systems mainly follows two approaches: (a) Volume averaged modelling and (b) Pore-scale modelling.

Volume averaged models. Volume averaged models (Mesalhy et al. 2005; Tian and Zhao 2011; Srivatsa et al. 2014; Zhang et al. 2017; Yang et al. 2018; Sundarram and Li 2014; Kumar and Saha 2018) assume that the entire composite structure is a porous medium and formulates the governing equations for energy balance for this porous medium. Two different approaches are taken. Basic models assume that

the metal foam and PCM are in local thermal equilibrium and thus a single nodal temperature variable can specify the temperature evolution of the system. All the properties at the discretized nodes are calculated based on volume averaging the foam and PCM properties. For these models, a single energy balance equation in terms of the average temperature is sufficient to simulate the system. The volume averaged energy equation for this case can be written as

$$\rho_{av}\frac{\partial(C_{pav}T+\varepsilon f_l L)}{\partial t}+\varepsilon\rho_{PCM}\nabla.(\vec{U}C_{pPCM}T)=\nabla.(k_{eff}\nabla T) \tag{11.1}$$

In Eq. 11.1, T is the temperature, ρ is the density, C_p is the specific heat, $\vec{U}$ is the velocity of liquid PCM, f_l is the liquid fraction of PCM, L is the latent heat of fusion of PCM, and subscripts '*av*' and '*PCM*' denote the average values and values for PCM, respectively. k_{eff} is the effective thermal conductivity which can be formulated in terms of the metal foam porosity ε. The main drawback of the single equation approach is that it does not capture the local thermal non-equilibrium between the metal and PCM and thus cannot calculate the heat transfer between the metal foam and PCM.

The other approach for volume averaged models considers separate energy balance equations for the metal foam and for the PCM (Yang et al. 2018; Kumar and Saha 2018). The energy equation for metal foam can be written as follows.

$$(1-\varepsilon)\rho_m\frac{\partial(C_{pm}T_m)}{\partial t}=\nabla.(k_{m,eff}\nabla T_m)-h_{int}a_{int}(T_m-T_{PCM}) \tag{11.2}$$

The energy equation for the PCM can be written as follows.

$$\begin{aligned}\varepsilon\rho_{PCM}\frac{\partial(C_{pPCM}T_{PCM}+f_l L)}{\partial t}+\varepsilon\rho_{PCM}\nabla.(\vec{U}C_{pPCM}T_{PCM})\\ =\nabla.(k_{PCM,eff}\nabla T_{PCM})-h_{int}a_{int}(T_{PCM}-T_m)\end{aligned} \tag{11.3}$$

In Eqs. 11.2 and 11.3, T_m and T_{PCM} denote the temperature of the metal foam and PCM, respectively. Subscripts '*m*' and '*PCM*' denote the properties of metal and PCM. The last terms in each equation represent the interface heat transfer between the metal foam and PCM. h_{int} is the interface heat transfer coefficient and a_{int} is the specific area of the interface. For equilibrium models, it is assumed that the temperature of PCM and metal at the PCM-metal foam interface is equal, i.e. $T_m = T_{PCM}$. On the other hand, non-equilibrium models assume that the temperature of PCM and metal are different at the interface. For this case, the two energy equations are coupled by using the interface heat transfer term, $h_{int}a_{int}(T_m - T_{PCM})$, as given in Eqs. 11.2 and 11.3. Although these models can capture the local temperature differences between the metal and PCM, defining the interface heat transfer coefficient (h_{int}) between the metal and PCM is challenging. Different models have been proposed for metal

foam-PCM systems using the two equation non-equilibrium approach with different interface heat transfer coefficients (Mesalhy et al. 2005; Srivatsa et al. 2014; Yang et al. 2018).

Volume averaged models can predict the overall heat transfer characteristics and melting pattern. However, they cannot capture the localized heat transfer between the metal foam and PCM accurately. This is particularly problematic for systems which have similar porosities but different foam structures as the governing equations for the volume averaged models are functions of porosities. These models also may not capture the convection pattern accurately as convection in metal foams is dependent on the foam structure itself.

Pore-scale models. The primary distinguishing feature of pore-scale models (Ren et al. 2017, 2018; Dinesh and Bhattacharya 2019; Abishek et al. 2018; Deng et al. 2017) is that they resolve the metal foam structure in the model. Metal foam geometry is modelled by using various geometry creation techniques (Dinesh and Bhattacharya 2019; Boomsma et al. 2003; Wang and Pan 2008; Abishek et al. 2017). It is assumed that the porous region in the metal foam is filled with PCM. These models can capture the heat transfer between the metal foam and PCM accurately as the effect of foam structure is present in the model. Simulations based on these models have shown that the pore structure plays an important role in determining the energy transfer characteristics of the system (Ren et al. 2017; Dinesh and Bhattacharya 2019). The main drawback of pore-scale models is the increased computational effort required as very fine numerical grid is necessary to capture the foam structure. A typical pore-scale model (Dinesh and Bhattacharya 2019) has been discussed in details in Sect. 11.5.1.

11.5 Case-Studies

11.5.1 Numerical Model and Problem Description

In this section, the effects of important design parameters described in Sect. 11.3 are studied by performing pore-scale simulations of melting for a metal foam-PCM composite energy storage system. Five different comparative studies are performed to see the effect of different foam material, different PCM, change in porosity, change in pore size and overall system size. For performing the simulations, the model described in (Dinesh and Bhattacharya 2019) is used. The main characteristics of the model are described briefly in the subsequent paragraphs. For more details, one can refer to Dinesh and Bhattacharya (2019).

Problem description. For the comparative studies, a cuboidal domain with heating from the bottom is considered. It is assumed that all the other sides are insulated. The domain is initially held at a certain temperature below the melting temperature

of the PCM. Heat transfer occurs due to heating from the bottom boundary and at first sensible energy absorption occurs. Subsequently, the PCM starts melting and energy is absorbed as latent heat.

Geometry creation model. For simulating the stated problem a coupled method is used (Dinesh and Bhattacharya 2019). The method combines a geometry creation model with a melting and solidification solver. The geometry creation model assumes that the 3-dimensional cuboidal domain is filled with overlapping pores of different sizes. The entire geometry creation process is performed using the following algorithm.

- At first, the cuboidal domain is created based on the length of its three sides.
- Pores are represented by spheres. Each sphere is defined by its radius (r) and co-ordinates of its center (x_c, y_c, z_c). The minimum and maximum sphere radius (r_{min}, r_{max}) are input parameters specified by the user. To insert a sphere in the domain, a random location within the domain is selected as the center coordinates for the sphere. The radius of the sphere is randomly selected using a random number generator subjected to the upper and lower bounds of r_{max} and r_{min}, i.e. $r_{min} \leq r \leq r_{max}$. After the coordinates of its center (x_c, y_c, z_c) and radius (r) are fixed, a sphere can be considered to be generated in the domain.
- To insert the subsequent sphere, another parameter, the sphere overlap, needs to be defined. The sphere overlap parameter denotes whether two spheres intersect each other or not. The distance between the centers of the two spheres can be calculated using $d = \sqrt{(x_n - x_c)^2 + (y_n - y_c)^2 + (z_n - z_c)^2}$ where x_n, y_n, z_n are the coordinates of the center of the new sphere. Sphere overlap is defined as $q = d/(r + r_{new})$ where r_{new} is the radius of the new sphere. If q is less than 1, it means that the two spheres intersect each other. This type of interaction between the spheres will lead to open cell type foam structure. If q is greater than 1, it means that the two spheres do not intersect each other leading to closed cell foam structure. At the limiting value of 1, the two spheres touch each other at a single point. For the geometry creation model, the minimum and maximum values of pore overlap are specified by the user.
- To insert a second sphere, the sphere radius is randomly assigned using the criteria $r_{min} \leq r_{new} \leq r_{max}$ and a random location is selected as the coordinates for the center of the second sphere with random overlap subjected to the minimum and maximum overlap bounds specified previously.
- Subsequently, spheres are generated one by one in a sequential manner following the same procedure. For each sphere, its overlap with all the existing spheres has to be checked. However, to make the algorithm computationally efficient, only the spheres within a certain distance from the center of the new spheres are considered for this overlap calculation.
- After generation of each sphere, the total volume occupied by the spheres is calculated and the resultant porosity is checked. If the resultant porosity reaches or exceeds the specified foam porosity, the generation of spheres is stopped.

- After the spheres are generated, the generated geometry needs to be mapped to a metal volume fraction parameter, (φ), to differentiate the metal and PCM in the discretized problem domain. To do this, the entire domain is divided into a very fine uniform grid structure. The grid points which are within any of the spheres are assigned a value of 0 and the grid points outside all the spheres are assigned a value of 1. Subsequently, a new relatively coarse mesh is generated. Each grid point in the new mesh correspond to several grid points in the original mesh. The value of metal volume fraction (φ) is calculated for each grid point of the new mesh by summing all the values of 1 and 0 for the corresponding grid points in the original mesh and dividing by the number of original grid points corresponding to a single grid point in the new mesh.
- The value of φ for all the grid points in the new mesh denote the metal fraction for the entire geometry. This new mesh is used for all the subsequent calculations and the old mesh is discarded. The volume fraction of PCM at each node is equal to $(1 - \varphi)$.

Figure 11.2a shows a typical metal foam surface generated using this method. Figure 11.2b shows the corresponding metal foam structure filled with PCM.

Phase change model. Melting and solidification of PCM is simulated by using the enthalpy method (Voller 2008; Bhattacharya and Dutta 2013). The process is governed by the energy conservation equation (Eq. 11.4) which is formulated in terms of volume averaged enthalpy as given in Eq. 11.5 (Dinesh and Bhattacharya 2019).

$$\rho \frac{\partial H}{\partial t} = \nabla.(K \nabla T) \tag{11.4}$$

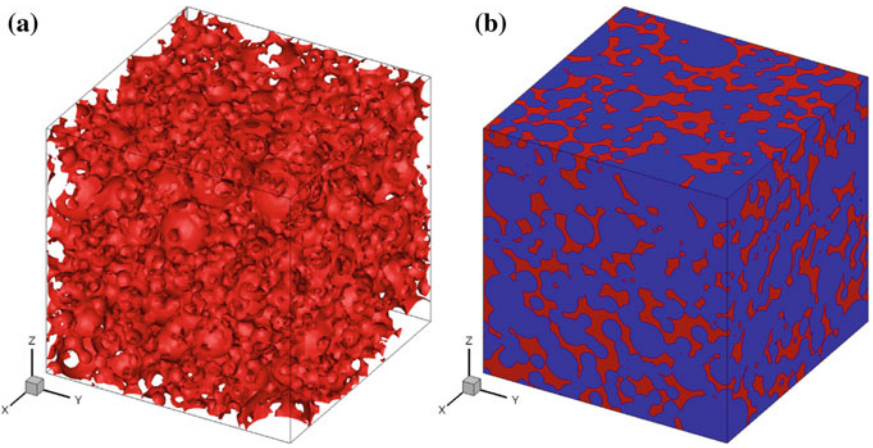

Fig. 11.2 Sample geometry generated by the model for 75% porosity. **a** Foam structure. **b** PCM-metal foam composite (red represents the metal foam and blue represents the PCM)

The volume average enthalpy is defined in terms of the sensible and latent heat as

$$H = [C_{p_{pcm}}(1-\varphi) + C_{p_m}\varphi]T + (1-\varphi)fL \tag{11.5}$$

The volume fraction of liquid PCM is tracked using the nodal melt fraction parameter f. In Eqs. 11.4 and 11.5, ρ is the average density, K is the average thermal conductivity and $C_{p_{pcm}}$ and C_{p_m} are the specific heat of PCM and metal, respectively. The detailed algorithm for solving the governing equation is described in Dinesh and Bhattacharya (2019). The model has been previously validated with experimental results given in Chen et al. (2014) and verified with 1D analytical solutions for melting and solidification (Dinesh and Bhattacharya 2019).

Standard case. In the present work, the model is applied to study the effect of the 5 different parameters described in Sect. 11.3. For all the 5 cases, a base system is considered with aluminum foam and paraffin as PCM and with the specifications given in Table 11.1. The thermo-physical properties of aluminum is specified in Table 11.2 while that for paraffin is presented in Table 11.3. A cuboidal domain is taken with a constant high temperature boundary condition of 373 K at the bottom surface. All the other sides are kept adiabatic. The entire domain is initially at 303 K. For each case, one of the parameter is changed while keeping all the other parameters constant and simulation results are compared to see its effect on temperature evolution and melting pattern. The total energy absorbed and the latent heat stored are also compared.

Table 11.1 Specifications for the base case

Parameter	Specification
Foam material	Aluminum
PCM	Paraffin
Foam porosity (%)	75
Minimum pore radius (cm)	0.5
Maximum pore radius (cm)	3
Domain side length (cm)	20
Initial temperature (K)	303
Hot boundary temperature (K)	373
Grid spacing for geometry model (mm)	0.625
Grid spacing for phase change model (mm)	2.5
Time step (s)	0.01

Table 11.2 Thermo-physical properties of aluminum (Al) and copper (Cu)

Property	Aluminum	Copper
Thermal conductivity (W/m K)	205	401
Specific heat (J/kg K)	910	385
Density (kg/m^3)	2830	8960

Table 11.3 Thermo-physical properties of paraffin and naphthalene

Property	Paraffin	Naphthalene
Latent heat (kJ/kg)	169	147.7
Thermal conductivity (W/m K)	0.2	0.132
Specific heat (J/kg K)	2100	1563
Density (kg/m^3)	880	976
Melting temperature (K)	335	353

11.5.2 Effect of Foam Material

For this comparison, two different cases are considered—one with aluminum foam and the other with copper foam. The thermo-physical properties of copper is specified in Table 11.2. All the other parameters, such as porosity, pore size, PCM and domain size are kept same as that mentioned in Table 11.1. Figure 11.3 shows the temperature contours for the two systems at time $t = 500$ and 1000 s. It can be seen that for the copper foam system the temperature evolution is faster. This is because of the

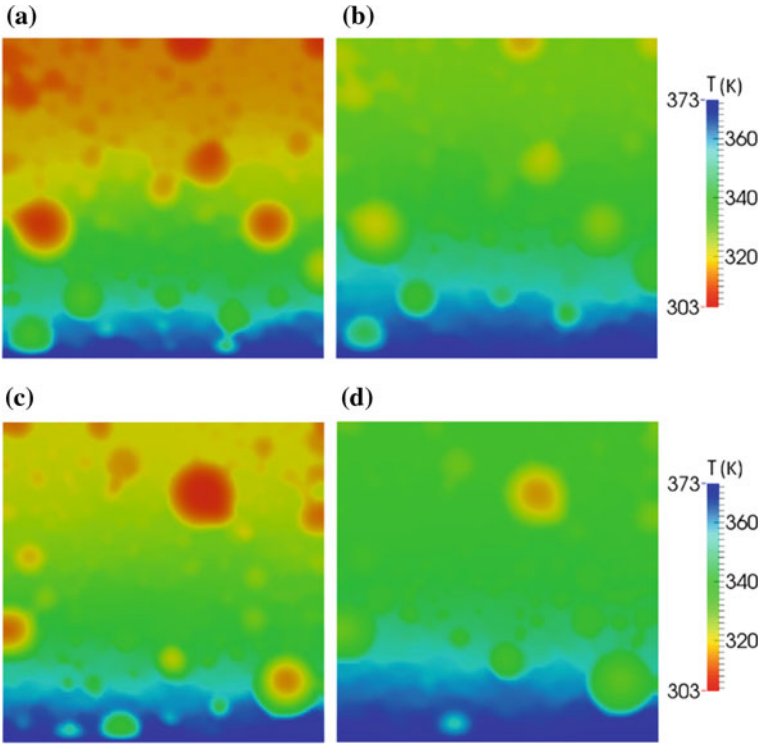

Fig. 11.3 Temperature contours at the mid-section. **a** Aluminum foam at $t = 500$ s. **b** Aluminum foam at $t = 1000$ s. **c** Copper foam at $t = 500$ s. **b** Copper foam at $t = 1000$ s

significantly higher thermal conductivity of copper. The density of copper is about 3 times as that of aluminum and thus the mass of copper is higher for the same overall porosity. However, copper has significantly lower specific heat as compared to aluminum. Thus the overall sensible heat absorption in copper is not markedly higher. The main difference in the system comes from the faster heat transfer to the PCM with use of copper foam which results in faster melting of PCM. This is evident from the liquid fraction contours for the two systems shown in Fig. 11.4.

The variation of total energy absorption and latent heat absorption with time is compared in Fig. 11.5a. It can be observed that use of Cu foam results in increase of approximately 20% in total heat absorption and approximately 23% in latent heat absorption for the given configuration. The variation of overall liquid fraction with time, as shown in Fig. 11.5b, confirms the higher melting rate of PCM with embedded Cu foam.

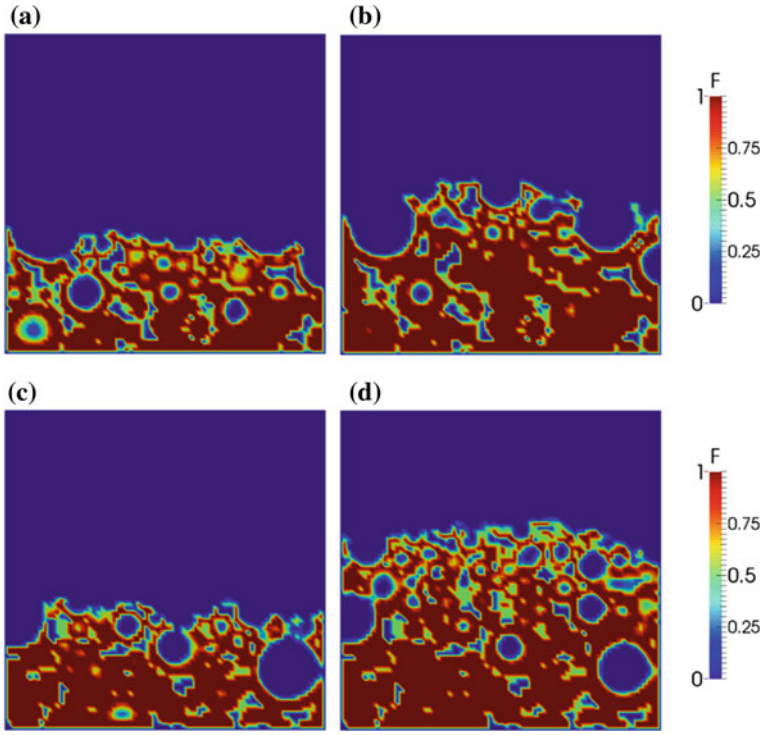

Fig. 11.4 Liquid fraction at the mid-section. **a** Aluminum foam at $t = 500$ s. **b** Aluminum foam at $t = 1000$ s. **c** Copper foam at $t = 500$ s. **d** Copper foam at $t = 1000$ s

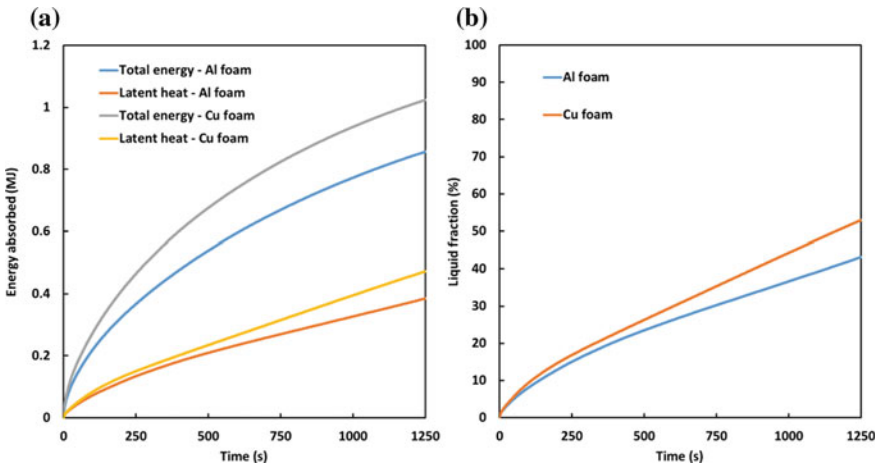

Fig. 11.5 Comparison of aluminum and copper foam. **a** Variation of energy absorption with time. **b** Variation of overall melt fraction with time

11.5.3 Effect of Phase Change Material

For this comparison, two different PCMs are considered—paraffin wax and naphthalene. All the other parameters are same as that stated in Table 11.1. The thermophysical properties of naphthalene is specified in Table 11.3. Figure 11.6 shows the temperature contours for the two systems at time $t = 500$ and 2000 s. It can be seen that the temperature is higher in the naphthalene based system. This is because of the higher melting temperature of naphthalene. Figure 11.7 shows the liquid fraction of PCM at time $t = 500$ and 2000 s. It can be seen that melting occurs at a faster rate for the paraffin based system. For this system, due to the lower melting temperature of paraffin, less sensible heating is required to reach the melting temperature and more energy can be stored as latent heat leading to higher melting rate.

The variation of total energy absorbed and the latent heat absorbed for the two systems with time are compared in Fig. 11.8a. It is seen that both the quantities are higher for the paraffin based system. However, the difference in latent heat absorption is significantly higher as compared to the total energy absorption. This suggest that the sensible heat absorption is higher for the naphthalene based system. For this case, most of the energy is absorbed as sensible heat during the initial period as the melting temperature of naphthalene is higher. Figure 11.8b shows a comparison of the variation of overall liquid fraction for the two systems with time. It confirms that the rate of melting is significantly higher for the paraffin based system. This study shows that the PCM should be selected depending on the energy absorption characteristics required and the necessary temperature range, as systems based on different PCM have significantly different heat absorption characteristics and melting pattern.

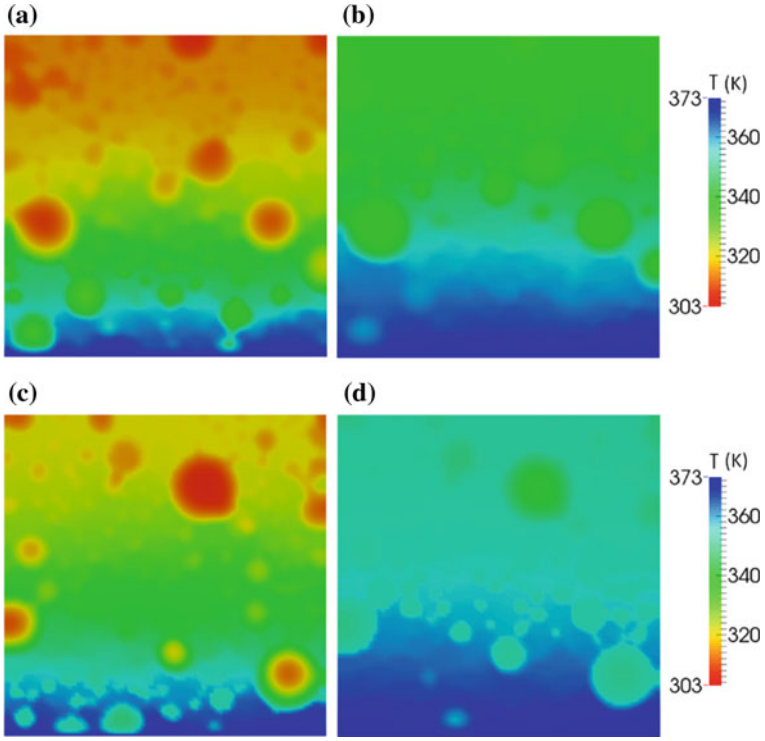

Fig. 11.6 Temperature contours at the mid-section. **a** With paraffin at $t = 500$ s. **b** With paraffin at $t = 2000$ s. **c** With naphthalene at $t = 500$ s. **d** With naphthalene at $t = 2000$ s

11.5.4 Effect of Porosity

To study the effect of porosity, two systems are considered—one with 75% porosity and the other with 50% porosity. Although the porosity is different, the pore size variation is kept at the same range. The geometries generated by the model for the two systems are presented in Fig. 11.9. It is observed that the 75% porosity system has considerably more number of pores. All the other parameters are kept same as that specified in Table 11.1. Figure 11.10 shows the temperature contours for the two systems at time $t = 500$ and 2000 s. It can be observed that the temperature is higher for the 50% porosity system. Also, there are localized low temperature regions which correspond to the interior sections for large pores filled with PCM. For the 75% porosity system, the temperature profile has a more uniform gradient from the bottom surface to the top surface. The corresponding liquid fraction contours are presented in Fig. 11.11. It is seen that, for the 50% porosity system, melting near the top surface starts faster. The 50% system has lower amount of PCM. As a result more energy can contribute towards sensible heating and the system reaches the melting

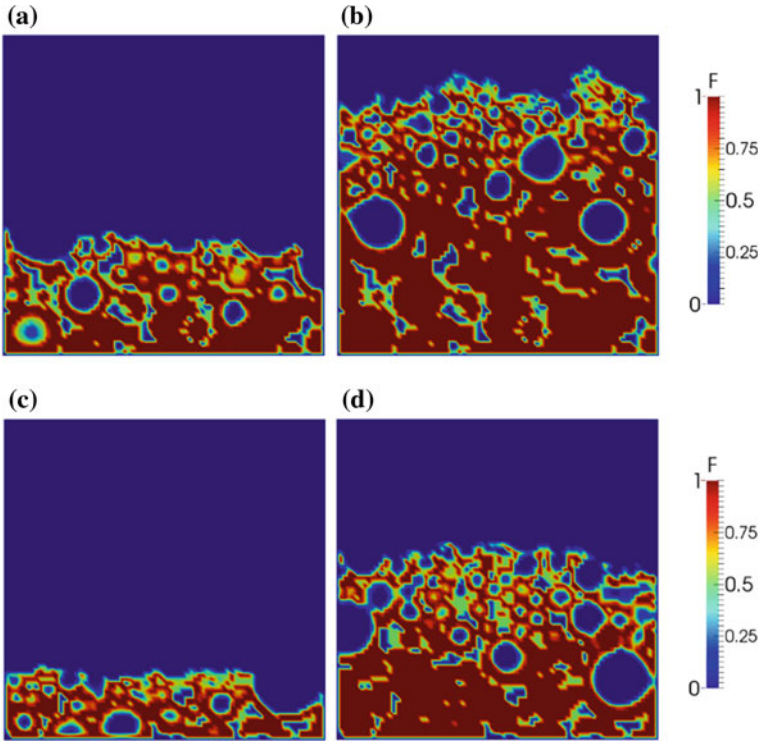

Fig. 11.7 Liquid fraction at the mid-section. **a** With paraffin at $t = 500$ s. **b** With paraffin at $t = 2000$ s. **c** With naphthalene at $t = 500$ s. **d** With naphthalene at $t = 2000$ s

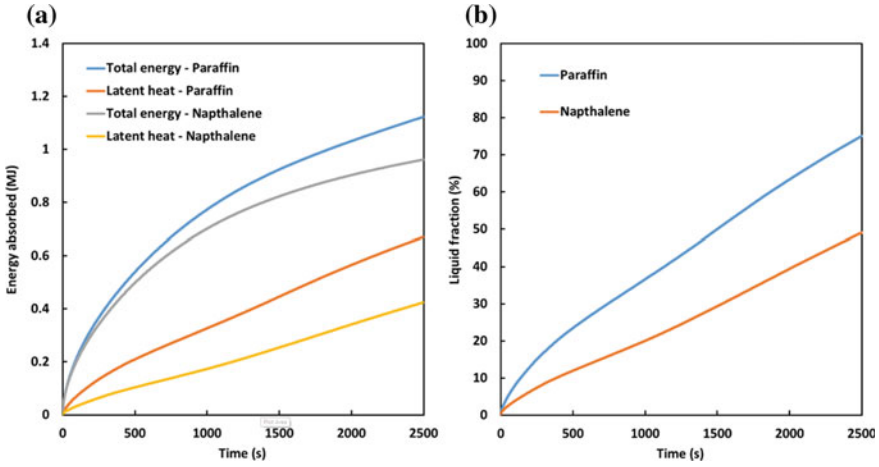

Fig. 11.8 Comparison of paraffin and naphthalene as PCM. **a** Variation of energy absorption with time. **b** Variation of overall melt fraction with time

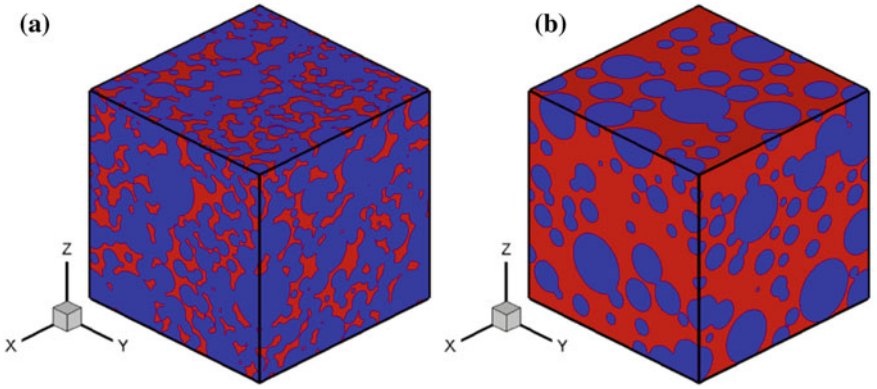

Fig. 11.9 Geometries generated for **a** 75% porosity; **b** 50% porosity (red represents the metal foam and blue represents the PCM)

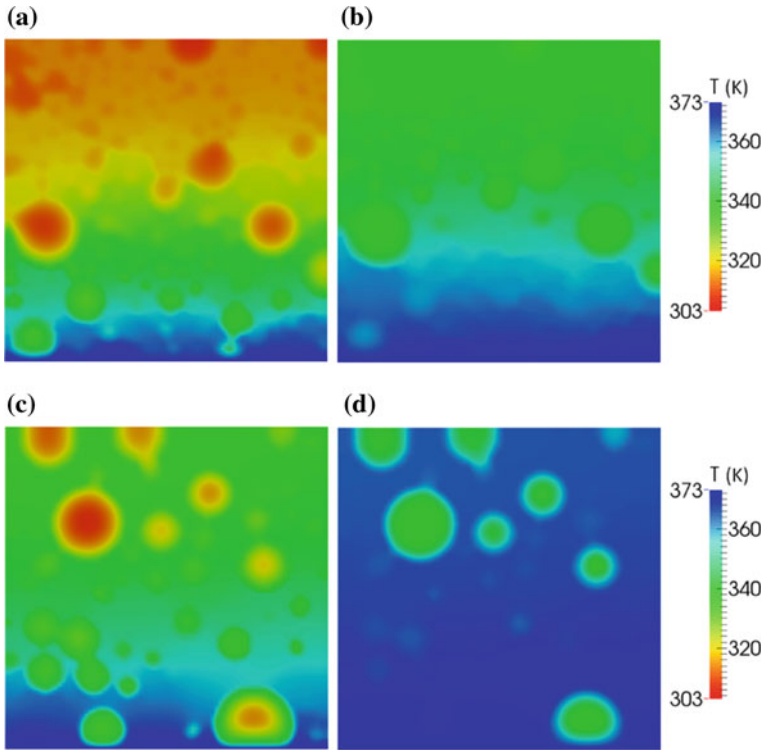

Fig. 11.10 Temperature contours at the mid-section with **a** 75% porosity at $t = 500$ s; **b** 75% porosity at $t = 2000$ s; **c** 50% porosity at $t = 500$ s; **d** 50% porosity at $t = 2000$ s

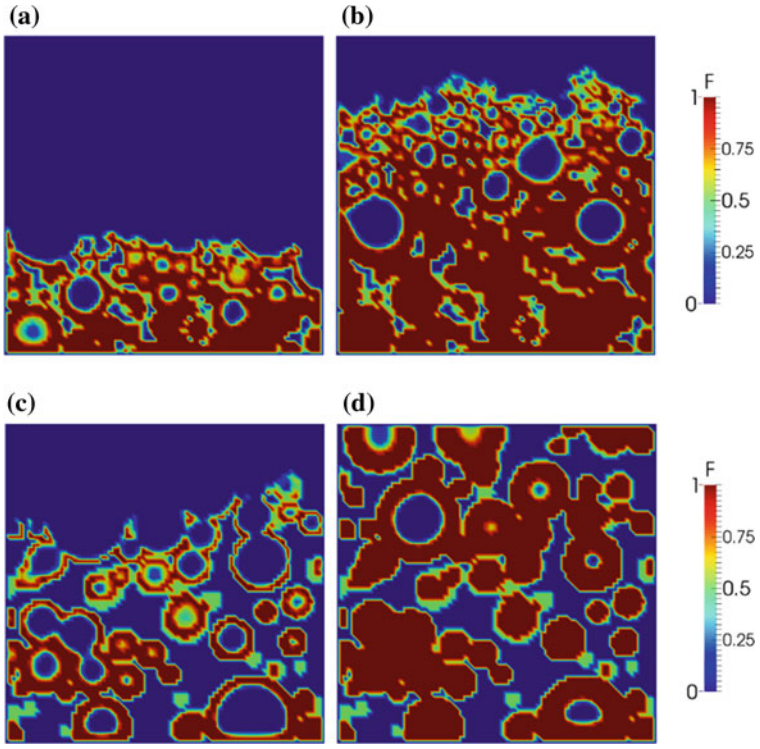

Fig. 11.11 Liquid fraction at the mid-section **a** 75% porosity at $t = 500$ s; **b** 75% porosity at $t = 2000$ s; **c** 50% porosity at $t = 500$ s; **d** 50% porosity at $t = 2000$ s

temperature of PCM faster. Also, in this case due to the higher amount of metal, the effective thermal conductivity of the system is higher leading to higher heat transfer rate.

The variation of total energy absorbed and the latent heat absorbed for the two systems with time are compared in Fig. 11.12a. It is observed that the rate of energy transfer is higher for the 50% porosity system. However, although the rate of latent heat absorption is initially higher for the 50% porosity system, at later time period, the 75% porosity system has higher latent heat transfer. This shows that sensible heating is significantly higher for the lower porosity system as larger volume fraction of metal is present in this case. Figure 11.12b shows the variation of liquid fraction with time for the two systems. It is seen that initially the liquid fraction increases at a faster rate for the 50% porosity system. However towards the end, it saturates as most of the PCM melts and only centers of large pores still remain solid. For the 75% porosity system the liquid fraction keeps on increasing steadily for the given time period. It should be noted here that, although the liquid fraction of PCM for the 75% porosity system is lower at the end of the simulation, the actual latent heat

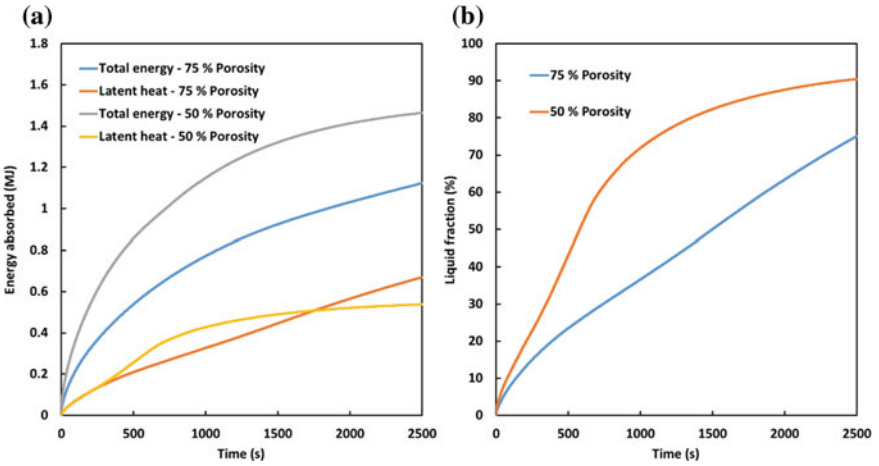

Fig. 11.12 Comparison of systems with 75% porosity and 50% porosity. **a** Variation of energy absorption with time. **b** Variation of overall melt fraction with time

absorption is higher as the total volume of PCM is higher for this system. Higher heat transfer rate with lower porosity of metal foam has been previously observed experimentally by Lafdi et al. (2007).

11.5.5 Effect of Pore Size

To study the effect of pore size, two systems are considered with varying pore sizes. The geometry for the first system is generated with a pore radius (r) range of 0.5–3.0 cm while for the second system, the geometry is created with a pore

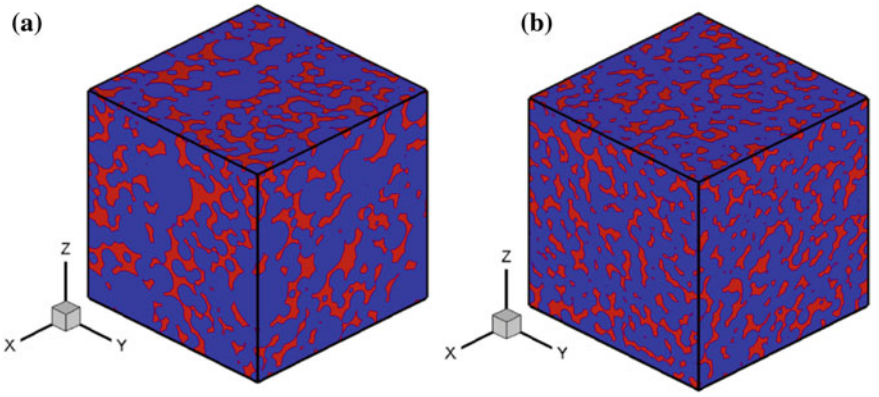

Fig. 11.13 Geometries generated for **a** pore size $0.5 < r < 3$ cm; **b** pore size $0.5 < r < 1$ cm (red represents the metal foam and blue represents the PCM)

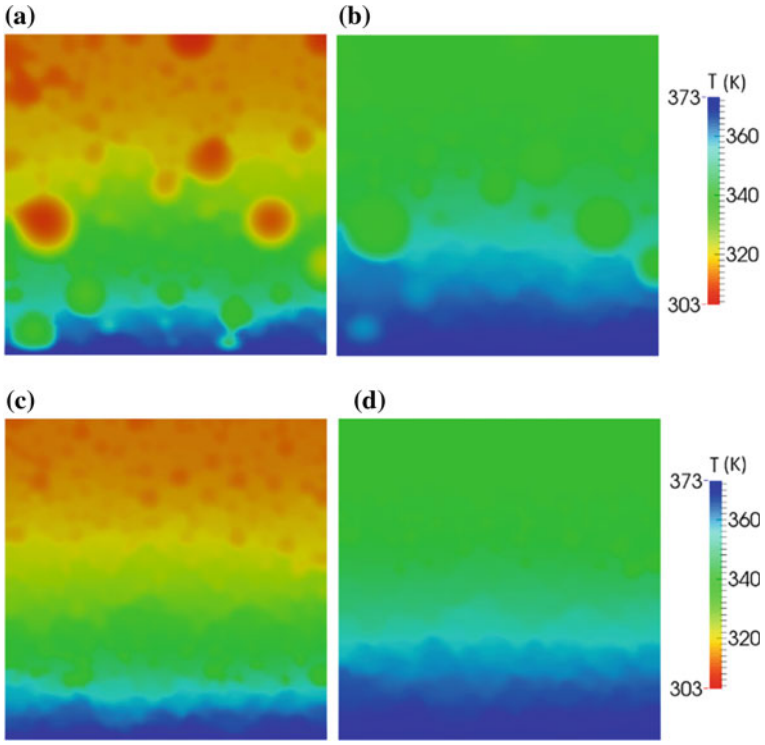

Fig. 11.14 Temperature contours at the mid-section with **a** $0.5 < r < 3$ cm at $t = 500$ s; **b** $0.5 < r < 3$ cm at $t = 2000$ s; **c** $0.5 < r < 1$ cm at $t = 500$ s; **d** $0.5 < r < 1$ cm at $t = 2000$ s

radius range of 0.5–1.0 cm. Hence the second system has significantly lower average pore size. It should be noted here that although the pore size is varied for the two systems the porosity is kept constant and equal to 75%. The geometries generated by the model for the two systems are presented in Fig. 11.13. It is observed that for the second system large pores are not present. All the parameters are kept same as that given in Table 11.1. Figure 11.14 shows the temperature contours for the two systems at time $t = 500$ and 2000 s. It is seen that the first system has localized low temperature regions as some of the pores are significantly large and energy transfer for those pores is very slow due to lower thermal conductivity of PCM. The second system shows uniform temperature gradient from the bottom surface to the top surface. For this case, as all the pores are smaller, all the PCM inside the pores are relatively near to metal foam structures and thus energy transfer can occur faster in this case. Figure 11.15 shows the corresponding liquid fraction contours. It confirms that the larger pores still contain a significant amount of solid PCM.

The variation of total energy absorbed and the latent heat absorbed for the two systems with time are compared in Fig. 11.16a. It is seen that both the quantities are slightly higher for the second system. As explained previously, the smaller pore

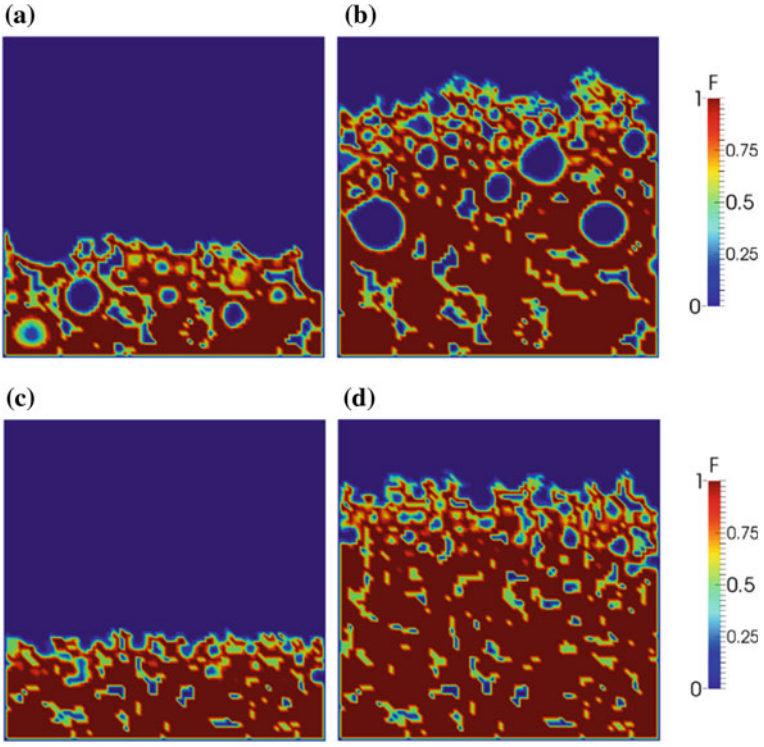

Fig. 11.15 Liquid fraction at the mid-section **a** $0.5 < r < 3$ cm at $t = 500$ s; **b** $0.5 < r < 3$ cm at $t = 2000$ s; **c** $0.5 < r < 1$ cm at $t = 500$ s; **d** $0.5 < r < 1$ cm at $t = 2000$ s

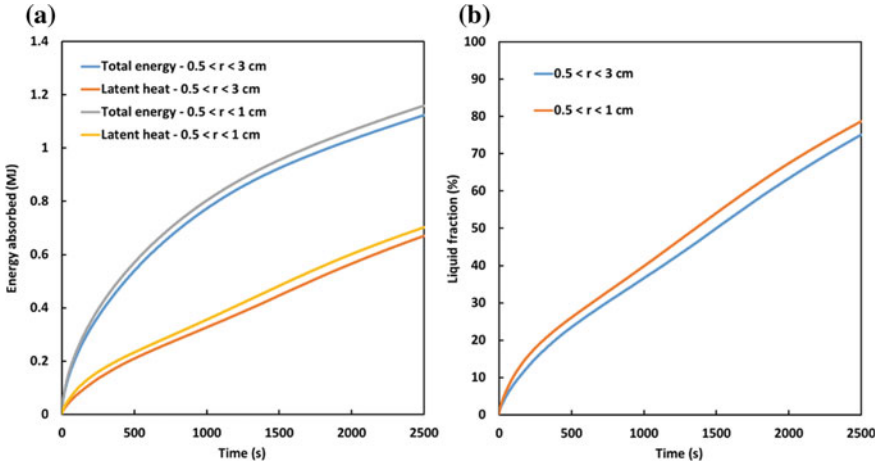

Fig. 11.16 Comparison of systems with different pore size distribution. **a** Variation of energy absorption with time. **b** Variation of overall melt fraction with time

size of the second system results in faster energy transfer to the PCM. The variation of liquid fraction with time for the two systems are compared in Fig. 11.16b which confirms that melting occurs at slightly faster rate if the average pore size is less. This study is important as it shows that although two systems may have exactly same material and porosity, variation of pore size leads to different energy absorption rates. Hence for designing a composite metal foam-PCM system, the pore size of the foam should also be taken into consideration. Similar results, predicting the increase in heat transfer with decrease in pore size, has been obtained by pore scale modelling by Ren et al. (2017).

11.5.6 Effect of Overall System Size

For this study two different cubic domains are considered—with side lengths of 20 and 10 cm, respectively. All the other parameters are same as that specified in Table 11.1. Figure 11.17 shows the temperature contours for the two systems at time

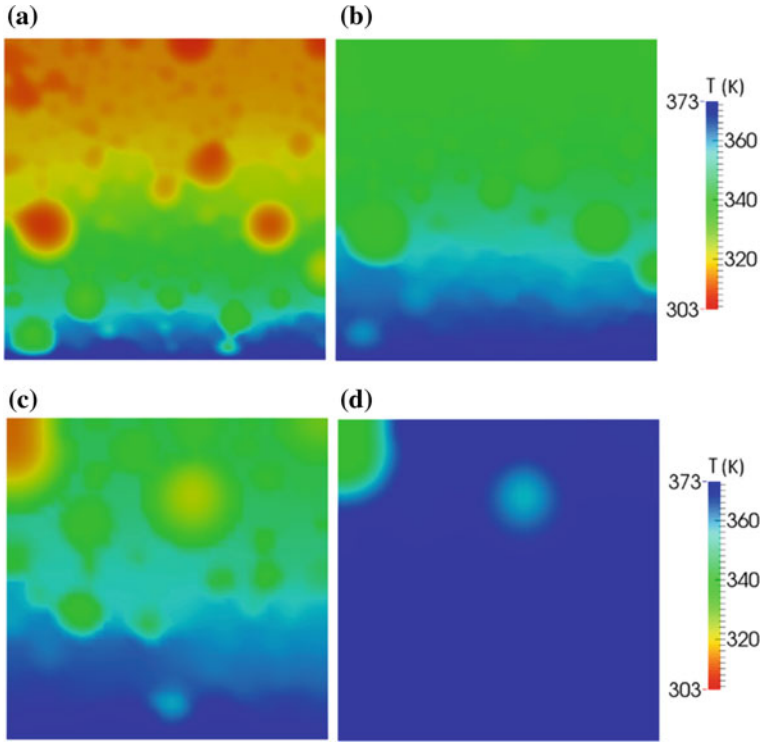

Fig. 11.17 Temperature contours at the mid-section for domain of side length **a** 20 cm at $t = 500$ s; **b** 20 cm at $t = 2000$ s; **c** 10 cm at $t = 500$ s; **d** 10 cm at $t = 2000$ s

$t = 500$ and 2000 s. Although the size is different, the plots for the small system are zoomed to the same size as those of the larger system. It is seen that the temperature is significantly higher for the smaller system as heat transfer occurs at a faster rate towards the top surface due to the lesser distance from the heating surface. This is also evident from the liquid fraction contours shown in Fig. 11.18 which shows that the initial melting rate is very high for the smaller system. It should be noted here that although the overall volume has been reduced by a factor of 8 for the second system, the heat transfer surface area is only 4 times smaller. Hence more heat transfer can occur per unit volume for the second case.

The variation of total energy absorbed and the latent heat absorbed for the two systems with time are compared in Fig. 11.19a. It is seen that both the quantities are higher for the larger system. However, although the system volume is 8 times more, the rate of energy absorption is significantly less than 8 times as that for the smaller system. This means that 8 smaller systems, which will have the same volume of PCM and metal as that for the larger system, will have significantly higher

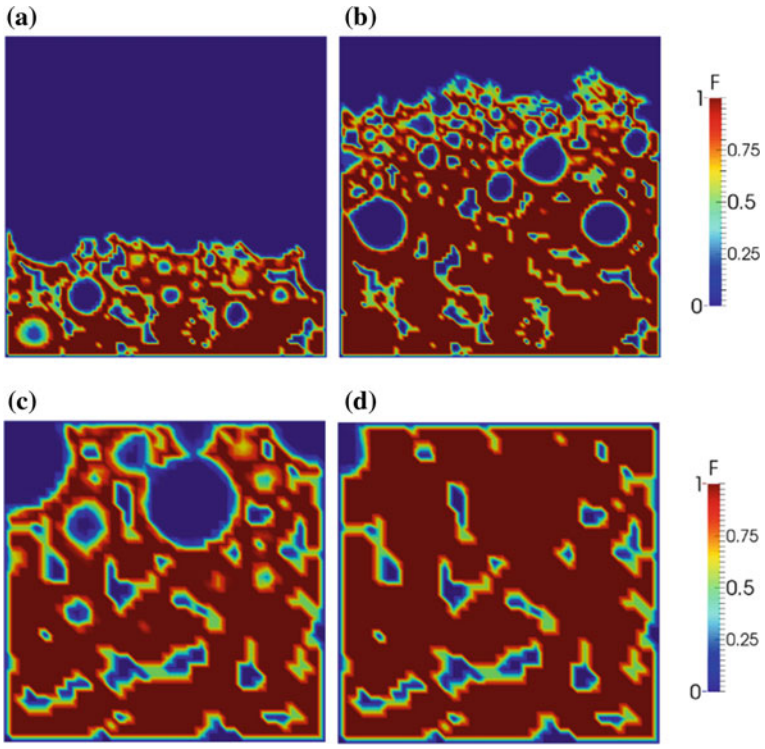

Fig. 11.18 Liquid fraction at the mid-section for domain of side length **a** 20 cm at $t = 500$ s; **b** 20 cm at $t = 2000$ s; **c** 10 cm at $t = 500$ s; **d** 10 cm at $t = 2000$ s

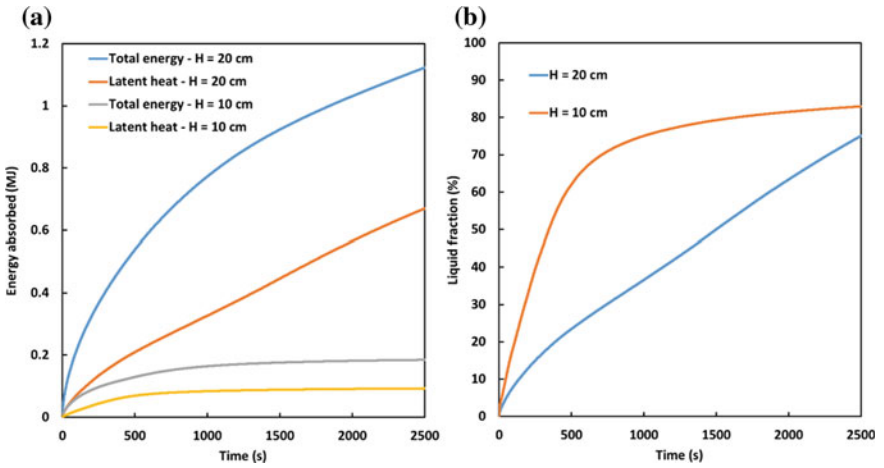

Fig. 11.19 Comparison of systems with different overall size. **a** Variation of energy absorption with time. **b** Variation of overall melt fraction with time

energy absorption rate. However, more heat transfer area will be required for this case. Figure 11.19b shows the variation of overall liquid fraction for the two systems which confirms that the rate of melting is higher for the smaller system.

11.6 Summary

This chapter presents a study of metal foam-PCM composite systems for energy storage. It has been previously shown that metal foams can be very effective in increasing the overall heat transfer rate for PCM based energy storage systems due to their high conductivity, intricate network and large surface area. In this chapter, various factors which can affect the energy absorption characteristics of metal foam-PCM systems are considered and analyzed. Pore-scale simulations of melting in metal foam-PCM systems are performed by varying parameters such as foam porosity, pore size distribution, foam and energy storage material and overall system size. The energy absorption characteristics, temperature evolution and melting pattern are compared to quantify the effect of these parameters. Results show that the each of these factors is important and hence should be taken into consideration while designing such systems.

References

Abishek S, King AJC, Mead-Hunter R, Golkarfard V, Heikamp W, Mullins BJ (2017) Generation and validation of virtual nonwoven, foam and knitted filter (separator/coalescer) geometries for CFD simulations. Sep Purif Technol 188:493–507

Abishek S, King AJC, Nadim N, Mullins BJ (2018) Effect of microstructure on melting in metal-foam/paraffin composite phase change materials. Int J Heat Mass Transf 127:135–144

Agyenim F, Hewitt N, Eames P, Smyth M (2010) A review of materials, heat transfer and phase change problem formulation for latent heat thermal energy storage systems (LHTESS). Renew Sustain Energy Rev 14(2):615–628

Bhattacharya A, Dutta P (2013) An enthalpy-based model of dendritic growth in a convecting binary alloy melt. Int J Numer Methods Heat Fluid Flow 23(7):1121–1135

Boomsma K, Poulikakos D, Ventikos Y (2003) Simulations of flow through open cell metal foams using an idealized periodic cell structure. Int J Heat Fluid Flow 24(6):825–834

Chen Z, Gao D, Shi J (2014) Experimental and numerical study on melting of phase change materials in metal foams at pore scale. Int J Heat Mass Transf 72:646–655

Deng Z, Liu X, Zhang C, Huang Y, Chen Y (2017) Melting behaviors of PCM in porous metal foam characterized by fractal geometry. Int J Heat Mass Transf 113:1031–1042

Dinesh BVS, Bhattacharya A (2019) Effect of foam geometry on heat absorption characteristics of PCM-metal foam composite thermal energy storage systems. Int J Heat Mass Transf 134:866–883

Fan L, Khodadadi JM (2011) Thermal conductivity enhancement of phase change materials for thermal energy storage: a review. Renew Sustain Energy Rev 15(1):24–46

Farid MM, Khudhair AM, Razack SAK, Al-Hallaj S (2004) A review on phase change energy storage: materials and applications. Energy Convers Manag 45(9–10):1597–1615

Hong ST, Herling DR (2006) Open-cell aluminum foams filled with phase change materials as compact heat sinks. Scripta Mater 55(10):887–890

Ibrahim NI, Al-Sulaiman FA, Rahman S, Yilbas BS, Sahin AZ (2017) Heat transfer enhancement of phase change materials for thermal energy storage applications: a critical review. Renew Sustain Energy Rev 74:26–50

Ji H, Sellan DP, Pettes MT, Kong X, Ji J, Shi L, Ruoff RS (2014) Enhanced thermal conductivity of phase change materials with ultrathin-graphite foams for thermal energy storage. Energy Environ Sci 7(3):1185–1192

Kenisarin M, Mahkamov K (2007) Solar energy storage using phase change materials. Renew Sustain Energy Rev 11(9):1913–1965

Kumar A, Saha SK (2018) Latent heat thermal storage with variable porosity metal matrix: a numerical study. Renew Energy 125:962–973

Lafdi K, Mesalhy O, Shaikh S (2007) Experimental study on the influence of foam porosity and pore size on the melting of phase change materials. J Appl Phys 102(8):083549

Lafdi K, Mesalhy O, Elgafy A (2008) Graphite foams infiltrated with phase change materials as alternative materials for space and terrestrial thermal energy storage applications. Carbon 46(1):159–168

Lin Y, Jia Y, Alva G, Fang G (2018) Review on thermal conductivity enhancement, thermal properties and applications of phase change materials in thermal energy storage. Renew Sustain Energy Rev 82:2730–2742

Liu L, Su D, Tang Y, Fang G (2016) Thermal conductivity enhancement of phase change materials for thermal energy storage: a review. Renew Sustain Energy Rev 62:305–317

Mancin S, Diani A, Doretti L, Hooman K, Rossetto L (2015) Experimental analysis of phase change phenomenon of paraffin waxes embedded in copper foams. Int J Therm Sci 90:79–89

Mesalhy O, Lafdi K, Elgafy A, Bowman K (2005) Numerical study for enhancing the thermal conductivity of phase change material (PCM) storage using high thermal conductivity porous matrix. Energy Convers Manag 46(6):847–867

Nazir H, Batool M, Osorio FJB, Isaza-Ruiz M, Xu X, Vignarooban K, Kannan AM (2019) Recent developments in phase change materials for energy storage applications: a review. Int J Heat Mass Transf 129:491–523

Pielichowska K, Pielichowski K (2014) Phase change materials for thermal energy storage. Prog Mater Sci 65:67–123

Qureshi ZA, Ali HM, Khushnood S (2018) Recent advances on thermal conductivity enhancement of phase change materials for energy storage system: a review. Int J Heat Mass Transf 127:838–856

Ren Q, He YL, Su KZ, Chan CL (2017) Investigation of the effect of metal foam characteristics on the PCM melting performance in a latent heat thermal energy storage unit by pore-scale lattice Boltzmann modeling. Numer Heat Transf Part A: Appl 72(10):745–764

Ren Q, Meng F, Guo P (2018) A comparative study of PCM melting process in a heat pipe-assisted LHTES unit enhanced with nanoparticles and metal foams by immersed boundary-lattice Boltzmann method at pore-scale. Int J Heat Mass Transf 121:1214–1228

Sharma A, Tyagi VV, Chen CR, Buddhi D (2009) Review on thermal energy storage with phase change materials and applications. Renew Sustain Energy Rev 13(2):318–345

Siahpush A, O'Brien J, Crepeau J (2008) Phase change heat transfer enhancement using copper porous foam. J Heat Transf 130(8):082301

Srivatsa PVSS, Baby R, Balaji C (2014) Numerical investigation of PCM based heat sinks with embedded metal foam/crossed plate fins. Numer Heat Transf Part A: Appl 66(10):1131–1153

Sundarram SS, Li W (2014) The effect of pore size and porosity on thermal management performance of phase change material infiltrated microcellular metal foams. Appl Therm Eng 64(1–2):147–154

Tian Y, Zhao CY (2011) A numerical investigation of heat transfer in phase change materials (PCMs) embedded in porous metals. Energy 36(9):5539–5546

Voller VR (2008) An enthalpy method for modeling dendritic growth in a binary alloy. Int J Heat Mass Transf 51(3–4):823–834

Wang M, Pan N (2008) Modeling and prediction of the effective thermal conductivity of random open-cell porous foams. Int J Heat Mass Transf 51(5–6):1325–1331

Wang C, Lin T, Li N, Zheng H (2016) Heat transfer enhancement of phase change composite material: copper foam/paraffin. Renew Energy 96:960–965

Xiao X, Zhang P, Li M (2013) Preparation and thermal characterization of paraffin/metal foam composite phase change material. Appl Energy 112:1357–1366

Xiao X, Zhang P, Li M (2014) Effective thermal conductivity of open-cell metal foams impregnated with pure paraffin for latent heat storage. Int J Therm Sci 81:94–105

Xu B, Li P, Chan C (2015) Application of phase change materials for thermal energy storage in concentrated solar thermal power plants: a review to recent developments. Appl Energy 160:286–307

Yang X, Bai Q, Guo Z, Niu Z, Yang C, Jin L, Yan J (2018) Comparison of direct numerical simulation with volume-averaged method on composite phase change materials for thermal energy storage. Appl Energy 229:700–714

Zalba B, Marın JM, Cabeza LF, Mehling H (2003) Review on thermal energy storage with phase change: materials, heat transfer analysis and applications. Appl Therm Eng 23(3):251–283

Zhang Z, Zhang N, Peng J, Fang X, Gao X, Fang Y (2012) Preparation and thermal energy storage properties of paraffin/expanded graphite composite phase change material. Appl Energy 91(1):426–431

Zhang Z, Cheng J, He X (2017) Numerical simulation of flow and heat transfer in composite PCM on the basis of two different models of open-cell metal foam skeletons. Int J Heat Mass Transf 112:959–971

Zhao CY, Lu W, Tian Y (2010) Heat transfer enhancement for thermal energy storage using metal foams embedded within phase change materials (PCMs). Sol Energy 84(8):1402–1412

Zhao W, France DM, Yu W, Kim T, Singh D (2014) Phase change material with graphite foam for applications in high-temperature latent heat storage systems of concentrated solar power plants. Renew Energy 69:134–146

Zheng H, Wang C, Liu Q, Tian Z, Fan X (2018) Thermal performance of copper foam/paraffin composite phase change material. Energy Convers Manag 157:372–381

Zhu ZQ, Huang YK, Hu N, Zeng Y, Fan LW (2018) Transient performance of a PCM-based heat sink with a partially filled metal foam: effects of the filling height ratio. Appl Therm Eng 128:966–972

Chapter 12
Direct Photo-Thermal Energy Storage Using Nanoparticles Laden Phase Change Materials

Deepak Moudgil and Vikrant Khullar

Abstract In the present work, we propose thermal energy storage by direct photo-thermal energy conversion (referred to as optical charging) using nanoparticles laden phase change materials (PCMs). In the conventional thermal storage systems, the absorbed solar energy is indirectly transferred to the PCM (primarily through conduction and convection heat transfer mechanisms) and is subsequently stored in the form of latent heat of the PCM (referred to as thermal charging). Opposed to the conventional thermal storage strategies; optical charging involves direct interaction of the sunlight with the phase change material (radiation being the predominant heat transfer mechanism). Broad absorption-based nanoparticles (amorphous carbon) have been seeded into the pristine phase change material (paraffin wax) to enhance photo-thermal conversion efficiency. Particularly, we investigate the effect of adding nanoparticles to conventional PCMs during optical charging process. To understand the role of nanoparticles; samples of pristine paraffin wax and nano-PCMs [different concentrations of nanoparticles (0.05, 0.1, 0.2, 0.4%, wt%) dispersed in the pristine paraffin wax] have been optically heated. Furthermore, optical charging has been compared with the conventional thermal charging process. As per the experimental observations, the optical charging scheme significantly improves the thermal charging rate (by more than 157%) at optimum nanoparticle concentration (0.2%, in the present study) as compared to conventional thermal charging.

Keywords Optical charging · Phase change material (PCM) · Nanoparticles

D. Moudgil · V. Khullar (✉)
Mechanical Engineering Department, Thapar Institute of Engineering and Technology Patiala, Patiala, Punjab 147004, India
e-mail: vikrant.khullar@thapar.edu

D. Moudgil
e-mail: dmoudgil_me17@thapar.edu

H. Tyagi et al. (eds.), *Solar Energy*, Energy, Environment, and Sustainability, https://doi.org/10.1007/978-981-15-0675-8_12

Nomenclature

English symbols

m	Mass
Tavg	Average temperature
Tatm	Atmospheric temperature

Subscripts

f	Fraction

Abbreviations

PCM	Phase change material
NPs	Nanoparticles
TES	Thermal energy storage
OC	Optical charging
TC	Thermocouple

12.1 Introduction

In today's world the energy demand in the industrial, household, agriculture and service sector vary on daily, weekly and seasonal basis. Thermal energy storage (TES) provides a simple an economic means of utilizing solar energy even during non-sunshine hours to satisfy our growing needs for heating and cooling. TES essentially involves three processes: charging, storage and discharging. Furthermore, thermal storage process could be either sensible TES or latent TES. In sensible heat storage, the material (concrete, rock, etc.) undergoes temperature change during charging and discharging processes; whereas in latent TES, the material (ice, salts, etc.) undergoes phase transformation during the charging and discharging processes (Dincer and Rosen 2002). Latent TES (employing PCMs) in particular offers range of capacities (quantity of energy stored) and capability of storing energy ranging from few hours to a few days at relatively high energy stored to volume ratio. PCMs could be classified into three basic types: organic (paraffins, fatty acids), inorganic (salt hydrates), eutectics (organic, inorganic) (Paksoy 2007). Conventionally, the charging process (melting of PCM) involves bleeding a part of the heated fluid from the

outlet of solar thermal system and circulating it in a pipe through the PCM containing storage tank. Herein, the heat of the fluid gets transferred to the PCM primarily through conduction and therefore the pipe material is invariable a highly conducting material (such as copper). Furthermore, researchers have used pipes with fins and employed various agitation techniques to enhance the heat transfer. Recently, the photon-transport based optical charging (OC) wherein, the solar irradiance directly interacts with the PCM has proven to significantly improve the charging process. Herein, nanoparticles have been seeded in the conventional PCMs to enhance its absorption capability; and the nanoparticle-laden PCM directly interacts with the incident sunlight through absorption and scattering mechanisms. Although, seeding nanoparticles into a transparent PCM is the most effective proposition but researchers have revealed that photon-transport based optical charging can still be applicable to nanoparticles-laden opaque PCMs (Wang et al. 2017). To enhance the charging rate researchers have dispersed various nanoparticles in PCMs (Cu NPs, Au NPs, Al_2O_3 NPs, metal foam copper, carbon nanotubes sponge, hybrid NPs etc.)—these could be broadly classified into plasmonic metallic nanoparticles or carbon-based broad absorption nanoparticles.

With the objective of optimizing the optical charging process, there have been efforts to understand the photon-nanoparticle laden PCM interaction mechanism and subsequently the melting process. Richardson et al., studied the light interaction with gold nanoparticles dispersed in ice matrix (Richardson et al. 2006). Chen et al., enhanced the enthalpy and thermal conductivity of PCM through usage of deformable carbon nano-tube sponge wherein energy storage is driven by illumination (Chen et al. 2012). Lin and Al-Kayiem used copper NPs to improve the thermophysical properties of PCMs for thermal energy storage (Lin and Al-Kayiem 2012). Usage of copper NPs in solar pond has been proven to reduce the charging and discharging time significantly (Karunamurthy et al. 2012). Alumina NPs dispersed into PCM to form a nano-PCM which has been used to increase the charging rate as compare to pure PCM (Pise et al. 2013). Hybrid nanoparticles have been used in solar heating systems to enhance the storage and nanofillers of graphene NPs have been found to enhance the thermal conductivity with increase in loading of NPs (Harikrishnan et al. 2014; Fan et al. 2013). Ultra-thin foam dispersed into PCM have shown to significantly increase the thermal conductivity at even low volume fractions (up to 18 times) and PCM filled spherical capsules have also been used to increase the thermal storage, cyclohexane with copper nanoparticles have been dispersed into PCM with porous medium to increase the energy storage (Ji et al. 2014; Khot et al. 2012; Hossain et al. 2015). The addition of metal foams has shown to increase the overall heat transfer up to 3–10 times. Researchers have also shown that usage of liquid metal gallium as nano-PCM reduces the melting time and improves thermal storage (Zhao et al. 2010; Wang et al. 2014; Alomair et al. 2017; Salyan and Suresh 2018).

The present work is essentially an attempt to further understand the optical charging and discharging process. This shall help in identifying the key parameters and processes impacting the melting rate of nanoparticle-laden PCMs. Firstly, we prepare the samples of nano PCM by using ultra-sonication method. Two set of experimental

set-ups have been designed, which are similar in all respects except that one simulates the surface heating i.e. the conventional charging mechanism and the other simulates the optical charging mode. Subsequently, charging rate of nano PCM at different concentrations have been carefully measured under optical charging mode.

12.2 Experimental Materials and Methods

In order to clearly understand the heat transfer mechanisms involved during thermal and optical heating two sets of experiments have been carefully designed. In the present work paraffin wax has been used as PCM and amorphous carbon nanoparticles (<100 nm SIGMA ALDRICH) of desired amount have been dispersed into PCM to form nano-PCM. All materials have been used without any further purification. For temperature measurements, K-type thermocouples were employed. In experiments glass and solar selective surface (black chrome coated copper sheet, 0.019 cm thick, Solchrome) were used as interface in two set-ups. Various nano-PCMs containing paraffin wax (10 g) and amorphous carbon nanoparticles (ACNs) with different mass fractions have been prepared and thermal conductivity has been measured using heat flow method (P.A Hilton Ltd., H112N) (see Table 12.1).

12.2.1 Ultra-sonication Process

Initially, paraffin wax has been melted in water bath and subsequently amorphous carbon nanoparticles of desired mass have been added to melted paraffin wax as shown in Fig. 12.1. Paraffin wax and amorphous carbon has been mixed by ultra-sonication process. All samples are prepared by using sonication process in which ultra-sonic waves leads to uniform mixing of the nanoparticles into the melted medium. This

Table 12.1 Nano-PCMs with different concentrations

Phase change material	Mass fractions, m_f %	Thermal conductivity (W m^{-1} K^{-1})
Paraffin wax (10 g)	0	0.278 ± 0.011
Paraffin wax (10 g) + ACNs (0.005 g)	0.05	0.324 ± 0.010
Paraffin wax (10 g) + ACNs (0.01 g)	0.1	0.388 ± 0.013
Paraffin wax (10 g) + ACNs (0.02 g)	0.2	0.359 ± 0.014
Paraffin wax (10 g) + ACNs (0.04 g)	0.4	0.329 ± 0.012

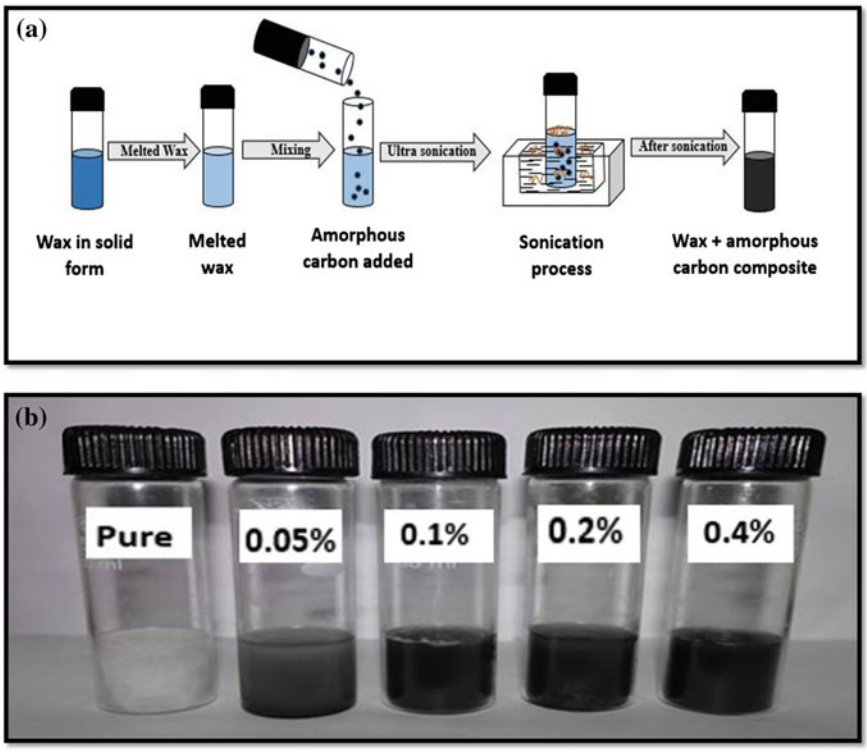

Fig. 12.1 **a** Schematic showing ultra-sonication process for preparing nano-PCM; **b** showing prepared samples of nano-PCM after ultra-sonication process

method is indirect method of sonication and the advantage of this method is that sonic energy is transmitted from horn through the water and into multiple samples i.e. a large number of nano-PCM samples could be prepared simultaneously. We use ultra-sonicator bath model SU-323 with load 3A by filling ¾ liquid in the tank (water). The process has been carried out for 15 min, subsequently, the as-prepared nano-PCM samples were cool down to atmospheric conditions. Figure 12.1b shows the picture of as-prepared nano-PCM samples after the ultra-sonication process.

12.3 Experimental Set-Up

Figure 12.2 shows the experimental set up consisting of 0.8 cm diameter optical light guide transporting the light from halogen lamp (250 W, 24 V Philips) connected with transformer and power supply. Intensity of light as measured by thermopile detector and power meter (1918-R, Newport) is 12.5 W/cm^2. Holding clamp is used to hold the optical light guide and the cylindrical tube housing the PCM is fixed at the base of

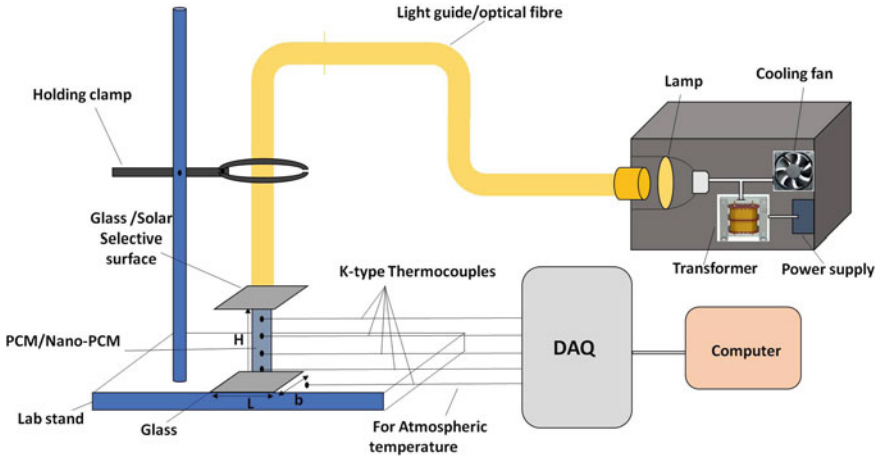

Fig. 12.2 Schematic showing experimental set-up for charging process of nano-PCM

the stand. Four equally spaced (0.5 cm apart) and calibrated K-type thermocouples have been placed in the cylindrical tube (1.7 cm × 1 cm) housing the PCM and fifth thermocouple is kept in open to record ambient temperature. As mentioned earlier, two sets of experimental were carried out i.e. volumetric (simulating optical charging) and surface (simulating thermal charging) heating. In volumetric heating, the cylindrical tube is covered with glass (2.5 cm × 2.1 cm) from both sides and in surface heating top is covered by solar selective surface (2.5 cm × 2.1 cm), bottom is covered with glass.

In both set of experiments, we fix the cylindrical tube at the base of the stand and also fix the positions of the thermocouples and optical light guide (see Fig. 12.3). Tube is filled with PCM/nano-PCM. Heating or charging process has been carried out for 1800 s, after which the power supply is turned off and the melted PCM/nano-PCM is allowed to cool for 1380 s (to ensure that the solidification process is completed and the PCM/nano-PCM is in equilibrium with the atmospheric conditions).

Each experiment has been performed for at least three times (to ensure repeatability of the results). Figure 12.3 shows the schematics of set-ups employed for surface and volumetric heating. The temperature field as measured by the thermocouples was logged using data acquisition (DAQ) system (NI).

12.4 Results and Discussion

Charging rates for two cases (namely interface-glass and interface-solar selective material) at various concentrations of the nanoparticles have been plotted in Figs. 12.4 and 12.5. Graphs clearly reveal that for a given illumination period (30 min in the

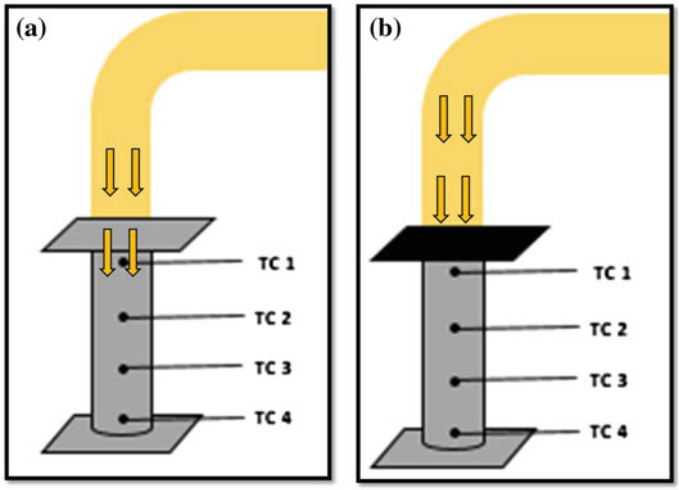

Fig. 12.3 Schematics showing the position of optical light guide and thermocouples for **a** volumetric heating, and **b** surface heating

present study), charging rate increases with increase in concentration of nanoparticles. Furthermore, volumetric heating is more effective as compare to surface heating.

In order to clearly understand the reasons for charging rate enhancements temperature distribution in each case was also analyzed. To understand the effect of nanoparticles in volumetric heating; samples of pristine paraffin wax and nano-PCMs [different concentrations of nanoparticles (0.05, 0.1, 0.2, 0.4%, wt%)] have been optically heated. From experimental observations we note that charging rate enhances, with increase in concentration. To understand the effect of nanoparticles in surface heating; samples of pristine paraffin wax and nano-PCMs [different concentrations of nanoparticles (0.05, 0.4%, wt%) have been heated. In case of surface heating (solar selective material used as interface) overall temperature distribution is less as compare to volumetric heating.

The temperature difference between the initial state and final state shows the charging process of nano-PCM. Four thermocouple positions give the temperature profiles to understand the thermal behavior of nano-PCM. These observations reveal that, the optical charging scheme significantly improves the thermal charging rate (by more than 157%) at optimum nanoparticle concentration (0.2%, in the present study) as compared to conventional thermal charging.

It may be noted that in case of thermal charging (surface heating), the light does not interact directly with the nanoparticles, instead it is absorbed by the solar selective surface and subsequently transferred to nanoparticle laden PCM through conduction. Thermal conductivity being nearly insensitive to the addition of nanoparticles, we need not carry out experiments for all mass fractions in case of surface heating. This is also confirmed through careful observation of the temperature distribution

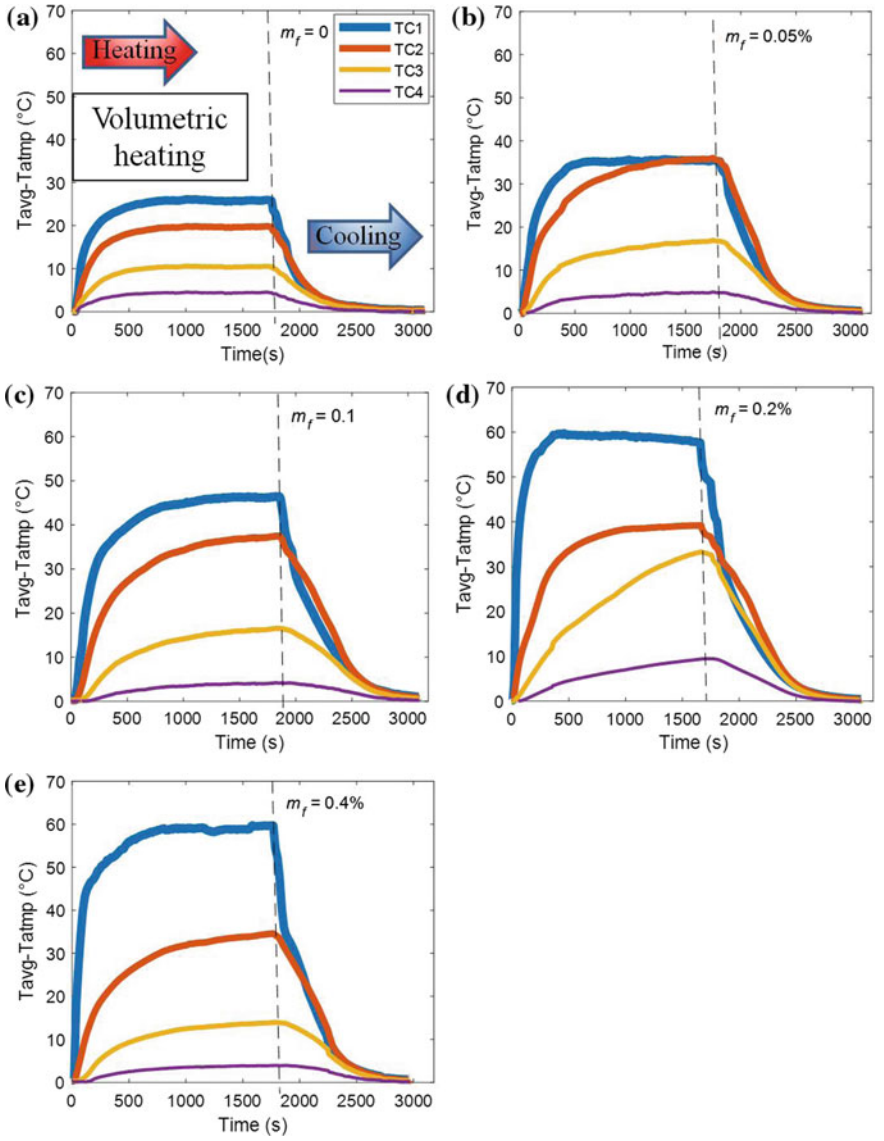

Fig. 12.4 Temperature field under OC mode as a function of time for four different concentrations of nanoparticles **a** pure paraffin wax, **b** NPs with concentration 0.05%, **c** NPs with concentration 0.1%, **d** NPs with concentration 0.2%, and **e** NPs with concentration 0.4%

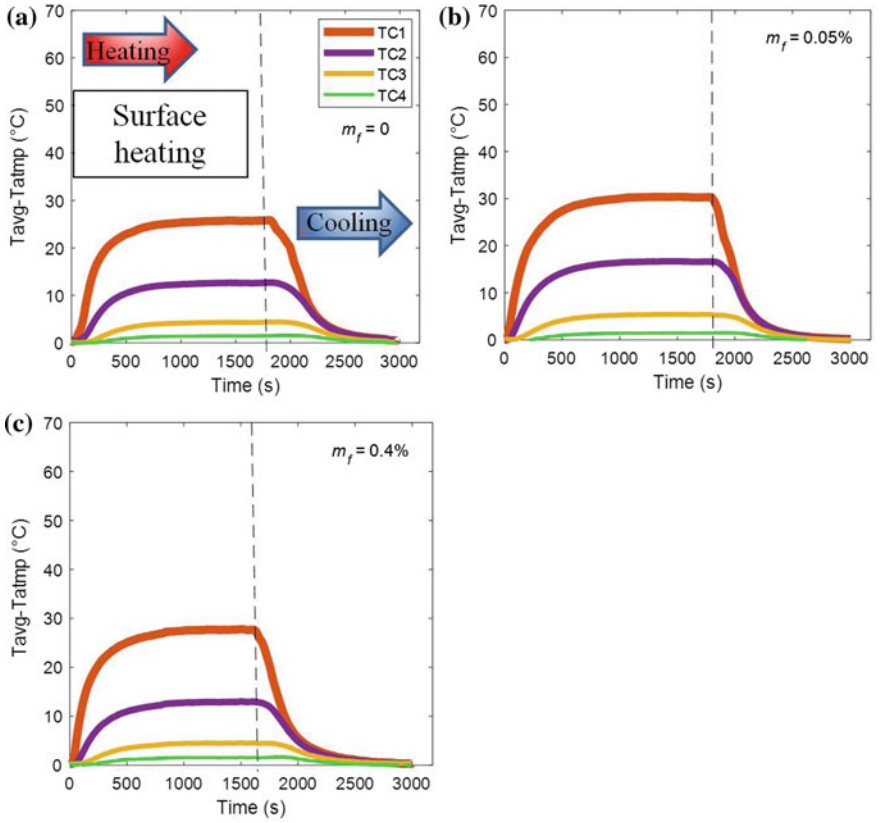

Fig. 12.5 Temperature field under thermal charging mode as a function of time for two different concentrations of nanoparticles **a** pure paraffin wax, **b** NPs with concentration 0.05%, and **c** NPs with concentration 0.4%

curves for various nanoparticle laden PCMs in case of surface heating (see Fig. 12.5). Finally, thermal images of various samples both under optical charging as well thermal charging modes have been captured (see Fig. 12.6) using IR camera (Keysight U5855A TrueIR thermal imager).

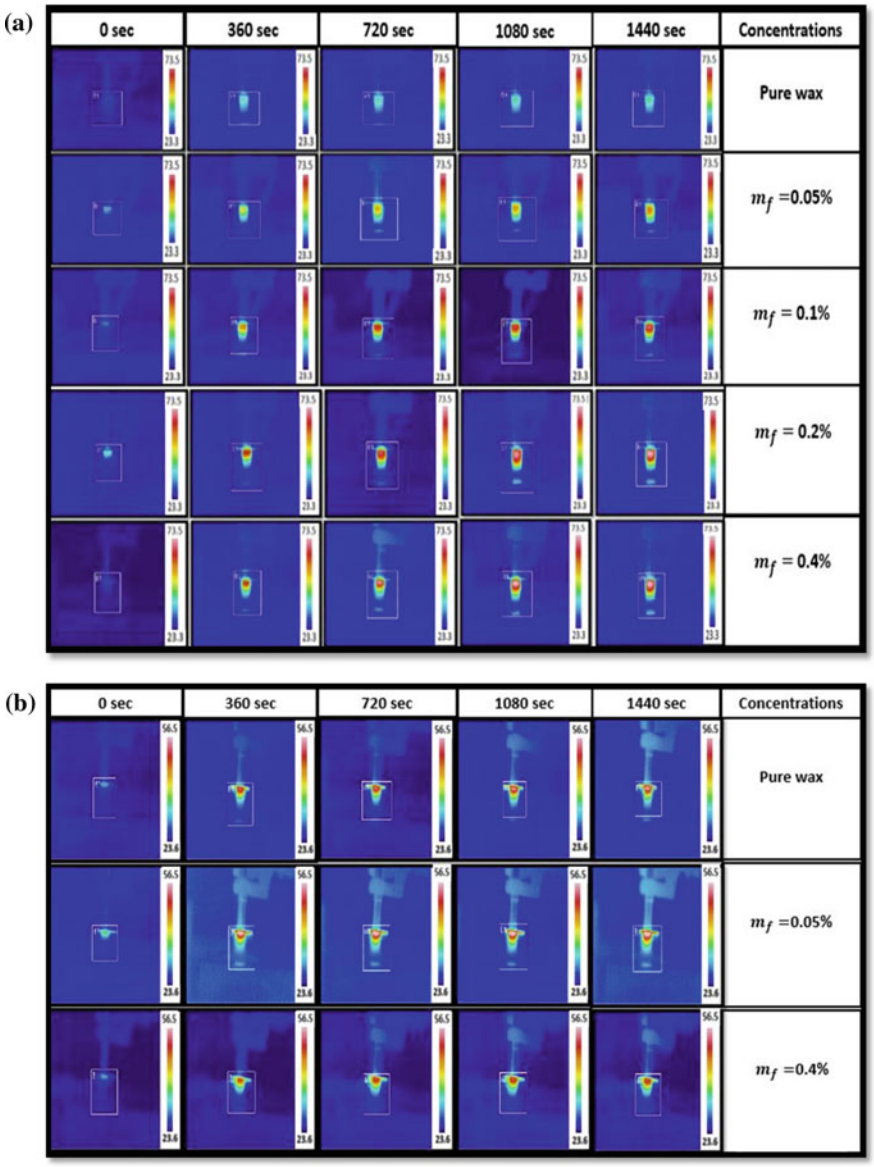

Fig. 12.6 Time-sequential thermal IR images of **a** pure paraffin and four different concentrations of nanoparticles [volumetric heating], and **b** pure paraffin and two different concentrations of nanoparticles [surface heating]

12.5 Conclusions

Experimental results reveal that addition of amorphous carbon nanoparticles can effectively improve the charging rate of PCMs. Furthermore, temperature distribution measurements show that optical heating of PCM in presence of nanoparticles could achieve more distributed energy absorption and hence proving to be an efficient and reliable method for charging PCMs. Volumetric heating gives more effective results as compared to conventional thermal charging under similar operating conditions. As a part of the future work, we intent to develop a comprehensive theoretical model simulating the optical charging process.

Acknowledgements The authors gratefully acknowledge the support provided by Mechanical Engineering Department, Thapar Institute of Engineering and Technology, Patiala, India.

References

Alomair MA, Alomair YA, Abdullah HA, Mahmud S, Tasnim S (2017) Nanoparticle enhanced phase change material in latent heat thermal energy storage system: an experimental study

Chen L, Zou R, Xia W, Liu Z, Shang Y, Zhu J, Wang Y, Lin J, Xia D, Cao A (2012) Electro- and photodriven phase change composites based on wax-infiltrated carbon nanotube sponges. ACS Nano 6(12):10884–10892

Dincer I, Rosen MA (2002) Thermal energy storage: systems and applications. Wiley, New York

Fan LW, Fang X, Wang X, Zeng Y, Xiao YQ, Yu ZT, Xu X, Hu YC, Cen KF (2013) Effects of various carbon nanofillers on the thermal conductivity and energy storage properties of paraffin-based nanocomposite phase change materials. Appl Energy 110:163–172

Harikrishnan S, Deepak K, Kalaiselvam S (2014) Thermal energy storage behavior of composite using hybrid nanomaterials as PCM for solar heating systems. J Therm Anal Calorim 115(2):1563–1571

Hossain R, Mahmud S, Dutta A, Pop I (2015) Energy storage system based on nanoparticle-enhanced phase change material inside porous medium. Int J Therm Sci 91:49–58

Ji H, Sellan DP, Pettes MT, Kong X, Ji J, Shi L, Ruoff RS (2014) Enhanced thermal conductivity of phase change materials with ultrathin-graphite foams for thermal energy storage. Energy Environ Sci 7(3):1185–1192

Karunamurthy K, Murugumohankumar K, Suresh S (2012) Use of CuO nano-material for the improvement of thermal conductivity and performance of low temperature energy storage system of solar pond. Dig J Nanomater Biostruct 7(4):1833–1841

Khot SA, Sane NK, Gawali BS (2012) Thermal energy storage using PCM for solar domestic hot water systems: a review. J Inst Eng (India): Ser C 93(2):171–176

Lin SC, Al-Kayiem HH (2012) Thermophysical properties of nanoparticles-phase change material compositions for thermal energy storage. In: Applied mechanics and materials, vol 232. Trans Tech Publications, pp 127–131

Paksoy HÖ (ed) (2007) Thermal energy storage for sustainable energy consumption: fundamentals, case studies and design, vol 234. Springer

Pise AT, Waghmare AV, Talandage VG (2013) Heat transfer enhancement by using nanomaterial in phase change material for latent heat thermal energy storage system. Asian J Eng Appl Technol 2(2):52–57

Richardson HH, Hickman ZN, Govorov AO, Thomas AC, Zhang W, Kordesch ME (2006) Thermooptical properties of gold nanoparticles embedded in ice: characterization of heat generation and melting. Nano Lett 6(4):783–788

Salyan S, Suresh S (2018) Liquid metal gallium laden organic phase change material for energy storage: an experimental study. Int J Hydrogen Energy 43(4):2469–2483

Wang Z, Tao P, Liu Y, Xu H, Ye Q, Hu H, Song C, Chen Z, Shang W, Deng T (2014) Rapid charging of thermal energy storage materials through plasmonic heating. Sci Rep 4:6246

Wang Z, Tong Z, Ye Q, Hu H, Nie X, Yan C, Shang W, Song C, Wu J, Wang J, Bao H (2017) Dynamic tuning of optical absorbers for accelerated solar-thermal energy storage. Nat Commun 8(1):1478

Zhao CY, Lu W, Tian Y (2010) Heat transfer enhancement for thermal energy storage using metal foams embedded within phase change materials (PCMs). Sol Energy 84(8):1402–1412

Chapter 13
Review on PCM Application for Cooling Load Reduction in Indian Buildings

Rajat Saxena, Dibakar Rakshit and S. C. Kaushik

Abstract Buildings use more than 40% of the total power consumed in India. Therefore, implementing energy conservation within buildings is of prime concern. Utilization of passive design parameters, such as Phase Change Material (PCM) incorporation, for energy conservation in buildings is thus a lucrative option. Incorporating PCMs within elements result in lowering of heat gain and temperature within the building. A number of simulation and experimental studies on PCM incorporated buildings, have been carried out. The advancements made in last forty years in the field of PCMs and their utilization as Thermal Energy Storage (TES) medium for buildings have been reviewed and presented in this study. This study focusses on PCM incorporation which is sensitive to its properties and climatic parameters of the location. Thus, there is a need of benchmarking the PCM for their application in buildings. Focus is on buildings in tropical hot climatic conditions, where reduction in cooling load is a challenge. This study lays emphasis on selection of appropriate PCMs based on its phase change temperature. Thermal conductivity, specific heat and latent heat are other properties which must be evaluated before PCM selection and implementation within buildings. The study also encompasses different methods of PCM incorporation being implemented across the world and have marked advantages and disadvantages of each followed by their impact in terms of energy savings.

Keywords Latent thermal energy storage · PCM · Passive system · Thermophysical properties · Building energy conservation

R. Saxena · D. Rakshit (✉) · S. C. Kaushik
Centre for Energy Studies, Indian Institute of Technology Delhi, Hauz Khas, New Delhi 110016, India
e-mail: dibakar@iitd.ac.in

R. Saxena
e-mail: rajat.saxena@ces.iitd.ac.in

S. C. Kaushik
e-mail: kaushik@ces.iitd.ac.in

H. Tyagi et al. (eds.), *Solar Energy*, Energy, Environment, and Sustainability, https://doi.org/10.1007/978-981-15-0675-8_13

13.1 Introduction

Energy exists in many forms and keeps transforming from one form to another. Energy utilization per person determines the economic and living standard of people within any country. Therefore, countries are aiming at increased rate of energy production year after year. The major problem to this is that there are limited resources available; thus, it is insufficient to just produce and use more energy. Thus, there is a need to utilize the available knowledge and technology for extracting energy from alternate sources, efficiently. The aim is to reduce the use of fossil fuel and replace them with utilization of alternate sources of energy.

Energy storage (ES) systems are an important component of alternate energy harnessed through solar, due to its intermittency. These systems store solar energy in different forms i.e. heat, chemical, biological, mechanical etc. Of these thermal (heat) energy storage systems are most studied and implemented world-wide for various applications. TES incorporation results in energy savings for cold climatic conditions as reported by Mehling and Cabeza (2008). With buildings having 40% share of the total electricity consumption (Saxena 2018), the focus is on reducing the power consumption of buildings in India. For tropical countries like India, the major power consumption during the greater part of the year is due to the cooling loads. There are several technologies being studied for cooling load reduction in buildings. This present study investigates the PCM implementation for buildings, as a passive measure, to reduce the cooling loads during peak hours of the day.

This chapter aims at providing a formidable solution to rapidly increasing building energy demands. The research emphasizes on careful selection of PCMs, as a passive storage option, for heating/cooling load abatement in buildings. PCMs are carefully selected based on their thermal characteristics, and mapped based on the climatic conditions of the place. This study also brings out how researchers have tried to incorporate PCMs within building elements followed by their assessment based on temperature reduction and energy conserved.

It is observed that PCMs in general have lower thermal conductivity thus, reducing their charge and discharge time. In order to ensure high rate of dispatchability of PCMs, it is necessary to investigate methods to increase their thermal conductivity. The nanoparticle dispersion is one such option which has also been discussed in this study.

13.2 TES Materials for Application in Buildings

A number of studies are available right from 1981, when concept of TES implementation in buildings was conceptualized and numerical model for a room with phase changing material (Kaushik et al. 1981) was developed. Further, a study in 1983, discussed the availability and application of different PCMs for storage of heat at low temperatures (0–120 °C). This study also discussed about the corrosion resistance

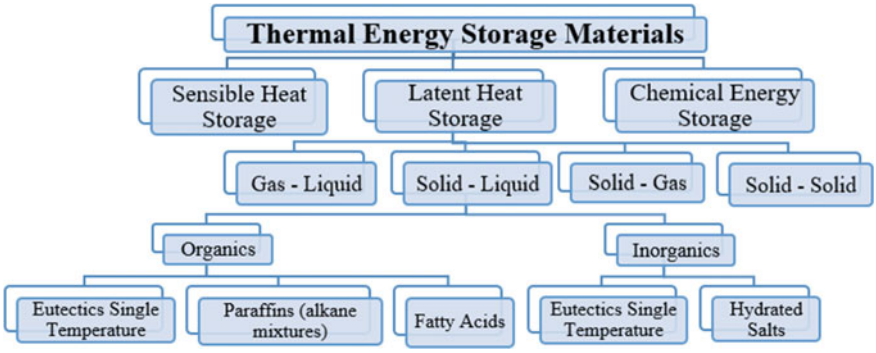

Fig. 13.1 TES material classification (Sharma et al. 2009)

and long term stability of these materials (Abhat 1983). Cabeza et al. (2011), Farid et al. (2004), Khudhair and Farid (2004), Sharma et al. (2009), Zalba et al. (2003) provides a detailed review on various types of PCMs and its applications. Material thermal properties, cost and compatibility are vital for them to be rendered suitable as TES material for any desired application. TES materials can be categorized as shown in Fig. 13.1.

13.2.1 Sensible Heat Storage Materials

Materials which absorb heat with rise in temperature and visa-versa, without undergoing phase change (in working range of temperatures) are referred to as sensible heat storage materials. Stored heat (Q_{sensible}) depends on specific heat of material as shown in Eq. 13.1. For example, in solar water heaters, the solar heat is utilized for heating water which subsequently results in its rise in temperature.

$$Q_{\text{sensible}} = m \int_{T_i}^{T_f} C_p.dT \tag{13.1}$$

Water maybe be referred to as best sensible heat storage materials owing to its highest specific heat. However, for temperature above 100 °C different salts, oils etc. maybe considered. Few sensible heat storage materials are as shown in Table 13.1 (Sharma et al. 2009; Solutia 1998; Benoit et al. 2016).

For high temperature solar thermal applications, molten metals and eutectic mixtures are also used. Heat stored per unit mass for sensible heat storage materials is relatively less followed by significant change in temperature, is observed. To overcome these drawbacks latent heat storage materials can be used.

Table 13.1 Different sensible heat storage solid and liquid materials

S. No.	Materials	Type	Specific heat (J/kg K)	Temperature/Range (°C)	Density (kg/m^{-3})
1	Rock	Solid	879	20	2560
2	Concrete	Solid	880	20	1900–2300
3	Brick	Solid	840	20	1600
4	Water	Solid	4190	0–100	1000
5	Caloriea HT43	Oil	2200	12–260	867
6	Diphenyl oxide (therminol VP-1)	Oil	1523–2600	12–393	1071–700
7	Ethanol	Organic liq.	2400	<79	790
8	Propanol	Organic liq.	2500	<98	800
9	Butanol	Organic liq.	2400	<119	810
10	Isobutanol	Organic liq.	3000	<100	808
11	Octane	Organic liq.	2400	<126	704
12	Hitec	Molten salt	–	142–535	1740
13	Hitec XL	Molten salt	–	120–500	1700
14	Solar salt	Molten salt	1553	220–600	1868
15	Liq. Sodium	Molten metal	1280	98–883	–
16	Lead bismuth eutectic (LBE)	Eutectic mixture	1260	125–1670	10529

13.2.2 Latent Heat Storage Materials

These materials have high specific heat capacity thus high concentration of energy is stored per unit mass due to latent heat involved. Another main advantage of using these materials is that they operate between small temperature differences while storing or retrieving the energy. These undergo solid- liquid or liquid-gas phase transition, in working range of temperature. The volumetric transition during liquid-gas phase change is quiet high as compared to solid-liquid PCM, hence are less suitable for building storage applications. Thus, solid-liquid transition storage systems are focused in this chapter. The heat stored within PCM storage is given in Eq. 13.2.

$$Q = m \int_{T_i}^{T_{\text{melt}}} C_{ps}.dT + m.L + m \int_{T_{\text{melt}}}^{T_f} C_{pl}.dT \tag{13.2}$$

The solid-liquid PCMs are further classified as inorganic and organic. Example of organic latent heat storage materials are paraffins, sugar alcohols, fatty acids etc. and example of inorganic PCMs are water, hydrated salts, molten salts, aqueous solutions etc. Moreover, two more miscible pure PCM constituents, having single melting/solidifying temperature are referred as eutectic mixtures. Use of hydrated salts as thermal energy storage materials is preferred, as they possess high energy density owing to higher density and latent heat. However, they show tendency of sub-cooling (or super-cooling) due to low nucleation rate thus, diminishing their usability significantly. Different PCMs are studied as potential TES materials, for temperature reduction within buildings and are illustrated in Table 13.2.

A significant number of researchers are working on organic PCMs i.e. on methods to increase their thermal conductivity which is a major drawback of using organic PCM. The research is going on to dope the nanoparticles into the PCM matrix to enhance their thermal conductivities. The methodology of mixing and characterizing the nano-enhanced PCMs is discussed in detail under Sect. 13.6.

13.2.3 Chemical Heat Storage Materials

Research is still under process to explore materials storing thermal energy as enthalpy change of a reaction. For e.g.:

$$\text{A} + \text{B} + \text{energy} \rightarrow \text{C} + \text{D} \tag{13.3}$$

In this interaction A and B absorb energy and convert into C and D thus the energy is stored as enthalpy change. It is important for reaction to be reversible so that energy can be retrieved when required. The challenge lies in finding such reactions that may hold true, must be stable and can be triggered as and when required. A perfect

Table 13.2 Solid-liquid PCMs for cooling load reduction in buildings

Material	Melting temperature (°C)	Thermal conductivity (W/m K)	Heat of fusion (kJ/kg)	Density (kg/m^3)	References
$LiClO_3$ $3H_2O$ (Hydrated salt)	8	–	253	1720 (solid)	Agyenim et al. (2010)
	8		155	1530 (liq.)	Agyenim et al. (2010)
Polyglycol E400 (organic)	8	0.187 (liq., 38.6 °C)	99.6	1125 (liq., 25 °C)	Cabeza and Mehling (2003)
	8	0.19	100	1228 (solid)	Agyenim et al. (2010)
Paraffin C_{15}	10	–	205	–	Sharma et al. (2009)
n-Pentadecane	10	–		770 (liq.)	Cabeza and Mehling (2003)
	9.9		193.9		Agyenim et al. (2010)
Caprylic acid (fatty acid)	16	0.149	148.5	901 (liq., 30 °C)	Zhou et al. (2012)
Paraffin C_{16}	16.7	–	237.1	–	Sharma et al. (2009)
45% capric acid + 55% lauric acid (organic)	17–21	–	143	–	Kant et al. (2017)
Glycerin (organic)	17.9	0.143	198.7	–	Zhou et al. (2012)
n-Heptadecane (organic)	19	0.21	240	760 (liq.)	Cabeza and Mehling (2003)
	20.8–21.7	–	171–172	–	Cabeza and Mehling (2003)
Butyl stearate (organic)	19	–	140	760 (liq.)	Cabeza and Mehling (2003)
	18–23	0.21	123–200	–	Sharma et al. (2009)
OM 21	22	0.14	174	891	Pluss Polymers (2017)
$FeBr_3 \cdot 6H_2O$ (Hydrated salt)	21	–	105	–	Zhou et al. (2012)
Octadecyl 3-mencaptopropylate (organic)	21	–	143	–	Sharma et al. (2009)

(continued)

Table 13.2 (continued)

Material	Melting temperature (°C)	Thermal conductivity (W/m K)	Heat of fusion (kJ/kg)	Density (kg/m^3)	References
Paraffin C_{17} (organic)	21.7	–	213	–	Zhou et al. (2012)
HS 22	23	0.56	167.6	1540	De Gracia and Cabeza (2015)
34% $C_{14}H_{28}O_2$ + 66% $C_{10}H_{20}O_2$	24	–	147.7	–	Zhou et al. (2012)
HS 24	26	0.55	1510	–	De Gracia and Cabeza (2015)
$Mn(NO_3)\cdot 6H_2O$ (hydrated salt)	25.5	–	125.9	1738 (liq., 20 °C)	(Sharma et al. 2009)
	25.8		125.9	1728 (liq., 40 °C)	(Cabeza and Mehling 2003)
Lactic acid (organic acid)	26	–	184	–	Sharma et al. (2009)
50% CH_3CONH_2 + 50% NH_2CONH_2 (organic eutectic)	27		163		Zhou et al. (2012)
n-Octadecane (organic)	28	0.148 (liquid)	244	774 (liq.), 814 (solid)	Zhou et al. (2012)
HS 29	29	0.382	190	1530	De Gracia and Cabeza (2015)
$LiNO_3\cdot 2H_2O$ (hydrated salt)	30	–	296	–	Zhou et al. (2012)
$LiNO_3\cdot 3H_2O$ (hydrated salt)	30	–	296	–	Sharma et al. (2009)
67% $Ca(NO_3)_2$ + 33% $Mg(NO_3)_2$ (Inorganic eutectic)	30	–	136	1670	Cabeza and Mehling (2003)
60% $Na(CH_3COO)\cdot 3H_2O$ + 40% $CO(NH_2)_2$ (Inorganic eutectic)	31.5	–	226	–	Cabeza and Mehling (2003)
OM 32	33	0.145	157	870	De Gracia and Cabeza (2015)
$Na_2SO_4\cdot 3H_2O$ (Hydrated salt)	32	–	251	–	Cabeza and Mehling (2003)
	32.4		241		Zhou et al. (2012)
$Na_2CO_3\cdot 10H_2O$ (hydrated salt)	32–36	–	246.5	1442	Cabeza and Mehling (2003)

(continued)

Table 13.2 (continued)

Material	Melting temperature (°C)	Thermal conductivity (W/m K)	Heat of fusion (kJ/kg)	Density (kg/m^3)	References
Paraffin C_{19} (organic)	32	–	222	–	De Gracia and Cabeza (2015)
Capric acid (fatty acid)	32	0.153	152.7	878 (liq., 45 °C)	De Gracia and Cabeza (2015)
	30.1–31.4		150–158		Sharma et al. (2009)
	31.5	0.152–0.149 (liquid)	153	886–1004	Cabeza and Mehling (2003)
62.6% lauric acid + 37.4% myristic acid	32.6	–	156	–	Cabeza and Mehling (2003)
64% lauric acid + 36% palmitic acid	32.8	–	165	–	Sharma et al. (2009)
$CaBr_2 \cdot 6H_2O$ (hydrated salt)	34	–	115.5	1956 (liq., 35 °C)	Cabeza and Mehling (2003)
Lauric acid + stearic acid (organic)	34	–	150	–	Cabeza and Mehling (2003)
66% lauric acid + 34% myristic acid	34.2	–	166.8	–	Cabeza and Mehling (2003)
$Na_2HPO_4 \cdot 12H_2O$ (hydrated salt)	35–44	0.514 (solid)	280	1522 (solid)	Cabeza and Mehling (2003)
	36	–	280	–	Farid et al. (2004)
	40	–	279	–	De Gracia and Cabeza (2015)
OM 35	35	0.16	171	870	De Gracia and Cabeza (2015)
Paraffin C_{20}	36.7	–	246	–	Farid et al. (2004)
OM 37	37	–	231	–	Pluss Polymers (2017)
$Mn(NO_3) \cdot 6H_2O$ (hydrated salt)	37.1	–	115	1738 (liq., 20 °C)	Cabeza and Mehling (2003)
	–	–		1795 (liq., 5 °C)	Farid et al. (2004)
1-Tetradecanol	38	–	205	–	Cabeza and Mehling (2003)
50% $Na(CH_3COO) \cdot 3H_2O$ + 50% $HCONH_2$	40.5	–	255	–	Liu et al. (2012)

(continued)

Table 13.2 (continued)

Material	Melting temperature (°C)	Thermal conductivity (W/m K)	Heat of fusion (kJ/kg)	Density (kg/m^3)	References
Heptadecanone	41	–	201	–	De Gracia and Cabeza (2015)
$KF{\cdot}2H_2O$ (Hydrated salt)	41.4	–		–	Farid et al. (2004)
$K(CH_3COO){\cdot}(1/2)\ H_2O$ (hydrated salt)	42	–	–	–	De Gracia and Cabeza (2015)
Lauric acid	42–44	0.147	178	870 (liq.)	Cabeza and Mehling (2003)

example is lead acetate batteries however, long term stability of these storage is still a topic of research. The advantage of these materials is high storage density near ambient temperature; thus, losses are greatly subsided.

This study however, deals with PCMs for application in Indian climatic conditions.

13.3 PCM Properties and Methods of Characterization

13.3.1 Desired PCM Properties and Their Inherent Problems

The PCM selection for a particular application is to be made judiciously, with the help of the following parameters (Mehling and Cabeza 2008):

- Suitable phase change temperature and high latent heat; specifically, temperature must be determined with high accuracy (as melting and solidification temperature plays a critical role in storage and release of heat at required temperature which is a pre-requisite for any thermal energy storage system);
- Other thermophysical properties: large heat capacity, low volume change ratio, large density and thermal conductivity, no phase segregation and lower super-cooling;
- Chemical parameters: high chemical stability, no corrosion, low toxicity, non-inflammable, compatible and non-polluting;
- Economic parameters: good recyclability, proper availability and cheap.

PCMs also possess certain inherent problems that should to be addressed before their application. Some of the major issues are as follows:

- Super-cooling (also referred as sub-cooling). It is the difference in melting and solidification temperature; PCMs are to be cooled below their solidification onset temperature to initiate nucleation which is followed by crystallization/solidification. For inorganic PCMs, sub-cooling is significantly higher.
- Phase segregation. PCMs (generally hydrated salts and eutectic mixtures) generally exhibit phase segregation. They separate out during melting thus making it inhomogeneous.
- Low thermal conductivity. It is problem for most of the PCMs. For organic PCMs the thermal conductivity is below 0.5 W/m K. For inorganic PCMs it is generally below 1 W/m K.

To overcome the above disadvantages the foremost priority is to assess the PCM properties with high accuracy and precision as there is divergence in data or data mismatch in the available literature followed by measures to enhance the PCM properties as per their specific field of application.

13.3.2 Material Characterization

The characterization plays a significant role in material selection for TES systems. It is necessary for design, modelling and implementation of these systems. The available knowledge on PCMs is limited and in some cases even found to be inaccurate/incomplete (Saxena et al. 2017). PCMs (salts in particular) show incongruent melting (with melting occurring non-uniformly) and also showing sub-cooling. Thus, there is a need to characterize these PCMs to determine the temperature dependence of different thermophysical properties Energy efficient building constructions, incorporating PCM storage require accurate assessment of PCM properties with respect to temperature as single data point may not define the system with accuracy. The specific heat, latent heat, phase change temperature, sub-cooling has been accurately determined using differential scanning calorimeter. Thermal conductivity is measured using thermal conductivity meter.

Differential Scanning Calorimetry: Differential Scanning Calorimetry is a method in which heat transfer to sample and reference pan is measured along with rise in temperature. The difference in heat flow and rise in temperature profile gives the latent heat, phase change temperature, specific heat of the sample. It also determines the sub-cooling as well. Differential scanning calorimeter (DSC) is used to accurately evaluate these thermal properties and their temperature dependence.

Thermal Conductivity Meter: It determines the dispatchability of the TES systems, which is one of the most important characteristic property for any energy storage system. The thermal conductivity measurement in different phases is generally done by two methods, that is steady-state and transient. The heat flow meter and guarded hot plate techniques are steady-state methods both based on Fourier's law, which suits the solid phase measurements, but requires a lot of time attain stable temperature gradient within the specimen. The transient techniques on the other hand measures thermal conductivity within minutes, therefore researchers now often use this method for PCMs. Transient plane source, transient hot wire and laser flash are the example of transient methods (Khodadadi et al. 2013).

13.4 Methods of PCM Incorporation

The integration of TES in buildings can be of two types i.e. active and passive. In Active systems, energy required is often derived from renewable resources whereas, passive systems concentrate on energy saving using seasonal shadings, blinds, increasing thermal mass or thermal insulation, focusing on reducing the energy demand. The thermal mass may be increased by PCM incorporation in building components. Thus, it is necessary to understand different methods that may be used for the purpose and their respective merits and demerits as discussed in Navarro et al.

For integrating PCMs into any building, five methods have been suggested, they are, direct incorporation, immersion, vacuum impregnation, encapsulation, shape and form stabilized materials (Navarro et al. 2016a; b).

13.4.1 Direct Incorporation

It deals with adding PCM directly to the building material such as concrete etc. Feldman et al. carried out direct incorporation of butyl stearate by 22% in the gypsum. The energy storage capacity was reported to have increased by ten-fold times (Feldman et al. 1991). However, there can be leaking problems as reported by Soares et al. (2013). Direct incorporation in concrete is still a topic of research as there are two major challenges first is that PCMs undergo phase change thus, they often leak or separate out from the mixture. Second, they readily do not mix with concrete and separate out which is to be taken care of, while mixing. Thus, other techniques/methods are used for PCM mixing.

13.4.2 Immersion

In this method, the construction elements are soaked or dipped in the container filled with PCM, which thus gets absorbed within the construction material. Immersion method requires many hours of soaking (Ling and Poon 2013). This method however is often not used due to leakage problems (Soares et al. 2013) and due to compatibility issues with certain building materials (Hawes et al. 1989). This method however, is slightly different from direct incorporation however, it faces similar constraints and problems in case of PCMs.

13.4.3 Vacuum Impregnation

In this method the air is first evacuated using the vacuum pump and soaked in the PCM container thereby replacing the air in the pores by the PCM. There is an effective reduction in the overall thermal conductivity of the sample. This method is generally suitable in case of foams etc. where thermal conductivity is to be reduced for insulation purpose. This method however has similar shortcomings for solid-liquid PCMs as previous cases.

13.4.4 Encapsulation

It is the process of encapsulating the PCM before being incorporated in the buildings. It is of two types: micro-encapsulation and macro-encapsulation and have been dealt in detail by many researchers. Different researches are being carried out to find out materials that are suitable for the sheath and also the size and shape to provide a proper transfer surface and area (Su et al. 2015; Konuklu et al. 2015; Khadiran et al. 2015). Navarro et al. has provided with a number of examples of micro and macro-encapsulated PCM test constructions in Spain, Paris and other parts of the world. For Indian conditions PCMs within sheet metal casing have been tested experimentally within bricks (Saxena et al. 2019). Cylindrical encapsulations are assumed by Kant et al. (2017) for simulating PCM incorporated bricks for Rae Bareilly, India.

13.4.5 Shape and Form Stabilized Composites

These basically aim at mixing supporting materials like HDPE by melting it along with the PCMs at higher temperature thereby creating composites on cooling and could be used in the construction material and avoid leakage of the PCM on melting (Navarro et al. 2016). These PCMs however, are still at the research stage and their long-term impact, cost and compatibility are to be studied in detail before implementation for building applications.

13.5 Assessment of PCM Incorporation within Buildings

To assess the impact of PCM incorporated buildings first it is necessary to assess the heat flow to non-conditioned room. This is followed by assessing the impact of PCM incorporation within buildings. Kaushik et al. (1981) carried out the thermal modelling of PCM incorporated room by assuming the solar influx with constant ambient air temperature. Jan Kosny et al. (2012) have implemented PCM over roof in East Tennessee and reported 30% reduction in heating load and 50% reduction in cooling load. Similar findings were observed by Sleiti and Naimester (2016) for USA and Entrop et al. (2016) for Netherlands, with stabilized inside temperature with reduction in heating loads. For India, it may be noted that the conditions are just the opposite of western countries, where outside temperature is higher and cooling is required to maintain comfortable temperature inside a building.

Heat flow to the control volume adds to the cooling load requirement for space conditioning. Thus, the heat, which is stored acts as waste heat. PCM incorporation results in overall increase in the thermal mass of the building as it absorbs latent heat by undergoing phase change, thus reducing the need of heavy construction. Biplab and Rakshit (2017) compared insulations and PCMs for different climatic

conditions in India. PCMs showed better results in terms of temperature reduction and heat transfer reduction. Pasupathy et al. (Pasupathy et al. 2008) have tested PCM incorporation over roof for Chennai through direct incorporation. However, long term impact was not carried out. Kant et al. (2017) carried out CFD simulation for PCM integrated brick, for March 15, in Rae Barelli, India. Temperature of different sections of bricks at different time of day was simulated. PCM suitability however, has not been studied in any of these studies.

The testing of PCM bricks in actual conditions under various PCM configurations has been carried out by Saxena et al. (2019). For this purpose, modified mud bricks were prepared using conventional Indian brick making process, as it is well established and could be scaled for future applications. The experiments were carried out for peak summer conditions with ambient temperature of 40 °C and above. The reduction of 6 °C was observed. Heat transfer reduction up to 12% was observed.

13.6 PCM Thermal Conductivity Enhancement with Nanoparticle Dispersion

Owing to the low thermal conductivities of PCMs there has been a considerable effort towards enhancement of thermal conductivity thereby increasing the dispatchability of TES systems. Inorganic PCMs are cheap and have better thermal conductivities than the organic PCMs however their stability over large number of cycles of charging and discharging is still an issue. Tendency of super-cooling is also higher in the case of inorganic salts. Due to super-cooling, the PCM is to be cooled below the freezing point temperature before it actually starts freezing and release heat. More importantly, it would not solidify unless this lower (nucleating) temperature is reached. However, the accompanying temperature in the new cycle it only absorbs the sensible heat. Thus, the usability of the inorganic PCMs is significantly lowered. Apart from this, inorganic materials also have compatibility issues with metal containers etc. Table 13.3 compares inorganic and organic PCM.

The researchers across the globe are working to overcome the problem of low thermal conductivities of PCMs. Particularly for organic PCMs, thermal conductivity enhancement seems to be only issue that is to be addressed for which a number of solutions have been suggested in the literature. The researchers are aiming at creating composite materials by enhancing organic PCMs using metallic foam, nano-particles of metal oxides and carbon. Babapoor and Karimi (2015) compared the results of adding SiO_2, Al_2O_3, Fe_2O_3, ZnO nano to PCMs to create a nano enhanced PCM (NEPCM). Of these, Al_2O_3 nano was found to give best results in terms of thermal conductivity enhancement. A comparison was made using DSC for different metal oxide nanoparticles including Al_2O_3 and TiO_2 being added to medium temperature PCM (Teng and Yu 2012). It was found that, of the five metal oxide nanoparticles, TiO_2 was the best.

Table 13.3 Comparison of inorganic and organic PCM (Sharma et al. 2009)

Inorganic PCMs (−10 to 117 °C)	Organic PCMs (−30 to 200 °C)
• Low thermal conductivity (K) (0.3–0.8 W/mK)	• Low thermal conductivity; lower than inorganic PCMs (0.13–0.4 W/mK)
• Storage capacity 105–300 kJ/kg	• Storage capacity 120–210 kJ/kg
• Problem of sub-cooling exists nucleators required	• Low degree of sub-cooling hence no nucleators required
• Have sharp phase change temperatures	• Lack sharp phase change temperatures. Fatty acids show sharp phase change temperature but are three times more expensive
• They break down into smaller compounds and hence are rendered useless after a few cycles and get segregated	• High cycle stability
• Cause corrosion in metal containers	• Chemically non-corrosive (exception: fatty acids are mildly corrosive)

PCM has high viscosity thus, direct mixing of nano to PCMs are difficult to blend and form a homogeneous composite. Thus, advanced wet impregnation method has been used for this purpose (Shi et al. 2013). In this method PCMs are dissolved in a solvent and nano particles are added and sonicated for around 30 min. Once homogenized the solvent is evaporated to form a homogenous nano enhanced PCM. Certain researchers in the case of inorganic salts use water as solvent for mixing, however to maintain the homogeneity, small amount of additive is mixed to this composite. These are known as surfactants (Singh et al. 2019). Then the composite mixture is heated to evaporate water thus inorganic NEPCM is left behind. For organic PCMs, generally, toluene or acetone is used as solvent, based on the solubility and compatibility. These composite PCMs are then characterized for determining the properties and improvement with the help of DSC and thermal conductivity meter. In building perspective, the impact of enhanced thermal conductivity for better discharge characteristics is yet to be tested experimentally. Apart from using composite PCMs another solution is to use different designs to assist heat transfer like the study of Hoogendoorn and Bart (Hoogendoorn and Bart 1992). This study discussed performance and modelling of latent heat storage materials and suggested use of thin film aluminum matrix embedded within PCM to reduce the solidification time due to increase in effective thermal conductivity.

13.7 PCM Selection and Mapping for Building Application in India

Extensive literature review is carried out on different types of PCMs, their thermophysical properties and specific application in buildings. Adding PCM to the building envelop increases the heat storage capacity of the building elements. This chapter

is focused towards assessing the PCMs suitability for different Indian conditions, find the impact of PCM incorporation within the building envelop. Before carrying out a detailed analysis first it is necessary to assess the potential PCMs that may be suitable for application, this is referred to as PCM mapping. This chapter assesses the average temperature of the place for different places followed by mapping of PCMs for different climatic conditions in India.

The weather of a place is determined based on its climatic conditions i.e. temperature, solar radiation falling, humidity, wind speed etc. Location, altitude, time of day and year, orientation are other important parameters which affect the solar radiation thereby controlling the temperature of a building. For example, buildings on a south facing slope in Leh will receive more radiation compared to other orientations.

Based on these factors, weather and climatic condition in India is divided into five zones. Table 13.4 provides description about each. Knowing the climatic condition, it becomes easier to designate particular PCM to suit the existing daily conditions. During the day, PCM will store most of the solar radiation. During the night, PCM temperature is greater than ambient thus, the heat flow direction is reversed and energy stored is now discharged to the ambient. It is important for a PCM to get discharged so as to be able to absorb heat the next day. To ensure PCM charging and discharging daily, it is necessary to carefully choose the PCM. The charging and discharging of PCM depends upon the temperature fluctuation of the place which is governed by its climatic condition and inherent PCM properties. Especially focusing the temperate regions, the heat stored in the PCMs can be sufficiently high, thus, would help in keeping the conditions comfortable or in some cases at least tolerable for any person inside the room.

For this study, certain cities were selected from each climatic zone and data for mean hourly temperature for all the months was taken from the literature for all these places. The following case studies are presented for Delhi, Jaipur, and Chennai to access the heat flow reduction during the peak hours. The surface is assumed to be covered with particular mapped PCM, so as to absorb or entrap solar energy during peak hours. A surface temperature of 27 °C is assumed on the other side (T_{wi}) of the PCM incorporated surface as shown in Fig. 13.2.

Table 13.4 Specification for different Indian climatic zones (Nayak and Prajapati 2006)

Criteria	Climate	R.H. (%)	Average monthly temperature (°C)
I	Warm and humid	>55 >75	>30 >25
II	Hot and dry	<55	>30
III	Temperate	<75	25–30
IV	Cold	All values	<25
V	Composite	If do not fulfill any of the above criteria for more than 6 months	

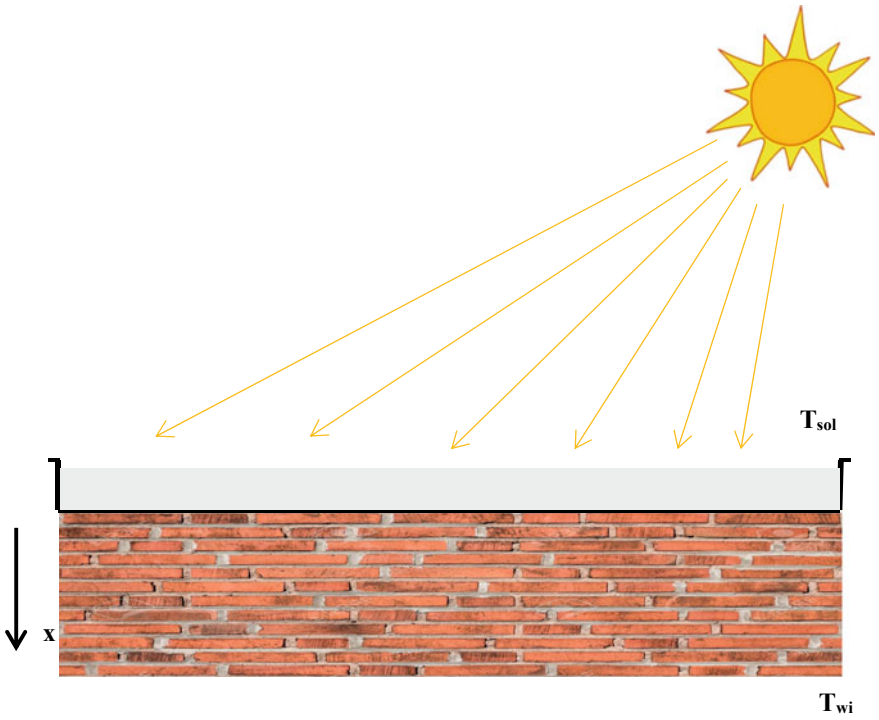

Fig. 13.2 Schematic geometry

13.8 Design Conditions

13.8.1 Case Study 1: Delhi (Altitude: 416° M, Latitude 28.6° N, Longitude 77.2° E)

It lies in type-V (composite) climatic zone. The mean average temperature in winter can be as low as 6.6 °C in the month of Dec-Jan and can be as high as 40.5 °C in June (Fig. 13.3). It is observed that significant amount of energy is utilized for cooling purpose. The cooling loads in Delhi are at peak between 11 a.m. and 4 p.m. This is when the solar intensity is at peak. Assuming the solar radiation to be 600 W/m^2 (April-October during peak hours) (actual value normally varies between 580 to 680 W/m^2 (Tyagi 2009) falling on a surface of dimension 4 × 2.5 m^2. For Delhi mean wind velocity was taken to be 10.8 km/h.

The average monthly minimum and maximum temperature of a place, is key for selecting the a PCM for that particular place. The phase change temperature must lie within the range of maximum and minimum temperature or else it would be rendered useless. Thus, the choice of the materials is made by mapping the minimum and maximum temperature of Delhi for the months of April to October and the energy

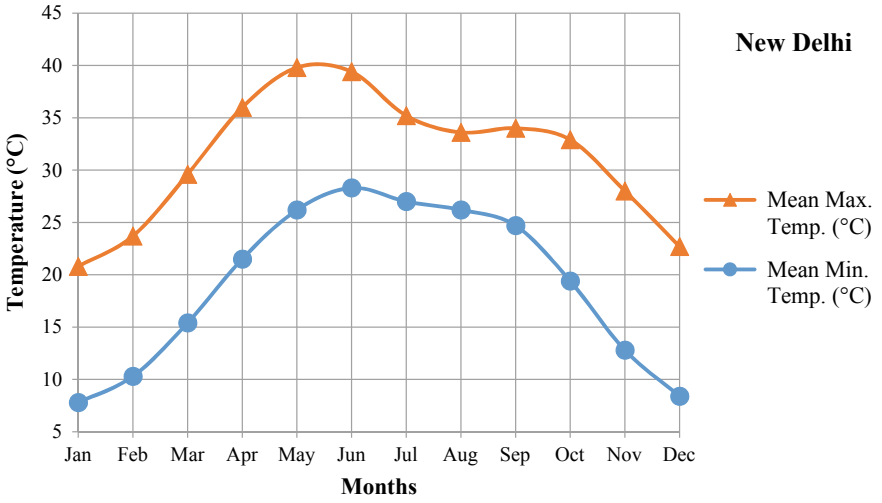

Fig. 13.3 Average monthly maximum and minimum temperature for New Delhi

savings per day was calculated on the basis of mean hourly temperature between 11 a.m. and 4 p.m. i.e. for five consecutive hours, in which cooling load is maximum. This energy saving is consequence of the solar insolation which falls on the surface and gets absorbed and is stopped from being transferred. The PCM is kept in a rectangular tray (of insulated material) having internal dimensions of 4 m × 2.5 m × 0.2 m. The PCM is filled in the tray and kept on the roof in the direct sunlight.

The solar air temperature is calculated from 11 a.m. to 4 p.m. Difference in sol air temperature and ambient temperature is significant and determines the heat flow to the inside. The total energy that could be transferred and stored in the different PCMs is calculated and the energy saving in kWh (unit of electricity) per day is calculated.

13.8.2 Case Study 2: Jaipur (Altitude: 431° M, Latitude 28.9° N, Longitude 75.8° E)

It lies in type-II (hot and dry) climatic zone. The mean average temperature in winter is 8.2 °C in the month of Dec-Jan and can be as high as 40.3 °C in June (Fig. 13.4). Assuming the solar radiation to be 660 W/m^2 (April-October during peak hours) (actual value normally varies between 640 and 690 W/m^2 (Tyagi et al. 2011) falling on a surface of dimension 4 × 2.5 m^2. For Jaipur mean wind velocity was taken to be 8 km/h.

Since the mean minimum temperature is below 30 °C hence same PCMs suit for the weather conditions in Jaipur as well. The mean hourly sol air temperature

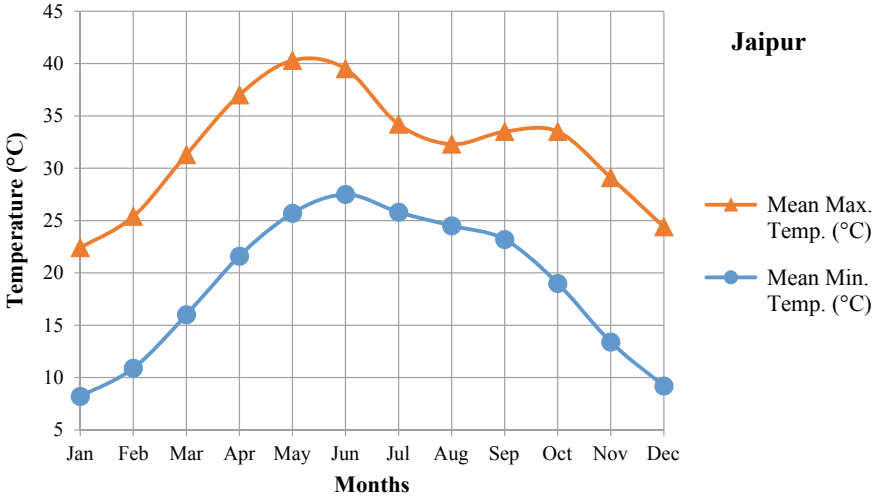

Fig. 13.4 Average monthly maximum and minimum temperature for Jaipur

is calculated and used in calculating heat absorbed by PCMs. The total energy that could be stored in different PCMs is calculated and hence the energy savings in kWh.

There is a relative increase in energy stored in the PCMs owing to the fact that the effective sol air temperature in Jaipur is higher, as h_o value is less due to lower wind speed than Delhi and higher solar insolation.

13.8.3 Case Study 3: Chennai (Altitude: 6° M, Latitude 13.1° N, Longitude 80.3° E)

It lies in type-I (warm and humid) climatic zone. The mean average temperature in winter is about 20.4 °C in the month of Dec-Jan and can be as high as 37.4 °C in May (Fig. 13.5). Assuming the solar radiation to be 630 W/m^2 (April-October during peak hours) (actual value normally varies between 620 and 660 W/m^2 (Tyagi 2009) falling on a surface of dimension 4 × 2.5 m^2. For Chennai, mean wind velocity is much higher than Delhi and Jaipur, and is taken to be 20 km/h.

Same PCMs suit for the temperatures at Chennai as well. Owing to the higher wind velocity in Chennai, the effective ho value is also much higher therefore sol air temperature is much lower in Chennai. Based on these values of the amount of energy that can be stored in the PCMs is calculated.

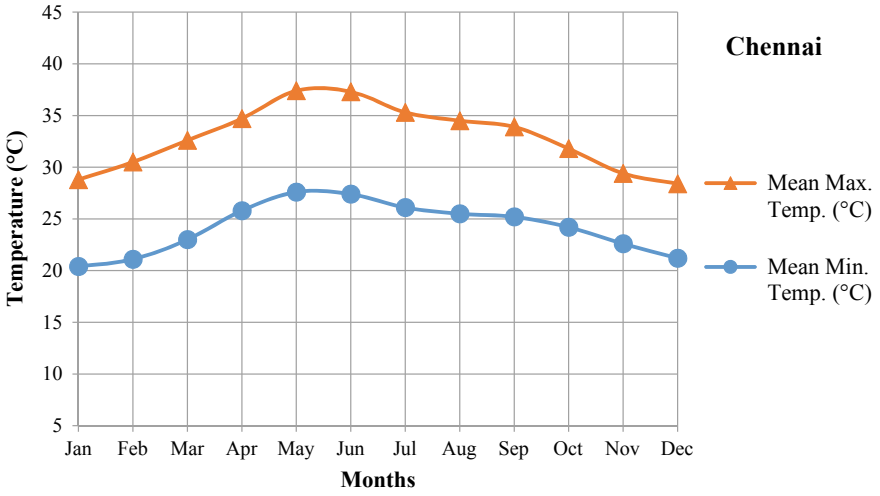

Fig. 13.5 Average monthly maximum and minimum temperature for Chennai

13.9 Thermal Calculations

In order to calculate the temperature difference, which would be driving the heat transfer to take place, the sol-air temperature needs to be defined. It is an effective outer surface temperature which considers both radiation and convection (Duffie and Beckman 2013). The sol air temperature (T_{sol}) is as follows:

$$T_{sol} = T_a + \left(\frac{\alpha \, \mathrm{I} - \varepsilon \, \Delta \mathrm{R}}{h_o} \right) \tag{13.4}$$

where, 'T_a' is ambient temperature, 'α' and 'ε' are absorptivity and emissivity of surface.

ΔR = Long wavelength radiative exchange from surface to sky.
ε.ΔR ≈ 60 W/m^2 for horizontal and 0 for vertical surfaces.
'I' is the global solar insolation and h_o is coefficient of heat transfer.

h_o is evaluated from Eq. 13.5 (McAdams (1954) relation):

$$h_o = 5.7 + 3.8\,\mathrm{s} \quad \text{for} \quad 0 < \mathrm{s} < 5\,\mathrm{m/s} \tag{13.5}$$

where, 's' is wind speed.

Heat transfer (Q) is calculated using:

$$Q = U_{ef} \mathrm{A}(T_{sol} - T_{wi}) \tag{13.6}$$

where, 'U_{ef}' is overall heat transfer coefficient and 'A' is exposed area.

$$\frac{1}{U_{ef}} = \frac{1}{h_o} + \frac{\delta_1}{k_1} + \frac{\delta_2}{k_2} + \frac{\delta_3}{k_3} \tag{13.7}$$

where, δ_1, δ_2, δ_3, k_1, k_2, k_3 are thickness and the thermal conductivity (W/mK) of PCM, tray material and brick respectively. k_2 is assumed to be very high hence term $\frac{\delta_2}{k_2} \approx 0$ (assumed).

13.10 Results and Discussion

The comparative values of mean ambient temperature and the sol air temperature for the month of May are plotted and shown in Fig. 13.6. The value of sol air temperatures for Chennai is relatively lower to that of Jaipur and New Delhi as the wind velocity in Chennai is much higher than the other two places, resulting in the higher value of convective heat transfer coefficient ho. This justifies the lower energy storage in the PCMs in Chennai.

Figure 13.7 shows a comparison between two different PCMs and a sensible heat storage material i.e. concrete for three different climatic conditions of New Delhi, Jaipur and Chennai. The comparison clearly shows that more energy can be stored using PCMs for all climatic conditions.

These initial calculations made affirms that PCM incorporation can save significant amount of energy however, detailed thermal modelling is required, considering a complete room incorporated with PCM.

A complete cyclic study is necessary as this study considers heat storage only during the peak hours. The PCM temperatures has not been modelled and assumed

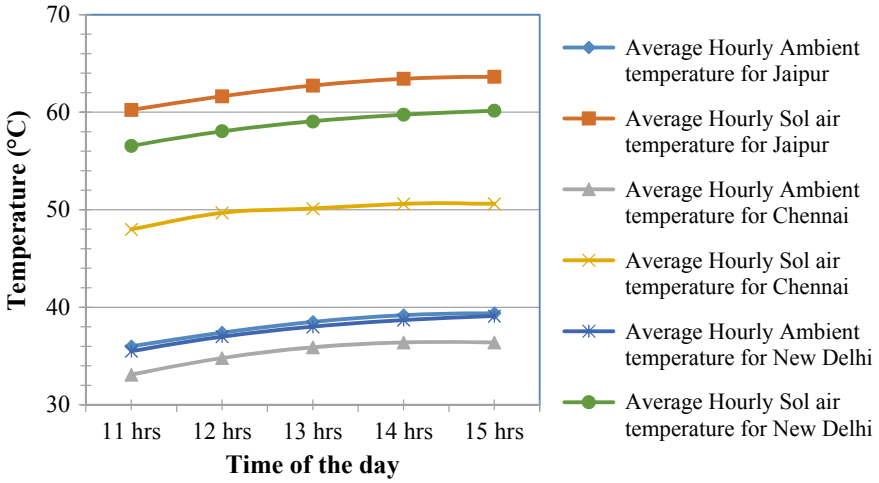

Fig. 13.6 Average hourly ambient and sol air temperatures for the month of May

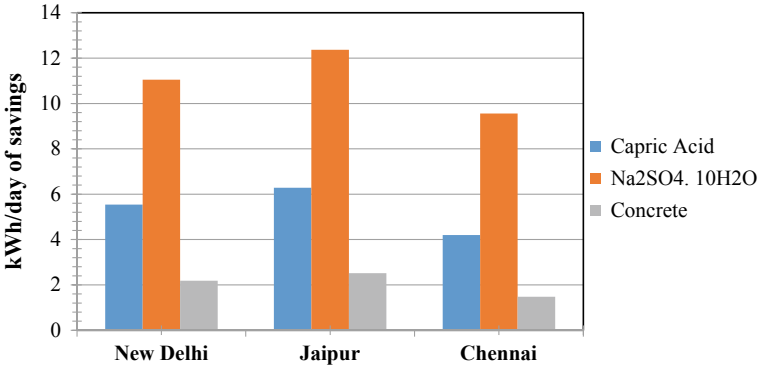

Fig. 13.7 Comparative kWh/day savings for different materials and places

to be constant at its phase change temperature as complete melting do not take place during the period of five hours. Further there is a need to assess the discharging of the PCM during the night, which is necessary for PCM to absorb heat on the subsequent day.

13.10.1 Mapping/Selection of PCM

Adding PCM to the building envelop increases the storage capacity of walls/roof. Mapping of different PCM is carried out for different climatic conditions in India. Selection of PCM is done based on the melting temperature (as given in literature) and the mean maximum and minimum temperature of the location. Both maximum and minimum temperatures are considered as higher temperature during day melts the PCM and when the temperature of the ambient is lower PCM releases heat and gets discharged. It is necessary for the PCM to get solidified during the night or else it will behave as a sensible heat storage, thus, reducing its storage capacity significantly. Figure 13.8 and Table 13.5 show different PCMs that are selected based on melting temperature and mean temperature of the places.

The PCMs are selected within the maximum and minimum temperature of the places. However, they must be simulated for a PCM incorporated room to assess their charging and discharging on implementation within buildings. This must be followed by characterization of these PCMs to assess their thermophysical properties and their temperature dependence to determine any mismatch in properties.

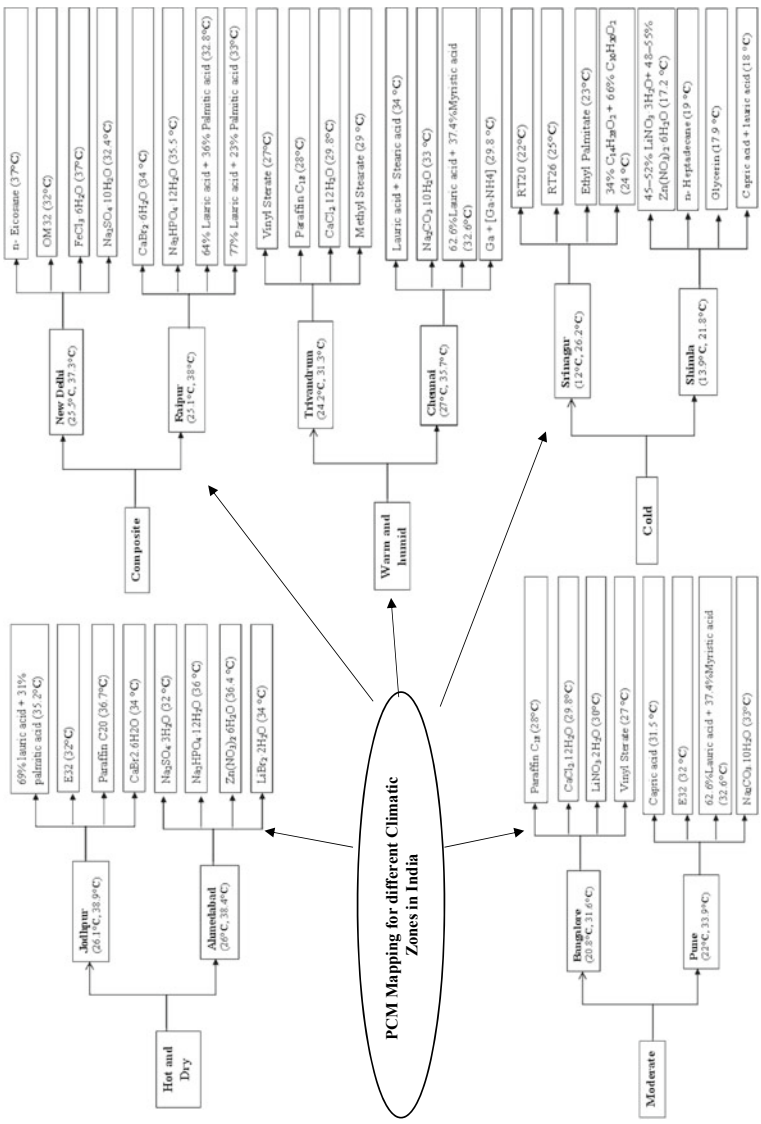

Fig. 13.8 PCM mapping for different climatic conditions in India

Table 13.5 PCM selected for different climatic conditions in India

Hot and dry				Cold						Moderate			
Jodhpur		Ahmedabad		Srinagar		Shimla		Leh		Bangalore		Pune	
Min avg temp (°C)	26.1	**Min avg temp (°C)**	26	**Min avg temp (°C)**	12.9	**Min avg temp (°C)**	13.9	**Min avg temp (°C)**	5	**Min avg temp (°C)**	20.8	**Min avg temp(°C)**	22
Max avg temp (°C)	38.9	**Max avg temp (°C)**	38.4	**Max avg temp (°C)**	26.2	**Max avg temp (°C)**	21.8	**Max avg temp (°C)**	18.8	**Max avg temp (°C)**	31.6	**Max avg temp (°C)**	33.9
PCM	**Melting point (°C)**	**PCM**	**Melting point (°C)**	**PCM**	**Melting point (°C)**	**PCM**	**Melting point (°C)**	**PCM**	**Melting point (°C)**	**PCM**	**Melting point (°C)**	**PCM**	**Melting point (°C)**
Climsel C32	32 (De Gracia and Cabeza 2015)	$Na_2SO_4 \cdot 3H_2O$	32 [Sharma et al. 2009]	RT20	22 (Sharma et al. 2009)	45–52% $LiNO_3 \cdot 3H_2O$ + 48–55% $Zn(NO_3)_2 \cdot 6H_2O$	17.2 (Sharma et al. 2009)	Caprylic acid	16 (Sharma et al. 2009)	Paraffin C_{18}	28 (De Gracia and Cabeza 2015; Mehling and Cabeza 2008; Sharma et al. 2009)	Climsel C32	32 (De Gracia and Cabeza 2015)
E32	32 (Liu et al. 2012)	80% lauric acid + 20% palmitic acid	32.7 (Liu et al. 2012)	RT26	25 (Sharma et al. 2009)	n-Heptadecane	19 (De Gracia and Cabeza 2015)	Climsel C15	15 (De Gracia and Cabeza 2015)	$CaCl_2.12H_2O$	29.8 (Mehling and Cabeza 2008)	E32	32 (Liu et al. 2012)

(continued)

Table 13.5 (continued)

Hot and dry				Cold						Moderate			
Jodhpur		Ahmedabad		Srinagar		Shimla		Leh		Bangalore		Pune	
Paraffin C_{20}	36.7 (Mehling and Cabeza 2008)	$Na_2HPO_4 \cdot 12H_2O$	36 (De Gracia and Cabeza 2015)	45% $Ca(NO_3)_2 \cdot 6H_2O$ + 55% $Zn(NO_3)_2 \cdot 6H_2O$	25 (Saxena et al. 2017)	61.5 mol% capric acid + 38.5 mol% lauric acid	19 (Liu et al. 2012)	48% butyl palmite + 48% butyl stearate + 3% other	17 (Liu et al. 2012)	$LiNO_3.2H_2O$	30 (Mehling and Cabeza 2008)	$Na_2CO_3 .10H_2O$	33 (De Gracia and Cabeza 2015)
69% lauric acid + 31% palmitic acid	35.2 (Liu et al. 2012)	$Zn(NO_3)_2 \cdot 6H_2O$	36.4 (De Gracia and Cabeza 2015)	Ethyl Palmitate	23 (Liu et al. 2012)	Glycerin	17.9 (Mehling and Cabeza 2008)	NaOH ·(3/2)H2O	15 (Liu et al. 2012)	Vinyl Sterate	27 (Sharma et al. 2009)	62.6% lauric acid + 37.4% myristic acid	32.6 (Liu et al. 2012)
$CaBr_2 \cdot 6H_2O$	34 (De Gracia and Cabeza 2015)	$LiBr_2 \cdot 2H_2O$	34 (Mehling and Cabeza 2008)	34% $C14H28O_2$ + 66% $C10H20O_2$	24 (Mehling and Cabeza 2008)	Capric acid + lauric acid	18 (Liu et al. 2012)	38.5% trimethylolethane + 31.5% water + 30% urea	14.4 (Liu et al. 2012)	TH29	29 (De Gracia and Cabeza 2015)	Paraffin C_{19}	32 (Mehling and Cabeza 2008)
$FeCl_3 \cdot 6H_2O$	37 (De Gracia and Cabeza 2015)	$Mn(NO_3) \cdot 6H_2O$	37.1 (Mehling and Cabeza 2008)	Climsel C24	24 (Sharma et al. 2009)	45% capric acid + 55% lauric acid	21 (Liu et al. 2012)	Dimethyl sulfoxide (DMSO)	16.5 (De Gracia and Cabeza 2015; Sharma et al. 2009)	RT30	28 (De Gracia and Cabeza 2015)	Capric acid	31.5 (De Gracia and Cabeza 2015)

(continued)

Table 13.5 (continued)

Warm and humid						Composite					
Trivandrum		Chennai		Guwahati		New Delhi		Lucknow		Raipur	
Min avg temp (°C)	24.2	**Min avg temp (°C)**	27	**Min avg temp (°C)**	23.1	**Min avg temp (°C)**	25.5	**Min avg temp (°C)**	24.4	**Min avg temp (°C)**	25.1
Max avg temp (°C)	31.3	**Max avg temp (°C)**	35.7	**Max avg temp (°C)**	31.3	**Max avg temp (°C)**	37.3	**Max avg temp (°C)**	37.5	**Max avg temp (°C)**	38.1
PCM	**Melting point (°C)**	**PCM**	**Melting point (°C)**	**PCM**	**Melting point (°C)**	**PCM**	**Melting point (°C)**	**PCM**	**Melting point (°C)**	**PCM**	**Melting point (°C)**
Vinyl Sterate	27 (Sharma et al. 2009)	Lauric acid + stearic acid	34 (Liu et al. 2012)	4.3% NaCl + 0.4% KCl + 48% CaCl2 + 47.3% H_2O	27 (Sharma et al. 2009)	n-Eicosane	37 (Saxena et al. 2018)	$Zn(NO_3)_2 \cdot 6H_2O$	36.4 (De Gracia and Cabeza 2015)	77% lauric acid + 23% palmitic acid	33 (Liu et al. 2012)
Paraffin C_{18}	28 (De Gracia and Cabeza 2015; Sharma et al. 2009)	$LiBr_2.2H_2O$	34 (Mehling and Cabeza 2008)	$LiNO_3 \cdot 3H_2O$	30 (De Gracia and Cabeza 2015; Sharma et al. 2009)	E32	32 (Liu et al. 2012)	62% lauric acid + 38% myristic acid	32.6 (Liu et al. 2012)	Capric acid	36 (De Gracia and Cabeza 2015)
$CaCl_2.12H_2O$	29.8 (Mehling and Cabeza 2008)	$Na_2CO_3 .10H_2O$	33 (De Gracia and Cabeza 2015)	47% $Ca(NO_3)2 \cdot 4H_2O$ + 53% $Mg(NO_3)_2 \cdot 6H_2O$	30 (De Gracia and Cabeza 2015)	Paraffin C_{20}	36.7 (Mehling and Cabeza 2008)	$Mn(NO_3) \cdot 6H_2O$	37.1 (Mehling and Cabeza 2008)	64% lauric acid + 36% palmitic acid	32.8 (Liu et al. 2012)
Ga	30 (Mehling and Cabeza 2008)	62.6% lauric acid + 37.4% myristic acid	32.6 (Liu et al. 2012)	$LiNO_3.2H_2O$	30 (Mehling and Cabeza 2008)	OM32	33 (Mehling and Cabeza 2008)	Polyglycol E 1000	35–40 (Sharma et al. 2009)	66% lauric acid + 34% myristic acid	34.2 (Liu et al. 2012)
Methyl stearate	29 (Liu et al. 2012)	Ga + [Ga-NH_4]	29.8 (Mehling and Cabeza 2008)	62.5% Trimethylolethane + 37% water	29.8 (Liu et al. 2012)	$FeCl_3 \cdot 6H_2O$	37 (De Gracia and Cabeza 2015)	80% lauric acid+20% palmitic acid	32.7 (Liu et al. 2012)	$CaBr_2 \cdot 6H_2O$	34 (De Gracia and Cabeza 2015)
n-Octadecane	28 (De Gracia and Cabeza 2015)	Capric acid	31.5 (De Gracia and Cabeza 2015)	RT30	28 (De Gracia and Cabeza 2015)	$Na_2SO_4 \cdot 10H_2O$	32.4 (De Gracia and Cabeza 2015)	$CaBr_2 \cdot 6H_2O$	34 (De Gracia and Cabeza 2015)	$Na_2HPO_4 \cdot 12H_2O$	35.5 (De Gracia and Cabeza 2015)

13.11 Conclusions

This chapter is key in selecting particular PCMs for heat flow reduction in buildings for different conditions in India. Studies carried out so far discuss about PCM integration however, proper method for PCM selection has been found missing for cooling load reduction of buildings in India. This study provides a comprehensive description about different PCMs, their properties, advantages, challenges and methods of implementation and incorporation followed by their assessment in buildings. The studies carried out in Indian context have been reviewed and impact of PCM incorporation for different cities has been discussed. PCMs have been categorized for cities lying in different climatic conditions based on their temperature variation and phase change temperature of the PCMs.

Significant energy savings can be achieved with PCM incorporation as shown in this study however, proper selection of PCMs is necessary in terms to their phase change temperature, thermal stability and compatibility. This study envisages that significant potential exits and more experimental studies need to be carried out to assess the overall savings through PCM implementation within buildings in India. This study can form the basis of initial PCM selection, benchmarking and their implementation within Indian buildings.

References

Abhat A (1983) Low temperature latent heat thermal energy storage: heat storage materials. Sol Energy 30:313–332. https://doi.org/10.1016/0038-092x(83)90186-x

Agyenim F, Hewitt N, Eames P, Smyth M (2010) A review of materials, heat transfer and phase change problem formulation for latent heat thermal energy storage systems (LHTESS). https://doi.org/10.1016/j.rser.2009.10.015

Babapoor A, Karimi G (2015) Thermal properties measurement and heat storage analysis of paraffinnanoparticles composites phase change material: comparison and optimization. Appl Therm Eng 90:945–951. https://doi.org/10.1016/j.applthermaleng.2015.07.083

Benoit H, Spreafico L, Gauthier D, Flamant G (2016) Review of heat transfer fluids in tube-receivers used in concentrating solar thermal systems: Properties and heat transfer coefficients. Renew Sustain Energy Rev 55:298–315. https://doi.org/10.1016/j.rser.2015.10.059

Biplab K, Rakshit D (2017) Comparative assessment of thermal comfort with insulation and phase change materials utilizations in building roofs and walls. Adv Mater Proc 2:393–397. https://doi.org/10.5185/amp.2017/609

Cabeza LF, Mehling H (2003) Review on thermal energy storage with phase change : materials, heat transfer analysis and applications

Cabeza LF, Castell A, Barreneche C, de Gracia A, Fernández AI (2011) Materials used as PCM in thermal energy storage in buildings: a review. Renew Sustain Energy Rev 15:1675–1695. https://doi.org/10.1016/j.rser.2010.11.018

De Gracia A, Cabeza LF (2015) Phase change materials and thermal energy storage for buildings. Energy Build 103:414–419. https://doi.org/10.1016/j.enbuild.2015.06.007

Duffie JA, Beckman WA (2013) Solar engineering of thermal processes. Wiley, Fourth

Entrop AG, Halman JIM, Dewulf GPMR, Reinders AHME (2016) Assessing the implementation potential of PCMs: the situation for residential buildings in the Netherlands. Energy Procedia 96:17–32. https://doi.org/10.1016/j.egypro.2016.09.090

Farid MM, Khudhair AM, Razack SAK, Al-Hallaj S (2004) A review on phase change energy storage: materials and applications. Energy Convers Manag 45:1597–1615. https://doi.org/10.1016/j.enconman.2003.09.015

Feldman D, Banu D, Hawes D, Ghanbari E (1991) Obtaining an energy storing building material by direct incorporation of an organic phase change material in gypsum wallboard. Sol Energy Mater 22:231–242. https://doi.org/10.1016/0165-1633(91)90021-C

Hawes DW, Banu D, Feldman D (1989) Latent heat storage in concrete. Sol Energy Mater 19:335–348. https://doi.org/10.1016/0165-1633(89)90014-2

Hoogendoorn CJ, Bart GCJ (1992) Performance and modelling of latent heat stores. Sol Energy 48:53–58. https://doi.org/10.1016/0038-092x(92)90176-B

Kant K, Shukla A, Sharma A (2017a) Advancement in phase change materials for thermal energy storage applications. https://doi.org/10.1016/j.solmat.2017.07.023

Kant K, Shukla A, Sharma A (2017b) Heat transfer studies of building brick containing phase change materials. Sol Energy 155:1233–1242. https://doi.org/10.1016/J.SOLENER.2017.07.072

Kaushik SC, Sodha MS, Bhardwaj SC, Kaushik ND (1981) Periodic heat transfer and load levelling of heat flux through a PCCM thermal storage wall/roof in an air-conditioned building. Build Environ 16:99–107. https://doi.org/10.1016/0360-1323(81)90026-3

Khadiran T, Hussein MZ, Zainal Z, Rusli R (2015) Encapsulation techniques for organic phase change materials as thermal energy storage medium: a review. Sol Energy Mater Sol Cells 143:78–98. https://doi.org/10.1016/j.solmat.2015.06.039

Khodadadi JM, Fan L, Babaei H (2013) Thermal conductivity enhancement of nanostructure-based colloidal suspensions utilized as phase change materials for thermal energy storage: a review. Renew Sustain Energy Rev 24:418–444. https://doi.org/10.1016/j.rser.2013.03.031

Khudhair AM, Farid MM (2004) A review on energy conservation in building applications with thermal storage by latent heat using phase change materials. Energy Convers Manag 45:263–275. https://doi.org/10.1016/S0196-8904(03)00131-6

Konuklu Y, Ostry M, Paksoy HO, Charvat P (2015) Review on using microencapsulated phase change materials (PCM) in building applications. Energy Build 106:134–155. https://doi.org/10.1016/j.enbuild.2015.07.019

KoŚny J, Biswas K, Miller W, Kriner S (2012) Field thermal performance of naturally ventilated solar roof with PCM heat sink. Sol Energy 86:2504–2514. https://doi.org/10.1016/j.solener.2012.05.020

Ling T-C, Poon C-S (2013) Use of phase change materials for thermal energy storage in concrete: an overview. Constr Build Mater 46:55–62. https://doi.org/10.1016/j.conbuildmat.2013.04.031

Liu M, Saman W, Bruno F (2012) Review on storage materials and thermal performance enhancement techniques for high temperature phase change thermal storage systems. Renew Sustain Energy Rev 16:2118–2132. https://doi.org/10.1016/j.rser.2012.01.020

McAdams WH (1954) Heat transmission. McGraw-Hill, New York, pp 252–262

Mehling H, Cabeza LF (2008) Heat and cold storage with PCM : an up to date introduction into basics and applications. Springer

Mehling H, Cabeza LF (2008) Heat and cold storage with PCM an up to date introduction into basics and applications. Springer

Navarro L, de Gracia A, Colclough S, Browne M, McCormack SJ, Griffiths P, Cabeza LF (2016a) Thermal energy storage in building integrated thermal systems: a review. Part 1. Active storage systems. Renew Energy 88:526–547. https://doi.org/10.1016/j.renene.2015.11.040

Navarro L, de Gracia A, Niall D, Castell A, Browne M, McCormack SJ, Griffiths P, Cabeza LF (2016b) Thermal energy storage in building integrated thermal systems: a review. Part 2 integration as passive system. Renew Energy 85:1334–1356. https://doi.org/10.1016/j.renene.2015.06.064

Nayak JK., Prajapati JA (2006) Chapter -2 climate and buildings. in: handbook on energy conscious buildings

Pasupathy A, Athanasius L, Velraj R, Seeniraj RV (2008) Experimental investigation and numerical simulation analysis on the thermal performance of a building roof incorporating phase change material (PCM) for thermal management. Appl Therm Eng 28:556–565. https://doi.org/10.1016/j.applthermaleng.2007.04.016

Pluss Polymers (2017) Pluss PCM technical data sheet

Saxena R, Biplab K, Rakshit D (2017) Quantitative assessment of phase change material utilization for building cooling load abatement in composite climatic condition. J Sol Energy Eng 140:011001. https://doi.org/10.1115/1.4038047

Saxena R, Rakshit D, Kaushik SC (2018) Experimental assessment of characterised PCMs for thermal management of buildings in tropical composite climate. https://doi.org/10.11159/htff18.170

Saxena R, Rakshit D, Kaushik SC (2019) Phase change material (PCM) incorporated bricks for energy conservation in composite climate: a sustainable building solution. Sol Energy 183:276–284. https://doi.org/10.1016/j.solener.2019.03.035

Sharma A, Tyagi VV, Chen CR, Buddhi D (2009) Review on thermal energy storage with phase change materials and applications. Renew Sustain Energy Rev 13:318–345. https://doi.org/10.1016/j.rser.2007.10.005

Shi J-N, Ger M-D, Liu Y-M, Fan Y-C, Wen N-T, Lin C-K, Pu N-W (2013) Improving the thermal conductivity and shape-stabilization of phase change materials using nanographite additives. Carbon N Y 51:365–372. https://doi.org/10.1016/j.carbon.2012.08.068

Singh RP, Xu H, Kaushik SC, Rakshit D, Romagnoli A (2019) Charging performance evaluation of finned conical thermal storage system encapsulated with nano-enhanced phase change material. Appl Therm Eng 151:176–190. https://doi.org/10.1016/J.APPLTHERMALENG.2019.01.072

Sleiti AK, Naimaster EJ (2016) Application of fatty acid based phase-change material to reduce energy consumption from roofs of buildings. J Sol Energy Eng 138:051003. https://doi.org/10.1115/1.4033574

Soares N, Costa JJ, Gaspar AR, Santos P (2013) Review of passive PCM latent heat thermal energy storage systems towards buildings energy efficiency. Energy Build 59:82–103. https://doi.org/10.1016/j.enbuild.2012.12.042

Solutia (1998) Technical bulletin 7239115C (supersedes 7239115B), therminol VP-1, heat transfer fluid

Su W, Darkwa J, Kokogiannakis G (2015) Review of solid-liquid phase change materials and their encapsulation technologies. Renew Sustain Energy Rev 48:373–391. https://doi.org/10.1016/j.rser.2015.04.044

Teng T-P, Yu C-C (2012) Characteristics of phase-change materials containing oxide nano-additives for thermal storage. Nanoscale Res Lett 7:611. https://doi.org/10.1186/1556-276X-7-611

Tyagi AP (2009) Solar radiant energy over India

Tyagi A, Singh OP, Singh SS, Kumar S (2011) Climate of Jaipur meteorological centre, Jaipur India meteorological department ministry of earth sciences government of India

Zalba B, Marín JM, Cabeza LF, Mehling H (2003) Review on thermal energy storage with phase change: materials, heat transfer analysis and applications. Appl Therm Eng 23:251–283. https://doi.org/10.1016/s1359-4311(02)00192-8

Zhou D, Zhao CY, Tian Y (2012) Review on thermal energy storage with phase change materials (PCMs) in building applications. Appl Energy 92:593–605. https://doi.org/10.1016/J.apenergy.2011.08.025

Chapter 14
Fabrication and Thermal Performance Evaluation of Metastable Supercooled Liquid PCM Based Heat Pack

Rohitash Kumar, Sumita Vyas, Bobin Mondal, Ravindra Kumar and Ambesh Dixit

Abstract Metastable supercooled liquid phase change material (MSLPCM) is prepared by homogeneous mixing of sodium acetate trihydrate (SAT), water and ethylene glycol (EG) in 92:5:3 weight fractions, respectively. A stainless steel (SS-306) triggering disk of size 20 mm (L) × 18 mm (W) × 0.2 mm (T) is fabricated by engraving grooves on SS disk for initiating nucleation in heat pack and release of heat at the time of requirement. The PCM heat pack containing 300 g PCM and a triggering disk is fabricated using high frequency PVC sealing machine. Thermal performance of identical PCM heat pack and water pack (300 g water) is carried out inside temperature history measuring setup at 0 °C ambient temperature. The temperature of PCM heat pack and water heat pack reduces from 70 to 30 °C in 210 and 48 min, respectively at 0 °C ambient temperature. The heating time of PCM heat pack is ~4.4 times more compared to water heat packs.

Keywords Phase change material · Supercooling · T-history · Latent heat · Heat packs

14.1 Introduction

The prolonged exposure of the human body to very low ambient temperature conditions may cause health problems such as frostbite and hypothermia. It is also very difficult to go outside for work in such ambient conditions. Therefore, it is desirable to use insulating clothing for thermal comfort and to reduce heat loss from the body to the environment, maintaining the safe temperature limits for a human body in an extreme cold environment. In the case of hypothermia and frostbite conditions, the external heating source is required to provide heat to the body, maintaining the body temperature in the safe limit for enhancing blood circulation and to reduce cold socks

R. Kumar · S. Vyas · B. Mondal · R. Kumar
Defence Laboratory, Ratanada, Jodhpur 342011, India
e-mail: dootrohit1976@gmail.com

R. Kumar · A. Dixit (✉)
Department of Physics, Indian Institute of Technology Jodhpur, Jodhpur 342037, India
e-mail: ambesh@iitj.ac.in

H. Tyagi et al. (eds.), *Solar Energy*, Energy, Environment, and Sustainability, https://doi.org/10.1007/978-981-15-0675-8_14

and related adverse effects. Various technologies such as hot water bottles, electric pads, electric blankets, and insulating clothing are being used to provide the thermal comfort for inhabitants living in extremely cold conditions (Watson and Watson 1976). The insulating clothing maintains body temperature by reducing the rate of heat transfer between the human body and surrounding ambient. This method may be effective for a shorter time duration as there is no heating source. The relief time using hot water bottles is less as it utilizes the specific heat of water (4 kJ kg^{-1}) and also provides heating in a large temperature window, not soothing to the human body. The electric power based heating products utilizes a temperature controller such as a thermostat to regulate the temperature of these devices. In the case of any failure of the temperature controller, the temperature of the heating device may shoot and cause serious skin burn causality. Further, these devices are not cost effective and not suitable for outdoor applications. The coal-based heating devices such as Kangaries, Bukharies release CO_2, CO gases and are dangerous for the health. These heating systems are also prone to the skin cancer incidences (Wani 2010). The phase change material (PCM) based technologies such as PCM heat packs are very promising for thermal comfort under such conditions and therapeutic applications at the time of requirement. It utilizes a phase change material as thermal energy storage media. The thermal energy storage capacity of PCM is very high as compared to the sensible storage materials such as water because of the latent heat of fusion of PCMs while changing the phase of material from solid to liquid. For example, the latent heat values (and melting temperature) of some of salt hydrates $CaCl_2.6H_2O$, $LiNO_3.3H_2O$, $Na_2CO_3.10H_2O$, $Na_2SO_4.10H_2O$ are 174–191 kJ kg^{-1} (29–30 °C), 296 kJ kg^{-1} (30 °C), 267 kJ kg^{-1} (32 °C), and 241 kJ kg^{-1} (32.4 °C), respectively (Barrett et al. 1984; Barrett and Best 1985). Further, it releases heat in the very limited temperature range (near phase change temperature of PCM), therefore it may be more effective for body heating applications. The hydrated salt PCMs are being used in the PCM heat packs. The hydrated salt PCMs are known for their large supercooling and may remain in a metastable supercooled liquid state far below PCM's melting temperature before solidification. This property of hydrated salts makes them very useful for storing heat at the time of availability and releasing it later at the time of requirement (Barrett et al. 1984; Barrett and Best 1985). These PCM heat packs are reusable, reliable, and cost-effective, providing heat at body soothing temperature (Ulman and Valentin 1983). Among numerous PCM based heat packs, the sodium acetate trihydrate (SAT) based heat packs has attracted more attention due to its high latent heat (~270 kJ kg^{-1}), suitable melting temperature (~58 °C), large supercooling (up to − 10 °C), and stability against large numbers of charging cycles, making it reusable, and very cost effective (Kimura and Kai 1985). These PCM based heat packs use a metallic disk containing multiple grooves to start nucleation in metastable supercooled liquid SAT for releasing heat at the time of requirement (Kapralis et al. 1990; Sandnes and Rekstad 2006). These heat packs can be recharged by heating packs in hot water for 25–30 min. Rohitash Kumar et al. developed SAT, ethylene glycol and water-based PCM suitable for body warming in extremely cold climates and medical applications such as treatment of muscle cramp, frostbite etc. (Kumar et al. 2017;

Kumar et al. 2016). In this study, authors have investigated the thermal performance of PCM heat packs containing 300 g PCM at ambient temperature ~0 °C and the results are compared with an identical water heat pack.

14.2 Materials and Methods

Ethylene glycol (EG) and Sodium acetate trihydrate (grade excel R) are procured from Alfa Assar and used without any modification to prepare a metastable supercooled liquid PCM for fabricating a heat pack. SAT, EG and deionized (DI) water are mixed in 92:5:3 weight fractions, respectively. The mixture is heated up to 80 °C and stirred for 25–30 min using magnetic stirrer. After homogeneous mixing of samples, the solution (~300 g) is filled in a PVC pack, as shown in Fig. 14.1a. Multiple grooves are incorporated on a metallic disk made of Stainless Steel (SS)-304 for initiating heat nucleation for releasing heat from PCM heat packs, shown in Fig. 14.1b. The size of this metallic disk is 20 mm (L) × 18 mm (W) × 0.2 mm (T). An identical PVC pack containing 300 g DI water is also fabricated to compare the thermal performance of PCM heat pack with a similar water pack. In-house developed temperature-history (T-history) setup is used to study the thermal performance of PCM and water heat packs (Fig. 14.1c; Kumar et al. 2016). K-type thermocouples are used to measure the temperature of packs and ambient temperature of the air chamber of T-history setup by connecting to the data logger (model: 34972A, make: Agilent) for recording temperature. The temperature data are recorded after every 10 s time intervals.

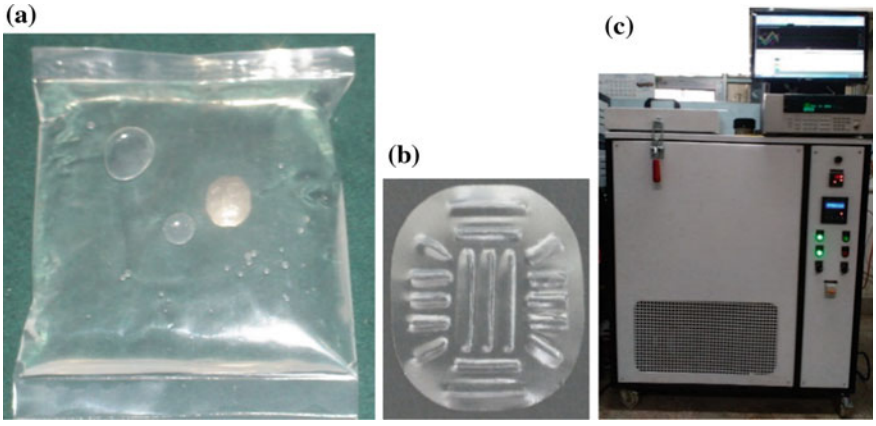

Fig. 14.1 Actual photograph of **a** PCM heat pack containing 300 g metastable supercooled liquid PCM, **b** metallic disk consisting multiple grooves on its surface, and **c** a photograph of in-house developed T-history measuring set up

14.3 Results and Discussion

14.3.1 Thermal Performance Evaluation of PCM Heat Pack

The metallic disk, consisting of multiple grooves, is used to start nucleation in the PCM heat pack at the desired temperature. The process of the heat release from PCM heat pack is explained in Fig. 14.2. The metastable supercooled liquid PCM based heat pack containing 300 g MSLPCM and a metallic disk is shown in Fig. 14.2a. The solid particles of SAT entrapped between two opposite surfaces of the metallic disk is released after pressing the metallic disk and nucleation is started in metastable supercooled liquid, shown in Fig. 14.2b. The nuclei in MSLPCM grow at a fast rate due to the stability of SAT phase below its melting temperature i.e. solid phase.

Initially, the PCM heat pack is kept inside a T-history air chamber at 80 °C temperature, above melting temperature ~56 °C of PCM for complete melting of PCM. After ensuring the complete melting of PCM, the air chamber temperature is reduced to 0 °C. The PCM pack surface temperature in conjunction with ambient temperature is measured using K type thermocouple at every 10 s time interval, and the recorded temperature-history data is plotted in Fig. 14.3.

The heat pack has shown initially cooling from 70 to 35 °C without any solidification and at this temperature the nucleation is initiated by pressing the metallic disk. The temperature of PCM heat pack is increased from 35 to 53 °C after initiating solidification due to the heat release, stored in the form of latent heat of fusion in SAT, Fig. 14.3. The MSLPCM solidifies in the phase change region and temperature of heat pack remain in the phase change temperature range of MSLPCM (56–46 °C) during phase change process. After complete solidification of PCM, the PCM pack releases heat in the form of specific heat of PCM. The PCM heat pack took about 210 min to cool from 70 to 30 °C.

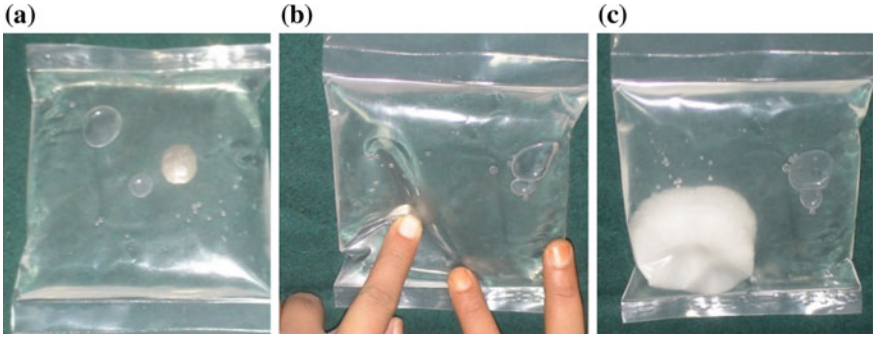

Fig. 14.2 Actual photographs of **a** PCM in metastable supercooled liquid state in a PVC pack, **b** initiating nucleation in MSLPCM by pressing metallic disk, and **c** growth of nucleation (solidification) in PCM heat pack after 5 s

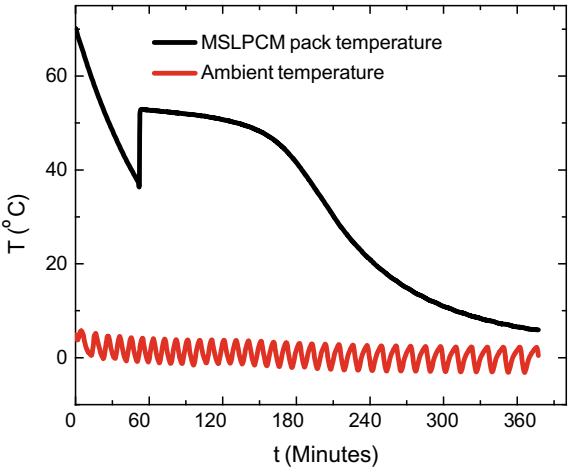

Fig. 14.3 Temperature response of MSLPCM heat pack at ambient temperature 0 °C, recorded from in-house developed T-history measurement setup. The small oscillations (<5 °C) in ambient temperature are attributed to the temperature feedback control, causing variations during its on-off cycles

14.3.2 Thermal Performance Evaluation of Water Heat Pack

A DI water heat pack, identical to the MSLPCM heat pack, is fabricated to compare the thermal performance with SAT based heat pack. The temperature of water heat pack is measured from 70 °C at ambient temperature 0 °C, and the results are shown in Fig. 14.4. The water heat pack took ~48 min for cooling from 70 to 30 °C, as normal sensible heat release process.

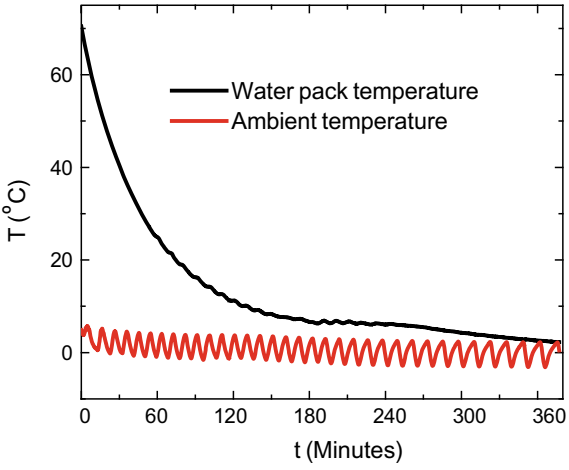

Fig. 14.4 Temperature response of water heat pack at ambient temperature 0 °C, used for comparison with SAT PCM heat pack. Here also small oscillations are attributed to on-off cycles of temperature feedback control while cooling the chamber

14.4 Conclusion

We designed MSLPCM based thermal heat packs for thermal comfort application and the thermal performance of metastable supercooled liquid phase change material based heat pack is evaluated against an identical water heat pack. The heating time of MSLPCM based heat pack is ~4.4 times more than that of water based heat pack. Thus, MSLPCM heat pack, showing excellent thermal performance, may be the promising thermal energy storage systems for providing thermal comfort to human beings in extreme cold environments in the form of body heating and also for medical applications such as treatment of muscle cramps, frostbite etc.

Acknowledgements Authors acknowledge Defence Research and Development Organization (DRDO) and Central Instrumentation Facility at IIT Jodhpur for supporting this work.

References

Barrett PF, Best BR (1985) Thermal energy storage in supercooled salt mixtures. Mater Chem Phys 12:529–536. https://doi.org/10.1016/0254-0584(85)90038-0

Barrett PF, Best BR, Oldham KB (1984) Thermal energy storage in supersaturated salt solutions. Mater Chem Phys 10:39–49. https://doi.org/10.1016/0254-0584(84)90077-4

Kapralis GI, Kapralis JE, Lowther J (1990) Inventors assignee. Imperforate groove trigger. United States patent US 4,899,727 A. 1990 Feb. 13

Kimura H, Kai J (1985) Phase change stability of sodium acetate trihydrate and its mixtures. Sol Energy 35:527–534. https://doi.org/10.1016/0038-092x(85)90121-5

Kumar R, Dixit A, Chandra L, Vyas S, Kumar R (2016) An experimental set-up for measuring thermodynamic response of low temperature phase change materials. In: 2016 First IEEE international conference on control, measurement and instrumentation (CMI), pp 107–109

Kumar R, Vyas S, Kumar R, Dixit A (2017) Development of sodium acetate trihydrate-ethylene glycol composite phase change materials with enhanced thermophysical properties for thermal comfort and therapeutic applications. Sci Rep 7:5203

Sandnes B, Rekstad J (2006) Supercooling salt hydrates: Stored enthalpy as a function of temperature. Sol Energy 80:616–625. https://doi.org/10.1016/j.solener.2004.11.014

Ulman A, Valentin B (1983) Investigations of sodium acetate trihydrate for solar latent-heat storage, controlling the melting point. Sol Energy Mater 92:177–181. https://doi.org/10.1016/0165-1633(83)90040-0

Wani I (2010) Kangri cancer. surgery 147:586–588. https://doi.org/10.1016/j.surg.2009.10.025

Watson SS, Watson WKR (1976) Inventors; kay laboratories, Inc., assignee. Constant temperature device. United States patent US 3,951,127A. Apr. 20

Part V
Solar Cells

Chapter 15
Yet to Be Challenged: TiO_2 as the Photo-Anode Material in Dye-Sensitized Solar Cells

Janethri B. Liyanage, Ishanie Rangeeka Perera and R. J. K. U. Ranatunga

Abstract Utilization of renewable sources can reduce the impact of increasing global energy demand on the rate of depletion of fossil fuels. One of the most studied and implemented routes to meet this energy demand is to harvest solar energy. Among solar-energy harvesting devices, dye-sensitized solar cells have been recognized as some of the cheapest and most environment friendly technologies, since they do not require high purity of starting materials or advanced fabrication techniques. A dye-sensitized solar cell is composed of a working electrode, in which the light absorbing sensitizer is chemisorbed onto the surface of a wide bandgap semiconductor; a redox electrolyte, that is placed in between two electrodes and functions to regenerate the sensitizer; and a counter electrode, which is a catalyst which accelerates a redox reaction with the electrolyte. Titanium dioxide (anatase phase) is the most widely used semiconductor material in dye-sensitized solar cells due to its low cost, chemical stability and optical properties. In this chapter, the literature on optimizing TiO_2 as a semiconductor material for n-type DSCs is reviewed. The evolution of TiO_2 nanostructures and techniques such as doping, composite preparation and surface modification are elaborated on. These methods have enhanced both the chemical and physical properties of TiO_2 nanostructures. Moreover, despite good overall performance, rapid recombination kinetics are a major disadvantage inherent in TiO_2. Thus, research has been carried out to substitute TiO_2 with alternative semiconductors. In view of this, other potential competitors for photo-anode material are reviewed and assessed. Finally, the prospects of an ideal semiconductor material for dye-sensitized solar cells is discussed.

J. B. Liyanage · I. R. Perera (✉) · R. J. K. U. Ranatunga (✉)
Department of Chemistry, University of Peradeniya, Peradeniya 20400, Sri Lanka
e-mail: ishanieperera@pdn.ac.lk

R. J. K. U. Ranatunga
e-mail: udyranatunga@pdn.ac.lk

J. B. Liyanage
e-mail: janethriliyanage@gmail.com

I. R. Perera · R. J. K. U. Ranatunga
Postgraduate Institute of Science, University of Peradeniya, Peradeniya 20400, Sri Lanka

H. Tyagi et al. (eds.), *Solar Energy*, Energy, Environment, and Sustainability, https://doi.org/10.1007/978-981-15-0675-8_15

Keywords Titanium dioxide · Photoanode · Dye-sensitized solar cells · Nanostructures

15.1 Introduction

The increasing demand for energy in conjunction with our dependence on fossil fuel has fast-tracked the reduction of the oil reserves of the earth. Moreover, the use of fossil fuel has resulted in severe ecological contamination and change. Renewable energy sources promise to alleviate both these problems and among these sources, solar energy has garnered much interest.

Photovoltaic cells, which convert solar radiation into electric current, are in the forefront of plans for sustainable energy. Presently, first generation solar cells based on crystalline or multi-crystalline Si hold a majority (>90%) of the market-share of solar cells. However, the adoption of Si photovoltaic cells has not reached desired levels, and research into more commercially viable technologies continues. Dye sensitized solar cells (DSCs) are third-generation, semiconductor photovoltaic devices that incorporate dyes to mediate efficient conversion of radiation. DSCs are considered a promising alternative (and complement) to single crystal silicon solar cells, due to their lower manufacture cost, easy fabrication on flexible substrates, and performance at ambient temperatures.

Although research into several materials has been reported, TiO_2 remains the most widely utilized photo-anode material for DSCs. In this chapter, we discuss modifications to the TiO_2 component which have been reported, and their effect on DSC performance. We begin with a general treatise on DSCs, and then move on to reviewing literature on modifications to TiO_2. Finally, we briefly discuss alternative semiconductor materials to TiO_2, in terms of DSC function.

A contemporary DSC utilizes five components for operation, namely;

1. Transparent conductive oxide, the anode of the device. This is the side of the device receiving solar radiation.
2. Semiconductor, deposited on the anode. This layer activates electronic conduction.
3. Sensitizer, a charge transfer dye bonded to the semiconductor.
4. Electrolyte, a redox mediator which restores the dye with each cycle.
5. Catalyst, coated on the cathode, which accelerates the redox reaction.

An illustration of the electron flow in a working DSC is given in Fig. 15.1. When the DSC is exposed to sunlight, electrons in the sensitizer can absorb a photon with energy $h\nu$, and excite to the LUMO. Dye sensitizers are chosen such that the LUMO has high energy, and excited electrons can inject into the conduction band (CB) of the working electrode (semiconductor) material. These electrons diffuse through the anode and can be used to drive an external circuit. Electrons returning from the counter electrode can reduce oxidized molecules of the redox-couple, which in turn undergo a redox reaction with dye, regenerating it and completing the cycle.

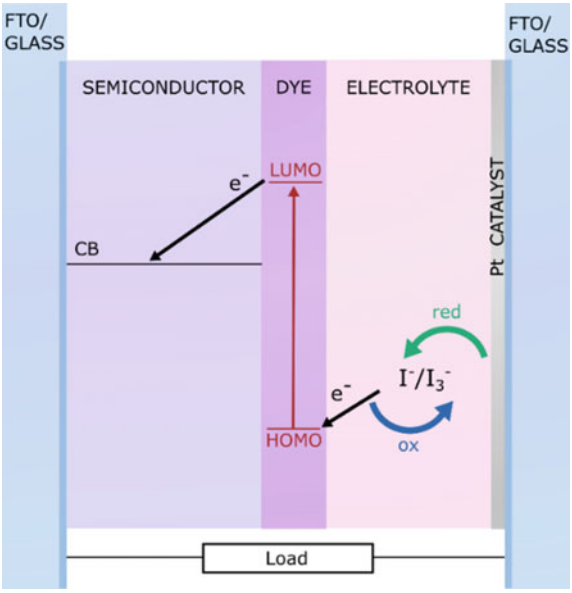

Fig. 15.1 Working diagram of DSC

In DSCs, the semiconductor layer functions as the support for the sensitizer, and as the transporter of photo-excited electrons from sensitizer to the external circuit. The semiconductor/sensitizer interface provides the platform for charges to separate after the photoexcitation of the dye, and consequently the injected charge carriers diffuse to the external circuit. Therefore, an ideal semiconductor should have a large surface area, for high dye loading; and fast charge transport, for efficient electron collection (Ye et al. 2015). Furthermore, strong binding with the dye keeps the dye in close proximity to the semiconductor; while suitable energy band potentials make the electron transfer process more efficient. Therefore, these characteristics can be considered qualifications for potential semiconductor materials (Gong et al. 2012).

The semiconductor is usually not fabricated as a monolith and is deposited as separate dense and mesoporous layers (see Fig. 15.2). The dense layer, a fine layer of the semiconductor material of about 100–200 nm thickness, prevents recombination reactions. The mesoporous layer is deposited on the dense layer, and is several micrometers thick. The mesoporous layer can be further divided into the transparent layer and the scattering layer. The transparent layer, having a thickness of about 1–15 μm, consists of particles of size 20–30 nm. A typical transparent layer ensures a large surface area of the nanocrystalline semiconductor, which allows higher dye adsorption. This leads to efficient light harvesting, especially for wavelengths under 600 nm. The scattering layer consist of much larger particles of a size about 300–400 nm and is coated on the transparent conductive oxide layer. This size of particles scatter light of longer wavelengths (red) back to the transparent layer, and enhances the absorption of light by the sensitizer (Ghadiri et al. 2010). The thickness

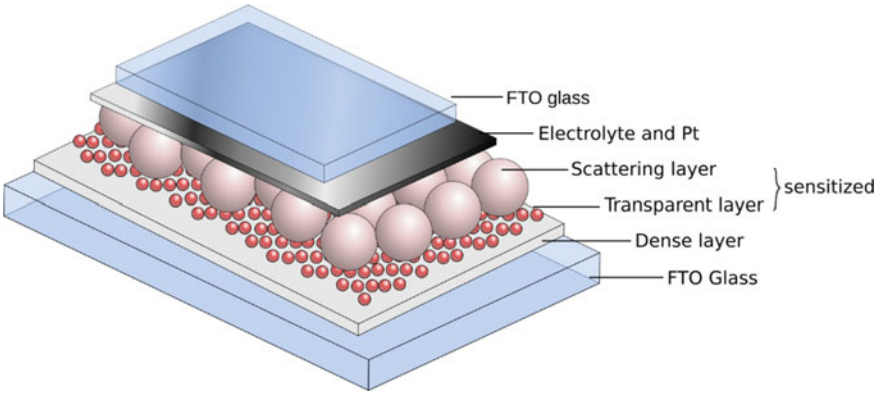

Fig. 15.2 Layered structure of material constituting a DSC

of the layer depends on the light absorbing ability of the dye and the deposition technique used.

DSCs have been fabricated using both n-type semiconductors, where the majority charge carriers are electrons, and p-type semiconductors, where the majority charge carriers are holes. This chapter focuses on the n-type TiO_2 semiconductor, which is still considered the gold-standard in DSC devices, and has been the most investigated semiconductor material since the 1970s. The long lifetime of excited electrons, remarkable resistance to photocorrosion, low-toxicity, while being a cheaper alternative, have made TiO_2 quite popular for solar energy applications (Roose 2015). TiO_2 nanostructures can be synthesized using sol-gel methods, hydrothermal synthesis, solvothermal synthesis, anodization, flame spray pyrolysis, among other methods.

Although the efficiency of the original DSC fabricated by Grätzel achieved only an efficiency of 7% (O'Regan and Grätzel 1991), subsequent optimization of devices and developments in the field have steadily improved efficiencies, until Chiba et al. reported the highest certified efficiency of ~11% (Chiba et al. 2006). In this chapter we review novel approaches in breakthroughs in optimizing the TiO_2 semiconductor material to produce better performing DSCs.

15.1.1 Characterizing DSSCs

Several parameters can be used to characterize the operation of a DSC:

Open circuit voltage (V_{OC}), the maximum voltage that the array provides when the terminals are not connected to any load. According to band gap theory, the difference between the quasi-Fermi level of the semiconductor layer and the electrolyte redox potential, controls the highest voltage generated under illumination.

Short circuit current (J_{SC}), the maximum current generated by the photovoltaic array when the output connectors are shorted together. J_{SC} depends on the incident photon to current efficiency (IPCE) and the incident photoflux. J_{SC} can be improved

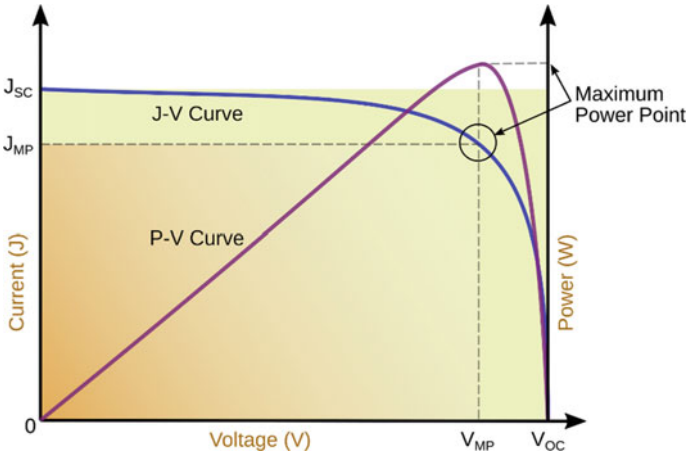

Fig. 15.3 Characteristic current-voltage and power-voltage curves of DSCs

by increasing the IPCE value using panchromatic dyes which can absorb incident light at a broader wavelength range.

Fill factor (FF), the ratio between maximum power the array can provide under normal conditions, and the product of V_{OC} and J_{SC}. The FF is related to the electron transfer and the internal resistance of the DSC, and can be optimized by minimizing the internal series resistance.

$$\text{Fill Factor(FF)} = \frac{Vmax \times Jmax}{Voc \times Jsc}$$

Efficiency (η), which is the ratio between the maximum electric power that the array can produce compared to the amount of solar irradiance incident hitting the array.

$$\text{Efficiency } (\eta) = \frac{Vmax \times Jmax}{Pin}$$

These parameters can be extracted from typical current-voltage (J–V) plots, as shown in Fig. 15.3.

15.1.2 Modifications to TiO_2

Throughout years of development, many modifications to TiO_2 have been carried out to increase the overall efficiency of DSCs through the enhancement of light harvesting efficiency, enhancing charge collection efficiency, and photogenerated charge transport efficiency (Kim et al. 2008). This chapter categorizes these modifications into three categories,

1. Morphology
2. Composites/hybrids
3. Doping.

In this chapter, we focus on changes in the structures and morphology, composites, and doping, in terms of their influence on the properties of TiO_2 DSCs. These three categories will be discussed separately. Apart from these surface modifications aim to improve the properties roughness, hydrophobicity, biocompatibility, surface energy, gas diffusion barrier etc. (De Jonge et al. 2008). In this chapter a separate space has not been allocated for the surface modifications done on TiO_2 as these are discussed under other modification techniques.

15.2 TiO_2 Morphology

The availability, ease of synthesis, and the intrinsic energy band structure are some reasons TiO_2 remains the forerunner among semiconductor materials for n-type DSCs. Apart from the material, the structure and morphology can have a considerable influence on the photogenerated electrons produced by a semiconductor. The multi-layered structuring of TiO_2 in conventional DSCs has many advantages, as described in the previous section. However, there are many facets of this architecture which have been targeted for optimization.

Increasing total dye adsorbed on the TiO_2 has been an objective in tuning the morphology. Raising the number of sensitizer molecules in contact with the semiconductor material enhances the light harvesting efficiency (O'Regan and Grätzel 1991). Either improving the binding of dye to the semiconductor or increasing the surface area of the material could elevate dye adsorption. Several studies have investigated the change in efficiency of cells when the porosity and particle size of TiO_2 are varied.

O'Regan et al. studied colloidal TiO_2, of average particle size of 15 nm, which was then deposited on a conducting glass sheet (O'Regan and Grätzel 1991). After the deposition a monolayer of the Ru based dye, the film turned into a deep reddish brown colour, shifting the absorption onset to 750 nm and giving a light harvesting efficiency of almost 100% below 550 nm, in the visible range ($\eta = 7.9\%$, at 10% sunlight; 7.12% at 100% sunlight).

After Grätzel and O'Regan's initial work the highest efficiency obtained so far, of 11.1% was attained by Chiba et al. They used the strategy of trapping incident light by incorporating submicron (400 nm) sized TiO_2 nanoparticles together with nanosized TiO_2 particles. The investigators optimized the haze, which is the portion of diffused light in total transmittance, at 800 nm to achieve high J_{SC}.

After decades, a similar study has been done on flexible substrates by Pichot et al., using a low temperature sintering method, without the use of an organic surfactant, which resulted in a high dye loading capacity, with respect to the film thickness, that compensated the lower efficiency of the DSC. The lower efficiency can be attributed

to the inefficient charge transport of electrons through the TiO_2 film, due to the pores of the film, causing recombination reactions before being collected (Pichot et al. 2000).

Another reason for optimizing the layer structure of TiO_2 is to lessen the grain boundaries of the material. This allows for faster transport of charges and lower recombination. Yu et al. lowered the thickness of the mesoporous layer from the conventional 10 μm, to 300 nm, leading to recombination only at the surface, and eliminating recombination with the oxidized dye and redox electrolyte. An added advantage was that at these thicknesses, the localized surface plasmon created at the FTO/TiO_2 interface was able to induce a relatively strong electric field at the TiO_2/dye interface, enhancing light absorption by the dyes and increasing cell efficiency. However, in this study, oxygen vacancy-Ti^{3+} type surface defects were formed, decreasing the efficiency almost linearly with the increased concentration of Ti^{3+} (Tributsch 2004). Defects can serve as recombination centers and pathways for electron back transfer, and decreased V_{OC} and FF. The lower efficiency can also be attributed to the lower dye adsorption, due to the smaller mesoporous layer, leading to a lower J_{SC} (Yu et al. 2012).

To address both the surface area and grain boundaries, several groups have investigated fabricating TiO_2 in nanostructures to yield materials with fewer grain boundaries, and well-defined conduction pathways. These materials have the potential of (1) improving of electron transport, (2) enhancing dye adsorption through increasing surface area, and (3) augmenting scattering of red light, where absorption of most molecular sensitizers is weak (Ghadiri et al. 2010). The nanostructured morphologies that have been tested for DSCs include hollow nanoparticles, nanorods and nanofibers, anodized nanotube arrays, and hierarchical 3D nanostructures (see Fig. 15.4).

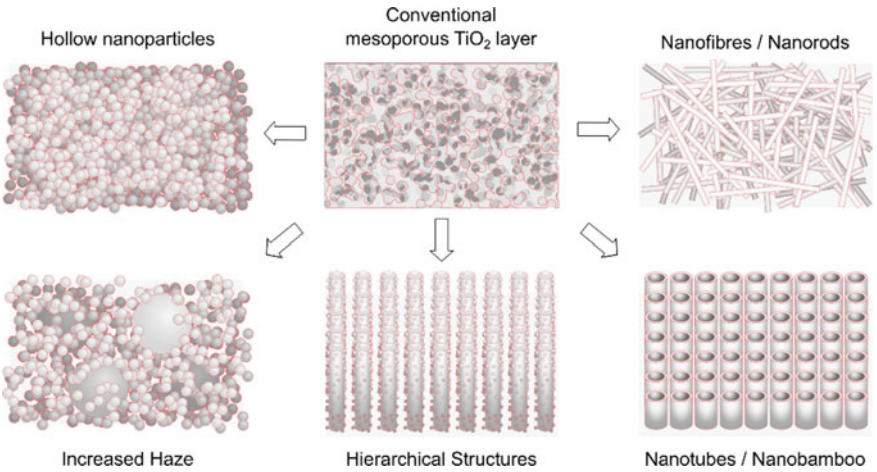

Fig. 15.4 Modification of the morphology of TiO_2

Another nanostructure that was considered for the development of TiO_2, as a better semiconductor material in DSCs, would be hollow nanoparticles. In 2008, Yang et al. synthesized quasi-ordered TiO_2 hollow hemispheres, using a colloidal template and radio frequency-sputtering, in order to obtain fast electron transport and high surface area in a thin photoelectrode, and obtained a photoconversion efficiency of 3.49%. The fact that the diameter, wall thickness and the height of these unique microstructures could be easily changed and the enhanced surface activity, encourages its application in DSCs (Yang et al. 2008). Koo et al. studied nano-embossed hollow spherical TiO_2 particles to obtain bifunctionality: light scattering and photoexcited electron generation, to obtain an efficiency of 10.34%. It has been confirmed that the nano-embossed hollow spheres containing layer was able to adsorb 5 times more of the dye while acting as the scattering layer (Koo et al. 2008). Similarly, Yu et al., studied hollow structured TiO_2 due to its low density, high surface area and its porous structure which affects the increase in light harvesting efficiency and fast motion of charge carriers. Under the optimal conditions, they were able to generate an efficiency of 4.82% (Yu and Zhang 2010).

Nanofibers have also been used as a structural modification implemented on to TiO_2, in the aim of improving the photovoltaic properties. Ghadiri et al. used cellulose fibers as a template material to synthesize the hollow TiO_2 nanofibers, by a stepwise hydrolysis and dehydration of a saturated Ti^{4+} solution. The unoriented nanostructure showed enhanced electron transport properties compared to the mesoporous layer made of spherical nanoparticles, leading to 7.15% efficiency under optimal conditions. The retardation of surface recombination, between the conduction band electrons and oxidized species in the electrolyte, observed in nanostructured fiber-based cells was able to balance out the adverse shift of the band edge toward positive potential and produce an open-circuit photovoltage of 760 mV, which is a gain compared to that of the DSC containing nanoparticles (Ghadiri et al. 2010), which is seen with the decrease of the photoactive layer. This shift of the conduction band edge towards the positive potential, has been generally observed for DSCs based on nanotubes and nanoparticles (Kuang et al. 2008). TiO_2 nanorods have been further studied by Pandanga et al. to optimize the morphology and dye uptake and to encourage fast electron transport avoiding recombination reactions (Pandanga et al. 2019).

Self-organized porous metal oxides with a nanotubular structure have attracted significant interest in recent years (Fraoucene et al. 2019). It possible to apply anodically formed TiO_2 nanotubes to photovoltaic devices, yielding semiconductor material with a large interconnected internal surface area (O'Regan and Grätzel 1991). Although considerable research has been concentrated on the development of nanotubular TiO_2 layers, there is no simple synthesis route to obtain a uniformly stretched nanotubular structure, other than by an electrochemical anodization process. However, electrons in the nanotube can also meet with many grain boundaries, defects, and trap sites, becoming a factor that retards the electron transport time (Kang et al. 2007).

Kai Zhu et al. reported that the light-harvesting efficiencies of nanotube (NT)-based DSCs were higher than those of nanoparticle (NP)-based DSCs. It was also

shown that by reducing the disorder that is typically present at the top of the NT layers, an increase in efficiency can be obtained as the dye uptake is increased, while the internal light scattering effect is seen to be strongly (Zhu et al. 2006, 2007).

It was later discovered that some of these advanced morphologies can be directly grown on the conductive substrate such as wires (Feng et al. 2008), templated rods (Liu and Aydil 2009) or self-organized anodic structures (Macak and Schmuki 2006; Stergiopoulos et al. 2008) that can be obtained as an oxide layer firmly attached to the Ti-(metal) substrate.

In the aim of allowing a longer, uninterrupted path for the photogenerated electrons, Kim et al. synthesized a bamboo type morphology, by controlled anodization of a Ti plate, for the increase in the photovoltaic efficiency. However, it was observed that there was no change in the transport properties or the recombination kinetics of bamboo type NTs and normal NTs. The only improvement observed was the dye loading capacity, as the bamboo type NTs allow the exterior as well as the interior coverage which enhanced the generated current, giving a maximum efficiency of 2.98%, which is greater than that obtained for normal NTs (Kim et al. 2008). But later on, several more studies have been done using this bamboo type NTs, in order to further increase the dye loading capacity. Luan et al., studied a two-step method, to form ridges on the surface of the bamboo type NTs and to obtain evenly lengthened NTs. It was noted that the ridge density and the length of the NT had a significant impact on the overall efficiency. Highest efficiency of 6.80% was obtained with the bamboo type NTs synthesized under a lower water content, which led to a longer tube length (Luan et al. 2012). Further studies were done by Ji et al. where they synthesized double walled bamboo type NTs. The dye loading was found to be significantly larger for the DSCs fabricated with NTs of higher ring density, leading to a better conversion efficiency (Ji et al. 2012). Wang et al. too studied a similar morphology which led to a reduced interfacial resistance and increased interfacial capacitance, compared to that of smooth walled NTs, resulting in a higher dye loading capability (Wang et al. 2014).

More recently, in 2019, research has been carried out to construct a hierarchical hetero-structured TiO_2 photoanode material, where anatase nano branches and rutile nanorods were used, aiming for a higher surface area (Jin et al. 2019). Also, research has been conducted to include TiO_2 hollow spheres as well as nanorods as a composite powder, to be applied as the light scattering layer in the photoanode of DSC. The increase in efficiency, up-to 9.58%, can be attributed to the two different scattering structures incorporated (Marandi et al. 2019) (Table 15.1).

15.3 TiO_2 Composites/Hybrid Materials

The VB of TiO_2 is composed of hybridized 2p orbitals of oxygen and the 3d orbitals of titanium, while the CB is purely 3d orbitals of titanium, which causes a decrease in the transition of electrons back to the VB, minimizing recombination reactions.

Table 15.1 Table with the maximum efficiencies obtained by modifications to the nanostructure or morphology

Modification	Efficiency (%)	References
TiO_2 submicron particles/nanoparticle mix	11.1	(Chiba et al. 2006)
TiO_2 hollow spheres and nanorods	9.58	(Marandi et al. 2019)
Colloidal TiO_2	7.9	(O'Regan and Grätzel 1991)
Nanofibres	7.15	(Ghadiri et al. 2010)

Due to the high surface area, TiO_2 in leads to efficient dye loading, and consequently high J_{SC}. The high Fermi level leads to a higher V_{oc}, which ultimately improves the overall efficiency.

However, inefficient electron transfer through the FTO/TiO_2 interface increases the back-electron transfer to the electrolyte. The electron trapping and the high density of grain boundaries present with spherical TiO_2 nanoparticles, also lowers conversion efficiency (Kopidakis et al. 2003). Therefore, much effort has been made to minimize the back-electron transfer and recombination. Using composites in DSC is one of the modifications done in order to minimize these problems.

Composites in DSCs use combinations of one or more materials including, metals, metal oxides, metal sulfides, etc. where the combination can be of the form of layered or core shell structures. DSCs using TiO_2 as a component can be produced by various methods such as chemical synthesis, solution or gas phase synthesis and template fabrication (Dahl et al. 2014). A composite material should have two main properties: (1) a CB band edge with energy between the TiO_2 CB and sensitizer LUMO (see Fig. 15.6), to facilitate the electron injection from the dye to the electrode; and (2) a high electron mobility (Mao et al. 2016). These properties would lead to a smoother, stepwise electron transport from the dye to the working electrode. Composites of TiO_2 can be tuned by controlling the composition of the material, in order to decrease the charge carrier recombination rate or adjust the band gap. Here, discussion of TiO_2 composites has been further broken down into subsections by the type of modifying material.

15.3.1 Metals

The most commonly used metallic nanoparticles in preparing composites with TiO_2 are silver and gold, as they can improve the optical absorption by inducing surface plasmons (Deepa et al. 2012) and form Schottky barriers at the metal-TiO_2 interface, which can reduce electron recombination (Chou et al. 2009). These can also increase the optical path length in electrodes, by reflecting and scattering incident light (Peng et al. 2013). Another important factor is that they can form electron transfer networks.

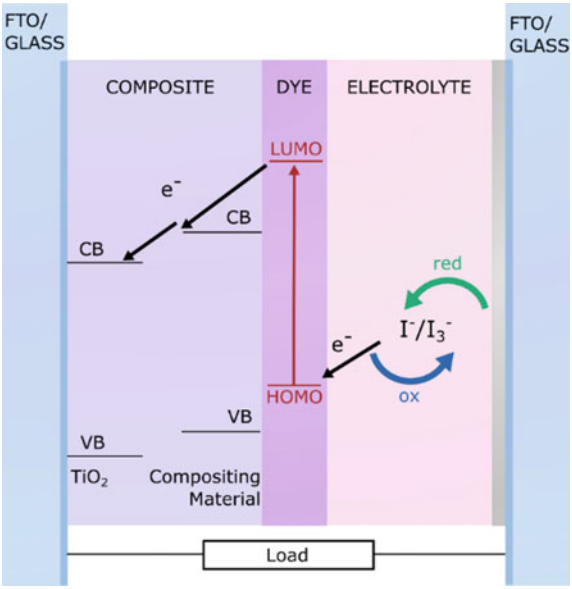

Fig. 15.6 Energy band structure of a DSC utilizing a TiO_2 composite material for the photoanode

Generally, there are two methods of preparing the metal composite. One is by simply mixing the metal and TiO_2, the other method is immersing TiO_2 in metal solution and reducing the adsorbed metal ions using either thermal evaporation or atomic laser deposition. Wu et al. have carried out a method to deposit the silver nanoparticles by chemical reduction with the aid of $NaBH_4$. The highest efficiency of 5.66% was observed at the highest concentration of $NaBH_4$ leading to a larger sized nanoparticle. The silver clusters formed on the surface TiO_2 would act as a scattering layer reflecting incident light, which increased the photocurrent. In this study, the dye adsorption was increased by an acid treatment (Wu et al. 2017). Silver has also been coated on TiO_2, using photo deposition and an overall efficiency of 6.86% was obtained. The investigators proposed that the silver layer lengthens the optical pathway and suppresses the charge transfer from surface states (Peng et al. 2013). Chou et al. prepared two composite mixtures containing silver and gold, using a dry coating method. This study concludes that the doping of metal nanoparticles improves the overall efficiency but the process of fabrication is very important for the overall efficiency of the DSC (Chou et al. 2009).

Similar studies have been done incorporating silver and gold as a composite material using a hydrothermal process (Muduli et al. 2012) and one-step electrospinning process (Nam et al. 2010). Studies have also been done using various nanostructures of TiO_2 along with metal, such as the use of hierarchical TiO_2 spheres containing needles with gold nanoparticles for a plasmonic enhancement (Bai et al. 2016) and the use of TiO_2 hollow spheres, nanoparticles, nanosheets with the metal nanoparticles and nanowires for an enhanced electron transport (Ran et al. 2018).

One of the drawbacks of using metals as composites is that I^-/I_3^-, the most commonly used redox electrolyte, is corrosive in the presence of metals, which would affect the durability of the system (Chou et al. 2009).

15.3.2 Metal Oxides

Metal oxides can be considered as the most commonly used material in preparing composites with TiO_2, for DSCs. Many have been studied so as to provide the electrons an easier transport with a stepwise conduction band edge. Among all metal oxides, Al_2O_3, ZnO, NiO, SiO_2 and SnO_2 have been studied extensively.

Zhang et al. studied the use of a blocking layer of Al_2O_3, so as to avoid recombination reactions, leading to a better V_{OC} and FF. Although V_{OC} and FF increase with greater thickness of the Al_2O_3 layer, confirming the function of the blocking layer, J_{SC} decreases. This may be due to the fact that the probability of electrons tunneling through the barrier has an exponential relationship with the tunneling length; or due to the decrease in dye adsorption due to the blocking layer. At an optimal coating the highest efficiency was obtained was 2.59% (Zhang et al. 2003).

Similar studies have been done by coating Al_2O_3 with reactive direct current magnetron sputtering (Wu et al. 2008), by stepwise condensation (Choi et al. 2008), using highly ordered TiO_2/Al_2O_3 (Kim et al. 2010) and also using highly ordered, vertically oriented TiO_2/Al_2O_3 nanotubes (Kim et al. 2014), where they have also made a modification to the structure.

Another popular material in preparing composites with TiO_2 is ZnO, due to its high electron mobility and band gap quite similar to that of TiO_2. However, using pure is thought to cause degradation of the dye forming Zn^{2+}-dye complexes. Manthina et al., studied the use of ZnO containing composites using 1D nanostructures. Overall dye uptake was lowered, but even taking this into account, it was observed that the performance of the pure TiO_2 system was greater than that of the ZnO-TiO_2 containing. The authors hypothesise that the transfer of electrons from TiO_2 to ZnO is attenuated as the CB edge of ZnO lies at a slightly more negative potential than that of TiO_2, and more work is needed to remove this barrier (Manthina et al. 2012).

Self-organized nanotubular metal oxides have attracted much interest in the recent past. But there is no simple synthesis method to obtain these structures other than anodization of the metal (Beranek et al. 2005), also leading to many grain boundaries, defects, and trap sites, becoming a factor that retards the electron transport time. Kang et al. tried to suppress the charge recombination by applying a wide band gap metal oxide, such as ZnO, to coat the TiO_2 film. The formation of an energy barrier by coating as a shell at the electrode/electrolyte interface was found to be essential for increasing the physical separation of the injected electrons from the cations of the redox electrolyte, thereby decreasing the rate of charge recombination. Here, in order to improve the FF, an H_2O_2 surface treatment was done, which reduced the thickness of the TiO_2 barrier layer. The ZnO coating was attributed to suppress electron flow

to the back-direction, which enhanced the V_{oc}, leading to a maximum efficiency of 0.906% after the H_2O_2 treatment (Kang et al. 2007).

ZnO as a composite material with TiO_2 has been studied by synthesizing a coaxial structure (Williams et al. 2012), as a photoanode material for an effective UV-visible active DSC (Noor et al. 2018), as multilayers (Bhatti et al. 2019) and as a core-shell nanostructure (Rajamanickam et al. 2019).

SnO_2 is another candidate for applications in DSCs. SnO_2 exhibits a band gap of 3.8 eV, larger than that of TiO_2, generating much fewer oxidative holes under illumination, therefore improving the long-term stability of the DSSCs and minimizing the degradation rate of the dye (Qian et al. 2009). Also, electron mobility in SnO_2 is much faster than in TiO_2. However, SnO_2 has the disadvantages of having poor dye loading capacity and fast charge recombination, when used in pure form within DSCs (Gao et al. 2012). These shortcomings can be overcome by the use of a TiO_2 barrier, which has been studied by Huo et al. The overall performance of the DSC was increased to 6.98%, compared to that of P25 and pure SnO_2 photoelectrodes, due to the high light scattering effect, fast electron transport due to the 1D structure and the enhanced dye loading capability (Huo et al. 2014).

Desai et al. has also studied similar hybrid materials using TiO_2 and SnO_2 (Desai et al. 2013). Further research based on the TiO_2–SnO_2 composite has been done using TiO_2 compact layer with nanocrystalline SnO_2 (Yang et al. 2014), using a core-shell structure (Knauf et al. 2015), by the synthesis of hybrid nanofibers (Wali et al. 2016) and also by the sol-gel and coprecipitation method (Endarko and Adawiyah 2019).

TiO_2 has also being incorporated with the p-type semiconductor NiO, by Hsu et al. They have used a flower like structure in order to enhance the light scattering, trapping for efficient photon harvesting and offering a large surface area for dye adsorption, thereby improved power conversion efficiency. The p-type component in TiO_2–NiO nanoparticles has significantly decreased the charge recombination, but its photovoltaic efficiency remains below 4% (Hsu et al. 2015).

Maçaira et al. prepared a SiO_2/TiO_2 composite photoelectrode to overcome the high number of grain boundaries and morphological defects, that cause recombination reactions, of a usual TiO_2 photoelectrode, while keeping the surface area at an optimum level. The high efficiency of 9.20% is due to the high surface area, and the low recombination (Maçaira et al. 2017). A similar study has been done by Cardoso et al. tuning anatase and rutile phase transition temperature (Cardoso et al. 2019). More recently, studies have been conducted using gold, SiO_2 and TiO_2 in a core/shell structure (Fadhilah et al. 2019; Li et al. 2019).

Furthermore, Fe_2O_3 has also been studied considering the cocktail effect of the two conduction bands, to prevent electron recombination (Im et al. 2011).

15.3.3 Metal Nitrides

Huang et al. have studied the composite gallium nitride (GaN) with TiO_2 as a photoelectrode material in order to enhance the power conversion. Here a maximum

efficiency of 4.90% has been obtained after optimizing the amount of GaN used in the composite mixture, which is an increase of about 60% when compared with that of a DSC of pure P25 nanoparticles. Here the photovoltaic performance has increased due to the decrease in charge transfer resistance and the increase in charge recombination resistance, at the electrolyte/dye/semiconductor interface (Huang et al. 2014).

Another metal nitride composite that has been studied is titanium nitride (TiN) with TiO_2. Higher content of TiN has shown a higher absorption of visible light. The V_{OC} has been increased as the flat band potential has shifted to a more negative value. The increase in FF can be attributed to the high conductivity of the film. However, this system yielded a decrease in J_{sc} which can be due to the low amounts of dye adsorption. Here an efficiency of 7.27% was observed, which is much higher than that obtained by simply using a P25 photoanode (Li et al. 2015).

15.3.4 Metal Sulfides

Photovoltaic properties of some metal sulfide-TiO_2 composites have been studied, several which have shown remarkable potential in solar cell applications. Ding et al. studied a one step, high temperature, solvothermal method to synthesize TiO_2-sulfide nanospheres. They were prepared using the respective hydrated sulfate. The considered composite materials are CdS (Wang et al. 2010), Cu_2S (Peng et al. 2014), ZnS (Sadikin et al. 2019) and Co_9S_8 (Yuan et al. 2017). These sulfide containing composites absorbed visible light and the high reaction temperature improved the crystallinity, making the composite mixtures suitable for DSSC application as well (Ding et al. 2012).

15.3.5 Carbon Nanostructures

Carbonaceous nanomaterials are an economic option to composite with TiO_2, which can result in enhanced efficiency of DSCs. The proposed activity of carbonaceous materials is either by excitation of the carbonaceous compound followed by charge injection to TiO_2 (Wang et al. 2005) or by formation of a Ti–O–C bond which leads to the creation of energy states within the band gap of TiO_2 (Pyrgiotakis et al. 2005), facilitating more efficient light absorption. The mechanism depends on the synthetic technique used. These composites also show improvement in dye adsorption and increased electron transport.

One of the most commonly used carbon nanostructures in preparing composites with TiO_2 are carbon nanotubes (CNT). As they not only have a large electrons-storage capacity, but also can show electronic conductivity similar to that of metals (Kongkanand et al. 2007). The 1D nano-structure and good electrical conductivity of CNT are beneficial to transport the electrons within TiO_2 films and enhance their photocatalytic and photoelectric conversion efficiencies (Yu et al. 2007).

Table 15.2 Table with the maximum efficiencies obtained by composites/hybrid materials

Modification	Efficiency (%)	References
SiO_2/TiO_2	9.20	(Maçaira et al. 2017)
TiN/TiO_2	7.27	(Li et al. 2015)
SnO_2 nanorods-TiO_2 hybrid material	6.98	(Huo et al. 2014)
Ag coated TiO_2	6.86	(Peng et al. 2013)

Yu et al. studied CNT with both P25 nanoparticles and TiO_2 hollow spheres and obtained an efficiency of 4.71%, under optimal conditions when hollow spheres were used. The improvement in the conversion efficiency is due to the fact that CNT can reduce the electrolyte/electrode interfacial resistance, the recombination rate of excited electrons and holes, and enhance the transport of electrons from the films to FTO substrates (Yu et al. 2011). More studies have been done using functionalized single-walled CNTs (Jang et al. 2004), using low temperature fabrication methods (Lee et al. 2008) and by the synthesis of a hybrid material with multi-walled CNTs (Mehmood et al. 2015).

Incorporating carbon nanofibres (CF) in TiO_2 has also been studied extensively. The CF/TiO_2 composite has been studied after using a spray-coating mechanism (Sigdel et al. 2014), coaxial electrospinning (Hieu et al. 2014) and bilayer structuring (TiO_2/CF and $Ag@TiO_2$ core-shell structure) (Lu et al. 2018).

Research has also been done using graphene and TiO_2 as the composite material, as graphene has excellent optical and electrical properties. Studies have used electrospun TiO_2-graphene nanofibers (Anish Madhavan et al. 2012) and simple inclusion of graphene in the composite material (Kusumawati et al. 2014; Zhu et al. 2014).

A unique study done with the use of graphene was by Chen et al., where they used a TiO_2/graphene/TiO_2 sandwich structures. The sandwich structure improved the performance of the DSC ($\eta = 3.93\%$) over pure TiO_2 and TiO_2/graphene containing photovoltaics. This improvement is associated with an increase in the absorption of light, a wide range of absorption wavelengths, shorter charge transportation distances, and the suppression of charge recombination when the graphene is applied (Chen et al. 2014).

Since graphene has a higher work function than TiO_2 (Dahl et al. 2014), it allows an increase in charge separation by electron injection into the graphene sheets. Chemical utilization of graphene has been established through reduction of graphene oxide sheets and has been used in DSC for the improvement of its photovoltaic properties (Low and Lai 2018; Suriani et al. 2019) (Table 15.2).

15.4 Modifications Done by Doping

Changes in the semiconductor electronic band structure can be accomplished by substitutional doping, which is the deliberate replacement of semiconductor atoms

in the host material with impurities, usually of similar atomic radius to the ion to be replaced in the lattice. Here, either electrons are donated by the dopant (n-type doping), where the valency is higher in the dopant than of the host material, or holes would be donated by the dopant (p-type doping), where the valency is lower than that of the host material. Figure 15.7 illustrates the changes in the energy band structure due to doping.

Doping in TiO_2 can be achieved by either the replacement of Ti^{4+} or O^{2-} in the lattice. Since the lower edge of the CB has a high contribution of Ti^{4+} 3d orbitals, replacing Ti^{4+} by a different cation is expected to heavily affect the CB structure. The upper edge of the VB consists of O^{2-}p orbitals and replacing O^{2-} by a different anion affects the VB energy (Roose 2015). Moreover, electron traps are caused by oxygen vacancies, titanium interstitials and the reduced crystal surface, which would lead to a higher conductivity. A positive shift of the flat band potential from the CB would lead to a better electron injection, giving a better J_{SC}, but a lower V_{OC} as the gap between the Fermi level and the potential of the redox electrolyte becomes smaller.

Even though adding an n-type dopant to the system would increase the number of free electrons in the TiO_2 system, these can also act as defects that trap charge carriers, encouraging electron-hole recombination reactions, which would decrease the photon-to-electron conversion efficiency (Duan et al. 2012) and V_{OC} (Roose 2015) at high dopant content. Thus, dopants, at any concentration, simply cannot improve the efficiency of a DSC. An improvement in the efficiency is only seen at an optimum concentration of the dopant.

Furthermore, as the (sensitizer) dye molecules anchor to Ti atoms, the replacement of Ti with another cation can also affect dye adsorption due to different binding strengths between the dye and the dopant, or because the dopant induces oxygen vacancies (De Angelis et al. 2010).

The most common method of depositing the dopant is by simply mixing the dopant with TiO_2, using either a sol–gel, hydrothermal, solvothermal, spray pyrolysis, atomic layer deposition, electrochemical deposition, sonochemical, microwave

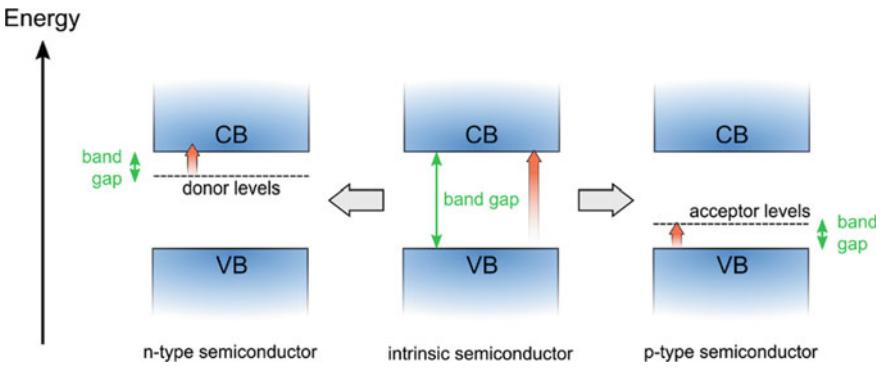

Fig. 15.7 Effects of doping on TiO_2

or electrospinning method. However, there are other methods of deposition possible, namely; pulse laser deposition, immersing the final TiO_2 sample in a solution of the dopant and applying a voltage, anodization and thermal oxidation.

Dopants of TiO_2 can be further categorized into four types: nonmetals, transition metals, post-transition metals, lanthanides.

15.4.1 Nonmetals

Even though they are not studied much, nonmetals have been used as a dopant for the improvement of TiO_2. Studies have been conducted by doping nitrogen, sulfur and fluorine, either by itself or as a combination of dopants.

TiO_2 is oxygen deficient, and produces species which can destroy both the dye and redox electrolyte. Ma et al. doped TiO_2 with nitrogen to overcome this problem. Nitrogen doped TiO_2 was synthesized by heating commercial anatase TiO_2 in the presence of N_2. The doped TiO_2 system showed an outstanding efficiency of 8% compared to those of the other two types of commercially available TiO_2 nanoparticles [P25 and Solaronix, Ti-Nanoxide D (SL-D)] included in the study. As the V_{OC} among the three systems had no drastic change, it can be assumed the N doping had not significantly affected the CB edge. However, N doping not only enhanced the effective surface area for dye adsorption, leading to an efficient photoresponse in the visible region, N doped TiO_2 was stable under extended thermal stress (Ma et al. 2005). It should be noted however that in this study the N doped TiO_2 was in the shape of needles, while the structure of P25 and SL-D were different.

Further, Simya et al. have shown that sulfur can be used as a co-dopant with N doped TiO_2 to decrease the band gap energy and improve light harvesting. DSCs fabricated with S and N-doped TiO_2 gave an efficiency of 1.80% in the visible region, which is 50% more when compared to pure TiO_2 (Simya et al. 2014). Fluorine has also been used as a co-dopant along with Ho^{3+} and Yb^{3+}, to synthesize a doped TiO_2, which exhibited upconversion properties (Yu et al. 2014). This would be further discussed under lanthanide dopants.

15.4.2 Transition Metals

Transition metal dopants can be considered as the most commonly used type of dopant with TiO_2, as studies are still being conducted using these metals. The main reason behind this could be the ability of most transition metals to shift the conduction band edge to a more negative potential, for efficient electron transport.

Among all the considered transition metals, niobium has been studied the most. Lee et al. coated Nb doped TiO_2 on the transparent conducting oxide and found that, under optimal amounts of the dopant, the Nb doped TiO_2 layer acted as a blocking layer, reducing the interfacial resistance compared to the undoped TiO_2 compact

layer by making an ohmic contact between FTO and the TiO_2 film. This system gave an efficiency of 6.58%, which is about 21.2% enhancement when compared with bare FTO-based DSCs (Lee et al. 2009).

In 2010, Chandiran et al. studied doping of TiO_2 with Nb^{5+} to create donor levels below the conduction band and promote charge transport over recombination and improving the transparency. Under optimal conditions, doped with 0.5% Nb and post treatment with $TiCl_4$, an overall efficiency of 8.7% was obtained. Here, Nb^{5+} would replace the Ti^{4+} in the lattice structure as they have similar radii and form strong hybridization with 4d and 3d orbitals. Due to the down-shift of the conduction band edge, doping with Nb^{5+} allows to drastically slow the dynamics of electron recombination with I_3^-, resulting in an increase of electron lifetime. The $TiCl_4$ post-treatment also acts to increase the electron lifetime. On the other hand, the gain achieved is partially compensated by a loss of electron transport (Chandiran et al. 2010). Lu et al. have performed a similar study, with the use of a water-soluble precursor, and have obtained a positive shift in the flat band potential along with an increase in the conductivity. An overall efficiency of 7.8% was obtained, and an increase of 18.2% compared to pure TiO_2 (Lü et al. 2010).

Another widely used transition metal used in doping is silver. Because the Nernstian potential of the conduction band in TiO_2 is lower than the standard electrode potential of Ag^+/Ag, the difference of potential is formed. Thus, the electron will be transferred from the conduction band of TiO_2–Ag^+ which was absorbed on the surface of TiO_2 nanospheres, and silver ions are reduced to silver atoms (Han et al. 2012).

Peng et al., studied the change in solar cell efficiency when silver is coated by photo-deposition. At the deposition time of 10 min, the conversion efficiency was improved from 5.97 to 6.86%. The Ag layer formed can reflect incident light and lengthen the optical path in electrodes, and in this case lead to an increase in J_{sc} up to 13.55 mA cm^{-2}. Furthermore, electron recombination was slowed down by Ag deposition, which led to a larger V_{OC} of 0.735 V. However, past the optimal deposition time, there was an increase in the series resistance due to the formation of the Ag barrier layer (Peng et al. 2013).

Wei and coworkers too have studied the use of the noble metal silver nanoparticles in TiO_2 nanotubes, using electrophoretic deposition. It was observed that the total dye adsorption was reduced with the deposition time, as silver nanoparticles on the surface of TiO_2, reduce adsorption capacity. The holes in the electrolyte and photoelectrons in TiO_2 recombine easily through the TiO_2–Ag-electrolyte interface (Wei et al. 2017), which lead to an overall efficiency of 5.01%, under optimum conditions of 30 min of deposition.

Similar doping methods have been done using zinc (Ghanbari Niaki et al. 2014), copper (Navas et al. 2012; Wijayarathna et al. 2008), nickel (Archana et al. 2013) and iron (Liu 2014), in order to improve photovoltaic properties.

Yttrium too has been used as a dopant as it is known to not change the band gap of TiO_2 (Li et al. 2009), even though the problems arise when considering the long-term stability of the DSC. With 1% Y-TiO_2, an efficiency of 9.1% was observed.

The improvement in performance can be attributed to the increase of electron lifetime in the new photoanode, which affords close to unity charge collection efficiency (Chandiran et al. 2011).

15.4.3 Post-transition Metal

As another part of the study done by Chandrian et al. in (2011), gallium too was doped to TiO_2, to improve the charge collection efficiency and the electrode transparency. The highest efficiency obtained with 1% gallium was 8.1%. With the increase in percentage of the Ga dopant, an increase in the open circuit voltage from 732 to 768 mV was observed. In turn, lower short circuit current led to a smaller overall efficiency. As the impurity levels increase the band gap of TiO_2 would also increase, making it favorable for electron transport. But having more positive conduction band potential would make it unfavorable for the electron to transport. Then again, having a more negative conduction band would also be unfavorable, which is why an optimum amount of the dopant must be used (Chandiran et al. 2011).

Another widely used post transitional metal as a dopant in TiO_2 is tin. Duan et al. studied tin as a dopant so as to improve the charge collection and electron transport while maintaining optimum J_{SC}. The Sn-doped TiO_2 nanoparticles showed a high V_{OC} of 722 mV, due to the negative shift of the flat band potential, and an enhanced J_{SC} of 16.01 mA cm^{-2}, due to the faster electron transport in the Sn-doped TiO_2 films (Duan et al. 2012).

Despite the lack of agreement on aluminium doped TiO_2, the substitution of Al into the TiO_2 lattice was confirmed by Pathak et al. It was suggested that Al doping reduces the number of sub-bandgap states, increasing the V_{OC} and electron conductivity, which led to an overall improvement in device performance of DSC (Pathak et al. 2014).

15.4.4 Lanthanides

Ytterbium and holmium, have been used, together with fluorine, as an upconversion material of TiO_2 by Yu et al. Upconversion materials have the ability to convert lower energy (near-infrared or infrared) radiation into high energy radiation (ultraviolet or visible) via multiphoton absorption and energy transfer (ET) processes (Zou et al. 2012). The improved DSCs conversion efficiency of 8.93% observed is associated with closer attachment of the upconversion process, enhanced light harvesting, and photogenerated electron–hole pair separation, as well as elevated Fermi level. Ho^{3+}–Yb^{3+}–F^- tridoped TiO_2 had excellent NIR-to-green upconversion ability helping dye sensitized solar cells to utilize more NIR light (Yu et al. 2014).

Erbium and ytterbium have also been used as co-dopants, in an upconversion material in the work of Shan et al. (Shan and Demopoulos 2010).

Table 15.3 Table with the maximum efficiencies obtained by doping TiO_2

Modification	Efficiency (%)	References
1% Y^{3+} doped TiO_2	9.00	(Chandiran et al. 2011)
Ho^{3+}–Yb^{3+}–F^- tridoped TiO_2	8.93	(Yu et al. 2014)
0.5% Nb doped TiO_2	8.7	(Chandiran et al. 2010)
1% Ga doped TiO_2	8.1	(Chandiran et al. 2011)
N_2 doped TiO_2	8.00	(Ma et al. 2005)

Other lanthanides that have been used as dopant to improve photovoltaic properties of TiO_2 are neodymium (Yao et al. 2006), lanthanum (Zhang et al. 2010) and cerium (Zhang et al. 2012) (Table 15.3).

15.5 Potential Competitors

After the first report of O'Regan and Grätzel in the application of nano-sized TiO_2 porous film electrodes in DSCs (O'Regan and Grätzel 1991), TiO_2 has been investigated under numerous modifications, some of which have been reviewed in this chapter. Modifications attempted to improve the surface area, light scattering effect, charge collection efficiency and interface quality. Although the development of TiO_2 based DSCs have shown much promise, many more competitors have arisen in the past decade, challenging TiO_2 as the semiconductor material for DSCs.

Two of the main factors affecting performance in DSC is efficient electron injection from the dye and rapid electron transport. TiO_2 nanoparticle based photoanodes have some limitations due to the presence of a large number of grain boundaries, and leads to electron recombination losses and also poor efficiency in the near infrared region (Sugathan et al. 2015).

Some researchers consider ZnO as the most promising alternative to TiO_2. There are several reasons behind this, such as the fact that both TiO_2 and ZnO have similar band gaps (~3.2 eV and ~3.3 eV, respectively) and electron affinities. However, comparing the two, ZnO has a much higher electron diffusivity and electron mobility of about 115–155 $cm^2\ V^{-1}\ s^{-1}$, which implies efficient electron transport and the reduction of recombination rates (Vittal and Ho 2017). Apart from the large excitation binding energy, low cost and stability against photocorrosion (Anta et al. 2012) the crystalline structure of ZnO is conducive to anisotropic growth (Baxter et al. 2006), unlike that of TiO_2, making it a prime candidate for DSCs with photoanodes consisting of nanorods, nanowires or nanosheets.

Many recent studies show the application of ZnO nanostructures for photoelectrodes with enhanced photovoltaic performance of DSCs. Some studies have

focused on the effect of morphologies such as nanofibre network mats (Kim et al. 2007), nano-sheets (Li et al. 2012) and among others (Giannouli and Spiliopoulou 2012; Zhang et al. 2009). While others have investigated synthesis procedures (Zhao et al. 2008).

After much study, the maximum reported efficiency for pure ZnO based DSC, using a liquid electrolyte is 7.5% (Memarian et al. 2011), which is much lower than that of TiO_2 based DSC. The low conversion efficiencies of ZnO-based systems are most likely due to the dissolution of ZnO to Zn^{2+} by the adsorbed acidic dye, followed by the formation of an insulating layer of Zn^{2+} and dye molecules, blocking the injected electrons from the dye molecules to the semiconductor by the insulating layer (Hiroaki Horiuchi et al. 2003). As ZnO is more basic than TiO_2, it is more prone to be attacked by acidic dyes. In order to avoid the formation of the insulating layer, many core-shell structures have been developed by coating a buffer layer on the ZnO surface. SiO_2 has been demonstrated to be a very effective shell material on ZnO, which prevents the formation of aggregates through a strong interaction between Si^{4+} and O^{2-} ions (Shin et al. 2007). Many core–shell structures have been developed using ZnO nanocrystals and ZnO nanowires, by coating a buffer layer of Al_2O_3 (Matt Law et al. 2006), TiO_2 (Matt Law et al. 2006), and even ZnO (Guillén et al. 2013) on their surfaces, to prevent the formation of the insulating Zn^{2+}/dye complex. ZnO has also been studied with CuO, with and without TiO_2 blocking layer, in the presence of Co^{2+}/Co^{3+} redox electrolyte (Habibi et al. 2014).

Most nanostructures of the semiconductor material, have been synthesized so as the final product would give a large surface area for the dye adsorption. ZnO and Fe_2O_3 have been taken into consideration as they are both suitable to prepare thin films, have good electrical conductivity, are inexpensive, and have a very good chemical stability. These reasons have led to use these materials in energy storage and photoelectrochemistry (Livage and Ganguli 2001). Reda et al. have used ZnO and Fe_2O_3 as photoanode materials, and studied the photovoltaic characteristics by changing the annealing temperature, in order to obtain a higher incident light to electrical energy conversion and has obtained a maximum efficiency of 2.2% for ZnO and 1.2% for Fe_2O_3 (Reda 2010). Moreover, due to the suitable band gap of about 2.2 eV Fe_2O_3, various nanostructures have been synthesized, including nanocubes (Ozaki et al. 1984), nano-rings (Jia et al. 2008), dendrites (Liang et al. 2010) and polyhedron (Lv et al. 2010). Fe_2O_3 has also been studied as a photoanode material in DSCs, using a one-pot, low temperature synthesis method (Manikandan et al. 2014).

Another possible alternative to TiO_2 is Nb_2O_5, due to the larger band gap of 3.49 eV, leading to a higher conduction band edge of −1.32 eV compared to that of TiO_2 (Ghosh et al. 2011), which could lead to higher V_{OC}. Moreover, in terms of IPCE Nb_2O_5 has the second value of 18%, after that of TiO_2, which has 45% (Jose et al. 2009). Ghosh et al. synthesized a nanoforest of Nb_2O_5 using laser ablation, under several gas compositions and pressure conditions, which was quite similar to vertically aligned nanocrystals to Gratzel's TiO_2 nanoforest. This study has also encouraged the growth of photoanode material, with high conduction band levels such as Ta_2O_5 and $SrTiO_3$, in a similar manner, for future studies in DSCs (Ghosh et al. 2011).

Another upcoming class of competitors for TiO_2, are metal-organic frameworks (MOFs), which are porous crystalline material made up of inorganic nodes, which are mostly metal cations or clusters; and organic linkers, which are organic ligands (Li et al. 2014). The light harvesting properties of MOFs were found to depend on the properties of the linker. Since the linkers are organic molecules having p-electrons, they absorb energy from the UV and blue regions in the electromagnetic spectrum for electronic transitions. As result, metal-to-ligand or ligand-to-metal energy transfer processors are possible, depending on the selection of the linker and metal type. Apart from this, the controllable architecture, adjustable pore size and high surface area of MOFs encouraged the application of them in DSCs. Most MOFs are insulators. However, MOF-5 has exhibited semiconductor behavior due to the geometric type of metal clusters containing ZnO units in the network which can act as quantum dots (Llabrés i Xamena et al. 2007). Various studies have been done by incorporating MOFs into either the working electrode, counter electrode, dye or the electrolyte medium, that is, any component of a DSC. The highest efficiency of 8.49%, has so far been attained by the Al-MOG MOF used in the electrolyte medium by Fan et al. (Fan et al. 2014). So far MOFs have only been incorporated into n-type DSCs and studies are yet to be done for p-type DSCs.

15.6 Conclusion

This chapter has discussed four aspects of modifying TiO_2, in order to improve the efficiency of a TiO_2 based DSCs. All these four modifications have a different approach to improve photovoltaic properties. The main purpose of changing the nanostructure would be to increase the dye adsorption, by enhancing the effective surface area. One-dimensional nanostructures are widely adopted to improve the electron transport, and minimizing recombination reactions. Surface modifications aim to decrease in grain boundaries which can act as trapping sites of the injected electrons, leading to recombination; and also, to strengthen and increase the attachment of the dye to the surface. Composites aim to provide a smoother, step-like electron

Table 15.4 Table with maximum efficiencies obtained by each modification

Modification		Efficiencies (%)	References
Structure and morphology	Nanoparticle (haze)	11.1	(Chiba et al. 2006)
	Nano-embossed hollow spheres	10.34	(Koo et al. 2008)
Composites	TiO_2–SiO_2 composite	9.20	(Maçaira et al. 2017)
Doping	Doping with 1% Y^{3+}	9.00	(Chandiran et al. 2011)
	Optimizing the amount of Ho^{3+}-Yb^{3+}-F^- tri doped TiO_2/pure TiO_2	8.93	(Yu et al. 2014)

transport from the dye to the working electrode, minimizing electron back transfer and recombination. Doping can improve the photovoltaic properties in two methods: better electron injection, and improved dye adsorption. The highest efficiencies obtained under these modifications have been tabulated in Table 15.4.

Even after extensive studies to improve the efficiency of DSCs, the highest efficiency is still 11.1% obtained by tuning the used TiO_2 nanoparticle sizes (Chiba et al. 2006). Even so, the improvement seen in the overall efficiency of DSCs along with these modifications, can be said to be promising for a more efficient and greener energy source.

References

Anish Madhavan A, Kalluri SK, Chacko D, Arun TA, Nagarajan S, Subramanian Nair KRV, Sreekumaran A, Nair SV, Balakrishnan A (2012) Electrical and optical properties of electrospun TiO_2-graphene composite nanofibers and its application as DSSC photo-anodes. RSC Adv 2:13032

Anta JA, Guillén E, Tena-Zaera R (2012) ZnO-based dye-sensitized solar cells. J Phys Chem C 116:11413–11425

Archana PS, Naveen Kumar E, Vijila C, Ramakrishna S, Yusoff MM, Jose R (2013) Dalt Trans 42:1024–1032

Bai L, Liu X, Li M, Guo K, Luoshan M, Zhu Y, Jiang R, Liao L, Zhao X (2016) Plasmonic enhancement of the performance of dye-sensitized solar cells by incorporating hierarchical TiO_2 spheres decorated with Au nanoparticles. Electrochim Acta 190:605–611

Baxter JB, Walker AM, van Ommering K, Aydil ES (2006) Synthesis and characterization of ZnO nanowires and their integration into dye-sensitized solar cells. Nanotechnol 17:S304–S312

Beranek R, Tsuchiya H, Sugishima T, Macak JM, Taveira L, Fujimoto S, Kisch H, Schmuki P (2005) Enhancement and limits of the photoelectrochemical response from anodic TiO_2 nanotubes. Appl Phys Lett 87:243114

Bhatti KA, Khan MI, Saleem M, Alvi F, Raza R, Rehman S (2019) Analysis of multilayer based TiO_2 and ZnO photoanodes for dye-sensitized solar cells. Mater Res Express 6:075902

Cardoso BN, Kohlrausch EC, Laranjo MT, Benvenutti EV, Balzaretti NM, Arenas LT, Santos MJL, Costa TMH (2019) Tuning anatase-rutile phase transition temperature: TiO_2 /SiO_2 nanoparticles applied in dye-sensitized solar cells. Int J Photoenergy 2019:1–9

Chandiran AK, Casas-Cabanas M, Comte P, Zakeeruddin SM, Graetzel M (2010) Doping a TiO_2 photoanode with Nb5+ to enhance transparency and charge collection efficiency in dye-sensitized solar cells. J Phys Chem C 114:15849–15856

Chandiran AK, Etgar L, Graetzel M (2011) 9232–9240

Chen L, Hsu C, Chan P, Zhang X, Huang C (2014) Improving the performance of dye-sensitized solar cells with TiO_2/graphene/TiO_2 sandwich structure. Nanoscale Res Lett 9:1–7

Chiba Y, Islam A, Watanabe Y, Komiya R, Koide N, Han L (2006) Dye-sensitized solar cells with conversion efficiency of 11.1%. Jpn J Appl Phys 45:L638–L640

Choi H, Kim S, Kang SO, Ko J, Kang M-S, Clifford JN, Forneli A, Palomares E, Nazeeruddin MK, Grätzel M (2008) Stepwise cosensitization of nanocrystalline TiO_2 films utilizing Al_2 O_3 layers in dye-sensitized solar cells. Angew Chem Int Ed 47:8259–8263

Chou C-S, Yang R-Y, Yeh C-K, Lin Y-J (2009) Preparation of TiO_2 /nano-metal composite particles and their applications in dye-sensitized solar cells. Powder Technol 194:95–105

Dahl M, Liu Y, Yin Y (2014) Composite titanium dioxide nanomaterials. Chem Rev 114:9853–9889

De Angelis F, Fantacci S, Selloni A, Nazeeruddin MK, Grätzel M (2010) First-principles modeling of the adsorption geometry and electronic structure of Ru(II) dyes on extended TiO_2 substrates for dye-sensitized solar cell applications. J Phys Chem C 114:6054–6061

De Jonge LT, Leeuwenburgh SCG, Wolke JGC, Jansen JA (2008) Organic-inorganic surface modifications for titanium implant surfaces. Pharm Res 25: 2357–2369

Deepa KG, Lekha P, Sindhu S (2012) Efficiency enhancement in DSSC using metal nanoparticles: a size dependent study. Sol Energy 86:326–330

Desai UV, Xu C, Wu J, Gao D (2013) Hybrid TiO_2 –SnO_2 nanotube arrays for dye-sensitized solar cells. J Phys Chem C 117:3232–3239

Ding S, Yin X, Lü X, Wang Y, Huang F, Wan D (2012) One-step high-temperature solvothermal synthesis of TiO_2 /sulfide nanocomposite spheres and their solar visible-light applications. ACS Appl Mater Interfaces 4:306–311

Duan Y, Fu N, Liu Q, Fang Y, Zhou X, Zhang J, Lin Y (2012) Sn-doped TiO_2 photoanode for dyesensitized solar cells. J Phys Chem C 116:8888–8893

Endarko E, Adawiyah SR (2019) Experimental study of TiO_2 nanoparticles fabrication by sol-gel and coprecipitation methods for TiO_2/SnO_2 composite thin film as photoanode. J ILMU DASAR 20:61

Fadhilah N, Pratama DY, Sawitri D, Risanti DD (2019) Preparation of Au@TiO_2@SiO_2 core-shell nanostructure and their light harvesting capability on DSSC (dye sensitized solar cells). In: AIP conference proceedings. AIP Publishing LLC, p 060007

Fan J, Li L, Rao H-S, Yang Q-L, Zhang J, Chen H-Y, Chen L, Kuang D-B, Su C-Y (2014) A novel metal–organic gel based electrolyte for efficient quasi-solid-state dye-sensitized solar cells. J Mater Chem A 2:15406

Feng X, Shankar K, Varghese OK, Paulose M, Latempa TJ, Grimes CA (2008) Vertically aligned single crystal TiO_2 nanowire arrays grown directly on transparent conducting oxide coated glass: synthesis details and applications. Nano Lett 8:3781–3786

Fraoucene H, Sugiawati VA, Hatem D, Belkaid MS, Vacandio F, Eyraud M, Pasquinelli M, Djenizian T (2019) Optical and electrochemical properties of self-organized TiO_2 nanotube arrays from anodized Ti−6Al−4V alloy. Front Chem 7:66

Gao C, Li X, Lu B, Chen L, Wang Y, Teng F, Wang J, Zhang Z, Pan X, Xie E (2012) A facile method to prepare SnO_2 nanotubes for use in efficient SnO_2–TiO_2 core–shell dye-sensitized solar cells. Nanoscale 4:3475

Ghadiri E, Taghavinia N, Zakeeruddin SM, Gra M (2010) Enhanced electron collection efficiency in dye-sensitized solar cells based on nanostructured TiO_2 hollow fibers. Nano Lett 10:1632–1638

Ghanbari Niaki AH, Bakhshayesh AM, Mohammadi MR (2014) Double-layer dye-sensitized solar cells based on Zn-doped TiO_2 transparent and light scattering layers: improving electron injection and light scattering effect. Sol Energy 103:210–222

Ghosh R, Brennaman MK, Uher T, Ok MR, Samulski ET, McNeil LE, Meyer TJ, Lopez R (2011) Nanoforest Nb_2O_5 photoanodes for dye-sensitized solar cells by pulsed laser deposition. ACS Appl Mater Interfaces 3:3929–3935

Giannouli M, Spiliopoulou F (2012) Effects of the morphology of nanostructured ZnO films on the efficiency of dye-sensitized solar cells. Renew Energy 41:115–122

Gong J, Liang J, Sumathy K (2012) Review on dye-sensitized solar cells (DSSCs): fundamental concepts and novel materials. Renew Sustain Energy Rev 16:5848–5860

Guillén E, Azaceta E, Vega-Poot A, Idígoras J, Echeberría J, Anta JA, Tena-Zaera R (2013) ZnO/ZnO core–shell nanowire array electrodes: blocking of recombination and impressive enhancement of photovoltage in dye-sensitized solar cells. J Phys Chem C 117:13365–13373

Habibi MH, Karimi B, Zendehdel M, Habibi M (2014) Preparation of nanostructure mixed copper-zinc oxide via co-precipitation rout for dye-sensitized solar cells: the influence of blocking layer and Co(II)/Co(III) complex redox shuttle. J Ind Eng Chem 20:1462–1467

Han Z, Zhang J, Yu Y, Cao W (2012) A new anode material of silver photo-deposition on TiO_2 in DSSC. Mater Lett 70:193–196

Hieu NT, Baik SJ, Jun Y, Lee M, Chung OH, Park JS (2014) Electrospun coaxial titanium dioxide/carbon nanofibers for use in anodes of dye-sensitized solar cells. Electrochim Acta 142:144–151

Horiuchi H, Katoh R, Hara K, Yanagida M, Murata S, Arakawa H, Tachiya M (2003) Electron injection efficiency from excited N3 into nanocrystalline ZnO films: effect of (N3-Zn^{2+}) aggregate formation. J Phys Chem B 107:2570–2574

Hsu WWC, Chen MWC, Zhang X, Sutanto I, Taguchi T, Zhi J, Chen A, Cui H, Huang F, Williams VO, Jeong NC, Prasittichai C, Farha OK, Pellin MJ, Hupp JT (2015) NiO-decorated mesoporous TiO_2 flowers for an improved photovoltaic dye sensitized solar cell. Phys Chem Chem Phys 80:6185–6196

Huang Y-R, Huang T-W, Wang T-H, Tsai Y-C (2014) Improved performance of dye-sensitized solar cells using gallium nitride–titanium dioxide composite photoelectrodes. J Colloid Interface Sci 428:128–132

Huo J, Hu Y, Jiang H, Huang W, Li C (2014) SnO_2 nanorod@TiO_2 hybrid material for dye-sensitized solar cells. J Mater Chem A 2:8266–8272

Im JS, Lee SK, Lee Y-S (2011) Cocktail effect of Fe_2O_3 and TiO_2 semiconductors for a high performance dyesensitized solar cell. Appl Surf Sci 257:2164–2169

Jang S-R, Vittal R, Kim K-J (2004) Incorporation of functionalized single-wall carbon nanotubes in dyesensitized TiO_2 solar cells. Langmuir 20:9807–9810

Ji Y, Zhang M, Cui J, Lin K-C, Zheng H, Zhu J-J, Samia ACS (2012) Highly-ordered TiO_2 nanotube arrays with double-walled and bamboo-type structures in dye-sensitized solar cells. Nano Energy 1:796–804

Jia C-J, Sun L-D, Luo F, Han X-D, Heyderman LJ, Yan Z-G, Yan C-H, Zheng K, Zhang Z, Takano M, Hayashi N, Eltschka M, Kläui M, Rüdiger U, Kasama T, Cervera-Gontard L, Dunin-Borkowski RE, Tzvetkov G, Raabe J (2008) Large-scale synthesis of single-crystalline iron oxide magnetic nanorings. J Am Chem Soc 130:16968–16977

Jin Z, Chen S, Zhang Y, Wang Y, Zhang X, Liu Y (2019) Construction of hierarchical hetero-structured TiO_2 photoanodes for dye-sensitized solar energy conversion: case study of anatase nanobranches on rutile nanorod arrays. Chem Phys 522:129–133

Jose R, Thavasi V, Ramakrishna S (2009) Metal oxides for dye-sensitized solar cells. J Am Ceram Soc 92:289–301

Kang SH, Kim J, Kim Y, Kim HS, Sung Y (2007) Surface modification of stretched TiO_2 nanotubes for solid-state dye-sensitized solar cells. J Phys Chem C 111:9614–9623

Kim I-D, Hong J-M, Lee BH, Kim DY, Jeon E-K, Choi D-K, Yang D-J (2007) Dye-sensitized solar cells using network structure of electrospun ZnO nanofiber mats. Appl Phys Lett 91:163109

Kim D, Ghicov A, Albu SP, Schmuki P (2008) 16454–16455

Kim J-Y, Kang SH, Kim HS, Sung Y-E (2010) Preparation of highly ordered mesoporous Al_2O_3 /TiO_2 and Its application in dye-sensitized solar cells. Langmuir 26:2864–2870

Kim J-Y, Lee K-H, Shin J, Park SH, Kang JS, Han KS, Sung MM, Pinna N, Sung Y-E (2014) Highly ordered and vertically oriented TiO_2/AlO_3 nanotube electrodes for application in dye-sensitized solar cells. Nanotechnology 25:504003

Knauf RR, Kalanyan B, Parsons GN, Dempsey JL (2015) Charge recombination dynamics in sensitized SnO_2/TiO_2 core/shell photoanodes. J Phys Chem C 119:28353–28360

Kongkanand A, Domínguez RM, Kamat PV (2007) Single wall carbon nanotube scaffolds for photoelectrochemical solar cells. Capture and transport of photogenerated electrons. In: Nano Letters. American Chemical Society, pp. 676–680

Koo H-J, Kim YJ, Lee YH, Lee WI, Kim K, Park N-G (2008) Nano-embossed hollow spherical TiO_2 as bifunctional material for high-efficiency dye-sensitized solar cells. Adv Mater 20:195–199

Kopidakis N, Benkstein KD, van de Lagemaat J, Frank AJ (2003) Transport-limited recombination of photocarriers in dye-sensitized nanocrystalline TiO_2 solar cells. J Phys Chem B 107:11307–11315

Kuang D, Brillet J, Chen P, Takata M, Uchida S, Miura H, Sumioka K, Zakeeruddin SM, Grätzel M (2008) Application of highly ordered TiO_2 nanotube arrays in flexible dye-sensitized solar cells. ACS Nano 2:1113–1116

Kusumawati Y, Martoprawiro MA, Pauporté T (2014) Effects of graphene in graphene/TiO_2 composite films applied to solar cell photoelectrode. J Phys Chem C 118:9974–9981

Law M, Greene LE, Radenovic A, Kuykendall T, Liphardt J, Yang P (2006) ZnO-Al_2O_3 and ZnO-TiO_2 coreshell nanowire dye-sensitized solar cells. J Phys Chem B 110:22652–22663

Lee K-M, Hu C-W, Chen H-W, Ho K.-C (2008) Incorporating carbon nanotube in a low-temperature fabrication process for dye-sensitized TiO_2 solar cells. Sol Energy Mater Sol Cells 92:1628–1633

Lee S, Noh JH, Han HS, Yim DK, Kim DH, Lee J-K, Kim JY, Jung HS, Hong KS (2009) Nb-doped TiO_2: a new compact layer material for TiO_2 dye-sensitized solar cells. J Phys Chem C 113:6878–6882

Li J, Yang X, Yu X, Xu L, Kang W, Yan W, Gao H, Liu Z, Guo Y (2009) Rare earth oxide-doped titania nanocomposites with enhanced photocatalytic activity towards the degradation of partially hydrolysis polyacrylamide.. Appl Surf Sci 255:3731–3738

Li H, Zhang Y, Wang J (2012) ZnO nanosheets derived from surfactant-directed process: growth mechanism, and application in dye-sensitized solar cells. J Am Ceram Soc 95:1241–1246

Li Y, Chen C, Sun X, Dou J, Wei M (2014) Metal–organic frameworks at interfaces in dye-sensitized solar cells. ChemSusChem 7:2469–2472

Li CT, Li SR, Chang LY, Lee CP, Chen PY, Sun SS, Lin JJ, Vittal R, Ho KC (2015) Efficient titanium nitride/titanium oxide composite photoanodes for dye-sensitized solar cells and water splitting. J Mater Chem A 3:4695–4705

Li Mingyue, Yuan N, Tang Y, Pei L, Zhu Y, Liu J, Bai L, Li Meiya (2019) Performance optimization of dye-sensitized solar cells by gradient-ascent architecture of SiO_2@Au@TiO_2 microspheres embedded with Au nanoparticles. J Mater Sci Technol 35:604–609

Liang J, Li L, Song W, Fang J, Luo M, Li Y (2010) Rapid synthesis of dendrite- and platelet-like α-Fe_2O_3 via a hydrothermal oxidation route. Cryst Res Technol 45:405–408

Liu Q-P (2014) Analysis on dye-sensitized solar cells based on Fe-doped TiO_2 by intensity-modulated photocurrent spectroscopy and Mott–Schottky. Chin Chem Lett 25:953–956

Liu B, Aydil ES (2009) Growth of oriented single-crystalline rutile TiO_2 nanorods on transparent conducting substrates for dye-sensitized solar cells. J Am Chem Soc 131:3985–3990

Livage J, Ganguli D (2001) Sol-gel electrochromic coatings and devices: a review. Sol Energy Mater Sol Cells 68:365–381

Llabrés i Xamena FX, Abad A, Corma A, Garcia H (2007) MOFs as catalysts: activity, reusability and shapeselectivity of a Pd-containing MOF. J Catal 250:294–298

Low FW, Lai CW (2018) Reduced graphene oxide decorated TiO_2 for improving dye-sensitized solar cells (DSSCs). Curr Nanosci 14

Lu D, Qin L, Liu D, Sun P, Liu F, Lu G (2018) High-efficiency dye-sensitized solar cells based on bilayer structured photoanode consisting of carbon nanofiber/TiO_2 composites and Ag@TiO_2 core-shell spheres. Electrochim Acta 292:180–189

Lü X, Mou X, Wu J, Zhang D, Zhang L, Huang F, Xu F, Huang S (2010) Improved-performance dye-sensitized solar cells using Nb-doped TiO_2 electrodes: efficient electron injection and transfer. Adv Funct Mater 20:509–515

Luan X, Guan D, Wang Y (2012) Facile synthesis and morphology control of bamboo-type TiO_2 nanotube arrays for high-efficiency dye-sensitized solar cells. J Phys Chem C 116:14257–14263

Lv B, Liu Z, Tian H, Xu Y, Wu D, Sun Y (2010) Single-crystalline dodecahedral and octodecahedral α-Fe_2O_3 particles synthesized by a fluoride anion-assisted hydrothermal method. Adv Funct Mater 20:3987–3996

Ma T, Akiyama M, Abe E, Imai I (2005) High-efficiency dye-sensitized solar cell based on a nitrogen-doped nanostructured titania electrode. Nano Lett 5:2543–2547

Maçaira J, Andrade L, Mendes A (2017) Highly efficient SiO_2/TiO_2 composite photoelectrodes for dyesensitized solar cells. Sol Energy 158:905–916

Macak JM, Schmuki P (2006) Anodic growth of self-organized anodic TiO_2 nanotubes in viscous electrolytes. Electrochim Acta 52:1258–1264

Manikandan A, Saravanan A, Antony SA, Bououdina M (2014) One-pot low temperature synthesis and characterization studies of nanocrystalline α-Fe_2O_3 based dye sensitized solar cells. J Nanosci Nanotechnol 15:4358–4366

Manthina V, Pablo J, Baena C, Liu G, Agrios AG (2012) ZnO-TiO_2 nanocomposite films for high light harvesting efficiency and fast electron transport in dye-sensitized solar cells. J Phys Chem C 116:23864–23870

Mao X, Zhou R, Zhang S, Ding L, Wan L, Qin S, Chen Z, Xu J, Miao S (2016) High efficiency dyesensitized solar cells constructed with composites of TiO_2 and the hot-bubbling synthesized ultra-small SnO_2 nanocrystals. Sci Rep 6:19390

Marandi M, Bayat S, Naeimi Sani Sabet M (2019) Hydrothermal growth of a composite TiO_2 hollow spheres/TiO_2 nanorods powder and its application in high performance dye-sensitized solar cells. J Electroanal Chem 833:143–150

Mehmood U, Hussein IA, Harrabi K, Mekki MB, Ahmed S, Tabet N (2015) Hybrid TiO_2–multiwall carbon nanotube (MWCNTs) photoanodes for efficient dye sensitized solar cells (DSSCs). Sol Energy Mater Sol Cells 140:174–179

Memarian N, Concina I, Braga A, Rozati SM, Vomiero A, Sberveglieri G (2011) Hierarchically assembled ZnO nanocrystallites for high-efficiency dye-sensitized solar cells. Angew Chem Int Ed 50:12321–12325

Muduli S, Game O, Dhas V, Vijayamohanan K, Bogle KA, Valanoor N, Ogale SB (2012) TiO_2–Au plasmonic nanocomposite for enhanced dye-sensitized solar cell (DSSC) performance. Sol Energy 86:1428–1434

Nam SH, Shim H-S, Kim Y-S, Dar MA, Kim JG, Kim WB (2010) Ag or Au nanoparticle-embedded one-dimensional composite TiO_2 nanofibers prepared via electrospinning for use in lithium-ion batteries. ACS Appl Mater Interfaces 2:2046–2052

Navas J, Fernández-Lorenzo C, Aguilar T, Alcántara R, Martín-Calleja J (2012) Improving open-circuit voltage in DSSCs using Cu-doped TiO_2 as a semiconductor. Phys Status Solidi 209:378–385

Noor S, Sajjad S, Leghari SAK, Shaheen S, Iqbal A (2018) ZnO/TiO_2 nanocomposite photoanode as an effective UV-vis responsive dye sensitized solar cell. Mater Res Express 5:095905

O'Regan B, Grätzel M (1991) A low-cost, high-efficiency solar cell based on dye-sensitized colloidal TiO_2 films. Nature 353:737–740

Ozaki M, Kratohvil S, Matijević E (1984) Formation of monodispersed spindle-type hematite particles. J Colloid Interface Sci 102:146–151

Pandanga JJ, Nursam NM, Shobih, Prastomo N (2019) Synthesis and application of TiO_2 nanorods as photoanode in dye-sensitized solar cells. J Phys Conf Ser 1191:012023

Pathak SK, Abate A, Ruckdeschel P, Roose B, Gödel KC, Vaynzof Y, Santhala A, Watanabe S-I, Hollman DJ, Noel N, Sepe A, Wiesner U, Friend R, Snaith HJ, Steiner U (2014) Performance and stability enhancement of dye-sensitized and perovskite solar cells by Al doping of TiO_2. Adv Funct Mater 24:6046–6055

Peng W, Zeng Y, Gong H, Leng Y, Yan Y, Hu W (2013) Silver-coated TiO_2 electrodes for high performance dye-sensitized solar cells. Solid State Electron 89:116–119

Peng Z, Liu Y, Zhao Y, Chen K, Cheng Y, Chen W (2014) Incorporation of the TiO_2 nanowire arrays photoanode and Cu 2S nanorod arrays counter electrode on the photovoltaic performance of quantum dot sensitized solar cells. Electrochim Acta 135:276–283

Pichot F, Pitts JR, Gregg BA (2000). Low-temperature sintering of TiO_2 colloids: application to flexible dyesensitized solar cells. Electrochim Acta 135:276–283

Pyrgiotakis G, Lee S-H, Sigmund W (2005) Advanced photocatalysis with anatase nano-coated multi-walled carbon nanotubes. MRS Proc 876:R5.7

Qian J, Liu P, Xiao Y, Jiang Y, Cao Y, Ai X, Yang H (2009) TiO_2-coated multilayered SnO_2 hollow microspheres for dye-sensitized solar cells. Adv Mater 21:3663–3667

Rajamanickam N, Kanmani SS, Jayakumar K, Ramachandran K (2019) On the possibility of ferromagnetism and improved dye-sensitized solar cells efficiency in TiO_2/ZnO core/shell nanostructures. J Photochem Photobiol A Chem 378:192–200

Ran H, Fan J, Zhang X, Mao J, Shao G (2018) Enhanced performances of dye-sensitized solar cells based on Au-TiO_2 and Ag-TiO_2 plasmonic hybrid nanocomposites. Appl Surf Sci 430:415–423

Reda SM (2010) Synthesis of ZnO and Fe_2O_3 nanoparticles by solgel method and their application in dyesensitized solar cells. Mater Sci Semicond Process 13:417–425
Roose B, Pathak S, Steiner U (2015) Doping of TiO_2 for sensitized solar cells. Chem Soc Rev 44:8326–8349
Sadikin SN, Rahman MYA, Umar AA (2019) Zinc sulphide-coated titanium dioxide films as photoanode for dye-sensitized solar cells: effect of immersion time on its performance. Superlattices Microstruct 130:153–159
Shan G-B, Demopoulos GP (2010) Near-infrared sunlight harvesting in dye-sensitized solar cells via the insertion of an upconverter-TiO_2 nanocomposite layer. Adv Mater 22:4373–4377
Shin YJ, Lee JH, Park JH, Park NG (2007) Enhanced photovoltaic properties of SiO_2-treated ZnO nanocrystalline electrode for dye-sensitized solar cell. Chem Lett 36:1506–1507
Sigdel S, Dubey A, Elbohy H, Aboagye A, Galipeau D, Zhang L, Fong H, Qiao Q (2014) Dye-sensitized solar cells based on spray-coated carbon nanofiber/TiO_2 nanoparticle composite counter electrodes. J Mater Chem A 2:11448
Simya OK, Selvam M, Karthik A, Rajendran V (2014) Dye-sensitized solar cells based on visible-light-active TiO_2 heterojunction nanoparticles. Synth Met 188:124–129
Stergiopoulos T, Ghicov A, Likodimos V, Tsoukleris DS, Kunze J, Schmuki P, Falaras P (2008) Dyesensitized solar cells based on thick highly ordered TiO_2 nanotubes produced by controlled anodic oxidation in non-aqueous electrolytic media. Nanotechnol 19:235602
Sugathan V, John E, Sudhakar K (2015) Recent improvements in dye sensitized solar cells: a review. Renew Sustain Energy Rev 52:54–64
Suriani AB, Muqoyyanah, Mohamed A, Mamat MH, Othman MHD, Ahmad MK, Abdul Khalil HPS, Marwoto P, Birowosuto MD (2019) Titanium dioxide/agglomerated-free reduced graphene oxide hybrid photoanode film for dye-sensitized solar cells photovoltaic performance improvement. Nano-Struct Nano-Object 18:100314
Tributsch H (2004) Dye sensitization solar cells: a critical assessment of the learning curve. Coord Chem Rev 248:1511–1530
Vardys VS (1979) Democray in the baltic states 1918–1934: the stage and the actors. J Balt Stud 10:320–336
Vittal R, Ho KC (2017) Zinc oxide based dye-sensitized solar cells: a review. Renew Sustain Energy Rev 70:920–935
Wali Q, Bakr ZH, Manshor NA, Fakharuddin A, Jose R (2016) SnO_2–TiO_2 hybrid nanofibers for efficient dye-sensitized solar cells. Sol Energy 132:395–404
Wang W, Serp P, Kalck P, Faria JL (2005) Visible light photodegradation of phenol on MWNT-TiO_2 composite catalysts prepared by a modified sol–gel method. J Mol Catal A Chem 235:194–199
Wang H, Bai Y, Zhang H, Zhang Z, Li J, Guo L (2010) CdS quantum dots-sensitized TiO_2 nanorod array on transparent conductive glass photoelectrodes. J Phys Chem C 114:16451–16455
Wang S, Zhou X, Xiao X, Fang Y, Lin Y (2014) An increase in conversion efficiency of dye-sensitized solar cells using bamboo-type TiO_2 nanotube arrays. Electrochim Acta 116:26–30
Wei X, Nbelayim PS, Kawamura G, Muto H, Matsuda A (2017) Ag nanoparticle-filled TiO_2 nanotube arrays prepared by anodization and electrophoretic deposition for dye-sensitized solar cells. Nanotechnol 28:135207
Wijayarathna TRCK, Aponsu GMLP, Ariyasinghe YPYP, Premalal EVA, Kumara GKR, Tennakone K (2008) A high efficiency indoline-sensitized solar cell based on a nanocrystalline TiO_2 surface doped with copper. Nanotechnol 19:485703
Williams VO, Jeong NC, Prasittichai C, Farha OK, Pellin MJ, Hupp JT (2012) Fast transporting ZnOTiO_2 coaxial photoanodes for dye-sensitized solar cells based on ALD-modified SiO_2 aerogel frameworks. ACS Nano 6:6185–6196
Wu S, Han H, Tai Q, Zhang J, Xu S, Zhou C, Yang Y, Hu H, Chen B, Zhao X (2008) Improvement in dye-sensitized solar cells employing TiO_2 electrodes coated with Al_2O_3 by reactive direct current magnetron sputtering. J Power Sources 182:119–123
Wu W-Y, Hsu C-F, Wu M-J, Chen C-N, Huang J-J (2017) Ag–TiO_2 composite photoelectrode for dyesensitized solar cell. Appl Phys A Mater Sci Process 123:357

Yang S-C, Yang D-J, Kim J, Hong J-M, Kim H-G, Kim I-D, Lee H (2008) Hollow TiO2 hemispheres obtained by colloidal templating for application in dye-sensitized solar cells. Adv Mater 20:1059–1064

Yao Q, Liu J, Peng Q, Wang X, Li Y (2006) Nd-Doped TiO_2 nanorods: preparation and application in dye-sensitized solar cells. Chem An Asian J 1:737–741

Ye M, Wen X, Wang M, Iocozzia J, Zhang N, Lin C, Lin Z (2015) Recent advances in dye-sensitized solar cells: from photoanodes, sensitizers and electrolytes to counter electrodes. Mater. Today.

Yu J, Zhang J (2010) A simple template-free approach to TiO_2 hollow spheres with enhanced photocatalytic activity. Dalt Trans 39:5860. https://doi.org/10.1039/c0dt00053a

Yu H, Quan X, Chen S, Zhao H (2007) TiO_2-multiwalled carbon nanotube heterojunction arrays and their charge separation capability. J Phys Chem C 111:12987–12991

Yu J, Fan J, Cheng B (2011a) Dye-sensitized solar cells based on anatase TiO_2 hollow spheres/carbon nanotube composite films. J Power Sources 196:7891–7898

Yu J, Fan J, Cheng B (2011b) Dye-sensitized solar cells based on anatase TiO_2 hollow spheres/carbon nanotube composite films. J Power Sources 196:7891–7898

Yu Y, Wu K, Wang D (2011) Dye-sensitized solar cells with modified TiO_2 surface chemical states: The role of Ti3. Appl Phys Lett 99:97–100

Yu J, Yang Y, Fan R, Liu D, Wei L, Chen S, Li L, Yang B, Cao W (2014) Enhanced near-infrared to visible upconversion nanoparticles of Ho^{3+}-Yb^{3+}-F^- tri-doped TiO_2 and its application in dye-sensitized solar cells with 37% improvement in power conversion efficiency. Inorg Chem 53:8045–8053

Yuan Z, Tang R, Zhang Y, Yin L (2017) Enhanced photovoltaic performance of dye-sensitized solar cells based on Co9S8nanotube array counter electrode and TiO2/g-C3N4 heterostructure nanosheet photoanode. J Alloys Compd 691:983–991

Zhang XT, Sutanto I, Taguchi T, Tokuhiro K, Meng QB, Rao TN, Fujishima A, Watanabe H, Nakamori T, Uragami M (2003) Al2O3-coated nanoporous TiO2 electrode for solid-state dye-sensitized solar cell. Sol Energy Mater Sol Cells 80:315–326

Zhang Q, Dandeneau CS, Zhou X, Cao G (2009) Nanostructures for dye-sensitized solar cells. Adv Mater 21:4087–4108

Zhang J, Zhao Z, Wang X, Yu T, Guan J, Yu Z, Li Z, Zou Z (2010) Increasing the oxygen vacancy density on the TiO2 surface by la-doping for dye-sensitized solar cells. J Phys Chem C 114:18396–18400

Zhang J, Peng W, Chen Z, Chen H, Han L (2012) Effect of cerium doping in the TiO2 photoanode on the electron transport of dye-sensitized solar cells. J Phys Chem C 116:19182–19190

Zhao D, Peng T, Lu L, Cai P, Jiang P, Bian Z (2008) Effect of annealing temperature on the photoelectrochemical properties of dye-sensitized solar cells made with mesoporous TiO2 nanoparticles. J Phys Chem C 112:8486–8494

Zhu K, Neale NR, Miedaner A, Frank AJ (2006)

Zhu K, Vinzant TB, Neale NR, Frank AJ (2007) Enhanced charge-collection efficiencies and light scattering in dye-sensitized solar cells using oriented TiO2 nanotubes arrays. Nano Lett

Zhu M, Li X, Liu W, Cui Y (2014) An investigation on the photoelectrochemical properties of dye-sensitized solar cells based on graphene–TiO2 composite photoanodes. J Power Sources 262:349–355

Zou W, Visser C, Maduro JA, Pshenichnikov MS, Hummelen JC (2012) Broadband dye-sensitized upconversion of near-infrared light. Nat Photonics 6:560–564

Chapter 16
p-Type Dye Sensitized Solar Cells: An Overview of Factors Limiting Efficiency

Sasanka Peiris, R. J. K. U. Ranatunga and Ishanie Rangeeka Perera

Abstract The energy crisis is a global problem that drives investment on renewable energy sources worldwide. Utilization of solar energy has become an effective strategy for sustainable energy generation, as it has the potential to fill the energy gap created due to the depletion of fossil fuel. On the ever-extending ladder of solar harvesting technologies, third generation dye-sensitized solar cells (DSCs) have the advantages of better cost effectiveness and environmental footprint when compared to the first-generation silicon solar cells and second-generation thin film photovoltaics. The ultimate goal of constructing high-efficiency multi-junction devices has set the target of improving single junction components of DSCs (n- and p-type), separately. The pace of development of single junction p-DSCs has been much slower than that of n-DSCs. Discovery of suitable materials and techniques have lifted the performance of n-DSCs to more than 14% since it was first reported in 1991. On the other hand, p-DSCs have a maximum efficiency of 2.51%. It is important to bridge the gap between the efficiencies of these single junction configurations, in order to adopt the concept of multi-junction/tandem-DSCs that have the potential to reach higher efficiencies by harvesting a larger fraction of the solar spectrum. This chapter focuses on reviewing literature on development of p-DSCs. First, as an introduction, the structure, function and kinetics of p-DSCs are described. Next, the two main factors that affect the overall performance of a p-DSC; light harvesting capacity, and energy loss within the device, are comprehensively discussed.

Keywords p-type · Solar energy · Dye-sensitized solar cells

S. Peiris
Sri Lanka Institute of Nanotechnology, Homagama 10200, Sri Lanka

R. J. K. U. Ranatunga · I. R. Perera (✉)
Department of Chemistry, Faculty of Science, University of Peradeniya, Peradeniya 20400, Sri Lanka
e-mail: ishanieperera@pdn.ac.lk

Postgraduate Institute of Chemistry, University of Peradeniya, Peradeniya 20400, Sri Lanka

H. Tyagi et al. (eds.), *Solar Energy*, Energy, Environment, and Sustainability, https://doi.org/10.1007/978-981-15-0675-8_16

16.1 Introduction

Photovoltaic (PV) energy conversion strategies have attracted huge attention in the scientific world today. With the depletion of fossil fuel deposits, the world is at the brim of facing an energy crisis; Utilization of solar energy is a hot spot of current research in this regard. Although photovoltaics date back nearly 175 years, development of photovoltaic cells progressed sporadically, and only became a viable energy source with the discovery of p-n junction silicon photocells, which could achieve an efficiency of 6%. Advances have improved efficiencies to over 20%, and currently, silicon based solar cells are a prime candidate for efficient photo current generation (Nattestad et al. 2016; Fraas 2014; Hagfeldt et al. 2010; Venkatraman et al. 2018).

Silicon being the most abundant element on the earth's crust facilitates easy access. Moreover, using Si cells are stable to ambient temperatures (Chapin et al. 1957), minimize reflection losses and monocrystalline silicon solar cells have relatively high photo conversion efficiencies. These cells are thought of as first-generation solar cells. Since the purification process of silicon is expensive, it has become the bottleneck for large scale commercial application. As a result, thin film solar cells composed of amorphous silicon, CIGS (copper indium gallium diselenide), and CdTe, which belong to the second generation of solar cells, came into play. However, the photo conversion efficiencies obtained with these devices are lower compared to those of monocrystalline silicon (Hagfeldt et al. 2010). Among other thin film solar cells, amorphous silicon is the most established technology due to advantages like lower temperature coefficient for power loss, low toxicity and cost effectiveness (Shah et al. 1995). A vast array of scientific approaches is being implemented to develop affordable and clean energy based on silicon solar cells (Chapin et al. 1954, 1957; Hagfeldt et al. 2010).

A subsequent stage in the field of photovoltaics was the development of the dye-sensitized solar cell (DSC), which is one of the outstanding inventions with an environmentally friendly, low cost and feasible practical application. DSCs are regarded as a bridge that directs the functionality of solar cells towards the third generation (O'regan and Grätzel 1991). Michael Grätzel and Brian O'Regan published their seminal work on DSCs in 1991, reporting a 7% overall light-to-electricity energy conversion yield under diffused sunlight (Hagfeldt et al. 2010; Baxter 2012). From that point onwards many developments and advancements to DSCs have brought about higher efficiencies. In 2006, Chiba et al. achieved an efficiency of 11.1%, which is the highest certified energy conversion reported (Chiba et al. 2006). By 2013, Kakiage et al. reported a conversion efficiency over 14% by co-photosensitization with an alkoxy silyl-anchor dye and a carboxy-anchor organic dye (Kakiage et al. 2015). This illustrates the fast evolution of DSCs within a few years. Michael Grätzel states "Our present needs could be met by covering 0.1% of the Earth's surface with PV installations that achieve a conversion efficiency of 10%" (Fraas 2014; Grätzel 2007). Consequently, it is possible PVs could dominate the world's energy market; bringing sustainable energy generation with low levels of pollution. Figure 16.1 shows renewable electricity generation, with projections to 2050, published by U.S.

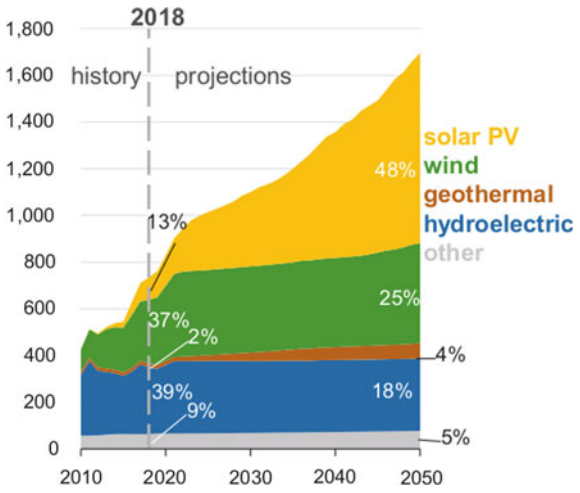

Fig. 16.1 Renewable electricity generation (in billions of kilowatt hours) in the United States of America, including end-use. *Source* U.S. Energy Information Administration (2018)

Energy Information Administration. Accordingly, wind and solar power is expected to monotonously increase, accounting for nearly 900 BkWh (94%) of the total growth. Furthermore, it is expected that solar photovoltaic (PV) usage will increase due to advancement in cost effectiveness. Figure 16.2 is also an extract from the above report, representing the annual electricity generating capacity additions and retirements, that predicts, solar PV will be a prominent generation mode by 2050 (Outlook 2018).

Although the first DSCs were fabricated, using a single n-type or p-type semiconductor material (single-junction devices), a contemporary push is to develop cells with both n-type and p-type concurrently functioning in a tandem (multijunction)

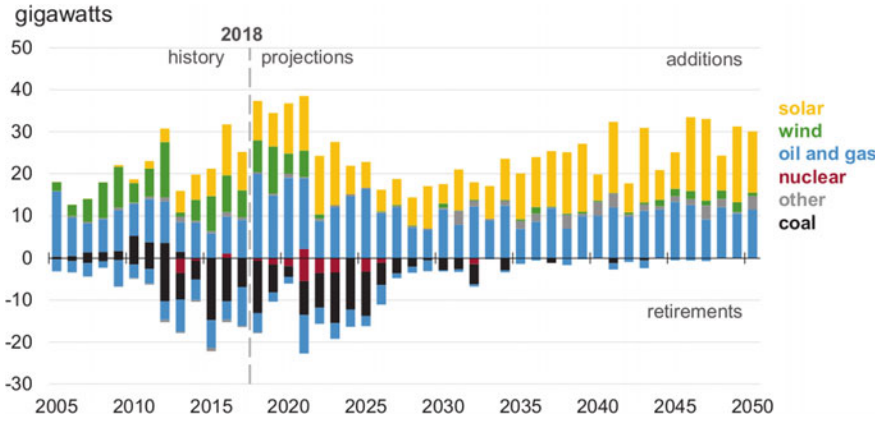

Fig. 16.2 Annual electricity generating capacity additions and retirements in USA. *Source* U.S. Energy Information Administration (2018)

device. The performance of tandem devices depends on the performance of each junction. Although n-type DSCs have been optimized extensively, the progress of p-DSCs is as yet, lacking (Odobel and Pellegrin 2013; Yu et al. 2012; Yum et al. 2011).

This chapter reviews the factors that limit the achievement of high photon to current conversion efficiencies in single junction p-DSCs. First a brief introduction on the structure, function and kinetics of a p-DSC will be discussed. Secondly, an overview of factors affecting the overall device performance such as light harvesting efficiency and charge collection and transport efficiency will be discussed in detail. Finally, the future prospects of p-DSCs will be elaborated.

16.2 Structure of DSCs

The art and the architecture of a typical DSC is interesting in its own right. Assembly of a working electrode (WE) and a counter electrode (CE) formulates a single DSC, in which an electrolyte is wedged between the two (Perera et al. 2019). Figure 16.3 illustrates the arrangement of basic components in a typical DSC. Proper fabrication of the WE are crucial in producing high photo conversion efficiencies. A transparent layer of a semiconductor material is placed on a glass substrate which is made conductive by coating with fluorine-doped tin oxide (FTO) (Hagfeldt et al. 2010; Zhang et al. 2016). The semiconductor material (with a wide bandgap) is deposited as a thin film having a large surface area, by producing Nano crystallites 10–20 nm in size, and then sintering to form a thin film of ~16 μm thickness (Baxter 2012; Perera et al. 2019). A high surface area is desired, to improve the dye loading capability, and thereby increase the light harvesting efficiency (Baxter 2012). The sensitizers are generally organic, or metal based, having the ability to transition to excited states with the absorption of solar energy. This will be elaborately discussed in the section b.

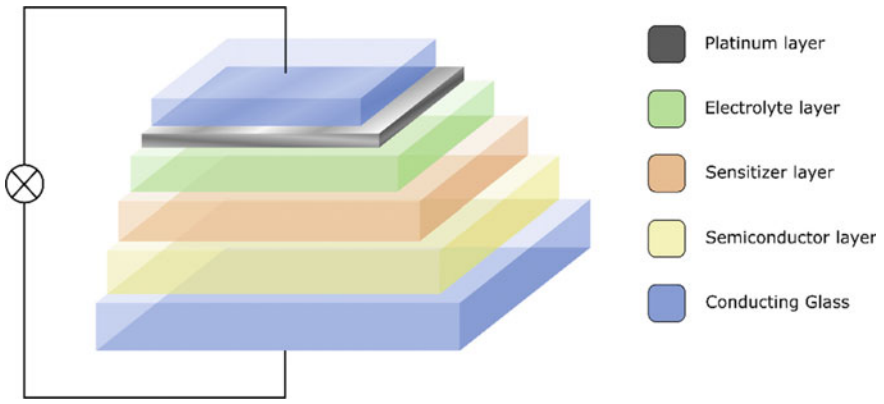

Fig. 16.3 Schematic Illustration of a typical DSCs

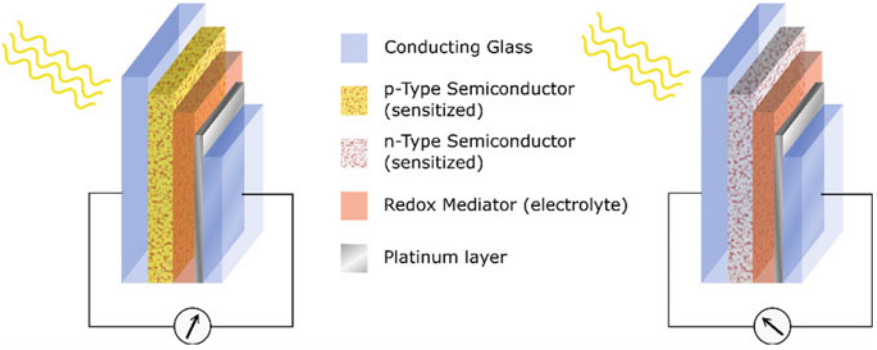

Fig. 16.4 Schematic diagram of components of a p-DSC (left), and n-DSC (right), respectively

The electrolyte containing a redox mediator, which is placed between two electrodes, could be in the form of a liquid, a quasi-solid, or a solid (Hagfeldt et al. 2010; Perera et al. 2019).

Based on the semiconductor material and the operation, DSCs can be categorized as n-type or p-type; both of which are considered as single junction DSCs. Electrons are considered as the major charge carriers in n-DSCs while holes are the major charge carriers in p-DSCs. In the fabrication process, n-type semiconductor materials such as TiO2 and ZnO are used in n-DSCs while p-type semiconductor materials like NiO, Cu_2O and $CuCrO_2$ are used in p-DSCs (Zhang et al. 2016; Gong et al. 2017). Figure 16.4 shows the arrangement of components in both n- and p-DSCs, respectively. So far, n-DSCs have been developed and utilized more widely, reaching efficiencies higher than 14% (Kakiage et al. 2015), while p-DSCs require further advancement with the highest reported efficiency currently at 2.51% (Nattestad et al. 2016; Perera et al. 2015).

16.3 Kinetics of Single Junction DSCs

Kinetics and charge movement dynamics in DSCs have been investigated by making use of experimental methods as well as computational modeling. The chemical kinetics in DSCs are complex, to an extent that it is difficult to apply simple rate laws. In spite of this, the protocol of expressing the half-life relevant to different processes is the current practice of conveying the kinetics of DSCs (Baxter 2012). The processes are interdependent and changes in one of them can influence the overall performance of the cell. Figure 16.5 show the time scale corresponding to different reactions. The injection rate of electrons into the semiconductor layer must be faster than the relaxation of dye molecules (Hagfeldt et al. 2010). For example, generally the relaxation time of a typically used Ru dye is around 50 ns while the electron injection into the semiconductor takes place in less than one picosecond (Baxter 2012). Another

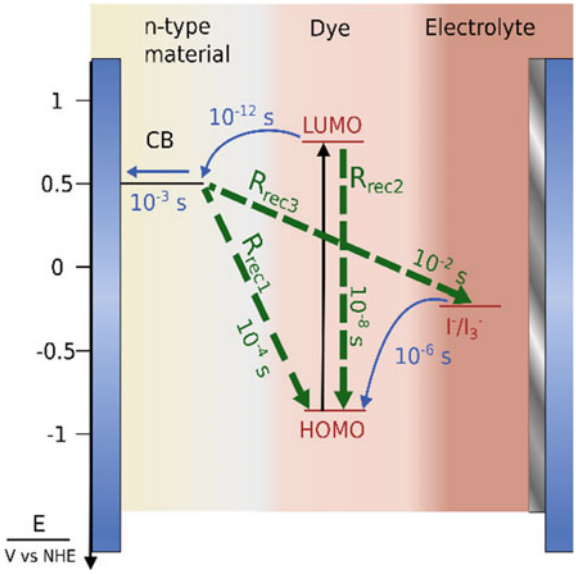

Fig. 16.5 Time scale corresponding to different processes in a DSC

important requirement is the regeneration of dye from the redox mediator should be much faster (microseconds) than that of the recombination, that occurs by back transfer of electrons from the semiconductor to the dye (hundreds of microseconds) reactions a, b, and c in Fig. 16.7 represents the possible recombination reactions taking place in a DSC (Hagfeldt et al. 2010).

R_{rec1} indicates the recombination reaction between the injected electrons at the CB of the semiconductor and the oxidized dye molecules. Similarly, R_{rec3} depicts the recombination of injected electrons with the oxidized species of the electrolyte. R_{rec3} has been suppressed with the development of the device components, which represents the relaxation of excited dye molecules prior to electron injection.

16.4 Current–Voltage Characteristics of a DSC

Photoelectrochemical parameters related with characterization techniques in DSCs are short-circuit current density (J_{SC}), open-circuit voltage (V_{OC}), fill factor (FF), and overall power conversion efficiency (η) (Gong et al. 2017). These are derived from current density (J) vs voltage (V) curves (see Fig. 16.6). In a J-V curve the intercept of Y axis which represents a zero-bias condition (short circuit condition) is the JSC of the device which can be defined as the photocurrent per unit area under short-circuit condition. The intercept of the X axis, which represents zero current density (open circuit condition), is taken as the V_{OC}, which is the working potential, produced by the device. It is the difference between redox potential of the electrolyte and the fermi level of the semiconductor material. The power conversion efficiency (η) is

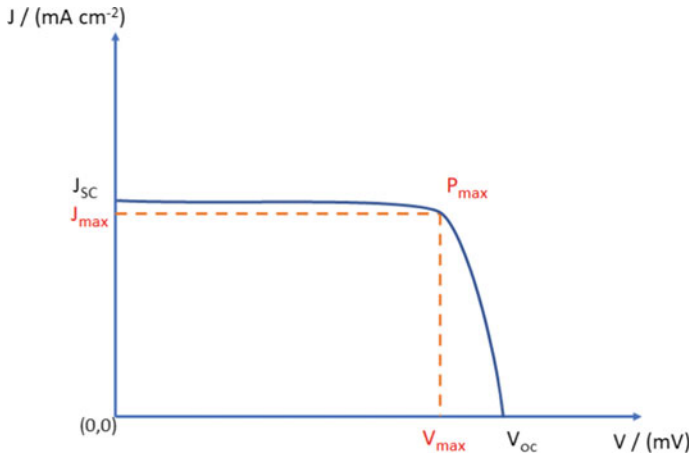

Fig. 16.6 General current versus voltage curve for DSCs

given by the ratio of maximum power output (P_{max}) to the incident solar power (P_{in}). Maximum power output is the product of J_{SC}, V_{OC} and FF (Eq. 16.1). Also, it can be calculated when the current and the voltage of the device reaches their maximum possible values, J_{max} and V_{max}, respectively (Eq. 16.3). The value of the FF lies in between 0 and 1 and it can be calculated using Eq. 16.2 (Perera et al. 2019). It can also be defined as the rectangularity of the J-V curve (Perera et al. 2019; Grätzel 2007).

$$\eta = P_{max}/P_{in} = J_{SC}V_{OC}FF/P_{in} \tag{16.1}$$

$$FF = P_{max}/J_{SC}V_{OC} \tag{16.2}$$

$$P_{max} = J_{max}V_{max} \tag{16.3}$$

16.5 p-Type DSCs

The development and optimization of p-DSCs are still in its infancy. NiO has predominantly been used as the semiconductor material, however, it suffers from low efficiency. Therefore, novel p-DSCs semiconductor materials such as Cu_2O_8, $CuCrO_2$ and $CuGaO_2$ are being developed (Zhang et al. 2016). Further, the advance research trends focusing on overall performance of p-DSC devices, pursue in tailoring novel sensitizers, (triphenylamine dyes, ruthenium dyes, cyclometalated iridium dye) electrolytes ($[Co(en)_3]^{2+/3+}$, $[Fe(acac)_3]^{0/1-}$) and CEs (CoS, $NiCo_2S_4$) (Xu et al. 2014; Xiong et al. 2013; Zhu et al. 2014; Lyu et al. 2016; Perera et al. 2015).

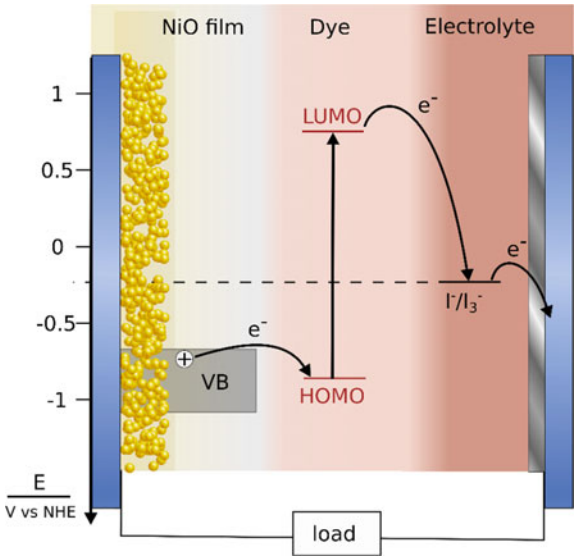

Fig. 16.7 Electron flow of a functioning p-DSC

Functioning principle of p-DSC can be explained using a few separate reactions, which are depicted in Fig. 16.7. The pilot reaction initiates with the photoexcitation of sensitizer (dye) molecules followed by injection of holes into the semiconductor layer, that leads to transfer electrons from the valence band (VB) of the semiconductor to the HOMO level of the dye, relaxing the excited state. The holes then diffuse through the mesoporous oxide film, and after passing through the external circuit, finally they reach the CE. The oxidized species of the electrolyte regenerates the reduced dye at CE by accepting the electrons and then, regenerate itself by collecting holes at the CE (Nattestad et al. 2016; Grätzel 2009; Hagfeldt et al. 2010).

16.6 Tandem DSCs

Lindquist proposed that by replacing the platinized CE of a single junction DSC, with a serial connection to another dye sensitized photo electrode, the photo conversion efficiency could be boosted. By connecting both n- and p-type semiconductors in a single device, tandem-DSCs (multi junction DSCs) are created (Odobel and Pellegrin 2013; Yu et al. 2012; Lefebvre et al. 2014). The theoretical photo conversion efficiency for a such tandem DSC was calculated to be 43% (Hagfeldt et al. 2010; Gong et al. 2017). The development of efficient tandem DSCs would be a breakthrough in photovoltaics because it allows the collection of photons with higher energy at one electrode and photons with lower energy at the other. This allows for a higher portion of incident solar energy to be used by the device. Figure 16.8, shows the alignment

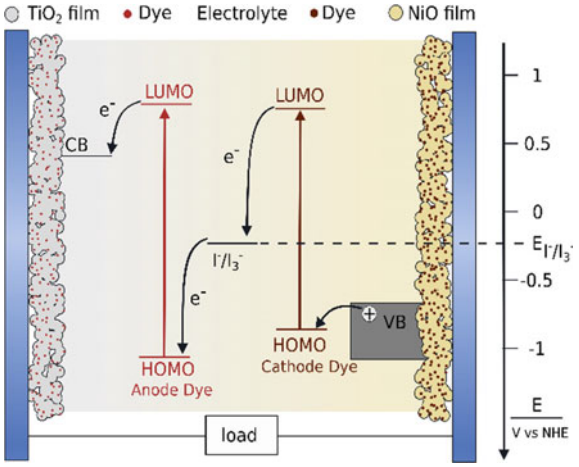

Fig. 16.8 Electron flow in a tandem DSC

of energy bands of the components in a tandem DSC and the electron flow within the device (Gong et al. 2017).

The V_{OC} value of a tandem-DSC can be approximated by the sum of V_{OC} values of n- and p- counterparts, whereas the J_{SC} is limited by the (low performing) photo-electrode. Due to the enhancement in V_{OC} the overall efficiency of a tandem-DSC is expected to be higher than the single junction counterparts. However, in many occasions the overall efficiency of a device does not fulfill its potential because of competition between the two sensitizers to capture photons within the same spectral range.

Although the promise of tandem DSCs is appealing, for these devices to be viable the overall efficiency must be improved significantly. At present the overall device performance of a tandem device which is limited to 2.42% (Yum et al. 2011), and this value is due to lower efficiency of the p-junction. Therefore, developing p-DSCs is important for the future of tandem DSCs (Hagfeldt et al. 2010; Yum et al. 2011; Baxter 2012; Perera et al. 2019).

16.7 Factors Affecting Overall Performances of p-Type DSCs

The developmental process of DSCs paves the way to create advanced technologies for generating affordable, efficient and green energy. In the field of energy generation, Thus, there is a concept been built known as the critical triangle, which is based on three main determinants: light-to electric energy conversion efficiency, stability, and cost. Among these determinants, the light-to-electricity energy conversion efficiency is given the most attention, and evolution of tandem DSCs is a major push towards fulfilling this requirement. Consequently, the development of p-DSCs is critical,

since contemporary tandem DSCs are limited by the power conversion efficiency of p-DSCs. This could be achieved by focusing on to two main strategies, namely, (1) maximizing the light harvesting, and (2) minimizing electron losses (Gong et al. 2017). Novel practices based on these strategies are elaborately discussed in this review, in Sects. 16.8 and 16.9, respectively.

Stability of the device is another aspect identified in the critical triangle that has been studied. A major hurdle in extending the lifetime of DSCs has been the use of liquid electrolytes, which can evaporate. A strategy to avoid this problem is to substitute liquid electrolytes with solid electrolytes, yielding in solid state dye-sensitized solar cells (ssDSCs). These devices are briefly discussed in Sect. 16.10.

16.8 Maximizing Light Harvesting

The light harvesting efficiency is predominantly determined by the performance of the photosensitizer. Photon capture is followed by excitation of the dye, causing injection of positive charge carriers into the valence band of the p-type semiconductor material. An efficient photo sensitizer should capture a maximum amount of sunlight, usually from photons with energy higher than the band gap; from wavelengths corresponding to UV and visible spectral region and reaching the near infrared (NIR) region of the electromagnetic spectrum. Since each absorption event can generate and push a pair of charges into the external circuit, enhancing the light harvesting capacity can increase the photocurrent density. An efficient sensitizer should also be strongly adsorbed on to the semiconductor surface so that the charge injection into the semiconductor is efficient. In addition, rapid regeneration of the sensitizer by the redox mediator is essential to minimize the recombination process, and importantly, the dye should be stable in both its excited and ground states. There are few novel sensitizers that are being used in p-DSCs: donor-π-acceptor systems, push-pull dyes, cyclometalated dyes, quaraines, and ku Quinones (Lyu et al. 2016; Ji et al. 2013; Jiang et al. 2014; Bonomo et al. 2017b).

Donor-(π linker)-acceptor systems have common structural motif including the integrants arranged in the order as donor–π–acceptor (see Fig. 16.9). The absorption and redox properties of the dye can be fine-tuned by changing the individual components. For example, arylamines are common donors while, cyanoacrylates are common acceptors, and the pi-bridge, which is the linker, may contain one or more thiophene units. Scientists have developed novel dyes by modifying these donor, linker and acceptor units. According to one investigation, when carboxylic acid groups are used as the acceptor, surface protonation of NiO occurs, causing a negative shift of the valence band edge. This leads to reduce the hole-injection and the photovoltage (Cui et al. 2014). Jin Cui et al. have developed a novel donor-π-acceptor organic sensitizer incorporating pyridine as the anchoring group that could overcome this problem. Under full sunlight (AM 1.5G,100 mW cm^{-2}) the reported conversion efficiency was ~0.16%, while V_{OC} is 117.9 mV, J_{SC} is 4.05 mA cm^{-2} and FF is 0.34. This causes positive shifting of VB edge of NiO, minimizing interfacial

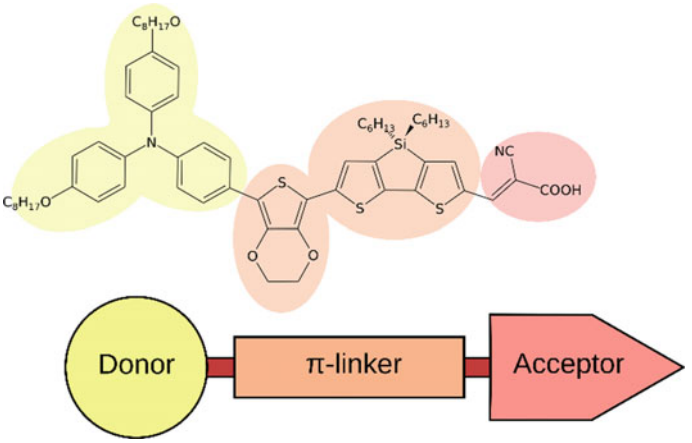

Fig. 16.9 Typical arrangement of units in a donor-π-acceptor type sensitizer

charge recombination with binding linkage that improves the potential for efficient p-DSCs (Cui et al. 2014).

Sheibani et al. also have produced two oligomer dyes for p-DSCs, incorporating different electron acceptor groups. Triphenylamine and oligothiophene with bulky alkyl chains have been used as the electron donor and the linker, respectively (Sheibani et al. 2016) Two different dyes were produced by including napthoilene-1,2-benzimidazole (NBI) (E1) and malononitrile (E2) as electron acceptors which are electron withdrawing. This is the first application of NBI as an electron acceptor in organic dyes for p-DSCs. When investigating the charge-separation kinetics, an important finding obtained from transient absorption spectroscopy (TAS) is that there is a prolonged Dye-NiO(+) charge separation lifetime identified for the NBI unit. According to the results, it shows beneficial characteristics for regeneration of the dye, since the dye can be stabilised when it is reduced. The narrower light absorption spectrum of E1 results in a relatively low photocurrent, which a drawback of the dye synthesized (Sheibani et al. 2016) (Table 16.1).

When comparing the studies carried out by Sheibani et al. and Jin Cui et al. which are based on modification of acceptors (in donor acceptor systems), work done by Jin Cui et al. which is incorporated with a pyridine ring exhibits a relatively high performance.

Table 16.1 Comparison of the photovoltaic performance of two dyes E1 and E2

Dye	V_{OC}/mV	J_{SC}/mA cm^{-2}	Fill factor	Efficiency/%
E1	320	0.93	0.44	0.130
E2	320	0.78	0.41	0.102

A study conducted by Zhu and coworkers has revealed how the bridging ligand could be modified to develop p-DSCs with a higher performance. Increasing the number of ter-thiophene groups in between triphenylamine and carboxylic acid resulted in power conversion efficiency of 0.19%, V_{OC} of 144 mV, J_{SC} of 4.01 mA cm^{-2} and FF of 0.33. The author proposed that ter-thiophene groups strongly affect the hole injection and prevent charge recombination, increasing power conversion efficiency. The investigators designed hexyl chains on the bridged thiophene rings that could avoid dye aggregation on the NiO film and block the electrolyte from approaching the surface of NiO; minimizing recombination between nickel oxide, electrolyte and semiconductor (Zhu et al. 2014).

It was reported that inclusion of Boradiazaindacene (bodipy) sensitizer is compatible with NiO based p-DSCs (Lefebvre et al. 2014). Bodipy dyes have large extinction coefficients, tunable absorption properties (i.e. to optically match photoanodes in tandem cells) and electrochemical stability. A further step for the improvement of charge separation has been taken by Lefebvre and coworkers. They have achieved an increase in charge-separated state lifetime of three orders of magnitude, by using triphenylamine-donor bodipy-acceptor design (JSC = 3 mA cm^{-2}, IPCE = 28%). The investigators state that further increase of yield and lifetime of the charge-separated state could be achieved by altering the electronic coupling through modifying the substituents on the bodipy (Lefebvre et al. 2014).

Push pull dyes can be considered as a further modification of the donor-(π linker)-acceptor system (Fig. 16.10). Insertion of a push-pull moiety into the donor-π-acceptor system is a novel method of enhancing the light harvesting and intermolecular charge transfer (ICT) between the electron donor and the electron acceptor. Table 16.2 lists different donors, acceptors, p-conjugated linkers and push-pull linkers that are frequently used. Donors like triphenylamine and diphenylamine are electron rich lewis-bases. The electron donor properties can be improved by increasing the number of methoxy substituents. Different combinations of these units can be applied to optimize the maximum possible light harvested by the photosensitizer in DSCs. The electron donor can be used in modification of the absorption spectra (Hadsadee et al. 2017).

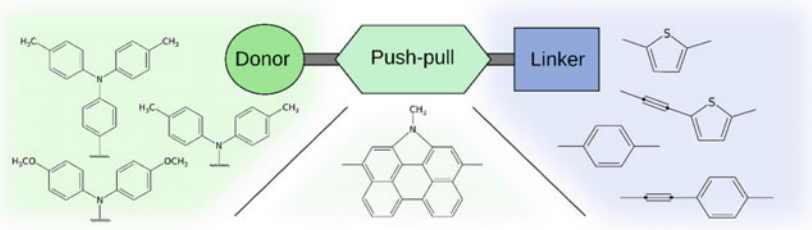

Fig. 16.10 Typical arrangement of units in a push-pull sensitizer, and examples of units used

Table 16.2 Examples representing Donors, Acceptors and linker

Donors	Triarylamine, indoline, perylene, fluorine, coumarin, carbazole, di(p-carboxyphenyl) amine
Acceptors	Cyanoacrylic acid, carboxylic acid, perylene monoamide
p-conjugated linkers	Thiophene, phenyl group
Push-Pull linkers	N-annulated perylene base

Zonghao Liu et al. have synthesized a series of novel push-pull arylamine-fluorene based organic dyes which are reported as, zzx-op1, zzx-op2, and zzx-op3 (featuring one, two, and three fluorene units as shown in Fig. 16.11). When they were applied in p-DSCs, with NiO nanoparticles as a semiconductor material and I^-/I_3^- as a redox couple, a significant energy conversion efficiency of 0.184% has been observed for zzx-op1 with a J_{SC} of 4.36 mA cm^{-2} under AM 1.5G condition and V_{OC} of 112 mV. The electron donor and acceptor of zzx-op1 are di(p-carboxyphenyl)amine (DCPA) and perylenemonoimide (PMID), respectively. A fluorene (FLU) unit with two aliphatic hexyl chains was used as a π-conjugated linker. According to the results, zzx-op1 showed 90.3% charge injection efficiency, which is higher than the other two dyes. In addition, when changing the linker from a single fluorene to a combination with 3,4-ethylenedioxythiophene and thiophene units, the absorption maximum was shifted towards longer wavelengths (300–420 nm), decreasing the energy conversion efficiency. Their investigation also demonstrates that electron-rich heterocyclic aromatic groups like 3,4-ethylenedioxythiophene and thiophene have the ability to raise HOMO energy levels and decrease the driving force for hole injection (Liu et al. 2014b).

Another paper published by Liu et al. on fine-tuning fluorene-based dye structures for high-efficiency p-DSCs, reveals how the application of optimized conditions

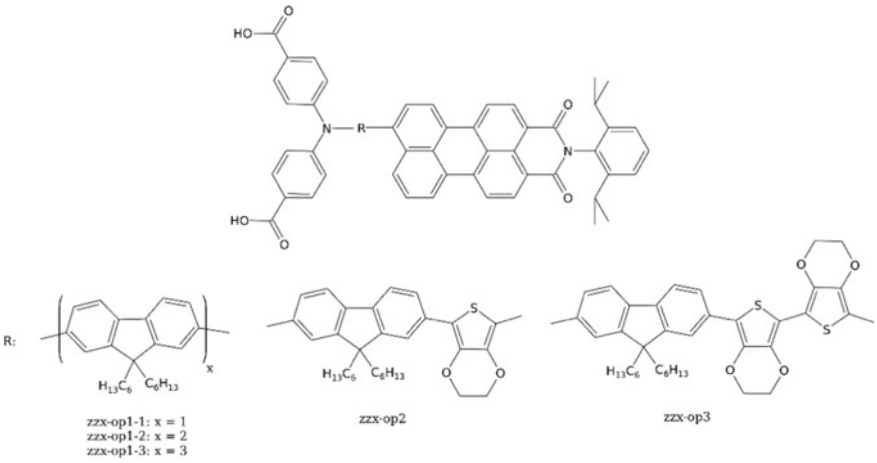

Fig. 16.11 zzx-op type push-pull dyes

could affect performance. They serendipitously found that the solvent system used to dissolve the dye could greatly influence cell performance. As a result of applying acetonitrile/THF solvent system in 1:1 ratio, the dye zzx-op1-2 outperformed the other two dyes (zzx-op1 and zzx-op1-3; Fig. 16.11) giving a photocurrent density of 7.57 mA cm^{-2} under full sun illumination (simulated AM 1.5G light illumination, 100 mW cm^{-2}, $V_{OC} = 117$ mV, FF = 0.4, $\eta = 0.353\%$). It is exciting that these cells with zzx-op1-2 dye, have excellent long-term stability. Moreover, it was found that this particular dye has comparatively longer hole lifetime, lower photocurrent losses and higher photogenerated hole density (Liu et al. 2014a).

Two novel donor–π acceptor push-pull dyes based on organometallic ruthenium di acetylide complexes, which could be applied for p-DSCs, were reported on by Lyu et al. Though these dyes are still not optimized, it is observed that their photovoltaic performance is relatively high compared to other ruthenium polypyridine complexes ($J_{SC} = 2.25$ mA cm^{-2}, $V_{OC} = 104$ mV, FF = 0.34, $\eta = 0.79\%$). According to the investigators lowering the energy level the HOMO will yield ruthenium diacetylide dyes with high performances due to enhancing injection Gibbs free enthalpy (Lyu et al. 2016).

Vasilis Nikolaou et al. synthesised the first covalently linked zinc porphyrin-fullerene (ZnP-C60) Donor-Acceptor dyads that can be used in p-DSCs. Three such structures (C60ZnPCOOH, C60-trZnPCOOH and C60trZnPtrCOOH) were synthesised and used as sensitizers in NiO-DSCs. Ultrafast transient absorption spectroscopy illustrates that there is a long-lived charge separation achieved with the shift of electrons from the porphyrin core (reduced) to the C60. Further, the transient experiments show that triazole ring also could expand the lifetime of charge separated state. In addition, they have examined the effect of introducing a spacer group with different lengths in between the electron acceptor and porphyrin macrocycle in order to reduce the charge recombination. The photo conversion efficiency of the best performing dyad with I_3^-/I^- electrolyte is 0.076% ($V_{OC} = 109$ mV; $J_{SC} = 1.86$ mA cm^{-2}; FF = 0.35) (Georgios Coutsolelos et al. 2018).

A zinc-porphyrin sensitizer has been also been designed by Jianfeng Lu et al. They have developed a D-π-A system by connecting the electron donor-di(p-carboxyphenyl)amine (DCPA) and the electron acceptor- perylenemonoimide (PMI) through a zinc(II) porphyrin having alkyl chains which act as a π- conjugated bridge. When the dye is fabricated into a p-DSC, with NiO semiconductor and tris(acetylacetonato) iron(III/II) redox mediator a power conversion efficiency of 0.92% has been observed under simulated 100 mW cm^{-2} (AM 1.5G irradiation) (Lu et al. 2018).

Hanni Wu et al. have developed Zn porphyrin-polyoxometalate hybrids incorporating different p-linkers which can be utilized as sensitizers in p-DSCs. They have made use of density functional theory method and time dependant density functional theory method to investigate the impact created on sensitizers by the p-linkers and have observed higher delocalization with longer p-linkers (Wu et al. 2016).

The groups of Koten (He et al. 2014) and Grätzel (Bessho et al. 2009) separately used cyclometalated Ru(II) complexes in n-DSCs. A significant recognition is given to these complexes due to their electrochemical and photochemical stability, and

the presence of a broad metal-to-ligand charge transfer (MLCT) band of significant intensity. Not like the other classes of sensitizers, cyclometalated $[Ru(N^{\wedge}N)_2(C^{\wedge}N)]^+$ provide flexibility to be used in both n- and p-type DSCs by varying the functional group. When it is used in a n-DSCs, the C^N ligand bears an ancillary role (similar to electron pushing in a 'push-pull' dye architecture) but when it comes to a carboxylic or phosphonic acid group in p-DSC it acts as the anchoring unit (Marinakis et al. 2017). Through functionalization of the C,N-ligand in $[Ru(N^{\wedge}N)_2(C^{\wedge}N)]^+$ complex (N^N ¼ bidentate N,N^0-ligand, C^N4 ¼ cyclometalated C,N-ligand), the electronic properties can be changed due to the localization of the highest-occupied molecular orbital (HOMO) on the Ru/C^N domain (Bomben et al. 2011, 2012; Ji et al. 2012, 43; He et al. 2014; Marinakis et al. 2017).

The first application of cyclometalated ruthenium complexes of the type Ru-$[(N^{\wedge}N)_2(C^{\wedge}N)]^+$, as sensitizers for NiO p-DSCs, was reported by Ji et al. (2012). These dyes demonstrated broad absorption in the visible region. Furthermore, hole injection to the VB of the semiconductor is promoted by the carboxylic anchoring group attached to the phenylpyridine ligand. Rigid phenyl linkers have been inserted to systematically vary the distance between the Ru-$[(N^{\wedge}N)_2(C^{\wedge}N)]^+$ core and the carboxylic anchoring group. Increasing the number of phenylene linkers depressed charge recombination losses and thereby, improved the photogenerated hole lifetime. Therefore, the devices fabricated by incorporating dyes with longer spacer groups reached higher efficiencies as well as higher J_{SC} and V_{OC} (With O12 dye, V_{OC} = 82 mV, J_{SC} = 1.84 mA cm^{-2}, FF = 0.34 and η = 0.015%) (Ji et al. 2012).

Zhiqiang Ji et al. have also studied the behavior of the triphenylamino linker attached to the para position of the ruthenium–carbon bond of the [N^C] ligand. This could improve the electronic coupling for hole injection and thereby generate comparatively higher J_{SC} values than the prior sensitizers with phenylene linkers. They have synthesized the sensitizers using 2,2′-bipyridine (O3), 1,10-phenanthroline (O13), and bathophenanthroline (O17), in a manner that increases the conjugation of N^N ligand, leading to intensification of the extinction coefficient, and a concurrent red-shift in absorption. Nevertheless, the O3 sensitizer exhibits comparatively higher Jsc of 3.04 mA cm^{-2}. But the V_{OC} is 93 mV which is low yielding a lower efficiency of 0.099% and fill factor is 0.35. However, the results suggest that O3 can perform efficient dye regeneration and slow charge recombination (Ji et al. 2013).

Another panchromatic cyclometalated Ru(II) complex (O18) is reported by He et al. (2014). which has the capability of absorbing photons from visible to near-IR region of the electromagnetic spectrum extending up to 800 nm. O18 has an improved molar extinction coefficient ($\varepsilon = 1.9 \times 104\ M^{-1}\ cm^{-1}$ at 593 nm in solution) that could stabilize the LUMO level of the dye. Due to the use of a π-conjugated system of 2,2′-bipyridyl (bpy) ligands they have increased the absorption cross section. Overall performance is relatively good (Jsc = 3.43 mA cm^{-2} V_{OC} = 93 mV; FF = 0.33; η = 0.104%) (He et al. 2014).

In addition to the ruthenium dyes, iridium complexes are also being used as cyclometalated sensitizers for p-DSCs. Marcello Gennari and coworkers synthesised three new cyclometalated iridium dyes and surprisingly they have revealed slow charge recombination and a long-lived charge separation which is found to be unique

for these dyes. Thus, it is more compatible with other redox mediators allowing high open circuit voltage. From the three iridium complexes investigated, IrDPQCN2 shows higher photovoltaic performances ($V_{OC} = 508$ mV; $J_{SC} = 0.25$ mA cm^{-2}, ff $= 0.54$; $\eta = 0.068\%$) (Gennari et al. 2014).

Squaraines (SQs) are a novel group of sensitizers that have the potential to be used in p-DSCs. They are derived from squaric acid and generate intramolecular donor-acceptor-donor charge transfer state in both the ground and the excited states (Law and Bailey 1992). Squaraines have extremely high molar extinction coefficients, and intense narrow absorbance/fluorescence in the red-IR. Since the reactivity of the electrophilic cyclobutyl core is high, SQs easily react with nucleophiles, as well as bases, limiting the application possibilities. However, recent modifications have made them more stable (Jiang et al. 2014).

Three squaraines (VG1-C8, VG10-C8, VG11-C) have been synthesised and applied in p-DSCs by Matteo Bonomo and coworkers. Among the three dyes, VG11-C8 with a dicyano–vinyl substituent on the central squaric ring, produces comparatively higher conversion efficiency, than the other two dyes ($V_{OC} = 93$ mV; $J_{SC} = 1.16$ mA cm^{-2}; FF $= 0.36$; $\eta = 0.043\%$). This yields favourable external quantum efficiency (EQE) of NiO and imbues characteristics of lower resistance of charge transport, low interfacial recombination, shorter hole diffusion times, and larger hole diffusion coefficient, in comparison to other two dyes (Bonomo et al. 2016).

A novel class of quinoid compounds known as KuQuinones (see Fig. 16.12) have been applied to p-DSCs. The presence of a highly conjugated pentacyclic structure results in a broad absorption in the visible region with two intense bands between 450 and 630 nm, making them worthy candidates for light harvesting in p-DSCs. In addition, these dyes consist of a very low reduction potential (Sabuzi et al. 2016).

Bonomo and co-investigators have also incorporated KuQuinones (KuQ) as the sensitizer in NiO based pDSCs. They state the dye possesses HOMO/LUMO states that match with the redox potential of I^-/I_3^- and the upper edge of the NiO valence band. They have reported on KuQ substituted with carboxylic acid and with different alkyl chain. According to the results KuQ-sensitized cells show similarity to that of the benchmark sensitizer erythrosine B (Ery B) other than the absence of electronic conjugation between the light absorbing unit and the anchoring group. Due to this

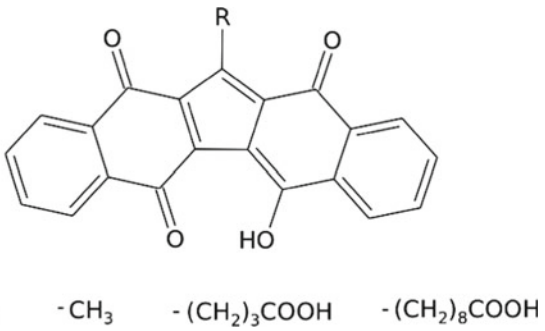

Fig. 16.12 General structure of KuQuinones

consequence, it is hypothesized, that chemical bonds are not involve in photoinduced charge transfer between the excited KuQ dyes and the NiO electrode, instead, it occurs through space. The KuQ-sensitized cells have a V_{OC} of 92.2 mV, J_{SC} of 0.74 mA cm^{-2}, FF of 35.9 and efficiency of 0.025% (Bonomo et al. 2017b).

16.9 Minimizing Electron Losses

After photoexcitation and injection of charge carriers into the semiconductor material by the photosensitizer, fast dye recombination, comparatively slow regeneration and lower charge mobility in the semiconductor material can contribute to loss of electrons within a DSC. Proper manipulation of the electrolyte and the semiconductor material could improve photoconversion efficiency. Novel electrolytes have been invented that could minimize the electron losses ensuring fast dye regeneration and minimum recombinations.

Powar et al. have fabricated efficient p-DSCs based on Tris(1,2-diaminoethane) Cobalt (II)/(III) electrolytes. They have observed $[Co(en)_3]^{2+/3+}$ redox couple could render energy conversion efficiencies of 1.3% at 100% sun (1.67% at 10% sun), with among the best performance indicators to date ($V_{OC} = 709$ mV, $J_{SC} = 4.44$ mA cm^{-2}; FF = 0.42). It is a transparent electrolyte, which can be easily applied into tandem DSCs. This electrolyte is best applicable with the NiO semiconductor; when it was used with TiO_2 the V_{OC} obtained was at a level around 475 mV (Powar et al. 2013).

Perera et al. have discovered a novel electrolyte based on tris(acetylacetonato)-iron (III)/(II) redox couple ($[Fe(acac)_3]^{0/1-}$) for p-DSCs. Interestingly they have improved the photocurrent by introducing a blocking layer on top of the NiO semiconductor material in the working electrode and by using chenodeoxycholic acid in the electrolyte. The device fabrication was done by incorporating perylene–thiophene–triphenylamine (PMI–6T–TPA) as the sensitizer and ($[Fe(acac)_3]^{0/1-}$) as the electrolyte. The best reported short circuit of $J_{SC} = 7.65$ mA cm^{-2} up to date has been achieved by them along with $\eta = 2.51\%$, FF = 0.51, $V_{OC} = 645$ mV. When analysing the measurement of dye regeneration kinetics of the redox mediator, the rate constant obtained (1.7×10^8 M^{-1} s^{-1}) is close to the maximum theoretical rate constant of 3.3×10^8 M^{-1} s^{-1}. As a result, considerably high dye-regeneration yield (>99%) has been obtained by these devices (Perera et al. 2015).

Xu et al. have introduced disulfide/thiolate electrolytes to improve the efficiency of p-DSCs. An organic redox couple of 1-methyl-1H-tetrazole-5-thiolate (T) and its disulfide dimer (T2) redox shuttle were used as an electrolyte in a p-DSC, of $CuCrO_2$ electrode and an organic dye (P1) sensitizer. Using this iodide-free transparent redox electrolyte with the sensitized heterojunction, they have gained a comparatively high V_{OC} of over 300 mV. And also studied on the application of CoS as the counter electrode and have observed an efficiency of 0.23%. This can be considered as the maximum efficiency gained for an organic redox couple (Xu et al. 2013).

More recently Marinakis and coworkers have investigated performance and long-term stability of p-DSCs with a cycloruthenated dye through electrolyte solvent tuning. Fabrication of p-DSC using NiO as the semiconductor material along with the zwitterionic cyclometalated ruthenium dye [Ru(bpy)2(H1)](H31¼(4-(2-phenylpyridin-4-yl)phenyl)phosphonic acid and I_3^-/I^-/acetonitrile (AN) electrolyte, produced a device with $V_{OC} = 95$ mV, $J_{SC} = 4.06$ mA cm^{-2}; and $\eta = 0.139\%$. With the use of propionitrile (PN), valeronitrile (VN) and 3-methoxypropionitrile (MPN) as electrolyte solvents, the trend of J_{SC} was observed as AN > PN > MPN > VN > NMP and V_{OC} follows the trend VN > PN > MPN > AN > NMP. This means there is an effect created by the electrolyte solvent on the efficiency of a DSC (Marinakis et al. 2017).

Effort to enhance the photoconversion efficiency of p-DSCs is mainly directed towards improving performance of individual components. Currently, numerous researches based on novel p-type semiconductor materials, sensitizers and electrolytes are underway. Though NiO is the primarily used semiconductor material in p-DSCs, there are few drawbacks that have been encountered when it is utilized. The VB of NiO lies at +0.50 V versus the NHE and if the typically used I^-/I_3^- redox mediator (+0.35 V vs. NHE) is used as the electrolyte, the V_{OC} will be limited to about 150 mV leading to a poor overall performance of the device (Zhang et al. 2016). On the other hand, NiO is a dark coloured compound which absorbs a significant amount of solar radiation. It has been reported that nearly 30–40% of incident photons are absorbed by a NiO film of thickness 2.3 μm (Yu et al. 2012). Furthermore, fast recombination reactions between the reduced sensitizers and the holes in NiO, cause a significant loss in the number of holes injected into the semiconductor (Ji et al. 2013), since the electronic conductivity of porous NiO is relatively low compared to TiO_2. The magnitude of hole diffusion coefficient in NiO (10^{-8} to 10^{-7} cm^2 s^{-1}) is three orders lower than that of the electron diffusion in TiO_2. As a result, the cathodic current is slowed down due to the delay of injection of holes and their collection back into the electrolyte. NiO also possesses lower dielectric constant and poor chromophore surface loading (Odobel and Pellegrin 2013). Scientists seek novel approaches to overcome these issues related with NiO and on the other hand, introduce different types of semiconductor material that can replace it. Flynn et al. have taken attempts to control the morphology and microstructure of NiO and bring about a methodology to synthesise high quality NiO hexagonal plates, which are ultra-thin and composed of a high density of nanoscale pores. They have observed more than a 10-fold improvement in the electrical mobility compared to conventional nanoparticles. Further, they revealed an increment of 20–30% of the performance of p-DSCs fabricated using these NiO plates. Although it is commonly suggested in literature that the black colour of NiO is due to mixed valence Ni^{2+}/Ni^{3+}, a study conducted by Adèle Renaud and coworkers show that it is due to the presence of Ni^0 and progressive oxidation could completely change the colour to pale green, and also create larger particle sizes that could lower the efficiency. According to their findings, the presence of elemental Ni does not seem to significantly affect the photovoltaic performances of p-DSCs (Renaud et al. 2013b). Zannotti et al. have tried using Ni/Mg mixed metal oxides for p-DSCs. When the concentration of MgO is

increased, photovoltage was increased due to the positive shift in fermi level of the semiconductor (NiO/MgO); however, the generated photocurrent drops with increasing the concentration of Mg^{2+}. Still they were able to show that a constitution of 5% MgO could balance the increased photo voltage and decreased photo current owning a large pore volume in both meso and macropore range (BET surface area of 35 $m^2\ g^{-1}$). The power conversion efficiency obtained by incorporating 5% MgO was higher than using NiO alone ($V_{OC} = 123$ mV; $J_{SC} = 5.09$ mA cm^{-2}; FF = 0.32; $\eta = 0.2\%$) (Zannotti et al. 2015).

Muhammad Awais et al. have revealed, that in addition to electrochemical parameters of individual components, the deposition method of NiO nanoparticles on indium tin oxide (ITO) substrate could affect the performance of p-DSCs. They have chosen spray deposition followed by sintering of nickel oxide nanoparticles to acquire a large surface area. A comparison of the J–V performance with NiO samples prepared using sol–gel method exemplified an enhanced performance in the NiO sample prepared using spray deposition due to higher mesoporosity obtained with this method (Awais et al. 2013).

Plasma-assisted microwave sintering (or rapid-discharge sintering, RDS) is a novel technique that was being employed by Awais et al. for the preparation of NiO thin films which can be used to fabricate photoactive electrodes in p-DSCs (Awais et al. 2014). The novelty of this method is the application of plasma bombardment treatment prior to the step of spray-deposition and heating of the FTO substrate. During the spray deposition, heating is controlled by the energy of microwaves. This method could ensure more efficient charge collection due to improved adhesion and electrical contact at the FTO/NiO interface. For comparison, they have used NiO nanoparticles synthesised by conventional sintering in furnace or through sol–gel procedures which are screen printed. They were able to produce NiO samples with better performance using RDS method when applied to p-DSCs sensitized with erythrosine B (Awais et al. 2014; Novelli et al. 2015) .

Current p-type semiconductor materials have been maneuvered towards a novel category of chemicals called delafossites. They belong to a family of transparent conducting oxides. Low electrical resistivity (high conductivity), high transparency, wide band gap, high energy conversion efficiency and low fabrication cost motivate their use as the semiconductor material in p-DSCs. More recognition is given to Cu (1) based $CuMO_2$ (M = Al, Cr, Ga, Cr, B, In) delafossites. Strong hybridization of 3d orbitals of Cu with 2p orbitals of O facilitate the delocalization of hole charge carriers, increasing the hole mobility (Ahmed et al. 2014; Jiang et al. 2016; Xu et al. 2014).

Yu et al. reported the first application of $CuGaO_2$ delafossite into pDSCs. The VB edge of $CuGaO_2$ is +0.6 V v.s. NHE and they have achieved V_{OC} of 357 mV by using $Co^{3+/2+}$(dtb-bpy) as the electrolyte (1 Sun AM 1.5 illumination). Increasing the illumination enhanced the V_{OC} up to 464 mV, which is known as the saturation photovoltage. Nano plates of $CuGaO_2$ that are stable up to to 350 °C have been made with an average diameter of 200 nm and thickness of 45 nm using a hydrothermal method. Since there is an off white colour in these nano plates, no competition exists against the sensitizer for capturing sunlight (Yu et al. 2012). Another research based

on $CuGaO_2$ plates conducted by Zhen Xu et al. produced devices with a remarkably high $J_{SC} = 2.05$ mA cm^{-2} incorporating I^-/I_3^- electrolyte as the redox mediator. Nanoplates of 100–200 nm diameter and thickness of 20–30 nm were obtained, and optimization of temperature for the hydrothermal synthesis was done (Xu et al. 2014). Adèle Renaud et al. have done further modification to $CuGaO_2$ based p-DSCs by doping Mg with assembly of PMI-NDI dyad as the dye, and tris(4,4′-bis-tert-butyl-2,2′-bipyridine)cobalt(II/III) as the electrolyte. They found out that there is a 73% increase in photovoltaic yield compared to undoped $CuGaO_2$, when doped with 1% of Mg. But this performance is lost when the doping is increased above 1% of Mg ($V_{OC} = 305$ mV; $J_{SC} = 0.415$ mA cm^{-2}; FF = 0.35; $\eta = 0.45$) (Renaud et al. 2013a).

$CuAlO_2$ is another type of delafossite which was synthesised by Ahmed and coworkers under controlled oxygen pressure (pO_2) of 105 atm and at a temperature of 775 °C. A uniform particle size of 35 nm was obtained and cathodic photocurrent with $J_{SC} = 0.954$ mA cm^{-2} under 1.5 sun illumination (Ahmed et al. 2014). Miclau et al. have conducted a study based on the effect of polymorphism on photovoltaic performance of $CuAlO_2$ delafossite nanomaterials by synthesizing nanocrystalline 3R or mixture of 2H and 3R polytypes. Key factors that cause the formation of poly types are temperature and autogenous pressure. Even a small concentration of 2H polytype caused raise energy conversion efficiency by 49% compared to pure 3R-$CuAlO_2$ polytype. The reason for higher efficiencies may be because of the presence of smaller Cu-Cu distance of 2H polytype compared to that of 3R polytype. As the electrical conductivity predominantly occurs through the Cu^+ plane, 2H polytype generates a higher photocurrent density (J_{SC}) (Miclau et al. 2017).

The first application of hydrothermally synthesised, Mg doped $CuCrO_2$ delafossite material in p-DSCs was reported by Xiong et al. They have observed an enhancement in optical transmittance and reduction of crystallite size, that leads to improvement of J_{SC} by approximately 27%, when $CuCrO_2$ was doped with Mg. Lower valence band edge and faster hole diffusion coefficient has been observed in $CuCr_{0.9}Mg_{0.1}O_2$ (in comparison to NiO), producing a V_{OC} of 201 mV and J_{SC} of 1.51 mA cm^{-2}. The efficiency obtained was 0.132% which is nearly three times higher compared to NiO-based reference devices with a V_{OC} of 0.449 (Xiong et al. 2013). Powar et al. have also worked on $CuCrO_2$ using $[Co(en)^3]^{2+/3+}$ based redox mediators ($V_{OC} = 734$ mV; $J_{SC} = 1.23 \pm 0.17$ mA cm^{-2}; FF = 0.53 ± 0.04; $\eta = 0.48 \pm 0.08$%). Though there is a comparatively higher V_{OC} value, the value of J_{SC} has been drastically decreased, due to insufficient hole-injection driving forces. Thus the efficiency was limited (Powar et al. 2014). Daniel et al. used hydrothermal synthesis to obtain nanocrystals of (Al, Mg)-Doped $CuCrO_2$ with smaller size (and therefore larger surface areas) compared with other delafossites. Doping of Al^{3+} causes shifting of the optical band gap by 0.05 eV, while dopic with Mg^{2+} causes it to shift by 0.27 eV. In the presence of Coumarin C343 as the sensitizer, the short-circuit density (J_{SC}) is increased by 11% for Al^{3+} doping and by 16% for Mg^{2+} doping (Daniel et al. 2017).

Ursu Daniela et al. have doped $CuCrO_2$ with Co to produce non-stoichiometric nanocrystals using a low-temperature hydrothermal method which increases the oxygen content of the delafossite structure. The electrical resistivity has been decreased

due to Co-substitution that increases the J_{SC} value 0.50 mA/cm^2, when using N719 and I^-/I_3^- as the sensitizer and the redox couple, respectively (Daniel et al. 2017).

Adèle Renaud et al. have successfully demonstrated the first DSC with p-type LaOCuS nanoparticles as the photocathode. Transparent LaOCuS is an oxysulfide material with similar VB potential to that of NiO, that enables effective hole injection from the excited sensitizer. When using PMI-NDI as the sensitizer, it could attain the following photovoltaic characteristics VOC = 150 mV, Jsc = 0.039 mA/cm^2, ff = 26%, $\eta = 0.002\%$ (Renaud et al. 2015).

An attractive discovery by Ze Yu et al. was based on finding p-type semiconducting property in degenerate n-type semiconductors, could open a novel avenue for research on p-DSCs. Indium tin oxide (ITO) is a n-type degenerate semiconductor having good charge transport properties, and sufficient transparency. With the application of ITO semiconductor in place of highly coloured NiO, and $[Fe(acac)_3]^{0/-}$ redox mediator, along with a new organic sensitizer, they have achieved a photo conversion efficiency of $1.96 \pm 0.12\%$ ($J_{SC} = 5.65$ mA cm^{-2}, $V_{OC} = 700$ mV). ITO owns a significant local density of states below −4.8 eV, enabling transfer of electrons to excited dye that produces a sustained photo cathodic current. A drawback of ITO is faster recombination rate at the ITO–electrolyte interface. In order to overcome this problem and attain higher efficiencies, the investigators have specifically designed and synthesised an extended oligothiophene π-bridging sensitizer (PMI-8T-TPA). Use of ITO as a blocking layer is another powerful modification that they have implemented to achieve a V_{OC} value of 758 mV in the presence of $[Co(en)_3]^{3+/2+}$ as the electrolyte and 712 mV in the presence of $[Fe(acac)_3]^{0/-}$ electrolyte (Yu et al. 2016).

Incorporation of porous metal–organic frameworks (MOFs) in fabrication of p-DSCs is a novel approach by Junkuo Gao et al. They have reported a Ti(IV)-based MOF, NTU-9, that shows p-type semiconductor behaviour with a bad gap of 1.72 eV. It absorbs in the visible range up to 750 nm and has good photocatalytic activity. Though there are numerous MOF applications related to n-DSCs, this is the first novel MOF which has been developed with a potential as a semiconductor material in p-DSCs. They also suggest that NTU-9 is a promising visible-light photocatalyst for energy conversion and environmental remediation (Gao et al. 2014).

In addition to the Cu based delafossite materials, Shi et al. have successfully introduced $NiCo_2S_4$ nanosheet films obtained from $NiCo_2O_4$, to be applied as a counter electrode in p-DSCs. Both $NiCo_2S_4$ and $NiCo_2S_4$ could be used to replace Pt and NiO, respectively. Cost effectiveness is a major advantage. $NiCo_2S_4$ is imbued with high catalytic activity towards I^-/I_3^- electrolyte, generating an improved J_{SC} = 2.989 mA cm^{-2} and $\eta = 0.248\%$ compared to when Pt is the counter electrode (1.824 mA/cm^2 and 0.158%, respectively) but V_{OC} is not improved (Shi et al. 2014).

Cuprous oxide (Cu_2O) is an important semiconducting material due to its high electron transmission. Studies on investigating electrodes made of pure Cu_2O are infrequent. Sisi et al. have demonstrated the possibility of applying Cu_2O into p-DSCs. They have compared commercial Cu_2O particles and electrodes prepared from Cu_2O powder. In comparison, prepared Cu_2O has shown better photovoltaic performance than commercial Cu_2O ($J_{SC} = 1.3$ mA cm^{-2}, $V_{OC} = 710$ mV, FF =

0.46, $\eta = 0.42\%$) due to high dye adsorption capability. They also verified factors such as the thickness of prepared $Cu_2O(2)$ film, uniformity and the grain size of material Cu_2O, affects the electrode performances (Du et al. 2014).

Daniel Ursu et al. have synthesized different morphologies of cuprous oxide, such as porous truncated octahedrons, and 3D hierarchical structures consisting of the micrometer dendritic rods, employing copper (II) acetate and ethyl cellulose as reactants. They have observed nearly 15% increase in V_{OC} and J_{SC} in the porous structure over the 3D hierarchical structure due to high dye loading capacity and the reduced recombination process at the oxide/dye/electrolyte interfaces (Ursu et al. 2018).

Despite the fact that attention given for the improvement of counter electrode is not very prominent, Mirko Congiu et al. have studied a novel application of transparent thin film of cobalt sulfide (CoS) as an anodic counter electrode in place of a Pt electrode. CoS is preferred over Pt due to low cost of the starting material and easier deposition. They have implemented a typical p-type cathode incorporated with mesoporous NiO-deposited via discharge sintering, erythrosin B as the photo sensitizer and I^-/I_3^- as the redox mediator along with the CoS anodic counter electrode. They report similar efficiency, J_{SC}, FF, and V_{OC} values to those obtained for DSCs with the Pt counter electrode ($V_{OC} = 74$ V, $J_{SC} = -1.051$ mA cm^{-2}, FF $= 0.325$, $\eta = 0.026\%$). Electrochemical impedance spectroscopy of CoS anodes in p-DSCs have shown higher electrocatalytic efficiency and lower charge-transfer resistance in comparison to platinized FTO anodes (Congiu et al. 2016).

The work done by Matteo Bonomo et al. has shown the limits on using cobalt sulfide as the anode of p-DSCs by employing a film of CoS of thickness <10 μm as the counter electrode with NiO photoactive cathode and I^-/I_3^- redox mediator. In comparison with Pt in the counter electrode CoS is unable to sustain photocurrent densities generated by NiO at a given potential, due to slower kinetics of iodide oxidation at the CoS anode. This could create 30 times larger charge transfer resistance of CoS with respect to Pt-FTO (130 Ω vs. 4.5 Ω). Furthermore, the behavior of CoS like a p-type semiconductor without a degeneracy, could induce the reverse bias of the photoelectrochemical cell. This displays a lower photoconversion efficiency ($V_{OC} = 128$ mV, $J_{SC} = -1.70$ mA cm^{-2}, FF $= 0.317$, $\eta = 0.07\%$) that is about 35% less than that of the analogous p-DSC with Pt-FTO anode (0.07 vs. 0.11%). However, there is no significant effect identified on the open circuit potential (130 mV) or the FF based on the nature of the anodic material (Bonomo et al. 2017a).

16.10 Solid State Dye Sensitized Solar Cells

One of the challenges encountered in liquid state DSCs is the instability of conventional liquid electrolytes due to volatilization. This affects the durability and the performance of solar cells. Consequently, scientists paid their attention towards employing solid or quasi solid hole conducting materials in place of liquid electrolytes like I^-/I_3^-. Both n-DSCs and p-DSCs are candidates for replacement of

liquid electrolytes. Among the p-semiconductors that act as hole transport materials, CuI plays a key role due to its higher stability and conductivity (Kato et al. 2018).

In 1998, Nature has published a letter by Grätzel putting forward the concept of a solid state dye-sensitized TiO_2 solar cells that can achieve high photon to electron conversion efficiency (Li et al. 2006; Bach et al. 1998). In 2014, Lei Zhang et al. fabricated the first solid state p-type dye-sensitized solar cell (p-ssDSC) using the electron conducting material, phenyl-C61-butyric acid methyl ester (PCBM) in the presence of NiO semiconductor and organic dye sensitizer. They have observed an admirable open circuit voltage ($V_{OC} = 620$ mV) due to the suppression of charge recombination losses. However, the J_{SC} value is very small (50 $\mu A\ cm^{-2}$) due to unsatisfactory lifetime of the excited state of the dye or slow regeneration of the dye. However, this attempt intensified the development of tandem solid-state dye-sensitized solar cells (t-ssDSCs) as well as dye-sensitized solar fuel devices (DSSFDs) (Zhang et al. 2016). The same group of scientists have developed an Indacenodithieno[3,2-b]thiophene (IDTT)-based organic dye (TIP) for further improvement of p-ssDSCs by minimizing the drawbacks of earlier research work. More recent work has produced comparatively higher performance ($\eta = 0.18\%$; $V_{OC} = 550$ mV; $J_{SC} = 0.86$ mA cm^{-2}). According to the charge lifetime experiments they have revealed that the TIP dye could significantly minimise recombination losses (Xu et al. 2019).

Lei Tian et al. have developed a core-shell NiO-dye-TiO_2 mesoporous film for the first time using a newly designed triphenylamine dye. Fabrication of the film has been done by employing atomic layer deposition technique. In this architecture, NiO nanoparticles are covered by TiO_2 layer that allows close contact of the dye and the semiconductor. Further, the dye alignment is well oriented for favourable electron/hole injection. This fabrication renders efficient and ultra-fast hole injection into NiO (>98%, $\leq$200 fs), followed by faster dye regeneration (70–93%, $\leq$500 fs), transferring electrons to TiO_2. This ensures much slower charge recombination than that in the absence of TiO_2 layer (t1/2 $\approx$ 100 ps). This is an interesting discovery which is applicable in ssDSCs (Tian 2019; Tian et al. 2017).

16.11 Summary and Outlook

Dye-sensitized solar cells represent one of the brightest prospects to address the energy crisis the world is facing. DSCs have the promise of being a commercially viable renewable energy source, due to the Research throughout the world has been directed towards a goal of discovering the best combination of components for DSCs. Currently, p-DSCs have gained attention in this regard, since it entails much more development to achieve the ultimate goal of fabricating efficient tandem-DSCs (Table 16.3).

Three major hurdles remain for viable p-DSC device, namely: (1) energy losses within the device, (2) coloration and high recombination rates of semiconductor material, and (3) poor light harvesting ability of the photocathode.

Table 16.3 Summary of photoelectrical performances corresponding to different components of pDSCs

	Modifications done for each component	Voc/(mV)	Jsc/mA cm^{-2}	FF	η/%
Semiconductor	Ni, Mg mixed metal oxides (Grätzel 2007)	123	5.09	0.32	0.2
	NiO prepared via RDS (Awais et al. 2014)	125	−2.84	0.34	0.121
	Delafossite ($CuGaO_2$) nano plates (Xu et al. 2014)	199.3	2.05	0.45	0.182
	Mg dopped $CuGaO_2$ (Renaud et al. 2013a)	305	0.415	0.35	0.045
	Delafossite $CuAlO_2$ nanoparticles (Ahmed et al. 2014)	155	0.954		
	Delafossite ($CuCrO_2$) nanoparticles (Powar et al. 2014)	734	1.23	0.48	0.53
	Delafossite ($CuCrO_2$) dopped with Mg (Xiong et al. 2013)	201	1.51	0.45	0.132
	Delafossite (LaOCuS) nanoparticles (Renaud et al. 2015)	150	0.039	0.26	0.002
	ITO (Yu et al. 2016)	712	5.65	0.49	1.96
	Cu_2O (Du et al. 2014)	710	1.3	0.46	0.42
Dye	Triphenylamine dyes (Zhu et al. 2014)	144	4.01	0.33	0.19
	Oligomer-acceptor dyes (Sheibani et al. 2016)	320	0.93	0.44	0.13
	Pyridine Ring Anchoring Group (Cui et al. 2014)	117.9	4.05	0.16	0.34
	Fluorene-based light absorbers (Liu et al. 2014b)	112	4.36	0.38	0.184

(continued)

Table 16.3 (continued)

	Modifications done for each component	Voc/(mV)	Jsc/mA cm^{-2}	FF	η/%
	Fluorene-based dye structures (Liu et al. 2014a)	117	7.57	0.4	0.353
	Push-pull rhutheniumm diacetylidedyes (Lyu et al. 2016)	104	2.25	0.34	0.079
	Cyclometallated ruthenium dye with triphenylamino group (Ji et al. 2013)	93	3.04	0.35	0.099
	Panchromatic cyclometallated ruthenium dye (He et al. 2014)	93	3.43	0.33	0.104
	Cyclometallated iridium dye (Gennari et al. 2014)	508	0.25	0.54	0.068
	Squaraines (Bonomo et al. 2016)	93	−1.16	0.36	0.043
	KuQuinones (Bonomo et al. 2017b; Powar et al. 2013)	92.2	0.74	0.35	0.023
	Porphyrine (Georgios Coutsolelos et al. 2018)	109	1.86	0.35	0.076
Electrolyte	Tris(1,2-diaminoethane)Cobalt (II)/(III) (Powar et al. 2013)	709	4.44	0.42	1.3
	Tris(acetylacetonato)-iron (III)/(II) (Perera et al. 2015)	645	7.65	0.51	2.51
	Disulfide/thiolate electrolytes (Xu et al. 2013)	304	1.73	0.44	0.023
ssDSCs	(Xu et al. 2019)	550	0.86	0.4	0.18
Counter-electrode	CoS anode (Congiu et al. 2016)	74	−1.051	0.33	0.026
	CoS anode (Bonomo et al. 2017a)	128	−1.7	0.32	0.07
	$NiCo_2S_4$ (Shi et al. 2014)	148.6	2.989	0.56	0.248

Energy losses associated with the redox process of I^-/I_3^-, which is the typically used electrolyte, have been overcome by discovering/designing novel redox mediators such as Co (II/II) and Fe (II/II) systems. These materials have reached high VOC, even though the slow diffusion of ions is still a significant issue for most of the studied mediators. The developed Fe (II/III) systems have seemingly overcome this limitation by exhibiting diffusion rates near the theoretical limit, but the light absorption profiles of these colored redox mediators compete for light with the sensitizer, lowering the overall device performance. Hence, further development of redox mediators with high diffusion rates and low light absorption remains a challenge in p-DSC research. Fine-tuning existing coordination complexes has been identified as one possible pathway to overcome this challenge.

The second major issue is replacing the widely used p-semiconductor material, NiO. It has been discussed here, and elsewhere, that the coloration of NiO due to the presence of Ni^0 is a major issue, again due to competing for light absorption with the sensitizer. Further, it has been shown that the electrochromic nature of NiO reduces the light harvesting efficiency of the p-DSC near V_{OC}. Moreover, the existence of trap states and the low conductivity of bulk NiO both contribute to unfavourable charge recombination reactions. However, NiO is still under investigation due to its capability of generating high photocurrents and the low-lying VB edge (−5.1 eV vs. vacuum) compared to other p-type semiconductors. Other p-type semiconductors with a VB edge between −5 and −6 eV (vs. Vacuum) are yet to be discovered. Thus, extensive research on alternative p-type semiconductor materials may be required to outperform NiO.

Further, in order to realize high light harvesting efficiencies it is important to develop sensitizers with broader absorption wavelength rage that extends from visible to near-IR region of the electromagnetic spectrum. Even though a lot of research has been done developing p-type sensitizers, the main focus has been the improvement of charge separation but not the light harvesting efficiencies. Since the charge separation challenge has been overcome with novel sensitizers, shifting focus to enhancing light harvesting efficiencies, while maintaining proper charge separation, for p-type sensitizers.

As elaborated throughout this chapter, remarkable development has occurred in the field of DSCs since the introduction of high-performance n-DSCs in 1999. Although n-DSCs are far ahead of p-DSCs in terms of efficiency at present, the historical improvements of n-DSC performance bode well for the advancement of p-DSCs too, particularly because there is no fundamental limitation to achieve high efficiencies. Although contemporary p-DSCs are limiting the overall performance of tandem-DSCs, the opportunities and avenues to upgrade these devices are clear and promising.

Acknowledgements Authors would like to express their gratitude to Mr. Dushan Wijewardena for the extended support.

References

Ahmed J, Blakely CK, Prakash J, Bruno SR, Yu M, Wu Y, Poltavets VV (2014) Scalable synthesis of delafossite CuAlO2 nanoparticles for p-type dye-sensitized solar cells applications. J Alloy Compd 591:275–279

Awais M, Dowling DD, Rahman M, Vos JG, Decker F, Dini D (2013) Spray-deposited NiO x films on ITO substrates as photoactive electrodes for p-type dye-sensitized solar cells. J Appl Electrochem 43:191–197

Awais M, Gibson E, Vos JG, Dowling DP, Hagfeldt A, Dini D (2014) Fabrication of efficient NiO photocathodes prepared via RDS with novel routes of substrate processing for p-type dye-sensitized solar cells. ChemElectroChem 1:384–391

Bach U, Lupo D, Comte P, Moser J, Weissörtel F, Salbeck J, Spreitzer H, Grätzel M (1998) Solid-state dye-sensitized mesoporous TiO_2 solar cells with high photon-to-electron conversion efficiencies. Nature 395:583

Baxter JB (2012) Commercialization of dye sensitized solar cells: present status and future research needs to improve efficiency, stability, and manufacturing. J Vacuum Sci Technol Vacuum Surf Films 30:020801

Bessho T, Yoneda E, Yum J-H, Guglielmi M, Tavernelli I, Imai H, Rothlisberger U, Nazeeruddin MK, Grätzel M (2009) New paradigm in molecular engineering of sensitizers for solar cell applications. J Am Chem Soc 131:5930–5934

Bomben PG, Thériault KD, Berlinguette CP (2011) Strategies for optimizing the performance of cyclometalated ruthenium sensitizers for dye-sensitized solar cells. Eur J Inorg Chem 2011:1806–1814

Bomben PG, Robson KC, Koivisto BD, Berlinguette CP (2012) Cyclometalated ruthenium chromophores for the dye-sensitized solar cell. Coord Chem Rev 256:1438–1450

Bonomo M, Barbero N, Matteocci F, Carlo AD, Barolo C, Dini D (2016) Beneficial effect of electron-withdrawing groups on the sensitizing action of squaraines for p-type dye-sensitized solar cells. J Phys Chem C 120:16340–16353

Bonomo M, Congiu M, de Marco ML, Dowling DP, di Carlo A, Graeff CF, Dini D (2017a) Limits on the use of cobalt sulfide as anode of p-type dye-sensitized solar cells. J Phys D Appl Phys 50:215501

Bonomo M, Sabuzi F, di Carlo A, Conte V, Dini D, Galloni P (2017b) KuQuinones as sensitizers for NiO based p-type dye-sensitized solar cells. New J Chem 41:2769–2779

Chapin DM, Fuller C, Pearson G (1954) A new silicon p-n junction photocell for converting solar radiation into electrical power. J Appl Phys 25:676–677

Chapin DM, Fuller CS, Pearson GL (1957) Solar energy converting apparatus. Google Patents

Chiba Y, Islam A, Watanabe Y, Komiya R, Koide N, Han L (2006). Dye-sensitized solar cells with conversion efficiency of 11.1%. Jap J Appl Phys 45:L638

Congiu M, Bonomo M, Marco MLD, Dowling DP, di Carlo A, Dini D, Graeff CF (2016) Cobalt sulfide as counter electrode in p-Type dye-sensitized solar cells. ChemistrySelect 1:2808–2815

Cui J, Lu J, Xu X, Cao K, Wang Z, Alemu G, Yuang H, Shen Y, Xu J, Cheng Y (2014) Organic sensitizers with pyridine ring anchoring group for p-type dye-sensitized solar cells. J Phys Chem C 118:16433–16440

Daniel U, Anamaria D, Sebarchievicia I, Miclau M (2017) Photovoltaic performance of Co-doped $CuCrO_2$ for p-type dye-sensitized solar cells application. Energy Procedia 112:497–503

Du S, Cheng P, Sun P, Wang B, Cai Y, Liu F, Zheng J, Lu G (2014) Highly efficiency p-type dye sensitized solar cells based on polygonal star-morphology Cu_2O material of photocathodes. Chem Res Chin Univ 30:661–665

Fraas LM (2014) History of solar cell development. Springer, Berlin

Gao J, Miao J, Li P-Z, Teng WY, Yang L, Zhao Y, Liu B, Zhang Q (2014) A p-type Ti (IV)-based metal–organic framework with visible-light photo-response. Chem Commun 50:3786–3788

Gennari M, Légalité F, Zhang L, Pellegrin Y, Blart E, Fortage J, Brown AM, Deronzier A, Collomb M-N, Boujtita M (2014) Long-lived charge separated state in NiO-based p-type dye-sensitized solar cells with simple cyclometalated iridium complexes. J Phys Chem Lett 5:2254–2258

Georgios Coutsolelos A, Nikolaou V, Plass F, Planchat A, Charisiadis A, Charalambidis G, Angaridis P, Kahnt A, Odobel F (2018) The effect of the triazole ring in hybrid electron donor-acceptor systems towards light harvesting in NiO-based devices

Gong J, Sumathy K, Qiao Q, Zhou Z (2017) Review on dye-sensitized solar cells (DSSCs): advanced techniques and research trends. Renew Sustain Energy Rev 68:234–246

Grätzel M (2007) Photovoltaic and photoelectrochemical conversion of solar energy. Philos. Trans. R. Soc. A: Math Phys Eng Sci 365:993–1005

Grätzel M (2009) Recent advances in sensitized mesoscopic solar cells. Acc Chem Res 42:1788–1798

Hadsadee S, Rattanawan R, Tarsang R, Kungwan N, Jungsuttiwong S (2017) Push-Pull N-annulated perylene-based sensitizers for dye-sensitized solar cells: theoretical property tuning by DFT/TDDFT. ChemistrySelect 2:9829–9837

Hagfeldt A, Boschloo G, Sun L, Kloo L, Pettersson H (2010) Dye-sensitized solar cells. Chem Rev 110:6595–6663

He M, Ji Z, Huang Z, Wu Y (2014) Molecular orbital engineering of a panchromatic cyclometalated Ru (II) dye for p-type dye-sensitized solar cells. J Phys Chem C 118:16518–16525

Ji Z, Natu G, Huang Z, Kokhan O, Zhang X, Wu Y (2012) Synthesis, photophysics, and photovoltaic studies of ruthenium cyclometalated complexes as sensitizers for p-type NiO dye-sensitized solar cells. J Phys Chem C 116:16854–16863

Ji Z, Natu G, Wu Y (2013) Cyclometalated ruthenium sensitizers bearing a triphenylamino group for p-type NiO dye-sensitized solar cells. ACS Appl Mater Interfaces 5:8641–8648

Jiang J-Q, Sun C-L, Shi Z-F, Zhang H-L (2014) Squaraines as light-capturing materials in photovoltaic cells. RSC Adv 4:32987–32996

Jiang T, Bujoli-Doeuff M, Farré Y, Blart E, Pellegrin Y, Gautron E, Boujtita M, Cario L, Odobel F, Jobic S (2016) Copper borate as a photocathode in p-type dye-sensitized solar cells. RSC Adv 6:1549–1553

Kakiage K, Aoyama Y, Yano T, Oya K, Fujisawa J-I, Hanaya M (2015) Highly-efficient dye-sensitized solar cells with collaborative sensitization by silyl-anchor and carboxy-anchor dyes. Chem Commun 51:15894–15897

Kato N, Moribe S, Shiozawa M, Suzuki R, Higuchi K, Suzuki A, Sreenivasu M, Tsuchimoto K, Tatematsu K, Mizumoto K (2018) Improved conversion efficiency of 10% for solid-state dye-sensitized solar cells utilizing P-type semiconducting CuI and multi-dye consisting of novel porphyrin dimer and organic dyes. J Mater Chem A 6:22508–22512

Law KY, Bailey FC (1992) Squaraine chemistry. Synthesis, characterization, and optical properties of a class of novel unsymmetrical squaraines:[4-(dimethylamino) phenyl](4'-methoxyphenyl) squaraine and its derivatives. J Organic Chem 57:3278–3286

Lefebvre J-F, Sun X-Z, Calladine JA, George MW, Gibson EA (2014) Promoting charge-separation in p-type dye-sensitized solar cells using bodipy. Chem Commun 50:5258–5260

Li B, Wang L, Kang B, Wang P, Qiu Y (2006) Review of recent progress in solid-state dye-sensitized solar cells. Sol Energy Mater Sol Cells 90:549–573

Liu Z, Li W, Topa S, Xu X, Zeng X, Zhao Z, Wang M, Chen W, Wang F, Cheng Y-B (2014a) Fine tuning of fluorene-based dye structures for high-efficiency p-type dye-sensitized solar cells. ACS Appl Mater Interfaces 6:10614–10622

Liu Z, Xiong D, Xu X, Arooj Q, Wang H, Yin L, Li W, Wu H, Zhao Z, Chen W (2014b) Modulated charge injection in p-type dye-sensitized solar cells using fluorene-based light absorbers. ACS Appl Mater Interfaces 6:3448–3454

Lu J, Liu Z, Pai N, Jiang L, Bach U, Simonov AN, Cheng YB, Spiccia L (2018) Molecular engineering of zinc-porphyrin sensitisers for p-type dye-sensitised solar Cells. ChemPlusChem 83:711–720

Lyu S, Farré Y, Ducasse L, Pellegrin Y, Toupance T, Olivier C, Odobel F (2016) Push–pull ruthenium diacetylide complexes: new dyes for p-type dye-sensitized solar cells. RSC Adv. 6:19928–19936

Marinakis N, Willgert M, Constable EC, Housecroft CE (2017) Optimization of performance and long-term stability of p-type dye-sensitized solar cells with a cycloruthenated dye through electrolyte solvent tuning. Sustain Energy Fuels 1:626–635

Miclau M, Miclau N, Banica R, Ursu D (2017) Effect of polymorphism on photovoltaic performance of $CuAlO_2$ delafossite nanomaterials for p-type dye-sensitized solar cells application. Mater Today 4:6975–6981

Nattestad A, Perera I, Spiccia L (2016) Developments in and prospects for photocathodic and tandem dye-sensitized solar cells. J Photochem Photobiol, C 28:44–71

Novelli V, Awais M, Dowling DP, Dini D (2015) Electrochemical characterization of rapid discharge sintering (RDS) NiO cathodes for dye-sensitized solar cells of p-type. Am. J. Anal. Chem 6:176–187

Odobel F, Pellegrin Y (2013) Recent advances in the sensitization of wide-band-gap nanostructured p-type semiconductors. Photovoltaic and photocatalytic applications. J Phys Chem Lett 4:2551–2564

O'regan B, Grätzel M (1991) A low-cost, high-efficiency solar cell based on dye-sensitized colloidal TiO_2 films. Nature 353:737

Outlook AE (2018) With projection to 2050, US Energy Information Administration (EIA), 6 Feb 2018

Perera IR, Daeneke T, Makuta S, Yu Z, Tachibana Y, Mishra A, Bäuerle P, Ohlin CA, Bach U, Spiccia L (2015) Application of the tris (acetylacetonato) iron (III)/(II) Redox Couple in p-Type Dye-Sensitized Solar Cells. Angew Chem Int Ed 54:3758–3762

Perera I, Hettiarachchi C, Ranatunga R (2019) Metal–organic frameworks in dye-sensitized solar cells. In: Advances in solar energy research. Springer, Berlin

Powar S, Daeneke T, Ma MT, Fu D, Duffy NW, Götz G, Weidelener M, Mishra A, Bäuerle P, Spiccia L (2013) Highly efficient p-Type dye-sensitized solar cells based on tris (1, 2-diaminoethane) cobalt (II)/(III) Electrolytes. Angew Chem Int Ed 52:602–605

Powar S, Xiong D, Daeneke T, Ma MT, Gupta A, Lee G, Makuta S, Tachibana Y, Chen W, Spiccia L (2014) Improved photovoltages for p-type dye-sensitized solar cells using $CuCrO_2$ nanoparticles. J Phys Chem C 118:16375–16379

Renaud AL, Cario L, Deniard P, Gautron E, Rocquefelte X, Pellegrin Y, Blart E, Odobel F, Jobic S (2013a) Impact of Mg doping on performances of $CuGaO_2$ based p-type dye-sensitized solar cells. J Phys Chem C 118:54–59

Renaud AL, Chavillon B, Cario L, Pleux LCL, Szuwarski N, Pellegrin Y, Blart E, Gautron E, Odobel F, Jobic SP (2013b) Origin of the black color of NiO used as photocathode in p-type dye-sensitized solar cells. J Phys Chem C 117:22478–22483

Renaud A, Cario L, Pellegrin Y, Blart E, Boujtita M, Odobel F, Jobic S (2015) The first dye-sensitized solar cell with p-type LaOCuS nanoparticles as a photocathode. RSC Adv 5:60148–60151

Sabuzi F, Armuzza V, Conte V, Floris B, Venanzi M, Galloni P, Gatto E (2016) KuQuinones: a new class of quinoid compounds as photoactive species on ITO. J Mater Chem C 4:622–629

Shah A, Platz R, Keppner H (1995) Thin-film silicon solar cells: a review and selected trends. Sol Energy Mater Sol Cells 38:501–520

Sheibani E, Zhang L, Liu P, Xu B, Mijangos E, Boschloo G, Hagfeldt A, Hammarström L, Kloo L, Tian H (2016) A study of oligothiophene–acceptor dyes in p-type dye-sensitized solar cells. Rsc Adv 6:18165–18177

Shi Z, Lu H, Liu Q, Cao F, Guo J, Deng K, Li L (2014) Efficient p-type dye-sensitized solar cells with all-nano-electrodes: $NiCo_2S_4$ mesoporous nanosheet counter electrodes directly converted from $NiCo_2O_4$ photocathodes. Nanoscale Res Lett 9:608

Tian H (2019) Solid-state p-type dye-sensitized solar cells: progress, potential applications and challenges. Sustain Energy Fuel*s*

Tian L, Föhlinger J, Pati PB, Zhang Z, Lin J, Yang W, Johansson M, Kubart T, Sun J, Boschloo G (2017) Ultrafast dye regeneration in a core–shell NiO–dye–TiO_2 mesoporous film. Phys Chem Chem Phys 20:36–40

Ursu D, Dabici A, Vajda M, Bublea N-C, Duteanu N, Miclau M (2018) Effect of Cu_2O morphology on photovoltaic performance of p-type dye-sensitized solar cells. Ann West Univ Timisoara-Phys 60:67–74

Venkatraman V, Raju R, Oikonomopoulos SP, Alsberg BK (2018) The dye-sensitized solar cell database. J Cheminform 10:18

Wu H, Zhang T, Wu C, Guan W, Yan L, Su Z (2016) A theoretical design and investigation on Zn-porphyrin-polyoxometalate hybrids with different π-linkers for searching high performance sensitizers of p-type dye-sensitized solar cells. Dyes Pigm 130:168–175

Xiong D, Zhang W, Zeng X, Xu Z, Chen W, Cui J, Wang M, Sun L, Cheng YB (2013) Enhanced performance of p-type dye-sensitized solar cells based on ultrasmall Mg-doped $CuCrO_2$ nanocrystals. Chemsuschem 6:1432–1437

Xu X, Zhang B, Cui J, Xiong D, Shen Y, Chen W, Sun L, Cheng Y, Wang M (2013) Efficient p-type dye-sensitized solar cells based on disulfide/thiolate electrolytes. Nanoscale 5:7963–7969

Xu Z, Xiong D, Wang H, Zhang W, Zeng X, Ming L, Chen W, Xu X, Cui J, Wang M (2014) Remarkable photocurrent of p-type dye-sensitized solar cell achieved by size controlled CuGaO 2 nanoplates. J Mater Chem A 2:2968–2976

Xu B, Wrede S, Curtze A, Tian L, Pati P, Kloo L, Wu Y, Tian H (2019) An indacenodithieno [3, 2-b] thiophene based organic dye for solid-state p-Type dye-sensitized solar cells. ChemSusChem

Yu M, Natu G, Ji Z, Wu Y (2012) p-type dye-sensitized solar cells based on delafossite CuGaO2 nanoplates with saturation photovoltages exceeding 460 mV. J Phys Chem Lett 3:1074–1078

Yu Z, Perera IR, Daeneke T, Makuta S, Tachibana Y, Jasieniak JJ, Mishra A, Bäuerle P, Spiccia L, Bach U (2016) Indium tin oxide as a semiconductor material in efficient p-type dye-sensitized solar cells. NPG Asia Mater 8:e305

Yum J-H, Baranoff E, Wenger S, Nazeeruddin MK, Grätzel M (2011) Panchromatic engineering for dye-sensitized solar cells. Energy Environ Sci 4:842–857

Zannotti M, Wood CJ, Summers GH, Stevens LA, Hall MR, Snape CE, Giovanetti R, Gibson EA (2015) Ni Mg mixed metal oxides for p-type dye-sensitized solar cells. ACS Appl Mater Interfaces 7:24556–24565

Zhang L, Boschloo G, Hammarström L, Tian H (2016) Solid state p-type dye-sensitized solar cells: concept, experiment and mechanism. Phys Chem Chem Phys 18:5080–5085

Zhu L, Yang HB, Zhong C, Li CM (2014) Rational design of triphenylamine dyes for highly efficient p-type dye sensitized solar cells. Dyes Pigm 105:97–104

Chapter 17
Conducting Polymers as Cost Effective Counter Electrode Material in Dye-Sensitized Solar Cells

Shanal Shalindra Bandara Gunasekera, Ishanie Rangeeka Perera and Samodha Subhashini Gunathilaka

Abstract Dye-sensitized solar cells (DSCs) are third generation photovoltaic devices capable of harvesting solar energy to generate electricity. DSCs have gained significant research interest during past decades due to its high theoretical power conversion efficiencies and most importantly the cost effectiveness and environment friendly fabrication process. Firstly, in this chapter, the function of the counter electrode (CE) in a DSC has been discussed in brief. The CE participates in the electron transfer from the external circuit back to the redox mediator thereby catalyzing its regeneration reaction. In the state of art DSCs, Pt has been the preferred CE material. Properties such as promising conductivity and high electrocatalytic activity towards the process of reduction of I_3^- to I^- which is the typical redox mediator, contributes to its applicability as the preferred CE material. However, the use of Pt CE adhere major drawbacks such as the high cost and its susceptibility to undergo corrosion. These limitations have emphasized the importance of exploring alternative cost effective functional materials with better conductivity and electrocatalytic properties. Subsequently, the limitations of using Pt as the CE materials, and the advantages and challenges associated with alternative materials have been elaborated. Conducting polymers with extended conjugate electron systems are a promising substitute material for Pt in DSCs. A wide range of conducting polymers and polymer hybrid composites have been investigated for their applicability as CEs in DSCs. These polymers have gained popularity not just due to cost effectiveness compared to Pt but also due to their promising conductivity, superior electrocatalytic properties, easy preparation and fabrication. Different types of conjugated polymers and polymer hybrid composites, their synthetic methods, fabrication processes and their respective photovoltaic performances are then reviewed. Finally, the future prospects of conducting polymers as CE material has been discussed.

S. S. B. Gunasekera · I. R. Perera · S. S. Gunathilaka (✉)
Department of Chemistry, Faculty of Science, University of Peradeniya, Peradeniya 20400, Sri Lanka
e-mail: subhashinig@pdn.ac.lk

S. S. B. Gunasekera
e-mail: shanalgunasekera@gmail.com

I. R. Perera
e-mail: ishanieperera@pdn.ac.lk

H. Tyagi et al. (eds.), *Solar Energy*, Energy, Environment, and Sustainability, https://doi.org/10.1007/978-981-15-0675-8_17

Keywords CE · Platinum · Conducting polymers · Dye-sensitized solar cells

17.1 Introduction

The demand for energy is increasing rapidly with the growth of population and industrialization. According to International Energy Outlook 2016 by U.S. Energy Information Administration, the world energy demand is expected to be increased by 48% from 2012–2040 for a period of 28 years (DOE/EIA-0484 (2016)). The world energy production mainly depends on primary energy sources including oil, coal followed by natural gases. The statistics indicate that, oil contributes around 33% to the total energy demand being the world's leading fuel. The global demand for oil in 2014 was 92.4% which is projected to be increased up to 99.1% by 2020 (World Energy Resources 2016, World Energy Council). The second primary energy source in terms of consumption is coal and the demand for coal to produce energy has increased by 64% from 2000 to 2014 (World Energy Resources 2016, World Energy Council). The third primary energy source; natural gasses contributes 24% to the global energy demand (World Energy Resources 2016, World Energy Council). Although the demand for the primary energy sources shows a dramatic increase, these petroleum based sources are depleting at an alarming rate. Moreover, combustion of such fuels has led to increase in harmful greenhouse gases emitted into the atmosphere. These adverse effects have led the scientists to focus research on harvesting energy from renewable energy sources such as wind, tide, geothermal and solar energy (World-nuclear.org. (2019), Renewables 2014-Global Status report).

Among many renewable energy sources, the use of solar power has been exponentially increased over the past decades as it is the most abundant, constant and least polluting energy source which can be harvested (Lee 2019). The amount of energy falling on the surface of the earth from the sun is about 3×10^{24} J year^{-1} or 10^4 times the consumption of the world. Covering 0.1% of the total area of the earth by using 10% efficient solar cells (SCs) would be adequate to meet up the global energy demand (Grätzel 2005).

Silicon based SCs are the most popular SCs in the market which give efficiencies up to 15–17% (Lee et al. 2014). Major problem with SCs are their high manufacturing cost, because it requires highly pure silicon (99.9999% of purity) making the SC expensive (Braga et al. 2008). Promising solution for this problem was given by Grätzel (2003) with the breakthrough on dye-sensitized solar cell (DSC) with many desirable properties such as higher flexibility for the choice of starting materials, higher transparency and less environmental pollution in addition to being low-cost (O'Regan and Grätzel 1991; Grätzel 2003).

17.1.1 Operational Principle of Dye-Sensitized Solar Cells

A dye-sensitized solar cell (DSC) typically consists of three main components; the dye sensitized semiconductor oxide photoanode/working electrode (WE), redox electrolyte and a counter electrode (CE)/cathode (Grätzel 2001; Hagfelt and Grätzel 2000). The photoanode is a transparent electrode made out of transparent conductive oxide (TCO) coated on a glass substrate, generally indium doped tin oxide (ITO) (Tahar et al. 1998) or fluorine doped tin oxide (FTO) (Yang 2009) are used that facilitate electrical conductivity and light transmittance. A mesoporous semiconductor layer (typically TiO_2) is deposited on the TCO in order to enhance and activate electronic conduction. Additionally the surface of the mesoporous oxide layer is covalently bonded to a monolayer charge transfer dye which contributes to enhance light absorption and eventually generate charge carriers. The porous nature and the morphology of the TiO_2 layer is selected such that it assures a greater degree of absorption of the dye at the surface thus accommodating a greater area of reaction sites (Gong et al. 2012).

Figure 17.1 depicts the function of a typical DSC. Upon illumination with sunlight the sensitizer molecules harvest incoming photons and undergo excitation from the ground state to the excited state. Subsequently the excited electron will be injected into the conduction band of the TiO_2 semiconductor material, which leads to the formation of an oxidized sensitizer. These electrons generated will diffuse to the anode and will be eventually migrated along an external circuit to the CE. The CE is made out of a TCO glass substrate which is coated with a catalyst, most commonly Pt (Thomas et al. 2014; Maiaugree et al. 2015). This platinised CE facilitates smooth electron flow and catalyse the redox reaction in the electrolyte. Pt is used

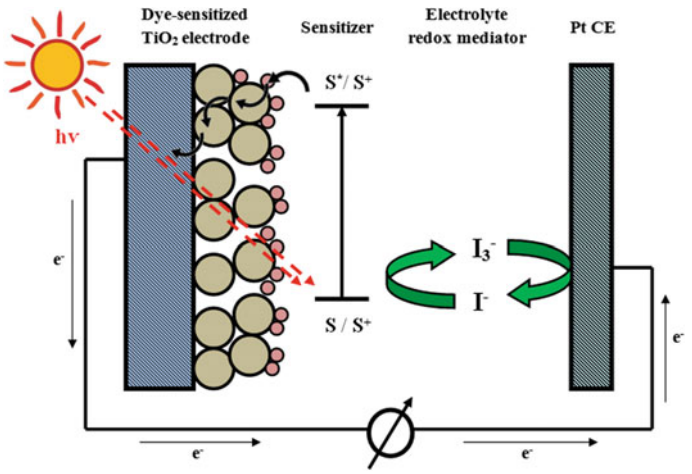

Fig. 17.1 Schematic diagram of typical DSC and the electron transfer process involved in energy conversion

as a preferred CE material due to its favourable characteristics such as high catalytic activity and good electrical conductivity (Yun et al. 2015). A liquid electrolyte is present between the WE and the CE. This electrolyte contains a redox mediator and typically iodide/triiodide redox couple is used in liquid electrolyte (Chiba et al. 2006) whereas organic hole transport materials such as spiro-OMeTAD (Bach et al. 1998) and polymer materials such as polyethyleneglycol, polyacrylonitrile and poly(vinylidine) fluoride-co-hexauoropropylene (Upadhyaya et al. 2006; Cao et al. 1995; Wang et al. 2003) are the common mediators in solid state and quasi-solid state electrolytes respectively. The function of the electrolyte is the regeneration of the oxidized dye via electrochemical redox reaction thus completing the cycle. The dye molecules subjected to oxidation are been reduced by the reduced species migrating through the electrolyte medium and meanwhile the redox couple regeneration occurs by means of reduction at the CE (Hagfelt and Grätzel 2000).

The Eqs. (17.1)–(17.6) summarise the operational principle of a typical DSCs fabricated with I^-/I_3^- redox couple (Nogueira et al. 2004)

$$TiO_2|S + h\nu \rightarrow TiO_2|S^* \tag{17.1}$$

$$TiO_2|S^* \rightarrow TiO_2|S^+ + e_{CB}^- \tag{17.2}$$

$$TiO_2|S^+ + e_{CB}^- \rightarrow TiO_2|S \tag{17.3}$$

$$TiO_2|S^+ + 3/2\, I^- \rightarrow TiO_2|S + 1/2\, I_3^- \tag{17.4}$$

$$1/2\, I_3^- + e_{(Pt)}^- \rightarrow 3/2\, I^- \tag{17.5}$$

$$I_3^- + 2e_{CB}^- \rightarrow 3I^- \tag{17.6}$$

The substrate of the photo electrode plays a major role in the WE functioning; acting as a charge collector and providing support for the semiconductor layer. They need to possess high optical transparency such that natural sunlight is allowed to pass down to the semiconductor material without unwanted absorption and high electrical conductance to facilitate the electron transfer process (Gong et al. 2012). ITO and FTO are commonly used as substrate materials (Sima et al. 2010). There are drawbacks associated with their usage due to material's brittle nature, high cost and limited availability of indium, lack of sufficient transparency and the fact that they are temperature and pH sensitive (Chen et al. 2001). This has led to the investigation of novel material such as graphene films as substitute materials for the use as a substrate (Zhu et al. 2009).

The semiconductor material at the WE which is under extensive investigation is TiO_2 (Park et al. 2000). In addition to this ZnO (Law et al. 2005), SnO_2 (Fonstad and Rediker 1971) and chalcogenides (Gong et al. 2012) are also commonly used. These semiconductors have a characteristic conductive electronic structure consisting of

valence band and conduction band with a band gap having energy in the range of UV region in the electromagnetic spectrum, hence a photon with energy that matches the band gap can cause the excitation of an electron leaving behind a hole in the valence band. These charges are been migrated to the external circuit to provide electrical current. TiO_2 is the semiconductor material most commonly used and it is been used either in the form of rutile or anatase or a mixed composition of both these natural forms. The morphology and network geometry has a significant impact on the efficiency and photoelectrochemical performance of DSCs. A multilayered structure of mesoporous network of TiO_2 has yielded high cell efficiency (Wang et al. 2004). Highly ordered nano structure of TiO_2 such as network structure of TiO_2 crystal like nanowires (Adachi et al. 2004), structure consisting of submicrometer-sized mesoporous TiO_2 beads (Chen et al. 2009) and hollow TiO_2 hemisphere films deposited on substrate material (Yang et al. 2008) have been developed with high photovoltaic performances. In addition plasma enhanced polymerized aniline/TiO_2 DSCs with favourable photovoltaic performances have been developed and investigated (Ameen et al. 2009).

There are specific criteria to be satisfied by the dye sensitizer material. Most importantly the LUMO level of the sensitizer material must be closer (about 150 mV) in energy and must match the conduction band edge of the semiconductor in order to decrease energetic potential losses associated with the transfer of electrons. The HOMO level of the sensitizer material should be at a sufficient low level to enable acceptance of electrons from an electrolyte or hole conducting material. Additionally it needs to absorb all incident light below the near IR wavelength. The sensitizer material should be composed of carboxylate/phosphate group for anchorage onto the semiconductor oxide surface. Furthermore the sensitizer material needs to possess the endurance to withstand multiple turnovers and prolonged exposure to sunlight without degradation (Grätzel 2001). Initially ruthenium(II) based dyes such as the N3 dye (Nazeeruddin et al. 1993) and the black dye (Nazeeruddin et al. 1997) had been commonly used as the sensitizer material with considerable efficiency but their usage had been restricted due to the high cost and limited availability of Ru metal. Afterwards metal free organic dyes had been used (Mishra et al. 2009) and currently the use of natural dyes (Zhou et al. 2011) with structure modification is investigated as a substitute material for the sensitizer material with considerable efficiencies (Gong et al. 2012).

The electrolyte which is responsible for the electron collection at the CE and electron transportation back to the oxidized dye molecule needs to satisfy specific criteria such as rapid electron transfer kinetics, sufficient driving force to regenerate the dye, low light absorption and ability to regenerate at minimum overpotential at the CE. The most commonly used electrolyte is the iodide/triiodide (Boschloo et al. 2009) redox couple in an organic matrix usually acetonitrile. Alternative redox couples such a Br^-/Br_3^-, $SCN^-/(SCN)_2$, $SeCN^-/(SeCN)_3^-$, $[Fe(CN)_6]^{3-/4-}$, Co(II)/Co(III) (Daeneke et al. 2012), $[Mn(acac)_3]^{0/1+}$ (Perera et al. 2014) and disulfide/thiolate are used (Wang et al. 2010). Although liquid electrolytes as mentioned above offer favourable kinetics there are challenges in its usage in terms of long term durability

and operational stability due to leakage of toxic organic solvent and increase in internal resistance due to evaporation of volatile components such as iodine. Hence as an alternative the use of ionic liquid, quasi-solid state and solid state electrolytes have been investigated. The use of room temperature ionic liquids such as 1,3-dialkylimidazolium, 1,2,3-trialkylimidazolium and N-alkylpyridinium (Gorlov et al. 2007) are investigated and it had been possible to achieve significant efficiency with ionic electrolytes of eutectic salts (Bai et al. 2008).

The CE is responsible for the electron transfer from the external circuit back to the redox mediator thus completing the circuit. A CE material needs to possess excellent catalytic activity for redox electrolyte reduction, low resistance, high chemical stability and low production cost (Rahman et al. 2016). A typical CE is made out of a transparent conductive oxide glass on which a catalyst is fabricated (Thomas et al. 2014). The applicability of a wide variety of CE materials in DSCs has been extensively investigated in the recent years, this is been discussed in detail under Sect. 17.1.2 as this is the main focus of the chapter.

The preliminary characterization method for a DSC is current density-voltage (J-V) curves. The overall performance of a DSC can be evaluated in terms of cell efficiency (η) and fill factor (FF) that can be derived from a typical J-V curve. η is described as the quantum yield of photogenerated electron for the incident photonflux. The FF is another parameter that has an influence on the cell efficiency which relies on internal resistance and electron transfer. In addition to these two parameters the short circuit current density (J_{sc}) and open-circuit voltage V_{oc}) can also be derived from J-V curves (Gong et al. 2012).

The main focus of this chapter is the applicability of conducting polymers as promising substitute material for Pt CE in DSCs with a brief introduction on DSCs and their operational principle. The advantages and the drawbacks associated with the usage of the typical Pt CE is discussed followed by a description of other promising candidates as a substitute for the Pt CE. Then the use of conducting polymers as a CE material is reviewed focussing on three of the most promising conducting polymers and polymer hybrid composites. These conducting polymers and polymer hybrid composites are discussed in detail focussing on their synthetic methods, fabrication processes and their respective photovoltaic performances.

17.1.2 CE Materials

Pt has been utilized as the preferred CE material with regard to its high conductivity, high electrocatalytic activity towards reduction of I_3^- to I^- which is the typical redox mediator in DSCs and high light to electric energy conversion efficiency. A DSC with an exceptionally high efficiency of 12.3% was reported with the use of thermally decomposed platinum (Yella et al. 2011). The applicability of a variety of Pt materials as CE in DSCs has been investigated. Pt nano particles synthesized by means of decomposition of chloroplatinic acid thermally and electrochemical reduction of hexachloro platinic acid (Fu et al. 2012) was found to be a promising CE material

due to favourable characteristics such as low charge transfer resistance, promising electrical conductivity, high surface area and corrosion resistance. The applicability of Pt composite materials as CE in DSCs has also been studied (Xu et al. 2008; Yen et al. 2012). Although platinum based CEs yields high photovoltaic performances, platinum is an expensive noble metal and its usage in DSCs makes it one of the most expensive components in a DSC. In addition to its expensiveness, Pt is corrosive when used with electrolytes consisting of the redox mediator I_3^-/I^-. It has been discovered that Pt decomposes into PtI_4 in the presence of redox mediator I_3^-/I^- which would result in an adverse impact on the long term stability of the CE (Xiao et al. 2014).

The high cost and corrosion susceptibility has led to the exploration of substitute materials in place of Pt as a CE material. Hence carbon based material such as graphene (Xu et al. 2014a, b), conducting polymer-graphene nanocomposites (Huang et al. 2011), metal organic frameworks (MOFs) (Sun et al. 2016), conducting polymers and polymer hybrid composites (Rahman et al. 2016) have been investigated as alternative CE materials and they have shown favourable photovoltaic performances.

Carbon is used as a promising counter electrode material due to favourable properties such as high conductivity, appreciable catalytic activity towards many redox mediators, corrosion resistivity and cost effectiveness. The use of carbon based materials such as carbon black, graphene, mesoporous carbon, carbon nanotubes and graphene based composite materials; as CE material has been explored. The use of carbon black as a CE material was investigated and it yielded an efficiency around 9% (Murakami et al. 2006). The highest efficiency achieved with the use of a graphene CE was reported by Kakiage et al., in which an efficiency of 14.7% was yielded with the use of a graphene/gold CE (Kakiage et al. 2015).

The applicability of MOFs as CE materials has been explored. The use of CoS_2 embedded within carbon nanocages synthesized using ZIF-67 template achieved an efficiency of 8.2% (Cui et al. 2016). An outstanding efficiency of 8.69% was yielded by the use of CE material ZnSe embedded N-doped carbon cubes synthesized using MOFs with Zn nodes and benzimidazole linkers (Jiang et al. 2018).

17.2 Conducting Polymers as CE Material

Conducting polymers are organic polymers that possess an orbital system that assures the mobility of charge carriers. These polymers show extensive conjugation with overlapping π orbitals along the polymer backbone of sp^2 hybridized carbons. As a result of the delocalization of the π electrons these polymers reveal appreciable conductivity that ranges from 10^{-8} to 10^5 S/cm (Rahman et al. 2016). Conducting polymers are considered as favourable candidates for CE materials in DSCs due to characteristics such as efficient catalytic activity, promising conductivity and superior stability. Moreover the usage of conducting polymers is further favoured due to high surface area associated with the porous nature of the material thus enhancing catalytic activity and their facile cost effective synthesis. Various conducting polymers such as polypyrrole, polyaniline, polythiophene, poly(3,4-ethylenedioxythiphene) and

poly(styrene sulfonate) doped poly(3,4-ethylenedioxythiophene) have been investigated as cost effective Pt-free CEs (Thomas et al. 2014; Hou et al. 2012; Tang et al. 2013). They have revealed promising electrocatalytic activities and low charge transfer resistance. However conducting polymers associates a major challenge in their applicability due to been insoluble and mechanically weak. Due to this reason nanomaterials are been added such as carbon nanotubes, boron nanotubes, graphene, fullerene in order to improve and enhance their mechanical, electrical properties (Lee et al. 2008). The use of nanographite/polyaniline composites as CE in DSCs has yielded an efficiency of 7.07% (Huang et al. 2011). The favourable properties and appreciable efficiencies of conducting polymer based CEs have inspired extensive investigation of them as promising CE materials in Pt free DSCs.

17.2.1 Polyaniline (PANI) as a CE in DSCs

PANI is a conducting polymer consisting of a reactive NH group with two phenyl rings on either sides of it. The reactive NH group can undergo protonation and deprotonation. Hence conductivity of PANI depends not only on the oxidation state but also the degree of protonation and the dopant type. Figure 17.2 summarises the different forms of PANI that exist with different oxidation states. PANI is a promising material as a CE due to its favourable characteristics such as low cost, high electro chemical activity and high thermal and chemical stability (Saranya et al. 2015). PANI

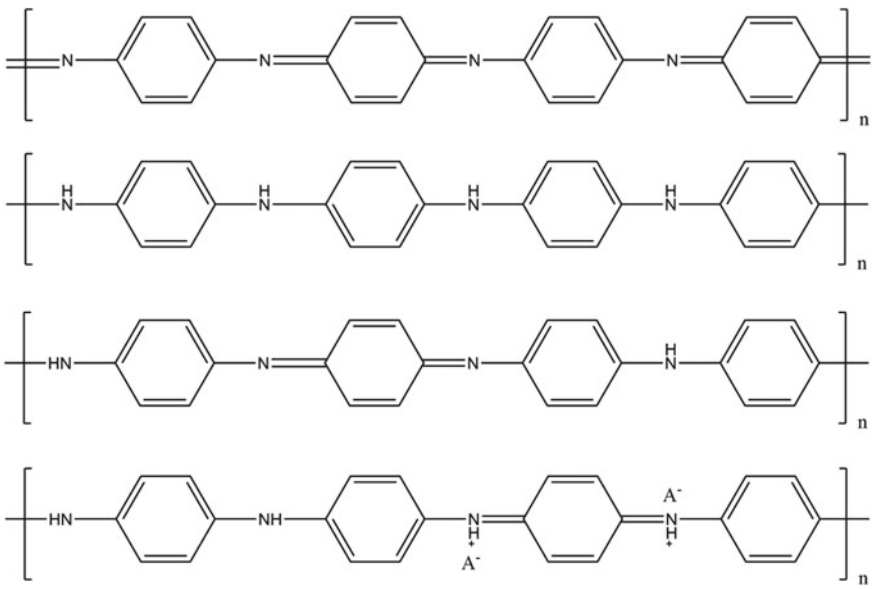

Fig. 17.2 Oxidative forms of PANI

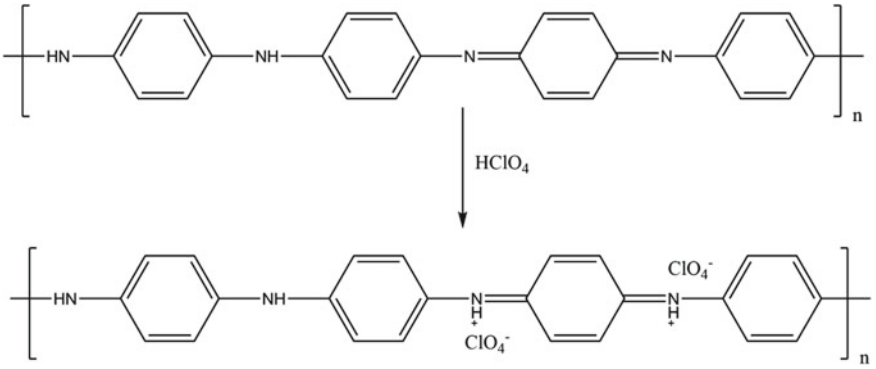

Fig. 17.3 Doping of PANI with $HClO_4$

can be synthesized using two distinct methods, chemical polymerization method and electropolymerization method.

Microporous polyaniline synthesized using oxidative chemical polymerization has been used as a substitute CE material with a size diameter of 100 nm; and a higher overall energy conversion efficiency had been achieved (Li et al. 2008). Here PANI had been synthesized by means of aqueous oxidative polymerization reaction with ammonium persulfate using perchloric acid as the dopant (Fig. 17.3).

PANI nanoparticles synthesized using this methodology had been coated on a conducting FTO glass by dip tugging method thus preparing a PANI CE. The PANI nanoparticles with 100 nm size diameter and microporosity contributes to enhance the surface area of the PANI CE thus improving the catalytic activity and trapping liquid electrolytes in microporomerics in DSCs.

Cyclic voltagrams provide evidence for the fact that this PANI CE has a reduced charge transfer resistance and high electricatalytic activity towards I_3^-/I^- redox couple. Furthermore PANI CE had achieved a 7.15% overall energy conversion efficiency which is greater with respect to the usage of Pt CE under same conditions (Li et al. 2008).

The electropolymerization method of synthesizing PANI is considerably simpler and cost effective with respect to chemical polymerization. This method enables the preparation of CE material with controllable surface morphology and it assures effective adhesion to the substrate surface. Several techniques of electropolymerization are used in the synthesis of PANI CE material such as cyclic voltammetry, constant potential, constant current, pulse current, and pulse potentiostatic methods (Xiao et al. 2013).

PANI CEs prepared using constant potential method is the conventional synthetic methodology. PANI CE prepared using the synthetic methodology of pulse potentiostatic polymerization has revealed high electrochemical stability and excellent electrocatalytic activity for the I_3^-/I^- redox reaction with respect to conventional PANI CEs prepared using constant potential synthetic methodology. PANI CEs prepared using pulse potentiostatic polymerization results in a higher cathodic peak

current revealed from CV tests and lower charge transfer resistance. These conducting polymers have a rough surface morphology and due to this high surface area the electrocatalytic activity is been enhanced. Although the power conversion efficiency is not as high as Pt CE (up to 90% PCE of DSCs using Pt CE) in this case of conducting PANI polymers, it is a preferred CE material due to its cost effectiveness and facile synthesis methodology (Xiao et al. 2013).

The two step cyclic voltammetry approach for the synthesis of PANI CE material has also been able to achieve substantial power conversion efficiency. This method enables the preparation of well controlled and short branched PANI nanofibres with high performance. It involves a pre electropolymerization step in which a larger potential range (0–1.3 V) is applied for few cycles (typically one) followed by PANI electropolymerization subjected to a smaller potential range (0–0.9 V) for a larger number of cycles (10 cycles). It reveals high electrocatalytic activity towards I_3^-/I^- redox couple due to high cathodic peak current and lower charge transfer resistance as evident from CV tests. This is also due to the enhanced surface area attributed to PANI nanofibres due to short branched surface morphology. The conversion efficiency of these two step PANI CEs can be enhanced to achieve up to 97% of the power conversion efficiency observed when platinised CEs are been used. But their applicability is favoured due to cost effective nature (Xiao et al. 2014).

The surface morphology of electropolymerized PANI has a significant impact on the electrocatalytic activity and charge transfer resistance in DSCs. This surface morphology of electropolymerized PANI CEs varies with the usage of different dopant anions such as SO_4^{2-}, ClO_4^-, BF_4^-, Cl^- and p-toluene sulfonate (Rahman et al. 2016).

The use of H_2SO_4-doped dense PANI nanoparticles CE has enabled a higher power conversion efficiency of 7.30% in DSCs. The long conjugation structure, high level of doping and extensive electron delocalization contributes for favourable electrical conductance and enhanced electrocatalytic activity towards I_3^-/I^- redox species thus owing to an overall higher power conversion efficiency (Rahman et al. 2016).

The electrocatalytic activity and power conversion efficiency of sulfamic acid-doped PANI nanofibres have been enhanced due to the fact that sulfamic acid contributes to create voids in the fibrous network of PANI nanofibres. This doping allows a 27% improvement in the photon-conversion efficiency (Ameen et al. 2010).

The usage of PANI nano wire arrays as a CE material enables a very high power conversion efficiency of 8.24%. The oriented PANI nano wire arrays are prepared by means of in situ polymerization owing to a greater surface area and hence a high catalytic activity towards the redox mediator. It had been found that a greater electrocatalytic activity is recorded towards Co^{2+}/Co^{3+} redox mediator. The usage of PANI nano wire arrays also associates the advantage of been able to be grown on flexible substrate material (Wang et al. 2013).

Furthermore transparent PANI CEs have been used for the fabrication of novel bifacially active DSCs that can be illuminated from both sides. Such bifacially active DSCs prepared using transparent PANI CEs enables high power generating efficiency due to the ability of utilizing light from both sides. Bifacial DSCs require transparency in the CEs; hence the use of a Pt CE is unfavoured due to its high reflectance of

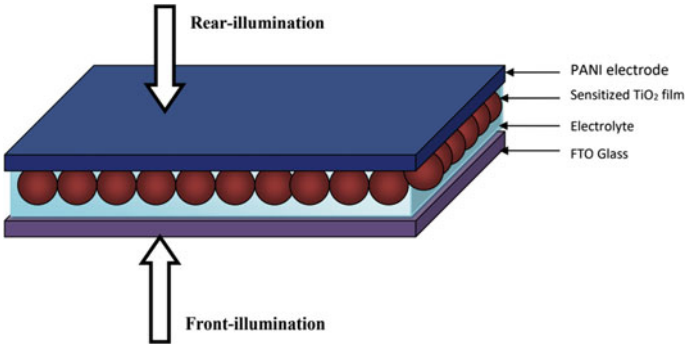

Fig. 17.4 Schematic diagram of a Bifacial DSC with transparent PANI CE. Adapted from Tai et al. (2011)

light. Carbon material based CEs cannot be used as it requires them to possess substantial thickness to achieve desirable conductivity and electrocatalytic activity which diminishes the transparency of the CE. However there are methods of preparing high quality transparent PANI films that can be substituted as CEs in bifacial DSCc such as in situ polymerization of aniline on FTO glass to produce novel transparent PANI CE. In addition the emaralidine PANI possess complementary absorption in the visible region of the electromagnetic spectrum with the N3 dye and this is crucial for the high performance of the Bifacial DSCs. CV tests provide evidence to show that PANI CEs in bifacial DSCs yields a greater peak current density than Pt CEs, hence PANI is the more efficient CE in bifacial DSCs (Tai et al. 2011) (Fig. 17.4).

The use of PANI CE has enabled the yield of a power conversion efficiency of 6.54% which is closer to that of a DSC with a Pt CE which is 6.69% (Table 17.1). But in the bifacial DSCs in addition, the rear illumination yields a power conversion efficiency of 4.26%. This distinct feature of bifacial DSCs been able to utilize light from both front illumination and rear illumination encourages its applicability in building integrated photovoltaics such as power generating windows (Tai et al. 2011).

Table 17.2 summarises the photovoltaic parameters of DSCs with Pt free PANI CEs having outstanding efficiencies. The number of active sites available for the redox reaction can be improved by increasing the thickness. It is possible to enhance the electrochemical catalytic properties of PANI CE by the use of special morphologies which can be attained using electrochemical polymerization method. The main challenge associated with the use of PANI CE is the difficulty of coating a uniform

Table 17.1 Electrical impedance spectroscopy (EIS) and J-V parameters of DSCs with Pt and PANI CEs

Electrodes	V_{oc} (mV)	J_{sc} (mA/cm^2)	FF	PCE (%)
FTO/Pt	706	14.75	0.643	6.69
FTO/PANI	710	15.24	0.604	6.54

Table 17.2 Photovoltaic performances of different PANI CEs

Type of PANI	Preparation methodology	FF	PCE (%)	Refs.
Microporous PANI	Oxidative polymerization	0.69	7.15	Li et al. (2008)
Transparent PANI	Chemical deposition	0.65	8.35	Wu et al. (2014)
H_2SO_4 doped PANI	Chemical deposition	0.59	7.30	Xu et al. (2014a, b)
PANI film	Technique employing Hexafluoro-isopropanol (HFIP) solution	0.67	8.80	Chiang et al. (2013)

film with appreciable conductivity and surface area. Therefore when considering the use of dopants in efficiency enhancement, both its ability to enhance conductivity and act as a pore former increasing surface area; needs to be taken into account (Saranya et al. 2015).

17.2.2 Polypyrrole (PPy) as a CE in DSCs

PPy is another substitute material that can be used in place of Pt as the CE. Besides its good mechanical, chemical stability and high conductivity, PPy shows good catalytic behaviour for I_3^- reduction when used as the CE but have slightly lower fill factor and lower power conversion efficiency with regard to Pt CE (Rahman et al. 2016; MacDiarmid 1997). However by means of controlling the morphology of the PPy CE it is possible to improve the power conversion efficiency. The use of PPy as a CE material is also favoured due to simple preparation procedure and low cost (Fig. 17.5).

PPy nano particles synthesized using chemical oxidative method and coated on conducting FTO glass reveals higher electrocatalytic activity and greater power conversion efficiency in comparison to Pt CEs. PPy had been easily synthesized by

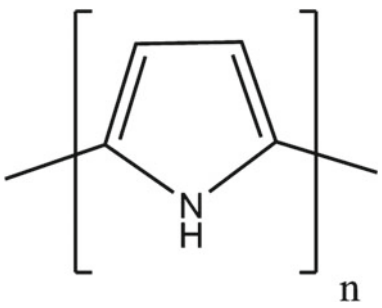

Fig. 17.5 Structure of polypyrrole

Table 17.3 Photoelectric properties of DSCs with PPy and Pt CEs

Electrode	J_{sc} (mA/cm^2)	FF	PCE (%)
PPy	15.01	0.69	7.66
Pt	14.47	0.68	6.90

means of chemical oxidative polymerization in the presence of iodine and these PPy nanoparticles (40–60 nm) were coated on FTO glass to prepare the CE (Wu et al. 2008).

Condition: Liquid electrolyte contains 0.1 M KI, 0.01 M I_2 and 0.6 M tetrabutyl ammonium iodide and acetonitrile.

The CV tests reveal that the use of PPy CEs results in smaller charge transfer resistance and higher electrocatalytic activity towards I_3^-/I^- redox reaction than the Pt CE. The overall power conversion efficiency when using PPy CE is 7.66% which is 11% greater than when using Pt CE provided the same conditions (Table 17.3).

The improved photovoltaic performances can be attributed to its high surface area, low charge transfer resistance and high electrocatalytic activity. In addition to the excellent photoelectric properties of PPy, its simple synthesis, fabrication and cost effectiveness also contributes to its credibility as a substitute for Pt CEs (Wu et al. 2008).

The use of PPy synthesized using vapour phase polymerization, as CE material in DSCs has been investigated. PPy synthesized using vapour phase polymerization (VPP) shows favourable catalytic behaviour, but associates a slightly lower fill factor and a lower power conversion efficiency compared to Pt CE material. The lower power conversion efficiency can be attributed to insufficient contact between the polymer films and FTO glass and also due to low oxidant concentrations. Therefore it is possible to improve photovoltaic performances by manipulating the morphology of PPy and its adhesion to the FTO substrate and the oxidant concentration (Rahman et al. 2016). PPy was synthesized by exposing FTO glass spin coated with iron (iii) p-toluenesulfonate (Fe-TsO) to pyrrole vapour which resulted in the preparation of VPP-PPy homogenous individual particles demonstrating a particle size in the range of 100–150 nm. The VPP-PPy CEs yield power conversion efficiency in the range of 2.0–3.4% depending on the oxidant concentration which is lower than the power conversion efficiency observed for Pt CE material which is 4.4% (Table 17.4). It was discovered that the photovoltaic performances were improved with an increase in Fe-TsO oxidant concentration (Xia et al. 2011).

Table 17.4 Photoelectric properties of DSCs with PPy and Pt CEs

Electrode	J_{sc} (mA/cm^2)	FF	PCE (%)
Pt	9.5	0.65	4.4
5% VPP-PPy	8.3	0.51	2.8
20% VPP-PPy	9.2	0.54	3.4

There has been a recorded increase in the power conversion efficiency in VPP-PPy CEs when the Fe-TsO oxidant concentration is increased from 5% (PCE of 2.8%) to 20% (PCE of 3.4%). From cyclic voltammetry it has been revealed that VPP-PPy possess high electrocatalytic activity for I^-/I_3^- redox system. Despite its lower power conversion efficiency its substitution of Pt CE is favoured due to its cost effectiveness and facile synthesis (Xia et al. 2011).

Furthermore traditional electrochemical polymerization methods are employed to synthesize PPy to be used as a CE in DSCs. The use of potentiostatic mode of polymerization at 1.2 V (vs. Ag/AgCl) for polymerization of pyrrole in acetonitrile solution to prepare EP-PPy had been investigated. This enables the synthesis of PPy particles around the size of 300 nm and assures full coverage of FTO substrate. PPy CE prepared by electropolymerization exhibits a power conversion efficiency of 3.2% which is comparable with regard to optimized VPP-PPy CE's power conversion efficiency. Although its power conversion efficiency is less than that of Pt CE material they show good catalytic behaviour with respectable J_{sc}. In terms of electropolymerization the use of bulky sized inert doping anions such as ClO_4^- are preferred in the preparation of PPy, due to their high mobility which contributes to achieve high current density. In addition to its respectable photovoltaic performances; feasibility of electropolymerization synthesis and inexpensiveness contributes to the credibility of EP-PPy as a substitute material for CEs (Xia et al. 2011).

The use of novel self-assembled PPy nanotube membrane as CE material in Pt-free DSCs has been reported by Peng et al. (2013). Free standing paper like membranes composed of PPy nanotubes have been synthesized and used to prepare FTO and Pt free CEs. Usually PPy CE is fabricated by deposition of the polymer on FTO substrate and in situ polymerization and both these methods require FTO substrate. This method allows the preparation of FTO free CEs consisting of PPy nanofibres only, hence flexible DSCs with considerable mechanical properties. This facile synthetic methodology involves heating of pulp like homogenous suspensions at low temperature followed by doping in HCl solution. Finally the PPy nanotubes allowed to self-assemble into paper like flexible PPy membranes under a vacuum atmosphere at high temperature (Rahman et al. 2016).

The high surface area of the PPy nanofibres and good electrolyte penetration in the poriferous PPy membrane contributes to the respectable electrocatalytic activity as revealed from the photovoltaic performance data shown in Table 17.5. This PPy membranes yield a power conversion efficiency of 5.27%. That is 84% of the power conversion efficiency for platinised CE under same conditions. Despite the slightly lower power conversion efficiency the use of self-assembled PPy nanotube membranes as a substitute material for Pt CE material is favoured due to inexpensiveness,

Table 17.5 Photovoltaic performance data of DSCs with different CEs

Electrode	J_{sc} (mA/cm^2)	FF	PCE (%)
Pt/FTO	13.41	0.65	6.25
PPy	13.10	0.56	5.27

facile synthesis and most importantly the ability to prepare flexible DSCs consisting of FTO free CEs (Peng et al 2013).

Therefore it is possible to understand that PPy is a credible substitute material for Pt as the CE in DSCs and the performance of PPy based CEs depends on factors such as method of polymer synthesis and conditions, type of dopant anions, type of oxidant species used and film morphology (Peng et al. 2013).

Furthermore the use of PPy CEs in quasi solid state DSCs has been investigated by Makris et al. Quasi-solid state DSCs have been constructed using nanocrystalline titania, ureasil based nanoconposite gel electrolyte and PPy functionalized CE. PPy was electrodeposited on FTO substrate under potentiostatic conditions using the pyrrole precursor monomer in aqueous medium thus synthesizing PPy functionalized CE.

Despite the fact that DSC with Pt CE exhibits higher open circuit voltage and a better fill factor relative to PPy functionalized CE, they possess higher short circuit current density which accounts to its superior electrocatalytic activity. The thickness of the PPy film plays a pivotal role in the photovoltaic performances of the DSCs and this thickness is controllable by the deposition time. PPy films having a thickness of 750 nm gave rise to the optimum photovoltaic performances which are summarized in Table 17.6. The employment of PPy functionalized CEs in quasi-solid state DSCs is preferred due to inexpensiveness, durability feasibility of synthesis and the fact that it can achieve substantial power conversion efficiency which is only 30% less efficient with respect to platinised CEs (Makris et al. 2011).

Table 17.7 summarises the photovoltaic parameters of DSCs with Pt free PPy CEs having outstanding efficiencies. The efficiency of PPy CE is highly dependent on the nature of the dopant, synthetic methodology and surface morphology. They

Table 17.6 Photovoltaic performance data of DSCs with different counter electrodes

Electrode	J_{sc} (mA/cm^2)	FF	PCE (%)
Pt	13.5	0.69	6.7
PPy	15.9	0.45	4.6

Table 17.7 Photovoltaic performances of different PPy CEs

Type of PPy	Preparation methodology	FF	PCE (%)	Refs.
PPy nanoparticles	Synthetic chemical method	0.69	7.66	Wu et al. (2008)
Ultra-thin PPy nanosheets	Organic single crystal surface induced polymerization	0.62	6.80	Hwang et al. (2014)
Spherical PPy	Chemical oxidative polymerization	0.64	7.73	Jeon et al. (2011)
Porous PPy	In situ polymerization	0.52	5.74	Bu et al. (2013)

tend to yield comparatively lower efficiencies associated with higher R_{ct} and lower conductivity (Saranya et al. 2015). But despite the lower efficiencies relative to Pt CEs its applicability as a CE material is preferred due to cost effectiveness and facile synthesis.

17.2.3 Poly(3,4-Ethylenedioxythiophene)/(PEDOT) as a CE in DSCs

PEDOT is another type of conducting polymer which is extensively studied as a substitute for Pt CE material. It is an efficient catalyst in DSCs due to its nanoporous structure, high conductivity at room temperature, electrochemical reversibility and high chemical and thermal stability (Fig. 17.6).

The use PEDOT polymerized via constant current electropolymerization as CE material has been reported by Gao et al. (2014). PEDOT films were synthesized on FTO substrate by means of aqueous galvanostatic polymerization technique at current density of 0.5 mA cm^{-2}. These PEDOT CEs show variable photovoltaic performances based on the surface morphologies which can be controlled using the polymerization time.

From CV and EIS data it is evident that the polymerization time has an impact on the photovoltaic performances of the DSCs. The PEDOT CEs showed faster reaction rates and higher electrocatalytic activity as the polymerization time was increased. The PEDOT CE polymerized at 40 s possessed higher electrocatalytic activity towards I_3^- and charge transfer resistance which is comparable with that of Pt CE. It was possible to achieve a power conversion efficiency of 6.46% by optimized PEDOT CE which is greater than the power conversion efficiency yielded by Pt CE under same conditions which is 6.33% (Table 17.8). Therefore PEDOT

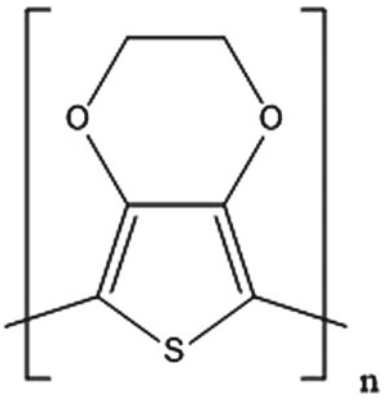

Fig. 17.6 Structure of Poly(3,4-ethylenedioxythiophene)/PEDOT

Table 17.8 Photovoltaic performances of DSCs of various CEs

Electrodes	J_{sc} (mA/cm^2)	FF	PCE (%)
Pt	15.27	0.61	6.33
PEDOT-10s	15.58	0.54	5.38
PEDOT-40s	16.66	0.57	6.46

films are regarded as promising alternative materials that can be used in place of Pt as the CE in DSCs (Gao et al. 2014).

PEDOT nanoporous layers synthesized via electro-oxidative polymerization using room temperature hydrophobic ionic liquids as a medium; was investigated as a source of CE material that can substitute Pt in DSCs (Rahman et al. 2016). In this synthetic methodology room temperature ionic liquids are used as the polymerization medium. This enables the provision of favourable growth conditions to produce grains in the nanometer size range which is desirable as the grain size dictates the catalytic behaviour of the polymer. The applicability of π-conjugated polymer electrochemical devices is limited due to poor environmental stability and electrochemical cycling between oxidation states. These problems arise partly due to the electrolytes used in these devices, but room temperature ionic liquids are electrochemically stable and hence they are ideal solvents for long life electrochemical processes. Therefore the use of PEDOT CEs associates the advantage of reproducible high cycling life (Ahmad et al. 2010).

The photovoltaic performance has been monitored by increasing the thickness of PEDOT film by means of increasing the polymerization time. As the thickness of PEDOT film increased the J_{sc} has increased but in contrast the open circuit voltage has decreased. It could be understood from the above data tabulated that the photovoltaic performance increases when the PEDOT film thickness decreases as thin films have favourable catalytic properties. These PEDOT CEs achieved a power conversion efficiency of 7.93% which is only slightly lower than when using platinised CE in DSCs (Table 17.9). Therefore in terms of inexpensiveness, feasibility of synthesis, reproducible high cycling life and respectable photovoltaic performances PEDOT is a credible alternative for Pt CEs (Ahmad et al. 2010).

Furthermore a significant photovoltaic performance was reported with the use of nanostructured PEDOT which were electrochemically prepared, as the CE material in DSCs (Rahman et al. 2016). Here PEDOT nanofibres were synthesized having high catalytic activity and they were used as the CE material in DSCs. The

Table 17.9 Photovoltaic performances of DSCs for various CEs

Electrode	J_{sc} (mA/cm^2)	FF	PCE (%)
Pt	15.9	0.73	8.71
PEDOT-30s	15.0	0.76	7.93
PEDOT-60s	15.2	0.75	7.86

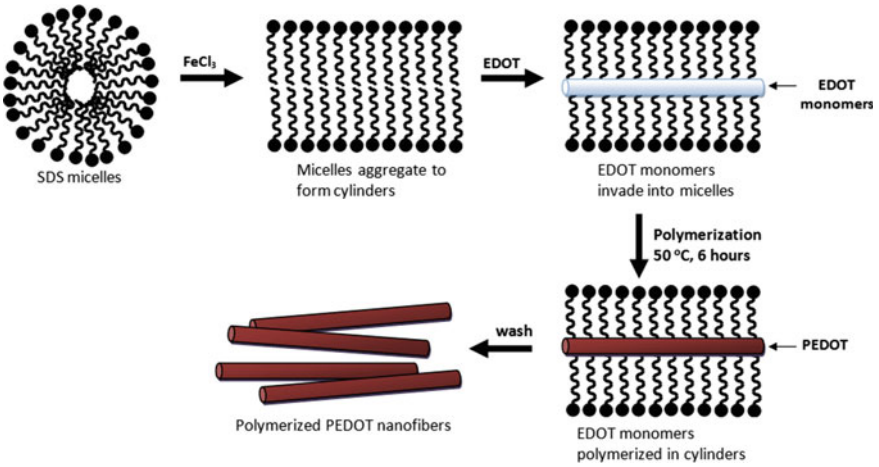

Fig. 17.7 Schematic illustration of the synthesis of PEDOT nanofibres. Adapted from Jeon et al. (2013)

synthetic methodology consists of chemical oxidative polymerization in aqueous medium in the presence of sodium dodecyl sulphate (SDS) and $FeCl_3$ using 3,4-ethylenedioxythiophene (EDOT) monomer. The schematic diagram above illustrates the synthetic methodology employed to prepare the PEDOT nanofibres (Jeon et al. 2013) (Fig. 17.7).

The nanofibrous PEDOT CE with high electrical conductivity and large surface area behaves as a CE material with high catalytic activity. The nanofibrous structure is porous and possess a rough morphology which enables penetration of the electrolyte to facilitate and catalyse redox reactions. This is evident from the photovoltaic performance data obtained (Table 17.10) from CV and EIS tests (Jeon et al. 2013).

Both J_{sc} and V_{oc} recorded for PEDOT-NF CE is greater than in DSCs with Pt CE resulting in a higher conversion efficiency of 8.34%. In comparison to platinised CE PEDOT-NF CE shows higher redox current revealed from CV tests which is attributed to the larger number of catalytic active sites associated with the large surface area. Therefore due to its distinct photovoltaic performances PEDOT-NF CEs are a credible alternative for platinised CEs (Jeon et al. 2013).

The polymer morphology plays a pivotal role in terms of efficiency of conducting polymer CEs (Rahman et al. 2016). This is evident from the investigation of the use of PEDOT films having nano-meadows morphology as CE material in DSCs. Here

Table 17.10 Photovoltaic performances of DSCs assembled with different CEs

Electrodes	J_{sc} (mA/cm^2)	FF	PCE (%)
Pt	16.6	0.60	7.20
PEDOT-NF	17.3	0.67	8.34

Table 17.11 Photovoltaic performances of different PEDOT CEs

Type of PEDOT	Preparation methodology	FF	PCE (%)	Refs.
PEDOT film	Electropolymerization	0.69	8.87	Li et al. (2014)
PEDOT-NFs	Chemical oxidative polymerization—organic liquid electrolyte	0.67	8.34	Jeon et al. (2013)
PEDOT-EG film	Electropolymerization	0.64	8.50	Zhang et al. (2013)
PEDOT film	HFIP solution	0.67	9.00	Chiang et al. (2013)

PEDOT films were synthesized using electropolymerization employing pulse potentiostatic method. The PEDOT nano-meadows were eletcropolymerized onto multi walled carbon nanotubes (MWCNT) and fabricated onto FTO glass substrate. The PEDOT/MWCNT CEs demonstrated greater power conversion efficiency (7.03%) relative to DSCs with Pt CE (5.88%) under the same conditions. Therefore due to the high electrocatalytic activity attributed to high specific surface area and high photovoltaic performances PEDOT CE with nano-meadows morphology is a promising alternative CE material (Xiao et al. 2012).

Table 17.11 summarises the photovoltaic parameters of DSCs with Pt free PEDOT CEs having outstanding efficiencies. PEDOT exhibits the highest electrocatalytic activity towards I_3^-/I^-; amongst all conducting polymers (Bay et al. 2006). By different polymerization methods it is possible to synthesize PEDOT with high conductivity. Hence PEDOT CEs yield outstanding efficiencies relative to other conducting polymer CEs (Saranya et al. 2015). Furthermore, its applicability as a CE is favoured also due to its cost effectiveness and feasibility of synthesis.

17.2.4 Polymer Hybrid Composites as CEs in DSCs

Polymer hybrids are a blend of different types of polymers and their applicability as CEs is under extensive investigation due to synergistic effect it generates in terms of enhancing electrocatalytic activity (Yue et al. 2012). The preparation of CEs by means of electrodeposition of PEDOT:PSS (polystyrenesulfonate) has yielded an outstanding efficiency of 8.3% (Zhang et al. 2013).

Carbon is another cost effective substitute for Pt as a CE material. Nevertheless its applicability as a CE material is limited due to its insolubility in most solvents. To subdue this drawback carbon materials could be utilized as a composite material with conducting polymers and conducting polymer blends thus giving rise to synergistic effects. In addition, the usage of such composite materials contributes to favourable mechanical properties. Therefore the applicability of conducting polymer/carbon composites are extensively investigated as CE materials. Various forms of carbon such as carbon black (CB), carbon nanotubes (CNT) and graphene have been used

to prepare composites with conducting polymers; that have emerged as promising candidates for CE materials (Saranya et al. 2015).

Graphene has emerged as promising CE material in DSCs with very good electrical conductivity and high electrocatalytic activity (Rahman et al. 2016). The surface functionalization of such carbon materials with conducting polymers have found to enhance the electrocatalytic activity, as conducting polymers such as PANI, PPy and PEDOT are promising conducting polymer candidates to replace Pt CEs in DSCs.

The use of reduced graphene oxide/PPy/PEDOT composite films as substitute material in place of Pt CE in DSCs has been investigated by Sekkarapatti et al. Here moderately reduced graphene oxide (RGO)/PPy/PEDTO composite films were fabricated employing a process of three steps. GO/PPy composites were initially prepared via in situ polymerization. Afterwards uniform thin films of graphene oxide/PPy were deposited on a transparent conductive electrode substrate and annealed at high temperature (300 °C) which results in the preparation of moderately reduced GO/PPy composite films by thermal reduction. Finally PEDOT was deposited on the RGO/PPy film by one-step electrodeposition as illustrated by Fig. 17.8. The RGO/PPy/PEDTO composites thus produced were employed as the CE in DSCs.

In the composite CE graphene and the conducting polymers, PPy and PEDOT provides synergistic properties in terms of conductivity and electrocatalytic activity which can be understood by the evaluation of data from CV and EIS analysis.

The composite CE yields J_{sc} and V_{oc} values that are comparable with Pt CEs (Table 17.12). Furthermore it exhibits good power conversion efficiency (7.1%)

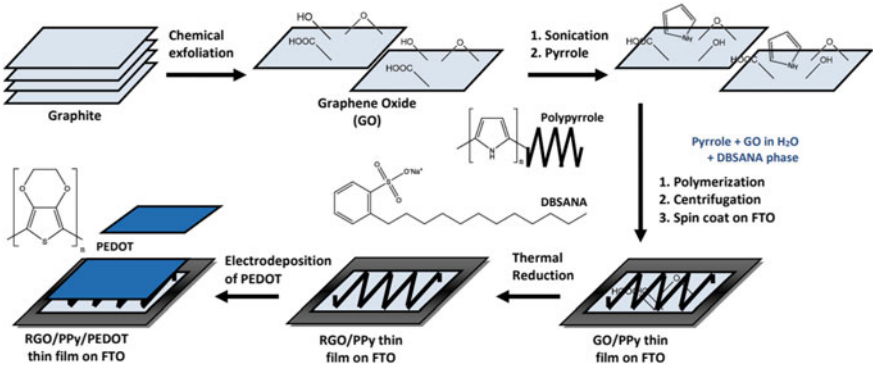

Fig. 17.8 Schematic illustration of the synthesis of RGO/PPy/PEDOT CE. Adapted from Sekkarapatti et al. (2015)

Table 17.12 Photovoltaic performances of various different CEs

Electrodes	J_{sc} (mA/cm^2)	FF	PCE (%)
Pt	19.2	0.62	9.3
RGO/PPy/PEDOT	17.0	0.55	7.1

Table 17.13 Photovoltaic performances of DSCs with different CEs

Electrodes	J_{sc} (mA/cm^2)	FF	PCE (%)
Pt	17.9	0.64	8.5
MWCNT/PEDOT:PSS	15.5	0.63	6.5

which is slightly less than in DSCs with Pt CEs. Hence RGO/PPy/PEDOT composite CEs reveal respectable electrocatalytic activity and sufficient photovoltaic performances. In addition to this its inexpensiveness and facile synthesis assures its credibility as a promising CE material (Sekkarapatti et al. 2015).

Furthermore conducting polymer/carbon nanotube composites are reported as promising CE materials in DSCs. Carbon nanotubes have remarkable potential as CE materials due to fast electron transfer and good conductivity. The composite solution was prepared by dispersal of multiwall carbon nanotubes (MWCNTs) in aqueous PEDOT:PSS solution via ultrasonication. The carbon nanotubes/conducting polymer composites were fabricated on FTO substrate by means of spin coating (Fan et al. 2008).

The photovoltaic performance data reveals that the composite CE exhibits comparable J_{sc} and V_{oc} with respect to Pt CE (Table 17.13). The power conversion efficiency demonstrated by DSCs with composite CE is only slightly less than that of DSCs with Pt CEs. Therefore due to respectable photovoltaic performance, facile synthesis and inexpensiveness, MWCNT/PEDOT:PSS composite material are credible as promising CE materials that can be used in place of Pt (Fan et al. 2008).

Table 17.14 summarises the photovoltaic parameters of DSCs with Pt free conducting polymer/carbon composite CEs having outstanding efficiencies. The use of such composites enables favourable electrical, optical and mechanical properties through synergistic effects (Saranya et al. 2015).

Table 17.14 Photovoltaic performances of different CP/carbon composite CEs

CP/carbon, CNT, graphene composites	Preparation methodology	FF	PCE (%)	Refs.
PEDOT:PSS/carbon	Doctor blade method	0.69	7.60	Yue et al. (2013a, b)
PEDOT:PSS/graphite	Chemical polymerization	0.73	7.36	Sun et al. (2010)
PPy/SWCNT	Reflux method	0.71	8.30	He et al. (2014)
PEDOT:PSS/MWCNT film	Spin coating	0.71	8.30	Guan et al. (2013)
PPy/RGO composite	Rapid mixing method	0.64	8.14	Gong et al. (2013)
Graphene/PEDOT:PSS	Electropolymerization	0.65	7.86	Yue et al. (2013a, b)

17.3 Summary

The CE is a vital component in DSCs which is responsible for the transfer of electrons from the external circuit back to the redox mediator and regeneration of redox couple. The CE electrode typically comprises of a transparent conductive oxide glass on which a catalyst is fabricated. The applicability of a wide variety of CE materials has been investigated out of which Pt has been utilized as the preferred CE material due to its high conductivity and high electrocatalytic activity towards I_3^-/I^-. The applicability of Pt as a CE is limited due to its high cost and susceptibility to undergo corrosion. Hence the use of substitute materials in place of Pt as the CE; such as carbon based materials, metal organic frameworks, conducting polymers and polymer hybrid composites have been extensively investigated.

Conducting polymers are considered as promising CE material due to their high conductivity, high electrocatalytic activity and good stability. Furthermore their applicability as CE materials is favoured due to cost effectiveness and feasibility of synthesis. Various conducting polymers such as PANI, PPy, PEDOT and polymer hybrid composites have been extensively investigated as cost effective CE materials in Pt free DSCs. PANI based CE material is a promising prospect in DSCs due to appreciable photovoltaic performances and cost effectiveness. PANI reveals favourable characteristics such as low cost, high electrochemical activity, high environmental stability and facile synthesis. PANI used as CE material is synthesized by means of either chemical polymerization or electropolymerization method. It is possible to enhance the electrochemical catalytic properties of PANI CEs by the use of special morphologies. In PANI CEs, dopants are selected such that it enhances conductivity and increases surface area by acting as a pore former. The use of PPy based CEs in DSCs yield relatively lower efficiencies due to low conductivity and high R_{ct}. Nevertheless its efficiency is improved by selection of proper dopants, effective synthetic methodologies and manipulating surface morphologies. Despite lower efficiencies their applicability as a CE material is preferred due to cost effective facile synthesis and fabrication of PPy based CEs. PEDOT yields the highest efficiency and electrocatalytic activity towards I_3^-/I^- amongst other conducting polymers in Pt free DSCs. The applicability of PEDOT CEs is limited due to its cost which is comparable with that of Pt CE. Furthermore, carbon materials are used as composite materials with conducting polymers and conducting polymer blends to prepare CEs with enhanced conductivity, electrocatalytic properties and favourable mechanical properties derived through synergistic effects. The use of composite materials consisting of conducting polymers and carbon materials such as CB, CNTs and graphene; as CE material has yielded outstanding efficiencies in Pt fee DSCs. Hence the prospect of substitution of Pt CE with conducting polymers and polymer hybrid composites and preparing cost effective environmentally friendly DSCs seems promising in the future.

References

Adachi M, Murata Y, Takao J, Jiu J, Sakamoto M, Wamg F (2004) Highly efficient dye-sensitized solar cells with a titania thin-film electrode composed of a network structure of single-crystal-like TiO_2 nanowires made by the oriented attachment mechanism. J Am Chem Soc 126:14943–14949

Ahmad S, Yum J-H, Xianxi Z, Gratzel M, Butt H-J, Nazeeruddin MK (2010) Gye-sensitized solar cells based on poly (3,4,-ethylenedioxythiophene) counter electrode derived from ionic liquids. J Mater Chem 20:1654–1658

Ameen S, Shaheer Akhtar M, Kim G-S, Kim YS (2009) Plasma-enhanced polymerized aniline/TiO_2 dye-sensitized solar cells. J Alloy Compd 487:382–386

Ameen S, Akhtar MS, Kim YS, Yang O-B, Shin H-S (2010) Sulfamic acid-doped polyaniline nanofibres thin-film based counter electrode: application in dye-sensitized solar cells. J. Phys. Chem. 114(10):4760–4764

Bach U, Lupo D, Comte P, Moser JE, Weissortel F, Salbeck J, Spreitzer H, Gratzel M (1998) Solid-state dye-sensitized mesoporous TiO_2 solar cells with high photon-to-electron conversion efficiencies. Nature 395(6702):583–585

Bai Y, Cao Y, Zhang J, Wang M, Li R, Wang P, Zakeeruddin SM, Gratzel M (2008) High-performance dye-sensitized solar cells based on solvent-free electrolytes produced from eutectic melts. Nat Mater 7:626–630

Bay L, West K, Winther-Jensen B, Jacobsen T (2006) Electrochemical reaction rates in a dye-sensitised solar cell—the iodide/tri-iodide redox system. Solar Energy Mater Solar Cells 90(3):341–351

Boschloo G, Hagfeldt A (2009) Characteristics of the iodide/triiodide redox mediator in dye-sensitized solar cells. Acc Chem Res 42(11):1819–1826

Braga A, Moreira S, Zampieri P, Bacchin J, Mei P (2008) New processes for the production of solar-grade polycrystalline silicon: a review. Sol Energy Mater Sol Cells 92(4):418–424

Bu C, Tai Q, Liu Y, Guo S, Zhao X (2013) A transparent and stable polypyrrole counter electrode for dye-sensitized solar cell. J Power Sources 221:78–83

Cao F, Oskam G, Searson PC (1995) A solid state, dye sensitized photoelectrochemical cell. J Phys Chem 99(47):17071–17073

Chen Z, Cotterell B, Wang W, Guenther E, Chua SJ (2001) A mechanical assessment of flexible optoelectronic devices. Thin Solid Films 394(1):201–205

Chen D, Huang F, Cheng Y, Caruso RA (2009) Mesoporous anatase TiO_2 beads with high surface areas and controllable pore sizes: a superior candidate for high-performance dye sensitized solar cells. Adv Mater 21:2206–2210

Chiang C-H, Chen S-C, Wu C-G (2013) Preparation of highly concentrated and stable conducting polymer solutions and their application in high-efficiency dye-sensitized solar cell. Org Electron 14(9):2369–2378

Chiba Y, Islam A, Watanabe Y, Komiya R, Koide N, Han LY (2006) Dye-sensitized solar cells with conversion efficiency of 11.1%. Jpn J Appl Phys Part 2 45 (24–28):L638–L640

Cui X, Xie Z, Wang Y (2016) Novel CoS_2 embedded carbon nanocages by direct sulfurizing metal-organic frameworks for dye-sensitized solar cells. Nanoscale 8(23):11984–11992

Daeneke T, Uemura Y, Duffy NW, Mozer AJ, Koumura N, Bach U, Spiccia L (2012) Aqueous dye-sensitized solar cell electrolytes based on the ferricyanideferrocyanide redox couple. Adv Mater

Fan B, Mai X, Sun K, Ouyang J (2008) Conducting polymer/carbon nanotube composite as counter electrode of dye sensitized solar cells. Appl. Phys. Lett. 93:143103

Fonstad C, Rediker R (1971) Electrical properties of high-quality stannic oxide crystals. J Appl Phys 42(7):2911–2918

Fu D, Huang P, Bach U (2012) Platinum coated counter electrodes for dye-sensitized solar cells fabricated by pulsed electrodeposition—correlation of nanostructure, catalytic activity and optical properties. Electrochim Acta 77:121–127

Gao L, Mao X, Zhu H, Xiao W, Gan F, Wang D (2014) Electropolymerization of PEDOT on CNTs conductive network assembled at water/oil interface. Electrochim Acta 136(1):97–104
Gong J, Liang J, Sumathy K (2012) Review on dye-sensitized solar cells (DSSCs): fundamental concepts and novel materials. Renew Sustain Energy Rev 16:5848–5860
Gong F, Xu X, Zhou G, Wang Z-S (2013) Enhanced charge transportation in a polypyrrole counter electrode via incorporation of reduced graphene oxide sheets for dye-sensitized solar cells. Phys Chem Chem Phys 15(2):546–552
Gorlov M, Pettersson H, Hagfeldt A, Kloo L (2007) Electrolytes for dye-sensitized solar cells based on interhalogen ionic salts and liquids. Inorg Chem 46(9):3566–3575
Grätzel M (2001) Photoelectrochemical cells. Nature 414(6861):338–344
Grätzel M (2003) Dye-sensitized solar cells. J Photochem Photobiol C 4(2):145–153
Grätzel M (2005) Solar energy conversion by dye-sensitized photovoltaic cells. Inorg Chem 44(20):6841–6851
Guan G, Yang Z, Qiu L, Sun X, Zhang Z, Ren J (2013) Oriented PEDOT:PSS on aligned carbon nanotubes for efficient dyesensitized solar cells. J Mater Chem A 1(42):13268–13273
Hagfeldt A, Grätzel M (2000) Molecular photovoltaics. Acc Chem Res 33(5):269–277
He B, Tang Q, Luo J, Li Q, Chen X, Cai H (2014) Rapid charge-transfer in polypyrrole–single wall carbon nanotube complex counter electrodes: improved photovoltaic performances of dyesensitized solar cells. J Power Sour 256:170–177
Hou S, Cai X, Wu H, Lv Z, Wang D, Fu Y, Zou D (2012) Flexible, metal-free composite counter electrodes for efficient fiber-shaped dye-sensitized solar cells. J Power Sour 215:164–169
Huang KC, Huang JH, Wu CH, Liu CY, Chen HW, Chu CW, Lin CL, Ho KC (2011) Nanographite/polyaniline composite films as the counter electrodes for dye-sensitized solar cells. J Mater Chem 21:10384–10389
Hwang DK, Song D, Jeon SS, Han TH, Kang YS, Im SS (2014) Ultrathin polypyrrole nanosheets doped with HCl as counter electrodes in dye-sensitized solar cells. J Mater Chem A 2(3):859
Jeon SS, Kim C, Ko J, Im SS (2011) Spherical polypyrrole nanoparticles as a highly efficient counter electrode for dye-sensitized solar cells. J Mater Chemi 21(22):8146–8151
Jeon N, Hwang DK, Kang YS, Im SS, Kim D-W (2013) Quasi-solid state dye-sensitized solar cells assembled with polymeric ionic liquid and poly(3,4,-ethylenedioxythiophene) counter electrode. Electrochem Commun 34:1–4
Jiang X, Li H, Li S, Huang S, Zhu C, Hou L (2018) Metal-organic framework-derived Ni–Co alloy@carbon microspheres as high-performance counter electrode catalysts for dye-sensitized solar cells. Chem Eng J 334:419–431
Kakiage K, Aoyama Y, Yano T, Oya K, Fujisawa J-I, Hanaya M (2015) Highly-efficient dye-sensitized solar cells with collaborative sensitization by silyl-anchor and carboxy-anchor dyes. Chem Commun 51(88):15894–15897
Law M, Greene LE, Johnson JC, Saykally R, Yang P (2005) Nanowire dye-sensitized solar cells. Nat Mater 4(6):455–459
Lee P (2019) Solar energy. In: Managing global warming-an interface of technology and human issues, pp 317–332
Lee C, Wei X, Kyssar JW, Hone J (2008) Measurement of the elastic properties and intrinsic strength of monolayer graphene. Science 321:385–388
Lee Y, Kim B, Ifitiquar S, Park C, Yi J (2014) Silicon solar cells: Past, present and the future. J Korean Phys Soc 65(3):355–361
Li Q, Wu J, Tang Q, Lan Z, Li P, Lin J, Fan L (2008) Application of microporous polyaniline counter electrode for dye-sensitized solar cells. Electrochem Commun 10:1299–1302
Li C-T, Lee C-P, Fan M-S, Chen P-Y, Vittal R, Ho K-C (2014) Ionic liquiddoped poly(3,4-ethylenedioxythiophene) counter electrodes for dye-sensitized solar cells: cationic and anionic effects on the photovoltaic performance. Nano Energy 9:1–14
Macdiarmid AG (1997) Polyaniline and polypyrrole: where are we headed. Synth Met 84:27–34
Maiaugree W, Lowpa S, Towannang M, Rutphonsan P, Tangtrakarn A, Pimanpang S, Maiaugree P, Ratchapolthavisin N, Sang-aroon W, Jarernboon W, Amornkitbamrung V (2015) A dye sensitized

solar cell using natural counter electrode and natural dye derived from mangosteen peel waste. Sci Rep 5:15230
Makris T, Dracopoulos V, Sterigiopoulos T, Lianos P (2011) A quasi solid-state dye-sensitized solar cell made of polypyrrole counter electrodes. Electrochim Acta 56:2004–2008
Mishra A, Fischer MKR, Bauerle P (2009) Metal-free organic dyes for dye-sensitized solar cells: from structure: property relationships to design rules. Angewandte Chemie Int Ed 48(14):2474–2499
Murakami TN, Ito S, Wang Q, Nazeeruddin MK, Bessho T, Cesar I, Liska P, Humphry-Baker R, Comte P, Péchy P, Grätzel M (2006) Highly efficient dye-sensitized solar cells based on carbon black counter electrodes. J Electrochem Soc 153(12):A2255–A2261
Nazeeruddin MK, Kay A, Rodicio I, Humphry-Baker R, Mueller E, Liska P, Vlachopoulos N, Graetzel M (1993) Conversion of light to electricity by cis-X2bis (2,20-bipyridyl-4,40-dicarboxylate) ruthenium (II) charge-transfer sensitizers (X¼ Cl^-, Br^-, I^-, CN^-, and SCN^-) on nanocrystalline titanium dioxide electrodes. J Am Chem Soc 115(14):6382–6390
Nazeeruddin MK, Pechy P, Gratzel M (1997) Efficient panchromatic sensitization ¨ of nanocrystalline TiO_2 films by a black dye based on atrithiocyanatoruthenium complex. Chem Commun 18:1705–1706
Nogueira AF, Longo C, De Paoli MA (2004) Polymers in dye sensitized solar cells: overview and perspectives. Coord Chem Rev 248:1455–1468
O'Regan B, Grätzel M (1991) A low-cost, high-efficiency solar cell based on dye-sensitized colloidal TiO_2 films. Nature 353(6346):737–740
Park NG, van de Lagemaat J, Frank AJ (2000) Comparison of dye-sensitized rutile and anatase-based TiO_2 solar cells. J Phys Chem B 104(38):8989–8994
Peng T, Sun W, Huang C, Yu W, Sebo B, Dai Z, Guo S, Zhao XZ (2013) Self-assembled free-standing polypyrrole nanotube membrane as an efficient FTO- and Pt-free counter electrode for dye-sensitized solar cells. ACS Appl Mater Interfaces 6:14–17
Perera IR, Gupta A, Xiang W, Baeneke T, Bach U, Evans RA, Spiccia L (2014) Introducing manganese complexes as redox mediators for dye-sensitized solar cells. Phys. Chem. Chem. Phys. 16(24):12021–12028
Rahman MS, Hammed WA, Yahya RB, Mahmud HNME (2016) Prospects of conducting polymer and graphene as counter electrodes in dye-sensitized solar cells. J Polym Res 23:192–205
Saranya K, Rameez Md, Subramania A (2015) Developments in conducting polymer based counter electrodes for dye-sensitized solar cells—an overview. Eur Polymer J 66:207–227
Sekkarapatti M, Nikolakapoulou A, Raptis D, Dracopoulos V, Paterakis G, Lianos P (2015) Reduced graphene oxide/Polypyrrole/PEDOT composite films as efficient Pt-free counter electrode for dye-sensitized solar cells. 173:276–281
Sima C, Grigoriu C, Antohe S (2010) Comparison of the dye-sensitized solar cells performances based on transparent conductive ITO and FTO. Thin Solid Films 519(2):595–597
Sun H, Luo Y, Zhang Y, Li D, Yu Z, Li K (2010) In situ preparation of a flexible polyaniline/carbon composite counter electrode and its application in dye-sensitized solar cells. J Phys Chem C 114(26):11673–11679
Sun X, Li Y, Dou J, Shen D, Wei M (2016) Metal-organic frameworks derived carbon as a high-efficiency counter electrode for dye-sensitized solar cells. J Power Sources 232:93–98
Tahar RBH, Ban T, Ohya Y, Takahashi Y (1998) Tin doped indium oxide thin films: electrical properties. J Appl Phys 83(5):2631–2645
Tai Q, Chen B, Guo F, Xu S, Hu H, Sebo B, Zhao X-Z (2011) In situ prepared transparent polyaniline electrode and its application in bifacial dye-sensitized solar cells. ACS Nano 5:3795–3799
Tang Q, Cai H, Yuan S, Wang X (2013) Counter electrodes from double-layered polyaniline nanostructures for dye-sensitized solar cell applications. J Mater Chem A 1(2):317–323
Thomas S, Deepak TG, Anjusree GS, Arun TA, Nair SV, Nair AS (2014) A review on counter electrode materials in dye-sensitized solar cells. J Mater Chem A 2(13):4474–4490

Upadhyaya HM, Hirata N, Haque SA, de Paoli M-A, Durrant JR (2006) Kinetic competition in flexible dye sensitised solar cells employing a series of polymer electrolytes. Chem Commun 8:877–879

U.S. Energy Information Administration (2016) International energy outlook-2016

Wang P, Zakeeruddin SM, Moser JE, Nazeeruddin MK, Sekiguchi T, Grätzel M (2003) A stable quasi-solid-state dye-sensitized solar cell with an amphiphilic ruthenium sensitizer and polymer gel electrolyte. Nat Mater 2(6):402–407

Wang Z-S, Kawauchi H, Kashima T, Arakawa H (2004) Significant influence of TiO_2 photoelectrode morphology on the energy conversion efficiency of N719 dye-sensitized solar cell. Coord Chem Rev 248:1381–1389

Wang M, Chamberland N, Breau L, Moser JE, Humphry-Baker R, Marsan B, Zakeeruddin SM, Gratzel M (2010) An organic redox electrolyte to rival triiodide/iodide in dye-sensitized solar cells. Nat Chem 2(5):385–389

Wang H, Feng Q, Gong F, Li Y, Zhou G, Wang Z-S (2013) In situ growth of oriented polyaniline nano wires array for efficient cathode of Co(III)/Co(II) mediated dye-sensitized solar cell. J Mater Chem A 1:97–104

World Energy Council (2016). https://www.worldenergy.org/wp-content/uploads/2016/10/World-Energy-Resources-Full-report-2016.10.03.pdf

World Nuclear Association (2019) Renewable Energy and electricity, sustainable energy, renewable energy. http://www.world-nuclear.org/information-library/energy-and-the-environment/renewable-energy-and-electricity.aspx)

Wu J, Li Q, Fan L, Lan Z, Li P, Lin J, Hao S (2008) High-performance polypyrrole nanoparticles CE for dye-sensitized solar cells. J Power Sources 181:172–176

Wu J, Li Y, Tang Q, Yue G, Lin J, Huang M (2014). Bifacial dyesensitized solar cells: a strategy to enhance overall efficiency based on transparent polyaniline electrode. Sci Rep 4

Xia J, Chen L, Yanagida S (2011) Application of polypyrrole as a CE for a dye-sensitized solar cell. J Mater Chem 21:4664–4649

Xiao YM, Lin JY, Wu JH, Tai SY, Chou S-W, Yue GT, Wu J (2012) Pulse electropolymerization of high performance PEDOT/MWCNT CEs for Pt-free dye sensitized solar cells. J Mater Chem 22:19919–19925

Xiao Y, Lin J-Y, Wang W-Y, Tai S-Y, Yue G, Wu J (2013) Enhanced performance of low-cost dye-sensitized solar cells with pulse-electropolymerized polyaniline CEs. Electrochim Acta 90:468–474

Xiao Y, Han G, Li Y, Li M, Chang Y (2014) High performance of Pt-free dye-sensitized solar cells based on two-step electropolymerized polyaniline CEs. J Mat Chem A 2:3452–3460

Xu M, Li R, Pootrakulchote N, Shi D, Guo J, Yi Z, Zakeeruddin SM, Grätzel M, Wang P (2008) Energy-level and molecular engineering of organic D-p-A sensitizers in dye-sensitized solar cells. J Phys Chem C 112(49):19770–19776

Xu J, Li M, Wu L, Sun Y, Zhu L, Gu S, Liu L, Bai Z, Fang D, Xu W (2014a) A flexible polypyrrole-coated fabric counter electrode for dye-sensitized solar cells. J Power Sour 257:230–236

Xu P, Tang Q, Chen H, He B (2014b) Insights of close contact between polyaniline and FTO substrate for enhanced photovoltaic performances of dye-sensitized solar cells. Electrochim Acta 125:163–169

Yang F (2009) Thin film solar cells grown by organic vapor phase deposition. Princeton University

Yang S-C, Yang D-J, Kim J, Hong J-M, Kim H-M, Kim H-d, Lee H (2008) Hallow TiO_2 hemispheres obtained by colloidal templating for application in dye-sensitized solar cells. Adv Mater 20:1059–1064

Yella A, Lee HW, Tsao N, Yi C, Chandiran AK, Nazeeruddin MK, Diau EW, Yeh CY, Zakeeruddin SM, Grätzel M (2011) Porphyrin-sensitized solar cells with cobalt (II/III)-based redox electrolyte exceed 12% efficiency [science (629)]. Science 334(6060):1203

Yen Y-S, Chou H-H, Chen Y-C, Hsu C-Y, Lin JT (2012) Recent developments in molecule-based organic materials for dye-sensitized solar cells. J Mater Chem 22(18):8734–8747

Yue G, Wu J, Xiao Y, Lin J, Huang M, Lan Z (2012) Application of poly(3,4- ethylenedioxythiophene):polystyrenesulfonate/polypyrrole counter electrode for dye-sensitized solar cells. J Phys Chem C 116(34):18057–18063

Yue G, Wu J, Xiao Y, Lin J, Huang M, Fan L (2013a) A dye-sensitized solar cell based on PEDOT:PSS counter electrode. Chin Sci Bull 58(4–5):559–566

Yue G, Wu J, Xiao Y, Lin J, Huang M, Lan Z (2013b) Functionalized graphene/poly(3,4-ethylenedioxythiophene):polystyrenesulfonate as counter electrode catalyst for dye-sensitized solar cells. Energy 54:315–321

Yun S, Freitas JN, Nogueira AF, Wang Y, Ahmad S, Wang Z (2015) Dye sensitized solar cells employing polymers. Progr Polymer Sci 59:1–40

Zhang T-L, Chen H-Y, Su C-Y, Kuang D-B (2013) A novel TCO- and Pt-free counter electrode for high efficiency dye-sensitized solar cells. J Mater Chem A 1(5):1724

Zhou H, Wu L, Gao Y, Ma T (2011) Dye-sensitized solar cells using 20 natural dyes as sensitizers. J Photochem Photobiol A Chem 219(2–3):188–194

Zhu H, Wei J, Wang K, Wu D (2009) Applications of carbon materials in photovoltaic solar cells. Sol Energy Mater Sol Cells 93(9):1461–1470

Chapter 18
Interfacial Materials for Organic Solar Cells

Amaresh Mishra

Abstract Organic solar cell (OSC) is one of the promising photovoltaic technology for next generation low-cost renewable energy sources. The power conversion efficiencies (PCE) of OSCs have reached above 14% in single-junction and ~17% in tandem OSCs. This rapid increase in the performance is mostly profited from the synergetic advances in rational molecular design, device processing and interfacial layer modifications. In addition to the development of efficient photoactive materials, interfacial design plays a crucial role in the improvement of device performance and stability. Most importantly, the interfacial layer is responsible for establishing good ohmic contact in the device, thus minimize the resistance, interfacial recombination and improve charge selectivity. In this chapter, we present the recent development in the electron and hole transporting interfacial materials design for both single-junction and tandem OSCs. Special attention will be paid to the design principles of interfacial materials which includes inorganic metal oxides, composite materials, oligomeric and polymeric molecules and their use as cathode and anode interlayer for high efficiency devices. The structure-property relationships of various interfacial materials will be analyzed as an approach towards high performance OSCs. Finally, we will discuss the current challenges with possible solutions and perspectives for performance enhancement in OSCs.

Keywords Interfacial material · Organic semiconductor · Cathode interlayer · Anode interlayer · Organic solar cell

18.1 Introduction

Solution-processed organic solar cells (OSC) using π-conjugated organic materials as active layer components have shown significant advance in recent years with power conversion efficiency (PCE) in the range from 10–14% in single bulk-heterojunction devices (Mishra and Bäuerle 2012; Li et al. 2019; Zhang et al. 2018a, b; Xiao et al.

A. Mishra (✉)
School of Chemistry and Nano Research Centre, Sambalpur University, Jyoti Vihar, Sambalpur, India
e-mail: amaresh.mishra@suniv.ac.in

H. Tyagi et al. (eds.), *Solar Energy*, Energy, Environment, and Sustainability, https://doi.org/10.1007/978-981-15-0675-8_18

2017; Mishra and Sahu 2019). In tandem cells the PCE of around 17% was recently being reported (Meng et al. 2018). Theoretically it has been demonstrated that PCE close to 20% is not so far to realize for tandem cell based on the optimized device configuration, material bandgaps alignment and high achievable fill factors (FF) (Li et al. 2014a). A typical bulk-heterojunction solar cells (BHJSC) comprise of donor (D):acceptor (A) based organic photoactive layer sandwiched between two electrodes. The excitons (electron-hole pair) generated in the photoactive layer after light excitation needs to move towards D: A interface to separate holes and electrons which then transport to the respective electrodes through highest occupied molecular orbital (HOMO) and lowest unoccupied molecular orbital (LUMO). The holes travel towards the anode and electrons collected at the cathode (Fig. 18.1). In BHJ devices the energy level offset between the D and A and their contact with the respective electrodes plays a crucial role in driving the potential out of the device. Therefore, a barrier-less contact (Ohmic contact) with the electrodes is necessary for efficient charge transport and extraction, which is very challenging to manipulate between organic and metal electrode interface. Generally, a Schottky barrier formed at the electrodes creates loss of potential thus lower the open circuit voltage (V_{OC}) (Yip and Jen 2012).

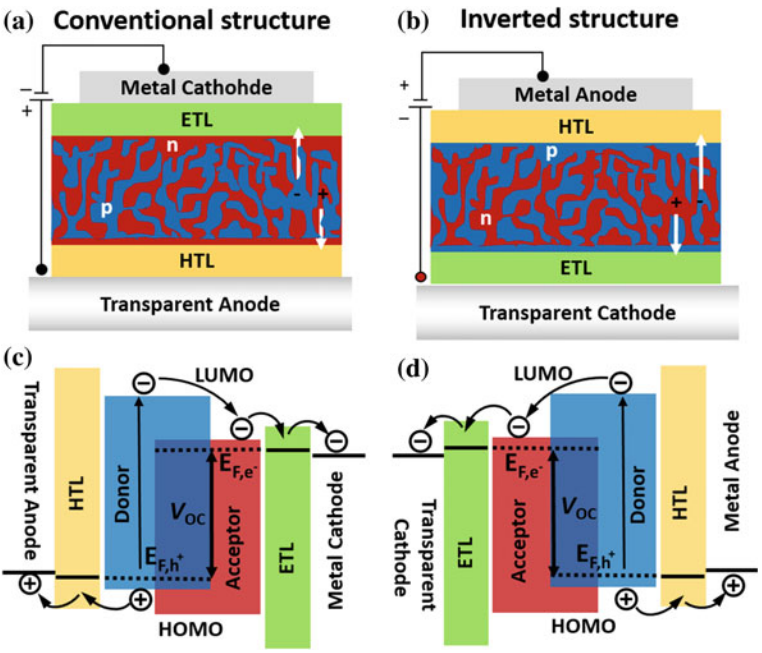

Fig. 18.1 Device architecture of **a** conventional OSC and **b** inverted OSC, **c** and **d** are the corresponding energy level alignment with interfacial layers providing Ohmic contacts and charge selectivity at both electrodes

In addition to the synthesis of novel active layer materials and updated device fabrication conditions, the design and implementation of interfacial materials is also very crucial in the device performance improvement. An ideal interfacial design is most important for efficient charge transport as they not only establish good Ohmic contact but also regulate other device parameters like film morphology, control energy level alignment, alter work functions (WF) of both anode and cathode, minimize resistance with high charge selectivity, reduce charge recombination rate, enhance charge extraction and improve device stability (Ma et al. 2010; Chen et al. 2010). The WF is defined as the energy difference between Fermi energy and vacuum level which is the minimum amount of energy necessary to withdraw an electron from the metal. In order to match the energy levels for efficient charge transport and collections various cathode and anode interfacial layers have been introduced between the active layer and electrodes. To date, several reports have revealed the underlying mechanisms for the tuning of WF by interfacial materials at the active layer/electrode interfaces (van Reenen et al. 2014; Lee et al. 2014a; Wang et al. 2015). The interfacial modification influence the formation of interfacial dipole resulting in permanent shifting of the vacuum level to different degrees at the interface which depends on the direction of the dipole (Fig. 18.2). The solar cell performance completely depends on the direction of the dipole. The net interfacial dipole directed towards the metal electrode reduces the device performance, while when the net dipole directed away from the metal improves the device performance due to increase in the built-in voltage.

In conventional OSCs, poly(3,4-ethylenedioxythiophene):poly(styrene sulfonate) (PEDOT:PSS) has been widely used as anode interface layer (AIL) to modify indium tin oxide (ITO)-coated glass surface for efficient hole extraction. In these devices LiF or Ca generally are used to modify low WF metal cathode like Al. However, due to polar and acidic nature of PEDOT:PSS they are very sensitive to low WF metal, oxygen and moisture. Therefore, many groups have developed inverted device structure where high WF metals such as Ag and Au used as top electrode and low WF metal

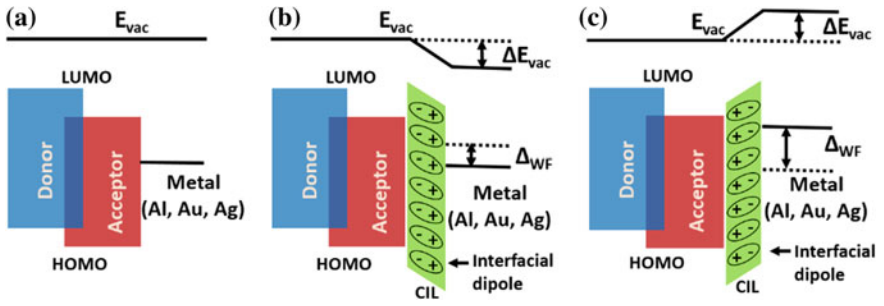

Fig. 18.2 Schematic representation of the band energy alignment for OSCs **a** without interfacial layer **b** and **c** tuned by the introduction of dipolar CIL above the active layer surface with the spontaneous dipole formation and work function modification of the metal cathode. The dipole introduces an electrostatic potential shift for charges crossing the interface, shifting the vacuum level between the metal and organic, **b** interfacial dipole directed towards metal surface **c** interfacial dipole directed away from metal surface and increases the built-in voltage

oxide such as TiO_2, ZnO as cathode interfacial layer (CIL) to modify ITO surface (Fig. 18.2). Subsequently, various organic and polymeric materials were synthesized for their use as interlayer material in solution-processed OSCs. The interfacial layer is very important to fine tune the device performance such as V_{OC}, short-circuit current density (J_{SC}) and FF, therefore the overall PCE. Along with the photoactive layers it is also highly important to optimize the charge extracting interfacial layer in single-junction and charge recombination layer in tandem cell to achieve high performance OSCs. The interconnecting layer (ICL) in tandem cell is highly responsible for extraction of holes and electrons from the adjacent subcells. Hence, the choice of ICL plays a detrimental role in the device performance improvement. Mihailetchi et al. observed a variation in the V_{OC} of polymer:fullerene-based conventional solar cells (~0.4 to 0.85 V) by using metal cathodes of variable WFs which is due to the Fermi level pinning of the electrodes to the active layer which enables Ohmic contact at the cathode (Mihailetchi et al. 2003). The low WF metals (Ag, Al, Ca etc.) generally forms Ohmic contact with the LUMO of the acceptor, while the high WF metals (Au, Pd etc.) forms Ohmic contact with the HOMO of the donor material. Jen group demonstrated the influence of metal anodes on the V_{OC} of an poly-(3-hexylthiophene) (P3HT): [6,6]-phenyl C_{60} butyric acid methyl ester ($PC_{61}BM$) based inverted solar cell using ZnO-NPs/C_{60}-self-assembled monolayer as interfacial material and found that only Pd with high WF can form good Ohmic contact for hole extraction from the donor (Hau et al. 2010).

In recent years major efforts have been devoted to develop interfacial layers for single-junction and tandem OSCs. The interfacial layers are mostly used to modify the energy level alignment between active layer and electrode, adjust the polarity of the electrodes for charge selectivity, control the surface energy by modulating active layer morphology, as well reduce carrier recombination and improve stability of photoactive layer and electrodes interface by preventing the metal ions from diffusion into the organic layer (van Reenen et al. 2014; Yip and Jen 2012; Manders et al. 2013; Bilby et al. 2014; Jørgensen et al. 2012; Ma et al. 2010). The interfacial materials have been designed in such a way that they can be processed from orthogonal solvent relative to the active layer and thus, can be processed from solution. In the last few years, the number of publications on interfacial material design and their implementation in various OSC devices have been considerably increased. Recently, some of the reviews have comprehensively summarized the role of interfacial layers in OSCs (Lai et al. 2013; Chueh et al. 2015; Wang et al. 2015; Yin et al. 2016; Yip and Jen 2012; Li et al. 2018a). Frey and co-workers discussed the mechanistic studies on the driving force for interlayer formation and their influence on device performance (Vinokur et al. 2016). In this chapter we systematically discuss some important progress on solution-processed interfacial materials including organic-inorganic hybrids, transition metal oxide, composite materials, oligomeric and polymeric molecules, and their implementation as cathode and anode interfacial layer for high efficiency single-junction OSCs. Finally, structure-property and device performance relationship and challenges of the interfacial materials towards high performance devices will be deduced.

18.2 Interfacial Design for Efficient Organic Solar Cells

The metal:organic interface plays a crucial role in overall device performance improvement. Insertion of an interfacial layer between the metal and organics can dramatically alter the interface properties. They can control the charge transfer and recombination process and minimize the contact resistance in the device and lower the series resistance thus improve the FF, thus overall PCE. The processing conditions and wettability between the components are also very important for device performance improvement. Another important aspect is the charge selectivity at the electrode interface. The interfacial layer should ensure selective charge extraction by blocking the flow of unfavorable charge carrier. The interfacial layers can improve the charge selectivity at the organic: electrode interface by selectively transporting either electrons or holes, thus acting as an electron-transport layer (ETL) and block holes to flow through, and a hole-transport layer (HTL) by blocking electron to flow through (Irwin et al. 2008; Walzer et al. 2007). Till date numerous small molecules and polymers have been developed and used as interfacial materials in OSCs and successfully improved the device PCE and most importantly the stability. Below we will discuss the design and development some efficient CIL and AIL and their performance in high efficiency OSCs.

18.2.1 Electron Transport Materials as Cathode Interface Layers

The prerequisite for a cathode interfacial layer is low WF to match with the LUMO of the organic acceptor for efficient charge extraction, electron transport with hole blocking properties, lower the energy loss and reduce interfacial defects. The CIL should have transparent in nature for inverted devices in order for efficient transmission of light and good stability to prevent metal electrode diffusion in conventional devices. Till date a variety of ETL, such as low WF metal oxide, composite materials, organic molecules and polymers, have been used in high performance OSCs. Here we will focus some of the recent advance in the use of CIL including their development and performance in OSC devices and deduce some structure-performance relationships.

18.2.1.1 Metal Oxides as CIL

n-Type metal oxides such as TiO_2, ZnO, SnO_x, Al_2O_3, ZrO_2 were used as CIL materials due to their low lying energy levels (~4.3 to 4.4 eV) (Waldauf et al. 2006; Trost et al. 2012; Hau et al. 2008; Trost et al. 2015; Jheng et al. 2013). These materials have good optical transparency in the visible region and efficiently transport

electrons. Recently, some ternary oxides, like Al-doped ZnO, Mg-doped ZnO, Li-doped ZnO, Ga-doped ZnO, In-doped ZnO) have also emerged as effective materials for CIL (Shin et al. 2010; Yin et al. 2014; Soultati et al. 2019; Stubhan et al. 2013; Liao et al. 2014). TiO_2 and ZnO, are the most widely used CILs in OSCs because of their good transparency, environmentally stable, they can be solution-processed, nontoxic and low cost. The WF of TiO_x (−4.3 eV, LUMO ~4.4 eV) and ZnO (−4.3 eV, LUMO ~4.1 eV) are suitable for collecting electron and efficiently block hole. The low WF of about 4.3 eV is suitable to modify the WF of both the ITO in inverted devices or metal electrodes in conventional devices. The photovoltaic parameters of some representative devices using various ETLs are summarized in Table 18.1.

The TiO_X layer was prepared by sol-gel method from tetrabutyl titanate in isopropanol by spin-coating and efficiently used as CIL in inverted OSCs (Bao et al. 2014; Liu et al. 2012b). It has been found that the precursor and annealing temperature strongly influence the optoelectronic properties of the TiO_X layer. In conventional device TiO_X layer acts as optical spacer to enhance light absorption and also acts as ETL/HBL. Kim et al. reported that by exchanging the isopropyl ligands of titanium isopropoxide with 2-methoxyethanol formed an ETLs that need a shorter illumination time to fill shallow electron traps and improve the PCEs due to increase in both J_{SC} and V_{OC} (Kim et al. 2013).

Lee et al. presented very stable OSC devices using sol-gel derived TiO_X as ETL in conventional device. Although the devices with and without TiO_x generated very similar PCEs ~4.0%, the air stability with TiO_X layer was significantly enhanced by two orders of magnitude (Lee et al. 2007). Park et al. reported PCEs of 6.1% for PCDTBT:$PC_{71}BM$ based devices with internal quantum efficiency close to 100% using TiO_x as CIL (Park et al. 2009). Mor et al. demonstrated a PCE of 4.1% in P3HT:$PC_{61}BM$-based device using vertically aligned transparent TiO_2 nanotube arrays. The pore size of the nanotube was tailored to infiltrate the polymer into the nanotubes to form self-aligned aggregates. The devices displayed excellent external quantum efficiency (EQE) up to 80% resulting from efficient charge separation at both the P3HT-TiO_2 and P3HT-$PC_{61}BM$ interfaces (Mor et al. 2007). Sharma et al. demonstrated an increased in the PCE from 2.8 to 4.1% by the introduction of TiO_2 layer between active layer (P3HT:fullerene free acceptor CSORG5) and Al metal electrode in conventional device (Sharma et al. 2014).

The performance improvement of TiO_X based solar cells generally required light soaking to improve carrier densities, and reduce oxygen defect. The light soaking significantly reduced the s-shape of *J-V* curve enhancing the FF from 0.26 to 0.60 and PCE from 1.3 to 3.3% (Lin et al. 2013). It has been shown that the n-doped TiO_X synthesized via controlling the nitrogen doping concentration in sol-gel synthesis overcome the light-soaking process. N-doping significantly reduced the WF of TiO_X on the ITO (from 4.8 to 4.2 eV) and improved the Ohmic contact with the active layer, thus increased the PCE from 2.13% (for undoped TiO_X) to 8.82% without light soaking (Kim et al. 2015).

Yan et al. reported a light soaking free inverted solar cell by doping TiO_2 with titanium oxide bis(2,4-pentanedionate) (TOPD). The treatment of TiO_2/TOPD film with UV light and then with ethanolamine eliminate the light soaking of the device

Table 18.1 Summary of photovoltaic performance based on representative metal oxide based CILs

Cathode structure	Active layer	Anode structure	V_{OC} (V)	J_{SC} (mA cm^{-2})	FF	PCE (%)	References
ITO/TiO_X	P3HT/$PC_{71}BM$	MoO_3/Ag	0.63	11.8	0.63	4.65	Bao et al. (2014)
FTO/TiO_2 NT	P3HT:$PC_{61}BM$	PEDOT:PSS/Au	0.64	12.4	0.51	4.07	Mor et al. (2007)
TiO_2/Au	P3HT:CSORG5	ITO/PEDOT:PSS	0.98	7.28	0.56	4.16	Sharma et al. (2014)
TiO*x*/Al	P3HT:$PC_{61}BM$	ITO/PEDOT:PSS	0.62	10.8	0.61	4.10	Lee et al. (2007)
TiO*x*/Al	PCDTBT:$PC_{71}BM$	ITO/PEDOT:PSS	0.88	10.6	0.66	6.10	Park et al. (2009)
ITO/TiO*x*	PCDTBT:$PC_{71}BM$	MoO_3/Al	0.85	10.8	0.60	5.50	Liu et al. (2012b)
ITO/TiO*x*	PTB7-Th:$PC_{71}BM$	MoO_3/Ag	0.79	15.5	0.72	8.82	Kim et al. (2015)
ITO/TiO_2:TOPD (UV and EA treatments)	PTB7-Th:$PC_{71}BM$	MoO_3/Ag	0.79	18.8	0.71	10.6	Yan et al. (2017)
ITO/TiO_2	PTB7:$PC_{71}BM$	MoO_3/Ag	0.70	14.4	0.64	6.39	You et al. (2012)
ITO/TiO_2-Cs	PTB7:$PC_{71}BM$	MoO_3/Ag	0.72	14.7	0.66	7.01	You et al. (2012)
ITO/ZnO	P3HT:$PC_{61}BM$	PEDOT:PSS/Ag	0.62	11.2	0.54	3.78	Hau et al. (2008)
ITO/ZnO	P3HT:$PC_{61}BM$	Ag	0.57	9.60	0.50	2.70	Takanezawa et al. (2007)
ITO/ZnO	PTB7:$PC_{71}BM$	MoO_3/Ag	0.72	14.7	0.69	7.34	You et al. (2012)
ITO/ZnO	PDTG–TPD:$PC_{71}BM$	MoO_3/Ag	0.86	14.1	0.67	8.10	Chen et al. (2012)
ITO/ZnO	PTB7:$PC_{71}BM$	MoO_3/Ag	0.71	13.7	0.69	6.71	Lee et al. (2014b)
ITO/ZnO/MeOH	PTB7:$PC_{71}BM$	MoO_3/Ag	0.72	14.7	0.73	7.72	Lee et al. (2014b)
ITO/ZnO/2–ME + EA(1%)	PTB7:$PC_{71}BM$	MoO_3/Ag	0.71	16.8	0.73	8.69	Lee et al. (2014b)

(continued)

Table 18.1 (continued)

Cathode structure	Active layer	Anode structure	V_{OC} (V)	J_{SC} (mA cm^{-2})	FF	PCE (%)	References
ZnO/Al	PTB7:$PC_{71}BM$	ITO/PEDOT:PSS	0.73	14.6	0.62	6.66	Dkhil et al. (2014)
ZnO/EA(1%)/Al	PTB7:$PC_{71}BM$	ITO/PEDOT:PSS	0.75	15.5	0.66	7.60	Dkhil et al. (2014)
ITO/ZnO	PCDTBT:$PC_{71}BM$	MoO_3/Ag	0.88	10.4	0.69	6.33	Sun et al. (2011)
ITO/ZnO	PffBT4T–2OD:$TC_{71}BM$	MoO_3/Al	0.77	18.8	0.75	10.8	Liu et al. (2014)
ITO/ZnO	PffBT4T–2OD:$PC_{71}BM$	MoO_3/Al	0.77	18.4	0.74	10.5	Liu et al. (2014)
ITO/ZnO	PIFTBT8:$PC_{71}BM$	MoO_3/Ag	1.04	9.74	0.50	5.05	Yin et al. (2013)
ITO/ZnO (patterned)	PTB7-Th:$PC_{71}BM$	MoO_3/Al	0.78	19.5	0.67	10.1	Chen et al. (2015)
ITO/ZnO	PTh_4FBT:$PC_{71}BM$	MoO_3/Ag	0.77	13.5	0.66	6.82	Jheng et al. (2013)
ITO/ZnO + TiO_2	PTB7:$PC_{71}BM$	MoO_X/Al	0.74	16.5	0.72	8.82	Li et al. (2014b)
ITO/SnO_X	P3HT:$PC_{61}BM$	MoO_3/Ag	0.52	10.4	0.55	3.00	Trost et al. (2012)
ITO/SnO_X	PCDTBT:$PC_{61}BM$	MoO_3/Ag	0.91	10.6	0.61	5.90	Trost et al. (2015)
ITO/SnO_2	PBDTT-DPP:$PC_{61}BM$	MoO_3/Al	0.73	11.7	0.61	5.24	Bob et al. (2013)
FTO/TiO_2/Al_2O_3	PTB7:$PC_{71}BM$	MoO_X/Al	0.72	14.3	0.69	7.10	Vasilopoulou et al. (2014)
FTO/TiO_2/ZrO_2	PTB7:$PC_{71}BM$	MoO_X/Al	0.71	14.0	0.69	6.90	Vasilopoulou et al. (2014)
ITO/$Cs_{0.5}MoO_3$	PBDTDTTT–S–T:$PC_{71}BM$	MoO_3/Ag	0.61	15.6	0.63	6.00	Li et al. (2014c)
ITO/CsV_2O_5	PBDTDTTT–S–T:$PC_{71}BM$	V_2O_5/Ag	0.63	15.8	0.61	6.08	Li et al. (2014c)
ITO/MoO_3	PBDTDTTT–S–T:$PC_{71}BM$	$Cs_{0.5}MoO_3$/Al	0.68	16.1	0.67	7.32	Li et al. (2014c)
ITO/V_2O_5	PBDTDTTT–S–T:$PC_{71}BM$	CsV_2O_5/Al	0.68	16.4	0.67	7.49	Li et al. (2014c)
ITO/Al doped MoO_3	PCDTBT:$PC_{71}BM$	MoO_3/Al	0.89	10.7	0.66	6.28	Liu et al. (2012a)

(continued)

Table 18.1 (continued)

Cathode structure	Active layer	Anode structure	V_{OC} (V)	J_{SC} (mA cm^{-2})	FF	PCE (%)	References
ITO/Mg doped ZnO	PTB7:$PC_{71}BM$	MoO_3/Ag	0.74	16.8	0.67	8.31	Yin et al. (2014)
ITO/Li doped ZnO	PTB7-Th:$PC_{71}BM$	MoO_3/Al	0.80	17.9	0.70	10.1	Soultati et al. (2019)
ITO/Li doped ZnO	PTB7-Th:IT-4F	MoO_X/Al	0.83	16.1	0.67	8.96	Soultati et al. (2019)
ITO/Li doped ZnO	PSEHTT:$IC_{60}BA$	PEDOT:PSS/MoO_X/Al	0.94	10.6	0.66	6.59	Yusoff et al. (2014)
ITO/Al doped ZnO	PTB7-Th:$PC_{71}BM$	MoO_X/Al	0.80	17.9	0.72	10.4	Liu et al. (2016a)
ITO/In doped ZnO	PTB7-Th:$PC_{71}BM$	MoO_3/Ag	0.79	16.3	0.70	9.11	Liao et al. (2014)
ITO/AZO-Ti	P3HT:$PC_{61}BM$	WO_X/Al	0.65	8.66	0.68	3.83	Gadisa et al. (2013)
ITO/ZnO/[BMIM]BF_4	PTB7-Th:$PC_{71}BM$	MoO_X/Ag	0.72	17.2	0.74	9.12	Yu et al. (2015)

(Yan et al. 2017). Further analysis suggested that the addition of TOPD into the TiO_2 nanoparticle films reduced the WF from 4.43 to 4.23 eV (by Kelvin probe measurements), which reduced the energy barrier for charge injection from active layer to electrode. Similar effect was observed for UV and ethanolamine treatment of TiO_2.

The optical properties of ZnO CILs can be tuned by preparation method, composition, film morphology, thickness of the layer. The most widely used preparation method of ZnO for OSC applications are chemical deposition (Park et al. 2013) sol-gel processing, (Kyaw et al. 2008; Yin et al. 2013) and nanoparticle approach. The choice of precursor solution and annealing temperature strongly influence the device performance of sol-gel prepared ZnO. Takanezawa et al. reported a PCE of 2.7% for P3HT-PC_{61}BM devices using ZnO nanorod array as ETL (Takanezawa et al. 2007). White et al. introduced a solution-processed ZnO as CIL in P3HT-PC_{61}BM devices with Ag as hole extraction back contact exhibiting a PCE of 2.58%. (White et al. 2006) The authors suggested efficient electron transfer without loss of energy at the PC_{61}BM:ZnO interface due to near equal LUMO of PC_{61}BM and conduction band of ZnO. However, stability was the major issue in those devices due to desorption of oxygen from ZnO in both air and inert atmosphere. Hau et al. revealed an excellent device stability with PCE of 3.78% by incorporating PEDOT:PSS as AIL in inverted device structure and ZnO nanoparticle as CIL processed by sol–gel method (Hau et al. 2008). The PEDOT:PSS worked as an oxygen-diffusion barrier in inverted devices. In addition, the WF with Ag was modified to −5.0 eV by oxidizing to Ag_2O in presence of air, thus matching well with the PEDOT:PSS HOMO level (−5.1 eV) and improve electrical contact at the interface.

You et al. used TiO_2, ZnO, or TiO_2:Cs with similar WF ~4.2 eV as CILs in inverted device using PTB7:PC_{71}BM as active layer (You et al. 2012). PCE as high as 7.3% with high stability have been achieved with ZnO nanoparticle. Chen et al. reported a PCE of 8.1% using UV ozone treated ZnO nanoparticle as CIL (Chen et al. 2012). The UV ozone treatment reduced the trap state and surface defects on the nanoparticle surface.

Lee et al. demonstrated the reduction of energy barrier between the LUMO of acceptor and conduction band of ZnO by treating the ZnO surface by polar solvents like 2-methoxyethanol (2-ME) + ethanolamine (EA) as co-solvent (Lee et al. 2014b). The polar solvent lowers the contact barrier for electron transport and extraction, reduce contact resistance thus series resistance and bimolecular recombination resulting in dramatic improvement in PCE from 6.71 to 8.69% for PTB7:PC_{71}BM devices. The PCE improvement was due to increase in J_{SC} and FF. The device with Methanol treatment also improved the device PCE by about 1% compared to the untreated ZnO. Using ethanolamine (EA) treated ZnO nanoparticle as optical spacer and PEDOT:PSS as HTL in PTB7:PC_{71}BM based conventional devices the PCE could be increased from 5.8 to 7.6%. (Dkhil et al. 2014) The EA treatment lowered the WF from ~4.3 to 4.1 eV (calculated from XPS study), which can be assigned to dipolar polarization of the ZnO surface via the adsorption of EA. The enhancement was attributed to reduced contact barrier, reduced recombination and enhanced electron extraction at the cathode.

Using a low band gap polymer PCDTBT:$PC_{71}BM$ blend in combination with low temperature sol-gel prepared ZnO as CIL and MoO_x as HTL in an inverted device reached PCEs up to 6.33%. (Sun et al. 2011) Liu et al. reported further PCE improvement to 10.8 and 10.5% with high FF of 0.77 using PffBT4T-2OD:$TC_{71}BM$ and PffBT4T-2OD:$PC_{71}BM$ blend and sol-gel processed ZnO prepared from diethyl zinc as CIL (Liu et al. 2014). Yin et al. demonstrated that using sol-gel processed ZnO by controlling the film thickness and MoO_3 as AIL PCE up to 5.05% could be achieved with greater device stability compared to without ZnO. The V_{OC} in these devices was significantly enhanced from 0.22 V without ZnO to 1.04 V with ZnO (Yin et al. 2013). The use of Cu_2O, NiO and WO_3 as AIL showed comparatively lower performance compared to MoO_3 which is ascribed to their energy levels differences, and interfacial contacts with the active layer materials and metal anode. The starting precursor materials also make a significant difference in the device performance. MacLeod et al. revealed that using diethylzinc-derived ZnO as CIL a lower PCE but more stable device could be obtained compared to the device derived from zinc acetate precursor (MacLeod et al. 2015).

When a patterned ZnO prepared from sol-gel techniques was employed as CIL in PTB7-Th:$PC_{71}BM$ based devices and MoO_x/Al as top electrode the PCE could be increased to 10.1% compared to 8.5% for the reference device without ZnO (Chen et al. 2015). The improved performance was ascribed to collective effect of the patterned-induced anti-reflection, light scattering, surface plasmon resonance, reduced recombination probability and improved charge extraction at the ZnO:active layer interface.

Using a combination of ZnO nanoparticles and TiO_2 nanorods an enhancement in the PCE (8.82%) could be observed compared to bare ZnO nanoparticles (7.76%) and TiO_2 nanorods (7.66%). This improvement was mainly due to interfacial contact and reduced contact resistance and leakage current and facilitation of electron collection and transport efficiency (Li et al. 2014b).

Trost et al. used solution-processed SnO_x prepared from tetrakis(diethylamino)tin as reactive precursor in isopropanol solution as electron extraction layer in inverted OSC. The WF of SnO_x was −4.1 eV similar to that of TiO_x (−4.0 eV), thus generating very similar PCE of around 3.0%. (Trost et al. 2012) However, the SnO_x based devices showed remarkable stability in contrast to TiO_x at elevated temperature up to 80 °C in air without encapsulation. Deposition of SnO_X does not required any light soaking. The deposition of a thin layer of SnO_X (>20 nm) significantly change the WF from 4.8 eV of the ITO to the 4.2 eV of the SnO_X-coated ITO which is attributed to the formation of an interface dipole between ITO and SnO_X. Using SnO_X CILs prepared by atomic layer deposition (ALD) at 80 °C without UV-treatment a high PCE of 5.9% could be achieved compared to 0.4% for OSCs based on TiO_X and reduced the s-shape for PCDTBT:$PC_{71}BM$ devices. The results demonstrated that SnO_X acts as barrier-free electron extraction layer without UV-irradiation and does not change its WF (4.2 eV) upon illumination (Trost et al. 2015). However, a significant lowering of WF from 4.4 to 3.9 eV was observed for TiO_X after illumination.

Yang and co-workers revealed that the use of nanostructured gelled SnO_2 could significantly enhanced the PCE of PBDTT-DPP:$PC_{61}BM$-based device to 5.24%

(Bob et al. 2013). The PCE of bulk- or extended-SnO_2 as CILs reduced to 0.7% and 1.45%, respectively due to dramatic reduction in the V_{OC} and FF. The lower performance for bulk and extended SnO_2 were due to rough thin film formation (relatively large particles) that prevents electron transport and increased the shunting pathways.

Insulating low WF Al_2O_3 or ZrO_2 were applied to the TiO_2 layer by ALD method to passivate the surface trap states followed by a downward shift of the conduction band minimum. A range of polymer donors were tested and highest PCE of 6.9 and 7.1% were achieved for PTB7:$PC_{71}BM$ device using Al_2O_3 and ZrO_2 nanolayers due to significant suppression of charge recombination and enhanced electron extraction at the TiO_2/Al_2O_3 or ZrO_2/organic interface (Vasilopoulou et al. 2014).

By intercalating cesium into the V_2O_5 or MoO_3, the WF of metal oxides can be tuned over a wide range of 1.1 eV thus making them as both ETL and HTL (Li et al. 2014c). Using MoO_3/V_2O_5 and $Cs_{0.5}MoO_3/CsV_2O_5$ as HTL and ETL, the PBDTDTTT-S-T:$PC_{71}BM$-based devices exhibited PCEs of 6.0 and 6.08%, respectively. The best performance were achieved with the Cs:Mo and Cs:V mole ratios of 0.5:1. By using with 0.5 wt% of Cs the WF of MoO_3/V_2O_5 were tuned from 5.32 eV/5.41 eV to 4.28 eV/4.19 eV, respectively.

Similar to Cs-doping, Al-doping also tuned the WF of MoO_3 to acts as CIL. Liu et al. demonstrated an improvement in PCE for PCDTBT:$PC_{71}BM$-based OSCs using Al-doped MoO_3 as CIL and MoO_3/Al as anode. A high FF of 0.66% and a PCE of 6.28% was achieved. The MoO_3-Al composite films are highly transparent and exhibit a high WF of 4.09 eV with 55% Al doping compared to 5.5 eV for neat MoO_3, thus able to form Ohmic contact with the LUMO of $PC_{71}BM$. (Liu et al. 2012a) Li-doped ZnO (LZO) when used as CIL in PSEHTT:$IC_{60}BA$ generated a PCE of 6.59% compared to 5.36% for ZnO. LZO layer was further used as interconnecting layer in tandem and triple cell generating PCE up to 10.4 and 11.83% (Yusoff et al. 2014).

Using Mg-doped ZnO as CIL, Yin et al. obtained a PCE of 8.31% which was significantly higher than those of device without CIL (3.5%) or with only ZnO (7.1%) as CIL. (Yin et al. 2014) The WF can be tuned by changing the amount of Mg doping and also the device stability improved significantly. The insertion of various metal carbonates such as Li_2CO_3, K_2CO_3, Na_2CO_3, Cs_2CO_3, and $(NH_4)_2CO_3$ as gradient doping agent for ZnO layer can improve the electron extraction properties by modifying the energy levels without making any damage to the ZnO nanostructures (Nho et al. 2016). When 5 wt% Li-doped ZnO was used as CIL in PTB7-Th:$PC_{71}BM$ based devices the PCE was improved from 8.59 to 10.05% (Soultati et al. 2019). Fullerene-free solar cells based on the PTB7-Th:IT-4F blend exhibited PCEs up to 8.96% under similar device structure. It has been proposed that the Li ions are intercalated within the ZnO lattice as interstitial dopants and replace the defects which acts as trap state in ZnO, improve the electron conductivity and alter the WF of doped oxide.

The performance improvement was further visible with low temperature processed Al-doped ZnO (AZO) CIL. High PCE of 10.42% was achieved with PTB7-Th:$PC_{71}BM$ blend device and was found to be insensitive to the thickness of AZO. Additionally, due to low temperature processing flexible devices on poly(ethylene

terephthalate)/indium tin oxide substrates were also prepared showing PCE of 8.93% (Liu et al. 2016a). The conductivity of AZO was enhanced by three order of magnitude compared to neat ZnO, therefore a thicker film can be prepared with AZO (above 100 nm) (Stubhan et al. 2011). Similar enhancement in conductivity was also observed for Ga-doped ZnO and In-doped ZnO thus enabling thicker film formation up to 200 nm. (Shin et al. 2010; Puetz et al. 2011) The device performance was improved after doping due to improved electron transport/hole blocking properties.

Liao et al. present a high efficiency and stable inverted OSCs using sol-gel processed In–doped ZnO as CIL. The PTB7-Th:$PC_{71}BM$ device exhibited a PCE of 9.11% compared to 8.25% for undoped ZnO (Liao et al. 2014). The LUMO energy level lowered from 4.29 to 4.62 eV upon doping. In-doping also improved the electron mobility from 8.25×10^{-5} to 9.5×10^{-3} $cm^2\ V^{-1}\ s^{-1}$ and enhanced the conductivity from 0.015 to 8.51 S cm^{-1}.

Gadisa et al. prepared AZO nanoparticle stabilized with a TiO_X complex. The P3HT:$PC_{61}BM$ device prepared with modified CIL and WO_3 as AIL generated high FF of 0.68 due to efficient hole blocking property of AZO-Ti and could solve the issue related to interfacial recombination in the devices (Gadisa et al. 2013). Brabec and co-workers improved the device performance of P3HT:$PC_{61}BM$ device by employing a C_{60} self-assembled monolayer (SAM) containing phosphonic acid anchoring group (Stubhan et al. 2012). The series resistance in the device was reduced keeping the shunt resistance high. The use of ZnO-poly(vinyl pyrrolidone) (PVP) based composite films prepared using sol-gel method as ETL, demonstrated PCEs >8% under AM 1.5G illumination at 100 mW cm^{-2} (Small et al. 2012). ZnO/ionic liquid composite interlayer was also fabricated as CIL and show improved photovoltaic performance over 9%. The ionic nature of [BMIM]BF_4 form interfacial dipole between active layer and ZnO and facilitate charge transport. (Yu et al. 2015) Electrochemical impedance spectral analysis showed the reduction of charge transfer resistance from ZnO to ZnO/[BMIM]BF_4.

It has been realized that the binary and ternary metal oxides as well their doped state whenever required can be used as efficient CILs in BHJ solar cells. Most importantly, the low temperature processing methods using sol-gel approach is viable to apply in other electronic devices including flexible substrate.

18.2.1.2 Organic Molecules as CIL

In this section we will summarize the current development on the use of some selective organic molecules as CIL and discuss their molecular design and implementation in OSCs. In order to improve the device performance along with new donor and acceptor material design, it is important to get control over the interfacial properties. Toward this goal, many new organic interfacial material systems are being designed and synthesized to optimize the energy levels of electrodes in order to increase the device performance. Earlier, BCP has been extensively used as an efficient EBL in vacuum-processed devices (Peumans and Forrest 2001).

Wide bandgap materials such as bathocuproine (BCP) and bathophenanthroline (BPhen) were widely used as exciton blocking layer (EBL) to eliminate anomalous exciton quenching and formed a passivating layer at the organic: cathode interface (Peumans and Forrest 2001; Vogel et al. 2006; Chan et al. 2006). Gommans et al. demonstrated a significant enhancement of V_{OC} (from 0.07 V to 0.92 V) by the incorporation of BCP between the active layer and Al in a planar heterojunction solar cells containing subphthalocyanine (SubPc)/Buckminsterfullerene(C_{60}) active layer. The built-in potential in the device increased from 0.25 to 0.85 V showing a PCE improved from 0.05 to 3.0%. BCP layer also acts as optical spacer to improve the absorption of the active layer (Gommans et al. 2008). Zhao et al. used 4,7-bis(3,5-bis(trifluoromethyl)phenyl)-2,9-dimethyl-1,10-phenanthroline (BCP-2CF_3) as EBL between PCDTBT:PC_{61}BM device. In comparison to the reference cell (3.3%) without EBL, the use of BCP, BCP-2CF_3 improved the PCE to about 4.3 and 4.6% (Zhao et al. 2016). Furthermore, The BCP-2CF_3 sustain to annealing temperature up to 100 °C, while BCP revealed a loss of about 90% to its original PCE. It has been believe that the diffusion of EBL into the D: A layer is the main reason for device degradation.

In OSCs the WF of ITO (4.5–4.7 eV) lies between the HOMO and LUMO of conjugated organic materials thus can collect either electrons or holes efficiently. Thus, by using different interfacial layers the polarity of the ITO surface can be tuned to collect either holes or electrons. Li et al. demonstrated that the ITO surface polarity can be changed by using either cesium carbonate (Cs_2CO_3) or vanadium oxide (V_2O_5) as interfacial layer on ITO in P3HT:PC_{61}BM blend. A PCE of 2.25% was reported for ITO/Cs_2CO_3/active layer/V_2O_5/Al inverted device compared to 1.55% for conventional device using ITO/PEDOT:PSS/active layer/Cs_2CO_3/Al structure (Li et al. 2006).

Surface modification of interlayer using various self-assembled layers was also found to be an efficient route for performance improvement by changing the contact properties, phase morphology and manipulating the barrier height. Brabec and co-workers used 0.1 wt% polyoxyethylene tridecyl ether (PTE) as an organic interfacial layer between ITO and TiO_x to improve the quality of the TiO_x electron extraction layer. The P3HT:PC_{61}BM-based BHJ device (ITO/PTE/TiO_x/P3HT:PCBM/PEDOT:PSS/Ag) with modified interface generated a PCE of 3.6% with improved FF of 0.64 compared to 3.1% (FF = 0.55) without organic interlayer. Without any ETL the device performance was very poor with

PCE of only 1.6% (FF = 0.36). The PTE layer clearly alter the electron selectivity of ITO/PTE/TiO_x electrode. The use of Ag instead of Au top electrode gave a low absorption loss (Steim et al. 2008). The modification of ZnO surface by cesium stearate (CsSt) improve the surface microstructure, energy level, conductivity, exciton generation rate and dissociation probability. Inverted OSCs prepared using ZnO/CsSt CIL layer in PTB7:$PC_{71}BM$ devices a high PCE of 8.69% was achieved which is about 20% higher than the ZnO-only CIL. (Wang et al. 2014a) In another study an organic dye PAPTA was used as surface modifier for ZnO in PBDTTT-C-T/$PC_{71}BM$ device resulting in an improvement in the PCE from 3.27% for bare ZnO to 7.11% for the modified ZnO with a significant increase in V_{OC} and J_{SC} values. (Song et al. 2013) The dye layer reduced the leakage current and e^{-}-h^{+} recombination at the cathode interface by blocking hole injection to ZnO layer.

The interfacial layer between P3HT and TiO_2 was modified by cyanoacrylic acid containing anchoring group in TBTDA (Yu et al. 2012). The surface modification with TBTDA monolayer increased the electron affinity close to the TiO_2 surface and induced a molecular dipole oriented away from the surface of TiO_2 enabling simultaneous improvement in V_{OC} and J_{SC}. The PCE was improved from 0.2 to 2.87%. 4-*tert*-Butyl-pyridine (TBP) was co-deposited to reduce the unfavorable protonation effect of TiO_2 and retard the charge recombination in P3HT/TiO_2 interface.

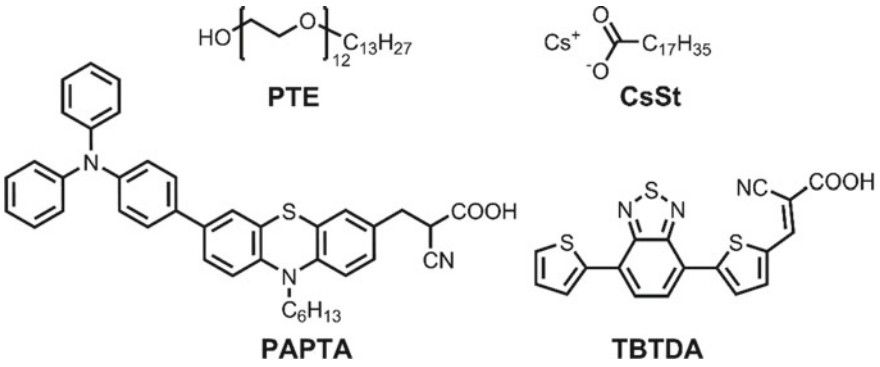

1,4,5,8-Naphthalenetetracarboxylic dianhydride (NTCDA) was also used as n-type material between organic/Ag interface and prevent electrical shorting of the cell due to the migration of vacuum-deposited Ag to the organic layer (Suemori et al. 2005; Hiramoto et al. 2006). Singh et al. incorporate BPhen and BCP as additional buffer layers between P3HT:$PC_{61}BM$ and LiF/Al (Singh et al. 2016). The device with BCP gave a PCE of 4.96% due to the combined effects of better hole-blocking capacity of BCP and low work function provided by LiF/Al. The use of Bphen and WO_3 as EBL and AIL increased the PCE of the CuPc/C_{60}-based OSC devices to 3.33% compared to the device without WO_3 layer (2.64%). The better electron transport and exciton blocking ability of Bphen were the major contribution to the increased device performance. The device without Bphen and WO_3 layer generated very low PCE of 0.84% (Chan et al. 2006). Despite of similar optical transparency,

the electron mobility of Bphen is two order of magnitude higher compared to BCP thus led to better electron transport.

Zhao et al. used amino-group containing small molecules such as dicyandiamide (DCDA) and urea as CIL in P3HT:PC_{61}BM BHJ solar cells. The PCE has been enhanced from 3.35% for the reference device to 4.25% and 4.39% respectively, due to increase in J_{SC} and FF values (Zhao et al. 2014). Further investigation of film morphologies revealed the interfacial dipole formation between the photoactive layer and Al cathode which might have lowered the WF of Al and facilitate electron extraction from PCBM. Also the amine groups can coordinate to the Al and prevent its interaction with P3HT.

Nam et al. successfully used a combination of pyromellitic dianhydride (PMDA)/LiF as CIL in P3HT:PC_{61}BM BHJ devices which showed superior photovoltaic performance (PCE = 3.9%) compared to the device with single CILs PMDA (PCE = 1.8%) or with only LiF (PCE = 3.3%) due to reduced leakage current and series resistance (Nam et al. 2012).

The use of organic dipolar interlayers for interfacial tuning of the electron-collecting buffer layer and the photoactive layer has been projected as an efficient way to improve the overall device performance. In this respect, various perylene derivatives have been used as CIL to modify the interface between cathode and organic layer. Chen et al. demonstrated the modification of ITO WF by coating with a cationic N,N′-bis[2-(trimethylammonium)ethylene]perylene-3,4,9,10-tetracarboxyldiimide ($PDIN^+I^-$) and anionic $PEDOT:PSS^-$ composite prepared by electrostatic layer by layer (eLbL) deposition technique to prepared $PDIN^+I^-$:$PEDOT:PSS^-$ composite and used as CIL (Fig. 18.3) (Chen et al. 2011). The interlayer was prepared by sequential deposition of precleaned ITO electrode into the cationic $PDIN^+I^-$ solution for 5 min followed by subsequent dipping in anionic PEDOT:PSS solutions for 5 min with immediate rinsing steps using water. Multiple repetition steps gave multilayer films on ITO surface. Odd-even effect of the interlayer can be clearly visible in the device performance. The WF of the modified ITO can be varied between 4.35 and 4.60 eV depending on the layer number. Li et al. obtained a reduction of ITO WF by coating a $PDIN^+I^-$ film and used as CIL which

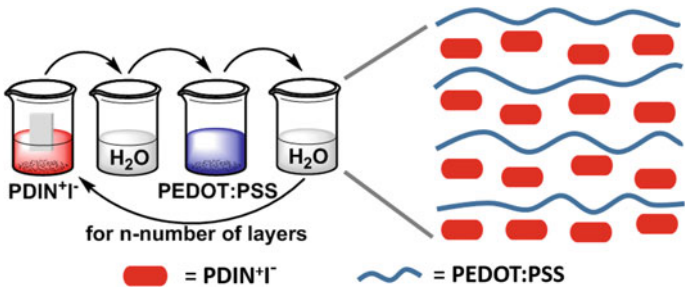

Fig. 18.3 Electrostatic layer by layer (eLbL) deposition technique to prepare multilayers of interfacial layer

gave improved PCE of 7.0 to 7.18% when used without or with LiF layer than that of device with bare Al cathode or only LiF/Al (Li et al. 2016).

Gregg and co-workers reported a self-doping, O_2-Stable water soluble dicationic perylene bis(2-ethyltrimethylammonium hydroxide imide ($PETMA^+$-OH^-) salt as CIL (Reilly III et al. 2012). The molecule doped by dehydration and de-doped by hydration. It has been shown that the conductivity for the doped state could be significantly increased from 4×10^{-3} to 2×10^{-3} S cm^{-1}.

Zhang et al. reported a thickness insensitive room temperature processed perylene derivatives comprising dimethylamino (PDIN) or dimethylamino-N-oxide (PDINO) as terminal groups and explore their use for CIL (Wang et al. 2014b). PDINO was synthesized from PDIN by treatment with H_2O_2. The large interfacial dipole formed by the perylene derivatives induced the vacuum level shift and change the WF of metal electrode. The LUMO energy levels of PDIN and PDINO are estimated to be –3.63 eV and –3.72 eV, respectively and close to the $PC_{71}BM$, while the HOMO levels are at −6.05 and −6.21 eV lowered enough to block the holes from the donors. Ultraviolet photoelectron spectroscopy (UPS) results revealed the shift of the WF of Al from 4.3 to 3.5 eV by deposition of a thin layer (5 nm) of either PDI derivatives. However, the WF of Ag and Au strongly depend on the type of PDI layer. For both electrodes, PDIN/PDINO treatment lowered the WF to ~3.93 eV/~3.60 eV allowing them to form good ohmic contacts with the fullerene acceptor. This change in the WF is related to the polar nature and dipole formation ability of the terminal amino or amino-N-oxide groups in PDIN and PDINO. The lowered WFs of PDI/metal cathodes also increase the built-in field used to break the electrical symmetry inside of the cells, beneficial for charge extraction and reduce recombination losses. Conventional device using PDIN/Al or PDINO/Al as CIL and PEDOT:PSS as AIL gave excellent PCE of 7.68–8.24% comparatively higher than that of Ca/Al CIL (PCE = 6.98%). Moreover, the perylene derivatives also lowered the WF of Au and Ag metal to use as cathode. Due to lowering of the WF, Ag or Au were also used as cathode generating high photovoltaic performance above 7% and high FF close to 0.73.

Min et al. used ZnO/PDINO as CIL in small molecule based OSC devices (BDTT-S-TR:$PC_{71}BM$) and Ag as top electrode. The ZnO/PDINO bilayer not only served as an effective cathode interlayer but also acts as a protective coating on top of the active layer. The device gave a PCE of 8.2%. They further fabricate all solution-processed OSCs using highly transparent Ag nanowire as top electrode resulting in a PCE of 3.62% (Min et al. 2016). When PDINO interlayer was implemented in conventional fullerene-free devices PCEs up to 14.04% have been achieved for PBDB-TF:IDIC-C4Ph blend after thermal annealing at 130 °C (Li et al. 2019).

Yu et al. reported a high performance fullerene-free OSC using PDIN as CIL and B-DIPDI:PTB7-Th as photoactive layer. PDIN helps in interfacial doping of B-DIPDI acceptor and facilitate the charge transport and extraction (Yu et al. 2016). The use of PDIN interlayer as a surface modifier on ZnO resulted in a $\approx$ 14% enhancement of the PCE than that of the pristine ZnO-based device. The grazing incident wide angle X-ray scattering (GIWAXS) study revealed a more crystalline face-on orientation of the BHJ film achieved due to compatibility of both PDI acceptor and interlayer. Lin et al. observed a PCE of 6.31% using PDIN CIL PTB7Th:IEIC

based devices (Lin et al. 2015). A polar solvent soluble zwitterion perylene diimide zwitterion (PDI-z) consisted of sulfobetaine ion as terminal units was prepared and employed as CIL. (Song et al. 2018) The fullerene-free PBDB-T:IT-M based devices under optical condition gave a PCE of 11.2%. PDI-z can also found to alter the high WF metals, such as Au, Cu, Ag, where PDI-z/Ag gave the best PCE of 9.38%. The device using PDIN as CIL also gave a high PCE of 10.25%. Fullerene-free ternary solar cells using PDIN interlayer have been fabricated showing excellent PCE of 11.6% (Hu et al. 2018). The enhanced performance was due to the strong and complementary absorption of the active layer and interfacial modification by PDIN layer improving the charge extraction and dissociation.

Sun et al. used a zwitterionic rhodamine 101 as CIL and tested the device performance using various metal as top electrodes. The PCDTBT:$PC_{71}BM$ device with Al as top electrode gave the best PCE 6.15% compared to 4.57 for Ca/Al or 3.8% for Al alone (Sun et al. 2012). Similar effect was also observed for other metal electrodes (Ag, Au, Cu) in combination with rhodamine 101.

By employing a water/alcohol soluble pyridinium salt F8PS (HOMO = 5.71 eV and LUMO = −3.31 eV) as CIL in PCDTBT:$PC_{71}BM$ devices simultaneous improvement of all photovoltaic parameters was observed. The PCE increased from 4.32% for the reference cell to 6.56% and V_{OC} from 0.76 to 0.94 V (Ye et al. 2013). The V_{OC} improvement was due to the generation of interface dipoles and excellent electron transfer/collection ability of the hydrophilic pyridinium salt.

Zhang et al. reported two hydrophobic materials FBF-N and FTBTF-N which served CIL to modulate the atop-BHJ morphology (Zhang et al. 2014). Thus, the PCE of PTB7:$PC_{71}BM$ device could be enhanced to 7.97 and 9.22% from 1.18% for bare ITO without interlayer. The hydrophobic nature of backbone formed better morphology and helped to improve the J_{SC} and FF.

Vacuum-deposition of N,N-Dioctyl-3,4,9,10-perylenedicarboximide (PTCDI-C8) over ZnO layer modified the interface properties, reduced the WF of ZnO and improve device performance of PTB7-Th:$PC_{71}BM$ device with PCE from 8.26 to 9.29% (Fan et al. 2017).

Ma and co-workers developed a CIL by doping sol-gel derived ZnO with a 1 wt% perylene derivative PBI-H, which formed an N − Zn bond with ZnO by thermal treatment and improved the electron mobility by an order of magnitude (5.10×10^{-4} for neat ZnO to 2.02×10^{-3} cm^2 V^{-1} s^{-1}). (Nian et al. 2015) The conductivity also improved to 4.50×10^{-3} S m^{-1}. OSC devices with PTB7:$PC_{71}BM$ and PTB7-Th:$PC_{71}BM$ photoactive layer generated an excellent PCEs of 9.01% and 10.5%, respectively, which is independent of CIL thickness and higher than the device with pure ZnO (7.4 and 8.3%). The WF of modified ITO/ZnO:PBI-H decreased to 3.8 eV compared to 4.2 eV for bare ITO/ZnO indicating increased electron population on the conduction band of ZnO and also pinned the WF of ITO near LUMO of $PC_{71}BM$ forming good Ohmic contact with $PC_{71}BM$. PBI-H blocks holes due to low lying HOMO energy level. Furthermore, the PBI-H interlayer form self-assembled J-type aggregate with absorption maximum at 650 nm, 80 nm red-shifted than the monomer and formed nanofibril networks by non-covalent interactions efficient for charge transport (Xie et al. 2015).

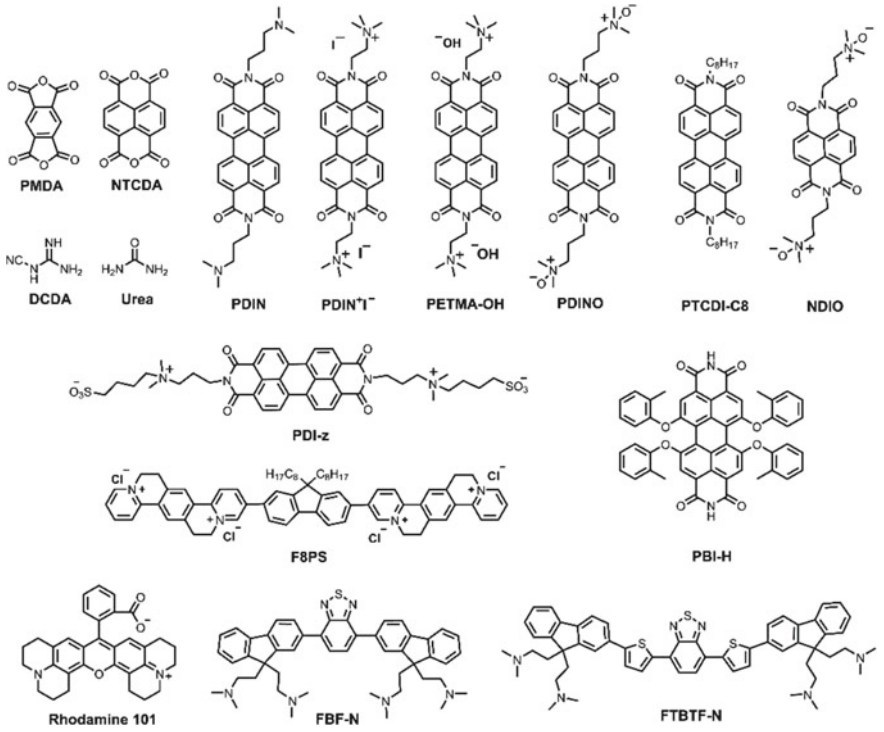

Hou and co-workers synthesized a water soluble interfacial material NDIO which showed high transparency in the visible region, suitable work-function, low roughness for excellent interface contact and aqueous processability. Incorporation of NDIO in PBDT-TS1:$PC_{71}BM$ based inverted devices gave high PCE of 9.51%, which was significantly higher compared to the device without CIL (PCE = 5.33%) (Zhao et al. 2015). Using ZnO or PEIE as CIL instead of NDIO in PBDT-TS1/PCBM-based devices gave comparable PCEs of 9.67% and 9.32%, respectively.

Cao and co-workers used a star-shaped triazine based CIL TzPyBr containing terminal pyridinium moieties. Inverted devices using PTB7:$PC_{71}BM$ photoactive layer gave a PCE of 6.84% almost double than that of reference device (3.5%) (Chen et al. 2014). The low-lying HOMO energy level of TzPyBr effectively blocks the holes travelling towards cathode and improve directional charge transport.

Recently, Wang et al. developed a series of star-shaped triphenylamine-based materials (namely, TFN, TFB, TFO, TFS) containing various polar pendant groups for CIL (Wang et al. 2016). The compounds were synthesized via Suzuki cross-coupling reactions of boronic ester of triphenylamine with different bromo derivatives. All compounds showed very similar HOMO/LUMO energy levels (~−5.45/~−2.5 eV). Conventional OSCs with PTB7:$PC_{71}BM$ using these CILs exhibited PCE improvement in the order as cast (6.8%) < methanol (8.0%) < TFN (8.6%) < PFN (8.7%) < TFS (8.7%) < TFO (9.7%) < TFB (10.1%). The results showed that TFB as the best cathode modifier reaching highest PCE of 10.1%. The

pendant ionic groups (quaternary ammonium bromide, amino N-oxide, and sulfobetaine ion) of ETMs formed strong interaction with Al electrode and induced dipole orientation towards active layer, thus, reduces the Al WF (from -4.3 eV to between −3.79 and −4.06 eV), lowering the energy barrier at the active layer: Al interface and increased the built-in potential (V_{bi}) to improve the V_{OC} values. It has also been shown that the mobile Br^- counterions of TFB can easily absorbed on the Al electrode and form the stronger and more regular dipole moments than those zwitterionic TFO and TFS with immobile counterions linked via covalent bond.

Wang et al. fabricated a CIL using a tetraphenylethylene-based small molecule TPE-2 terminated with zwitterionic aminopropane sulfonate groups (Wang et al. 2017). TPE-based molecule has strong tendency to show aggregation-induced emission (AIE) effect. PTB7:$PC_{71}BM$-based conventional device with TPE-2/Al cathode gave PCE of 8.94% compared to 3.89% for bare Al, 7.31% for Ca/Al, 7.83% for MeOH/Al and 8.33% for PFN/Al. This strong improvement of PCE was attributed to the well-organized lamellar structure, resulting from the self-assemble property of TPE-2.

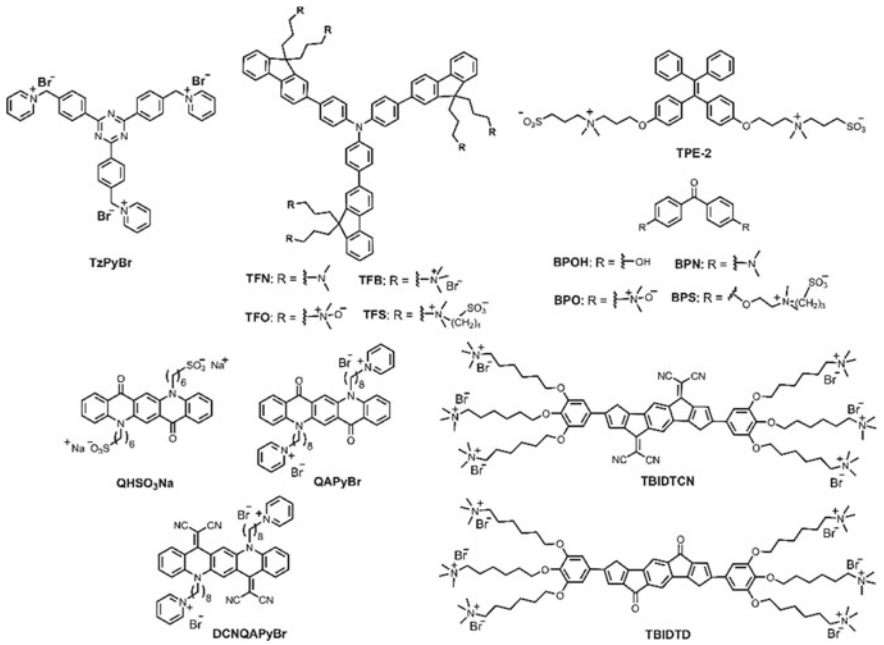

A series of benzophenone-based molecular CILs with different polar terminal groups comprising hydroxyl (BPOH), neutral amino (BPN), amino N-oxide (BPO), and sulfobetaine (BPS) ions were prepared. and used as CIL between PTB7:$PC_{71}BM$ and Al electrode. OSCs with solution-processed BPO-based interlayer showed a PCE of 9.34% with the highest J_{SC} and FF due to decreased series resistance and charge recombination compared to the devices with BPN, BPOH and BPS interlayers. It was

further noted that the methanol treatment plays an important role in performance improvement (PCE = 7.97%) by increasing the V_{bi} and passivating surface traps (Liu et al. 2017).

Fused ring quinacridone derivatives were developed and tested as CIL materials. Wudl and co-workers reported a water/alcohol soluble quinacridone-based molecule $QHSO_3Na$ which when used as CIL increased the device PCE from 4.34 to 5.17% (Pho et al. 2011). A significant improvement in the FF from 0.53 to 0.63 was observed, while the V_{OC} and J_{SC} values were similar to the reference cell. Chen et al. demonstrated an improvement in the PCE (6.70%) of PCDTBT:$PC_{71}BM$ devices using 4 nm thin QAPyBr CIL containing pyridinium pendent groups due to significant increase in the FF along with V_{OC} and J_{SC} higher than the Al-based devices (5.13%) (Chen et al. 2016). Further increase in CIL thickness (~20 nm) the PCE dropped to around 1.7% due to significant reduction in the J_{SC} and FF. Interestingly, the strong electron accepting group dicyanomethylene group containing CIL, DCNQAPyBr showed further improvement in the PCE due to enhanced electron transport ability and conductivity as well insensitive to thickness of the CIL. The best device gave a PCE of 6.96% using 13 nm thick DCNQAPyBr. The device gave maintain high PCE of 5.8% even up to 40 nm thickness showing the importance of cyano groups on the device performance improvement.

Indacenodithiophene (IDT), which has been successfully employed to develop various fullerene-free acceptors, was used to synthesize two new cationic electrolyte TBIDTD and TBIDTCN for CIL. Among the two CILs TBIDTCN gave the better performance with PCE of 9.19% compared to 8.62% for TBIDTD due to dramatic reduction of series resistance, lower LUMO energy level for efficient electron transport and extraction (Miao et al. 2018). The reference device gave 1.66 times lower performance.

18.2.1.3 Fullerene Derivatives as CIL

Various water/alcohol soluble fullerene derivatives have been prepared to use them as CIL and reviewed recently (Lai et al. 2014; Chueh et al. 2015). Due to similar energy levels with respect to $PC_{61}BM$/$PC_{71}BM$ they have been widely employed as CIL to modify the surface properties and enhance the photovoltaic performance. Some representative examples are discussed below and the photovoltaic parameters are presented in Table 18.2.

Zhang et al. synthesized an alcohol soluble poly(ethylene glycol) end-capped fullerene derivative, PEGN-C_{60}, for its used as EBL with different active layers, such as P3HT:$PC_{61}BM$, PBDTTT-C:$PC_{71}BM$, and PBDTTT-C-T:$PC_{71}BM$. The optimal PCEs of the these devices reached values of up to 3.84%, 6.22%, 7.45%, respectively, and close to the values obtained using Ca/Al based CIL and significantly higher compared to without EBLs (Zhang et al. 2013).

Li and co-workers prepared two fullerene derivatives namely, PCBDAN and PCBDANI and studied their ability to act as CIL (Li et al. 2013). PCBDANI was synthesized by the reaction of PCBDAN with methyl iodide. These CILs formed interfacial

Table 18.2 Summary of photovoltaic performance based on representative small molecule CILs

Cathode structure	Active layer	Anode structure	V_{OC} (V)	J_{SC} (mA cm^{-2})	FF	PCE (%)	References
BCP/Al	SubPc/C_{60}	ITO	0.92	5.42	0.60	3.03	Gommans et al. (2008)
BCP/LiF/Al	P3HT:$PC_{61}BM$	ITO/PEDOT:PSS	0.60	13.5	0.61	4.96	Singh et al. (2016)
ITO/PETMA$^+$-OH$^-$	P3HT:$PC_{61}BM$	V_2O_5/Al	0.51	9.87	0.51	2.52	Reilly III et al. (2012)
PDIN$^+$I$^-$/LiF/Al	PBTI3T: $PC_{71}BM$	ITO/PEDOT:PSS	0.86	11.2	0.75	7.18	Li et al. (2016)
PDINO/Al	PTB7:$PC_{71}BM$	ITO/PEDOT:PSS	0.75	15.9	0.73	8.24	Wang et al. (2014b)
PDIN/Al	PTB7:$PC_{71}BM$	ITO/PEDOT:PSS	0.76	14.3	0.71	7.68	Wang et al. (2014b)
ZnO/PDINO/Ag	BDTT-S-TR:$PC_{71}BM$	ITO/PEDOT:PSS	0.96	13.1	0.65	8.21	Min et al. (2016)
PDINO/Al	PBDB-TF:IDIC-C4Ph	ITO/PEDOT:PSS	0.94	19.1	0.78	14.0	Li et al. (2019)
ITO/ZnO/PDIN	PTB7-Th:B-DIPDI	MoO_3/Ag	0.78	13.0	0.62	6.29	Yu et al. (2016)
PDIN/Al	PBDB-T:IT-M	ITO/PEDOT:PSS	0.94	16.1	0.68	10.3	Song et al. (2018)
PDIN-z/Al	PBDB-T:IT-M	ITO/PEDOT:PSS	0.94	16.1	0.74	11.2	Song et al. (2018)
PDIN/Al	J71:IT-M:ITIC	ITO/PEDOT:PSS	0.98	18.1	0.66	11.6	Hu et al. (2018)
Rhodamine 101/Al	PCDTBT:$PC_{71}BM$	ITO/PEDOT:PSS	0.94	11.1	0.59	6.15	Sun et al. (2012)
F8PS/Al	PCDTBT:$PC_{71}BM$	ITO/PEDOT:PSS	0.94	11.3	0.62	6.56	Ye et al. (2013)
ITO/FBF-N	PTB7:$PC_{71}BM$	MoO_3/Al	0.75	15.5	0.68	7.97	Zhang et al. (2014)
ITO/FTBTF-N	PTB7:$PC_{71}BM$	MoO_3/Al	0.74	17.2	0.72	9.22	Zhang et al. (2014)
ITO/ZnO/PTCDI-C8	PTB7-Th:$PC_{71}BM$	MoO_3/Ag	0.81	18.3	0.63	9.29	Fan et al. (2017)
ITO/ZnO:PBI-H	PTB7:$PC_{71}BM$	MoO_3/Al	0.75	17.2	0.70	9.01	Nian et al. (2015)

(continued)

Table 18.2 (continued)

Cathode structure	Active layer	Anode structure	V_{OC} (V)	J_{SC} (mA cm^{-2})	FF	PCE (%)	References
ITO/ZnO:PBI-H	PTB7-Th:$PC_{71}BM$	MoO_3/Al	0.82	17.5	0.73	10.5	Nian et al. (2015)
ITO/NDIO	PBDT-TS1:$PC_{71}BM$	MoO_3/Al	0.79	18.02	0.67	9.51	Zhao et al. (2015)
ITO/TzPyBr	PTB7:$PC_{71}BM$	MoO_3/Al	0.70	15.6	0.62	6.84	Chen et al. (2014)
TFN/Al	PTB7:$PC_{71}BM$	ITO/PEDOT:PSS	0.73	15.6	0.72	8.60	Wang et al. (2016)
TFB/Al	PTB7:$PC_{71}BM$	ITO/PEDOT:PSS	0.78	17.6	0.74	10.1	Wang et al. (2016)
TFO/Al	PTB7:$PC_{71}BM$	ITO/PEDOT:PSS	0.76	17.4	0.73	9.70	Wang et al. (2016)
TFS/Al	PTB7:$PC_{71}BM$	ITO/PEDOT:PSS	0.75	16.4	0.71	8.70	Wang et al. (2016)
PFN/Al	PTB7:$PC_{71}BM$	ITO/PEDOT:PSS	0.75	17.1	0.68	8.70	Wang et al. (2016)
TPE-2/Al	PTB7:$PC_{71}BM$	ITO/PEDOT:PSS	0.76	16.8	0.70	8.94	Wang et al. (2017)
BPN/Al	PTB7:$PC_{71}BM$	ITO/PEDOT:PSS	0.76	16.9	0.70	8.98	Liu et al. (2017)
BPO/Al	PTB7:$PC_{71}BM$	ITO/PEDOT:PSS	0.76	17.1	0.72	9.34	Liu et al. (2017)
BPS/Al	PTB7:$PC_{71}BM$	ITO/PEDOT:PSS	0.76	16.9	0.70	9.03	Liu et al. (2017)
$QHSO_3Na$/Al	PCDTBT:$PC_{71}BM$	ITO/PEDOT:PSS	0.84	9.83	0.63	5.17	Pho et al. (2011)
QAPyBr/Al	PCDTBT:$PC_{71}BM$	ITO/PEDOT:PSS	0.90	11.2	0.66	6.70	Chen et al. (2016)
DCNQAPyBr/Al	PCDTBT:$PC_{71}BM$	ITO/PEDOT:PSS	0.91	11.3	0.68	6.96	Chen et al. (2016)
TBIDTD/Al	PTB7:$PC_{71}BM$	ITO/PEDOT:PSS	0.77	16.2	0.69	8.62	Miao et al. (2018)
TBIDTCN/Al	PTB7:$PC_{71}BM$	ITO/PEDOT:PSS	0.77	16.6	0.72	9.19	Miao et al. (2018)
PEGN-C_{60}/Al	P3HT:$PC_{61}BM$	ITO/PEDOT:PSS	0.63	9.21	0.67	3.84	Zhang et al. (2013)

(continued)

Table 18.2 (continued)

Cathode structure	Active layer	Anode structure	V_{OC} (V)	J_{SC} (mA cm^{-2})	FF	PCE (%)	References
PEGN-C_{60}/Al	PBDTTT-C:$PC_{71}BM$	ITO/PEDOT:PSS	0.74	14.0	0.61	6.22	Zhang et al. (2013)
PEGN-C_{60}/Al	PBDTTT-C-T:$PC_{71}BM$	ITO/PEDOT:PSS	0.79	14.8	0.63	7.45	Zhang et al. (2013)
PCBDAN/Al	PBDTTT-C-T/$PC_{71}BM$	ITO/PEDOT:PSS	0.78	17.4	0.57	7.70	Li et al. (2013)
PCBDANI/Al	PBDTTT-C-T/$PC_{71}BM$	ITO/PEDOT:PSS	0.78	17.3	0.57	7.69	Li et al. (2013)
C_{60}-N/Ag	PTB7-Th:$PC_{71}BM$	ITO/PEDOT:PSS	0.78	16.8	0.71	9.35	Page et al. (2014)
C_{60}-SB/Ag	PTB7-Th:$PC_{71}BM$	ITO/PEDOT:PSS	0.75	16.9	0.68	8.57	Page et al. (2014)
ITO/C_{60}-SB	PTB7-Th:$PC_{71}BM$	MoO_3/Ag	0.75	18.2	0.66	9.08	Liu et al. (2015a)
ITO/B-PCPO	PCDTBT:$PC_{71}BM$	MoO_3/Al	0.89	9.50	0.62	6.20	Duan et al. (2012)
ITO/ZnO-C_{60}	PTB7:$PC_{71}BM$	MoO_3/Ag	0.73	15.4	0.73	8.21	Liao et al. (2013)
ITO/ZnO-C_{60}	PTB7-Th:$PC_{71}BM$	MoO_3/Ag	0.80	15.7	0.74	9.35	Liao et al. (2013)
ITO/ZnO-C_{60}	PBDT-BT:$PC_{71}BM$	MoO_3/Ag	0.92	15.4	0.66	9.40	Subbiah et al. (2015)

dipole between the active layer and Al metal and demonstrated very similar OSC performance with PCEs around 7.7% for PBDTTT-C-T/$PC_{71}BM$ devices and showed greater stability compared to Ca/Al or only Al.

The trade-off between stability due to oxidation and WF of electrode is a major challenge in the field of OSCs. Page et al. used amine-functionalized C_{60}-N and sulfobetaine-substituted zwitterionic C_{60}-SB as cathode independent buffer layer in conventional device (Page et al. 2014). Specifically, using a thin layer of C_{60}-N the effective WF of Ag, Cu, and Au electrodes can be significantly reduced to 3.65 eV. C_{60}-SB was prepared from C_{60}-N by reaction with 1,3-propanesultone via ring opening. The insertion of C_{60}-N between active layer and metal electrodes resulted in good Ohmic contact for electron injection, and a large built-in potential difference for efficient charge extraction in OSCs. Devices with devices with C_{60}-N or C_{60}-SB interlayers yielded PCE values 9.35% and 8.57%, respectively. Lower PCEs were obtained for devices with Al (8.65%), Cu (8.67%) or Au (8.56%) cathodes, relative to Ag (9.35%) cathodes, which can be credited to the lower reflectivity of Cu and Au.

Russell and co-workers further implemented C_{60}-SB as CIL in an inverted device, which showed exceptional improvement of PCE to 9.23% for PTB7-Th:$PC_{71}BM$ blend compared to 1.96% with bare ITO (Liu et al. 2015a). The CIL also acts as an electron acceptor and modified the WF of ITO from 4.5 eV to ~ 4.0 eV as measured by UPS. The highest performance was achieved with the CIL thickness of ~40 nm and remain above 8.0% for the entire thickness range above 10 nm. The work function modification of ITO by C_{60}-SB may arised from orientation of the permanent dipole at the interface, due to the preferential interactions of the sulfobetaine zwitterion with the ITO surface.

Cao group developed an alcohol soluble phosphate-containing fullerene bis-adducts, B-PCPO as CIL in inverted OSCs to improve the electron transport and collection efficiency (Duan et al. 2012). It was observed that the B-PCPO interlayer could effectively decrease the WF of ITO to 3.9 eV and thereby enhance the electron collection at the ITO electrode. The device resulted in PCE increased from 4.83 to 6.20% by using a B-PCPO interlayer, compared to 5.31% for ZnO and 4.83% for device without interlayer.

Chen et al. developed a CIL ZnO-C_{60} by reacting zinc acetate with hydroxyl containing fullerene derivative PCBE-OH (Liao et al. 2013). This ZnO-C_{60} CIL provides dual functionalities for enhanced electron collection, producing a fullerene-rich cathode surface and promote compatibility of the BHJ layer at the interface. The C_{60}-doped ZnO lower the LUMO level to −4.53 eV compared to pristine ZnO (−4.1 eV) promoting better electron transport pathways. Inverted BHJ devices comprising PTB7-Th:$PC_{71}BM$ blend exhibited excellent PCEs of 9.35% higher than that bare ZnO. Subbiah et al. reported a PCE of 9.4% using a ZnO−C_{60} interlayer at the cathode contact (Subbiah et al. 2015). The surface modification eliminates of oxygen vacancies on the ZnO surface that can act as electron traps and reduced carrier recombination.

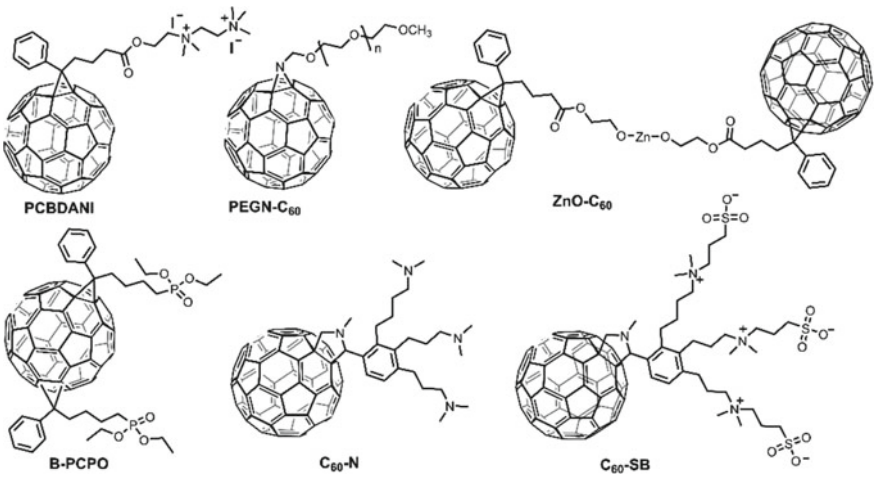

In summary, hydrophilic fullerene derivatives would be a promising family of interfacial materials for highly efficient OSCs. Although the synthesis and purification of these fullerene derivatives somehow complicated and for their implementation as efficient CIL efficient preparation methods need to be developed.

18.2.1.4 Organic Polymers as CIL

The use of water/alcohol soluble polymers as CIL was widely interpreted as interfacial dipole formation model (He et al. 2011b, 2012). These CILs can effectively modify the WF of the metal cathode by forming interfacial dipole between the oganic: metal interface, thus improve the electron injection and transport in the device (Duan et al. 2013c; Hu et al. 2014; Tang et al. 2014). Various water soluble non-conjugated, such as PEIE and PEI as cathode modifier and π-conjugated polymers such as PFN, PFN-Br and others have effectively implemented as CILs in various OSC devices (He et al. 2011a, 2012; Zhou et al. 2012a; Kang et al. 2012). The conjugated chain improve the delocalization of electrons and the polar pendant groups makes them process from polar water/alcohol, thus does not affects the active layer processed from complementary organic solvents (Duan et al. 2013c). The shift of the vacuum level by interfacial dipoles could increase the V_{bi} of the device and thus increases the V_{OC}. Depending on the types of interfacial materials the work function of ITO can be reduced by 0.3−0.6 eV. The increased V_{bi} does not alter the energetics of the active layer and therefore improvement in all photovoltaic parameters can be expected. The photovoltaic data are presented in Table 18.3.

Shao et al. used a poly(ethylene oxide) (PEO)-modified ZnO composite as an ETL (Shao et al. 2013). The surface modification using 0.05% of PEO effectively passivate the surface trap state in ZnO, thus suppressed the recombination losses, reduced series resistance, thus enhanced the PCE to 5.64 and 6.59% for TQ1:$PC_{71}BM$ and PCDTBT:$PC_{71}BM$, respectively. Using polyallylamine (PAA) as polyelectrolyte

Table 18.3 Summary of photovoltaic performance based on representative polymer CIL

Cathode structure	Active layer	Anode structure	V_{OC} (V)	J_{SC} (mA cm^{-2})	FF	PCE (%)	References
ITO/PEO:ZnO	TQ1:$PC_{71}BM$	MoO_3/Ag	0.88	9.60	0.67	5.64	Shao et al. (2013)
ITO/PEO:ZnO	PCDTBT:$PC_{71}BM$	MoO_3/Ag	0.88	11.4	0.65	6.59	Shao et al. (2013)
ITO/ZnO/PEIE	p–DTS(FBTTh$_2$)$_2$:$PC_{71}BM$	MoO_3/Ag	0.77	15.2	0.67	7.88	Kyaw et al. (2013)
ITO/PEIE protonated	PTB7-Th:IEICO-4F	MoO_3/Ag	0.70	27.2	0.69	13.2	Xiong et al. (2019)
MSAPBS/Al	PTB7:$PC_{71}BM$	ITO/PEDOT:PSS	0.76	19.2	0.68	10.0	Ouyang et al. (2015)
DSAPS/Al	PTB7:$PC_{71}BM$	ITO/PEDOT:PSS	0.76	18.2	0.70	9.79	Liu et al. (2016b)
ZnO/DSAPS	PTB7:$PC_{71}BM$	MoO_3/Al	0.75	17.0	0.70	9.10	Liu et al. (2016b)
ITO/PEI/F_{16}CuPc	PTB7:$PC_{71}BM$	MoO_3/Ag	0.72	20.2	0.66	9.51	Li et al. (2018b)
ITO/ZnO/APTES	PTB7-Th:$PC_{71}BM$	MoO_3/Ag	0.78	17.1	0.71	9.46	Fu et al. (2017)
ITO/ZnO/APTMS	PTB7-Th:$PC_{71}BM$	MoO_3/Al	0.80	16.7	0.68	9.07	Wei et al. (2018)
ITO/ZnO/PDEPB	PTB7:$PC_{71}BM$	MoO_3/Ag	0.73	16.0	0.70	8.14	Nam et al. (2017)
ITO/ZnO/PDEPB	PTB7-Th:$PC_{71}BM$	MoO_3/Ag	0.79	18.6	0.71	10.4	Nam et al. (2016)
ITO/ZnO/PPy1	PTB7:$PC_{71}BM$	MoO_3/Ag	0.75	15.3	0.72	8.29	Aryal et al. (2018)
ITO/ZnO/Ppy1	PTB7-Th:$PC_{71}BM$	MoO_3/Ag	0.81	17.1	0.68	9.37	Aryal et al. (2018)
ITO/PEI/SnO_2/PFN	PCDTBT:$PC_{71}BM$	MoO_3/Ag	0.85	14.2	0.60	7.18	Guo et al. (2019)
ITO/P3TBPHT:PEDOTPSS	PCDTTPD:$PC_{71}BM$	V_2O_5/Al	0.91	11.2	0.55	5.60	Worfolk et al. (2012)
P3TMAHT:SDS/Al	P3HT:$PC_{71}BM$	ITO/PEDOT:PSS	0.62	9.54	0.68	4.01	Chang et al. (2012)

(continued)

Table 18.3 (continued)

Cathode structure	Active layer	Anode structure	V_{OC} (V)	J_{SC} (mA cm^{-2})	FF	PCE (%)	References
P3IMDHT/Al	PCDTBT:$PC_{71}BM$	ITO/PEDOT:PSS	0.87	12.0	0.59	6.69	Kesters et al. (2013)
P3TMAHT/Al	PCDTBT:$PC_{71}BM$	ITO/PEDOT:PSS	0.88	11.8	0.58	6.48	Kesters et al. (2013)
ITO/P3IMDHT	PCDTBT:$PC_{71}BM$	MoO_3/Ag	0.84	11.2	0.51	4.80	Zilberberg et al. (2013)
PCDTBT-N/Al	PCDTBT:$PC_{71}BM$	ITO/PEDOT:PSS	0.92	10.2	0.57	5.32	Duan et al. (2013a)
ITO/ZnO/PBN	PTB7:$PC_{71}BM$	MoO_3/Ag	0.75	15.8	0.72	8.60	Kim et al. (2014)
PFN/Ca/Al	PTB7:$PC_{71}BM$	ITO/PEDOT:PSS	0.76	15.4	0.71	8.20	He et al. (2012)
ITO/PFN	PTB7:$PC_{71}BM$	MoO_3/Al	0.74	17.2	0.72	9.20	He et al. (2012)
PFNSO/Al	PTB7:$PC_{71}BM$	ITO/PEDOT:PSS	0.73	16.4	0.73	8.74	Duan et al. (2013b)
ITO/PFN-OX	PBDT-DTNT: $PC_{71}BM$	MoO_3/Ag	0.74	17.6	0.66	8.62	Hu et al. (2014)
PFN/Al	PCDTBT:$PC_{71}BM$	ITO/PEDOT:PSS	0.91	12.1	0.62	6.73	He et al. (2011b)
ITO/ZnO/PFN	PTB7:$PC_{71}BM$:ICBA	MoO_3/Ag	0.77	16.5	0.72	9.30	Han et al. (2016)
PFN-Br/Ag	PTB7:PDIBDT-IT	ITO/PEDOT:PSS	0.74	13.6	0.60	6.06	Liu et al. (2018)
ITO/ZnO/PFN-Br	PBDB-TF:IT-4F	MoO_3/Al	0.87	20.2	0.79	13.8	Zheng et al. (2019)
PFN/Al	P1:DCI-2	ITO/PEDOT:PSS	0.8	13.8	0.63	6.94	Mishra et al. (2017)

(continued)

Table 18.3 (continued)

Cathode structure	Active layer	Anode structure	V_{OC} (V)	J_{SC} (mA cm^{-2})	FF	PCE (%)	References
PFN/Al	TPA-SN5-DCV:$PC_{71}BM$	ITO/PEDOT:PSS	0.74	14.2	0.69	7.24	Mishra et al. (2018)
ITO/PFS	PDBT-TS1:$PC_{71}BM$	PFS/Al	0.78	18.0	0.66	9.48	Xu et al. (2016)
PFN/Ag	PBDB-T:ITIC	ITO/PEDOT:PSS	0.91	15.8	0.58	8.60	Sun et al. (2017)
PFN-2TNDI/Ag	PBDB-T:ITIC	ITO/PEDOT:PSS	0.92	16.6	0.70	11.1	Sun et al. (2017)
PT_2NDISB/Ag	PBDTT-TT:$PC_{71}BM$	ITO/PEDOT:PSS	0.76	18.8	0.70	10.1	Liu et al. (2015b)
ITO/PNDIT10 N	PTB7-Th:$PC_{71}BM$	MoOx/Ag	0.73	16.4	0.55	7.0	Bjuggren et al. (2018)

PCE of 6.3% was achieved with poly(thieno[3,4-b]thiophene-alt-benzodithiophene) (PTB):$PC_{71}BM$ devices. The lowering of the ITO WF was originated from the strong electrostatic self-assembled dipoles formed by the presence of protonated amines within the ITO/PAA cathodes, forming a good Ohmic contact with LUMO of $PC_{71}BM$ (Kang et al. 2012).

A ionic polyacetylene-based conjugated polymer electrolyte poly(N-dodecyl-2-ethynylpyridiniumbromide) (PDEPB) was developed and used as interfacial dipole layer to modify the ZnO surface and reduced its WF. Performance improvement was observed for the ZnO/PDEPB modified interlayer due to lowering of interfacial resistance (probed by impedance spectroscopy measurement) and surface defects on ZnO (Nam et al. 2017). PDEPB layer lowered the WF of the electron transporting ZnO layer (by UPS measurement) and increased the built-in potential, hence enabling efficient charge transport/extraction. The PCE was further improved to over 10% using PTB7Th:$PC_{71}BM$ as photoactive layer and ZnO/PDEPB (0.5 mg/mL) interlayer (Nam et al. 2016). The increase in the V_{OC} with PDEPB interlayers can be due to the increased V_{bi} caused by the dipolar interactions between PDEPB and ZnO, basically contributing to accelerate the charge transport process.

Aryal et al. synthesized a series of polyacetylene-based pyridinium salts (PPy1-PPy3) and used as cathode modifier of ZnO layer. Interfacial modification improved the PCE from 7.46% for a ZnO-based control device to ~8.3% for PTB7:$PC_{71}BM$ and to ~9.3% for PTB7-Th:$PC_{71}BM$ based devices (Aryal et al. 2018). Incorporation of CIL suppressed the charge recombination and thus facilitated charge extraction. The interlayer also protect the device from oxygen and humidity contamination and improved the device stability (88% retention after ~1000 h).

After the successful use of non-conjugated polyelectrolytes PEI and PEIE as neutral surface modifier by Kippelen and co-wokers, these materials have found significant importance in the single junction and tandem photovoltaic device fabrications (Zhou et al. 2012a, b). These materials successfully tune the WFs of metal electrodes, reduce the interfacial energy barrier and increase the build-in potential. For example the WF of ITO can be reduced from ~4.4 to ~3.3 eV (measured by UPS) by depositing thin film of solution-processed PEI or PEIE, originating from the strong electrostatic self-assembled dipoles formed due to polar amine groups.

Heeger and Bazan group introduced 80% ethoxylated PEIE on the top of the ZnO forming a composite film to enhance the device efficiency by lowering the work function of ZnO (Kyaw et al. 2013). Inverted OSCs using a small molecule p-DTS($FBTTh_2$)$_2$:$PC_{71}BM$ active layer demonstrated PCEs up to 7.88% using ZnO/PEIE CIL which is higher compared to bare ZnO (6.29%) or PEIE (5.18%). PEIE coating on ZnO lowered the WF of ZnO from 4.5 to 3.8 eV by creating a dipole moment at the interface and thus supresses the trap-assisted recombination. The increased V_{OC} for ZnO/PEIE based devices (0.77 V) compared to bare ZnO (0.72 V) can be attributed to the reduced WF of cathode after PEIE deposition.

Recently, Zhou and co-workers demonstrated that the PEIE interlayer can reduce the performance of fullerene-free devices by reacting with the acceptor molecules with amine leading to s-shaped *J*-*V* curve. The authors deactivate the chemical interaction by protonating the PEIE electrolyte processing from aqueous solution. OSCs

using PTB7-Th:IEICO-4F active layer and the protonated PEIE interfacial layer exhibited an excellent PCE of 13.2%, which is higher than the reference devices with ZnO interlayer (12.6%). Also the device processed from water eliminates further thermal annealing treatment (Xiong et al. 2019). It is important to note that the PEIE processed from alcohols such as isopropanol, ethanol, methanol gave <10% PCE due to low FF of 0.53–0.57 arising from s-shape character of the *J-V* curve.

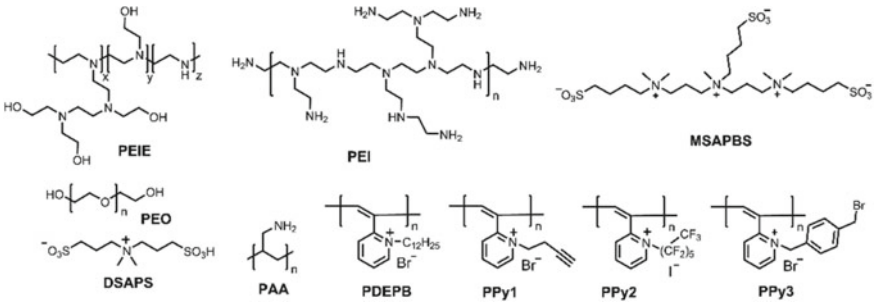

ooseness-1Ge and co-workers reported a non-conjugated zwitterionic MSAPBS which was used to modify the Al cathode and offer good ohmic contact for photogenerated charge carrier collection. Conventional device using ITO/PEDOT:PSS/PTB7:$PC_{71}BM$/MSAPBS/Al device structure gave a high PCE of 10.0%, much higher compared to PFN/Al (8.2%) and Ca/Al (7.99%) cathode (Ouyang et al. 2015). It has been shown that treatment of zwitterionic interlayer DSAPS dissolved in methanol eliminate the trade-off between V_{OC} and J_{SC}. The MeOH treatment increased the built-in voltage and surface potential, thus contributes to the V_{OC} enhancement and the CIL improve the charge transport and thus the J_{SC} and FF. The PCE of both conventional and inverted devices with PTB7/$PC_{71}BM$ blend improved from 3.89 to 9.79% and 7.34 to 9.10% (Liu et al. 2016b).

Li et al. adopted a vacuum-evaporation method to deposit fluorinated copper phthalocyanine ($F_{16}CuPc$) layer over the ITO/PEI buffer layer to modify the surface properties. The composite layer increase the electronic coupling between the ITO and organic layer and induce forward charge transfer by decreasing recombination of charges (Li et al. 2018b). The $F_{16}CuPc$ also regulates the growth of organic layer and control morphology. Optimized inverted device displayed the best PCE of 9.52% with 6 nm thick $F_{16}CuPc$ layer over PEI compared to 7.147% of the device without $F_{16}CuPc$. The PEI layer lowered the WF of ITO and reduce the Schottky barrier. The introduction of $F_{16}CuPc$ decreases the potential difference between ITO and active layer and helps to transport electrons to ITO cathode and also acts as hole blocking layer.

Fu et al. developed a modified ZnO ETL by surface ligand exchange of the hydroxyl group with 3-aminopropyl triethoxysilane (APTES) (Fu et al. 2017). The silane group can form crosslinking and modify the metal oxide surface by covalent bonding. The ZnO/APTES modified CIL gave an improved PCE of 9.46% for device

based on PTB7-Th/$PC_{71}BM$ active layer, a higher value than the control device without linker (8.47%). The aminosilane linker plays dual function to enhance the PCE, which includes (1) passivating the ZnO surface via silane groups and decreasing the surface WF of ZnO to 3.9 eV and (2) interaction with active layer to reduce the interface contact resistance. Recently, Ma and co-workers used the similar strategy to prepared air stable 3-aminopropyltrimethoxysilane (APTMS)-capped ZnO nanoparticle, which reduced the surface adsorbed oxygen defects, improved the charge transfer efficiency and most importantly suppressed the light-soaking effect of ZnO (Wei et al. 2018). The PCE of PTB7-Th/$PC_{71}BM$ using ZnO@APTMS gave a PCE of 9.07%, much higher than the bare ZnO (4.39%). It is interesting to note that the PCE of modified ZnO-based device does not influenced by the light soaking, however, the ZnO-based device was almost doubled after UV light soaking. The devices with modified interlayer also showed excellent air stability for a year.

Various polythiophene derivatives were prepared using pendant amino functionalities, such as *t*–butylpyridinium (P3TBPHT), trimethylammonium (P3TMAHT) and imidazolium (P3IMDHT). The polymers were synthesized by quaternization reaction of poly[3-(6-bromohexyl)thiophene] with the corresponding amines. The P3TBPHT and PEDOT:PSS were deposited on the ITO surface using eLbL technique discussed above. The number of layers control the WF of ITO from 4.6 to 3.8 eV and successfully used as cathode buffer layer. The OSCs prepared using P3TBPHT:PEDOT layer gave excellent PCEs of 5.6% and outstanding device stability retaining >90% of initial performance when stored over 1000 h in air compared to other metal oxides (Worfolk et al. 2012). Yang and co-workers P3TMAHT:SDS (sodium dodecylbenzene sulfonate) complex by simple mixing of both compounds and successfully used as polyelectrolyte in P3HTP:$C_{61}BM$ BHJ achieving PCE of 4.0% almost double compared to only Al (2.12%) due to large improvement in the V_{OC} and FF (Chang et al. 2012). Kesters et al. used an imidazolium-substituted polythiophene P3IMDHT as ETL, which perform close to the value of other analogous conjugated polyelectrolytes (CPE) (Kesters et al. 2013). The device performance also depends on the molecular weight (MW) of P3IMDHT and high MW gave the best performance. The interlayer creates an extra built-in electric field promoting charge transfer from the BHJ layer into the interlayer as investigated by scanning probe microscopy (Drijkoningen et al. 2014). Zilberberg et al. used an ultrathin layer of P3IMDHT as CIL in an PCDTBT:$PC_{71}BM$ inverted device which achieved very similar PCE (~4.8%) to that obtained for device with TiO_2 interlayer (Zilberberg et al. 2013). P3MAHT CPE when used over ITO/AZO layer an improved device performance was observed (Min et al. 2013).

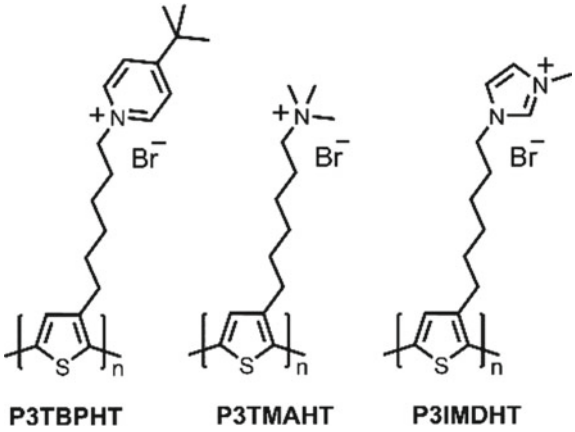

Cao and co-workers developed various alcohol-/water-soluble conjugated polymers, poly[(9,9-bis(3′-(*N,N*-dimethylamino)propyl)-2,7-fluorene)-alt-2,7-(9,9–dioctyldioctylfluorene)] (PFN) and poly[(9,9-bis(3′-((*N,N*-dimethyl)-*N*-ethylammonium)-propyl)-2,7-fluorene)-*alt*-2,7-(9,9-dioctylfluorene)] dibromide (PFN-Br) and used as the ITO surface modifier (Huang et al. 2004). Using an inverted device architecture a certified PCE of 9.2 and 8.2% for conventional structure was achieved which offered Ohmic contact for photogenerated charge carrier collection and improve photon harvesting (He et al. 2012). The same group further developed an alcohol soluble polyelectrolyte poly[(9,9-bis((*N*-(4-sulfonate-1-butyl)-*N,N*-dimethylammonium)propyl)-2,7-fluorene)-alt-2,7-(9,9-dioctylfluorene)] (PFNSO) containing sulfobetaine zwitterionic groups on their side chains to use as CIL. (Duan et al. 2013b) A PCE of 8.74% could be achieved using PTB7:$PC_{71}BM$ photoactive layer resulting from the small leakage current and lower series resistance. The same group further developed alcohol soluble thermal cross-linkable, conjugated polyfluorene, poly[(9,9-bis(6′-(N,N-dimethylamino)propyl)-2,7-fluorene)-alt-2,7-(9,9-bis(3-ethyl(oxetane-3-ethyloxy)-hexyl)-fluorene)] (PFN-OX). (Hu et al. 2014) PFN-OX electron extraction layer can be completely crosslinked at 140 °C forming a smooth layer over ITO and modify the WF of ITO to 3.5 eV to match with the LUMO level of $PC_{71}BM$. Inverted BHJ device using PBDT–DTNT:$PC_{71}BM$ exhibited a PCE of 8.62% with a BHJ film thickness of 280 nm. While device without PFN-OX layer gave very low PCE of 1.42% due to very low V_{OC} (0.32 V) and FF (0.31). Remarkable PCE of 7.24% has also been measured with BHJ thickness of 1000 nm demonstrating high hole mobility and ordered molecular structure of donor polymer.

Cao and co-workers demonstrated the incorporation of PFN as CIL between PCDTBT:$PC_{71}BM$ blend and Al simultaneously improved the V_{OC}, J_{SC} and FF, thus the PCE from 4.02 to 6.73% (He et al. 2011b). The V_{OC} was improved from 0.71 to 0.91 V and FF from 0.49 to 0.62. It has been shown that the device with PFN/Al exhibited a high turn-on voltage of 0.8–1.0 V compared to bare Al device (0.5–0.6 V), indicating the enhancement of V_{bi} across the device with PFN layer which is key to the V_{OC} improvement. The role of PFN layer was further studied by

scanning Kelvin probe microscopy (SKPM) measurement, which revealed the PFN interlayer can effectively prevent the built-up of space charge under light, thus have a strong impact on the charge carrier transport. The PFN layer formed a microscopic electric dipole and the direction of the dipole was aligned with the V_{bi}.

Han et al. used ZnO/PFN bilayer as CIL in which the ZnO nanoparticles can function as an efficient ETL to reduce series resistance, while the PFN can improve the energy level alignment through the formation of an interfacial dipole between ZnO and photoactive layer. The inverted device gave high performance using bilayer ZnO/PFN compared to only ZnO or PFN-based devices (Han et al. 2016).

Guo et al. demonstrated an enhancement of the OSC performance with ternary PEI/SnO_2/PFN composite interlayer by modulating the energy level between the active layer and electrode and reduced the interfacial defects (Guo et al. 2019). The inverted device using this ternary interlayer led to a dramatic increase in the device performance with PCE of 7.18% compared to 5.5% larger shunt resistance (R_{sh}) and a decrease of series or contact resistance (R_s) were observed, which could prevent the leakage current, resulting in the increased J_{SC} and FF.

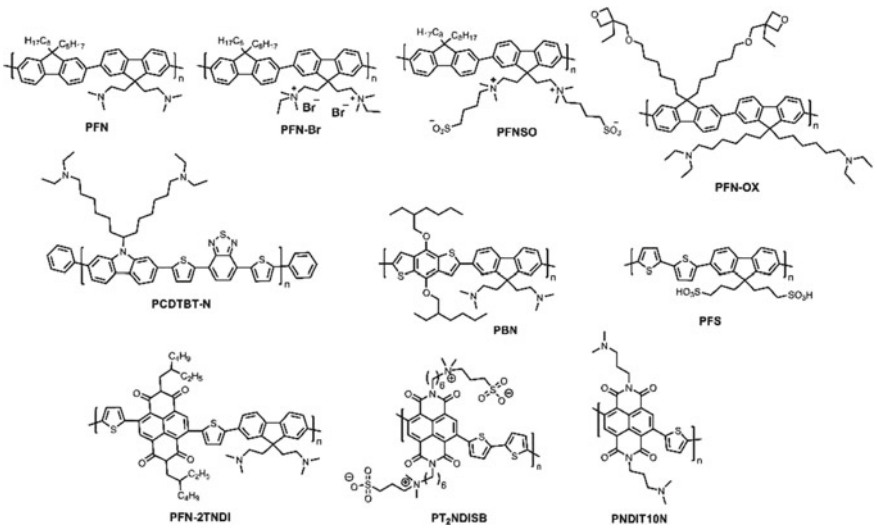

Recently, using PFN-Br/Ag as CIL in PTB7-Th:PDIBDT-IT based fullerene-free devices generated a PCE of 6.06% (Liu et al. 2018). PFN-Br was used to effectively alleviate the interfacial energy barrier in the device. Hou and co-workers demonstrated that by mixing ZnO nanoparticles with PFN-Br the surface free energy of ZnO layers can be tuned from 51.23 to 76.62 mN m^{-1} (Zheng et al. 2019). BHJSCs constructed from PBDB-TF:IT-4F photoactive layer excellent PCE of 13.82% was achieved together with a record FF value of 0.79. Transient photovoltage measurement revealed longer electron lifetime suggesting retardation of charge carrier recombination as well boost the exciton dissociation efficiency. The introduction of PFN-Br

into ZnO ETL, the stability of ETL increased and is related to the suppressed aggregations of ZnO nanoparticles.

Mishra et al. demonstrated a low energy loss (E_{loss}) in conventional fullerene-free solar cells using P1:DCI-2 blend and PFN as CIL. The device exhibited a PCE of 6.94% with low E_{loss} of 0.39 V showing the importance of PFN layer on device performance (Mishra et al. 2017). The authors further reported a PCE of 7.24% using a D: A based organic molecule TPA-SN5-DCV:$PC_{71}BM$ blend using PFN/Al cathode after solvent additive treatment followed by thermal annealing (Mishra et al. 2018).

Duan et al. developed a conjugated alcohol soluble PCDTBT-N functionalized with tertiaryamine pendant groups and used as buffer layer in metal: organic interface to improve electron collection efficiency (Duan et al. 2013a). The amino groups formed complex with C_{70} and act as hole traps as well shift the Fermi level from about 4.6–4.2 eV. PCDTBT:$PC_{71}BM$-based devices gave PCE of 5.32% compared to without interlayer due to the reduced transport loss for efficient electron collection through the n-doping of $PC_{71}BM$.

Kim et al. prepared a conjugated polyelectrolyte PBN consisting of benzodithiophene and fluorine units as CIL for ZnO surface modification (Kim et al. 2014). PBN creates an interfacial dipoles at the ZnO/organic interface and improve the contact between the layers thus enhanced the PCE of PTB7:$PC_{71}BM$ by about 21% i.e. from 7.1 to 8.6%.

Hou group developed a unique polymer poly[9,9-bis(1-sulfopropane-3-yl)-fluorene-2,7-diyl-alt-(2,2′-bithiophene-5,5′)-diyl] (PFS) comprising sulfonic acid containing fluorene and bithiophene unit which acts as both anode and cathode interfacial layers. The device with PDBT-TS1:$PC_{71}BM$ achieved a high PCE of 9.48% and comparable to device with PEDOT:PSS (9.76%) or Mg (9.63%) as anode and cathode interlayers (Xu et al. 2016).

Sun et al. reported fullerene-free OSCs with a PCE of over 11% by introducing n-type PFN or PFN-2TNDI as CIL (Sun et al. 2017). The results revealed that the contact between the n-type interlayer and the donor provides an extra interface for charge dissociation and the matching of energy levels between the interlayer and the acceptor allows efficient electron extraction from the BHJ at the interface. Furthermore, in contrast to PFN, PFN-2TNDI layer is suitable for exciton dissociation due to appropriate energy level offset between the donor and interlayer resulting in enhanced photocurrent generation.

A conjugated polymer PT_2NDISB containing napthalenediimide and bithiophene with pendant zwitterionic groups was synthesized via Suzuki coupling reaction and incorporated as interlayer between active layer and Ag in OSCs. A thin layer of polymer interlayer (~8 nm) increased the device efficiency from 3.17 to 10.19%. The interlayer lowered the WF to 3.8 eV, increase the V_{bi} and reduces the pinholes formation. The CIL act as optical spacers to enhance total photocurrent generated within the active layer (Liu et al. 2015b). Using a NDI derivative PNDIT10 N as CIL and MoO_x as AIL, the inverted device using PTB7-Th:$PC_{71}BM$ gave a PCE of 7.0% (Bjuggren et al. 2018). UPS spectroscopy demonstrated reduction in the ITO work function after surface modification which is related to the formation of interfacial

dipole by the electron pair present in the pendant nitrogen atoms which facilitates electron collection and transport to the ITO cathode (van Reenen et al. 2014; Lee et al. 2018). The PNDIT10 N also acts as hole blocking layer due to its low lying HOMO energy level.

18.2.2 Hole Transport Materials as Anode Interface Layers

For materials to be used as AIL, the WF should be high enough to match with the HOMO of the donor for efficient hole extraction. An efficient hole transport led to reduction in the series resistance. The AIL materials should possess high optical transparency, good chemical stability, good optical transmittance, a high ionization potential and suitable electron blocking ability. AIL has similar importance as CIL in order to obtain high performance devices (Xu and Hou 2018). The reaction between the active layer and metal electrode due to diffusion of metal ion resulted in detrimental effect on device performance forming interfacial dipole barrier and defect states. Earlier, it has been shown that the s-shape current density-voltage (*J-V*) curve resulted from the interfacial barrier (Trost et al. 2013; Tress et al. 2011). Variation of hole selective layer can strongly affect the s-shape in the device. Sims et al. reported that by introducing 1,4,5,8,9,11-hexaazatriphenylenehexacarbonitrile (HATCN) to the N,N′-bis(3-methylphenyl)-N,N′-bis(phenyl)benzidine (TPD) layer the WF and mobility of the hole selective layer can be tuned and effectively reduce the s-shape and improve the FF (Sims et al. 2014). Here HATCN worked as inert buffer layer which prevent diffusion and chemical reaction at the interface. Subbiah et al. used a bilayer of MoO_3/MTDATA (4,4′,4″-tris(3-methylphenylphenylamino) triphenylamine) processed by vacuum-deposition as AIL and improved the device performance of an inverted device 5.8–6.45% suggesting an improvement of the hole extraction from the photoactive layer to the anode, effectively blocks the electrons and allowed favourable vertical morphology of active layer blend (Subbiah et al. 2012). Various triarylamine based HTMs have been successfully utilized to improve the hole transporting process in vacuum-process OSCs (Walzer et al. 2007; Mishra et al. 2011; Fitzner et al. 2011, 2012; Schulze et al. 2006).

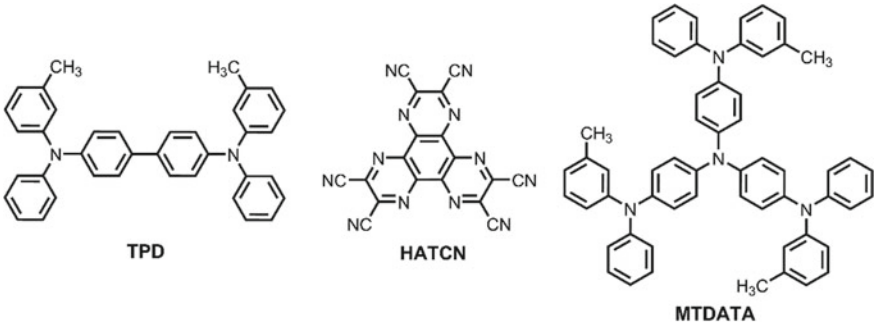

Conventional solution-processed OSCs generally used PEDOT:PSS (WF ≈ 5.1 eV) as AIL and many high performance devices have been reported. However, PEDOT:PSS influences the device long term stability due to its acidic nature. To improve the device performance and stability PEDOT:PSS has been modified with metal nanoparticles, such as Ag and Au. The photovoltaic data of some representative devices with various HTLs are presented in Table 18.4. Using colloidal Ag nanoprism embedded with PEDOT:PSS as AIL and modified bis-C_{60} as CIL, enhancement in the PCE from 7.7 to 9.0% has been observed due to enhanced optical absorption. (Yao et al. 2014) Au@Ag core–shell nanocube (NC) showing strong plasmonic light scattering effect than Au nanoparticles when used as AIL with PEDOT:PSS the PCE of PCDTBT:PC_{71}BM solar cells improved from 5.3 to 6.3% and for PTB7:PC_{71}BM PCE improved from 7.9 to 9.2% (Baek et al. 2014). The Ag shell acted to enhance the plasmonic scattering and improve the absorption of Au@Ag nanocube. Solution-processable MoO_x as AIL have improved the photovoltaic performance and device stability compared to PEDOT:PSS. (Tan et al. 2013) NiO nanoparticle when used as AIL in PTB7:PC_{71}BM blend achieved a high PCE of 9.16% which is higher than that of PEDOT:PSS based devices (8.6%) (Jiang et al. 2015).

Solution-processed OSCs using dithieno[3,2-*b*:2′,3′-*d*]pyrrole (DTP)-based small molecule donor and PC_{61}BM acceptor as active layer and either PEDOT:PSS or V_2O_5 as AIL were prepared. Devices with V_2O_5 gave much better performance with very high FF up to ~0.60 compared to PEDOT:PSS (~0.50) was ascribed to the improved hole collection at the anode associated with a better match between the WF of V_2O_5 and the HOMO of the donor as well different surface energy at the interface. When polydimethylsiloxane (PDMS) was used as solvent additive the PCE with V_2O_5 AIL was improved to 5.3% (Schulz et al. 2016). Small molecule OSCs employing CuSCN as AIL obtained a PCE of 8.22% (V_{OC} = 0.86, FF = 0.68) compared to 7.54% (V_{OC} = 0.84, FF = 0.65) for PEDOT:PSS AIL (Mishra et al. 2016). Both device gave nearly similar photocurrent values which could be ascribed to the similar transparencies in the visible region. The improvement in the FF was related to the formation of better ohmic contact between the active layer and CuSCN, because of the high WF of CuSCN than PEDOT:PSS. The high V_{OC} was due to better alignment of HOMO of the donor and valance band of CuSCN (−5.35 eV) which also acts as good electron blocking layer.

Various p-type small molecules and polymers have been prepared and used in conventional and inverted devices. Heeger and co-workers used chlorobenzoic acid (CBA) as surface modifier of ITO electrode which produce a high WF electrode with better transparency as an alternative to PEDOT:PSS. The benzoic acid bound to the surface and chlorine atom pointed towards the organic layer forming a dipole. The PTB7:PC_{71}BM based device achieved an improved PCE of 8.5% for CBA AIL compared to 7.5% for PEDOT:PSS, ascribed improved light absorption and formation of an Ohmic contact for hole transport (Choi et al. 2015). Huang et al. demonstrated the enhancement of WF of ITO surface by self-assembling different benzoic acid and sulfonic acids on the ITO surface (Huang et al. 2016). The WF of SAM-modified ITO changed in the order CBSA (5.18 eV), CBA (4.91 eV), FBA (4.85 eV), and BA (4.75 eV) when applied with same concentration. Among all derivatives CBSA

Table 18.4 Summary of photovoltaic performance based on representative AILs

Anode structure	Active layer	Cathode structure	V_{OC} (V)	J_{SC} (mA cm^{-2})	FF	PCE (%)	References
MTDATA/MoO_3/Ag	PDTS-BTD:$PC_{71}BM$	ITO/ZnO	0.61	17.8	0.59	6.45	Subbiah et al. (2012)
ITO/PEDOT:PSS + Ag NPs	PIDTT-DFBT:$PC_{71}BM$	Bis-C_{60} + Ag NPs/Ag	0.96	14.4	0.63	9.02	Yao et al. (2014)
ITO/PEDOT:PSS + Au@Ag	PTB7:$PC_{71}BM$	TiO_X/Al.	0.75	17.5	0.70	9.19	Baek et al. (2014)
ITO/MoOx	P3HT:IC60BA	Ca/Al	0.85	10.4	0.72	6.29	Tan et al. (2013)
ITO/NiO_X	PTB7-Th:$PC_{71}BM$	Ca/Al	0.79	18.3	0.63	9.16	Jiang et al. (2015)
ITO/V_2O_5	DTP2THex:$PC_{61}BM$	LiF/Al	1.07	7.9	0.63	5.30	Schulz et al. (2016)
ITO/PEDOT:PSS	2IN:$PC_{71}BM$	Al	0.84	13.8	0.65	7.54	Mishra et al. (2016)
ITO/CuSCN	2IN:$PC_{71}BM$	Al	0.86	14.1	0.68	8.22	Mishra et al. (2016)
ITO/CBA	PTB7:$PC_{71}BM$	Al	0.74	16.5	0.70	8.48	Choi et al. (2015)
ITO/CBSA (0.1 mg/ml)	PTB7-Th:$PC_{71}BM$	PFN/Al	0.80	16.4	0.70	9.20	Huang et al. (2016)
ITO/CBA (1.0 mg/ml)	PTB7-Th:$PC_{71}BM$	PFN/Al	0.80	16.3	0.66	8.60	Huang et al. (2016)
ITO/FBA (1.0 mg/ml)	PTB7-Th:$PC_{71}BM$	PFN/Al	0.72	16.1	0.62	7.10	Huang et al. (2016)
ITO/BA (1.0 mg/ml)	PTB7-Th:$PC_{71}BM$	PFN/Al	0.66	15.2	0.61	6.10	Huang et al. (2016)
ITO/CBSC (1.0 mg/ml)	PTB7-Th:$PC_{71}BM$	PFN/Al	0.80	16.7	0.68	9.10	Huang et al. (2016)
ITO/PABTSi_2:TFB	P3HT:$PC_{61}BM$	LiF/Al	0.54	9.31	0.63	3.10	Hains et al. (2010)
ITO/TPDSi_2:TFB	P3HT:$PC_{61}BM$	LiF/Al	0.55	4.72	0.10	0.28	Hains et al. (2010)

(continued)

Table 18.4 (continued)

Anode structure	Active layer	Cathode structure	V_{OC} (V)	J_{SC} (mA cm^{-2})	FF	PCE (%)	References
ITO/TPDB	P3HT:$PC_{61}BM$	LiF/Al	0.55	8.62	0.64	3.03	Lu et al. (2013)
ITO/TPDB	PBDTTPD:$PC_{61}BM$	LiF/Al	0.87	11.5	0.65	6.51	Lu et al. (2013)
ITO/PCP-Na	PBDT-TS1:$PC_{71}BM$	Mg/Al	0.80	17.5	0.71	9.89	Cui et al. (2016)
ITO/PCF-Na	PBDT-TS1:$PC_{71}BM$	Mg/Al	0.80	17.5	0.68	9.45	Cui et al. (2016)
ITO/PFS-Na	PBDT-TS1:$PC_{71}BM$	Mg/Al	0.79	16.5	0.63	8.16	Cui et al. (2016)

showed the best PCE with 9.2% with PTB7–Th:$PC_{71}BM$ using 0.1 mg/mL CBSA. However, with increasing the concentration of CBSA the performance were reduces to 7.7% for 1.0 mg/mL. All other derivatives gave best performance with 1.0 mg/mL of surface modifiers. Considering the acidic nature of CBSA the authors also prepared SAM with chlorobenzenesulfonyl chloride (CBSC) which gave similar PCEs of 9.1% and significantly improved the device stability. A triple dipole effect for Cl-assisted self-assembled molecule on ITO has been proposed.

Mark et al. developed two AILs ($TPDSi_2$, $PBATSi_2$) and implemented in P3HT:$PC_{61}BM$ device (Hains et al. 2010). The molecules were anchor on the ITO surface via $SiCl_3$ groups and form cross linking by 1:2 blending with TFB polymer. The devices based on $PBATSi_2$:TFB interlayer gave PCE of 3.14% similar to PEDOT:PSS, while the $TPDSi_2$:TFB exhibited very poor PCE of only 0.28% and FF of 0.10 due to s-shape curve. This poor performance of $TPDSi_2$ the large HOMO energy mismatch of TPDSi2 (HOMO = −5.3 eV) and P3HT (−5.0 eV) forming a barrier to hole transport/collection at the anode. However, the HOMO energy of $PBATSi_2$ (−4.9 eV) align well with P3HT and the LUMO is high enough to block the electrons.

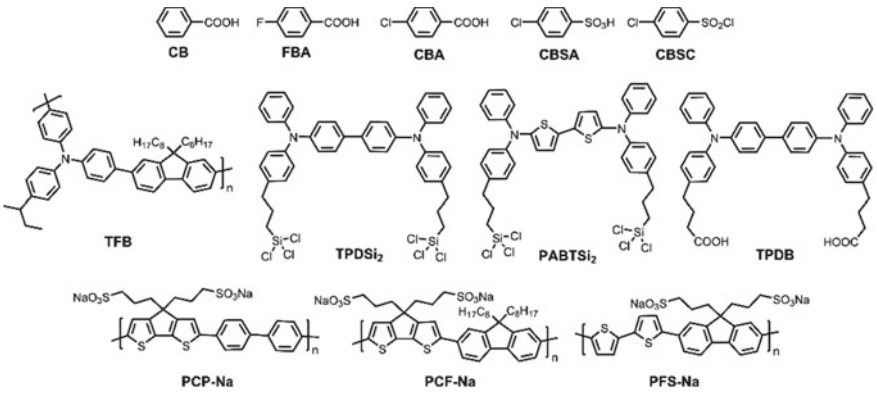

Small molecule TPDB comprising carboxyl side chains was implemented as AIL in P3HT:$PC_{61}BM$ and PBDTTPD:$PC_{61}BM$ based devices due to its high transparency in the visible region and appropriate energy level alignment for hole transporting and electron blocking capacity. The devices based on these new HTLs gave improved PCEs up to 6.51% compared to PEDOT:PSS buffer layer and better device stability (Lu et al. 2013).

Hou and co-workers developed three pH neutral conjugated polymers, namely PCP-Na, PCF-Na, and PFS-Na and tested AILs in conventional OSCs. Among the three polymers PCP-Na exhibited self-doping ability and with high electrical conductivity of 1.66×10^{-3} S cm^{-1}. OSCs prepared with PCP-Na as AIL recorded PCEs of up to 9.89% and possess thickness insensitivity over 300 nm, retaining FF of 70% (Cui et al. 2016).

18.3 Conclusions and Outlook

In this chapter we have explored some cathode and anode interfacial materials and their role in solution-processed organic solar cells. Together with the development of novel active layer materials (polymers or oligomers), the interfacial materials design have found equal importance toward their role in device performance improvement. These interlayer materials have gained tremendous interest in recent years and been successfully employed in high performance conventional and inverted devices. A structure-property device performance relationships have been established which is beneficial for the development of new interlayer materials. Furthermore, with an effort towards molecular design, from neutral to charged materials, the optical properties, energy levels, charge carrier mobilities, conductivity, work function as well as surface morphology and surface energy can be tuned, and therefore affecting the OSC performance. When these materials are combined with suitable donor: acceptor photoactive layers and device processing conditions high performance single junction solar cells reaching PCEs >10% have been achieved. Recently, record PCE exceeding 17% was reported for an inverted tandem cell using ZnO/PFN-Br as CIL, PEDOT:PSS/ZnO as interconnecting layer and MoO_3/Ag as AIL showing the importance of molecular design of different active layers, interlayers and device engineering (Meng et al. 2018). Apart from device efficiency, the device stability is also an important issue which was almost solved by the use of metal oxides as interlayer in inverted devices. Simultaneously, together with the performance the use of organic and polymeric interlayers have also shown tremendous improvement in device stability. Sometime very thin interlayer is sufficient to get high efficiency. However, for practical applicability of the technology it is also important to develop thickness insensitive interlayers which are very rare at this moment. Now it is also important to exploit the potential of various interlayer materials in different device configuration which could open up new opportunities towards performance improvement and PCE of >20% is not far to reach.

Acknowledgements The authors would like to acknowledge the Sambalpur University for providing research infrastructure and Department of Science and Technology (DST), New Delhi (DST/TMD/SERI/D05) for financial support.

References

Aryal UK, Chakravarthi N, Park H-Y, Bae H, Jin S-H, Gal Y-S (2018) Highly efficient polyacetylene–based polyelectrolytes as cathode interfacial layers for organic solar cell applications. Org Electron 53:265–272

Baek S-W, Park G, Noh J, Cho C, Lee C-H, Seo M-K, Song H, Lee J-Y (2014) Au@Ag core-shell nanocubes for efficient plasmonic light scattering effect in low bandgap organic solar cells. ACS Nano 8(4):3302–3312

Bao X, Sun L, Shen W, Yang C, Chen W, Yang R (2014) Facile preparation of TiO_X film as an interface material for efficient inverted polymer solar cells. J Mater Chem A 2(6):1732–1737

Bilby D, Frieberg B, Kramadhati S, Green P, Kim J (2014) Design considerations for electrode buffer layer materials in polymer solar cells. ACS Appl Mater Interfaces 6(17):14964–14974

Bjuggren JM, Sharma A, Gedefaw D, Elmas S, Pan C, Kirk B, Zhao X, Andersson G, Andersson MR (2018) Facile synthesis of an efficient and robust cathode interface material for polymer solar cells. ACS Appl Energy Mater 1(12):7130–7139

Bob B, Song T-B, Chen C-C, Xu Z, Yang Y (2013) Nanoscale dispersions of gelled SnO_2: material properties and device applications. Chem Mater 25(23):4725–4730

Chan MY, Lee CS, Lai SL, Fung MK, Wong FL, Sun HY, Lau KM, Lee ST (2006) Efficient organic photovoltaic devices using a combination of exciton blocking layer and anodic buffer layer. J Appl Phys 100(9):094506

Chang Y-M, Zhu R, Richard E, Chen C-C, Li G, Yang Y (2012) Electrostatic self-assembly conjugated polyelectrolyte-surfactant complex as an interlayer for high performance polymer solar cells. Adv Funct Mater 22(15):3284–3289

Chen L-M, Xu Z, Hong Z, Yang Y (2010) Interface investigation and engineering—achieving high performance polymer photovoltaic devices. J Mater Chem 20:2575–2598

Chen Q, Worfolk BJ, Hauger TC, Al-Atar U, Harris KD, Buriak JM (2011) Finely tailored performance of inverted organic photovoltaics through layer-by-layer interfacial engineering. ACS Appl Mater Interfaces 3(10):3962–3970

Chen S, Small CE, Amb CM, Subbiah J, Lai T-h, Tsang S-W, Manders JR, Reynolds JR, So F (2012) Inverted polymer solar cells with reduced interface recombination. Adv Energy Mater 2(11):1333–1337

Chen D, Zhou H, Cai P, Sun S, Ye H, Su S-J, Cao Y (2014) A water-processable organic electron-selective layer for solution-processed inverted organic solar cells. Appl Phys Lett 104(5):053304

Chen J-D, Cui C, Li Y-Q, Zhou L, Ou Q-D, Li C, Li Y, Tang J-X (2015) Single-junction polymer solar cells exceeding 10% power conversion efficiency. Adv Mater 27(6):1035–1041

Chen W, Lv J, Han J, Chen Y, Jia T, Li F, Wang Y (2016) N-Type cathode interlayer based on dicyanomethylenated quinacridone derivative for high-performance polymer solar cells. J Mater Chem A 4(6):2169–2177

Choi H, Kim H-B, Ko S-J, Kim JY, Heeger AJ (2015) An organic surface modifier to produce a high work function transparent electrode for high performance polymer solar cells. Adv Mater 27(5):892–896

Chueh C-C, Li C-Z, Jen AKY (2015) Recent progress and perspective in solution-processed Interfacial materials for efficient and stable polymer and organometal perovskite solar cells. Energy Environ Sci 8(4):1160–1189

Cui Y, Xu B, Yang B, Yao H, Li S, Hou J (2016) A novel pH neutral self-doped polymer for anode interfacial layer in efficient polymer solar cells. Macromolecules 49(21):8126–8133

Dkhil SB, Duché D, Gaceur M, Thakur AK, Aboura FB, Escoubas L, Simon J-J, Guerrero A, Bisquert J, Garcia-Belmonte G, Bao Q, Fahlman M, Videlot-Ackermann C, Margeat O, Ackermann J (2014) Interplay of optical, morphological, and electronic effects of ZnO optical spacers in highly efficient polymer solar cells. Adv Energy Mater 4(18):1400805

Drijkoningen J, Kesters J, Vangerven T, Bourgeois E, Lutsen L, Vanderzande D, Maes W, D'Haen J, Manca J (2014) Investigating the role of efficiency enhancing interlayers for bulk heterojunction solar cells by scanning probe microscopy. Org Electron 15(6):1282–1289

Duan C, Zhong C, Liu C, Huang F, Cao Y (2012) Highly efficient inverted polymer solar cells based on an alcohol soluble fullerene derivative interfacial modification material. Chem Mater 24(9):1682–1689

Duan C, Cai W, Hsu BBY, Zhong C, Zhang K, Liu C, Hu Z, Huang F, Bazan GC, Heeger AJ, Cao Y (2013a) Toward green solvent processable photovoltaic materials for polymer solar cells: the role of highly polar pendant groups on charge carrier transport and photovoltaic behavior. Energy Environ Sci 6:3022–3034

Duan C, Zhang K, Guan X, Zhong C, Xie H, Huang F, Chen J, Peng J, Cao Y (2013b) Conjugated zwitterionic polyelectrolyte-based interface modification materials for high performance polymer optoelectronic devices. Chem Sci 4:1298–1307

Duan C, Zhang K, Zhong C, Huang F, Cao Y (2013c) Recent advances in water/alcohol-soluble π-conjugated materials: new materials and growing applications in solar cells. Chem Soc Rev 42(23):9071–9104

Fan P, Zheng Y, Song J, Yu J (2017) N-type small molecule as an interfacial modification layer for efficient inverted polymer solar cells. Sol Energy 158:278–284

Fitzner R, Reinold E, Mishra A, Mena-Osteritz E, Ziehlke H, Körner C, Leo K, Riede M, Weil M, Tsaryova O, Weiß A, Uhrich C, Pfeiffer M, Bäuerle P (2011) Dicyanovinyl-substituted oligothiophenes: structure-property relationships and application in vacuum-processed small molecule organic solar cells. Adv Funct Mater 21(5):897–910

Fitzner R, Mena-Osteritz E, Mishra A, Schulz G, Reinold E, Weil M, Körner C, Ziehlke H, Elschner C, Leo K, Riede M, Pfeiffer M, Uhrich C, Bäuerle P (2012) Correlation of π-conjugated oligomer structure with film morphology and organic solar cell performance. J Am Chem Soc 134(27):11064–11067

Fu P, Guo X, Wang S, Ye Y, Li C (2017) Aminosilane as a molecular linker between the electron-transport layer and active layer for efficient inverted polymer solar cells. ACS Appl Mater Interfaces 9(15):13390–13395

Gadisa A, Hairfield T, Alibabaei L, Donley CL, Samulski ET, Lopez R (2013) Solution processed al-doped ZnO nanoparticles/tiox composite for highly efficient inverted organic solar cells. ACS Appl Mater Interfaces 5(17):8440–8445

Gommans H, Verreet B, Rand BP, Muller R, Poortmans J, Heremans P, Genoe J (2008) On the role of bathocuproine in organic photovoltaic cells. Adv Funct Mater 18(22):3686–3691

Guo J, Ren G, Han W, Sun Y, Wang M, Zhou Y, Shen L, Guo W (2019) Facilitating electron extraction of inverted polymer solar cells by using organic/inorganic/organic composite buffer layer. Org Electron 68:187–192

Hains AW, Ramanan C, Irwin MD, Liu J, Wasielewski MR, Marks TJ (2010) Designed bithiophene-based interfacial layer for high-efficiency bulk-heterojunction organic photovoltaic cells. Importance of Interfacial Energy Level Matching. ACS Appl Mater Interfaces 2(1):175–185

Han C, Cheng Y, Chen L, Qian L, Yang Z, Xue W, Zhang T, Yang Y, Cao W (2016) Enhanced performance of inverted polymer solar cells by combining ZnO nanoparticles and poly[(9,9-bis(3′-(N, N-dimethylamino)propyl)-2,7-fluorene)-alt-2,7-(9,9-dioctyfluorene)] as electron transport layer. ACS Appl Mater Interfaces 8(5):3301–3307

Hau SK, Yip H-L, Baek NS, Zou J, O'Malley K, Jen AKY (2008) Air-stable inverted flexible polymer solar cells using zinc oxide nanoparticles as an electron selective layer. Appl Phys Lett 92(25):253301–253303

Hau SK, O'Malley KM, Cheng Y, Yip H, Ma H, Jen AK (2010) Optimization of active layer and anode electrode for high-performance inverted bulk-heterojunction solar cells. IEEE J Sel Top Quantum Electron 16(6):1665–1675

He Z, Zhang C, Xu X, Zhang L, Huang L, Chen J, Wu H, Cao Y (2011a) Largely enhanced efficiency with a PFN/Al bilayer cathode in high efficiency bulk heterojunction photovoltaic cells with a low bandgap polycarbazole donor. Adv Mater 23(27):3086–3089

He Z, Zhong C, Huang X, Wong W-Y, Wu H, Chen L, Su S, Cao Y (2011b) Simultaneous enhancement of open-circuit voltage, short-circuit current density, and fill factor in polymer solar cells. Adv Mater 23(40):4636–4643

He Z, Zhong C, Su S, Xu M, Wu H, Cao Y (2012) Enhanced power-conversion efficiency in polymer solar cells using an inverted device structure. Nat Photon 6:591–595

Hiramoto M, Suemori K, Matsumura Y, Miyata T, Yokoyama M (2006) P-I-N junction organic solar cells. Mol Cryst Liq Cryst 455:267–275

Hu X, Yi C, Wang M, Hsu C-H, Liu S, Zhang K, Zhong C, Huang F, Gong X, Cao Y (2014) High-performance inverted organic photovoltaics with over 1-μm thick active layers. Adv Energy Mater 4(15):1400378

Hu Z, Zhang F, An Q, Zhang M, Ma X, Wang J, Zhang J, Wang J (2018) Ternary nonfullerene polymer solar cells with a power conversion efficiency of 11.6% by inheriting the advantages of binary cells. ACS Energy Lett 3(3):555–561

Huang F, Wu H, Wang D, Yang W, Cao Y (2004) Novel electroluminescent conjugated polyelectrolytes based on polyfluorene. Chem Mater 16(4):708–716

Huang L, Chen L, Huang P, Wu F, Tan L, Xiao S, Zhong W, Sun L, Chen Y (2016) Triple dipole effect from self-assembled small-molecules for high performance organic photovoltaics. Adv Mater 28(24):4852–4860

Irwin MD, Buchholz DB, Hains AW, Chang RPH, Marks TJ (2008) *p*-type semiconducting nickel oxide as an efficiency-enhancing anode interfacial layer in polymer bulk-heterojunction solar cells. Proc Nat Acad Sci 105(8):2783–2787

Jheng J-F, Lai Y-Y, Wu J-S, Chao Y-H, Wang C-L, Hsu C-S (2013) Influences of the non-covalent interaction strength on reaching high solid-state order and device performance of a low bandgap polymer with axisymmetrical structural units. Adv Mater 25(17):2445–2451

Jiang F, Choy WCH, Li X, Zhang D, Cheng J (2015) Post-treatment-free solution-processed non-stoichiometric NiOx nanoparticles for efficient hole-transport layers of organic optoelectronic devices. Adv Mater 27(18):2930–2937

Jørgensen M, Norrman K, Gevorgyan SA, Tromholt T, Andreasen B, Krebs FC (2012) Stability of polymer solar cells. Adv Mater 24(5):580–612

Kang H, Hong S, Lee J, Lee K (2012) Electrostatically self-assembled nonconjugated polyelectrolytes as an ideal interfacial layer for inverted polymer solar cells. Adv Mater 24(22):3005–3009

Kesters J, Ghoos T, Penxten H, Drijkoningen J, Vangerven T, Lyons DM, Verreet B, Aernouts T, Lutsen L, Vanderzande D, Manca J, Maes W (2013) Imidazolium-substituted polythiophenes as efficient electron transport materials improving photovoltaic performance. Adv Energy Mater 3(9):1180–1185

Kim JB, Ahn S, Kang SJ, Nuckolls C, Loo Y-L (2013) Ligand chemistry of titania precursor affects transient photovoltaic behavior in inverted organic solar cells. Appl Phys Lett 102(10):103302

Kim HI, Bui TTT, Kim G-W, Kang G, Shin WS, Park T (2014) A benzodithiophene-based novel electron transport layer for a highly efficient polymer solar cell. ACS Appl Mater Interfaces 6(18):15875–15880

Kim G, Kong J, Kim J, Kang H, Back H, Kim H, Lee K (2015) Overcoming the light-soaking problem in inverted polymer solar cells by introducing a heavily doped titanium sub-oxide functional layer. Adv Energy Mater 5(3):1401298

Kyaw AKK, Sun XW, Jiang CY, Lo GQ, Zhao DW, Kwong DL (2008) An inverted organic solar cell employing a sol-gel derived ZnO electron selective layer and thermal evaporated MoO_3 hole selective layer. Appl Phys Lett 93(22):221107

Kyaw AKK, Wang DH, Gupta V, Zhang J, Chand S, Bazan GC, Heeger AJ (2013) Efficient solution-processed small-molecule solar cells with inverted structure. Adv Mater 25(17):2397–2402

Lai T-H, Tsang S-W, Manders JR, Chen S, So F (2013) Properties of interlayer for organic photovoltaics. Mater Today 16(11):424–432

Lai Y-Y, Cheng Y-J, Hsu CS (2014) Applications of functional fullerene materials in polymer solar cells. Energy Environ Sci 7:1866–1883

Lee K, Kim JY, Park SH, Kim SH, Cho S, Heeger AJ (2007) Air-stable polymer electronic devices. Adv Mater 19(18):2445–2449

Lee BH, Jung IH, Woo HY, Shim H-K, Kim G, Lee K (2014a) Multi-charged conjugated polyelectrolytes as a versatile work function modifier for organic electronic devices. Adv Funct Mater 24(8):1100–1108

Lee BR, Jung ED, Nam YS, Jung M, Park JS, Lee S, Choi H, Ko S-J, Shin NR, Kim Y-K, Kim SO, Kim JY, Shin H-J, Cho S, Song MH (2014b) Amine-based polar solvent treatment for highly efficient inverted polymer solar cells. Adv Mater 26(3):494–500

Lee J-H, Jeong SY, Kim G, Park B, Kim J, Kee S, Kim B, Lee K (2018) Reinforcing the built-in field for efficient charge collection in polymer solar cells. Adv Funct Mater 28(10):1705079

Li G, Chu C-W, Shrotriya V, Huang J, Yang Y (2006) Efficient inverted polymer solar cells. Appl Phys Lett 88(25):253503

Li S, Lei M, Lv M, Watkins SE, Za Tan, Zhu J, Hou J, Chen X, Li Y (2013) [6,6]-Phenyl-C61-butyric acid dimethylamino ester as a cathode buffer layer for high-performance polymer solar cells. Adv Energy Mater 3(12):1569–1574

Li N, Baran D, Spyropoulos GD, Zhang H, Berny S, Turbiez M, Ameri T, Krebs FC, Brabec CJ (2014a) Environmentally printing efficient organic tandem solar cells with high fill factors: a guideline towards 20% power conversion efficiency. Adv Energy Mater 4(11):1400084

Li P, Sun C, Jiu T, Wang G, Li J, Li X, Fang J (2014b) High-performance inverted solar cells based on blend films of ZnO naoparticles and TiO_2 nanorods as a cathode buffer layer. ACS Appl Mater Interfaces 6(6):4074–4080

Li X, Xie F, Zhang S, Hou J, Choy WCH (2014c) Over 1.1 eV workfunction tuning of cesium intercalated metal oxides for functioning as both electron and hole transport layers in organic optoelectronic devices. Adv Funct Mater 24(46):7348–7356

Li Z, Yang D, Zhao X, Li Z, Zhang T, Wu F, Yang X (2016) New PDI-based small-molecule cathode interlayer material with strong electron extracting ability for polymer solar cells. RSC Adv 6(103):101645–101651

Li X, Zhang W, Usman K, Fang J (2018a) Small molecule interlayers in organic solar cells. Adv Energy Mater 8(28):1702730

Li Z, Liu C, Zhang X, Guo J, Zhang X, Guo W (2018b) Boosting electron extraction in polymer solar cells by introducing a N-Type organic semiconductor interface layer. J Phys Chem C 122(1):207–215

Li Y, Zheng N, Yu L, Wen S, Gao C, Sun M, Yang R (2019) A simple phenyl group introduced at the tail of alkyl side chains of small molecular acceptors: new strategy to balance the crystallinity of acceptors and miscibility of bulk heterojunction enabling highly efficient organic solar cells. Adv Mater 31(12):1807832

Liao S-H, Jhuo H-J, Cheng Y-S, Chen S-A (2013) Fullerene derivative-doped zinc oxide nanofilm as the cathode of inverted polymer solar cells with low-bandgap polymer (PTB7-Th) for high performance. Adv Mater 25(34):4766–4771

Liao S-H, Jhuo H-J, Yeh P-N, Cheng Y-S, Li Y-L, Lee Y-H, Sharma S, Chen S-A (2014) Single junction inverted polymer solar cell reaching power conversion efficiency 10.31% by employing dual-doped zinc oxide nano-film as cathode interlayer. Sci Rep 4:6813. https://doi.org/10.1038/srep06813

Lin Z, Jiang C, Zhu C, Zhang J (2013) Development of inverted organic solar cells with TiO2 interface layer by using low-temperature atomic layer deposition. ACS Appl Mater Interfaces 5(3):713–718

Lin Y, Zhang Z-G, Bai H, Wang J, Yao Y, Li Y, Zhu D, Zhan X (2015) High-performance fullerene-free polymer solar cells with 6.31% efficiency. Energy Environ Sci 8:610–616

Liu J, Shao S, Fang G, Meng B, Xie Z, Wang L (2012a) High-efficiency inverted polymer solar cells with transparent and work-function tunable MoO_3-Al composite film as cathode buffer layer. Adv Mater 24(20):2774–2779

Liu J, Shao S, Meng B, Fang G, Xie Z, Wang L, Li X (2012b) Enhancement of inverted polymer solar cells with solution-processed ZnO-TiO_X composite as cathode buffer layer. Appl Phys Lett 100(21):213906

Liu Y, Zhao J, Li Z, Mu C, Ma W, Hu H, Jiang K, Lin H, Ade H, Yan H (2014) Aggregation and morphology control enables multiple cases of high-efficiency polymer solar cells. Nat Commun 5:5293

Liu Y, Page Z, Ferdous S, Liu F, Kim P, Emrick T, Russell T (2015a) Dual functional zwitterionic fullerene interlayer for efficient inverted polymer solar cells. Adv Energy Mater 5(14):1500405

Liu Y, Page ZA, Russell TP, Emrick T (2015b) Finely tuned polymer interlayers enhance solar cell efficiency. Angew Chem Int Ed 54(39):11485–11489

Liu X, Li X, Li Y, Song C, Zhu L, Zhang W, Wang H-Q, Fang J (2016a) High-performance polymer solar cells with PCE of 10.42% via Al-Doped ZnO cathode interlayer. Adv Mater 28(34):7405–7412

Liu Z, Ouyang X, Peng R, Bai Y, Mi D, Jiang W, Facchetti A, Ge Z (2016b) Efficient polymer solar cells based on the synergy effect of a novel non-conjugated small-molecule electrolyte and polar solvent. J Mater Chem A 4(7):2530–2536

Liu Z, Li W, Peng R, Jiang W, Guan Q, Lei T, Yang R, Islam A, Wei Q, Ge Z (2017) Benzophenone-based small molecular cathode interlayers with various polar groups for efficient polymer solar cells. J Mater Chem A 5(21):10154–10160

Liu Y, Liu G, Xie R, Wang Z, Zhong W, Li Y, Huang F, Cao Y (2018) A rational design and synthesis of cross-conjugated small molecule acceptors approaching high-performance fullerene-free polymer solar cells. Chem Mater 30(13):4331–4342

Lu K, Yuan J, Peng J, Huang X, Cui L, Jiang Z, Wang H-Q, Ma W (2013) New solution-processable small molecules as hole-transporting layer in efficient polymer solar cells. J Mater Chem A 1(45):14253–14261

Ma H, Yip H-L, Huang F, Jen AK-Y (2010) Interface engineering for organic electronics. Adv Funct Mater 20(9):1371–1388

MacLeod BA, Tremolet de Villers BJ, Schulz P, Ndione PF, Kim H, Giordano AJ, Zhu K, Marder SR, Graham S, Berry JJ, Kahn A, Olson DC (2015) Stability of inverted organic solar cells with ZnO contact layers deposited from sol-gel precursors. Energy Environ Sci 8(2):592–601

Manders JR, Tsang S-W, Hartel MJ, Lai T-H, Chen S, Amb CM, Reynolds JR, So F (2013) Solution-processed nickel oxide hole transport layers in high efficiency polymer photovoltaic cells. Adv Funct Mater 23(23):2993–3001

Meng L, Zhang Y, Wan X, Li C, Zhang X, Wang Y, Ke X, Xiao Z, Ding L, Xia R, Yip H-L, Cao Y, Chen Y (2018) Organic and solution-processed tandem solar cells with 17.3% efficiency. Science 361(6407):1094–1098

Miao Y, Yu H, Zhang Y, Yan X, Zhang J, Wang Y (2018) Efficient polymer solar cells based on a cathode interlayer of dicyanomethylenated indacenodithiophene derivative with large π-conjugation and electron-deficient properties. J Mater Chem C 6(1):57–65

Mihailetchi VD, Blom PWM, Hummelen JC, Rispens MT (2003) Cathode dependence of the open-circuit voltage of polymer: fullerene bulk heterojunction solar cells. J Appl Phys 94(10):6849–6854

Min J, Zhang H, Stubhan T, Luponosov YN, Kraft M, Ponomarenko SA, Ameri T, Scherf U, Brabec CJ (2013) A combination of Al-doped ZnO and a conjugated polyelectrolyte interlayer for small molecule solution-processed solar cells with an inverted structure. J Mater Chem A 1(37):11306–11311

Min J, Bronnbauer C, Zhang Z-G, Cui C, Luponosov YN, Ata I, Schweizer P, Przybilla T, Guo F, Ameri T, Forberich K, Spiecker E, Bäuerle P, Ponomarenko SA, Li Y, Brabec CJ (2016) Fully solution-processed small molecule semitransparent solar cells: optimization of transparent cathode architecture and four absorbing layers. Adv Funct Mater 26(25):4543–4550

Mishra A, Bäuerle P (2012) Small molecule organic semiconductors on the move: promises for future solar energy technology. Angew Chem Int Ed 51(9):2020–2067

Mishra A, Sahu SN (2019) Fullerene-Free Molecular Acceptors for Organic Photovoltaics. In: Tyagi H, Agarwal AK, Chakraborty PR, S. Powar (eds) Advances in Solar Energy Research, Energy, Environment, and Sustainability. Springer Nature, Singapore Pte Ltd., pp 221–279

Mishra A, Uhrich C, Reinold E, Pfeiffer M, Bäuerle P (2011) Synthesis and characterization of acceptor-substituted oligothiophenes for solar cell applications. Adv Energy Mater 1(2):265–273

Mishra A, Rana T, Looser A, Stolte M, Würthner F, Bäuerle P, Sharma GD (2016) High performance A-D-A oligothiophene-based organic solar cells employing two-step annealing and solution-processable copper thiocyanate (CuSCN) as an interfacial hole transporting layer. J Mater Chem A 4(44):17344–17353

Mishra A, Keshtov ML, Looser A, Singhal R, Stolte M, Würthner F, Bäuerle P, Sharma GD (2017) Unprecedented low energy losses in organic solar cells with high external quantum efficiencies by employing non-fullerene electron acceptors. J Mater Chem A 5(28):14887–14897

Mishra A, Wetzel C, Singhal R, Bäuerle P, Sharma GD (2018) Low energy gap triphenylamine–heteropentacene–dicyanovinyl triad for solution-processed bulk-heterojunction solar cells. J Phys Chem C 122(21):11262–11269

Mor GK, Shankar K, Paulose M, Varghese OK, Grimes CA (2007) High efficiency double heterojunction polymer photovoltaic cells using highly ordered TiO_2 nanotube arrays. Appl Phys Lett 91(15):152111

Nam E, Oh S, Jung D, Kim H, Chae H, Yi J (2012) Organic photovoltaic devices with the bilayer cathode interfacial structure of pyromellitic dianhydride and lithium fluoride. Semicon Sci Tech 27(10):105004

Nam S, Seo J, Han H, Kim H, Hahm SG, Ree M, Gal Y-S, Anthopoulos TD, Bradley DDC, Kim Y (2016) >10% efficiency polymer: fullerene solar cells with polyacetylene-based polyelectrolyte interlayers. Adv Mater Interfaces 3(23):1600415

Nam S, Seo J, Song M, Kim H, Ree M, Gal Y-S, Bradley DDC, Kim Y (2017) Polyacetylene-based polyelectrolyte as a universal interfacial layer for efficient inverted polymer solar cells. Org Electron 48:61–67

Nho S, Baek G, Park S, Lee BR, Cha MJ, Lim DC, Seo JH, Oh S-H, Song MH, Cho S (2016) Highly efficient inverted bulk-heterojunction solar cells with a gradiently-doped ZnO layer. Energy Environ Sci 9(1):240–246

Nian L, Zhang W, Zhu N, Liu L, Xie Z, Wu H, Würthner F, Ma Y (2015) Photoconductive cathode interlayer for highly efficient inverted polymer solar cells. J Am Chem Soc 137(22):6995–6998

Ouyang X, Peng R, Ai L, Zhang X, Ge Z (2015) Efficient polymer solar cells employing a non-conjugated small-molecule electrolyte. Nat Photon 9:520–524

Page ZA, Liu Y, Duzhko VV, Russell TP, Emrick T (2014) Fulleropyrrolidine interlayers: tailoring electrodes to raise organic solar cell efficiency. Science 346(6208):441–444

Park SH, Roy A, Beaupre S, Cho S, Coates N, Moon JS, Moses D, Leclerc M, Lee K, Heeger AJ (2009) Bulk heterojunction solar cells with internal quantum efficiency approaching 100%. Nat Photon 3(5):297–302

Park H-Y, Lim D, Kim K-D, Jang S-Y (2013) Performance Optimization of Low-temperature-annealed Solution-processable ZnO Buffer Layers for Inverted Polymer Solar Cells. J Mater Chem A 1:6327–6334

Peumans P, Forrest SR (2001) Very-high-efficiency double-heterostructure copper phthalocyanine/C_{60} photovoltaic cells. Appl Phys Lett 79(1):126–128

Pho TV, Kim H, Seo JH, Heeger AJ, Wudl F (2011) Quinacridone-based electron transport layers for enhanced performance in bulk-heterojunction solar cells. Adv Funct Mater 21(22):4338–4341

Puetz A, Stubhan T, Reinhard M, Loesch O, Hammarberg E, Wolf S, Feldmann C, Kalt H, Colsmann A, Lemmer U (2011) Organic solar cells incorporating buffer layers from indium doped zinc oxide nanoparticles. Sol Energy Mater Sol Cell 95(2):579–585

Reilly TH III, Hains AW, Chen H-Y, Gregg BA (2012) A self-doping, O_2-stable, n-type interfacial layer for organic electronics. Adv Energy Mater 2(4):455–460

Schulz GL, Kar P, Weidelener M, Vogt A, Urdanpilleta M, Lindén M, Mena-Osteritz E, Mishra A, Bäuerle P (2016) The influence of alkyl side chains on molecular packing and solar cell performance of dithienopyrrole-based oligothiophenes. J Mater Chem A 4(27):10514–10523

Schulze K, Uhrich C, Schüppel R, Leo K, Pfeiffer M, Brier E, Reinold E, Bäuerle P (2006) Efficient vacuum deposited organic solar cells with high photovoltage based on a new low band-gap oligothiophene and fullerene C_{60}. Adv Mater 18:2872–2875

Shao S, Zheng K, Pullerits T, Zhang F (2013) Enhanced performance of inverted polymer solar cells by using poly(ethylene oxide)-modified ZnO as an electron transport layer. ACS Appl Mater Interfaces 5(2):380–385

Sharma GD, Anil Reddy M, Ramana DV, Chandrasekharam M (2014) A novel carbazole-phenothiazine dyad small molecule as a non-fullerene electron acceptor for polymer bulk heterojunction solar cells. RSC Adv 4:33279–33285

Shin K-S, Lee K-H, Lee HH, Choi D, Kim S-W (2010) Enhanced power conversion efficiency of inverted organic solar cells with a ga-doped ZnO nanostructured thin film prepared using aqueous solution. J Phys Chem C 114(37):15782–15785

Sims L, Hörmann U, Hanfland R, MacKenzie RCI, Kogler FR, Steim R, Brütting W, Schilinsky P (2014) Investigation of the s-shape caused by the hole selective layer in bulk heterojunction solar cells. Org Electron 15(11):2862–2867

Singh A, Dey A, Das D, Iyer PK (2016) Effect of dual cathode buffer layer on the charge carrier dynamics of rrP3HT:PCBM based bulk heterojunction solar cell. ACS Appl Mater Interfaces 8(17):10904–10910

Small CE, Chen S, Subbiah J, Amb CM, Tsang S-W, Lai T-H, Reynolds JR, So F (2012) High-efficiency inverted dithienogermole-thienopyrrolodione-based polymer solar cells. Nat Photon 6(2):115–120

Song CE, Ryu KY, Hong S-J, Bathula C, Lee SK, Shin WS, Lee J-C, Choi SK, Kim JH, Moon S-J (2013) Enhanced performance in inverted polymer solar cells with D–π–A-type molecular dye incorporated on ZnO buffer layer. Chemsuschem 6(8):1445–1454

Song C, Liu X, Li X, Wang Y-C, Wan L, Sun X, Zhang W, Fang J (2018) Perylene diimide-based zwitterion as the cathode interlayer for high-performance nonfullerene polymer solar cells. ACS Appl Mater Interfaces 10(17):14986–14992

Soultati A, Fakharuddin A, Polydorou E, Drivas C, Kaltzoglou A, Haider MI, Kournoutas F, Fakis M, Palilis LC, Kennou S, Davazoglou D, Falaras P, Argitis P, Gardelis S, Kordatos A, Chroneos AI, Schmidt-Mende L, Vasilopoulou M (2019) Lithium doping of ZnO for high efficiency and stability fullerene and non-fullerene organic solar cells. ACS Appl Energy Mater 2(3):1663–1675

Steim R, Choulis SA, Schilinsky P, Brabec CJ (2008) Interface modification for highly efficient organic photovoltaics. Appl Phys Lett 92(9):093303

Stubhan T, Oh H, Pinna L, Krantz J, Litzov I, Brabec CJ (2011) Inverted organic solar cells using a solution processed aluminum-doped zinc oxide buffer layer. Org Electron 12(9):1539–1543

Stubhan T, Salinas M, Ebel A, Krebs FC, Hirsch A, Halik M, Brabec CJ (2012) Increasing the fill factor of inverted P3HT:PCBM solar cells through surface modification of Al-doped ZnO via phosphonic acid-anchored C_{60} SAMs. Adv Energy Mater 2(5):532–535

Stubhan T, Litzov I, Li N, Salinas M, Steidl M, Sauer G, Forberich K, Matt GJ, Halik M, Brabec CJ (2013) Overcoming interface losses in organic solar cells by applying low temperature, solution processed aluminum-doped zinc oxide electron extraction layers. J Mater Chem A 1:6004–6009

Subbiah J, Amb CM, Irfan I, Gao Y, Reynolds JR, So F (2012) High-efficiency inverted polymer solar cells with double interlayer. ACS Appl Mater Interfaces 4(2):866–870

Subbiah J, Purushothaman B, Chen M, Qin T, Gao M, Vak D, Scholes FH, Chen X, Watkins SE, Wilson GJ, Holmes AB, Wong WWH, Jones DJ (2015) Organic solar cells using a high-molecular-weight benzodithiophene–benzothiadiazole copolymer with an efficiency of 9.4%. Adv Mater 27(4):702–705

Suemori K, Miyata T, Yokoyama M, Hiramoto M (2005) Three-layered organic solar cells incorporating a nanostructure-optimized phthalocyanine: fullerene codeposited interlayer. Appl Phys Lett 86(6):063509–063503

Sun Y, Seo JH, Takacs CJ, Seifter J, Heeger AJ (2011) Inverted polymer solar cells integrated with a low-temperature-annealed sol-gel-derived ZnO film as an electron transport layer. Adv Mater 23(14):1679–1683

Sun K, Zhao B, Murugesan V, Kumar A, Zeng K, Subbiah J, Wong WWH, Jones DJ, Ouyang J (2012) High-performance polymer solar cells with a conjugated zwitterion by solution processing or thermal deposition as the electron-collection interlayer. J Mater Chem 22:24155–24165

Sun C, Wu Z, Hu Z, Xiao J, Zhao W, Li H-W, Li Q-Y, Tsang S-W, Xu Y-X, Zhang K, Yip H-L, Hou J, Huang F, Cao Y (2017) Interface design for high-efficiency non-fullerene polymer solar cells. Energy Environ Sci 10(8):1784–1791

Takanezawa K, Hirota K, Wei Q-S, Tajima K, Hashimoto K (2007) Efficient charge collection with ZnO nanorod array in hybrid photovoltaic devices. J Phys Chem C 111(19):7218–7223

Tang Z, Tress W, Bao Q, Jafari MJ, Bergqvist J, Ederth T, Andersson MR, Inganäs O (2014) Improving cathodes with a polymer interlayer in reversed organic solar cells. Adv Energy Mater 4:1400643

Tress W, Leo K, Riede M (2011) Influence of hole-transport layers and donor materials on open-circuit voltage and shape of I–V curves of organic solar cells. Adv Funct Mater 21(11):2140–2149

Trost S, Zilberberg K, Behrendt A, Riedl T (2012) Room-temperature solution processed SnOx as an electron extraction layer for inverted organic solar cells with superior thermal stability. J Mater Chem 22:16224–16229

Trost S, Zilberberg K, Behrendt A, Polywka A, Görrn P, Reckers P, Maibach J, Mayer T, Riedl T (2013) Overcoming the "Light-Soaking" issue in inverted organic solar cells by the use of Al:ZnO electron extraction layers. Adv Energy Mater 3(11):1437–1444

Trost S, Behrendt A, Becker T, Polywka A, Görrn P, Riedl T (2015) Tin oxide (SnOx) as universal "Light-Soaking" free electron extraction material for organic solar cells. Adv Energy Mater 5(17):1500277

van Reenen S, Kouijzer S, Janssen RAJ, Wienk MM, Kemerink M (2014) Origin of work function modification by ionic and amine-based interface layers. Adv Mater Interfaces 1(8):1400189

Vasilopoulou M, Georgiadou DG, Soultati A, Boukos N, Gardelis S, Palilis LC, Fakis M, Skoulatakis G, Kennou S, Botzakaki M, Georga S, Krontiras CA, Auras F, Fattakhova-Rohlfing D, Bein T, Papadopoulos TA, Davazoglou D, Argitis P (2014) Atomic-layer-deposited aluminum and zirconium oxides for surface passivation of TiO_2 in high-efficiency organic photovoltaics. Adv Energy Mater 4(15):1400214

Vinokur J, Shamieh B, Deckman I, Singhal A, Frey GL (2016) Mechanisms for spontaneous generation of interlayers in organic solar cells. Chem Mater 28(24):8851–8870

Vogel M, Doka S, Breyer C, Lux-Steiner MC, Fostiropoulos K (2006) On the function of a bathocuproine buffer layer in organic photovoltaic cells. Appl Phys Lett 89(16):163501

Waldauf C, Morana M, Denk P, Schilinsky P, Coakley K, Choulis SA, Brabec CJ (2006) Highly efficient inverted organic photovoltaics using solution based titanium oxide as electron selective contact. Appl Phys Lett 89(23):233517

Walzer K, Männig B, Pfeiffer M, Leo K (2007) Highly efficient organic devices based on electrically doped transport layers. Chem Rev 107(4):1233–1271

Wang G, Jiu T, Tang G, Li J, Li P, Song X, Lu F, Fang J (2014a) Interface modification of ZnO-based inverted PTB7:PC71BM organic solar cells by cesium stearate and simultaneous enhancement of device parameters. ACS Sustainable Chem Eng 2(5):1331–1337

Wang J, Zhang Z-G, Qi b, Jin Z, Chi D, Qi Z, Li Y (2014b) Perylene diimides: a thickness-insensitive cathode interlayer for high performance polymer solar cells. Energy Environ Sci 7(6):1966–1973

Wang F, Za Tan, Li Y (2015) Solution-processable metal oxides/chelates as electrode buffer layers for efficient and stable polymer solar cells. Energy Environ Sci 8(4):1059–1091

Wang Z, Li Z, Xu X, Li Y, Li K, Peng Q (2016) Polymer solar cells exceeding 10% efficiency enabled via a facile star-shaped molecular cathode interlayer with variable counterions. Adv Funct Mater 26(26):4643–4652

Wang C, Liu Z, Li M, Xie Y, Li B, Wang S, Xue S, Peng Q, Chen B, Zhao Z, Li Q, Ge Z, Li Z (2017) The marriage of AIE and interface engineering: convenient synthesis and enhanced photovoltaic performance. Chem Sci 8(5):3750–3758

Wei J, Ji G, Zhang C, Yan L, Luo Q, Wang C, Chen Q, Yang J, Chen L, Ma C-Q (2018) Silane-capped ZnO nanoparticles for use as the electron transport layer in inverted organic solar cells. ACS Nano 12(6):5518–5529

White MS, Olson DC, Shaheen SE, Kopidakis N, Ginley DS (2006) Inverted bulk-heterojunction organic photovoltaic device using a solution-derived ZnO underlayer. Appl Phys Lett 89(14):143517

Worfolk BJ, Hauger TC, Harris KD, Rider DA, Fordyce JAM, Beaupré S, Leclerc M, Buriak JM (2012) Work function control of interfacial buffer layers for efficient and air-stable inverted low-bandgap organic photovoltaics. Adv Energy Mater 2(3):361–368

Xiao Z, Jia X, Ding L (2017) Ternary organic solar cells offer 14% power conversion efficiency. Sci Bull 62(23):1562–1564

Xie Z, Xiao B, He Z, Zhang W, Wu X, Wu H, Würthner F, Wang C, Xie F, Liu L, Ma Y, Wong W-Y, Cao Y (2015) Self-assembled perylene bisimide J-aggregates as promising cathode modifiers for highly efficient inverted polymer solar cells. Mater Horiz 2(5):514–518

Xiong S, Hu L, Hu L, Sun L, Qin F, Liu X, Fahlman M, Zhou Y (2019) 12.5% flexible nonfullerene solar cells by passivating the chemical interaction between the active layer and polymer interfacial layer. Adv Mater:1806616

Xu B, Hou J (2018) Solution-processable conjugated polymers as anode interfacial layer materials for organic solar cells. Adv Energy Mater 8(20):1800022

Xu B, Zheng Z, Zhao K, Hou J (2016) A bifunctional interlayer material for modifying both the anode and cathode in highly efficient polymer solar cells. Adv Mater 28(3):434–439

Yan Y, Cai F, Yang L, Li J, Zhang Y, Qin F, Xiong C, Zhou Y, Lidzey DG, Wang T (2017) Light-soaking-free inverted polymer solar cells with an efficiency of 10.5% by compositional and surface modifications to a low-temperature-processed TiO_2 Electron-transport layer. Adv Mater 29(1):1604044

Yao K, Salvador M, Chueh C-C, Xin X-K, Xu Y-X, deQuilettes DW, Hu T, Chen Y, Ginger DS, Jen AK-Y (2014) A general route to enhance polymer solar cell performance using plasmonic nanoprisms. Adv Energy Mater 4(9):1400206

Ye H, Hu X, Jiang Z, Chen D, Liu X, Nie H, Su S-J, Gong X, Cao Y (2013) Pyridinium salt-based molecules as cathode interlayer for enhanced performance in polymer solar cells. J Mater Chem A 1:3387–3394

Yin Z, Zheng Q, Chen S-C, Cai D (2013) Interface control of semiconducting metal oxide layers for efficient and stable inverted polymer solar cells with open-circuit voltages over 1.0 Volt. ACS Appl Mater Interfaces 5(18):9015–9025

Yin Z, Zheng Q, Chen S-C, Cai D, Zhou L, Zhang J (2014) Bandgap tunable $Zn_{1-x}Mg_xO$ thin films as highly transparent cathode buffer layers for high-performance inverted polymer solar cells. Adv Energy Mater 4:1301404

Yin Z, Wei J, Zheng Q (2016) Interfacial materials for organic solar cells: recent advances and perspectives. Adv Sci 3(8):1500362

Yip H-L, Jen AKY (2012) Recent advances in solution-processed interfacial materials for efficient and stable polymer solar cells. Energy Environ Sci 5:5994–6011

You J, Chen C-C, Dou L, Murase S, Duan H-S, Hawks S, Xu T, Son HJ, Yu L, Li G, Yang Y (2012) Metal oxide nanoparticles as an electron-transport layer in high-performance and stable inverted polymer solar cells. Adv Mater 24(38):5267–5272

Yu J, Shen T-L, Weng W-H, Huang Y-C, Huang C-I, Su W-F, Rwei S-P, Ho K-C, Wang L (2012) Molecular design of interfacial modifiers for polymer-inorganic hybrid solar cells. Adv Energy Mater 2(2):245–252

Yu W, Huang L, Yang D, Fu P, Zhou L, Zhang J, Li C (2015) Efficiency exceeding 10% for inverted polymer solar cells with a ZnO/ionic liquid combined cathode interfacial layer. J Mater Chem A 3(20):10660–10665

Yu J, Xi Y, Chueh C-C, Zhao D, Lin F, Pozzo LD, Tang W, Jen AKY (2016) A room-temperature processable pdi-based electron-transporting layer for enhanced performance in PDI-based non-fullerene solar cells. Adv Mater Interfaces 3(18):1600476

Yusoff ARBM, Kim D, Kim HP, Shneider FK, da Silva WJ, Jang J (2014) A high efficiency solution processed polymer inverted triple-junction solar cell exhibiting a power conversion efficiency of 11.83%. Energy Environ Sci 8:303–316

Za Tan, Qian D, Zhang W, Li L, Ding Y, Xu Q, Wang F, Li Y (2013) Efficient and stable polymer solar cells with solution-processed molybdenum oxide interfacial layer. J Mater Chem A 1:657–664

Zhang Z-G, Li H, Qi Z, Jin Z, Liu G, Hou J, Li Y, Wang J (2013) Poly(ethylene glycol) modified [60]fullerene as electron buffer layer for high-performance polymer solar cells. Appl Phys Lett 102(14):143902

Zhang W, Wu Y, Bao Q, Gao F, Fang J (2014) Morphological control for highly efficient inverted polymer solar cells via the backbone design of cathode interlayer materials. Adv Energy Mater 4(12):1400359

Zhang H, Yao H, Hou J, Zhu J, Zhang J, Li W, Yu R, Gao B, Zhang S, Hou J (2018a) Over 14% efficiency in organic solar cells enabled by chlorinated nonfullerene small-molecule acceptors. Adv Mater:1800613

Zhang S, Qin Y, Zhu J, Hou J (2018b) Over 14% efficiency in polymer solar cells enabled by a chlorinated polymer donor. Adv Mater 30(20):1800868

Zhao X, Xu C, Wang H, Chen F, Zhang W, Zhao Z, Chen L, Yang S (2014) Application of biuret, dicyandiamide, or urea as a cathode buffer layer toward the efficiency enhancement of polymer solar cells. ACS Appl Mater Interfaces 6(6):4329–4337

Zhao K, Ye L, Zhao W, Zhang S, Yao H, Xu B, Sun M, Hou J (2015) Enhanced efficiency of polymer photovoltaic cells via the incorporation of a water-soluble naphthalene diimide derivative as a cathode interlayer. J Mater Chem C 3(37):9565–9571

Zhao Y, Schwab MG, Kiersnowski A, Pisula W, Baumgarten M, Chen L, Müllen K, Li C (2016) Trifluoromethyl-functionalized bathocuproine for polymer solar cells. J Mater Chem C 4(21):4640–4646

Zheng Z, Zhang S, Wang J, Zhang J, Zhang D, Zhang Y, Wei Z, Tang Z, Hou J, Zhou H (2019) Exquisite modulation of ZnO nanoparticle electron transporting layer for high-performance fullerene-free organic solar cell with inverted structure. J Mater Chem A 7(8):3570–3576

Zhou Y, Fuentes-Hernandez C, Shim J, Meyer J, Giordano AJ, Li H, Winget P, Papadopoulos T, Cheun H, Kim J, Fenoll M, Dindar A, Haske W, Najafabadi E, Khan TM, Sojoudi H, Barlow S, Graham S, Brédas J-L, Marder SR, Kahn A, Kippelen B (2012a) A universal method to produce low-work function electrodes for organic electronics. Science 336(6079):327–332

Zhou Y, Fuentes-Hernandez C, Shim JW, Khan TM, Kippelen B (2012b) High performance polymeric charge recombination layer for organic tandem solar cells. Energy Environ Sci 5:9827–9832

Zilberberg K, Behrendt A, Kraft M, Scherf U, Riedl T (2013) Ultrathin interlayers of a conjugated polyelectrolyte for low work-function cathodes in efficient inverted organic solar cells. Org Electron 14(3):951–957